

REPORT DOCUMENTATION

AD-A238 706

Approved
10.0704-018

1a. REPORT SECURITY CLASSIFICATION Unclassified		11	
2a. SECURITY CLASSIFICATION AUTHORITY Unclassified		3. DISTRIBUTION/AVAILABILITY OF REPORT Approved for public release; Distribution unlimited	
2b. DECLASSIFICATION/DOWNGRADING SCHEDULE 1991		5. MONITORING ORGANIZATION REPORT NUMBER(S) AFOSR-TR- 91 0642	
4. PERFORMING ORGANIZATION REPORT NUMBER(S) CSPAR531791WU		7a. NAME OF MONITORING ORGANIZATION AFOSR	
6a. NAME OF PERFORMING ORGANIZATION The University of Alabama in Huntsville	6b. OFFICE SYMBOL (If applicable) UAH	7b. ADDRESS (City, State, and ZIP Code) Building 410 Bolling AFB DC 20332-6448	
6c. ADDRESS (City, State, and ZIP Code) Department of Mechanical Engineering Huntsville, AL 35899	9. PROCUREMENT INSTRUMENT IDENTIFICATION NUMBER AFOSR-88-0013		
8a. NAME OF FUNDING/SPONSORING ORGANIZATION Air Force Office of Scientific Research	8b. OFFICE SYMBOL (If applicable) AFOSR/NP	10. SOURCE OF FUNDING NUMBERS	
8c. ADDRESS (City, State, and ZIP Code) AFOSR/NP Building 410 Bolling AFB, DC 20332-6448	PROGRAM ELEMENT NO. 61102F	PROJECT NO. 2311/A1	TASK NO. 2311/A1 WORK UNIT ACCESSION NO.
11. TITLE (Include Security Classification) A Study of Coronal-Interplanetary Coupling Mechanisms			
12. PERSONAL AUTHOR(S) S. T. Wu			
13a. TYPE OF REPORT Final	13b. TIME COVERED FROM 11/1/87 TO 3/31/91	14. DATE OF REPORT (Year, Month, Day) 4/30/91	15. PAGE COUNT 134
16. SUPPLEMENTARY NOTATION			
17. COSATI CODES		18. SUBJECT TERMS (Continue on reverse if necessary and identify by block number)	
FIELD	GROUP	SUB-GROUP	
19. ABSTRACT (Continue on reverse if necessary and identify by block number) It is understood that the operations of military, as well as civilian, satellite and systems for communications, tracking and surveillance can be interrupted, degraded or even endangered as a result of powerful explosions on the surface of the sun called solar flares. These spectacular eruptions release shock waves, hot plasma clouds, highly accelerated atomic nuclei and burst of x-rays, ultra-violet and visible-band electromagnetic radiation into interplanetary space. When the path of propagation of these high-energy emissions intersects the Earth's magnetosphere, our terrestrial environment is impacted in various ways that may produce deleterious effects on military systems, both on the ground and in space. In this investigation, we have conducted a theoretical study of the dynamics of coronal-interplanetary coupling. It was demonstrated that photospheric shear motion could be a viable physical mechanism to understand the occurrence of solar flares. This study has laid the groundwork for solar flare prediction and their consequences on the geomagnetic storm. A total of sixteen papers were published in the open literature of these findings.			
20. DISTRIBUTION/AVAILABILITY OF ABSTRACT <input checked="" type="checkbox"/> UNCLASSIFIED/UNLIMITED <input checked="" type="checkbox"/> SAME AS RPT <input type="checkbox"/> DTIC USERS		21. ABSTRACT SECURITY CLASSIFICATION Unclassified	
22a. NAME OF RESPONSIBLE INDIVIDUAL Dr Henry R. Radoski		22b. TELEPHONE (Include Area Code) 202/767-4906	22c. OFFICE SYMBOL NP

TABLE OF CONTENTS

SUMMARY

- I. INTRODUCTION
- II. INVESTIGATION OF FUNDAMENTAL PHYSICAL MECHANISMS FOR SOLAR ACTIVITIES
 - II.1. MHD Simulation of Mass Injection: A Mechanism for the formation of Active Region Loops, in J. Adv. Space Res. Vol. 8, No. 11, 215-219, 1988.
 - II.2. A Dynamical Model of Prominence Loops, T. Yeh, in Solar Phys., Vol. 124, 251-269, 1989.
 - II.3. Soliton and Strong Langmuir Turbulence in Solar Flares Process in Astrophys. and Space Sci., Vol. 152, 287-311, 1989.
 - II.4. The Role of Condensation and Heat Conduction in the Formation of Prominences: A MHD Simulation, in Solar Phys., Vol. 125, 277-293, 1990.
- III. MAGNETOHYDRODYNAMIC WAVES IN THE SOLAR ATMOSPHERE
 - III.1. Magnetohydrodynamic Instabilities in Coronal Arcade in Astrophys. J., Vol. 337, 989-1002, 1989.
 - III.2. Propagating and Non-propagating Compression Waves in an Isothermal Atmosphere with Uniform Horizontal Magnetic Field in Astrophys. J., Vol. 344, 478-493, 1989.
 - III.3. Reflection and Trapping of Transient Alfvén Waves Propagating in an Isothermal Atmosphere with Constant Gravity and Uniform Magnetic Field in Astrophys. J., Vol. 345, 597-605, 1989.

Accession For	
ADAMS	<input checked="" type="checkbox"/>
ADAMS TAB	<input type="checkbox"/>
Unprocessed	<input type="checkbox"/>
Justification	
SS	
Distribution	
Availability Codes	
Dist	Avail and/or Special
A-1	

91-05947



IV. SOLAR INTERPLANETARY COUPLING STUDIES

- IV.1. Shear-Induced Instability and Arch Filament Eruption: An MHD Numerical Simulation in Solar Phys., (to appear) 1991.
- IV.2. Model Calculations of Rising Motions of Prominence Loops in Solar Phys. (to appear) 1991.
- IV.3. A Time-dependent, Three-dimensional, MHD Numerical Study of Interplanetary Magnetic Draping Around Plasmoid in the Solar Wind in J. of Geophysical Res. (to appear) 1991.

V. NUMERICAL MODELING OF GLOBAL SOLAR INTERPLANETARY ENVIRONMENT

- V.1. Numerical Simulation of Solar Disturbances and Their Interplanetary Consequences in 1990 IAU Symposium on "Basic Plasma Processes on the Sun" E. R. Priest and V. Krishan (eds), 331-340.
- V.2. Numerical Simulation of Extended Corona in J. Adv. Space Res. (to appear) 1991.

VI. FUNDAMENTAL METHODS FOR THE MODELING OF SOLAR INTERPLANETARY ENVIRONMENT

- VI.1. Magnetohydrodynamic (MHD) Modeling of Solar Active Phenomena via Numerical Methods, in Developments in Theoretical and Applied Mechanics, S. Y. Wang, R. M. Hackett, S. L. Deleuw and S. Am. Smith (eds), 62-70, 1988.
- VI.2. Application of Similitude Principle to the Numerical Simulation of Solar Atmospheric Dynamics in J. Adv. Space Res., Vol. 8, Number 11, 221-226, 1988.
- VI.3. On the Numerical Computation of Non-linear Force-free Magnetic Fields, in Astrophys. J., Vol. 362, 698-708, 1990.
- VI.4. A Comparison Between Progressive Extension Method (PEM) and Iterative Method (IM) for Magnetic Field Extrapolations in the Solar Atmosphere in J. of the Italian Astronomical Soc., Vol. 61, No. 2, 477-484, 1990.

CONCLUDING REMARKS

I. INTRODUCTION

In this report, we summarize the findings from a study on a number of fundamental problems in solar-terrestrial relationships supported by a three year grant from the Air Force Office of scientific Research (ASOSR-88-0013) in the time period November 1, 1987 - March 31, 1991. The specific emphasis of this study is to deal with those problems concerning the dynamics of photospheric/corona/interplanetary coupling mechanisms (PCIM).

It is understood that solar-terrestrial research has its ultimate goal in the development of the scientific capability of objective prediction of the earth's space environment. To attain this goal, it is necessary to acquire sufficient understanding about the physical processes in the photosphere, corona, and interplanetary space and to develop effective skills with numerical simulation of the dynamics in these processes.

In order to achieve these goals, we have taken a two-fold approach; we first identified a possible physical mechanism and performed a synthesis calculation using self-consistent magnetohydrodynamic (MHD) theory via numerical simulation as well as analytical methods. These results were then tested by available observations. If no observations were available, the results were used as a guide for future planned observations. The physical scenario for the present study can be described as follows:

First, we investigated solar surface activities. This was accomplished by using our newly developed nonlinear force-free (NLFF) model (Wu, et al., 1990, see Section VI-3) together with solar magnetograph data which were obtained by the Solar Optical Observational Network (SOON) system of the Air Force and NASA/Marshall Space Flight Center. Representative results are shown in the upper left panel of Figure 1 in which (a) shows the observed vector magnetic field at photospheric level and (b) shows the computed field lines of the observed structures extrapolating from data given in (a). In the lower

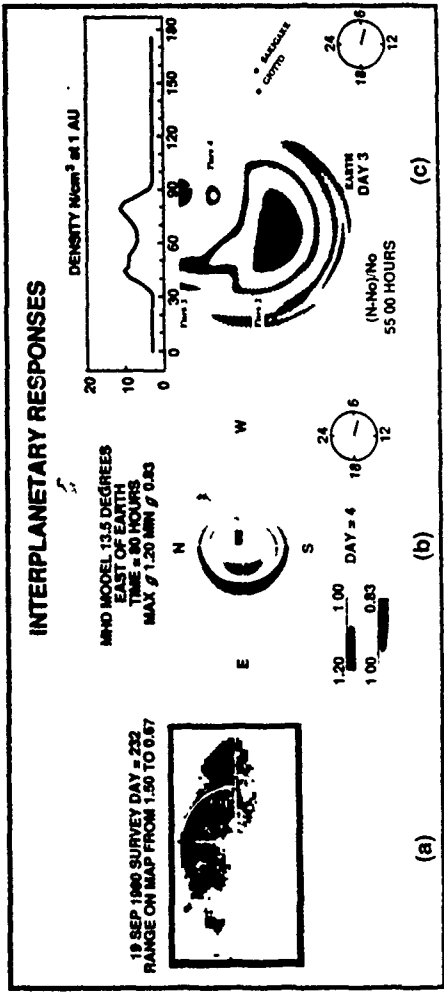
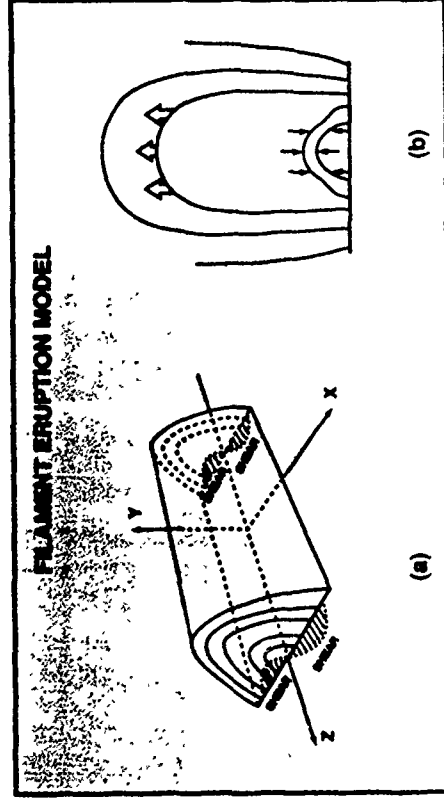
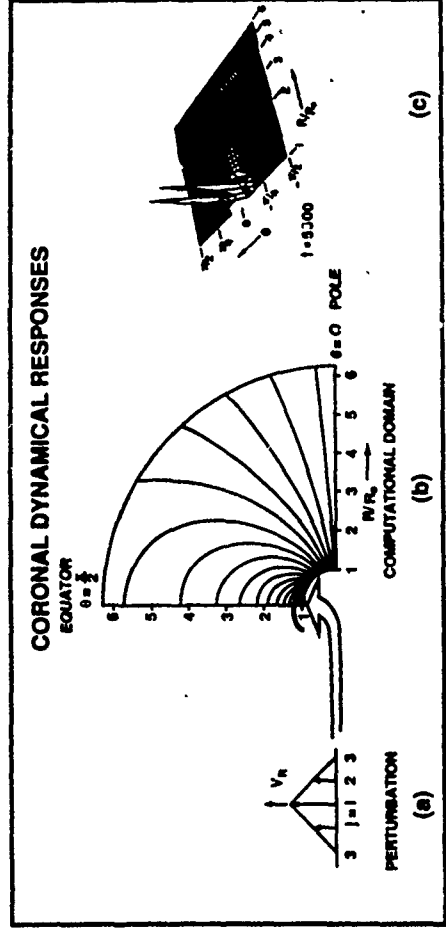
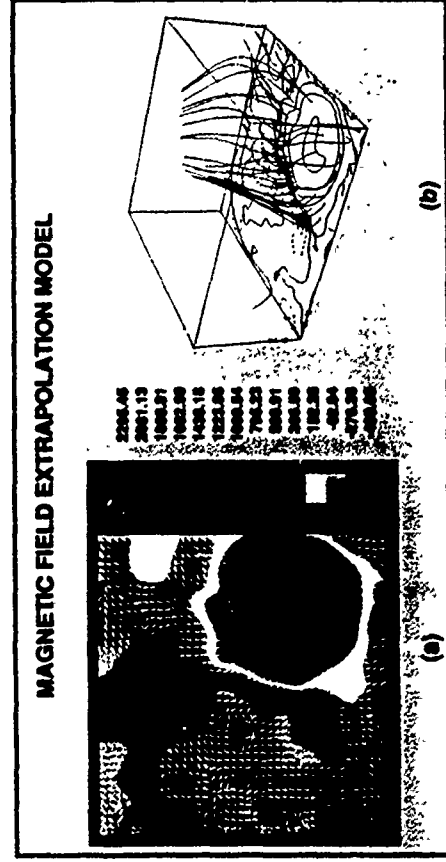
left panel of Figure 1 we present the results on the study shear-motion-induced non-equilibrium which may lead to the initiation of Coronal Mass Ejections (CMEs). In this study, we found that when the shear angle reaches a critical value, the arcade will become unstable and will be ejected to the middle atmosphere (i.e. the corona). This critical value of shear could be tested by observation. A detailed account of these findings is described in Section IV.1.

Next, we investigated the coronal responses due to the mass ejection. This result is shown in the upper right panel of Figure 1 where (a) shows the input to simulate the mass ejection by prescribing a mass flux flowing from the lower boundary, (b) shows the initial magnetic field configuration and the location of the input and (c) shows the results 5500 sec after introduction of the disturbance, which exhibits the non-linear interaction between mass motion and MHD waves. It clearly indicates that the outward propagation of MHD fast waves (or shocks) and MHD slow shocks in the inner region shown as the twin peaks in the upper right panel of Figure 1.

Finally, we studied the interplanetary responses as shown in the lower right panel of Figure 1. This panel (a) shows a radio astronomical interplanetary scintillation (IPS) observation of the disturbed solar wind density during an earlier period in September 1980 near solar maximum (cycle 21); (b) shows a three-dimensional MHD simulation of density compression regions (red) and rarefaction (blue). The resemblance between the observation and simulation is clearly indicated, (c) shows the solar wind density response in the ecliptic plane during a series of major solar flares and CMEs at solar minimum in February 1986; spacecraft data at the designated location (Earth, Giotto and Sakigake) were used for comparison with the MHD simulation. To facilitate these studies, a number of new numerical techniques were developed.

PHOTOSPHERE/CORONAL/INTERPLANETARY COUPLING STUDIES

GOAL: TO UNDERSTAND THE FUNDAMENTAL PHYSICS OF ENERGY AND MOMENTUM TRANSPORT FROM
SOLAR SURFACE THROUGH THE CORONA TO INTERPLANETARY SPACE VIA NUMERICAL SIMULATION



These findings are included in section VI. The subject of fundamental physical mechanisms of solar activities is presented in Section II. The results of solar atmospheric magnetohydrodynamic waves are presented in Section III. In Section IV we discuss the solar-interplanetary coupling studies. The numerical modeling of global solar interplanetary environment is included in Section V. Finally, the concluding remarks are presented in Section VII. In summary, a total of sixteen articles were published in Astrophysical Journal, Journal of Geophysical Research, Solar Physics, etc. to present our results in the public literature.

II. INVESTIGATION OF FUNDAMENTAL PHYSICAL MECHANISMS OF SOLAR ACTIVITIES

In this section, we employed both macroscopic theory of magnetohydrodynamics and microscopic kinetic theory (i.e. Boltzmann equations) to study the physical mechanisms which may explain the cause of solar activities. Four papers were included to report these results.

MHD Simulation of Mass Injection: A Mechanism for the formation of Active Region Loops, in J. Adv. Space Res. Vol. 8, No. 11, 215-219, 1988.

A Dynamical Model of Prominence Loops. T. Yeh, in Solar Phys., Vol. 124, 251-269, 1989.

Soliton and Strong Langmuir Turbulence in Solar Flares Process in Astrophys. and Space Sci., Vol. 152, 287-311, 1989.

The Role of Condensation and Heat Conduction in the Formation of Prominences: A MHD Simulation, in Solar Phys., Vol. 125, 277-293, 1990.

MHD SIMULATION OF MASS INJECTION: A MECHANISM FOR THE FORMATION OF ACTIVE REGION LOOPS

Chung-Chieh Cheng* and S. T. Wu**

*Naval Research Laboratory, Washington, DC 20375, U.S.A.

**University of Alabama in Huntsville, Huntsville, AL 35899, U.S.A.

ABSTRACT

We have used a 2-D nonlinear MHD numerical code to simulate the formation and dynamic evolution of active regions loops subjected to mass injections at the footpoints. We also calculated the UV and X-ray signatures of the plasmas. We find that it is possible to form loops in a low beta plasma that occur in the solar active regions.

INTRODUCTION

Observations in XUV and in X-ray from *Skylab* have shown that the solar active region is composed primarily of loop structures of various temperatures and sizes (cf. Vaiana *et al.* /1/, Tousey *et al.* /2/, Reeves *et al.* /3/). Although there are numerous theoretical studies of the heating of coronal loops (for a review see Kuperus, Ionson, and Spicer /4/), the problem of the formation of loops is largely not understood. In this paper, we have numerically simulated, using a 2-D MHD code, the formation of coronal loop structures in active regions under the assumption of mass injections from the loop footpoints. We have also applied a spectroscopic code to the numerical results to obtain the XUV and X-ray signatures of the evolution of the dynamics of the mass injection. We find that it is possible to form loop structures in active regions from the mass injections if the magnetic field is strong enough (i.e., low plasma beta). In contrast, Wu *et al.* /5/ and An *et al.* /6/ have found that mass injection will result in the formation of a quiescent prominence in a Kippenhahn-Schluter configuration if the plasma beta is high (e.g., beta=2).

NUMERICAL MODEL

The numerical simulation is done with a 2-D, non-planar, time dependent non-ideal MHD code. The governing MHD equations are given by Wu *et al.* /7/, except now thermal conduction and radiative losses are included in the energy equation. The numerical algorithm is based on the method of the fully implicit continuous Eulerian scheme (Hu and Wu /8/; Wu and Wang /9/). The computation domain is 8000 km in height and 16000 km in width. Mass injection is treated as an initial boundary value problem, and the characteristic method (Hu and Wu, /8/) is used to specify some of the boundary conditions. The upper boundary is treated as a non-reflective surface.

For the present simulation, mass is injected at the lower boundary of a gravitationally stratified plasma permeated with an initially dipole magnetic field (Fig. 1). The atmosphere is assumed to be initially hydrostatic and isothermal with a temperature of 10^6 K and a number density of $5 \times 10^9 \text{ cm}^{-3}$ at the lower boundary. The mass is injected with a density and temperature at the lower boundary. Choice of the initial atmosphere corresponds to the conditions of solar active regions.

RESULTS

MHD Evolution of the Plasma

Figure 2 shows the dynamic evolution of the magnetic field, the temperature and the density for the symmetric case for which the mass injection velocity is 40 km/sec and the initial plasma beta is 0.5. We see that after 800 sec, the regions on the side of the injection locations became more dense and cooler than the initial atmosphere. At 1600 sec, the temperature in the condensed regions has decreased about 10% and the density increased about 30% as compared with the surroundings. At $t=3146$ sec, the temperature there has decreased

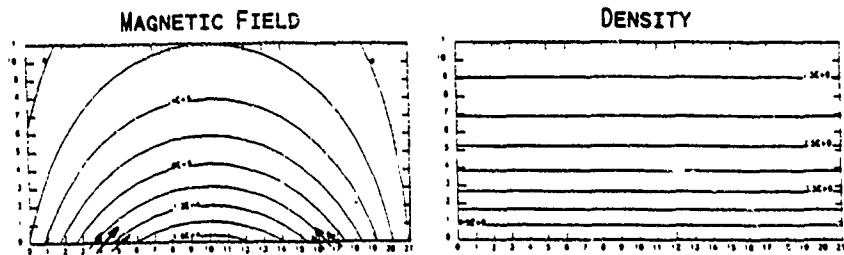


Fig. 1 Initial model. The atmosphere is initially isothermal and hydrostatic with a temperature of 10^6 K and a number density of $5 \times 10^9 \text{ cm}^{-3}$ at the lower boundary. The arrows indicate the locations of mass injection.

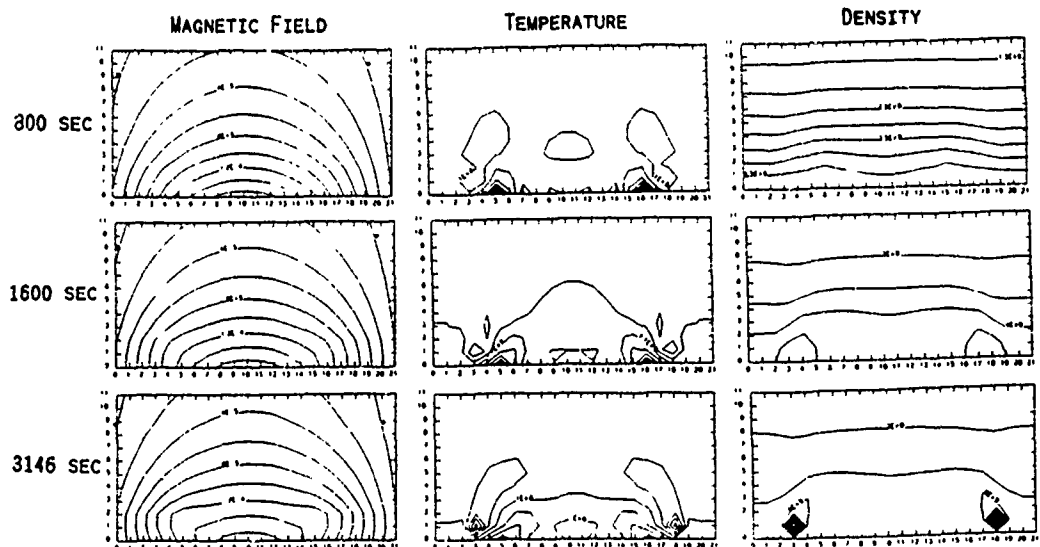


Fig. 2 Time evolution of the plasma for the symmetric mass injection case with injection velocity of 40 km/sec. Initial plasma beta is 0.5

to less than 7×10^5 K, and the density increased to more than 10^{10} cm^{-3} . As we can see from the figure, as mass injection proceeds the adjacent magnetic field is squeezed which compresses the plasma there and causes condensation. Note that the magnetic field is strong enough to support the plasmas, and no pit is formed as in the case of high beta cases studied by Wu *et al.* /5/, and An *et al.* /6/.

XUV and X-Ray Spectroscopic Signatures

Once we know the evolution of the temperature and density of the plasmas, we can calculate the XUV and X-ray radiation signatures. We have calculated the emission distribution (photons/ $\text{cm}^3 \text{ sec}$) for the lines: N V 1238 Å (1.6×10^5 K), Ne VII 465 Å (5×10^5 K), Mg VIII 437 Å (8×10^5 K), Mg IX 368 Å (1×10^6 K), and O VII 22 Å (2×10^6 K). The temperatures indicated for each line is the temperature at which the emission for that line is at maximum. These lines are typical of the solar transition region and corona. The results show that the N V emissions are concentrated in bright kernels at the location of mass injections, while the Ne VII line shows extensions toward higher altitudes, and the coronal O VII line shows loop-like structures. Figures 3 and 4 show the emission distributions at various times for selected lines.

The results for the case with higher mass injection velocity of 60 km/sec and plasma beta=0.5 are similar to the above case, except now the evolution progresses faster, and the formation of the loop-like structures occurs much earlier. At $t=1600$ sec, loop-like structures can be observed in the coronal line O VII.

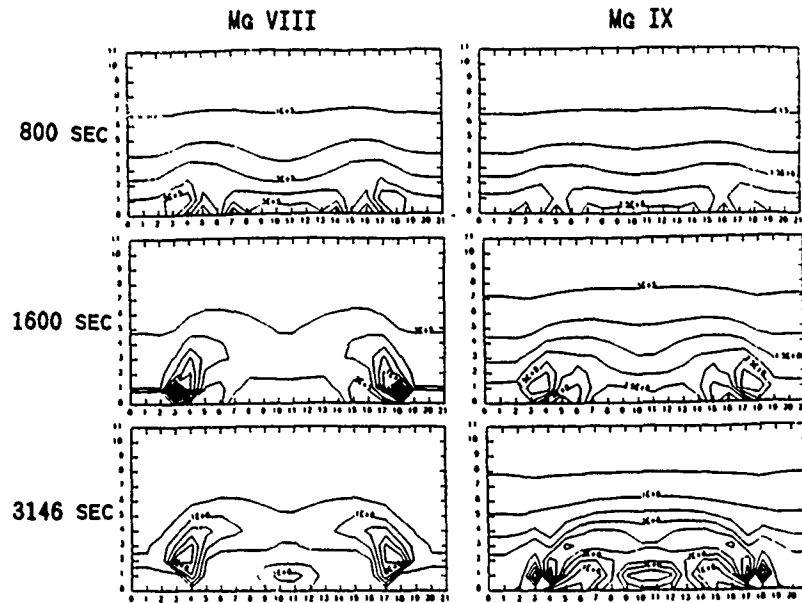


Fig. 3 Emission distribution of the Mg VIII and Mg IX lines at various times for the symmetric mass injection case.

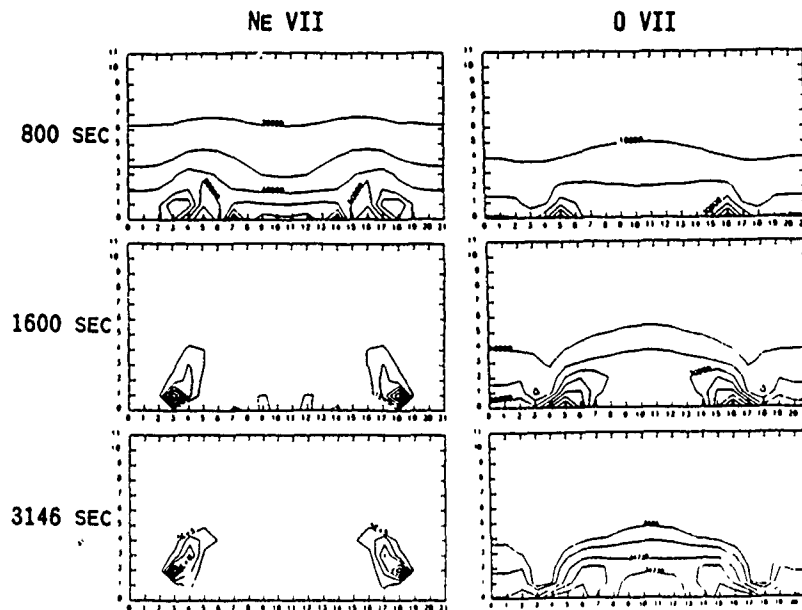


Fig. 4 Emission distribution of the Ne VII and O VII lines at various times for the symmetric mass injection case.

Figures 5 and 6 show the results for an asymmetric mass injection with velocity of 100 km/sec in an initial atmosphere with $\beta=1.0$. Again, the dynamic evolution is similar to the symmetric injection case. However, in contrast to the symmetric cases, the loop structure seen in O VII has asymmetric emission distribution with one side of the loop much brighter than the other.

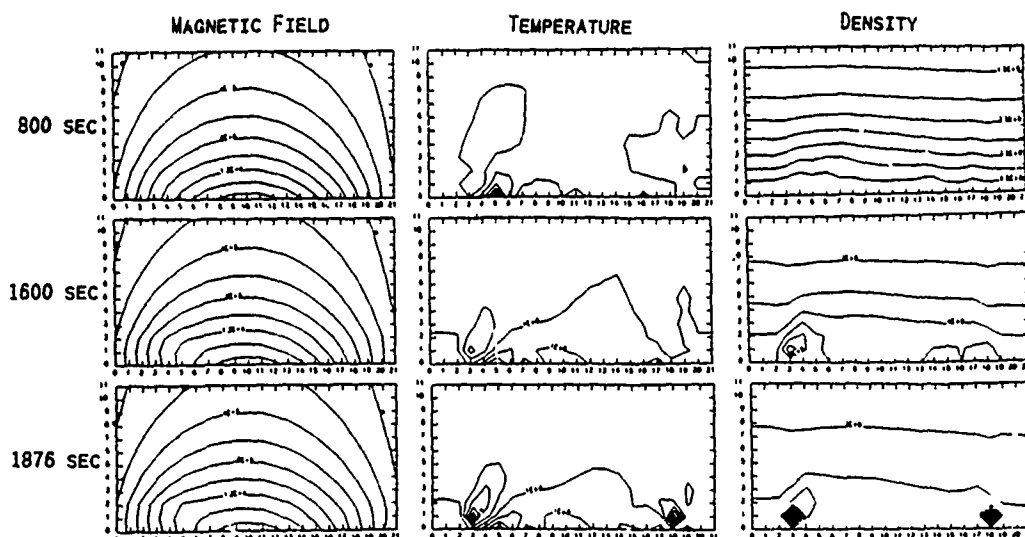


Fig. 5 Time evolution of the plasma for the asymmetric mass injection case with an injection velocity of 100 km/sec. Initial plasma beta is 0.5

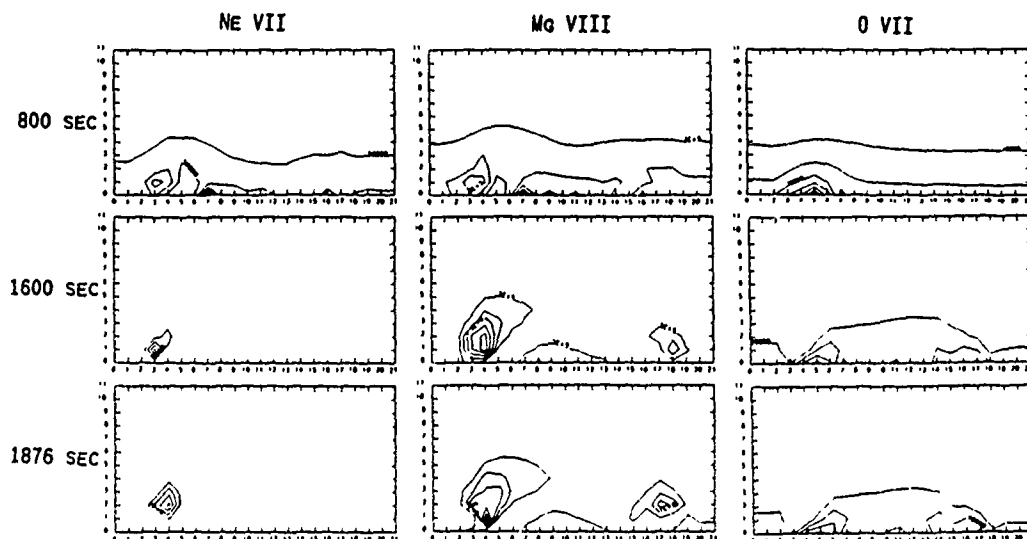


Fig. 6 Emission distribution for the Ne VII, Mg VIII, and O VII lines at various times for the asymmetric mass injection case.

DISCUSSION

We have numerically simulated the dynamic evolution of mass injections in a solar atmosphere and calculated the XUV and X-ray signatures. We find that for an atmosphere with small plasma beta, mass injection produces condensations and provides the mass of loop-like structures. The dense and cooler regions will be observed in the transition regions lines such as Ne VII as elongated emission structures reminiscent of the incomplete loops so often observed from Skylab. In the hotter coronal lines such as O VII we will observe loop-like structures similar to those observed in X-ray images from Skylab. We note that the mass injection velocities we used in this paper are somewhat high compared to those generally observed in the active region, although the mass injection could correspond to spicule-like events that occur in the active regions. Our primary purpose here is to try to understand the physics involved in the interaction between the mass injection and the confining magnetic field. We have seen that mass injection into the magnetic configuration from the footpoint could produce loop-like structures provided that the magnetic field is

strong enough to support the injected material. Thus mass injection could be a mechanism of loop formation in the active regions. In future simulations, more realistic mass injection velocities of a few kilometers per sec will be used. These low evaporation velocities could be produced by heating at lower levels at the footpoints.

The work done by S.T. Wu was supported by NASA under grant NAGW-9 and by Air Force under grant AFOSR-88-00013.

REFERENCES

1. Vaiana et al. 1973, Ap. J. (Letters), 185, L47.
2. Tousey et al. 1973, Solar Phys., 33, 265.
3. Reeves, et al. 1976, in Progress in Astronautics and Aeronautics, 48, 73.
4. Kuperus, M., Ionson, J.A., and Spicer, D.S. 1981, Ann. Rev. Astron. Astrophys., 19, 7.
5. Wu, S.T., Bao, J.T., An, C.H., and Tandberg-Hanssen, E., 1987, in Proc. of the Workshop on Dynamics and Structure of Solar Prominences (Palma De Mallorca, Spain, Nov. 18-20, 1987).
6. An, C.H., Wu, S.T., Bao, J.J., and Suess, S.T. 1988, in Proc. of 10th Korea Symposium for Science and Technology.
7. Wu, S.T., Hu, Y.Q., Nakagawa, Y., and Tandberg-Hanssen, E., 1983, Ap. J., 266, 866.
8. Hu, Y.Q. and Wu, S.T., 1984, J. Comp. Phys., 55, 33.
9. Wu, S.T., and Wang, J.F., 1987, Computer Methods in Appl. Mech. and Eng., 25.

A DYNAMICAL MODEL OF PROMINENCE LOOPS

TYAN YEH

Space Environment Laboratory, NOAA Environmental Research Laboratories, Boulder, CO 80303, U.S.A.

(Received 10 August, 1988; in revised form 26 June, 1989)

Abstract. A dynamical model of prominence loops is constructed on the basis of the theory of hydromagnetic buoyancy force. A prominence loop is regarded as a flux rope immersed in the solar atmosphere above a bipolar region of the photospheric magnetic field. The motion of a loop is partitioned into a translational motion, which accounts for the displacement of the centroidal axis of the loop, and an expansional motion, which accounts for the displacement of the periphery of the loop relative to the axis. The translational motion is driven by the hydromagnetic buoyancy force exerted by the surrounding medium of the solar atmosphere and the gravitational force exerted by the Sun. The expansional motion is driven by the pressure gradient that sustains the pressure difference between internal and external gas pressures and the self-induced Lorentz force that results from interactions among internal currents. The main constituent of the hydromagnetic buoyancy force on a prominence loop is the diamagnetic force exerted on the internal currents by the external currents that sustain the pre-existing magnetic field. By spatial transformation between magnetic and mechanical stresses, the diamagnetic force is manifested through a mechanical force acting at various mass elements of the prominence. For a prominence loop in equilibrium, the gravitational force is balanced by the hydromagnetic buoyancy force and the Lorentz force of helical magnetic field is balanced by a gradient force of gas pressure.

1. Introduction

Solar prominences are cool, dense plasmas trapped in the hot, tenuous coronal atmosphere near the solar surface (see Tandberg-Hanssen, 1974). They consist of a system of bundles of magnetic flux and the material constricted therein. Long-lived quiescent prominences are formed in the neighborhoods of weak bipolar regions of the photospheric magnetic field, with orientation almost along the polarity neutral lines (see McIntosh, 1979). Short-lived active prominences associated with stronger magnetic fields and short-lived postflare loop prominences appear above active regions near sunspots. The weight of the prominence material is apparently supported by forces that result from interactions among currents. Much of the past theoretical work has been aimed at revealing the magnetic configurations that provide the requisite uplifting magnetic force (e.g., Kippenhahn and Schlüter, 1957; Anzer and Tandberg-Hanssen, 1970; Kuperus and Raadu, 1974; Low, 1981). These models of quiescent prominences are based on mathematical solutions to the equations of magnetohydrostatic equilibrium.

A quiescent prominence may lose its equilibrium when it is subject to disturbances. A perturbed prominence may find a new equilibrium or may run away in an eruption and eventually disintegrate. In the process of eruption, each prominence loop evolves dynamically and maintains itself as a separate object from the ambient medium. So does a loop in active prominences in the absence of the catastrophic occurrence of magnetic reconnection. Therefore, it is desirable to construct dynamical models for prominence

loops and to treat their quiescent states as special situations when there are no unbalanced forces (Sakurai, 1976; Pneuman, 1984). Such a theoretical approach is very much like that for looplike coronal mass ejections (Yeh, 1982).

Based on the theory of hydromagnetic buoyancy force for flux ropes (Yeh, 1985), we construct a new dynamical model of prominence loops. This model differs from Pneuman's model in the inclusion of the accelerations of translational and expansional motions for a prominence loop. Pneuman prescribes the translational motion kinematically, without specifying the force that overcomes the gravitational pull, and assumes that the Lorentz force is balanced by the gradient force of gas pressure which matches the external conditions. In the new model, we regard the flux rope that represents a prominence loop as an extraneous body immersed in the magnetized medium of the solar atmosphere. Other loops in the prominence system are regarded as being far away and not causing significant interaction. Polarization currents are induced at the interface to maintain the separation of the loop's helical magnetic field lines from the bipolar magnetic field lines of the external medium. The ambient hydromagnetic pressure exerts a hydromagnetic buoyancy force on the prominence loop. In turn, through the spatial transmission of stress and the spatial transformation between magnetic and mechanical stresses, the hydromagnetic buoyancy force is manifested as an externally-caused gradient force of gas pressure in the prominence. The main constituent of the hydromagnetic buoyancy force is the diamagnetic force that amounts to the force exerted on the currents in the prominence loop by the currents that sustain the bipolar magnetic field.

Accordingly, the motion of an individual mass element of the prominence loop consists of two parts: a translational motion shared by various mass elements and an expansional motion relative to the centroidal axis of the loop. The translational motion is driven by the hydromagnetic buoyancy force and the gravitational force. The expansional motion is driven by the internally-caused gradient force that sustains the pressure difference between internal and external gas pressures and the self-induced Lorentz force that results from interactions among internal currents. In the special situation of equilibrium, the gravitational force is balanced by the hydromagnetic buoyancy force and the Lorentz force of helical magnetic field is balanced by the internally-caused gradient force of gas pressure.

In this paper, we expound the new dynamical model of prominence loops with the simplification that there is no variation along the axis of the prominence. The effect of the curvature of the axis and the longitudinal stretching of the prominence in its motion will be considered in future work. Thus, the present treatment may be regarded as dealing with the top portion of a prominence loop, which is represented by a section of a straight flux rope of circular cross-section. The cylindrical symmetry is merely a mathematical convenience. The realistic geometry of arbitrary cross-sections that appear in the temporal change of the shape of a flux rope will be considered in future work. The prominence loop is immersed in an arcaded bipolar magnetic field near the solar surface. For the sake of simplicity, the loop will be assumed to have its axis aligned to the magnetic arcade.

2. Currents and Magnetic Fields

We use cylindrical coordinates (z, q, ϕ) with the z -axis aligned with the axis of the prominence loop and the angle ϕ measured from the radial line in the upward direction. The cross-sectional radius of the loop will be denoted Q . The whole space is partitioned into three regions: an interior region $q < Q$ occupied by the loop, an exterior region $q > Q$ filled by the surrounding medium, and a peripheral region $q = Q$ which is a thin layer of negligible mass and concentrated current. The currents that flow in the exterior region to sustain the bipolar magnetic field are the external currents. The internal currents consist of the currents that are carried by the intruding prominence in the interior region and the currents that are induced in the peripheral region. The immersion of the prominence loop as an extraneous body in the magnetized medium of the solar atmosphere causes the induction of polarization currents. The induced currents maintain the magnetic separation of the internal and external field lines. By virtue of the high electrical conductivity of the solar plasmas, the induced currents concentrate spatially to form a surface current at the periphery.

By virtue of the interaction among the three current systems, there are several kinds of field-line linkage. The field lines in the interior region are helical. The field lines in the peripheral region are circumferential. Field lines in the exterior region are mainly bipolar. The internal magnetic field is produced by the currents in the interior region alone. This is so because the interior region is shielded from the effect of the external currents by the polarization currents in the peripheral region. In other words, the external currents and the polarization currents together produce a null magnetic field in the interior region. On the other hand, the external magnetic field is produced jointly by all currents in the exterior, peripheral, and interior regions. It is the sum of the pre-existing magnetic field produced by the external currents and the perturbant magnetic field; the latter is produced by the conduction currents carried by the intruding loop and the polarization currents induced in the interaction.

First, we consider the pre-existing magnetic field produced by external currents. In a two-dimensional treatment, the invariance in the longitudinal direction allows a uniform longitudinal component in the magnetic field. The bipolar transverse component of the magnetic field can be described in terms of a couple of line monopoles as the source and sink of magnetic flux, in lieu of currents. This is merely a mathematical expediency. The currents that produce the longitudinal magnetic field are very far away so that the latter can be regarded uniform. Let the photospheric flux source of monopole strength Ψ_M be located at $q = a, \phi = \pi - \alpha$ and the photospheric flux sink of monopole strength $-\Psi_M$ be located at $q = a, \phi = \pi + \alpha$ (see Figure 1). The distance a and the half-angle α are related to the heliocentric distance r_0 of the loop's axis and the heliocentric half-angle θ_M subtended by the couple of monopoles by the geometric relationships

$$a^2 = R_\odot^2 - 2 R_\odot r_0 \cos \theta_M + r_0^2, \quad \frac{\sin \alpha}{R_\odot} = \frac{\sin \theta_M}{a}.$$

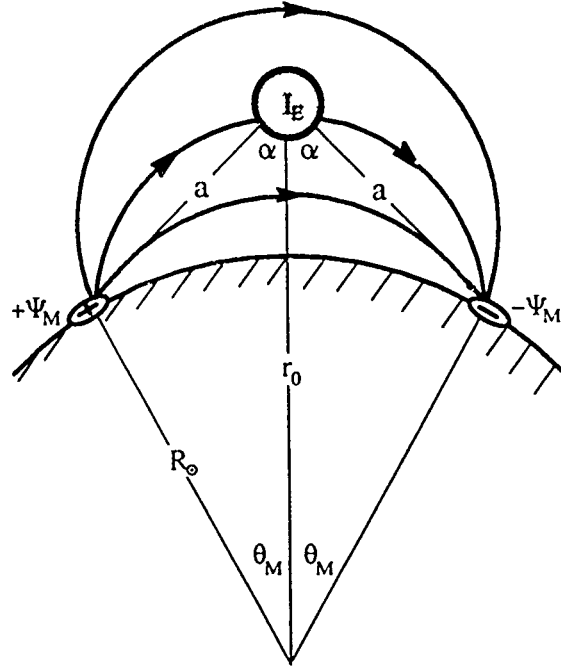


Fig. 1. A prominence loop of circular cross-section above a pair of line monopoles.

The magnetic field associated with this source-sink pair has the flux function

$$\begin{aligned} \psi^{(\infty)} = & \frac{\Psi_M}{2\pi} \operatorname{atn} \frac{q \sin \phi - a \sin(\pi - \alpha)}{q \cos \phi - a \cos(\pi - \alpha)} + \\ & + \frac{-\Psi_M}{2\pi} \operatorname{atn} \frac{q \sin \phi - a \sin(\pi + \alpha)}{q \cos \phi - a \cos(\pi + \alpha)}. \end{aligned} \quad (1)$$

Thus, the pre-existing magnetic field, given by $\mathbf{1}_z B_{\parallel \infty} + \mathbf{1}_z \times (-\nabla \psi^{(\infty)})$ can be written as

$$\begin{aligned} \mathbf{B}^{(\infty)} = & \mathbf{1}_z B_{\parallel \infty} + \frac{\Psi_M}{2\pi} \frac{\mathbf{1}_q [q + a \cos(\phi + \alpha)] - \mathbf{1}_\phi a \sin(\phi + \alpha)}{q^2 + 2aq \cos(\phi + \alpha) + a^2} + \\ & + \frac{-\Psi_M}{2\pi} \frac{\mathbf{1}_q [q + a \cos(\phi - \alpha)] - \mathbf{1}_\phi a \sin(\phi - \alpha)}{q^2 + 2aq \cos(\phi - \alpha) + a^2}. \end{aligned} \quad (2)$$

Here $B_{\parallel \infty}$ denotes the uniform longitudinal magnetic field. The field lines are helical arcs, with circular projections, from the flux source to the flux sink. At the site $q = 0$, where the prominence loop intrudes, the pre-existing magnetic field has the local strength

$$\mathbf{B}_\infty = \mathbf{1}_z B_{\parallel \infty} + \mathbf{1}_r \times \mathbf{1}_z B_{\perp \infty} \quad (3)$$

with the transverse magnetic field given by

$$B_{\perp \infty} = \frac{\Psi_M}{\pi} \frac{\sin \alpha}{a}. \quad (4)$$

The associated magnetic pressure has the local gradient

$$\left(-\nabla \frac{1}{2\mu} B^2 \right)_{\infty} = \mathbf{1}_r \frac{2 \cos \alpha}{\mu a} B_{\perp \infty}^2. \quad (5)$$

We use here rationalized mks units with the magnetic permeability $\mu = 4\pi \times 10^{-7}$ henry m^{-1} . Here $\mathbf{1}_r$ is a unit vector in the $\phi = 0$ direction which is opposite to the solar gravity. We remark that the radius of curvature for the circular projection of the bipolar field line that passes through the point $q = 0$ is $a/2 \cos \alpha$.

Next, we consider the perturbation to the pre-existing magnetic field, caused by the intrusion of the prominence loop. An axisymmetric distributed current carried by the loop will produce an azimuthal magnetic field $\mathbf{1}_{\phi} \mu I_E / 2\pi q$ outside the loop, as though the total longitudinal current $I_E \equiv \int_0^Q J_z 2\pi q dq$ were concentrated at the axis $q = 0$. The polarization currents induced at the periphery produce another potential magnetic field in the exterior region. The latter perturbation is as though it were produced by a couple of line monopoles located inside the loop. By the method of images, in analogy to image charges in electrostatics, the photospheric monopoles $\pm \Psi_M$ at $q = a$, $\phi = \pi \mp \alpha$ induce images consisting of monopoles of strength $\pm \Psi_M$ at the inverse points $q = Q^2/a$, $\phi = \pi \mp \alpha$ (cf. Yeh, 1938). From the flux function

$$\begin{aligned} \psi = & \frac{\mu I_E}{2\pi} \log \frac{1}{q} + \frac{\Psi_M}{2\pi} \left[\text{atn} \frac{q \sin \phi - a \sin \alpha}{q \cos \phi + a \cos \alpha} + \text{atn} \frac{q \sin \phi - (Q^2/a) \sin \alpha}{q \cos \phi + (Q^2/a) \cos \alpha} \right] + \\ & + \frac{-\Psi_M}{2\pi} \left[\text{atn} \frac{q \sin \phi + a \sin \alpha}{q \cos \phi + a \cos \alpha} - \text{atn} \frac{q \sin \phi + (Q^2/a) \sin \alpha}{q \cos \phi + (Q^2/a) \cos \alpha} \right], \end{aligned} \quad (6)$$

we obtain the perturbed magnetic field

$$\begin{aligned} \mathbf{B} = & \mathbf{1}_z B_{\parallel \infty} + \mathbf{1}_{\phi} \frac{\mu I_E}{2\pi q} + \\ & + \frac{\Psi_M}{2\pi} \left\{ \frac{\mathbf{1}_q [q + a \cos(\phi + \alpha)] - \mathbf{1}_{\phi} a \sin(\phi + \alpha)}{q^2 + 2aq \cos(\phi + \alpha) + a^2} + \right. \\ & + \left. \frac{\mathbf{1}_q [q + (Q^2/a) \cos(\phi + \alpha)] - \mathbf{1}_{\phi} (Q^2/a) \sin(\phi + \alpha)}{q^2 + 2(Q^2/a)q \cos(\phi + \alpha) + (Q^2/a)^2} \right\} + \\ & + \frac{-\Psi_M}{2\pi} \left\{ \frac{\mathbf{1}_q [q + a \cos(\phi - \alpha)] - \mathbf{1}_{\phi} a \sin(\phi - \alpha)}{q^2 + 2aq \cos(\phi - \alpha) + a^2} + \right. \\ & + \left. \frac{\mathbf{1}_q [q + (Q^2/a) \cos(\phi - \alpha)] - \mathbf{1}_{\phi} (Q^2/a) \sin(\phi - \alpha)}{q^2 + 2(Q^2/a)q \cos(\phi - \alpha) + (Q^2/a)^2} \right\}. \end{aligned} \quad (7)$$

The longitudinal component of the magnetic field is not perturbed.

The field-line topology of the transverse magnetic field, given in Equation (7), depends on the ratio $\mu I_E / \Psi_M$. In the case of $I_E = 0$, there are only a pair of X-type magnetic neutral points, located at $q = Q$, $\phi = \pi \mp \arccos[2(a/Q + Q/a)^{-1} \cos \alpha]$ (see Figure 2(a)). In the case of $I_E \neq 0$, there are additional neutral points in the exterior and interior regions, besides the aforementioned pair. They stay on the periphery if $\mu I_E / \Psi_M$ has a value between $-4Qa \sin \alpha / (Q^2 - 2Qa \cos \alpha + a^2)$ and $4Qa \sin \alpha / (Q^2 + 2Qa \cos \alpha + a^2)$ (see Figure 2(b)), and coalesce to be outside the periphery otherwise (see Figure 2(c)). The additional neutral point in the exterior region is of hyperbolic type, so that the two line monopoles are encircled by field lines in the

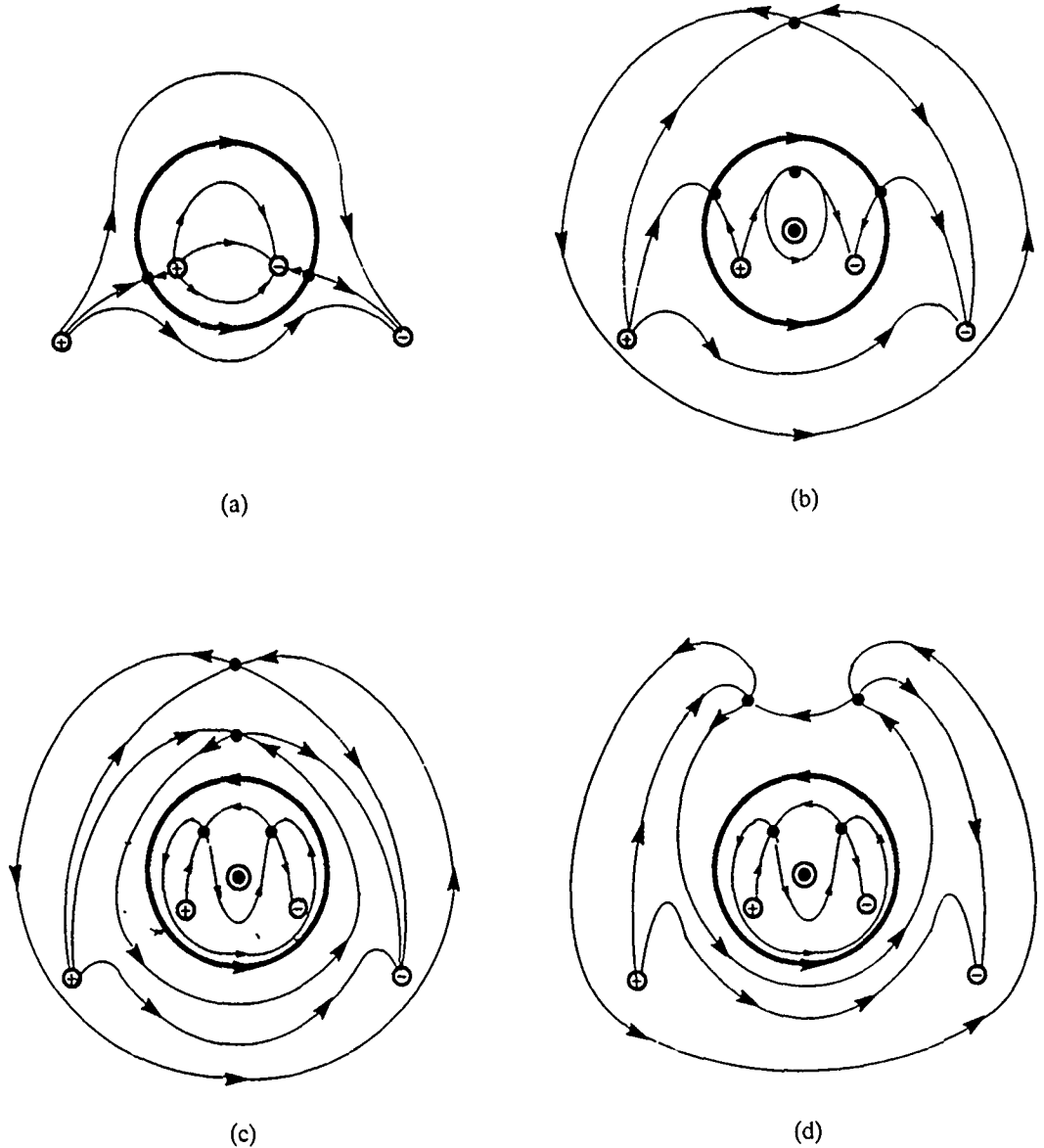


Fig. 2. Field line topology for the transverse magnetic field. (a) With $I_E = 0$, (b) with $0 < \mu I_E / \Psi_M < 4Qa \sin \alpha / (Q^2 + 2Qa \cos \alpha + a^2)$, (c) with $\mu I_E / \Psi_M$ slightly greater than $4Qa \sin \alpha / (Q^2 + 2Qa \cos \alpha + a^2)$, (d) with $\mu I_E / \Psi_M$ significantly greater than $4Qa \sin \alpha / (Q^2 + 2Qa \cos \alpha + a^2)$.

distant region of large radii. On the other hand, the additional neutral point in the interior region is of parabolic type if $\mu I_E / \Psi_M$ is in the above-mentioned range (see Figure 2(b)) and bifurcates into a pair of X-type neutral points otherwise (see Figures 2(c) and 2(d)), so that the line current at the center is encircled by field lines in the near region of small radii. If $|\mu I_E / \Psi_M|$ is very large, the two neutral points outside the periphery will be on the two sides of the line $\phi = 0$ or π instead of on the line $\phi = 0$ or π (see Figure 2(d)). The above discussion includes the interior region for the sake of global clarity. Physically, Equation (7) is valid only for the exterior region.

To be in conformance with the accepted idea that the normal component of the photospheric magnetic field is not altered by the coronal currents, we may include the polarization currents induced on the photosphere (Kuperus and Raadu, 1974). This will remove the additional polarity neutral lines, which appeared spuriously in Figure 2. By the method of images the polarization currents on the photosphere amount to couples of line current and couples of line monopole inside the cylinder whose surface represents the photosphere. These induced photospheric currents together with all the currents in the prominence loop produce a magnetic field that has no normal component on the photospheric surface. In turn, the photospheric polarization currents induce their own image currents inside the prominence loop so that the magnetic field resulting from all currents remains tangential on the surface of the prominence loop. The additional induced currents in the prominence loop also amount to current couples and monopole couples inside the prominence loop (see Appendix).

3. Hydromagnetic Buoyancy Force on a Prominence

The magnetized medium surrounding a prominence loop exerts its hydromagnetic pressure on the immersed loop as an extraneous body. The surface integral of the ambient hydromagnetic pressure yields the hydromagnetic buoyancy force

$$\mathbf{F} = \int_0^{2\pi} -\mathbf{1}_q \left(p_A + \frac{1}{2\mu} \mathbf{B}_A^2 \right) Q d\phi \quad (8)$$

on the immersed loop.

The ambient magnetic field at the periphery $q = Q$ is

$$\begin{aligned} \mathbf{B}_A(\phi) = \mathbf{1}_z B_{\parallel \infty} + \mathbf{1}_\phi \left\{ B_{\perp \infty} \frac{1}{\sin \alpha} \left[\frac{-a^2 \sin(\phi + \alpha)}{Q^2 + 2Qa \cos(\phi + \alpha) + a^2} + \right. \right. \\ \left. \left. + \frac{a^2 \sin(\phi - \alpha)}{Q^2 + 2Qa \cos(\phi - \alpha) + a^2} \right] + \frac{\mu I_E}{2\pi Q} \right\}, \end{aligned} \quad (9)$$

from Equation (7). Accordingly, the ambient magnetic pressure is

$$\begin{aligned} \frac{1}{2\mu} \mathbf{B}_A^2 = & \frac{1}{2\mu} B_{\parallel\infty}^2 + \frac{1}{2\mu} B_{\perp\infty}^2 - \frac{1}{\sin^2 \alpha} \left[\frac{-a^2 \sin(\phi + \alpha)}{Q^2 + 2Qa \cos(\phi + \alpha) + a^2} + \right. \\ & \left. + \frac{a^2 \sin(\phi - \alpha)}{Q^2 + 2Qa \cos(\phi - \alpha) + a^2} \right]^2 + \frac{I_E}{2\pi Q} B_{\perp\infty} \frac{1}{\sin \alpha} \times \\ & \times \left[\frac{-a^2 \sin(\phi + \alpha)}{Q^2 + 2Qa \cos(\phi + \alpha) + a^2} + \frac{a^2 \sin(\phi - \alpha)}{Q^2 + 2Qa \cos(\phi - \alpha) + a^2} \right] + \frac{1}{2} \frac{\mu I_E^2}{(2\pi Q)^2}. \end{aligned} \quad (10)$$

Only the two circumferentially inhomogeneous terms, one proportional to $I_E B_{\perp\infty}$ and the other proportional to $B_{\perp\infty}^2$, will contribute to the integral $\int_0^{2\pi} -\mathbf{l}_q \frac{1}{2\mu} \mathbf{B}_A^2 Q d\phi$ for the diamagnetic buoyancy force (Yeh, 1983). The former term yields $\mathbf{l}_r I_E B_{\perp\infty}$. It signifies the force on the line current that accounts for the conduction current in the interior region exerted by the two monopoles that account for the external currents. The latter term yields the force on the two image monopoles that account for the polarization currents in the peripheral region exerted by the two external monopoles (see Figure 3). The result is a diamagnetic force in the direction of \mathbf{l}_r . Its magnitude is

$$F^{(m)} = I_E B_{\perp\infty} + \Gamma \frac{2 \cos \alpha}{\mu a} B_{\perp\infty}^2 \pi Q^2 \quad (11)$$

per unit axial length. The geometric coefficient

$$\Gamma = \frac{2a^6}{(a^2 - Q^2)(a^4 - 2a^2 Q^2 \cos 2\alpha + Q^4)} \quad (12)$$

has the limiting value of 2 for very small value of Q/a . This diamagnetic force can be written

$$\mathbf{F}^{(m)} = \mathbf{I}_E \times \mathbf{B}_{\infty} + \Gamma \left(-\nabla \frac{1}{2\mu} \mathbf{B}^2 \right)_{\infty} \pi Q^2 \quad (13)$$

in terms of the current carried by the intruding loop and the pre-existing magnetic field and magnetic pressure gradient produced by the external currents. Here $\mathbf{I}_E \equiv \mathbf{l}_z I_E$ is the volume integral of the current per unit axial length. The azimuthal current density has a volume integral equal to zero. So does the volume integral of the polarization currents. Inclusion of the polarization currents on the photosphere will incur an additional force acting on the prominence loop. The additional force is essentially $\mathbf{l}_r \mu I_E^2 / 4\pi(r_0 - R_{\odot})$. It is significant when the prominence loop is close to the photosphere (see Appendix).

In addition to diamagnetic force the hydromagnetic buoyancy force also includes hydrostatic and hydrodynamic buoyancy forces. In the absence or neglect of motion for

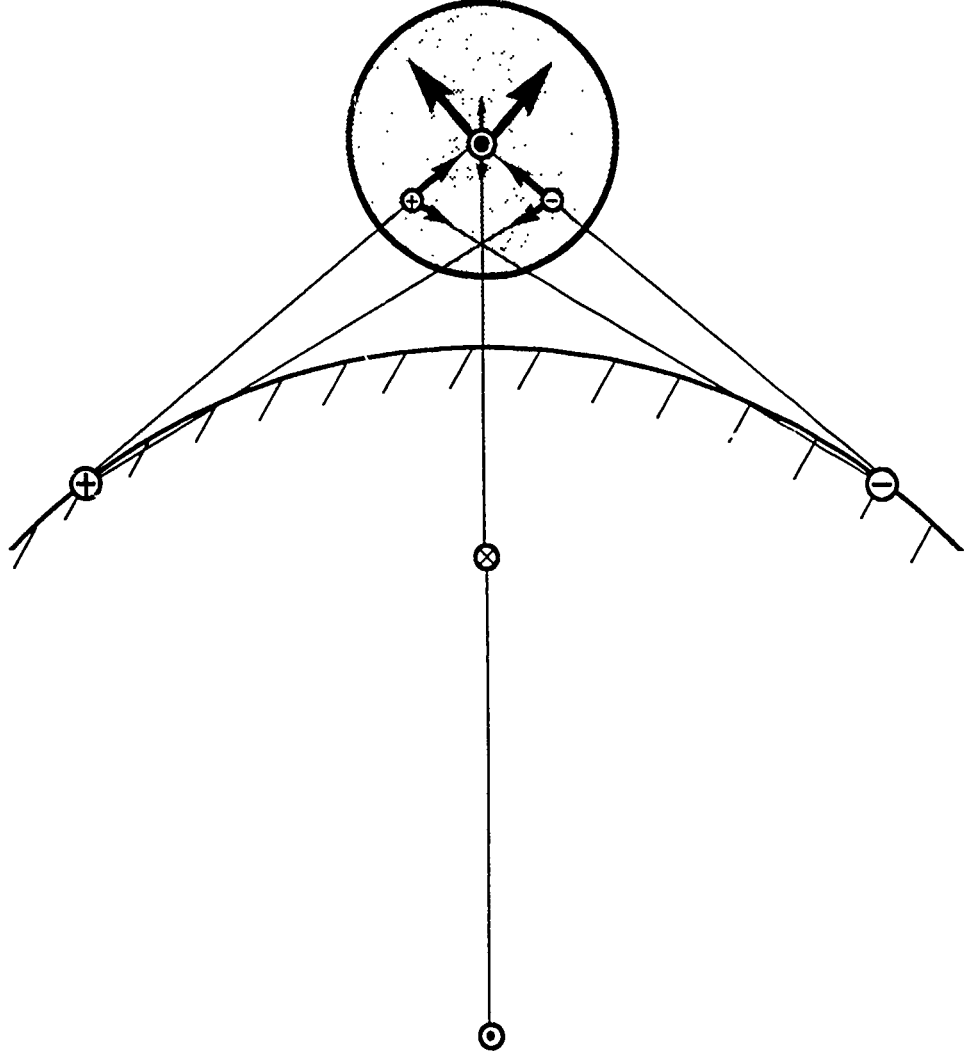


Fig. 3 Biot-Savart forces on the line currents and monopoles inside the prominence cylinder exerted by the line currents and monopoles outside.

the surrounding medium, the external gas pressure is entirely hydrostatic. Hydrostatic pressure impresses directly on the periphery of an immersed body, without modification. Thus, the ambient gas pressure is

$$p_A(\phi) = p_\infty - \rho_\infty g Q \cos \phi, \quad (14)$$

with $g \equiv GM_\odot/r_\odot^2$ being the gravitational acceleration at $q = 0$. Here G is the gravitational constant and M_\odot is the solar mass. For our present discussion, we consider the situation when the straight axis of the loop lies perpendicular to the solar gravity $\mathbf{g} \equiv -\mathbf{1}_r g$. By virtue of the hydrostatic relationship $\nabla p^{(s)} = \rho_\infty \mathbf{g}$ between the hydrostatic pressure $p^{(s)}$, the mass density ρ_∞ of the external medium, and the solar gravity, we obtain the hydrostatic buoyancy force (Archimedes' law)

$$\mathbf{F}^{(s)} = -\rho_\infty \mathbf{g} \pi Q^2, \quad (15)$$

from the integral $\int_0^{2\pi} -\mathbf{1}_q p_A Q d\phi$. It is in the direction opposite to the solar gravity. The

magnitude of this hydrostatic buoyancy force is

$$F^{(s)} = \rho_{\infty} \frac{GM_{\odot}}{r_0^2} \pi Q^2. \quad (16)$$

4. Hydromagnetic Stress in a Prominence Loop

Now, we describe the helical magnetic field inside the prominence loop. The current in the interior region must be so distributed that not only the current density but also the solenoidal magnetic field are tangential at the peripheral boundary. In a straight cylindrical region, an axisymmetric current density without a radial component will produce an axisymmetric magnetic field without a radial component too. We consider the current distribution

$$\mathbf{J}_E(q) = \mathbf{1}_z J_0 + \mathbf{1}_{\phi} \frac{B_0}{\mu Q} \frac{q/Q}{(1 - q^2/Q^2)^{1/2}}. \quad (17)$$

It produces the magnetic field

$$\mathbf{B}_E(q) = \mathbf{1}_z \int_q^Q \mu J_{\phi} dq + \mathbf{1}_{\phi} \frac{1}{q} \int_0^q \mu J_z q dq = \mathbf{1}_z B_0 \left(1 - \frac{q^2}{Q^2}\right)^{1/2} + \mathbf{1}_{\phi} \frac{1}{2} \mu J_0 q \quad (18)$$

with helical field lines. At the axis $q = 0$, where the azimuthal components of the current density and the magnetic field are necessarily zero, the axial current density has the value J_0 and the axial magnetic field has the value B_0 . At the boundary $q = Q$, where the longitudinal component of the magnetic field is zero, the boundary magnetic field is

$$\mathbf{B}_B(\phi) = \mathbf{1}_{\phi} \frac{\mu I_E}{2\pi Q} \quad (19)$$

with

$$I_E = J_0 \pi Q^2. \quad (20)$$

The pitch angle of the helical field line, given by $\arctan(B_{\phi}/B_z)$, increases from 0° at the axis to 90° at the boundary.

The spatial transition between the ambient and boundary magnetic fields at the outer and inner surfaces, respectively, of the thin peripheral layer is accommodated by the polarization current. From the expression $\mathbf{1}_q \times (\mathbf{B}_A - \mathbf{B}_B)$, we obtain the surface density of the polarization current

$$\begin{aligned} \mathbf{i}_p = & \mathbf{1}_z \frac{1}{\mu} B_{\perp \infty} \times \\ & \times \frac{2a^2(Q^2 + a^2) \cos \phi + 4Qa^3 \cos \alpha}{[Q^2 + 2Qa \cos(\phi - \alpha) + a^2][Q^2 + 2Qa \cos(\phi + \alpha) + a^2]} - \mathbf{1}_{\phi} \frac{1}{\mu} B_{\parallel \infty} \end{aligned} \quad (21)$$

per unit length.

The peripheral layer is a thin region of concentrated current without significant mass accumulation. Its mass is negligible, so it cannot sustain a non-zero force. Accordingly, the magnetic force associated with the polarization current must be balanced by the mechanical force associated with the gas pressure because the gravitational force is nil there. In other words, the hydromagnetic pressure is invariant across the thin peripheral layer. Namely,

$$p_A + \frac{1}{2\mu} B_A^2 = p_B + \frac{1}{2\mu} B_B^2. \quad (22)$$

Since the gas pressure in the exterior region is hardly perturbed by the intrusion of the prominence loop, the ambient gas pressure is essentially equal to the pre-existing external gas pressure at the periphery. The external gas pressure, even not perturbed, may have a significant inhomogeneity caused by the effect of the solar gravity.

Substitution of Equations (9), (14), and (19) into Equation (22) yields

$$\begin{aligned} p_B(\phi) = p_\infty - \rho_\infty g Q \cos \phi + \frac{1}{2\mu} B_{\perp\infty}^2 + \\ + \frac{1}{2\mu} B_{\perp\infty}^2 \frac{1}{\sin^2 \alpha} \left[\frac{-a^2 \sin(\phi + \alpha)}{Q^2 + 2Qa \cos(\phi + \alpha) + a^2} + \frac{a^2 \sin(\phi - \alpha)}{Q^2 + 2Qa \cos(\phi - \alpha) + a^2} \right]^2 + \\ + \frac{I_E}{2\pi Q} B_{\perp\infty} \frac{1}{\sin \alpha} \left[\frac{-a^2 \sin(\phi + \alpha)}{Q^2 + 2Qa \cos(\phi + \alpha) + a^2} + \frac{a^2 \sin(\phi - \alpha)}{Q^2 + 2Qa \cos(\phi - \alpha) + a^2} \right]. \end{aligned} \quad (23)$$

The internal gas pressure varies from the boundary value p_B at $q = Q$ to the axial value p_0 at $q = 0$. Thus, the spatial variation of the gas pressure inside the loop can be accounted for by two parts:

$$p_E = p_E^{(e)} + p_E^{(i)}. \quad (24)$$

The externally-caused part,

$$p_E^{(e)} = -\frac{F^{(s)}}{\pi Q^2} (r - r_0) - \frac{F^{(m)}}{\pi Q^2} q \cos \phi, \quad (25)$$

varies from the value of zero at the axis to a circumferentially undulatory value $-(F^{(s)} + F^{(m)}) \cos \phi / \pi Q$ at the boundary. The internally-caused part varies from p_0 at the axis to $p_B + (F^{(s)} + F^{(m)}) \cos \phi / \pi Q$ at the boundary. It is well represented by

$$p_E^{(i)} = p_0 \left(1 - \frac{q^2}{Q^2} \right) + \bar{p}_B \frac{q^2}{Q^2} \quad (26)$$

with

$$\bar{p}_B = p_\infty + \frac{1}{2\mu} B_{\perp\infty}^2 \quad (27)$$

signifying the circumferential average of $p_E^{(i)}$. The externally-caused gradient of the gas pressure provides the externally-caused mechanical force density

$$-\nabla p_E^{(e)} = \frac{\mathbf{F}^{(s)}}{\pi Q^2} + \frac{\mathbf{F}^{(m)}}{\pi Q^2} \quad (28)$$

that manifests the hydromagnetic buoyancy force. The internally-caused gradient of the gas pressure provides the internally-caused mechanical force density

$$-\nabla p_E^{(i)} = \mathbf{1}_q 2 \frac{p_0 - \bar{p}_B}{Q} \frac{q}{Q} \quad (29)$$

Accordingly, the resultant mechanical force density is

$$\begin{aligned} -\nabla p_E = & -\rho_\infty \mathbf{g} + \frac{\mathbf{I}_E \times \mathbf{B}_\infty}{\pi Q^2} + \Gamma \left(-\nabla \frac{1}{2\mu} \mathbf{B}^2 \right)_\infty + \\ & + \mathbf{1}_q 2 \frac{p_0 - (p_\infty + \frac{1}{2}\mu^{-1} B_{||\infty}^2)}{Q} \frac{q}{Q} \end{aligned} \quad (30)$$

The magnetic force density in the interior region is readily obtained from Equations (17) and (18). The result

$$\mathbf{J}_E \times \mathbf{B}_E = \mathbf{1}_q \left(\frac{B_0^2}{\mu Q} - \frac{1}{2} \mu J_0^2 Q \right) \frac{q}{Q} \quad (31)$$

indicates that the self-induced Lorentz force exerting at various mass elements of the prominence is in the radial direction. Its magnitude is zero at the axis, where the azimuthal components of both the current density and the magnetic field are zero. By axisymmetry, the volume integral of the Lorentz force density is zero. This self-induced magnetic force is the force exerted on a part of internal current by other parts of the internal currents, without involving the external currents.

5. Motion of a Prominence Loop

We have partitioned the hydromagnetic force density acting at various mass elements of a prominence loop into two parts:

$$\mathbf{f}_E = \mathbf{1}_r f_0 + \mathbf{1}_q H \frac{q}{Q} \quad (32)$$

The externally-caused force density

$$f_0 = -\rho_E \frac{GM_\odot}{r_0^2} + \frac{F^{(s)} + F^{(m)}}{\pi Q^2} \quad (33)$$

is uniform over the cross-section of the loop. The internally-caused force density is proportional to the distance from the axis of the loop. The latter has the value

$$H = 2 \frac{(p_0 + \frac{1}{2}\mu^{-1}B_0^2) - (p_\infty + \frac{1}{2}\mu^{-1}B_{q\infty}^2)}{Q} - \frac{1}{2}\mu J_0^2 Q \quad (34)$$

at the periphery. In a similar manner, the velocity of a mass element of the loop may be partitioned into two parts:

$$\mathbf{u}_E = \mathbf{1}_r u_0 + \mathbf{1}_q V \frac{q}{Q} \quad (35)$$

Here u_0 is the common speed of the translational motion and V is the peripheral speed of the expansional motion. The translational velocity is uniform over the cross-section whereas the expansional velocity is proportional to the distance from the axis. The ratio q/Q associated with an individual mass element is invariant in time. In accordance with Newton's law,

$$\rho_E \frac{d}{dt} \mathbf{u}_E = -\nabla p_E + \mathbf{J}_E \times \mathbf{B}_E + \rho_E \mathbf{g}, \quad (36)$$

the translational motion of the loop as a whole is driven by the externally-caused mechanical force and the gravitational force whereas the expansional motion of the loop relative to its centroidal axis is driven by the internally-caused mechanical force and the self-induced Lorentz force. Accordingly, the dynamical evolution of the prominence loop is described by the equations

$$\frac{d}{dt} r_0 = u_0, \quad (37)$$

$$\rho_E \frac{d}{dt} u_0 = f_0 \quad (38)$$

for the translational motion and

$$\frac{d}{dt} Q = V, \quad (39)$$

$$\rho_E \frac{d}{dt} V = H \quad (40)$$

for the expansional motion.

Additional equations for the dynamical evolution are provided by conservation of mass and magnetic flux carried by the prominence loop and conservation of energy in the physical processes involved. The mass of the loop is $\rho_E \pi Q^2$ per unit axial length.

Hence,

$$\frac{d}{dt} \rho_E Q^2 = 0. \quad (41)$$

It follows from Equation (18) that the longitudinal magnetic flux of the loop is $\frac{2}{3}B_0\pi Q^2$ and the azimuthal magnetic flux is $\frac{1}{4}\mu J_0 Q^2$ per unit axial length. Hence,

$$\frac{d}{dt} B_0 Q^2 = 0, \quad (42)$$

$$\frac{d}{dt} J_0 Q^2 = 0. \quad (43)$$

As to the conservation of energy, the energy in a prominence loop increases or decreases by the amount of energy gained or lost through energy transportation across the peripheral surface and energy deposition to the volume. The former includes work done by ambient pressure, heat transfer by thermal conduction, and longitudinal flow of energy toward the footpoints of the prominence loop. The latter includes work done by gravitational force, energy deposit by electrical current, absorption of irradiation, emission of radiation, and deposition of mechanical energy. Upon the use of equation of motion and equation of mass conservation, the equation of energy conservation

$$\frac{d}{dt} \iiint \left(\frac{1}{2} \rho_E \mathbf{u}_E^2 + \frac{3}{2} p_E \right) dV = \oint \mathbf{u}_A \cdot p_A d\mathbf{A} + \iiint (\mathbf{u}_E \cdot \rho_E \mathbf{g} + \mathbf{J}_E \cdot \mathbf{E}_E) dV + S$$

yields the entropy equation

$$\frac{d}{dt} \iiint \frac{3}{2} p_E dV + \iiint p_E (\nabla \cdot \mathbf{u}_E) dV = S.$$

Here S denotes the net source term for all entropy-generating processes. By virtue of $\nabla \cdot \mathbf{u}_E$ being equal to $2Q^{-1} dQ/dt$ according to Equations (35) and (39), the entropy equation can be written

$$Q^{-4/3} \frac{d}{dt} Q^{4/3} \iiint \frac{3}{2} p_E dV = S,$$

which is nothing but

$$Q^{-4/3} \frac{d}{dt} \left[\frac{3}{2} \left(\frac{1}{2} p_0 + \frac{1}{2} \bar{p}_B \right) \pi Q^{2+4/3} \right] = S, \quad (44)$$

since the volume integral for the thermal energy is equal to $\frac{3}{2} \left(\frac{1}{2} p_0 + \frac{1}{2} \bar{p}_B \right) \pi Q^2$.

The above eight Equations (37)–(44) serve to determine the temporal changes of the eight variables: r_0 , u_0 , Q , V , ρ_E , B_0 , J_0 , and p_0 in terms of the conditions for the external medium. The latter are specified by ρ_∞ , p_∞ , $B_{||\infty}$, and $B_{\perp\infty}$.

The above analysis is done quantitatively for the case of uniform mass density in the prominence loop. In reality, the mass is likely to concentrate in the pit of the helical field. Spatial variation of the mass density can be accounted for by suitable modifications. For example, the axisymmetric variation $\rho_E = \rho_0(1 - q^2/Q^2) + \bar{\rho}_B q^2/Q^2$ will incur the following modifications. The quantity ρ_E in Equations (33), (38), and (41) is to be replaced by the average mass density $\bar{\rho}_E = \frac{1}{2}\rho_0 + \frac{1}{2}\bar{\rho}_B$, but the one associated with the expansional inertial force in Equation (40) is to be replaced by $\frac{2}{5}\rho_0 + \frac{3}{5}\bar{\rho}_B$, which is the average of ρ_E weighted by q/Q .

6. Equilibrium Configuration for a Prominence Loop

A prominence loop in equilibrium with its surrounding medium has neither translational motion nor expansional motion. In other words, the hydromagnetic buoyancy force counterbalances the gravitational force, and the internally-caused gradient force of gas pressure counterbalances the Lorentz force of helical magnetic field. From Equations (38) and (40) with $u_0 = 0$ and $V = 0$ we obtain

$$J_0 = \frac{\rho_E - \rho_\infty}{B_{\perp\infty}} \frac{GM_\odot}{r_0^2} - \Gamma \frac{2 \cos \alpha}{\mu a} B_{\perp\infty}^2, \quad (45)$$

$$p_0 + \frac{1}{2\pi} B_0^2 = p_\infty + \frac{1}{2\mu} B_{\parallel\infty}^2 + \frac{1}{4} \mu J_0^2 Q^2. \quad (46)$$

These two constraints are necessary for equilibrium. Any changes of the parameters from the equilibrium values will initiate motion. Eruption of a quiescent prominence loop is then described by the dynamical evolution given by Equations (37)–(44).

It should be remarked that inclusion of the mirror-current effect will modify Equation (45) to

$$\begin{aligned} & -(\rho_E - \rho_\infty) \pi Q^2 \frac{GM_\odot}{r_0^2} + I_E B_{\perp\infty} + \Gamma \frac{2 \cos \alpha}{\mu a} B_{\perp\infty}^2 \pi Q^2 + \\ & + \mu I_E^2 \frac{R_\odot^2}{2\pi r_0(r_0^2 - R_\odot^2)} = 0. \end{aligned} \quad (47)$$

This condition of equilibrium for no translational motion reduces to that obtained by Van Tend and Kuperus (1978) in the limit of $r_0 - R_\odot \ll R_\odot$ and $Q \ll a$.

7. Discussion

Prominences appear in various morphologies. They all involve a system of complex or simple bundles of magnetic flux. We consider a prominence loop to be a flux rope that intrudes into the solar atmosphere as an extraneous body immersed in a separately magnetized medium. The time-scale of interaction between the two current systems is

not long enough to allow magnetic interconnection between the two kinds of field lines of different connectivity. The magnetic separation is maintained by currents induced at the interface of the two flux systems. By virtue of the high electrical conductivity of the solar plasmas, the induced currents concentrate spatially to form a surface current at the periphery. This is in keeping with the cellular structures common in astrophysical plasmas, with thin boundary layers separating plasma regions of widely different characteristics. The polarization currents have paths separate from the two interacting current systems. The spatial transformation between magnetic and mechanical stresses across the peripheral layer of the polarization currents means that the plasma beta (viz., the ratio of gas pressure to magnetic pressure) can vary significantly from one region to another region. With the gas pressure higher inside, the plasma beta can have a higher value in the prominence loop than in the surrounding medium, although its value is likely still less than unity.

The dynamical model of moving flux ropes presented in this paper is applicable to the helical prominences observed by Vršnak, Ruždjak, and Brajša (1988). It could also be applied to flare loops. Recent observations obtained by the HXIS and FCS instruments on board the Solar Maximum Mission spacecraft suggest that the hot loops seen in X-rays are at much higher altitudes than the cool loops visible later in H-alpha after cooling (Švestka *et al.*, 1987). These post-flare loops are likely formed during the process of flaring. Their descending motion is accompanied by shrinking in volume. It would be of interest to explain the latter feature by the dynamics of flux ropes.

Appendix. Photospheric Effect

The presence of a prominence loop in the photospheric magnetic field involves the interaction of two systems of magnetic fluxes. One of them is associated with the currents carried by the prominence loop and the other with the subphotospheric currents. In the interaction, polarization currents are induced on the surface of the prominence loop and the photospheric surface so that field lines do not penetrate the former surface and no additional field lines go through the latter surface. In other words, the resulting magnetic field is tangential on the surface of the prominence loop and has an unaltered normal component on the photospheric surface.

By the method of images (cf. Yeh, 1988), the induced currents can be accounted for by current couples and monopole couples if we approximate the photospheric surface by a cylinder. As shown in Figure 4, the conduction current I_E at $q = 0$ induces a couple of currents: $+I_E$ at $q = r_0$ and $-I_E$ at $q = r_0 - R_O^2/r_0$. The image induces its own image: $-I_E$ at $q = Q^2/r_0$ and $+I_E$ at $q = Q^2/(r_0 - R_O^2/r_0)$. The induction of images of image yields a series of current couples:

$$+I_E \text{ at } q = b_{2n} \text{ and } -I_E \text{ at } q = b_{2n+1}, \quad n = 0, 1, 2, \dots$$

inside the photospheric cylinder and another series,

$$-I_E \text{ at } q = Q^2/b_{2n} \text{ and } +I_E \text{ at } q = Q^2/b_{2n+1}, \quad n = 0, 2, \dots,$$

inside the photospheric cylinder. Here $a_0 = a$, $\alpha_0 = \alpha$, and

$$a_{n+1}^2 = r_0^2 - 2r_0 \frac{R_\odot^2}{r_{n+1}} \cos \theta_{n+1} + \frac{R_\odot^4}{r_{n+1}^2},$$

$$\sin \alpha_{n+1} = \frac{R_\odot^2/r_{n+1}}{a_{n+1}} \sin \theta_{n+1}, \quad n = 0, 1, 2, \dots$$

with

$$r_{n+1}^2 = r_0^2 - 2r_0 \frac{Q^2}{a_n} \cos \alpha_n + \frac{Q^4}{a_n^2},$$

$$\cos \theta_{n+1} = \frac{r_0^2 + r_{n+1}^2 - Q^4/a_n^2}{2r_0 r_{n+1}}, \quad \sin \theta_{n+1} = \frac{Q^2/a_n}{r_{n+1}} \sin \alpha_n.$$

These two series of monopole couples together with the pair of photospheric monopoles produce a magnetic field that also satisfies the required boundary conditions.

The resultant magnetic field yields the ambient magnetic field

$$\begin{aligned} \mathbf{B}_A = & \mathbf{1}_\phi \left\{ \frac{\mu I_E}{2\pi Q} + \right. \\ & + \sum_{n=0}^{\infty} \left[\frac{\mu I_E}{\pi} \frac{Q + b_{2n} \cos \phi}{Q^2 + 2Qb_{2n} \cos \phi + b_{2n}^2} + \frac{-\mu I_E}{\pi} \frac{Q + b_{2n+1} \cos \phi}{Q^2 + 2Qb_{2n+1} \cos \phi + b_{2n+1}^2} \right] + \\ & \left. + \sum_{n=0}^{\infty} \left[\frac{\Psi_M}{\pi} \frac{-\alpha \sin(\phi + \alpha_n)}{Q^2 + 2Qa_n \cos(\phi + \alpha_n) + a_n^2} + \frac{-\Psi_M}{\pi} \frac{-a_n \sin(\phi - \alpha_n)}{Q^2 + 2Qa_n \cos(\phi - \alpha_n) + a_n^2} \right] \right\} \end{aligned}$$

on the surface of the prominence loop. The integral $\int_0^{2\pi} -\mathbf{1}_q \frac{1}{2} \mu^{-1} \mathbf{B}_A^2 Q d\phi$ yields the diamagnetic buoyancy force

$$\begin{aligned} F^{(m)} = & \mathbf{1}_r \left\{ I_E \Psi_m \sum_{n=0}^{\infty} \frac{\sin \alpha_n}{\pi a_n} \left[1 + Q^2 a_n^2 \sum_{m=0}^{\infty} (b_{2m} - b_{2m+1}) \times \right. \right. \\ & \times \frac{a_n^2(b_{2m} + b_{2m+1}) + 2a_n b_{2m} b_{2m+1} \cos \alpha_n - Q^2(b_{2m} + b_{2m+1} + 2a_n \cos \alpha_n)}{(Q^4 - 2Q^2 a_n b_{2m+1} \cos \alpha_n + a_n^2 b_{2m+1}^2)(Q^4 - 2Q^2 a_n b_{2m} \cos \alpha_n + a_n^2 b_{2m}^2)} \left. \right] + \\ & + \frac{1}{\mu} \Psi_M^2 \sum_{n=0}^{\infty} \frac{4}{\pi} Q^2 a_n \sin \alpha_n \sum_{m=0}^{\infty} a_m^2 \sin \alpha_m \times \\ & \times \frac{a_n a_m \cos \alpha_n - Q^2 \cos \alpha_m}{[Q^4 - 2Q^2 a_n a_m \cos(\alpha_n - \alpha_m) + a_n^2 a_m^2][Q^4 - 2Q^2 a_n a_m \cos(\alpha_n + \alpha_m) + a_n^2 a_m^2]} + \end{aligned}$$

$$+ \mu I_E^2 \sum_{n=0}^{\infty} \left[\frac{1}{2\pi} \left(\frac{1}{b_{2n+1}} - \frac{1}{b_{2n}} \right) + Q^2 (b_{2n} - b_{2n+1}) \sum_{m=0}^{\infty} (b_{2m} - b_{2m+1}) \times \right. \\ \left. \times \frac{(b_{2n} + b_{2n+1}) b_{2m} b_{2m+1} - Q^2 (b_{2m} + b_{2m+1})}{(b_{2n+1} b_{2m+1} - Q^2) (b_{2n} b_{2m+1} - Q^2) (b_{2n+1} b_{2m} - Q^2) (b_{2n} b_{2m} - Q^2)} \right] \Bigg\}$$

acting on the prominence loop. It is equal to the vector sum of the Biot-Savart forces (see Yeh, 1983) on the conduction and polarization currents in the prominence loop exerted by the conduction and polarization currents on the photosphere. From its leading part,

$$1_r \left[I_E \Psi_M \frac{\sin \alpha}{\pi a} + \frac{1}{\mu} \Psi_M^2 \frac{4a^3 Q^2 \sin^2 \alpha \cos \alpha}{\pi (a^2 - Q^2) (a^4 - 2a^2 Q^2 \cos 2\alpha + Q^4)} + \mu I_E^2 \frac{R_\odot^2}{2\pi r_0 (r_0^2 - R_\odot^2)} \right],$$

it is seen that the additional force due to the photospheric effect is significant when the prominence loop is close to the photospheric surface. The term proportional to I_E^2 represents the mirror-current effect discussed by Van Tend and Kuperus (1978).

Acknowledgements

The author thanks Dr William Wagner and Dr Shi-Tsan Wu for helpful discussions. The treatment of the photospheric effect was suggested by the referee, to whom the author is grateful. This work was supported by U.S. Air Force Office of Scientific Research under the contract AFOSR-88-0013.

References

- Anzer, U. and Tandberg-Hanssen, E.: 1970, *Solar Phys.* **11**, 61.
 Kippenhahn, R. and Schlüter, A.: 1957, *Z. Astrophys.* **43**, 36.
 Kuperus, M. and Raadu, M. A.: 1974, *Astron. Astrophys.* **31**, 189.
 Low, B. C.: 1981, *Astrophys. J.* **246**, 538.
 McIntosh, P. S.: 1979, *Annotated Atlas of H α Synoptic Charts*, World Data Center A Report UAG-70, NOAA, Boulder.
 Pneuman, G. W.: 1984, *Solar Phys.* **94**, 299.
 Sakurai, T.: 1976, *Publ. Astron. Soc. Japan* **28**, 177.
 Švestka, Z. F., Fontenla, J. M., Machado, M. E., Martin, S. F., Neidig, D. F., and Poletto, G.: 1987, *Solar Phys.* **108**, 237.
 Tandberg-Hanssen, E.: 1974, *Solar Prominences*, D. Reidel Publ. Co., Dordrecht, Holland.
 Van Tend, W. and Kuperus, M.: 1978, *Solar Phys.* **59**, 115.
 Vršnak, B., Ruždjak, V., and Brajša, R.: 1988, *Solar Phys.* **116**, 45.
 Yeh, T.: 1982, *Solar Phys.* **78**, 287.
 Yeh, T.: 1983, *Astrophys. J.* **264**, 630.
 Yeh, T.: 1985, *Solar Phys.* **95**, 83.
 Yeh, T.: 1988, *Astrophys. J.* **328**, 954.

SOLITON AND STRONG LANGMUIR TURBULENCE IN SOLAR FLARE PROCESSES

M. T. SONG* and S. T. WU

*Center for Space Plasma and Aeronomic Research,
The University of Alabama at Huntsville, Huntsville, Alabama, U.S.A.*

and

M. DRYER

Space Environment Lab/ERL/NOAA, Boulder, Colorado, U.S.A.

(Received 1 September, 1988)

Abstract. The occurrence of modulational instability in the current sheet is investigated. Particular attention is drawn to the plasma micro-instability in this current sheet (i.e., the diffusion region) and its relation to the flare process. It is found that the solitons or strong Langmuir turbulence is likely to occur in the diffusion region under solar flare conditions in which the electric resistivity could be greatly enhanced by several orders of magnitude in this diffusion region. The result is a significant heating and stochastic acceleration of particles. Physically, the occurrence of soliton and strong Langmuir turbulence can be identified with a sudden eruption of an electric current leading to a local vacuum in which an electric potential is formed and results in the release of a huge amount of free energy. A numerical example is used to demonstrate the transition of the magnetic field, velocity, and plasma density from the outer MHD region into the diffusive (resistive) region and, then, back out again with the completion of the energy conversion process. This is all made possible by an increase of resistivity by 4–5 orders of magnitude over the classical value.

1. Introduction

The solar flare has been recognized as a violent electromagnetic phenomenon accompanied with the release of a huge amount of energy ($\sim 10^{28}$ – 10^{32} ergs) in a rather short time (i.e., time-scales ranging from a few seconds to about a thousand seconds). Based on both observation and theoretical study, it has been agreed that this release is derived from the huge amount of energy that is stored in the various configurations of the magnetic field (see Figure 1). It has been suggested that during the onset of a flare, this stored free energy is converted into heat and kinetic energy of the particles through magnetic reconnection. This process is believed to be triggered in a current sheet either spontaneously by the resistive instability such as the tearing mode (Furth *et al.*, 1963; Ugai and Tsuda, 1977; Van Hoven *et al.*, 1980) or driven from outside when topologically separate flux systems are pushed together (Priest, 1983; Sonnerup, 1983).

It can be seen from the schematic magnetic topologies in Figure 1 that when the two different polarity flux systems are pushed together (i.e., Figures 1(a), 1(b)), the region near the X-point collapses and current sheets are then formed (Dungey, 1953; Syrovatskii, 1966). When magnetic flux tubes are braided together (Figure 1(c)), no equilibrium can be obtained in which the current sheets may also form (Syrovatskii,

* Permanent address: Purple Mountain Observatory, Nanjing, People's Republic of China.

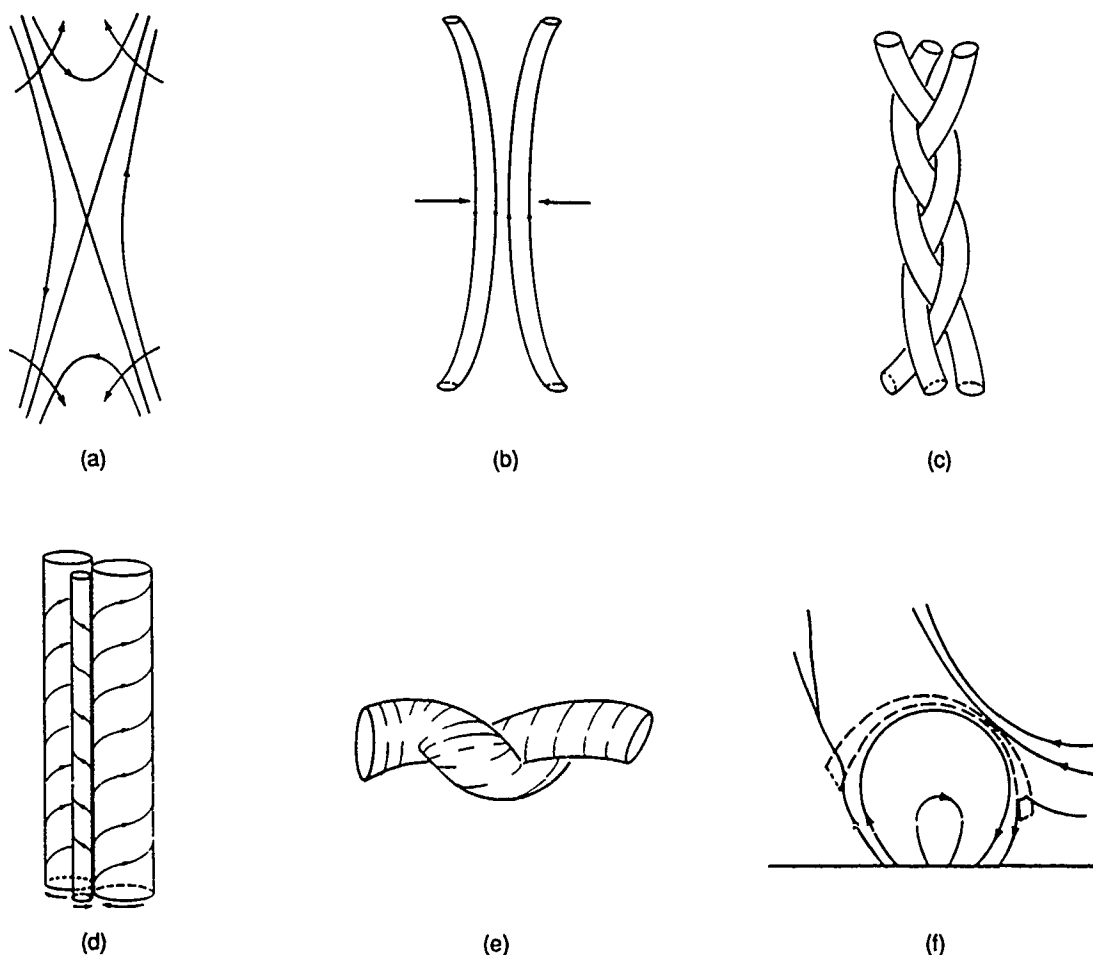


Fig. 1. Current sheet formation in variously-proposed magnetic topologies.

1978). However, when these flux tubes are twisted with the same direction of neighbouring flux tubes, then the current sheets can also be formed as shown in Figure 1(d).

Furthermore, the current sheet can be formed through ideal magnetohydrodynamics (MHD) instability processes such as the kink instability as shown in Figure 1(e) (Spicer, 1977; Parker, 1979; Hood and Priest, 1979). There is one additional possibility: as new magnetic flux emerges from below the photosphere (i.e., from the convective zone), it will create a current sheet at the interface of the overlying magnetic field as studied by Heyvaerts *et al.* (1977). Practically, the formation of a current sheet can be considered to be a dynamic process; therefore, the concept of driven reconnection in a flare process suggested by Sweet–Parker–Petschek seems to be a commendable one. Now, we shall examine this model briefly.

As shown in Figure 2, a slow steady-state inflow (along the x -axis of two oppositely-directed strongly-magnetized plasma flows), moves toward the current sheet. Subsequently, a rapid outflow of weakly magnetized plasma will be generated along the sheet (i.e., y -axis). According to Bernoulli's law,

$$p_{\infty} + \frac{B_{\infty}^2}{8\pi} = p_{\infty} + \frac{1}{2}\rho_{\infty}v_{\text{out}}^2;$$

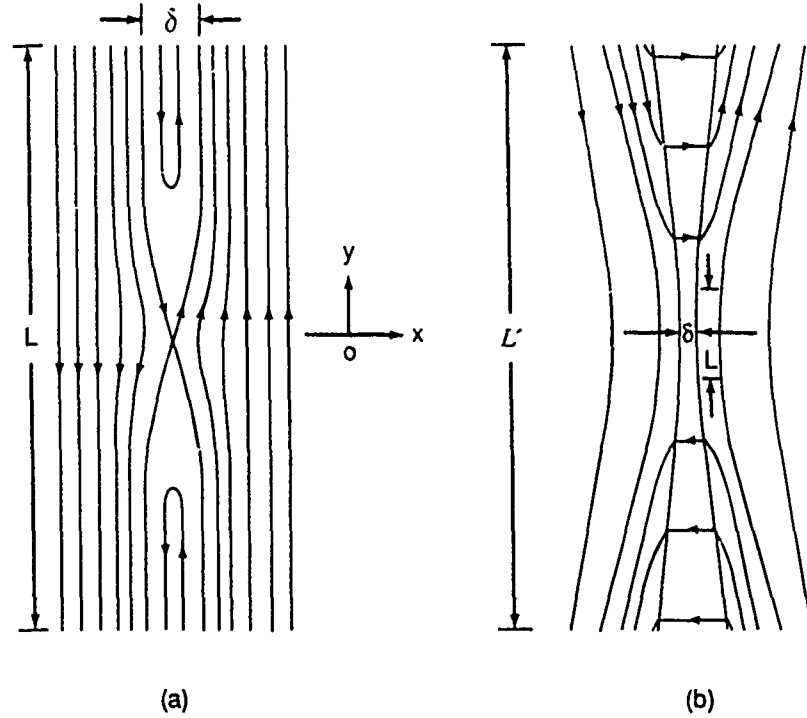


Fig. 2. Flare models. (a) Sweet-Parker model; (b) Petschek model. The resistive MHD region (with dimensions L and δ) is surrounded by the ideal MHD region everywhere else.

and thus the outflow velocity is equal to the Alfvén speed

$$V_{A\infty} = \frac{B_{\infty}}{\sqrt{4\pi\rho_{\infty}}}.$$

From the law of conservation of mass, we may write

$$\delta V_{\text{out}} = L V_{\text{in}}, \quad (1)$$

where δ and L are the thickness and length of the current sheet, respectively. The current intensity within this sheet,

$$j = \frac{c}{4\pi} |\nabla \times \mathbf{B}| \sim \frac{c}{4\pi} \frac{B_{\infty}}{\delta}$$

along the z -axis. Employing Ohm's law, we get,

$$\frac{c}{4\pi} \frac{B_{\infty}}{\delta} = j = \sigma E_{\text{inside}} = \sigma E_{\text{outside}} = \sigma \frac{B_{\infty}}{c} V_{\text{in}}; \quad (2)$$

with c and σ being the speed of light and electrical conductivity. Combination of Equations (1) and (2) yields,

$$V_{\text{in}} = V_{A\infty} \left[\frac{4\pi}{c^2} \sigma L V_{A\infty} \right]^{-1/2} = \frac{V_{A\infty}}{\sqrt{R_m}}, \quad (3)$$

with R_m being the magnetic Reynolds number.

For a typical pre-flare state (typically taken to be: $N_0 \sim 2 \times 10^{11} \text{ cm}^{-3}$, $B_\infty \sim 500 \text{ G}$, $L \sim 10^9 \text{ cm}$, $T \sim 10^4 \text{ K}$, $\sigma \sim 10^7 T^{3/2} \sim 10^{13} \text{ s}^{-1}$, $V_{A\infty} \sim 2.8 \times 10^8 \text{ cm s}^{-1}$), (then), $R_m \sim 3.4 \times 10^{10}$. However, the inflow velocity which represents the annihilation speed of magnetic field becomes too small to explain the rising time of a flare (i.e., $\sim 10^2$ – 10^3 s) as discussed by Parker (1963). In order to remedy this deficiency, Petschek (1964) devised a new model referred to as the Petschek mechanism for reconnection. In this model, Petschek introduced a slow magnetoacoustic shock to divide the flare region into three parts: the outer or MHD region; the wave or jet region; and the diffusion region. In the outer region, there is a strong magnetic field and slow speed flow. The wave region is just the opposite where there is a weak magnetic field and high speed flow. The diffusion region is a very small one such as $2y^* \times 2x^*$ as shown in Figure 2(b) where $(1/2)L$ and $(1/2)\delta$ decrease to y^* and x^* , respectively.

Taking the compressible factor $\alpha = 1$, the maximum annihilation rate could be computed,

$$V_{\text{in}} = V_{A\infty} \left(\frac{\pi}{4} \right) \{ \ln [2R_m (V_{\text{in}}/V_{A\infty})^2] \}^{-1} \simeq \\ \simeq 0.042 V_{A\infty} \sim 1.02 \times 10^7 \text{ cm s}^{-1}. \quad (4)$$

The annihilation time becomes

$$L/V_{\text{in}} \sim 10^2 \text{ s}; \quad (5)$$

the length of the diffusion region becomes

$$y^* = c^2 / [8\pi\sigma V_{A\infty} (V_{\text{in}}/V_{A\infty})^2] \sim 8.3 \text{ cm}, \quad (6)$$

and the thickness of the diffusion region becomes

$$x^* = (c^2/4\pi\sigma)/V_{\text{in}} = 0.702 \text{ cm}. \quad (7)$$

From these numerical results, we find that the model could match the rising time of a flare. However, the dimension of the diffusion region becomes unrealistically small; more specifically, the thickness (i.e., x^*) becomes close to or even smaller than the Larmor radius.

By taking the extreme compressible factor α to be 2.75×10^{-5} as suggested by Parker (1963), we find that $V_{\text{in}} \sim 3.6 \times 10^7 \text{ cm s}^{-1}$, $L/V_{\text{in}} \sim 27.7 \text{ s}$, $y^* \sim 2.43 \times 10^{-4} \text{ cm}$ and $x^* = 0.199 \text{ cm}$. This implies that the diffusion region of a flare would be degenerated to a point (i.e., the origin as shown in Figure 2) or the separator. Based on this idea, a number of authors (Coppi and Friedland, 1971; Sonnerup, 1973) developed a similarity solution which allows V_{in} to approach the Alfvén speed ($V_{A\infty}$). Obviously, such a tiny diffusion region is insignificant energetically and acts only as a source for producing the slow MHD shocks. These slow MHD shocks create hot fast jets of plasma with typically $\frac{3}{5}$ of the inflowing magnetic energy being converted into kinetic energy and $\frac{2}{5}$ into heat as demonstrated by Priest (1983).

The above description is a modified Petschek model that has been developed for years

when the original Petschek's model confronted great difficulty since its presentation in 1964.

Another way to remove this deficiency is by introducing the tearing mode instability into the flare process. This instability can break the current sheet into small fragments thereby reducing the length L and then increasing the annihilation rate (see Equation (3), and also refer to Coppi and Friedland, 1971). Friedman and Hamberger (1968, 1969) drew attention to the role of microturbulence in the current sheet; this additional physical process may enhance the annihilation rate and provide a realistic physical dimension of the diffusion region. Also, experiments indicate that the passage of a sufficiently dense current through a plasma leads to microturbulence which obstructs the electron drift and gives an anomalously small plasma electric conductivity. Thus, as soon as the microturbulence appears within the current sheet, the rate of magnetic diffusion greatly increases and would also give a reasonable physical dimension (i.e., thickness and length) of the current sheet.

In this study, we shall demonstrate that Petschek's mechanism for reconnection during the onset of a flare could be improved by introducing the microturbulence process within the current sheet. In Section 2, the theoretical model for Petschek's mechanism, in which strong microturbulence or modulational instability can occur, is described. In Section 3, the governing equations for the modulational instability are presented and investigated. The effect of solitons within the current sheet is discussed in Section 4. Final remarks on our flare model are presented in Section 5.

2. Theoretical Analysis

In a flare region, the estimated initial state (as given above) are typically: plasma number density $N_0 \sim 2 \times 10^{11} \text{ cm}^{-3}$, $B_\infty = 0.5 \text{ kG}$, characteristic length scale $L \sim 10^9 \text{ cm}$ and temperature $T_0 \sim 10^4 \text{ K}$. Within the current layer (i.e., $B \sim 0$), the total pressure balance gives a plasma compression factor $\alpha = N_0 k T_0 / N_m k T \sim N_0 k T_0 / (B_\infty^2 / 8\pi) \sim 2.76 \times 10^{-5}$. The Larmor radius of electrons ($\sim m V_\perp c / e B$) for the magnetic field strength of $B \sim 10$ to 100 G is in the range of 0.4 – 0.04 cm . The thermal velocity ($V_{Te} = (kT/m_e)^{1/2}$) is $3.89 \times 10^7 \text{ cm s}^{-1}$; electron plasma frequency $\omega_{pe} = (4\pi N_e e^2 / m_e)^{1/2} = 2.52 \times 10^{10} \text{ s}^{-1}$; and the Debye length $\lambda_d = k_d^{-1}$ (wave number corresponding to electron plasma oscillation) $= V_{Te} / \omega_{pe} = 1.54 \times 10^{-3} \text{ cm}$. The classical electric conductivity (σ) depends on the electron-ion effective collision frequency ν_{eff} which is the reciprocal of the Maxwellian relaxation time, ($\tau_a = \sqrt{m_e} (2kT)^{3/2} (8\pi n_e e^4 \ln \Lambda)^{-1}$ with $\ln \Lambda = \ln[(kT)^{3/2} e^{-3} (\pi n_e)^{-1/2}] \sim 9.8$. Then $\nu_{eff} = (\tau_a)^{-1} \sim 1.9 \times 10^7 \text{ s}^{-1}$, such that $\sigma = ne^2 / m_e \nu_{eff} = 2.62 \times 10^7 T^{3/2} / \ln \Lambda$. Subsequently, the mean free-path among particles is $\lambda_c = V_{Te} / \nu_{eff} \sim 1.9$ to 7.8 cm .

It has been known that the validity of the magnetohydrodynamic approximation in the current layer may be characterized by $\lambda \gg \lambda_c$, $\tau \gg \tau_a$ with λ and τ being the characteristic length and time in which plasma parameters may show significant inhomogeneity (Boyd and Sanderson, 1969). Based on these characteristics, the classical Petschek's model cannot meet the described criterion wherein x^* (the Petschek's characteristic length) ~ 0.2 to 0.7 cm and $\lambda < \lambda_c = 1.9 \sim 7.8 \text{ cm}$.

One of the means to resolve this difficulty is to increase the effectiveness of the resistivity (σ^{-1}). The description given in Equations (4), (6), and (7) indicates that, if σ^{-1} were to increase by 4 orders of magnitude, then the critical spatial characteristics x^* and y^* would be increased by the same order of magnitude without any appreciable change of the inflow plasma velocity (V_{in}). Accordingly, this possibility would lead to physically meaningful dimensions of the current layer in a solar flare process. That is: x^* would increase to 2×10^3 or even 7×10^3 cm, and y^* would increase to 8×10^4 or even 8×10^8 cm. Now, the question is: can σ^{-1} be enhanced by 4 orders of magnitude with a realistically physical process in the solar atmosphere?

Under a thermal equilibrium state, the resistivity (i.e., $\sim \sigma^{-1} = (m_e/e^2)(v_{eff}/n)$) depends on the temperature only. Thus, we may express $(v_{eff}/n)_{therm}$, in terms of the energy density W_T^l of Langmuir waves at thermal equilibrium conditions, as

$$\begin{aligned} \left(\frac{v_{eff}}{n}\right)_{therm} &= \frac{\omega_{pe}}{n} \frac{W_T^l}{nk_B T} = \left(\frac{\omega_{pe}}{V_{Te}}\right)^3 \frac{k_B T}{2\pi^2} = \\ &= \frac{16\sqrt{2}e^4 \ln \Lambda}{\sqrt{m_e}(2k_B T)^{3/2}}. \end{aligned} \quad (8)$$

If we consider that there is a turbulence of ion-acoustic waves whose energy density is W^s in the process, the effective ion-acoustic collision frequency between electrons and ions can be expressed (Tsytovich, 1970) by

$$\left(\frac{v_{eff}}{n}\right)_{ion-acoustic} \simeq \frac{\pi}{2} \left(\frac{\omega_{pe}}{n}\right) \frac{W^s}{nk_B T} = \frac{\pi\alpha}{2} \left(\frac{T_e}{T_i}\right)^{1/2} \left(\frac{v_{eff}}{n}\right)_{therm}, \quad (9)$$

where T_e and T_i are the temperatures of electrons and ions, respectively, and α is the ratio of W^s/W_T^s , with W_T^s being the energy density of ion-acoustic wave at thermal equilibrium (i.e., $W_T^s = W_T^l(T_e/T_i)^{1/2}$).

According to the order of estimation, it was found (according to the solar conditions assumed above) that $W_T^l/nk_B T \sim W_T^s/nk_B T \sim 10^{-4}$. Under these conditions there exists linear wave or weak ion-acoustic wave turbulence, the ratio of $W^s/nk_B T$ becomes 10^{-2} , thus the value of α could be on the order of 10^2 . However, when the nonlinear wave or strong turbulence is excited, $W^s/nk_B T$ could be unity and then $\alpha \sim 10^4$. This implies, according to Equation (9), the resistivity ($\sim \sigma^{-1}$) could be 10^4 orders of magnitude larger than its classical value at thermal equilibrium when the strong turbulence is excited. It is worth noting that Spicer (1977) has been able to show that anomalous resistivity in the current layer can only be 10^2 (order of magnitude) larger than its classical value.

The present proposed improved Petschek type flare model is similar to the work of Coppi and Friedland (1971) except that we have included the strong turbulence effect in the resistive region. Thus, the basic governing equation appropriate for this study can be described by a set of two-dimensional time-stationary, MHD flow equations such

as,

$$\nabla \cdot (\rho \mathbf{V}) = 0, \quad (10)$$

$$\rho(\mathbf{v} \cdot \nabla) \mathbf{v} = -\nabla(c_s^2 \rho) + \frac{1}{c} \mathbf{j} \times \mathbf{B} + \mu \nabla^2 \mathbf{v} + \frac{1}{3} \mu \nabla(\nabla \cdot \mathbf{v}), \quad (11)$$

$$\nabla \cdot \mathbf{B} = 0, \quad \nabla \times \mathbf{B} = \frac{4\pi}{c} \mathbf{J}, \quad (12)$$

$$\nabla \times \mathbf{E} = 0, \quad \mathbf{J} = \eta^{-1} \left(\mathbf{E} + \frac{1}{c} \mathbf{v} \times \mathbf{B} \right), \quad (13)$$

where c_s is the sound speed (i.e., $c_s = \sqrt{p/\rho}$) being almost a constant except in the current sheet. Since plasma turbulence exists in the current sheet, the resistivity (η) could not be a constant. However, the electric field $\mathbf{E} (= V_{in} B_{\infty}/c) \hat{\mathbf{Z}}$ and viscosity (μ) are considered to be constant. To seek a solution, we introduce the magnetic field potential and velocity potential as:

$$\rho \mathbf{v} = \nabla \times \psi, \quad \mathbf{B} = \nabla \times \mathbf{A};$$

where

$$\mathbf{A} = A(x, y) \hat{\mathbf{Z}}, \quad \psi = \psi(x, y) \hat{\mathbf{Z}}.$$

Thus the set of basic governing equations becomes,

$$[(\nabla \times \psi) \nabla - \mu \nabla^2 - \frac{1}{3} \mu \nabla \nabla] \left(\frac{\nabla \times \psi}{\rho} \right) + \frac{\nabla^2 A}{4\pi} \nabla A + \nabla(c_s^2 \rho) = 0, \quad (14)$$

$$\hat{\mathbf{Z}}(D_m \nabla^2 A + v_{in} B_{\infty}) + \rho^{-1} (\nabla \times \psi) \times (\nabla \times \mathbf{A}) = 0, \quad (15)$$

with $D_m = \eta c^2/4\pi$.

Now, the task left for us is to seek a solution for this set of Equations (14) and (15) with proper boundary conditions in both the ideal MHD and in the resistive MHD regions, respectively, as shown in Figure 2. In the ideal MHD region the viscosity and resistivity terms can be neglected; Equation (14) reduces to $\nabla^2 A = 0$, because the terms of $\nabla \times \psi$ and $\nabla(c_s^2 \rho)$ vanish thereby implying that the magnetic field must be a potential field (i.e., no current). If we regard ρ being constant or known, ψ can be solved from Equation (15). This solution represents an asymptotic one in the outer region (i.e., ideal MHD region). In the resistive region ($|x| < 10^4$ cm, $|y| < 10^7$ cm), the viscosity effect is ignored because the density and turbulence are not strong enough in this region. With this assumption, Equations (14) and (15) turn out to be three equations for three

variables ρ , A , and ψ . Using the boundary conditions at the origin ($x = 0$, $y = 0$); $\rho \rightarrow a_1$,

$$A \rightarrow \frac{1}{2} a_2 \left[\left(\frac{y}{\lambda_E} \right)^2 - (1 + a_2^{-1}) \left(\frac{x}{\lambda_E} \right) \right] b \quad \text{and} \quad \psi \rightarrow -a_3 xy.$$

Together with continuous properties at the interface between the MHD and resistive regions, the inside solution can be consistent with the outside solution. The asymptotic features of \mathbf{B} and \mathbf{V} near x - and y -axis are shown in Figure 3. These solutions are similar to those given by Coppi and Friedland (1971) and Vasyliunas (1975) except for the fact that the present solution gives more realistic physical dimensions for the resistive region.

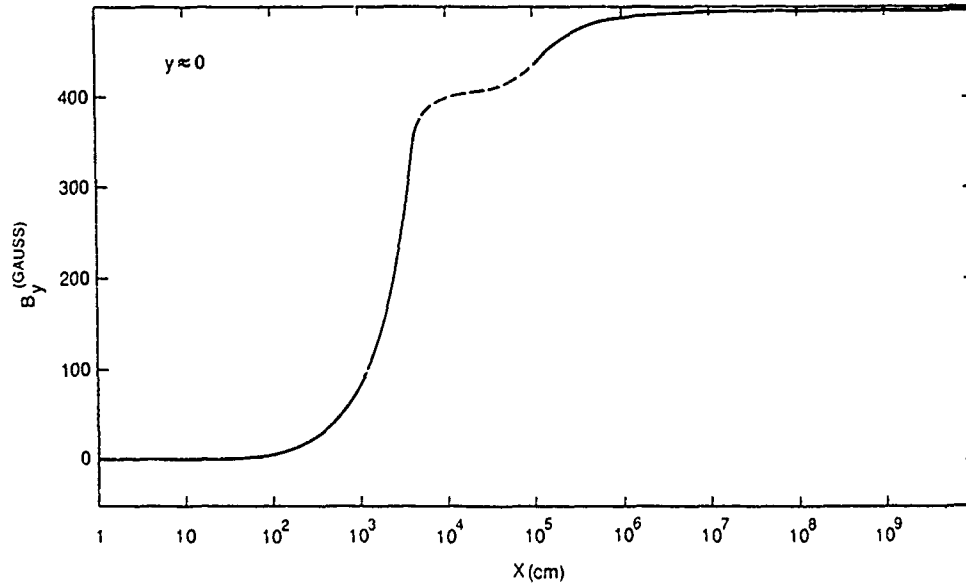


Fig. 3a.

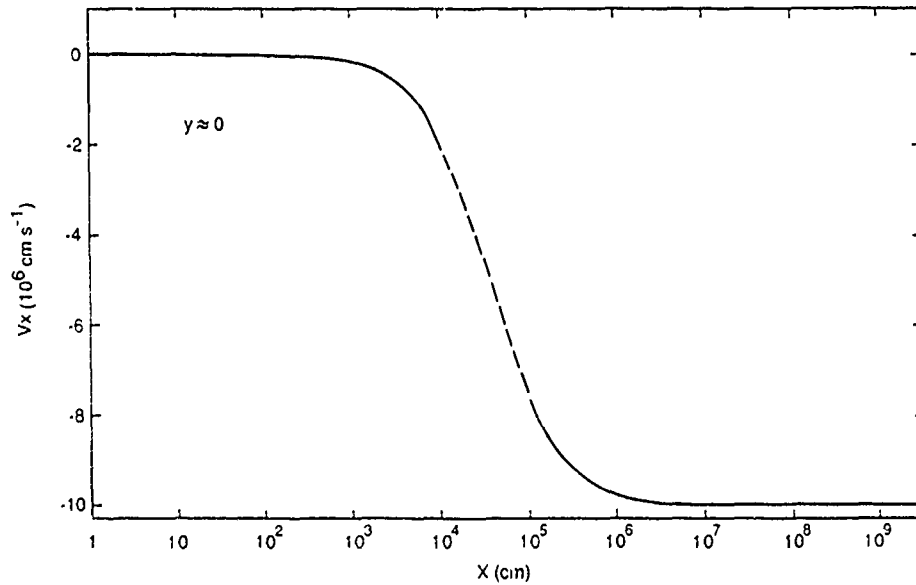


Fig. 3b.

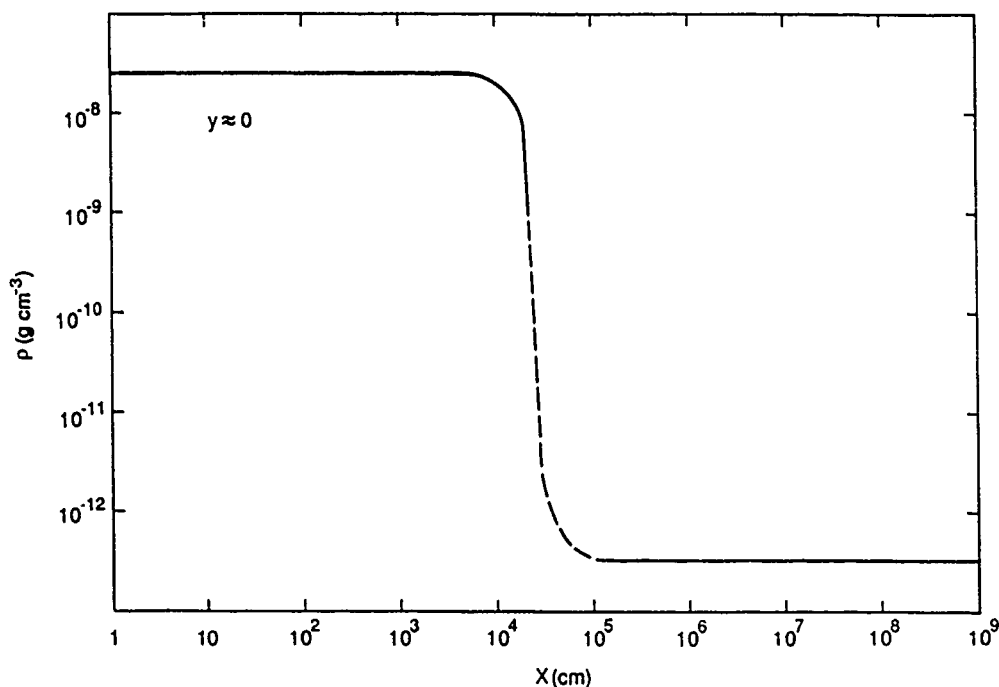


Fig. 3c.

Fig. 3. Magnetic field, velocity, and density profile transitions from the ideal MHD region into the resistive MHD region along the x -axis (i.e., $y = 0$). (a) B_y profile (b) v_x profile; (c) density profile. (See Section 4 for details.)

3. Electrohydrodynamics and Modulational Instability in Current Layer

It has been pointed out by Alfvén and Carlquist (1967) that the necessary condition for a sudden release of free-energy stored in a electromagnetic flow system is the requirement that the average particle velocity should exceed the thermal speeds (i.e., $v_i, v_e \gg v_{Ti}, v_{Te}$). In the laboratory case, when electric current exceeds some threshold the interruption of the circuit will occur, a situation which can lead to an explosion that destroys the equipment. As discussed in the previous section, there exists a strong electric current in the resistive region (i.e., the flare current layer). This situation allows us to apply the EHD (electrohydrodynamics) and modulation instability in this region for our investigation.

In order to carry out this study, we must distinguish the difference between two characteristic scales in relation to these two methods (i.e., MHD and modulation instability). When $\lambda \sim 10$ cm, $\tau \sim 1$ s, the resistive region could be described by means of an MHD model because small angle collisions play a dominant role in this region. On the other hand, when $\lambda \sim 10^{-2}$ cm, $\tau \sim 10^{-8}$ s, the resistive region should be considered as a collisionless plasma. Since $v_i, v_e > v_{Ti}, v_{Te}$, the effect of collisions (or thermal motion) can be neglected compared with the coherent action produced by self-consistent fields (Boyd and Sanderson, 1969). Thus, Vlasov's equation should be used in the resistive region, namely,

$$\frac{\partial f}{\partial t} + \mathbf{v} \cdot \frac{\partial f}{\partial \mathbf{r}} + \frac{\mathbf{F}}{m} \cdot \frac{\partial f}{\partial \mathbf{v}} = 0, \quad (16)$$

where the force $\mathbf{F} = \mathbf{E} + (1/c)\mathbf{v} \times \mathbf{B}$ is produced by self-consistent fields. In such a case, assuming a certain form (e.g., Maxwellian) of particle velocity distribution, the fluid description is also meaningful (Boyd and Sanderson, 1969) by taking the first and second moments of Equation (16). This procedure gives the conservation of momentum and mass for electrons and ions, respectively, as

$$\frac{\partial \mathbf{v}_e}{\partial t} + (\mathbf{v}_e \cdot \nabla) \mathbf{v}_e = \frac{e}{m_e} \mathbf{E} - \frac{e}{m_e c} (\mathbf{v}_e \times \mathbf{B}) - \frac{\gamma_e T_e k_B}{m_e n_e} \nabla n_e, \quad (17)$$

$$\frac{\partial \mathbf{v}_i}{\partial t} + (\mathbf{v}_i \cdot \nabla) \mathbf{v}_i = \frac{e}{m_i} \mathbf{E} + \frac{e}{m_i c} (\mathbf{v}_i \times \mathbf{B}) - \frac{\gamma_i T_i k_B}{m_i n_i} \nabla n_i, \quad (18)$$

$$\frac{\partial n_e}{\partial t} + \nabla \cdot (n_e \mathbf{v}_e) = 0, \quad (19)$$

$$\frac{\partial n_i}{\partial t} + \nabla \cdot (n_i \mathbf{v}_i) = 0; \quad (20)$$

and the approximate energy equation for ions and electrons are

$$P_{i,e} = \gamma_{i,e} k_B T_{i,e} n_{i,e}.$$

The self-consistent field quantities (i.e., \mathbf{E} and \mathbf{B}) are given by Maxwell's equations

$$\left. \begin{aligned} \nabla \cdot \mathbf{E} &= 4\pi e(n_i - n_e), \\ \nabla \times \mathbf{E} &= -\frac{1}{c} \frac{\partial \mathbf{B}}{\partial t}, \\ \nabla \times \mathbf{B} &= \frac{1}{c} \frac{\partial \mathbf{E}}{\partial t} + \frac{4\pi}{c} e(n_i \mathbf{v}_i - n_e \mathbf{v}_e), \\ \nabla \cdot \mathbf{B} &= 0. \end{aligned} \right\} \quad (21)$$

Under the flare conditions, there are accelerated ions having high speed (sound speed $c_s \geq (k_B T_e/m_i)^{1/2} \sim 9.09 \times 10^5 \text{ cm s}^{-1}$) in the current layer, thus, $v_i > v_{Ti}$. Since strong E_{outside} exists, the electrons have velocity greater than 10^7 cm s^{-1} , thus, these electrons oscillate between groups of protons having high speed which may lead to fast fluctuation of particle density. It is this fluctuation that produces very strong self-consistent fields. In the meantime, it is necessary to distinguish the slow oscillation and slow time-scale (ω_{pi}^{-1}) from fast oscillation and fast time-scale (ω_{pe}^{-1}). It is understood that electrons can have both slow and fast time-scale but protons can only have slow time-scale. This principle is needed to treat plasma turbulence and modulation instability (Hasegawa, 1975; Rudakov and Tsytovich, 1978; Li, 1985).

To analyze the set of Equations (17) through (21), we have assumed that the average

of the fast component of a single quantity to be zero,

$$\begin{aligned}
 n_i &= n_{is}, & n_e &= n_{es} + n_f^T, \\
 \langle n_f^T \rangle &= 0, \\
 \langle n_i - n_e \rangle &= 0, & \text{or } n_{is} &= n_{es} = n_s, \\
 \mathbf{v}_e &= \mathbf{v}_{es} + \mathbf{v}_f^T, & \langle \mathbf{v}_f^T \rangle &= 0, \\
 \mathbf{v}_i &= \mathbf{v}_{is}, \\
 \mathbf{E} &= \mathbf{E}_s + \mathbf{E}_f^T, & \langle \mathbf{E}_f^T \rangle &= 0, \\
 \mathbf{B} &= \mathbf{B}_f^T, & \langle \mathbf{B}_f^T \rangle &= 0.
 \end{aligned} \tag{22}$$

Inserting Equation (22) into Equation (17), we obtain

$$\begin{aligned}
 \frac{\partial}{\partial t} (\mathbf{v}_{es} + \mathbf{v}_f^T) + [(\mathbf{v}_{es} + \mathbf{v}_f^T) \nabla] (\mathbf{v}_{es} + \mathbf{v}_f^T) = \\
 = -\frac{e}{m_e} (\mathbf{E}_s + \mathbf{E}_f^T) - \frac{e}{m_e c} (\mathbf{v}_{es} \times \mathbf{B}_f^T + \mathbf{v}_f^T \times \mathbf{B}_f^T) - \\
 - \frac{\gamma_e k_B T_e}{m_e n_s} \nabla (n_s + n_f^T).
 \end{aligned} \tag{23}$$

Averaging Equation (23) over many fast time-interval of ω_{pe}^{-1} , we find that

$$\begin{aligned}
 \frac{\partial}{\partial t} (\mathbf{v}_{es}) + (\mathbf{v}_{es} \cdot \nabla) \mathbf{v}_{es} + \langle (\mathbf{v}_f^T \cdot \nabla) \mathbf{v}_f^T \rangle = \\
 = -\frac{e}{m_e} \mathbf{E}_s - \frac{e}{m_e c} \langle \mathbf{v}_f^T \times \mathbf{B}_f^T \rangle - \frac{\gamma_e k_B T_e}{m_e n_s} \nabla n_s,
 \end{aligned} \tag{24}$$

Physically, Equation (24) represents slow motion under the slow time-scale and

$$-\langle (\mathbf{v}_f^T \cdot \nabla) \mathbf{v}_f^T \rangle - \frac{e}{m_e c} \langle \mathbf{v}_f^T \times \mathbf{B}_f^T \rangle$$

represents the force produced by the fast oscillation of electrons. Subtracting Equation (24) from Equation (23) gives the equation of fast component, \mathbf{v}_f^T (see Appendix A for details)

$$\frac{\partial \mathbf{v}_f^T}{\partial t} = -\frac{e}{m_e} \mathbf{E}_f^T - \frac{\gamma_e T_e k_B}{m_e n_s} \nabla n_f^T. \tag{25}$$

To obtain this equation, the following conditions are used:

$$k_d/k \gg 1, \quad W_f \sim 1, \quad W_s \sim 10^{-2}. \tag{26}$$

Obviously, the fast component magnetic field \mathbf{B}_f^T is produced by the fast motion of electrons \mathbf{v}_f^T . Using Equations (21) and (25), we found that

$$-\frac{1}{c} \frac{\partial \mathbf{B}_f^T}{\partial t} = \nabla \times \mathbf{E}_f^T = -\frac{m_e}{e} \nabla \times \left(\frac{\partial \mathbf{v}_f^T}{\partial t} \right).$$

Integrating the above equation we obtain

$$\mathbf{B}_f^T = -\frac{m_e c}{e} \nabla \times (\mathbf{v}_f^T). \quad (27)$$

Then the force term becomes

$$-\langle (\mathbf{v}_f^T \cdot \nabla) \mathbf{v}_f^T \rangle - \frac{e}{m_e c} \langle \mathbf{v}_f^T \times \mathbf{B}_f^T \rangle = -\frac{1}{2} \nabla \langle (\mathbf{v}_f^T)^2 \rangle,$$

which is called the striction force (Rudakov *et al.*, 1978) or modulation force. Then Equation (24) can be expressed by

$$\frac{\partial \mathbf{v}_{es}}{\partial t} + (\mathbf{v}_{es} \cdot \nabla) \mathbf{v}_{es} = -\frac{e}{m_e} \mathbf{E}_s - \frac{\gamma_e k_B T_e}{m_e n_s} \nabla n_s - \frac{1}{2} \nabla \langle (\mathbf{v}_f^T)^2 \rangle. \quad (28)$$

As there is no slow component of \mathbf{B} , Equation (18) gives

$$\frac{\partial \mathbf{v}_{is}}{\partial t} + (\mathbf{v}_{is} \cdot \nabla) \mathbf{v}_{is} = \frac{e}{m_i} \mathbf{E}_s - \frac{\gamma_i k_B T_i}{m_i n_s} \nabla n_s. \quad (29)$$

Let us now examine Equations (28) and (29) to determine the conditions under which $\mathbf{v}_{es} = \mathbf{v}_{is}$ and then modulation instability could occur. From Equation (25), it follows that

$$v_f^T \sim \frac{e}{m_e \omega_{pe}} E_f^T = W_f^{1/2} v_{Te},$$

$$W_f^T \equiv (E_f^T / 4\pi) / n_s k_B T_e.$$

For strong turbulence, $W_f^T \sim 1$, then $v_f^T \sim 3.69 \times 10^7 \text{ cm s}^{-1}$ and $E_f^T \approx 1.77\text{--}177 \text{ statvolt cm}^{-1}$. (These estimations are based on $\alpha = 1, 10^{-4}$, $n_0 = 2 \times 10^{10-11}$ at $T_0 = 10^4 \text{ K}$, respectively.)

From Equation (29), we may estimate the slow scale component of ion speed as

$$v_{is} \sim \frac{e}{m_i \omega_{pi}} E_s = W_s^{1/2} \sqrt{\frac{m_e}{m_i}} v_{Te}.$$

If we take $W_s \sim 0.01$, then $v_{is} > 8.6 \times 10^4 \text{ cm s}^{-1}$, $E_s \sim 0.19\text{--}19 \text{ statvolt cm}^{-1}$. From these estimated values, it is obvious that expressions of Equations (28) and (29) are compatible when $\nabla \langle (\mathbf{v}_f^T)^2 \rangle$ and $(\gamma_e T_e k_B / m_e n_s) \nabla n_s$ have the same order of magnitude as $(e/m_i) E_s$, if we choose the length scale $\lambda (\lambda = k^{-1})$ adequately.

For example, if we take k being 10^2 and 10^4 (corresponding to compression factor α being 1 and 10^{-4} , respectively), $k \ll k_d$ which satisfies Equation (26) immediately. The values for other terms are:

$$\nabla \langle (v_f^T)^2 \rangle \sim k(3.7 \times 10^7)^2 \sim 1.37 \times 10^{17},$$

$$\frac{\gamma_e T_e k_B}{m_e n_s} \nabla n_s \sim 4.54 \times 10^{17},$$

$$\frac{e}{m_e} E_s \sim 9.81 \times 10^{16}.$$

In obtaining these results, we have chosen $\alpha = 1$ and $\gamma_e = 3$ (for strong turbulence).

According to these estimations, we should be able to choose

$$\mathbf{v}_{i,s} = \mathbf{v}_{e,s} = \mathbf{v}_s. \quad (30)$$

By combining Equations (28) and (29), we get

$$\frac{\partial \mathbf{v}_s}{\partial t} + (\mathbf{v}_s \cdot \nabla) \mathbf{v}_s = -(\gamma_e T_e + \gamma_i T_i) \frac{k_B \cdot \nabla n_s}{m_i n_s} - \frac{m_e}{2m_i} \nabla \langle (v_f^T)^2 \rangle. \quad (31)$$

Let us return to Equation (26) and set

$$\left. \begin{aligned} n_s &= n_0 + \delta n, \quad \text{with } n_0 \equiv \text{const. } |\delta n| \ll n_0, \\ \mathbf{v}_f^T &= \frac{1}{2} \mathbf{v}(\mathbf{r}, t) e^{-i\omega_{pe}t} + \frac{1}{2} \mathbf{v}^*(\mathbf{r}, t) e^{i\omega_{pe}t}, \\ \mathbf{E}_f^T &= \frac{1}{2} \mathbf{E}(\mathbf{r}, t) e^{-i\omega_{pe}t} + \frac{1}{2} \mathbf{E}^*(\mathbf{r}, t) e^{i\omega_{pe}t}, \end{aligned} \right\} \quad (32)$$

By aid of Equation (25), Equation (31) becomes

$$\frac{\partial \mathbf{v}_s}{\partial t} = -k_B(\gamma_e T_e + \gamma_i T_i) \frac{\nabla(\delta n)}{m_i n_0} - \frac{e^2}{4m_i m_e \omega_{pe}^2} \nabla |\mathbf{E}(\mathbf{r}, t)|^2, \quad (33)$$

where $|\mathbf{E}(\mathbf{r}, t)|^2 \equiv \mathbf{E}(\mathbf{r}, t) \cdot \mathbf{E}^*(\mathbf{r}, t)$ represents the square of the amplitude of the fast oscillating electric field.

Observation of Equation (33) shows that the slow motion is controlled by the gradient of density fluctuations and modulational force. Similarly, substitution of Equation (22) into Equations (19) and (20) together with condition Equation (26) provides simplified expressions for fast and slow components of particle density of the form

$$\frac{\partial n_f^T}{\partial t} + \text{div}(n_s \mathbf{v}_f^T) = 0, \quad (34)$$

$$\frac{\partial n_s}{\partial t} + \text{div}(n_s \mathbf{v}_s + \langle n_f^T \mathbf{v}_f^T \rangle) = 0. \quad (35)$$

Because $n_s \mathbf{v}_s \gg \langle n_f^T \mathbf{v}_f^T \rangle$, Equation (35) becomes

$$\frac{\partial n_s}{\partial t} + \text{div}(n_s \mathbf{v}_s) = 0.$$

Using Equation (32), we obtained,

$$\frac{\partial(\delta n)}{\partial t} + n_0 \text{div} \mathbf{v}_s = 0. \quad (36)$$

By use of Equation (27), the induced magnetic field \mathbf{B}_f^T could be estimated, such as, $B_f^T \sim (m_e c / e) k V_f^T \sim 2 \times 10^2 - 2 \times 10^4$ G for $\alpha = 1 - 10^{-4}$, respectively. This condition confirms our previous description that the self-consistent fields in the current layer are much larger than those outside. These values can be summarized as

$$\begin{aligned} E_f^T &\sim 1.8 - 180, & E_{\text{outside}} &\sim 0.3; \\ B_f^T &\sim 10^4, & B_{\text{outside}} &\sim 10 - 50 \text{ G}. \end{aligned}$$

Since the fast oscillating electric field (\mathbf{E}_f^T) would propagate in the current layer, its propagation equation under the condition of Equation (26) can be expressed by

$$\begin{aligned} \nabla \times \mathbf{B}_f^T &= \frac{1}{c} \frac{\partial \mathbf{E}_f^T}{\partial t} - \frac{4\pi e}{c} (n_s \mathbf{v}_f^T + n_f^T \mathbf{v}_s + n_f^T \mathbf{v}_f^T - \langle n_f^T \mathbf{v}_f^T \rangle) \simeq \\ &\simeq \frac{1}{c} \frac{\partial \mathbf{E}_f^T}{\partial t} - \frac{4\pi e}{c} n_s \mathbf{v}_f^T. \end{aligned}$$

Then

$$-c^2 \nabla \times (\nabla \times \mathbf{E}_f^T) = c \nabla \times \frac{\partial \mathbf{B}_f^T}{\partial t} = \frac{\partial^2 \mathbf{E}_f^T}{\partial t^2} - 4\pi e n_s \frac{\partial \mathbf{v}_f^T}{\partial t}. \quad (37)$$

The term $\mathbf{v}_f^T (\partial n_s / \partial t)$ has been ignored in Equation (37) because it is much smaller than $n_s (\partial \mathbf{v}_f^T / \partial t)$. Inserting Equation (25) into Equation (37), we obtain

$$\frac{\partial^2 \mathbf{E}_f^T}{\partial t^2} + c^2 \nabla \times (\nabla \times \mathbf{E}_f^T) + \frac{4\pi e^2}{m_e} n_s \mathbf{E}_f^T - \frac{i_e T_e k_B}{m_e} \nabla (\nabla \cdot \mathbf{E}_f^T) = 0, \quad (38)$$

where $-4\pi e n_s^T = \nabla \cdot \mathbf{E}_f^T$ (see Equation (21)). It could be noted that Equation (38) represents the propagation equation for \mathbf{E}_f^T .

Substituting Equation (32) into Equation (38) and ignoring the term $\frac{1}{2} (\partial^2 \mathbf{E}(\mathbf{r}, t) / \partial t^2) e^{-i\omega_{pe} t}$ (in comparison with the term: $-2i\omega_{pe} (\partial \mathbf{E}(\mathbf{r}, t) / \partial t) e^{-i\omega_{pe} t}$), we obtain two equations to govern the fields $\mathbf{E}(\mathbf{r}, t)$ and $\mathbf{E}^*(\mathbf{r}, t)$ with one being the conjugate of the other. Thus, it is enough to write down one of the two as

$$\begin{aligned} -2i\omega_{pe} \frac{\partial \mathbf{E}(\mathbf{r}, t)}{\partial t} + c^2 \nabla \times (\nabla \times \mathbf{E}(\mathbf{r}, t)) - \frac{i_e k_B T_e}{m_e} \nabla (\nabla \cdot \mathbf{E}(\mathbf{r}, t)) + \\ + \frac{\delta n}{n_0} \omega_{pe}^2 \mathbf{E}(\mathbf{r}, t) = 0. \end{aligned} \quad (39)$$

Finally, we obtain a set of equations (i.e., Equations (33), (36), and (39); Li, 1985) for the investigation of the modulation instability in the flare current layer; the first two equations being the conservation laws of momentum and mass, and the third one is the propagation equation for the electric field. According to Vedenov and Rudakov (1965), the criterion for the occurrence of the modulation instability is $W/nk_B T_e > \zeta(\Delta k)r_d^2$ with $\zeta \sim 1$. Vedenov and Rudakov (1965) state that, when this condition is attained, the striction force $(-\frac{1}{2}\nabla \langle v_f^2 \rangle)$ removes both electrons and ions from the density rarefaction. This leads to an increase of the 'lens effect', thus more Langmuir waves will be trapped and the striction force increases. Subsequently, the modulation interactions begin to develop, which confirms our analysis as stated above that, when the particle velocities exceed their thermal speeds and the electrons have great drifting velocity (as high as their thermal speeds), then the electrons will oscillate among a group of protons thereby leading to enhancement of the striction force.

At the onset of a flare, the effective electric field within the current layer approximately equals the electric field outside the current layer (E_{outside}): namely,

$$E_{\text{effective}} = \left| \mathbf{E} + \frac{1}{c} \mathbf{v} \times \mathbf{B} \right| \sim E_{\text{outside}} \sim \frac{1}{c} v_{\text{in}} B_{\infty} \sim 0.33$$

(where we took: $v_{\text{in}} \sim 10^7 \text{ cm s}^{-1}$, $B_{\infty} \sim 500 \text{ G}$), and then an electron will gain a velocity of 10^7 cm s^{-1} in a time-scale of ω_{pe}^{-1} (i.e., $(e/m_e)E_{\text{outside}}\omega_{pe}^{-1} = 6.3 \times 10^6 \text{ cm s}^{-1}$). In the meantime, both electrons and protons have group velocity near 10^6 cm s^{-1} . Therefore, under these two conditions (i.e., large driven current, $\mathbf{j} = \sigma E_{\text{outside}}$ and large ion speed, the modulational instability will occur in the flare current layer.

4. Soliton and Strong Langmuir Turbulence

We have made a more detailed numerical study of our analysis as it is applied to the Petschek model (as modified by Coppi and Friedland, 1971). We show that the plasma flow is first pushed along the x -axis into the resistive region where it gradually changes its direction and, finally, is expelled (with the required energy conversion) along the y -axis with an Alfvén speed of about $2 \times 10^8 \text{ cm s}^{-1}$. In the MHD region we choose the parameters (consistent with the above analysis) as follows: $L = 10^9 \text{ cm}$; $B_f = 500 \text{ G}$; $v_f = 10^7 \text{ cm s}^{-1}$; $T_f = 10^4 \text{ K}$; $n_f = 2 \times 10^{11} \text{ cm}^{-3}$; $\lambda = 10^5 \text{ cm}$. Hence, $x^* = x/\lambda$ and $y^* = 10^{-3} (y/\lambda)$. Near the x -axis, we take

$$B_y = B_f(1 - y^{*4}/80) [1 - (4x^*)^{-1}] .$$

$$v_x = -v_f [1 - (4x^*)^{-1}] .$$

Near the y -axis, we take

$$B_x = (B_f/24) [1 + x^{*4}/80] [1 - (4y^*)^{-1}] ,$$

$$v_y = 24v_f [1 + (4y^*)^{-1}] .$$

In the diffusion region, we choose: $T = 10^5$ K; $c_s = 3 \times 10^6$ cm s $^{-1}$; $\lambda_e = D_m/c_s = 2.4 \times 10^4$ cm; $D_m = \eta c^2/4\pi = [10^{-9}]$; $\mathbf{B} = v_f B_f/c_s = 10B_f/3$; $\bar{\rho} = v_a^2 v_f^2 \rho_f/c_s^4 = 2.45 \times 10^{-3}$ cm $^{-3}$. We also use the following approximate representations:

$$B_y = 1.2\bar{B}(x/\lambda_e),$$

$$B_x = 0.2(10B_f/3)(y/2.4 \times 10^4),$$

$$v_x = -c_s \sqrt{2}(x/\lambda_e)[1 - 0.9(x/\lambda_e)^2]^{-1},$$

$$v_y = \sqrt{2}c_s(y/\lambda_e)[1 - 1.2(y/\lambda_e)^2]^{-1}$$

and

$$\rho = (\bar{\rho})[1 - 1.2(x/\lambda_e)^2 - 0.9(y/\lambda_e)^2].$$

The results of our numerical experiment are shown in Figures 3 and 4 which show the magnetic field, velocity, and density profile transitions. Figure 3 shows these transitions along the x -axis ($y \simeq 0$) as the plasma flows from the MHD region into the resistive region toward the origin. Figure 4 shows the transitions along the y -axis ($x \simeq 0$) as the plasma [turns and] flows out of the resistive region back into the MHD region having completed the flare energy conversion process from magnetic to kinetic and thermal energies.

We have shown that the flow was first pushed along the x -axis into the resistive region, gradually changed its direction, and finally was expelled along the y -axis with Alfvén speed being $\sim 2 \times 10^8$ cm s $^{-1}$ (see Figure 4(b)). The effective electric field exists only in the z -direction. (Note, as in the MHD region, the effective electric field disappeared,

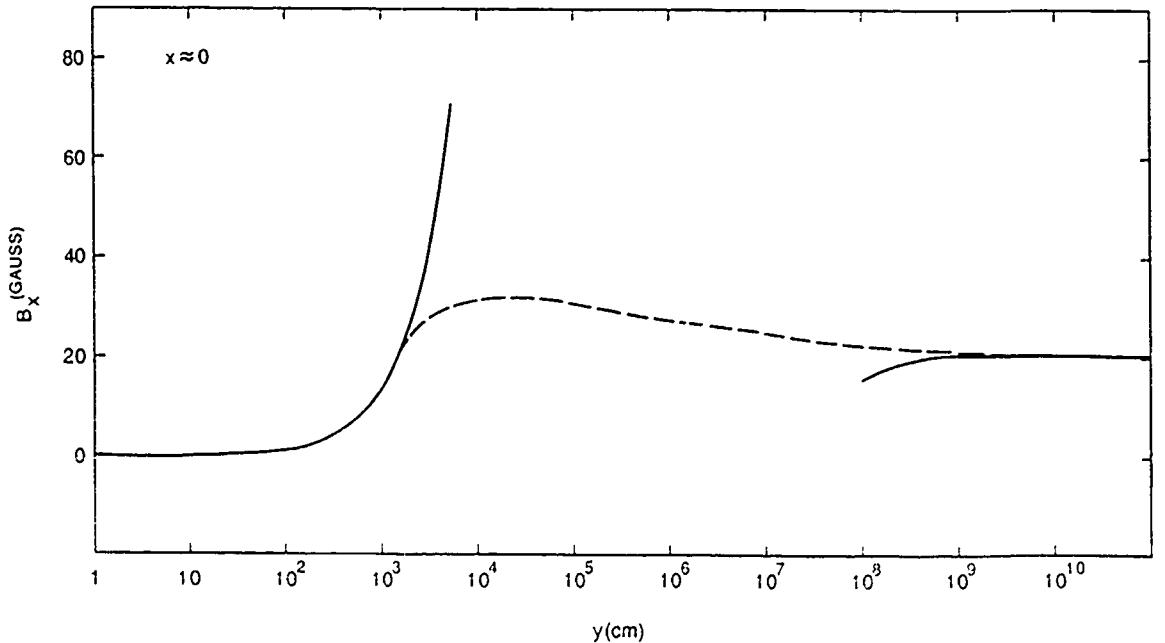


Fig. 4a.

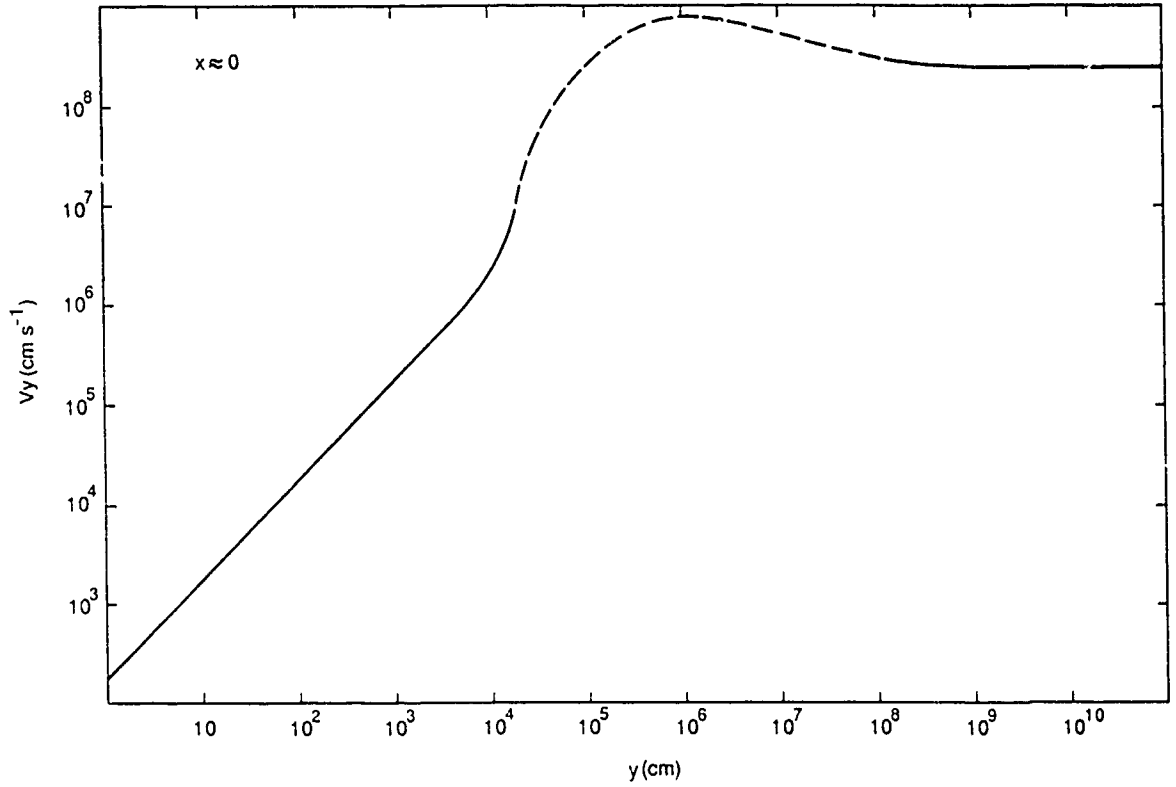


Fig. 4b.

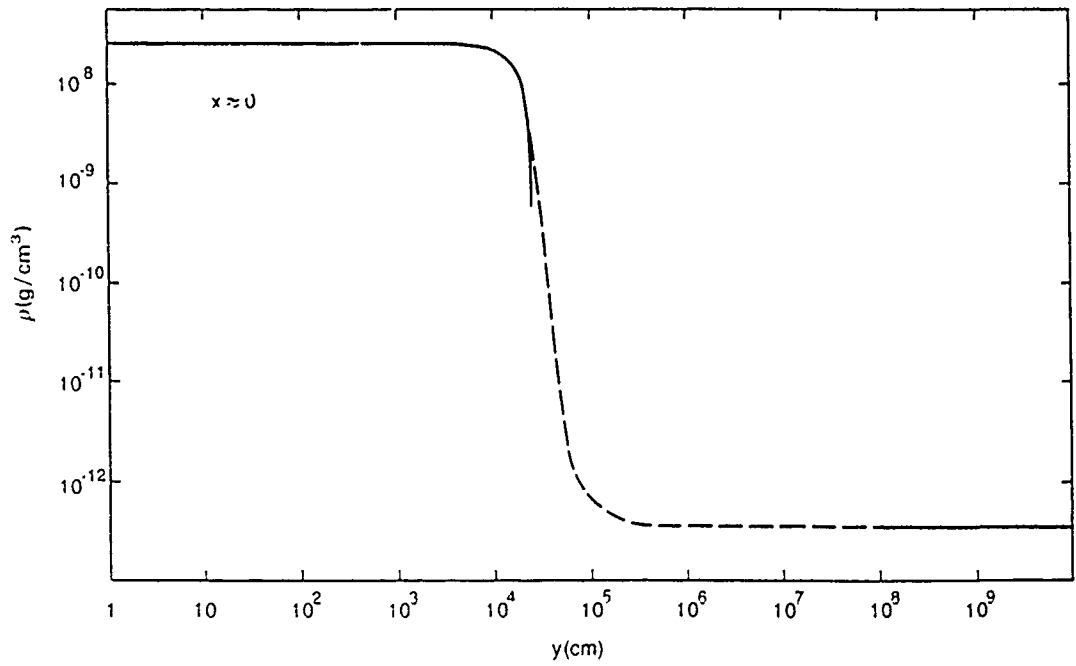


Fig. 4c.

Fig. 4. Magnetic field, velocity, and density profile transitions from the resistive MHD region into the ideal MHD region along the y -axis (i.e., $x \approx 0$). (a) B_x profile; (b) v_y profile; and (c) density profile. (See Section 4 for details.)

thus there is no particle acceleration along the z -axis.) Thus, in a short time ($\sim \omega_i^{-1}$), electrons and protons will gain their velocities in Z -direction exceeding their thermal speed, i.e., $v_e > 10^7 \text{ cm s}^{-1}$ and $v_i > 10^6 \text{ cm s}^{-1}$. Therefore, this induced driven-current would cause the modulation instability to occur along the Z -direction within the current layer of the solar flare. Since there is only a weak field (high β -plasma), it is permissible to treat this case as one-dimensional micro-instability problem. Thus, Equations (33), (36), and (39) become

$$\frac{\partial v_s}{\partial t} = - \frac{k_B(\gamma_e T_e + \gamma_i T_i)}{m_i} \frac{\partial}{\partial z} \left(\frac{\delta n}{n_0} \right) - \frac{e^2}{4m_i m_e \omega_{pe}^2} \frac{\partial}{\partial z} |E(z, t)|^2, \quad (33a)$$

$$\frac{\partial}{\partial t} \left(\frac{\delta n}{n_0} \right) + \frac{\partial v_s}{\partial z} = 0 \quad (36a)$$

and

$$-2i\omega_{pe} \frac{\partial E(z, t)}{\partial t} - \frac{\gamma_e k_B T_e}{m_e} \frac{\partial^2 E(z, t)}{\partial z^2} + \frac{\delta n}{n_0} \omega_{pe}^2 E(z, t) = 0. \quad (39a)$$

In order to seek a solution for this set of equations, we make the following substitutions:

$$t = t_0 \tau, \quad Z = \gamma_0 \xi, \quad \left(\frac{\delta n}{n_0} \right) = \bar{n}, \quad E(z, t) = \varepsilon_0 \varepsilon,$$

$$v_s = \bar{v} \cdot V;$$

with

$$\left. \begin{aligned} t_0 &= \omega_{pe}^{-1} (m_i/2m_e) \gamma_e T_e (\gamma_e T_e + \gamma_i T_i)^{-1} \\ \gamma_0 &= \omega_{pe}^{-1} (m_i/2m_e) \gamma_e T_e (\gamma_e T_e + \gamma_i T_i)^{-1} [(\gamma_e T_e + \gamma_i T_i)/m_i]^{1/2}, \\ \bar{n} &= (4m_e/m_i) (\gamma_e T_e + \gamma_i T_i) (\gamma_e T_e)^{-1}, \\ \varepsilon_0 &= 8[\pi n_0 (m_e/m_i) k_B (\gamma_e T_e + \gamma_i T_i)^2 (\gamma_e T_e)^{-1}]^{1/2}, \\ \bar{v} &= (4m_e/m_i) (\gamma_e T_e + \gamma_i T_i) (\gamma_e T_e)^{-1} [(\gamma_e T_e + \gamma_i T_i)/m_i]^{1/2}. \end{aligned} \right\} \quad (40)$$

After some mathematical manipulation, the dimensionless forms of Equations (33a), (36a), and (39a) become

$$\frac{\partial v}{\partial \tau} = - \frac{\partial n}{\partial \xi} - \frac{\partial \varepsilon}{\partial \xi} (\varepsilon \varepsilon^*), \quad (41)$$

$$\frac{\partial n}{\partial \tau} = - \frac{\partial v}{\partial \xi}, \quad (42)$$

$$i \frac{\partial \varepsilon}{\partial \tau} + \frac{\partial^2 \varepsilon}{\partial \xi^2} - n \varepsilon = 0. \quad (43)$$

After elimination of v from Equations (41) and (42), we obtain

$$\frac{\partial^2 n}{\partial \tau^2} - \frac{\partial^2 n}{\partial \xi^2} = \frac{\partial^2 (\varepsilon \varepsilon^*)}{\partial \xi^2}. \quad (14)$$

By observation, we realize that Equation (44) is the traveling wave equation; thus, the real quantities n and $\varepsilon \varepsilon^*$ could be represented by a functional form of $(\xi - u_0 \tau)$ with u_0 being the travelling wave group velocity. Thus, Equation (44) has a simple special solution as

$$\varepsilon \varepsilon^* = -(1 - u_0^2) \bar{n}, \quad (45)$$

where u_0 can be considered as an undetermined integration constant. Inserting Equation (45) into Equation (43) we obtain a nonlinear equation for dimensionless electric field ε :

$$i \frac{\partial \varepsilon}{\partial \tau} + \frac{\partial^2 \varepsilon}{\partial \xi^2} + (1 - u_0^2)^{-1} (\varepsilon \varepsilon^*) \varepsilon = 0, \quad (46)$$

where $u_0 < 1$, Equation (46) has a soliton solution (Li, 1985) of the form

$$\begin{aligned} \varepsilon = & \sqrt{\zeta_1} \left(\cosh \left\{ (\xi - u_0 \tau) \left[\frac{\zeta_1}{2(1 - u_0^2)} \right]^{1/2} \right\} \times \right. \\ & \times \exp \left[-i(u_0/2) (\xi - u_0 \tau) - i\phi \right] \Big)^{-1} \times \\ & \times \exp \left\{ i\tau \left[(\zeta_1/2) (1 - u_0^2)^{-1} + \left(\frac{u_0}{2} \right)^2 \right] \right\}, \end{aligned} \quad (47)$$

where ζ_1 and ϕ are integration constants. Physically $\sqrt{\zeta_1}$ represents dimensionless amplitude of fast oscillating electrical field, the initial phase. The term $(\zeta_1/2) (1 - u_0^2)^{-1} + (u_0/2)^2 \equiv \tilde{\omega}$ stands for dimensionless frequency shift, that is, the frequency of fast oscillation being $\omega_{pe} \sim \tau_0^{-1} \tilde{\omega}$. From Equation (45), the density fluctuation could be found as

$$\bar{n} = -\frac{\zeta_1}{1 - u_0^2} \operatorname{sech}^2 \{ (\xi - u_0 \tau) [\zeta_1/2(1 - u_0^2)]^{1/2} \}. \quad (48)$$

By examination of Equations (42) and (48), we found a solution for v , such as,

$$v = \frac{-u_0 \zeta_1}{1 - u_0^2} \operatorname{sech}^2 \{ (\xi - u_0 \tau) [\zeta_1/2(1 - u_0^2)]^{1/2} \}. \quad (49)$$

Before determining the parameters ζ_1 and u_0 , we shall calculate the three conservation quantities (Rudakov and Tsytovich, 1978) as follows:

$$\left. \begin{aligned} N &= \int_{-\infty}^{\infty} \varepsilon \varepsilon^* d\xi, \\ H &= \int_{-\infty}^{\infty} \left[\frac{\partial \varepsilon}{\partial \xi} \left(\frac{\partial \varepsilon^*}{\partial \xi} \right) + n \varepsilon \varepsilon^* + (n^2 + v^2)/2 \right] d\xi, \\ P &= \frac{1}{2} \int_{-\infty}^{\infty} \left[i \left(\varepsilon \frac{\partial \varepsilon^*}{\partial \xi} - \varepsilon^* \frac{\partial \varepsilon}{\partial \xi} \right) + 2nv \right] d\xi. \end{aligned} \right\} \quad (50)$$

Inserting Equations (47) through (49) into Equation (50) yields

$$N = 2[2\zeta_1(1 - u_0^2)]^{1/2}, \quad (51)$$

$$H = - \left(\frac{\sqrt{2}}{3} \zeta_1^{3/2} (1 - 5u_0^2) (1 - u_0^2)^{-3/2} + (\zeta_1/2)^{1/2} u_0^2 (1 - u_0^2) \right)^{1/2}, \quad (52)$$

$$P = \frac{4}{3} \sqrt{2} \zeta_1 u_0 (1 - u_0^2)^{-3/2} + \sqrt{2\zeta_1} u_0 (1 - u_0^2)^{-1/2}; \quad (53)$$

N , H , and P represent the number of Langmuir quanta, energy, and momentum of this soliton, respectively. Of all these the most important quantity is energy H which has to be negative if the soliton is stable. Like an atom in which electrons are trapped around the nucleus, it is just the negative energy which can trap particles within a soliton. From Equation (52), this soliton stability condition becomes

$$1 - 5u_0^2 > 0 \quad \text{or} \quad u_0 < \frac{1}{\sqrt{5}} \quad (54)$$

if $\zeta_1 \gg 1$ (corresponding to strong micro-turbulence). Using Equation (40) and $W_f^T = 0.9$ (or $E_f^T \sim 1.77$, $\alpha = 1$), we can estimate ζ_1 as

$$\begin{aligned} \zeta_1 &\sim (E_f^T)^2 \left[64\pi n_0 \left(\frac{m_e}{m_i} \right) k_B (\gamma_e T_e + \gamma_i T_i)^2 (\gamma_e T_e)^{-1} \right]^{-1} \sim \\ &\sim [64(m_e/m_i)]^{-1} (0.9) \sim 25.88. \end{aligned}$$

In view of this result, it is reasonable to choose $\sqrt{\zeta_1} = 5$, $u_0 = 0.2$. Determination of these two parameters will enable us to calculate the structure of this soliton. Thus; the propagation velocity of the soliton is given by

$$u_0 \frac{r_0}{\tau_0} = u_0 [(\gamma_e T_e + \gamma_i T_i)/m_i]^{1/2} = 0.2 \text{ (sound speed)} \sim 2 \times 10^5 \text{ cm s}^{-1}.$$

The dimension of this soliton is

$$2[2(1 - u_0^2)/\zeta_1]^{1/2} r_0 = \frac{0.277}{2} \omega_{pe}^{-1} \left(\frac{m_i}{m_e} \right) c_s \sim \\ \sim 1.01 \times 10^{-2} \text{ cm} \sim 10 \text{ Debye radius} .$$

The density fluctuation within the soliton is

$$\frac{\delta n}{n_0} \sim \bar{n} \frac{\zeta_1}{1 - u_0^2} = \frac{25}{0.96} \frac{4m_e}{m_i} \frac{\gamma_e T_e + \gamma_i T_i}{\gamma_e T_e} \sim 0.11 .$$

From these results, we note that only $\sim 10\%$ density fluctuation within an area of a 10^{-2} cm sized box could produce strong Langmuir turbulence (soliton) whose energy density of the electric field reaches a magnitude comparable to the order of the value of thermal energy density. It could be imaginable that there might be a much severe and violent phenomenon if, somewhere, a local vacuum really occurred!

From the conservation laws (i.e., Equations (51) through (53)), it could be noted that, when $u_0 \ll 1$, $N \sim \sqrt{\zeta_1}$, and $-H \sim \zeta_1^{3/2}$. This means that increasing u_0 diminishes the absolute value of the negative energy of the soliton. Thus, the solitons tend to fuse with each other and to be brought to rest independently of one another. In the case of the fusion of two identical solitons having equal energy H_0 , quanta numbers N_0 and amplitude $(\sqrt{\zeta_1})_0$, the characteristics of the soliton after the completion of the fusion process will be:

$$N_1 = 2N_0 , \quad (\sqrt{\zeta_1})_1 = 2(\sqrt{\zeta_1})_0$$

and

$$H_1 = -\frac{\sqrt{2}}{3} [2(\sqrt{\zeta_1})_0]^3 (1 - 5u_0^2) (1 - u_0^2)^{-3/2} = 8H_0 .$$

These results indicate that the soliton has gone through a transition process from a higher energy state to a lower energy state. Hence, $\Delta H = 2H_0 - H_1 = -6H_0 > 0$. This amount of energy can be converted into ion-sonic wave energy as has been demonstrated by numerical computations (Degtyarev *et al.*, 1976). These authors showed that the fusion of solitons is accomplished by ion-sonic emission. Those solitons with $\sqrt{\zeta_1} \ll 1$ do not fuse, and only those solitons with $\sqrt{\zeta_1} \geq 1$ are able to fuse. They have been able to show that the rate of fusion is proportional to $\sqrt{\zeta_1}$.

5. Concluding Remarks

In this paper, we have presented a detailed account of micro-physical processes which may enhance significantly the intensity of the flares over the level predicted by the classical flare theory. These micro-physical processes are the soliton and strong Langmuir turbulence. Overall, we may summarize as follows: when the condition for

modulational instability is reached, three modes of turbulence may occur. These three modes (soliton, free Langmuir waves, and ion-sound waves) will interact with each other, each one being converted to the others (Rudakov and Tsytovich, 1978). It could be noticed further that Langmuir waves can be trapped in solitons and that the energy released during the fusion of solitons is essentially taken up by ion-sound waves with only a negligible part of this energy being carried by free Langmuir waves (i.e., not trapped in solitons). Apart from the fusion of two identical solitons with the emission of ion-sound waves, there is a process in which ion-sound waves generated during the fusion of two solitons could destroy the third soliton. Also, a single soliton can be formed from a homogeneous Langmuir field accompanied by ion-sound emission which is called soliton condensation (Rudakov and Tsytovich, 1978.). From all these theoretical results, we may conclude that during the onset of a flare, when the converging particle velocity reaches $\sim 10^7 \text{ cm s}^{-1}$, the modulational instability begins to grow, and a set of solitons could be formed from the thermal Langmuir field. At the same time, the ion-sound turbulence increases rapidly to a high level comparable with the thermal energy density; $W_T^s \sim nk_B T$. Because of creation of such strong turbulence, the resistivity (σ^{-1}) becomes 4–5 orders of magnitude larger than the classical value. It is just this large resistivity which leads to an efficient conversion process in which an adequate part of the magnetic energy is converted to thermal energy, thereby illustrating the thermal phase of the flare.

In the classical flare model, the diffusion region is unrealistically small thereby making it very difficult to have magnetic energy converted to thermal energy. However, the present model with finite size of the diffusion region ($0.1 \text{ km} \times 10^2 \text{ km}$) plays a dual or twofold utilitarian role; on the one hand, greater resistivity enhances the temperature and, subsequently, enlarges the dimension of the diffusion region. Hence the efficiency of the energy conversion will be enhanced. On the other hand, strong turbulent electric field could accelerate particles stochastically. It has been pointed out by Sturrock (1975) that, in the first phase of the solar flare acceleration process, one of the most favourable mechanisms is stochastic acceleration with an RF electric field produced by plasma micro-instability. Since there is a diffusion region in the present model which leads to a much more efficient energy conversion process which also produces a high speed jet, there is no need to demand the existence of slow shocks as required by Petschek's model.

Acknowledgements

This work is supported by NASA Grant NAGW-9 (MTS and STW) and Air Force Contract AFOSR-88-0013 (STW). We also wish to thank Prof. S. Cuperman, Tel Aviv University, for his comments and suggestions.

Appendix A

First we will prove that the inequality

$$\left| \frac{\partial \pi}{\partial t} \right| \gg \left| \frac{\partial}{\partial x_i} \pi v_f^T \right| \quad \text{or} \quad \left| \frac{\partial}{\partial x_i} \pi v_s \right| \quad (\text{A1})$$

is valid under the condition (26). The right-hand side of Equation (29) has the same order of magnitude, so we can estimate v_s as

$$\frac{\partial v_s}{\partial t} \sim \frac{e}{m_i} E_s \quad \text{or} \quad v_s \sim \frac{e}{m_i \omega_{pi}} E_s = \sqrt{\frac{m_e}{m_i}} W_s^{1/2} v_{Te}.$$

Similarly, we can estimate v_f^T from Equations (23)–(24)

$$\frac{\partial v_f^T}{\partial t} \sim \frac{e}{m_e} E_f^T \quad \text{or} \quad v_f^T \sim \frac{e}{m_e \omega_{pe}} E_f^T = W_f^{1/2} v_{Te}.$$

Then

$$\left| \frac{\partial \pi}{\partial t} \right| \left/ \left| \frac{\partial}{\partial x_i} \pi v_f^T \right| \right. \sim \frac{k_d}{k} W_f^{-1/2},$$

$$\left| \frac{\partial \pi}{\partial t} \right| \left/ \left| \frac{\partial}{\partial x_i} \pi v_s \right| \right. \sim \frac{k_d}{k} [W_s (m_e/m_i)]^{-1/2}.$$

If we estimate v_s from (24)

$$\frac{\partial v_s}{\partial t} \sim \frac{e}{m_e} E_s \quad \text{for} \quad v_s \sim \frac{e}{m_e \omega_{pi}} E_s = \sqrt{\frac{m_i}{m_e}} W_s^{1/2} v_{Te}.$$

Then

$$\left| \frac{\partial \pi}{\partial t} \right| \left/ \left| \frac{\partial}{\partial x_i} \pi v_s \right| \right. \sim \frac{k_d}{k} \left[W_s \frac{m_i}{m_e} \right]^{-1/2}.$$

Therefore, in order to satisfy (A1), it is enough to take

$$k_d/d \gg 1, \quad W_f \sim 1, \quad W_s \sim 10^{-2}$$

which is just the condition (26).

Inserting (22) into (19) gives

$$\frac{\partial}{\partial t} (n_s + n_f^T) + \nabla \cdot [(n_s + n_f^T) (v_s + v_f^T)] = 0. \quad (\text{A2})$$

After averaging over the time-period ω_i^{-1} we obtain

$$\frac{\partial n_s}{\partial t} + \nabla \cdot (n_s v_s + \langle n_f^T v_f^T \rangle) = 0. \quad (\text{A3})$$

Subtracting (A3) from (A2) gives

$$\frac{\partial}{\partial t} n_f^T + \nabla \cdot (n_s \mathbf{v}_f^T + n_f^T \mathbf{v}_s + n_f^T \mathbf{v}_f^T - \langle n_f^T \mathbf{v}_f^T \rangle) = 0 \quad (\text{A4})$$

Considering (A1) we can write

$$\frac{\partial n_f^T}{\partial t} + \nabla \cdot (n_s \mathbf{v}_f^T) = 0. \quad (\text{A5})$$

Now, we simplify the representation of $\partial \mathbf{v}_f^T / \partial t$. Subtracting (24) from (23) gives

$$\begin{aligned} \frac{\partial \mathbf{v}_f^T}{\partial t} + (\mathbf{v}_s \cdot \nabla) \mathbf{v}_f^T + (\mathbf{v}_f^T \cdot \nabla) \mathbf{v}_s + (\mathbf{v}_f^T \cdot \nabla) \mathbf{v}_f^T - \langle (\mathbf{v}_f^T \cdot \nabla) \mathbf{v}_f^T \rangle = \\ = \frac{-e}{m_e} \mathbf{E}_f^T - \frac{e}{m_e c} [\mathbf{v}_s \times \mathbf{B}_f^T + (\mathbf{v}_f^T \times \mathbf{B}_f^T) - \langle \mathbf{v}_f^T \times \mathbf{B}_f^T \rangle] - \\ - \frac{\gamma_e k_B T_e}{m_e n_s} \nabla n_f^T. \end{aligned} \quad (\text{A6})$$

Comparing the three terms $-(e/m_e c) (\mathbf{v}_s^T \times \mathbf{B}_f^T)$, $-(e/m_e c) \mathbf{v}_f^T \times \mathbf{B}_f^T$, $-(e/m_e c) \times \langle \mathbf{v}_f^T \times \mathbf{B}_f^T \rangle$ with $-(e/m_e) \mathbf{E}_f^T$ and using Maxwell's equation $\nabla \times \mathbf{E}_f^T = -c^{-1} (\partial \mathbf{B}_f^T / \partial t)$, we can estimate them as:

$$\left| -\frac{e}{m_e c} (\mathbf{v}_f^T \times \mathbf{B}_f^T) \right| \left| -\frac{e}{m_e} \mathbf{E}_f^T \right| \sim k \omega_{pe}^{-1} W_f^{1/2} v_{Te} = \frac{k}{k_d} W_f^{1/2} \ll 1.$$

Similarly, the terms on the left-hand side of Equation (A6) compared with $\partial \mathbf{v}_f^T / \partial t$ can be proved to be very small, using Equation (A1).

Thus (A6) reduces to

$$\frac{\partial \mathbf{v}_f^T}{\partial t} = -\frac{e}{m} \mathbf{E}_f^T - \frac{\gamma_e T_e k_B}{m_e n_s} \nabla n_f^T.$$

References

- Alfvén, H. and Carlquist, P.: 1967, *Solar Phys.* **1**, 220.
 Boyd, T. J. M. and Sanderson, J. J.: 1969, *Plasma Dynamics*, Nelson, London.
 Coppi, B. and Friedland, A. B.: 1971, *Astrophys. J.* **169**, 379.
 DegTyarev, L. M., Zakharov, V. E., and Rudakov, L. I.: 1975, *Soviet Phys. JETP* **41**, 57.
 Dungey, J. W.: 1953, *Phil. Mag.* **44**, 725.
 Friedman, E. and Hamberger, S. M.: 1968, *Astrophys. J.* **152**, 667.
 Friedman, E. and Hamberger, S. M.: 1969, *Astrophys. J.* **8**, 104; 398.
 Furth, H. P., Killeen, J., and Rosenbluth, M. N.: 1963, *Phys. Fluids* **6**, 459.
 Hasegawa, A.: 1975, *Plasma Instabilities and Nonlinear Effects*, Interscience Publ., Inc., New York.
 Heyvaerts, J., Priest, E. R., and Rust, D. M.: 1977, *Astrophys. J.* **216**, 123.

- Hood, A. W. and Priest, E. R.: 1979, *Solar Phys.* **64**, 303.
- Li Xiao Qing: 1985, *Astrophys. Space Sci.* **112**, 13.
- Parker, E. N.: 1963, *Astrophys. J. Suppl. Ser.* **8**, 177.
- Parker, E. N.: 1979, *Cosmical Magnetic Fields*, Clarendon Press, Oxford.
- Petschek, H. E.: 1964, in W. N. Hess (eds.), *The Physics of Solar Flares*, NASA SP-50, p. 425.
- Priest, E. R.: 1983, 'Unstable Current Systems and Plasma Instabilities in Astrophysics', in M. Kundu and G. D. Holman (eds.), *IAU Symp.* **107**, 233.
- Rudakov, L. I. and Tsytovich, V. N.: 1978, *Phys. Rep.* **40C**, No. 1, 3.
- Sonnerup, B. U. O.: 1973, *High Energy Phenomena on the Sun*, Proceedings of a Symp. held at NASA Goddard Flight Center, p. 357.
- Sonnerup, B. U. O.: 1983, 'Unstable Current Systems and Plasma Instabilities in Astrophysics' in M. Kundu and G. D. Holman (eds.), *IAU Symp.* **107**, 5.
- Spicer, D. S.: 1977, *Solar Phys.* **53**, 305.
- Sturrock, P. A.: 1975, 'Coronal Disturbances', in G. Newkirk (ed.), *IAU Symp.* **57**, 437.
- Syrovatskii, S. I.: 1966, *Soviet Astron.* **10**, 270.
- Syrovatskii, S. I.: 1978, *Solar Phys.* **58**, 89.
- Tsytovich, V. N.: 1970, *Nonlinear Effects in Plasma*, Plenum Press, New York.
- Ugai, M. and Tsuda, T.: 1977, *J. Plasma Phys.* **17**, 337.
- Van Hoven *et al.*: 1980, 'The Preflare State', in P. A. Sturrock (ed.), *Solar Flares*, Skylab Solar Workshop II, Colorado Univ. Press, Boulder, p. 17.
- Vasyliunas, V. M.: 1975, *Rev. Geophys. Space Phys.* **13**, No. 1, 303.
- Vedenov, A. A. and Rudakov, L. I.: 1965, *Soviet Phys. Dokl.* **9**, 1073.

THE ROLE OF CONDENSATION AND HEAT CONDUCTION IN THE FORMATION OF PROMINENCES: AN MHD SIMULATION

S. T. WU, J. J. BAO, and C. H. AN

Center for Space Plasma and Aeronomic Research and Department of Mechanical Engineering, The University of Alabama in Huntsville, Huntsville, AL 35899, U.S.A.

and

E. TANDBERG-HANSEN

Space Science Laboratory, National Aeronautics and Space Administration, Marshall Space Flight Center, AL 35812, U.S.A.

(Received 13 June, 1989; in revised form 11 August, 1989)

Abstract. In this paper we investigate the effects of condensation and thermal conduction on the formation of Kippenhahn–Schlüter (K–S) type prominences in quiet regions (QP) due to symmetric mass injection. To implement this investigation, a self-consistent, two-dimensional, non-planar, time-dependent magnetohydrodynamic (MHD) simulation model is developed. In the model, we use various values of the injection velocity, density, and magnetic field strength to determine the most favorable conditions for the QP formation. Based on these simulation results, we find that the formation of a K–S-type field configuration should be considered as a dynamic process, which needs both condensation and mass injection to supply enough mass to maintain such a configuration to complete the formation process of quiescent prominence

1. Introduction

For decades, the formation of quiescent solar prominences has interested solar physicists, and many physical mechanisms for the formation have been advanced. For example, the formation of quiescent prominences by condensation from the surrounding coronal material has been investigated by a number of authors (Lust and Zirin, 1960; Field, 1965; Kuperus and Tandberg-Hanssen, 1967; Nakagawa, 1970; Raadu and Kuperus, 1973; Hildner, 1974). Such a condensation is expected to occur because the coronal plasma is in a radiatively unstable temperature regime (Parker, 1953; Cox and Tucker, 1969; An *et al.*, 1983). When a density perturbation causes radiative cooling to dominate in some region, the resultant net cooling decreases the temperature and pressure in the perturbed region and causes material inflow to form cool dense plasma material.

To date, most calculations of solar prominence formation, based on the assumption of coronal condensation, have only utilized linear or quasi-linear mathematical models (Kleczek, 1958; Uchida, 1963; Raju, 1968). Some models utilized self-consistent nonlinear magnetohydrodynamic models, but they dealt with very specific cases. Hildner (1974) employed the most sophisticated numerical MHD model at that time and showed that the local condensation is the key process for the solar prominence formation by adopting a parallel field configuration and ignoring thermal conduction. Low and Wu (1981) studied analytically the nonlinear interplay between magnetostatic equilibrium

and energy balance and showed that the thermal conduction parallel to the field is important for the energy balance in the Kippenhahn–Schlüter (K–S) type prominence sheet. The condensation of a coronal plasma may explain the origin of the cool dense prominence material, but it still leaves a number of unanswered questions; e.g., what is the mechanism of prominence support? Why does a prominence form along only a certain part of a neutral line? Furthermore, Saito and Tandberg-Hanssen (1973) showed observationally that condensation of coronal mass alone cannot supply enough mass for a prominence without collapsing a large part of the corona. The requirement for continuous mass supply from the chromosphere to a prominence led Pikel'ner (1969) to suggest a siphon mechanism for the prominence formation. Poland and Mariska (1986) studied the siphon mechanism for supplying mass in the prominence formation process using a one-dimensional flux tube model in which thermal conduction and radiation are included, but the effects from the magnetic field configuration and the MHD process on the condensation could not be accommodated properly. Recently, An, Bao, and Wu (1988) and An *et al.* (1988) employed a self-consistent time-dependent ideal MHD model (Wu *et al.*, 1983) to study the prominence formation by mass injection. They revealed the dynamic processes in the formation of the prominence field configuration, but the plasma parameters (i.e., density and temperature) could not match the observed values because of the limitation of the ideal MHD model without condensation and thermal conduction. In this paper, we shall present a two-dimensional, non-planar, time-dependent, self-consistent compressible magnetohydrodynamic model together with radiative cooling and thermal conduction in a gravitational field to investigate the roles of condensation and thermal conduction in the prominence formation. We discuss the present model and the initial and boundary conditions used for solving the model equations in Section 2. Numerical results obtained from the model and physical interpretations will be included in Section 3. Finally, concluding remarks concerning the model in both a mathematical and physical sense will be given in Section 4.

2. Description of the Model

In general, to set up a simulation model for a physical system we need to consider four parts: (i) mathematical description of the physical system of interest, (ii) appropriate computational boundary conditions corresponding to the physical system to be investigated, (iii) proper algorithm to execute the numerical computation, and (iv) the choice of the initial geometric configuration and proper interpretation of the numerical output.

2.1. MATHEMATICAL DESCRIPTION

To consider the dynamical behavior of the prominence formation, we choose to use the description of single fluid plasma theory, in which the theory of magnetohydrodynamics can be utilized. It is believed that the basic physics in the prominence formation is the interaction between the plasma and the magnetic field in a gravitational field with higher order transport effects (i.e., radiation and thermal conduction). Thus, we consider a

compressible fluid (plasma), initially at rest, imbedded in a stratified solar atmosphere with an arbitrary potential magnetic field. In addition, we also assume that the plasma is optically thin so that it is cooled by radiation in which condensation may be formed. The plasma is heated by absorption of mechanical energy; thermal conduction is included. However, the electric conductivity of the plasma is taken to be infinite and viscosity is set equal to zero.

The governing equations of this MHD model can be written as:

$$\frac{\partial \rho}{\partial t} + \nabla \cdot (\rho \mathbf{v}) = 0, \quad (1)$$

$$\frac{\partial (\rho \mathbf{v})}{\partial t} + \nabla \cdot (\rho \mathbf{v} \mathbf{v}) = -\nabla p + \frac{1}{c} \mathbf{J} \times \mathbf{B} + \rho \mathbf{g}, \quad (2)$$

$$\frac{\partial p}{\partial t} = -\gamma p (\nabla \cdot \mathbf{v}) - \mathbf{v} \cdot \nabla p + (\gamma - 1) [H - Q_R - Q_c], \quad (3)$$

$$\frac{\partial \mathbf{B}}{\partial t} = \nabla \times (\mathbf{v} \times \mathbf{B}), \quad (4)$$

$$p = \rho R T, \quad \mathbf{J} = \frac{c}{4\pi} \nabla \times \mathbf{B}, \quad \nabla \cdot \mathbf{B} = 0, \quad (5)$$

where the symbols ρ , p , T , \mathbf{v} , \mathbf{B} , and \mathbf{g} are the mass density ($\rho = \text{mn}$), pressure, temperature, velocity, magnetic field, and gravitational acceleration, respectively. All these quantities are space- and time-dependent except the gravitational acceleration. In addition, \mathbf{J} represents the electric current which is defined by Equation (5). The two constants γ and R are the ratio of specific heat and the universal gas constant. The independent variables are the spatial coordinates (i.e., horizontal (x) and vertical (z) coordinates) and time (t).

For the closure of the problem, there are three more quantities to be defined: viz., Q_c , Q_R , and H . Q_c represents heat conduction. The heat conduction parallel to magnetic field is much larger than the heat conduction perpendicular to the magnetic field for the magnetized prominence plasma, thus

$$Q_c \simeq -\nabla \cdot (k \nabla T), \quad (6)$$

with $k_{\parallel} = k_0 T^{5/2} \text{ erg K}^{-1} \text{ cm}^{-1} \text{ s}^{-1}$ and k_0 being 10^{-7} in cgs units.

The quantity Q_R represents the radiative cooling term which is chosen to have the form

$$Q_R = \Lambda_i n_e^2 T^{\alpha}, \quad (7)$$

where n_e is the electron number density. In the present approximation, it is simply equal to ρ/m where m is the hydrogen mass. The constants Λ_i and α define the temperature dependence which is identical to the one used by Hildner (1974) based on the optical

thin approximation given by Cox and Tucker (1969). The heating function, H , is not as well known as the cooling function. Thus, we simply choose a heating function of the following form:

$$H_0 = Q_{R0} = \chi \rho_0^2 T_0^2. \quad (8)$$

This choice assures us that in the initial atmosphere there is a balance between heating and radiative cooling at each point.

2.2. BOUNDARY CONDITIONS

It has been pointed out by Wu and Wang (1987) that the selection of appropriate boundary conditions is crucial for the correctness of the physical solutions. Thus, in this simulation study, self-consistently posed boundary conditions were used, based on projected normal characteristic boundary conditions (see Hu and Wu, 1984; Wu and Wang, 1987). The procedures can be summarized as follows:

(i) All the characteristic equations are taken along the projected characteristics in the $\mathbf{n} - t$ plane, where \mathbf{n} is normal to the boundary in question. In particular, those characteristic equations along the outgoing projected characteristics for which the corresponding characteristic velocity is pointing out of the calculation domain are identified with the compatibility equations (Hu and Wu, 1984).

(ii) For the lower physical boundary (as shown in Figure 1) used in the present calculation, the maximum number of boundary conditions can be arbitrarily specified to simulate the boundary disturbances. This number is equal to the number of incoming characteristics which are those characteristic velocities pointing into the calculation domain. Then, the given boundary conditions and the compatibility equations are combined into a complete system to determine the values of all the dependent variables on the boundary.

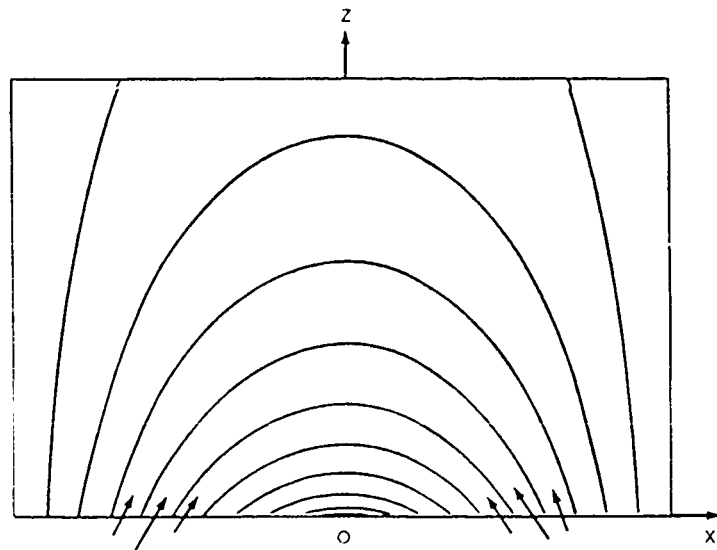


Fig. 1 Schematic representation of an initial potential magnetic field with symmetric mass injection as indicated by arrows and computational domain for the present study.

(iii) For the computational boundaries, i.e., the upper boundary and side boundaries in the present study, we choose again according to the rules given by Wu and Wang (1987). At the upper boundary, the non-reflecting boundary conditions are used: namely, all the spatial derivatives of the dependent variables in the characteristic equations are taken to be zero except those in the compatibility equations. Then, these non-reflecting boundary conditions are combined with the compatibility equations to determine the boundary values of the dependent variables. The side boundaries, as shown in Figure 1, have been chosen to be symmetric for mathematical convenience and physical acceptability.

2.3. NUMERICAL ALGORITHM

The algorithm used for this numerical simulation is the FICE (Full-Implicit-Continuous-Eulerian) scheme developed by Hu and Wu (1984). In the FICE scheme, all the quantities except the density (ρ), pressure, (p), and velocity (v) are computed explicitly through the values obtained at the immediate previous iteration step. Then, these values are substituted into the pressure equation for the routing iteration until the satisfactory results are reached. The detailed description of this scheme can be found in the work of Hu and Wu (1984).

2.4. INITIAL CONDITIONS

Prior to the introduction of the disturbances at the lower boundary (i.e., physical boundary), the initial solar atmosphere is supposed to be in hydrostatic equilibrium with a uniform temperature and is permeated by a potential magnetic field (i.e., $\nabla \times \mathbf{B} = 0$).

Under these physical conditions, the analytic conditions can be found from the set of governing equations (1) through (5) in two dimensions which have the following form:

$$\begin{aligned} \rho_0 &= \rho_i e^{-(\kappa RT)z}, \\ T_0 &= T_i, \\ v_0 &= 0, \\ B_{x0} &= B_i \cos \frac{\pi x}{2x_0} e^{-\pi z/2x_0}, \\ B_{z0} &= B_i \sin \frac{\pi x}{2x_0} e^{-\pi z/2x_0}, \\ B_{y0} &= 0, \end{aligned} \quad (9)$$

where ρ_i , T_i , and B_i are arbitrary constants of density, temperature, and magnetic field, respectively. This initial magnetic field configuration and computational domain are shown in Figure 1.

In order to simulate the mass injection, we have prescribed a velocity along the field lines in three grid points (see Figure 1) with a time ramp of five time steps. Subsequently, we have maintained this prescribed condition throughout the calculation.

3. Results

It is understood that the physical parameters which have significant effects on the simulation results are the initial plasma beta (i.e., the ratio of plasma pressure to magnetic pressure, $\beta_0 = 16\pi n_0 k T_0 / B_0^2$), the injection velocity (v_0), and amount of mass (ρ/ρ_0) injected into the system. Therefore, our calculations were performed for different combinations of these parameters to study the role of condensation and thermal conduction on the prominence formation processes due to mass injection as shown in Figure 2.

All these calculations are based on an initial isothermal atmosphere in hydrostatic equilibrium with a temperature of 10^6 K (i.e., T_c), a number density at the lower boundary of $5 \times 10^9 \text{ cm}^{-3}$ (i.e., ρ_c), and with a dipole current-free magnetic field. From these numerical experiments, we conclude that the best results for prominence formation occur for the following physical parameters: $\beta_0 = 2$ (i.e., $B_0 = 4.2$ g), $\rho/\rho_0 = 1.0$, and $v_0 = 10 \text{ km s}^{-1}$, i.e., point A in Figure 2. These results for magnetic field configuration, density contours, temperature contours, and velocity field at a time 6200 s after the initiation of the mass injection as shown in Figure 1 are presented in Figure 3. These results clearly indicate that a K-S quiescent prominence is formed; the magnetic field configuration shows a pit above the neutral line where a high density (i.e., 12.5 times higher than the original density) and cool ($\sim 90\%$ lower than the original temperature)

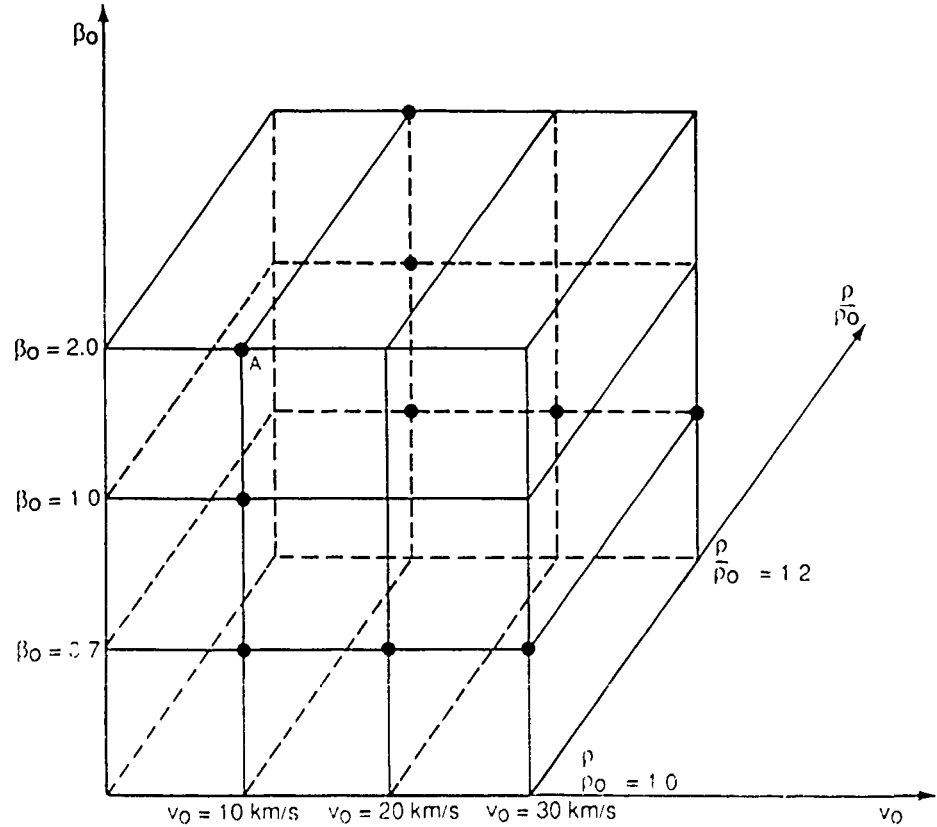


FIG. 2. Three-axes (v_0 , ρ/ρ_0 , β_0) representation of the physical parameters for which numerical simulations were performed.

material is formed. The cool dense material is formed by the condensation of surrounding coronal plasma as well as the injected plasma as exhibited in the velocity field: as the injected plasma starts to condense in the pit, the pressure deficit in the pit causes the coronal plasma to flow into the pit and condense.

In order to show the role of radiation and thermal conduction in the dynamical formation of the quiescent prominence we plot the density and temperature at the pit as shown in Figure 3 as a function of time for various combinations of radiation and thermal conduction; see Figure 4. The curves represented by *A*, *B*, *C*, and *D* are, respectively, the computed results for MHD with no thermal conduction or radiation, with thermal conduction only, (i.e., $[H - Q_R]_0 = 0$) with radiation only, and with both radiation and thermal conduction as noted in the caption of Figure 4. By comparison of curve *B* with *A*, we note that the heat conduction tries to smooth the temperature and density profiles along the field lines, resulting in a lower density accumulation and lower temperature drop in the pit than for the ideal MHD case. For both cases, the density and temperature evolution are far from those of a prominence. If the radiation is included in the model, the density and temperature are closer to those observed in a prominence; density enhances more than 10 times ($\sim 10^{11} \text{ cm}^{-3}$) and temperatures decreases $\sim 100\%$ over the initial value ($\sim 10^5 \text{ K}$) in the pit. Again by comparing the results of *C* and *D*, we find that heat conduction smooths the density and temperature distribution along the field lines. According to these simulation results, there are no doubts that radiation and thermal conduction have important roles in the formation of prominence. In particular, the radiation is essential to induce the condensation, and thermal conduction will modify the time-scale of the formation. We now may have a general scenario of the formation of quiescent prominences based on mass injection from the boundary with radiation and thermal conduction in our model. In the following we shall describe some detailed physics which may be revealed from this simulation study.

3.1. EFFECTS OF DIFFERENT INITIAL PLASMA BETA ($16\pi n_0 k T_0 / B_0^2$)

The plasma beta measures the relative importance of processes controlled by plasma pressure and processes controlled by magnetic pressure. During the prominence formation process with a fixed plasma pressure (i.e., $n_0 \sim 5 \times 10^9 \text{ cm}^{-3}$ and 10^6 K) at the lower boundary, it is necessary to have a proper magnetic field strength, in order for a K-S-type quiescent prominence to form. If the field is too strong, the field lines cannot bend enough to form a proper pit to hold the mass being injected, and the injected mass will fall back to the solar surface by gravitational pull. In that case a pit is not formed at the apex; instead a loop is created. If the field is too weak, it does not have enough strength to support the prominence material at the apex. Only for a proper value of field strength will the K-S-type prominence form. After a number of simulation studies, we present the field configurations and density contours with values of the plasma beta of 2.0 (4.2 G), 1.0 (5.9 G), and 0.7 (7.0 G) for the case of an injected mass velocity of 10 km s^{-1} and $\rho/\rho_0 = 1.0$ using the non-ideal MHD model in Figure 5. From these

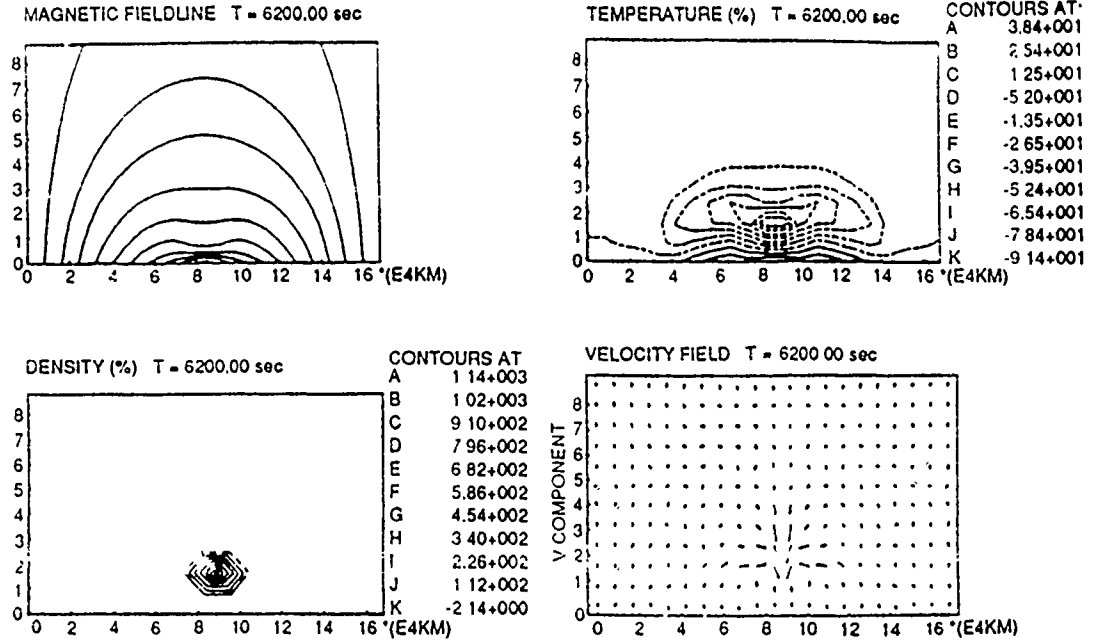


Fig. 3 Computed magnetic field lines, density contours $((\rho - \rho_0)/\rho_0)$, temperature contours $((T - T_0)/T_0)$ and vectorial velocity field at 6200 s after introduction of mass injection for $\beta_0 = 2.0$, $\rho/\rho_0 = 1.0$, and $v_0 = 10 \text{ km s}^{-1}$. The dotted lines represent the negative percentage which means the quantity has decreased to below the origin value.

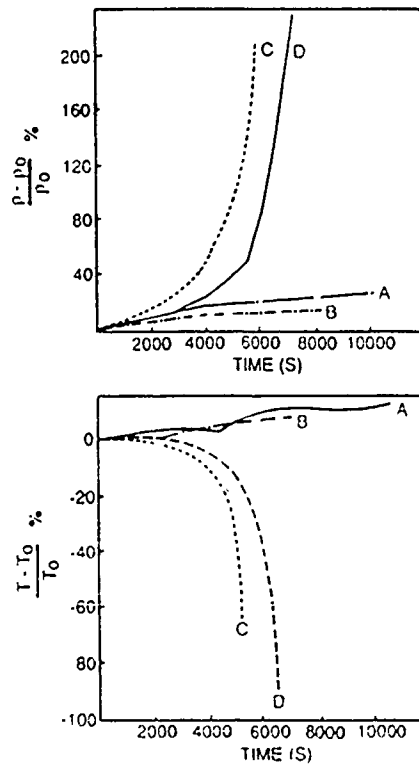


Fig. 4 The evolution of the density and temperature at the pit due to mass injection with $\beta_0 = 2.0$, $\rho/\rho_0 = 1.0$, and $v_0 = 10 \text{ km s}^{-1}$ for four cases (a) Ideal MHD (i.e., $Q_c = Q_R = 0$), (b) MHD with thermal conduction only (i.e., $Q_c \neq 0$, $Q_R = 0$), (c) MHD with radiation only (i.e., $Q_c = 0$, $Q_R \neq 0$), and (d) non-ideal MHD (i.e., $Q_c \neq 0$, $Q_R \neq 0$).

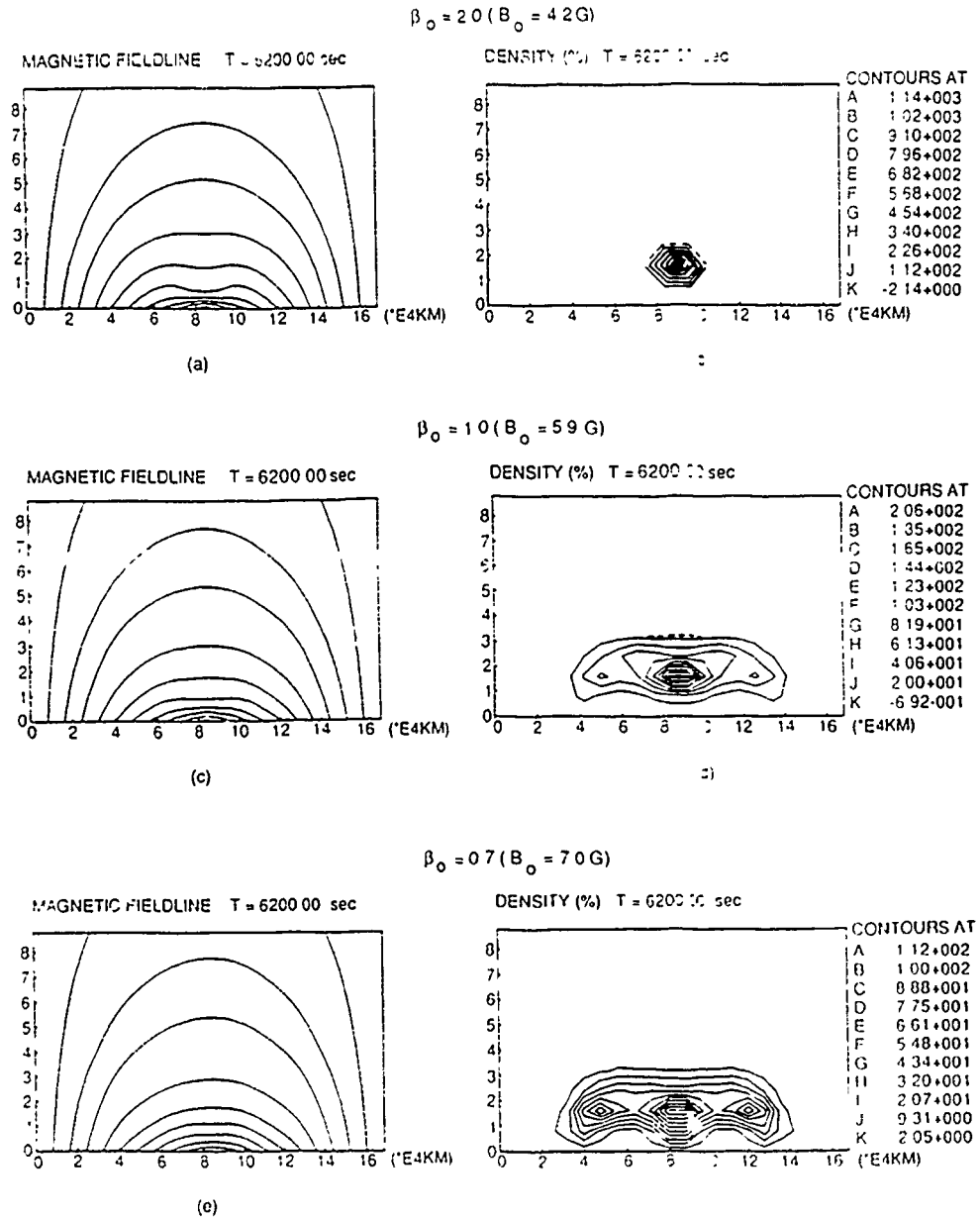


Fig 5. Computed magnetic field lines (left) and density contours (right) at 6200 s after mass injection for $v_0 = 10 \text{ km s}^{-1}$ and $\rho/\rho_0 = 1.0$ with various $\beta_0 = 0.7, 1.0$, and 2.0 , respectively, using non-ideal MHD model (present model)

numerical results we observe that the magnetic field configuration and density contours for $\beta_0 = 2.0$ best exhibit the expected features of a K-S-type prominence.

3.2. EFFECTS OF DIFFERENT INJECTION DENSITY (ρ/ρ_0) AND DIFFERENT INJECTION VELOCITY (v_0)

We have stated that the most favorable combination of physical parameters for the formation of a K-S-type prominence consists of a perturbed density ratio of 1.0, injection velocity (v_0) at 10 km s^{-1} , and a plasma beta value of 2.0. In order to

demonstrate that the formation process is sensitive to these parameters, we have shown the effects of the plasma beta value in the previous section. Now, we investigate the role of the perturbed density ratio and the magnitude of the injection velocity (v_0).

Figure 6 shows the magnetic field configuration, density contours, temperature contours, and vectorial representation of the velocity field at 6200 s for $\beta_0 = 2.0$ and $v_0 = 10 \text{ km s}^{-1}$, with a perturbed density of 1.0 on the left (a) and 1.2 on the right (b). It is immediately clear from these results that the case with $\rho/\rho_0 = 1.2$ does not lead to a K-S-type prominence, but exhibits a non-uniform loop structure as shown on the right side of Figure 6. This loop structure has high density at both legs and low density at

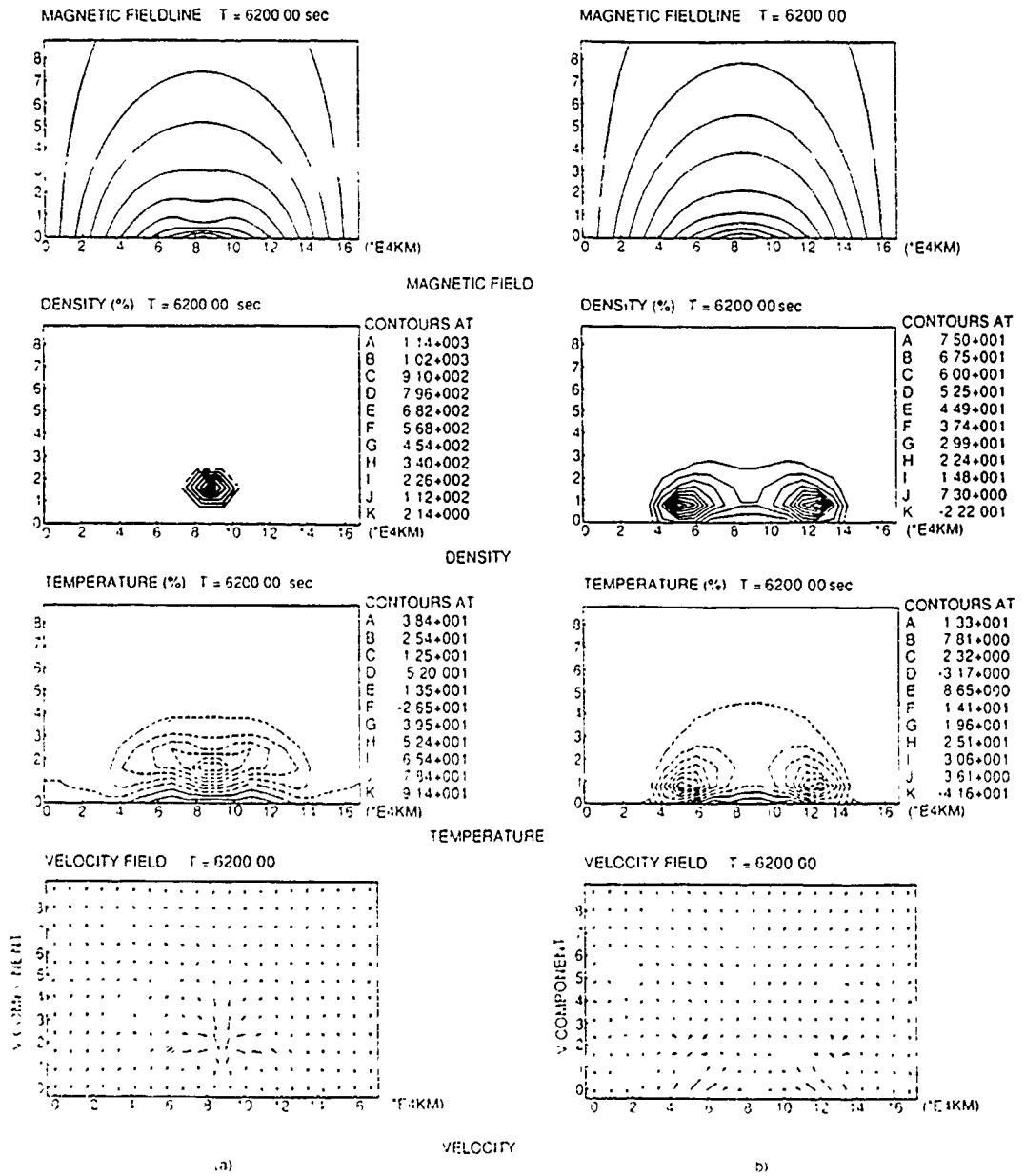


FIG. 6. Computed magnetic field, density, temperature, and velocity field at 6200 s after mass injections for $v_0 = 10 \text{ km s}^{-1}$ and $\beta_0 = 2.0$ with different injection density ratio (a) $\rho/\rho_0 = 1.0$ and (b) $\rho/\rho_0 = 1.2$.

the top. Observationally, it may reflect a loop having bright legs and less bright top. Physically, it may be understood because we have injected more (20% more than the case shown on the left side of Figure 6) mass into the system, and because of the effect of gravity on the condensation already triggered before the injected mass reaches the apex as shown by the velocity field in Figure 6.

In Figure 7, we show the effect of the injection velocity on the formation process. Again, the best physical parameters for K-S-type prominence formation are $\beta_0 = 2.0$,

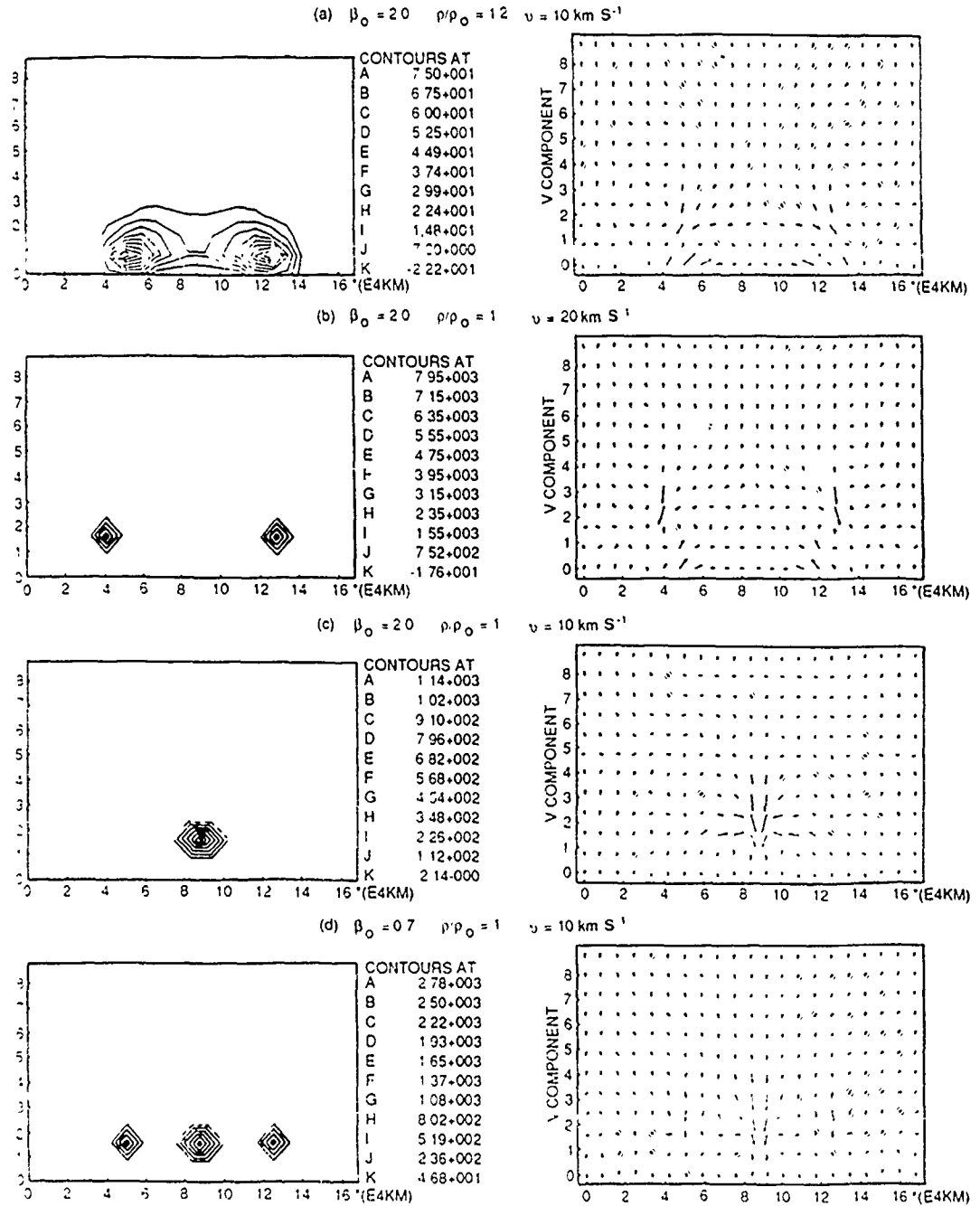


Fig. 7 Computed density contours (left) and velocity field (right) at 6200 s after mass injection for various cases (a) $\beta_0 = 2.0$, $\rho/\rho_0 = 1.2$, $v_0 = 10 \text{ km s}^{-1}$, (b) $\beta_0 = 2.0$, $\rho/\rho_0 = 1.0$, $v_0 = 20 \text{ km s}^{-1}$, (c) $\beta_0 = 2.0$, $\rho/\rho_0 = 1.0$, $v_0 = 10 \text{ km s}^{-1}$, and (d) $\beta_0 = 0.7$, $\rho/\rho_0 = 1.0$, $v_0 = 10 \text{ km s}^{-1}$

$\rho/\rho_0 = 1.0$, and $v_0 = 10 \text{ km s}^{-1}$. The density contours and vectoral representation of the velocity distribution are shown in Figure 7. From these results, we recognize the effects of the injection velocity by comparing the results shown in case (b) and case (c) in Figure 7, where only the density enhancement in the low injection velocity case (i.e., $v = 10 \text{ km s}^{-1}$) resembles the observed prominence features. It could be noticed further by comparison of Figures 7(c) and 7(d) that if the initial field strength increases (i.e., β_0 decreases), the observed feature of prominence density distribution fails to appear. Another important feature which could be seen by comparison of Figures 7(a) and 7(c) is the injection density which shows that when we increase 20% of the injection density, it forms a loop instead of prominence.

To summarize the present simulation studies, we show that the best combination of physical parameters for a K-S-type prominence formation is $\beta_0 = 2.0$ (i.e., 4.5 G), $\rho/\rho_0 = 1.0$, and $v_0 = 10 \text{ km s}^{-1}$, with condensation and thermal conduction processes

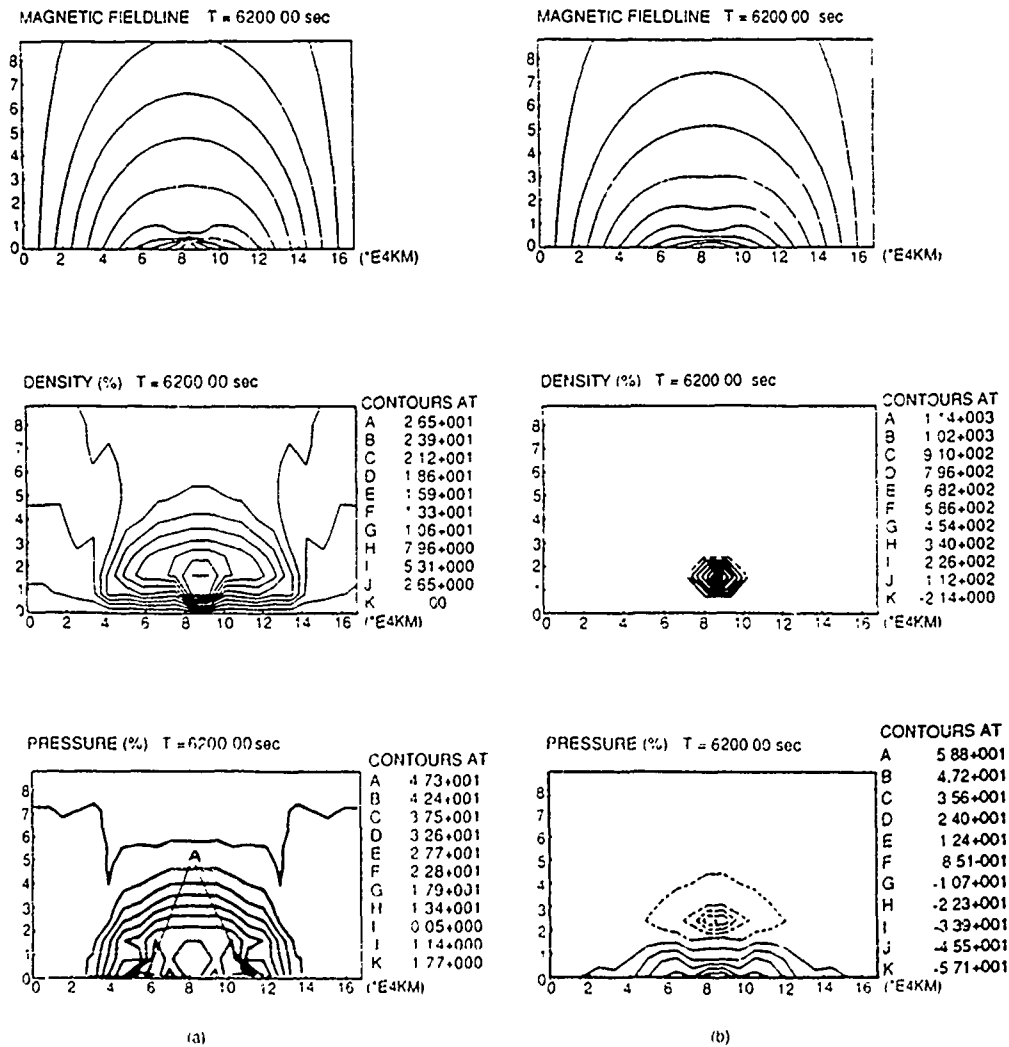
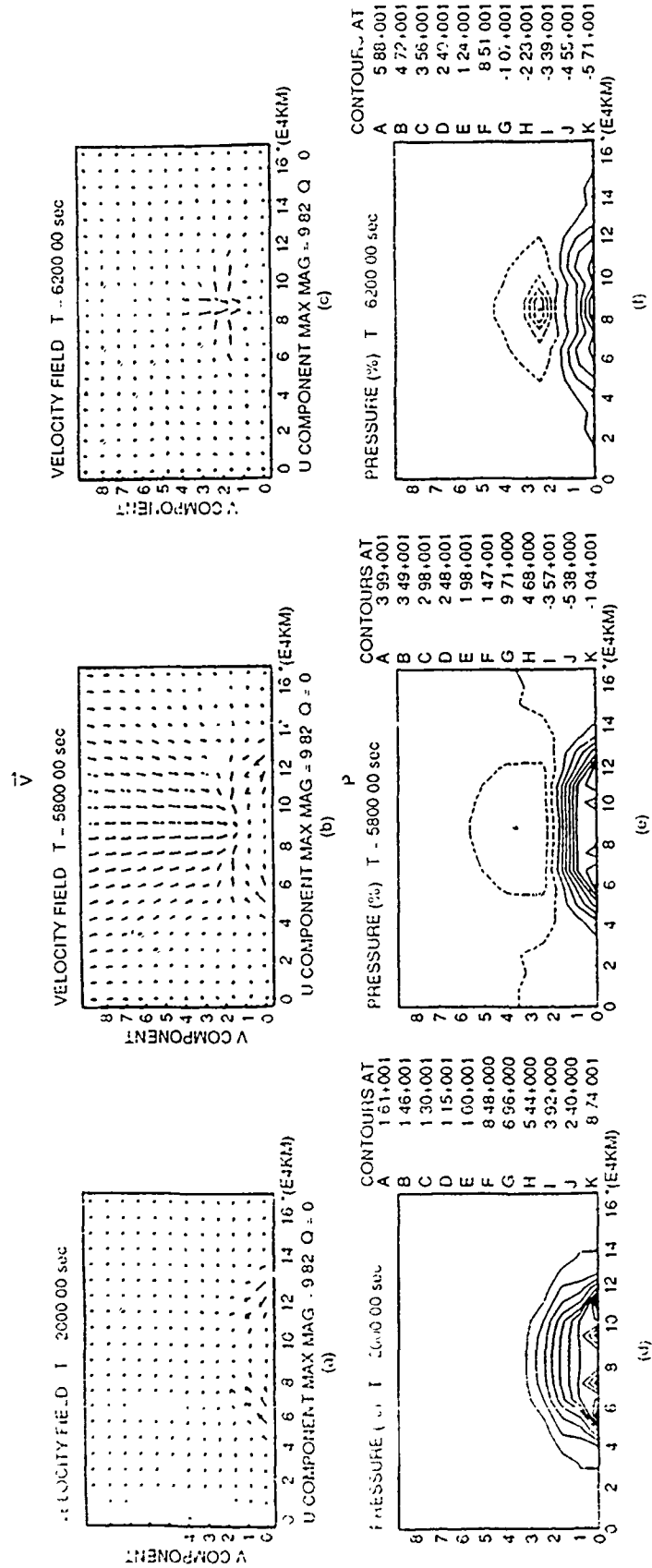


Fig 8 Comparison between the results of magnetic field, density, and pressure contours obtained from the ideal MHD model (left) and non-ideal MHD model (right) at 6200 s after mass injection for $\beta_0 = 2.0$, $\rho/\rho_0 = 1.0$, and $v_0 = 10 \text{ km s}^{-1}$.


 Fig. 9 Computed evolution of the velocity and pressure field due to mass injection for $\beta_0 = 2.0$, $\rho/\rho_0 = 1.0$, and $t_0 = 10 \text{ km s}^{-1}$ based on non-ideal MHD model

in the model (i.e., non-ideal MHD model). As discussed by An, Bao, and Wu (1988) and An *et al.* (1988) a K-S magnetic field configuration can be formed without condensation and thermal conduction. However, the resulting density contours do not resemble observations. These results for magnetic field configuration, density contours, and pressure contours are shown in Figure 8 for models with and without radiation and conduction.

Finally, we present the evolution of the vectorial representation of the velocity distribution and pressure distribution at various times (i.e., 2000, 5800, and 6200 s) in Figure 9. From these results we noted two important features:

(i) The development of a low pressure region on top of the apex as shown in Figure 9(f) may correspond to the cavity generally observed above prominences. Also, we can understand the cause of the cavity as due to the condensation (see Figure 9(c)) because there is no locality. We may notice further that this low pressure region is created by both density depletion ($\sim 2\%$, Figure 5(b)) and decreasing temperature ($\sim 91\%$, Figure 6).

(ii) The support of the prominence mass is due not only to the magnetic field but it also results from the momentum due to the injected mass as indicated by the high pressure contours on the lower boundary in Figure 9(d-f).

4. Discussion and Concluding Remarks

In comparison to previous studies of prominence formation, the present work incorporates the nonlinear dynamical effects of the magnetohydrodynamics together with condensation and thermal conduction in a fully self-consistent treatment. In order to sort out these complicated physical processes, it would be useful to estimate the characteristic time-scale for each of the physical processes. Employing dimensional analysis for the momentum and energy equations (i.e., Equations (2) and (3)), we obtain the following characteristic time-scales:

Hydrodynamic time-scale,

$$t_p = \left[\frac{x_0^2}{RT_0} \right]^{1/2} = \sqrt{\gamma} \frac{x_0}{c_s},$$

magnetohydrodynamic (MHD) time-scale,

$$t_m = \left[\frac{4\pi\rho_0 x_0^2}{B_0^2} \right]^{1/2} = \frac{x_0}{c_A},$$

conduction time-scale,

$$t_c = \frac{p_0}{(\gamma-1)Q_{c0}} = \frac{p_0 x_0^2}{(\gamma-1)k_0 T_0^2},$$

radiation time-scale,

$$t_R = \frac{p_0}{(\gamma-1)Q_{R0}} = \frac{p_0}{(\gamma-1)\lambda\rho_0^2 T_0^2}.$$

condensation time-scale.

$$t_{cds} = \frac{t_R t_c}{t_R - t_c},$$

where c_s is the sonic speed, c_A is the Alfvén speed, and the subscript 0 represents the reference value. In Table I, we present the results for these characteristic times for various initial conditions. Only the magnetohydrodynamic time-scale is affected by the plasma beta through the Alfvén time scale. The other time-scales are functions of plasma properties and geometric length. These characteristic time-scales have important effects on the determination of simulation time to assure meaningful physics and the under-

TABLE I
Characteristic time-scales with an initial atmosphere characterized
by $T = 10^6$ K, $\rho_0 = 8.35 \times 10^{-15}$ g cm $^{-3}$, $l_i = 2 \times 10^4$ km

β	0.7	1.0	2.0
t_p	170 s	170 s	170 s
t_m	92 s	110 s	156 s
t_c		8000 s	
t_R		3200 s	
t_{cds}		5400 s	

standing of the sequence of the physical processes. For example, we note from Figure 4 that the density increases and the temperature decreases significantly after 3000 s for the case where radiation is included. For the case of both radiation and thermal conduction, the density increases and the temperature decreases significantly beginning at ~ 5000 s. These two times correspond to our theoretically predicted radiation time scale and condensation time scale, respectively, which implies that our numerical simulation experiments behave properly. There are not any analytic results with which to compare our simulation, but the agreements with the above-mentioned time-scales may be considered to be an indication that the numerical results reflect correct physical situations.

We now estimate the amount of mass being accumulated in the 'pit' and examine the distribution between the injection mass and condensed mass. The total mass in the prominence can be obtained by numerically integrating the density distribution over the area which is considered to be the prominence (i.e., the pit). We find the total mass to be 6.4×10^2 g cm $^{-1}$. The amount of mass which is injected into the computational domain is 1.2×10^3 g cm $^{-1}$. However, not all of the mass can reach the pit which we identify with the prominence material. If we assume that only one-third of this injected mass reaches the pit, the amount of injected mass which can be considered as prominence mass is 4×10^2 g cm $^{-1}$. Taking the difference between the total prominence mass and the injected prominence mass to be the condensed mass from the corona, we find

that the latter is $2.4 \times 10^{12} \text{ g cm}^{-1}$. Because this is a two-dimensional model, the third dimension is arbitrary. If we take the length of the prominence to be 10^5 km , then the total mass in this simulated prominence is $6.4 \times 10^{12} \text{ g}$ of which 37.5% is coming from the coronal condensation and the rest (62.5%) is contributed by the injected mass from below. This scenario may resolve a classical problem in prominence formation as pointed by Saito and Tandberg-Hanssen (1973); i.e., with the mass injection present, the formation of prominence will not depend on the collapse of a very large part of the corona.

In summary, we have presented a self-consistent numerical simulation model for the understanding of the prominence formation process due to mass injection from the chromosphere. This model is based on a two-dimensional, time-dependent magneto-hydrodynamic theory with inclusion of radiation and thermal conduction effects. Based on the results from this simulation model, we conclude that

- (i) There is a unique combination of plasma beta, injection density, and velocity in which a K-S-type prominence may form at the neutral line. This might explain why there is no prominence at every neutral line.
- (ii) The mass injection does not supply the entire prominence mass but triggers a condensation of coronal mass to further supply the prominence mass.
- (iii) The prominence mass is not only supported by the magnetic field but also by an increase in the pressure gradient (see Figure 9) through the dynamic process of mass injection. This may be considered ballistic support.
- (iv) The combination of a high injection velocity and density with a small plasma beta is an unfavorable situation for the prominence formation. Instead, we see the formation of loops.
- (v) The formation of cool prominence mass is due to radiation, and the thermal conduction smooths the temperature distribution of the prominence along the field lines.
- (vi) The cavity formation may be considered as a dynamical process which happens because the surrounding coronal mass is condensed to the pit and there is not enough time for mass to be supplied to replace the condensed mass as demonstrated in Figures 5(b) and 9(c).
- (vii) Finally, we should note that the siphon effect is another mechanism which could get the mass into the pit because the creation of the cavity leads to an additional pressure gradient. However, this effect is small in comparison to the condensation and mass injection processes, since, the gravitational effect will enhance the process of condensed mass falling into the pit, but it will curtail the siphon mass from getting into it.

We conclude that this numerical simulation study reveals situations that resemble overall characteristics of a K-S-type prominence as concern field configuration, cool mass, and coronal cavity.

Acknowledgements

We acknowledge Ronald L. Moore for reading the manuscript and giving us valuable suggestions. The work done by STW and JJB was partially supported by NASA Grant

NAGW-9. The work done by CHA and STW was also partially supported by AFSOR-88-0013.

References

- An, C.-H., Bao, J. J., and Wu, S. T.: 1988, *Solar Phys.* **115**, 81.
 Ann, C.-H., Canfield, R. C., Fisher, G. H., and McClymont, A. N.: 1983, *Astrophys. J.* **267**, 421.
 Ann, C.-H., Bao, J. J., Wu, S. T., and Suess, S. T.: 1988, *Solar Phys.* **115**, 93.
 Cox, D. P. and Tucker, W. H.: 1969, *Astrophys. J.* **157**, 1157.
 Field, G. B.: 1965, *Astrophys. J.* **142**, 531.
 Hildner, E.: 1974, *Solar Phys.* **35**, 123.
 Hu, Y. Q. and Wu, S. T.: 1984, *J. Comp. Phys.* **55**(1), 33.
 Kleczek, J.: 1958, *Bull. Astron. Inst. Czech.* **9**, 115.
 Kuperus, M. and Tandberg-Hanssen, E.: 1967, *Solar Phys.* **2**, 39.
 Low, B. C. and Wu, S. T.: 1981, *Astrophys. J.* **248**, 335.
 Lust, R. and Zirin, H.: 1960, *Z. Astrophys. J.* **49**, 8.
 Nakagawa, Y.: 1970, *Solar Phys.* **12**, 419.
 Parker, E.: 1953, *Astrophys. J.* **117**, 431.
 Pikel'ner, S. B.: 1969, *Soviet Astron. - AJ* **13**, 259.
 Poland, A. I. and Mariska, J. T.: 1986, *Solar Phys.* **104**, 303.
 Raadu, M. A. and Kuperus, M.: 1973, *Solar Phys.* **28**, 77.
 Raju, P. K.: 1968, *Monthly Notices Roy. Astron. Soc.* **138**, 479.
 Saito, K. and Tandberg-Hanssen, E.: 1973, *Solar Phys.* **31**, 105.
 Uchida, Y.: 1963, *Publ. Astron. Soc. Japan* **15**, 376.
 Wu, S. T. and Wang, J. F.: 1987, *Compt. Math. Appl. Mech. Eng'g.* **64**, 267.
 Wu, S. T., Hu, Y. Q., Nakagawa, Y., and Tandberg-Hanssen, E.: 1983, *Astrophys. J.* **266**, 866.

III. MAGNETOHYDRODYNAMIC WAVES IN THE SOLAR ATMOSPHERE

It has been suggested that the coronal heating and solar wind acceleration may be related to the MHD waves in the solar atmosphere. Either to prove or to disprove these suggested concepts we have made a systematic study on the propagating, reflecting and trapping of MHD waves in the solar atmosphere. The results we obtained are not conclusive. Three papers were published in the Astrophysical Journal to report these results:

Magnetohydrodynamic Instabilities in Coronal Arcade in Astrophys. J., Vol. 337, 989-1002, 1989.

Propagating and Non-propagating Compression Waves in an Isothermal Atmosphere with Uniform Horizontal Magnetic Field in Astrophys. J., Vol. 344, 478-493, 1989.

Reflection and Trapping of Transient Alfvén Waves Propagating in an Isothermal Atmosphere with Constant Gravity and Uniform Magnetic Field in Astrophys. J., Vol. 345, 597-605, 1989.

MAGNETOHYDRODYNAMIC INSTABILITIES IN CORONAL ARCADES

CHANG-HYUK AN, S. T. SUESS,¹ AND S. T. WU

Center for Space Plasma and Aeronomic Research and Department of Mechanical Engineering, University of Alabama in Huntsville

Received 1988 February 29; accepted 1988 July 27

ABSTRACT

We have studied the MHD stability of coronal arcades with and without a detached flux tube using a two-dimensional linear MHD stability numerical model. For the study, we computed two-dimensional magnetohydrostatic equilibria with and without gravity. We have also studied the effect of gravity, magnetic shear (or field twist along a detached flux tube), and longitudinal wave number, n on stability.

We have found that a coronal arcade without a detached flux tube (or with all field lines tied to the lower boundary) is stable for any magnetic shear and for any longitudinal mode. On the other hand, an arcade with a detached flux tube is unstable for $n \neq 0$ perturbations and the instability mode structure and growth rate vary depending on the field twist and longitudinal wave number n . All the equilibria we have studied are stable to $n = 0$ perturbations.

Gravity has a stabilizing effect on the equilibria. The gravitational effect is measured by λ (the ratio of the standard arcade width to the gravitational scale height). As the λ increases from zero to 0.2 the $m = 0$ transverse mode growth rate decreases, but high m modes are stabilized. The equilibria we have studied are completely stabilized for $\lambda > 0.33$. This study enables us to understand the stable nature of coronal arcades and prominences, and gives us an insight into solar eruptive phenomena.

Subject headings: hydromagnetics — instabilities — Sun: corona

1. INTRODUCTION

The solar atmosphere exhibits various eruptive phenomena. Solar flares occur in active regions with highly sheared magnetic fields of several hundred Gauss along a neutral line. A very energetic solar flare is often associated with a prominence eruption in an active region. In a quiet region, where the magnetic field strength is ~ 10 G, a quiescent prominence resides along a neutral line for several days or weeks but can then erupt without any advance warning. Various mechanisms have been suggested for the onset of the eruptive phenomena. One mechanism is a critical shear beyond which no neighboring solution exists. The lack of neighboring solutions beyond the critical shear is considered to explain the onset of eruptive phenomena (Low 1977). Another is reconnection between emerging flux and overlying magnetic fields which triggers an eruptive phenomenon (Canfield, Priest, and Rust 1974; Heyvaerts, Priest, and Rust 1974; Heyvaerts, Priest, and Rust 1977). A third is an ideal MHD kink instability which causes an eruption of a magnetic flux tube (Moore 1988). In order for the critical shear or reconnection to be a possible eruptive mechanism the magnetic structure should be MHD stable before reaching the critical shear or reconnecting. If not, the magnetic structure would first be destroyed by fast MHD instabilities. On the other hand, in order for an eruption to be due to a kink instability, the magnetic structure should be MHD unstable. Here we conduct an MHD stability study as a first step to the understanding of eruptive phenomena. The stability study also enables us to understand the stable nature of quiescent prominences and coronal loops.

The stability of a coronal arcade with field lines tied to the photosphere has previously been studied (Hood and Priest 1980; Birn and Schindler 1981; Ray and Van Hoven 1983; Migliuolo and Cargill 1983; Hood and Anzer 1987) while

neglecting gravity and simplifying the field configuration to be in cylindrical geometry. The simplified one-dimensional MHD stability problem is extended to a two-dimensional MHD stability study by including solar gravity. Low (1984) constructed two-dimensional coronal arcades and studied the stability of specific equilibria using the energy principle (Bernstein *et al.* 1958; Hain, Lüst, and Schluter 1957). Galindo and Schindler (1984) also used the energy principle to prove that Kippenhahn-Schluter type prominence field configurations are stable to linear MHD instabilities. Melville, Hood, and Priest (1986) studied local modes analytically in two-dimensional coronal arcades without magnetic shear. These studies are restricted to the analysis of the stability of certain types of equilibria. Recently, Zwingman (1987) and Galindo (1987) developed numerical methods based on the energy principle for the study of the linear stability of general equilibria. Zwingman studied the stability of a sequence of equilibria with increasing pressure gradient for a given magnetic shear but restricted the calculation to a two-dimensional perturbation. Galindo studied the stability of several existing prominence models but did not study how line tying, gravity, magnetic shear, longitudinal wave number, and the surrounding ambient plasma and magnetic field affect the stability. In order to understand the nature of quiescent prominences and various eruptive phenomena we have to understand the consequences of these effects on stability. For the present study, we have developed a linear MHD numerical model. Our numerical model is different from the previous models in that we solve time-dependent linearized MHD equations as an initial boundary value problem instead of using the energy principle. We have also developed a numerical magnetohydrostatic equilibrium model for the computation of various equilibrium initial states. We will study the stability of equilibria with and without a detached flux tube and with and without gravity for various longitudinal wave numbers and various magnetic shear.

¹ NASA/Marshall Space Flight Center.

II. NUMERICAL MODEL

We solve the time-dependent linearized ideal MHD equations in dimensionless form:

$$\rho_0 \frac{\partial \mathbf{v}}{\partial t} = -\beta \nabla p_1 + \mathbf{J}_0 \times \mathbf{B}_1 + \mathbf{J}_1 \times \mathbf{B}_0 + \rho_1 \mathbf{g}, \quad (1)$$

$$\frac{\partial \rho_1}{\partial t} + \nabla \cdot (\rho_0 \mathbf{v}) = 0, \quad (2)$$

$$\frac{\partial p_1}{\partial t} + \mathbf{v} \cdot \nabla p_0 + \Gamma p_0 \nabla \cdot \mathbf{v} = 0, \quad (3)$$

$$\frac{\partial \mathbf{B}_1}{\partial t} = \nabla \times (\mathbf{v} \times \mathbf{B}_0), \quad (4)$$

$$\nabla \times \mathbf{B}_1 = \mathbf{J}_1, \quad (5)$$

$$p = \rho T, \quad (6)$$

Here a subscript 0 indicates equilibrium quantities, a subscript 1 indicates perturbed quantities, and \mathbf{v} , p , \mathbf{J} , \mathbf{B} , T , and ρ are velocity, pressure, current density, magnetic field, temperature and plasma density, respectively. In order to make the equations dimensionless we normalize \mathbf{v} , \mathbf{B} , p , and ρ with Alfvén velocity V_A , B_0 , P_0 , and ρ_0 at the lower boundary and time t is normalized by the Alfvén transit time across the width of an arcade. Lengths are normalized by the width of an arcade, and g is the dimensionless solar gravity defined as $g = \lambda \beta$ and directed in the negative y -direction; Γ is the ratio of specific heats, λ is the ratio of the width of a magnetic arcade to the gravitational scale height, and β is defined by $\beta = 4\pi P_0/B_0^2$ (note that this β is one half of the usual plasma β). Since we study the stability of two-dimensional magnetohydrostatic equilibria with symmetry in the z -direction, perturbed quantities have the form:

$$f_1(r, t) = f(x, y, t)e^{ikz}. \quad (7)$$

By using equation (7) for the perturbed quantities in equations (1)–(5) we obtain real and imaginary time-dependent linear MHD equations. The equations are integrated with time after a velocity perturbation is given to an initial equilibrium. The numerical method we use is essentially the same as that developed by Bateman *et al.* (1974) and is presented in the Appendix. We reproduced the results of Bateman *et al.* for verification of our numerical code. We calculate the linear growth rate assuming that perturbed quantities have an exponential time dependence. We integrate the kinetic energy, E , over the whole computing domain and calculate the growth rate at each time step using the equation:

$$\omega = [\ln E(t + \Delta t) - \ln E(t)]/\Delta t$$

until ω approaches a steady value. Since the kinetic energy is the square of velocity the real growth rate of a perturbation is half of ω .

Our problem is different from the problem of Bateman, Schneider, and Grossman (1974) in that we study the stability of gravitationally stratified coronal arcades with field lines tied to the lower boundary in an open space. We have to specify a line tying boundary condition at the lower boundary and an open boundary condition at the upper boundary, and have to add an artificial viscosity in the momentum equation to stabilize a numerical instability which may develop in a gravitationally stratified initial atmosphere. The numerical treatments

of line-tying, open boundary, and artificial viscosity are presented in detail in the Appendix.

III. EQUILIBRIUM INITIAL STATES

We compute a magnetohydrostatic equilibrium for an isothermal solar atmosphere by solving the force balance equation (we drop the subscript 0 for convenience),

$$\beta \nabla p = \mathbf{J} \times \mathbf{B} + \rho \mathbf{g}. \quad (8)$$

The vector form of the equation can be converted to a nonlinear second-order differential equation by using

$$\mathbf{B} = \nabla \times (A_z \mathbf{e}_z) + B_z \mathbf{e}_z. \quad (9)$$

Here A_z is the z -component of the vector potential \mathbf{A} . The differential equation (Low 1975) is

$$\nabla^2 A_z + f(A_z)e^{-\lambda y} + B_z \frac{dB_z}{dA_z} = 0. \quad (10)$$

$$p(x, y) = e^{-\lambda y} \left[p_0 + \frac{1}{\beta} \int f(A_z) dA_z \right], \quad (11)$$

$$\mathbf{J}_p = \frac{dB_z}{dA_z} \nabla A_z \times \mathbf{e}_z. \quad (12)$$

$$J_z = f(A_z)e^{-\lambda y} + B_z \frac{dB_z}{dA_z} = -\nabla^2 A_z. \quad (13)$$

We solve equation (10) by specifying source functions $f(A)$ and $B_z(A)$ as

$$f(A_z) = \alpha^2 A_z, \quad (14)$$

$$B_z(A_z) = \gamma(A_z - A_c)^2 \text{ for } A_c \leq A_z \leq 1,$$

$$B_z(A_z) = 0 \text{ for } A_z \leq A_c, \quad (15)$$

or

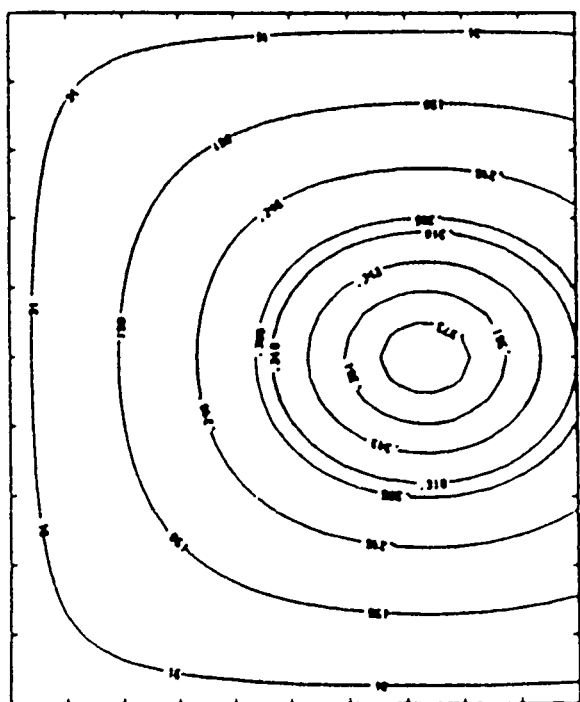
$$B_z(A_z) = \text{constant}. \quad (16)$$

By A_z we denote zero at the ends and the maximum at the center of the lower boundary, and A_c is an input parameter for localized magnetic shear. With the above source functions the plasma pressure in dimensionless form becomes

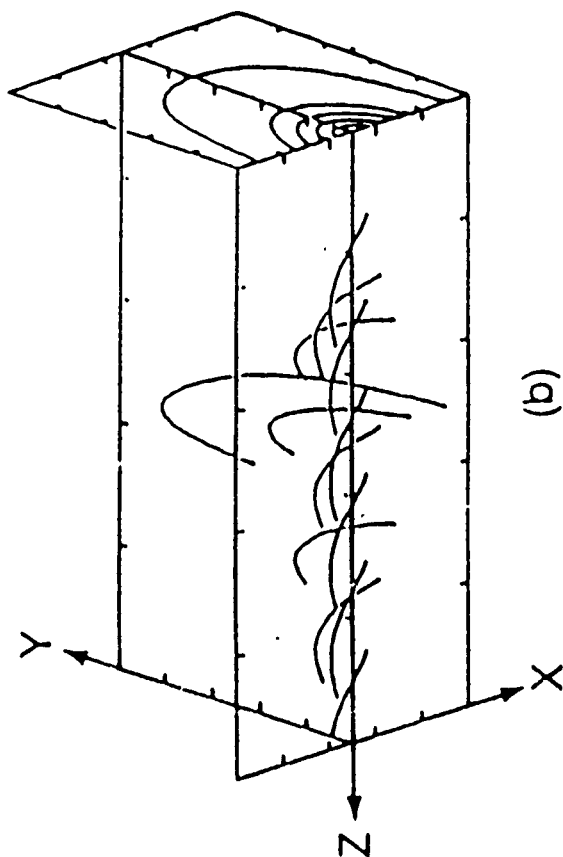
$$p(x, y) = e^{-\lambda y} (1 + 0.5x^2 A_z^2/\beta), \quad (17)$$

if we assume that $p(x, y) = 1$ for $y = 0$ and $A_z = 0$.

The source functions (14) and (15) imply that the longitudinal current is distributed over the whole arcade, with decreasing magnitude with height, and the transverse current is distributed locally to generate sheared magnetic field near the neutral line. The value of α determines the magnitude of longitudinal current and the non-force free component of magnetic field, γ determines the magnitude of magnetic shear, and A_c determines the localization of the shear. For a given α in equation (14) an increase of B_z in equation (16) does not change the transverse field, while an increase of γ in equation (15) inflates the transverse field lines. The isothermal equilibrium has a density profile identical to the pressure profile. From equation (17) we can see that the plasma pressure at the center of a loop increases as β decreases, resulting in an increase of the density in the detached flux tube. We compute two different equilibria in the x - y coordinate system, one is a coronal arcade with a detached flux tube and the other is without a detached flux tube. These equilibria are shown in Figure 1. $B_z = 0$ results in

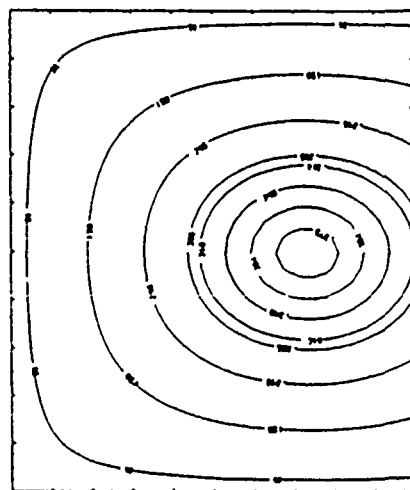


(a)

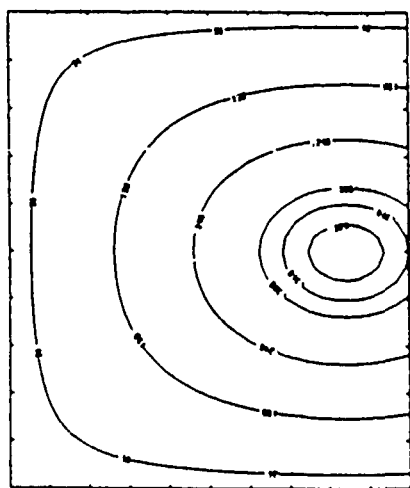


(b)

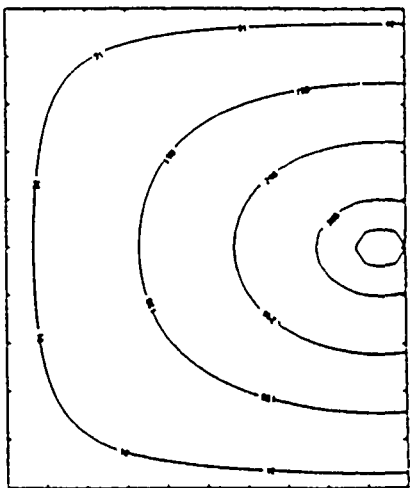
FIG. 1 (a) A coronal arcade with a detached flux tube and no gravity ($\lambda = 0$). We use eqs (14) and (16) to define source functions for eq (10) with $\alpha = 3.8$, $\gamma = 0$ (b) A coronal arcade with no detached flux tube and $\alpha = 0$. We use eqs (14) and (15) as source functions



(a)



(b)



(c)

FIG. 2 The effect of gravity on the magnetohydrostatic equilibrium solution for different λ values, (a) $\lambda = 0$, (b) $\lambda = 0.2$, and (c) $\lambda = 0.4$. As λ increases the size of the detached flux tube decreases

twisted magnetic field lines wrapped around the detached flux tube shown in cross section in Figure 1a with the twist decreasing as B_z increases. For the equilibrium we use equations (14) and (16) as source functions. Figure 1b shows a coronal arcade without a detached flux tube, obtained by using equations (14) and (15). The magnetic shear increases with γ in equation (15) until γ reaches a critical value beyond which no neighboring equilibrium exists. Our equilibrium numerical code is a part of the instability code with the same spatial algorithm and grid as used in the instability code. We will study the stability of the equilibrium shown in Figure 1 for different field twist and magnetic shear to show how they affect stability.

We will also study the effect of gravity on the stability by changing the value of λ . For given source functions $f(A_z)$ and $B_z(A_z)$, the field configuration changes with λ , as shown in Figure 2. The size of a detached flux tube shrinks as λ (or gravity) increases.

IV. STABILITY

a) Without Gravity

We first study the stability of a sequence of equilibria with a detached flux tube (Fig. 1a) for a various longitudinal magnetic field strengths, B_z , and for various longitudinal wave numbers, n . Here, the longitudinal wave number is defined as the number of longitudinal wavelengths in the arcade length (L_z) where the arcade length is equal to the aspect ratio times the width of the arcade. The longitudinal wave number n is expressed with wavevector k as $n = kL_z/2\pi$. We define the factor q to represent

the twist of a field line on a surface of a detached flux tube.

$$q = \frac{\int A_z B_z dl}{B_p(A_z)L_z} \quad (18)$$

Here, B_p is the transverse magnetic field. The integration is carried along a detached flux line of A_z . If q is less (larger) than 1, the field line wraps the flux tube more (less) than one turn along the length of the tube. For a circular cylindrical plasma pinch, the plasma is kink unstable for $q < 1$, implying that the magnitude of q determines the stability. As B_z increases, the magnetic shear of a field line tied to the photosphere and the q -value of a detached flux surface increase, affecting the stability. The relation between q and B_z for the equilibrium of Figure 1a is shown in Figure 3, which shows q at the center of the detached flux tube increasing nearly linearly with B_z .

The first example we study is the stability under a purely two-dimensional perturbation, i.e., the $n = 0$ wave. We find that the equilibrium shown in Figure 1a is stable to $n = 0$ perturbations for all values of B_z . Thus the equilibria we have studied, including the equilibria shown in Figure 1b, are stable to all two-dimensional perturbations. This result implies that a two-dimensional perturbation is not adequate for stability studies of a two-dimensional equilibrium, and we do not consider this case further.

Next, we study three-dimensional perturbations, namely $n \neq 0$ wave numbers. Figure 4 shows the instability growth rate ω versus B_z for $n = 1$ and 3. The dotted line is for $n = 3$ and $\beta = 1$, the solid line is for $n = 1$ and $\beta = 1$, and the light

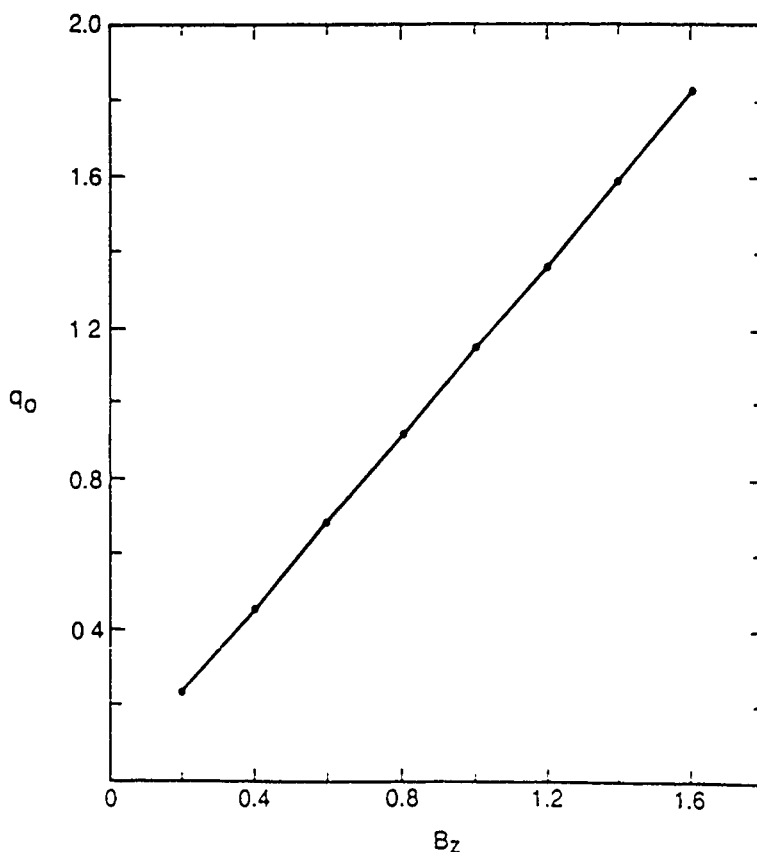


FIG. 3—The value q defined in eq. (18) vs B_z for the equilibrium of Fig. 1a. The value at the center of the detached flux tube is q_0 .

solid line is for $n = 1$ and $\beta = 0.1$. It can be seen from this figure that the growth rate versus B_z for $n = 1$ is much smaller than for $n = 3$. We will discuss these results in some detail.

Let us first examine the $n = 1$ mode. The growth rate for $n = 1$ and $\beta = 1$ (Fig. 4, solid line) shows that for B_z lower than 0.6 (or for q lower than 0.68), the equilibrium is unstable. The velocity structures for this perturbation are shown in Figure 5 for different initial perturbations but the same B_z . Figure 5a is for a random velocity perturbation. Figure 5b is for a symmetric v_x but antisymmetric v_y , and Figure 5c is for a symmetric v_y but antisymmetric v_x . Figure 5a shows that the random perturbation produces an asymmetric unstable mode structure, a surprising result because the initial equilibrium is

symmetric. If we combine the mode structures of Figures 5b and 5c, we see that the resultant mode structure is similar to that of Figure 5a. This figure thus implies that when we give a random perturbation, the two different modes of Figure 5b and 5c become the most unstable modes, producing, as a consequence, an asymmetric mode. We have checked the growth rate of each mode and find that the growth rates are the same for all three. We also notice that the initial perturbations of Figures 5b and 5c cause a faster approach to the linear growth rate than the random perturbation does. In most of this study, we use the perturbation of Figure 5c rather than the random perturbation, to reduce computation time. In analogy to the $m = 0$ mode in a circular cylindrical pinch (Bateman 1978,

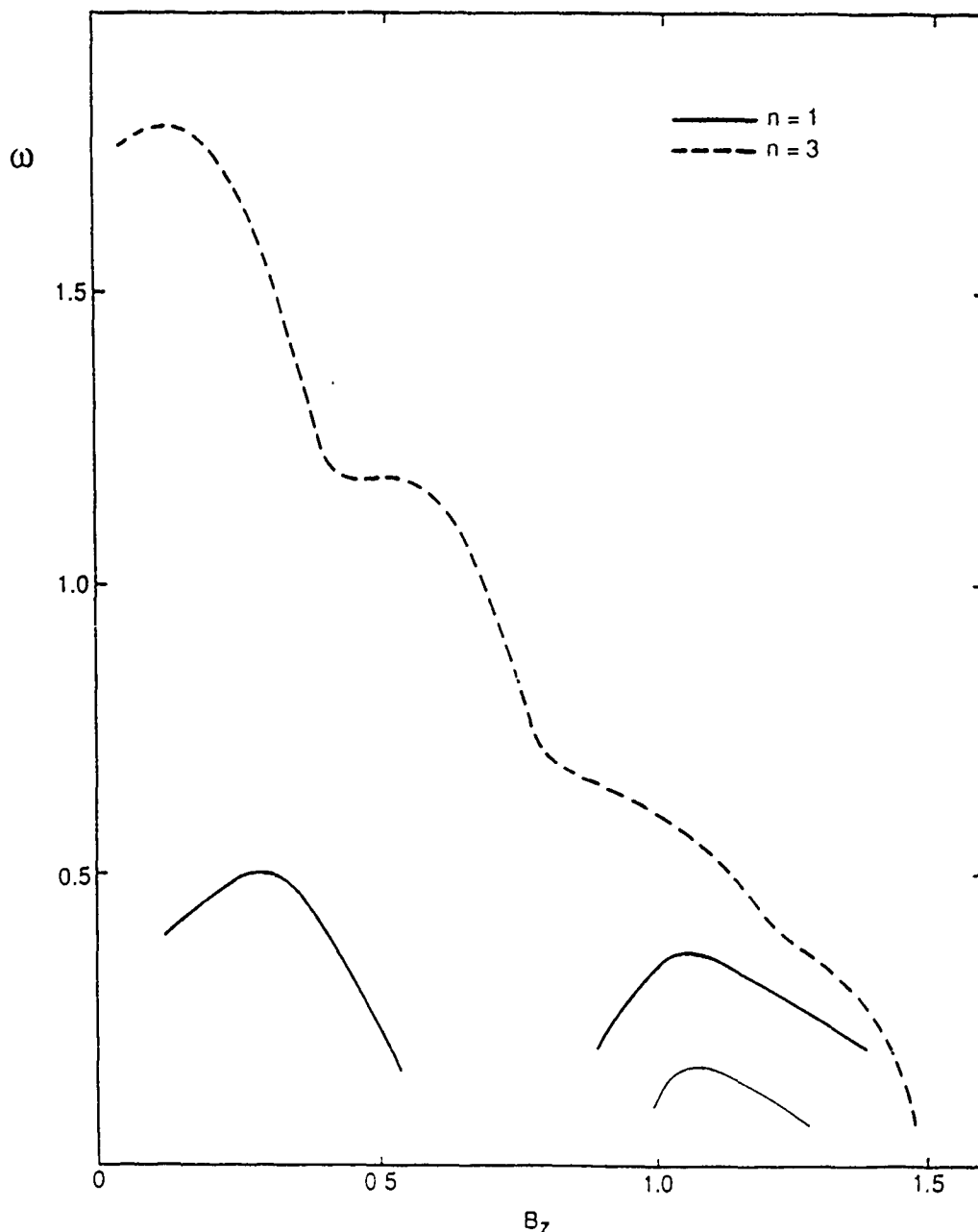


FIG. 4—Growth rate ω versus longitudinal magnetic field B_z for longitudinal mode numbers $n = 1$ and $n = 3$ and for $\lambda = 0$. The dotted line is for $n = 3$ and the solid line is for $n = 1$. For the two curves $\beta = 1$. The light solid line is for $n = 1$ and $\beta = 0.1$.

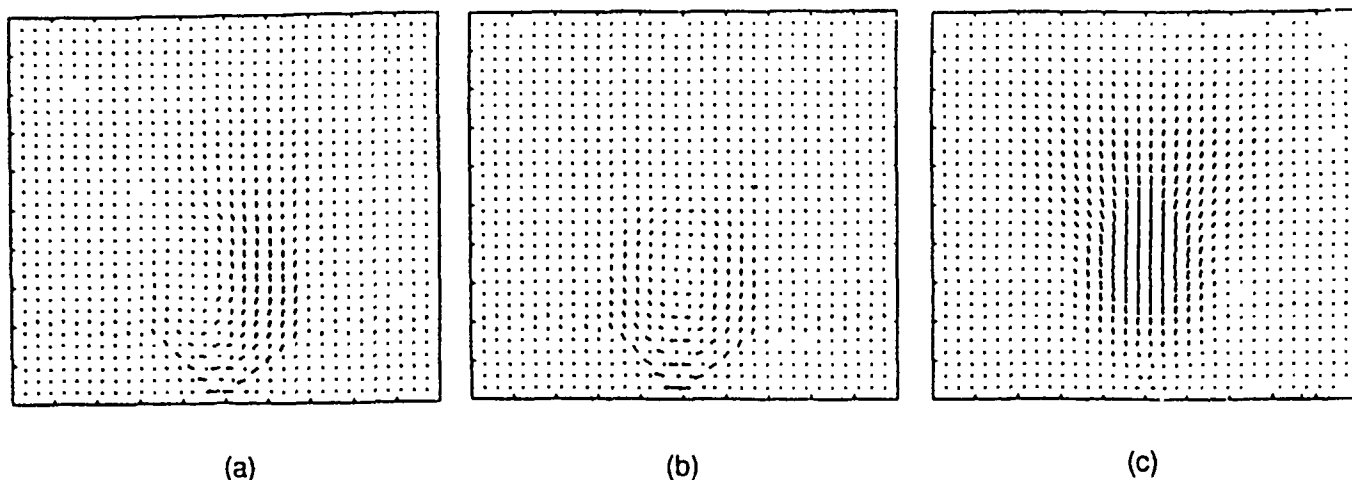


FIG 5—Velocity fields for the $m = 0$ unstable mode for different initial perturbations (a) random perturbation, (b) v_x is symmetric and v_y is antisymmetric, and (c) v_x is antisymmetric and v_y is symmetric. (a) and (b) show plasma moving fast along the lower boundary, even though line-tying boundary condition is given, because the field lines are detached from the lower boundary.

Chap. 6), we call this the $m = 0$ mode since it has no nodal lines in the x - y plane. For a cylindrical pinch, m represents a poloidal harmonic mode number which does not exist in this two-dimensional equilibrium configuration. When we say $m = 0, 1$, etc. in this study, we mean that the mode structures are similar to the $m = 0, 1$ (and so on) modes in a circular cylindrical pinch.

Figure 4 shows that the $n = 1$ mode is again unstable for $0.8 < B_z < 1.5$ (or $0.9 < q_0 < 1.7$) and the unstable mode structure is similar to the $m = 1$ mode of a circular cylindrical pinch as shown in Figure 6. This figure shows a tilted pair of vortex patterns, for a random perturbation (Fig. 6a), and a symmetric vortex that is localized in the detached flux tube for the perturbation used in Figure 5c. The mode structure shown in Figure 6b is a typical $m = 1$ mode in circular cylindrical pinch. The $m = 1$ mode is called a kink mode and is suggested to cause the eruption of prominences (Sakurai 1975). The $m = 0$ and 1 modes are separated from each other by a stable region where $0.6 < B_z < 0.8$. Figure 4 also shows that the growth rate for

$\beta = 0.1$ is one third of that for $\beta = 1$. The lower growth rate for $\beta = 0.1$ is due to the density for $\beta = 0.1$ being 10 times that for $\beta = 1$ at the center of the flux tube (see eq. [17]).

The $n = 3$ mode is shown in Figure 4 to have several times the growth rate of the $n = 1$ mode. It is ~ 4 times higher than for $n = 1$ for $B_z \approx 0$, but decreases rapidly to zero as B_z increases to 1.5. When B_z increases from zero to 1.5 the unstable structure changes from an $m = 0$ mode to an $m = 3$ mode continuously, without being separated by a stable region in B_z , which is a striking difference from the $n = 1$ mode. Since the $n = 3$ mode has a higher growth rate than the $n = 1$ mode for $B_z \leq 1.5$, a loop will eventually be subject to the $n = 3$ mode rather than $n = 1$ mode for a random perturbation in a longitudinal direction. This result implies that any prominence eruption is caused by higher n kink modes than $n = 1$, which seems contradictory to observations.

Figure 7 shows the growth rates versus n for $B_z = 1$ (or $q_0 = 1.14$). As n increases, the growth rate increases until $n = 3.4$ and then decreases for $n > 3.4$. The mode structure

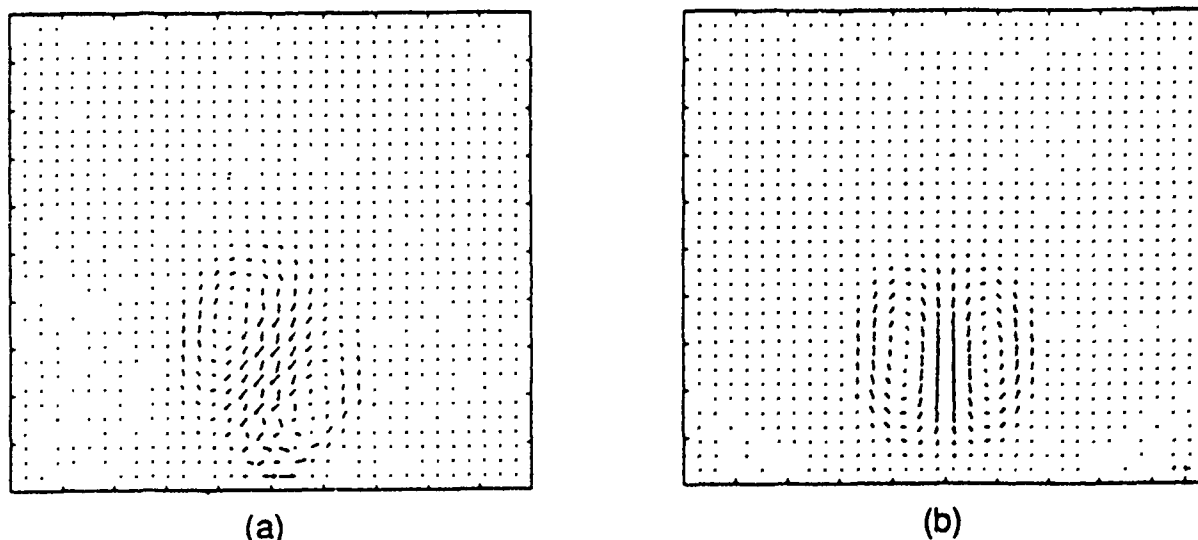


FIG 6—Velocity fields for the $m = 1$ unstable mode for two different initial perturbations (a) Random perturbation, (b) v_x is antisymmetric, and v_y is symmetric

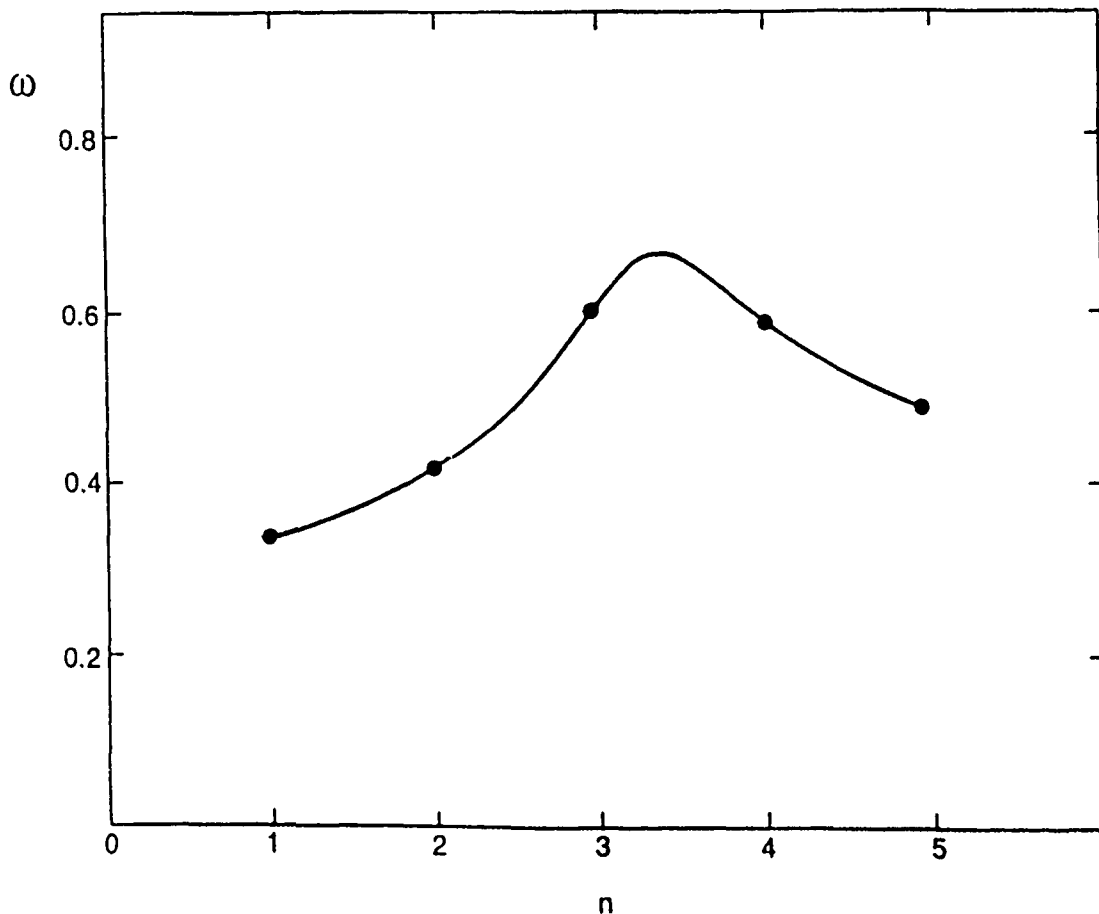


FIG. 7.—Growth rate vs longitudinal mode number n , for $B_z = 1$ and $\lambda = 0$. The longitudinal mode number n is usually an integer number, but we can also take a real value because $n = kL_z/2\pi$ and the wavevector k can be any number.

also changes from an $m = 1$ to an $m = 4$ mode continuously for increasing n . The mode structures for $n > 2$ are shown in Figure 8. The number of vortices increases as n increases and the modes are more broadly distributed in the upper region than near the lower boundary. The high m mode structures are similar to the ballooning modes in a tokamak (Bateman and Peng, 1977), which are strongly localized near the outer surface of the tokamak. The ballooning mode is considered dangerous to tokamak stability because of its mode structure. The implication of the ballooning-type mode structure shown in Figure 8 on the stability of a coronal arcade with a detached flux tube is not obvious.

Next, we study the stability of a sequence of equilibria not having a detached flux tube (Fig. 1b) in the presence of increasing magnetic shear. Since we specify $B_z(A_z)$ rather than magnetic shear, the sequence of equilibria does not necessarily correspond to quasistatic shear motion (Jockers 1976, 1977). However, the increase of γ in equation (15) does cause a monotonic increase of the shear. We find that the sequence of equilibria are all stable for γ less than the critical value over which no neighboring solution exists, implying that quasistatic evolution is possible up to a critical shear without any instability. Since no MHD instability is found during the quasi-static evolution, the critical phenomenon is a good candidate for indicating the onset of eruptive phenomena. This study could be further extended by studying the stability of a

sequence of equilibria with a specified continuously varying magnetic shear, rather than specified $B_z(A_z)$.

b) With Gravity

In § IVa, we have studied the stability of magnetic arcades without gravity. This is a valid approximation when the gravitational scale height is much larger than the typical size of a magnetic arcade. For a coronal arcade (or loop) with $T = 2 \times 10^6$ K, the gravitational scale height is $H_g \approx 6 \times 10^4$ km. On the other hand, the height of a coronal helmet streamer is $\sim 6 \times 10^5$ km, of the hot loops connecting two ribbon flares is $\sim 10^5$ km, and of a coronal X-ray loop is $\sim 10^4$ km (Priest 1984), which correspond to λ values of $\lambda \sim 10$, 2 and 0.2, respectively. For a solar prominence with $T = 10^4$ K, the scale height is $H_g \approx 3 \times 10^2$ km, much smaller than a mature quiescent prominence height of 5×10^4 km, which corresponds to $\lambda \sim 100$. These estimates of the heights imply that gravity cannot be neglected in all stability studies.

In § II, we defined dimensionless gravity, g , as $g = \lambda\beta$. For a given β value, the effect of gravity varies with λ . In order to understand the effect of gravity on the MHD stability we use various λ values and study the stability of a coronal arcade with a detached flux tube. Figure 9 shows the growth rates versus B_z of the $n = 1$ and $n = 3$ modes for $\lambda = 0.1$. The results should be compared with Figure 4 for $\lambda = 0$ to understand the effect of gravity. This comparison reveals the stabilizing effect

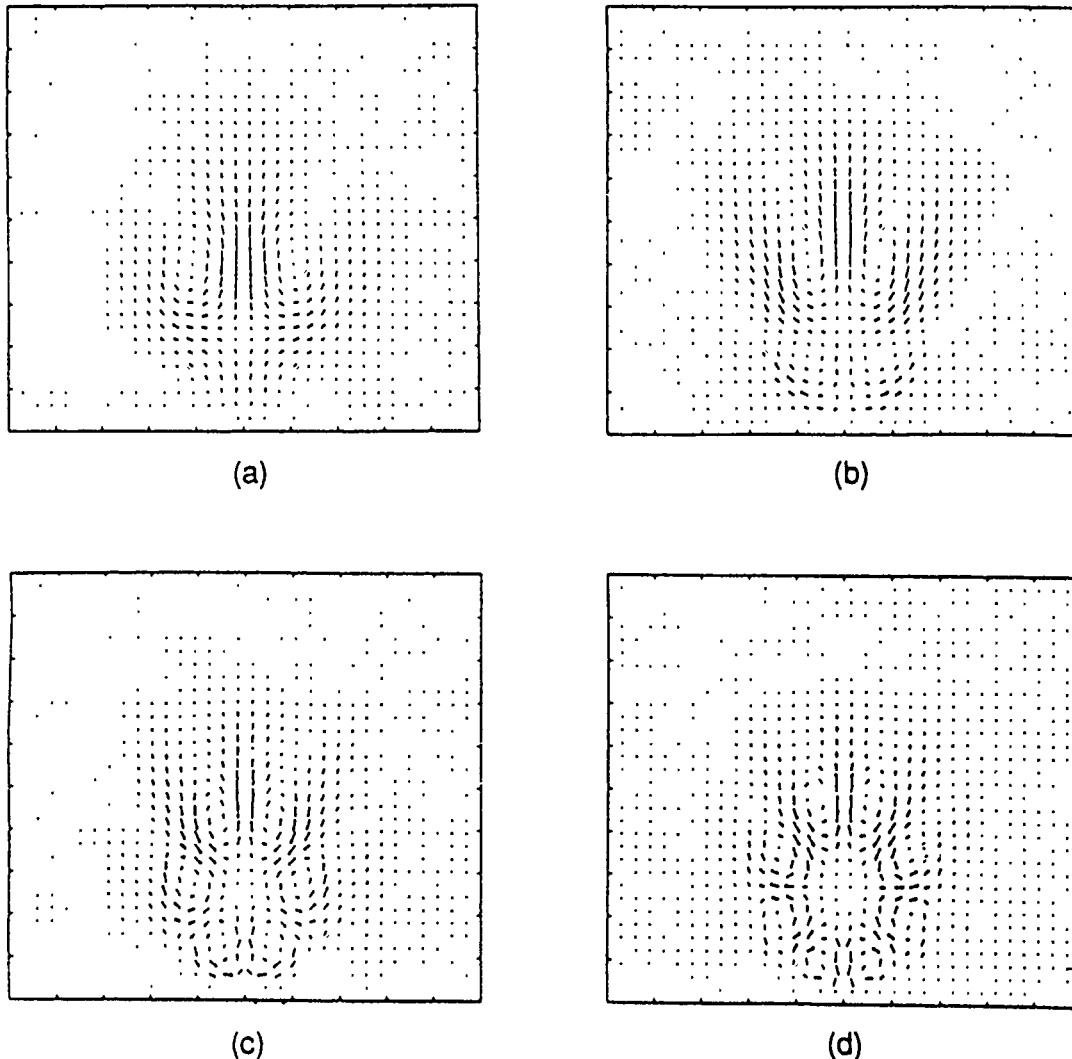


FIG. 8—Velocity fields for increasing longitudinal mode number n . $B_z = 1$, and $\lambda = 0$, (a) $n = 2$, (b) $n = 3$, (c) $n = 4$, and (d) $n = 5$. As n increases, the transverse mode number, m , increases.

of gravity. For $n = 1$, $\lambda = 0.1$ reduces the growth rate to half of that for $\lambda = 0$, and widens the stability region between the $m = 0$ and $m = 1$ modes from $0.6 < B_z < 0.8$ for $\lambda = 0$ to $0.4 < B_z < 0.9$ for $\lambda = 0.1$. For $n = 3$, gravity has a significant stabilizing effect especially on the $m \geq 2$ modes. Figure 4 shows that the mode structures for $n = 3$ with $B_z > 0.9$ are $m \geq 2$ modes and these high m modes are completely stabilized by gravity. Since gravity stabilizes the $n = 3$ but not the $n = 1$ kink mode for $B_z > 0.9$ we might see the eruption of a flux tube due to the $n = 1$ kink mode for a random perturbation in the longitudinal direction. This is an important difference from the $\lambda = 0$ case, in which the $n = 3$ mode dominates over the $n = 1$ mode for all B_z !

Since $\lambda = 0.1$ is unrealistically small for coronal arcades ($\lambda > 1$) and quiescent prominences ($\lambda \sim 100$), we have also studied the stability for larger values of λ . Figure 10 shows the variation of growth rates for $n = 1$ and $n = 3$ modes versus λ . The dotted lines are for the $n = 3$ modes, and the solid lines are for the $n = 1$ modes, with $B_z = 0.2$ or 1.0 as indicated. Since the $n = 3$ mode has its largest growth rate at $B_z = 0.2$ and the

$n = 1$ mode has its largest growth rate (for the kink mode) at $B_z = 1$, Figure 10 provides a very useful illustration of the overall stability change due to increasing λ . Considering only $n = 3$, as λ increases the growth rate for $B_z = 1.0$ decreases to zero at $\lambda = 0.09$ while the growth rate for $B_z = 0.2$ decreases to zero at $\lambda = 0.33$. For $\lambda < 0.09$, the growth rate for $B_z = 1.0$ is much lower than for $B_z = 0.2$. For $n = 1$, the growth rates for $B_z = 0.2$ and 1.0 both decrease to zero for λ near 0.2 and the difference between the two growth rates is not as large as for $n = 3$. As λ increases from zero, a detached flux tube with $B_z = 1.0$ is soon stabilized against the $n = 3$ mode but is unstable to the $n = 1$ kink mode until λ reaches 0.2 . For $B_z = 0.2$, the $n = 3$ mode dominates the $n = 1$ mode for $\lambda \leq 0.33$ and the transverse mode structure is the $m = 0$ mode. These results imply that if a detached flux tube has highly twisted field lines, the loop can disintegrate due to the $n = 3, m = 0$ mode for $\lambda \leq 0.33$, but the tube is stable for $\lambda > 0.33$. If the tube has twisted field lines of one turn along the tube length (i.e., $B_z \approx 1.0$) the tube can erupt due to the $n = 1, m = 1$ kink mode for $0.1 < \lambda < 0.2$ but will be stable for $\lambda > 0.2$.

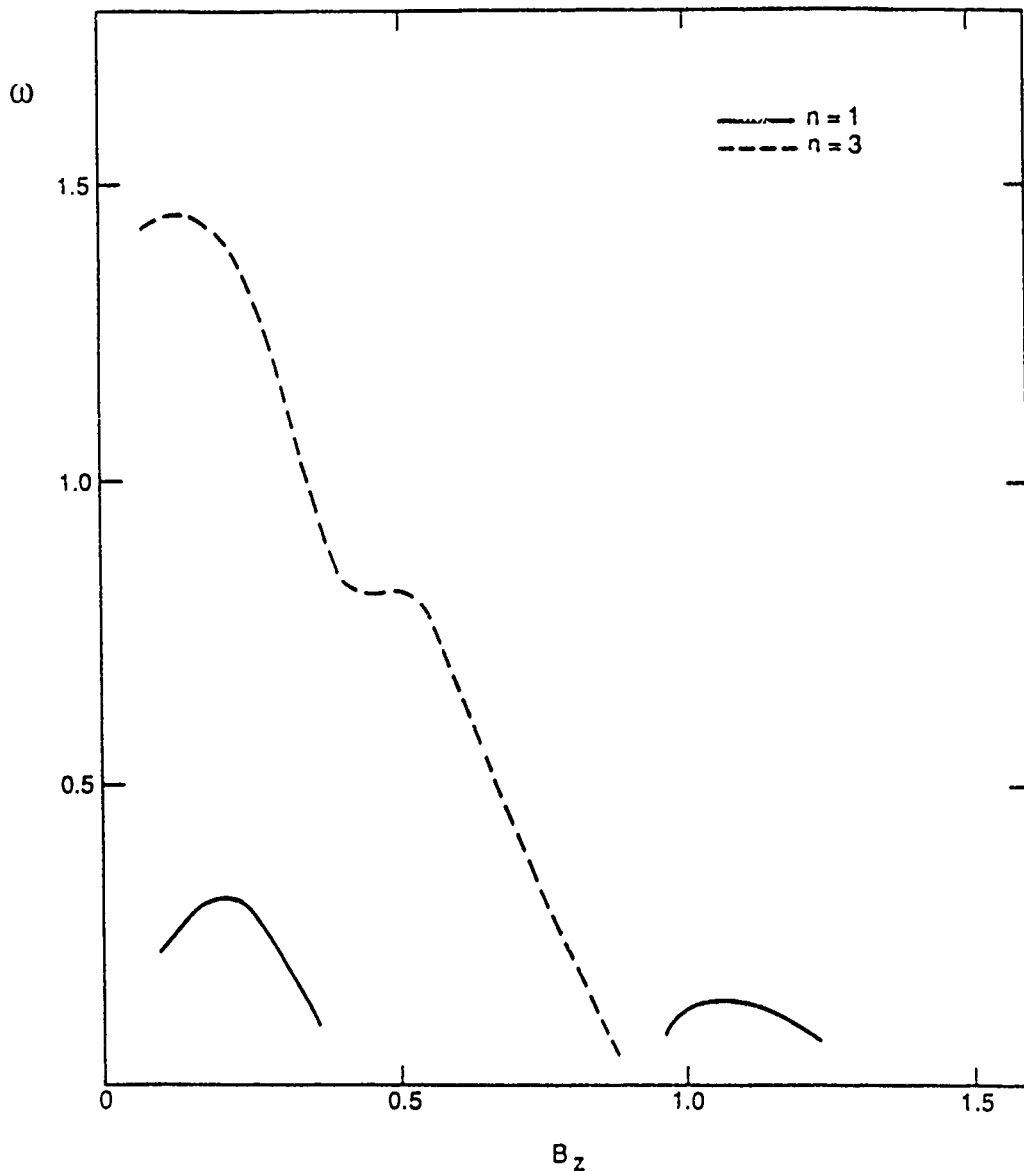


FIG. 9—Growth rate, ω , versus B_z for $\lambda = 0.1$. The solid line is for $n = 1$, and the dotted line is for $n = 3$. Note that for $B_z \geq 1$, the $n = 1$ kink mode is unstable while the $n = 3$ mode is stabilized by gravity.

V DISCUSSIONS AND CONCLUSIONS

We have studied the MHD stability of coronal arcades with and without a detached flux tube by using a two-dimensional linear MHD numerical model. For the study, we construct two-dimensional magnetohydrostatic equilibria with and without gravity with symmetry along the z -direction. We study the stability for different longitudinal wave numbers, n . For a given n , the transverse mode structure is represented by mode number m . The instability structure is found to vary, depending on the magnitude of B_z , which determines the degree of field twist and magnetic shear.

In the absence of gravity, we have found that a coronal arcade without a detached flux tube is stable for any magnetic shear less than a critical value, above which no neighboring solution exists. Furthermore, all the equilibria we have studied, even those with a detached flux tube are stable to two-dimensional perturbations for any B_z . However, three-

dimensional perturbations are unstable for equilibria with detached flux tubes and we find that the $n = 3$ modes have higher growth rates than the $n = 1$ modes for all B_z . For $n = 1$, the unstable transverse modes $m = 0$ and $m = 1$ are separated by a stable region in B_z , but for $n = 3$ the transverse mode structure changes continuously from the $m = 0$ to the $m = 4$ mode as B_z increases from zero to 1.5, without being separated by stable regions in B_z .

Liggett and Zirin (1984) observed rotational motions in several prominences and found that the motion continues through several turns while the eddy size remains constant. They found that the rotational motion is an actual motion of prominence material that does not destroy the prominences and pointed out the difficulty in understanding the motion in view of the conceptual model that prominences are being suspended in magnetic fields; the rotation must wind up the magnetic field, transferring energy to the field and slowing down or stopping the rotation. We notice that the rotational motion

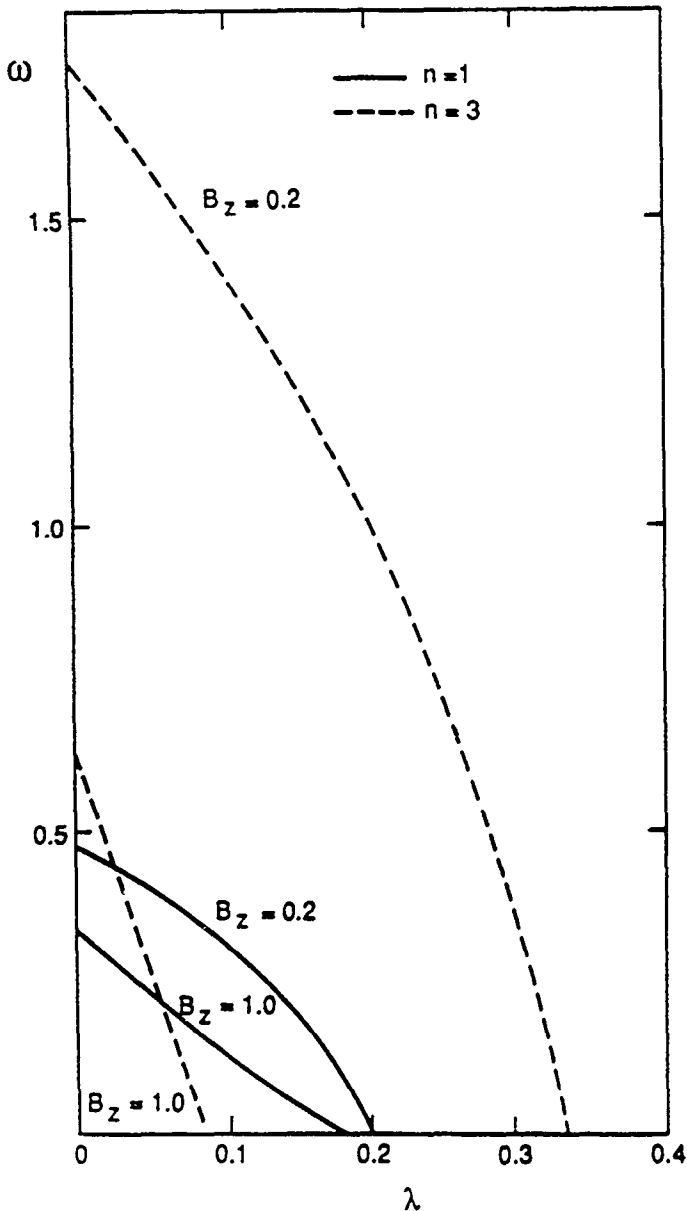


FIG. 10—Growth rate, ω , versus λ for $B_z = 0.2$ and 1.0 . The solid line is for $n = 1$ and the dotted line is for $n = 3$.

has a similar pattern to the $m = 0$ unstable velocity pattern shown in Figure 5a. In addition to this similarity, the $m = 0$ mode has the highest growth rate among various m modes even under gravity, and the mode does not cause prominence eruption. Therefore, we suggest that the rotational motion is due to the $m = 0$ unstable mode in a detached flux tube. The closed field lines in a detached flux tube may allow the rotational motion to exist through several turns without winding up the field lines. In order to confirm our suggestion, the field lines in the rotational region must be closed and highly twisted for the $m = 0$ mode.

The effect of gravity is measured with the parameter λ , which

is the ratio of the width of the coronal arcade to the gravitational scale height. The higher λ is, the stronger the effect of gravity. Gravity is shown to play a stabilizing role for all the equilibria we have studied in this paper. It is found that higher m modes are more strongly stabilized by gravity than lower m modes. For example, the $n = 3/m = 0$ mode is unstable for $\lambda < 0.33$ but $r = 3/m \geq 3$ modes are completely stabilized for $\lambda > 0.09$. Our equilibria are all stable for $\lambda \geq 0.35$, which is much lower than a realistic value for λ in coronal arcades (> 1) and quiescent prominences (~ 100). This result implies that quiescent prominences may not erupt due to MHD instabilities because of the strong stabilizing effect of gravity. In order for a prominence to erupt, the gravitational effect should be low ($\lambda < 1$). A low value of λ can be achieved by increasing the prominence temperature by two orders of magnitude. But, even though some observations show a heating prior to an eruption, no such temperature enhancement has been observed. The gravitational effect can also be reduced if plasma condenses to form a prominence and the mass is supported by the magnetic field. Due to magnetic support, the plasma density would change slowly in the vertical direction, causing a higher effective gravitational scale height than without magnetic support. If gravity stabilizes MHD instabilities in more realistic prominence magnetic fields in this manner, then the critical shear phenomenon is a good candidate for an eruptive mechanism.

Zwingman (1987) studied a critical shear mechanism for solar eruptive phenomena by solving the magnetohydrostatic equation. As he increased a pressure parameter, λ_p , successively to a critical value for a given magnetic shear, he eventually found no neighboring solution. He checked the MHD stability of the solutions against the $n = 0$ mode and found that the solutions are stable for λ_p less than a critical value. This stability study looks like a promising way to ensure that the critical phenomenon is an eruptive mechanism. However, our result indicates that the stability against $n = 0$ mode does not necessarily mean stability against $n \neq 0$ modes. The stability for $n \neq 0$ modes must also be considered to make sure that the sequence of the equilibrium solutions with λ_p less than critical value are stable.

Our numerical model for linear MHD stability differs from most previous studies in that we solve time-dependent linear MHD equations as an initial and boundary value problem while previous studies used the energy principle. One advantage of our method over the energy principle is that we can easily extend it to a nonlinear MHD problem and add non-ideal effects. By transforming the coordinates as shown in equation (18) we can also study the stability of coronal magnetic structures which have open field lines. But we note that the method is restricted to the study of the most unstable mode.

We thank Dr D. H. Hathaway for giving extensive advice on developing the numerical model and for reading and commenting on the manuscript. We also thank Dr. R. L. Moore for his valuable comments during the course of this research. This work is supported by NASA HQ Grant (NAGW-9) and Air Force Grant (AFOSR-88-0013) (CHA and STW) and also by NASA Solar and Heliospheric Physics Branch and Space Plasma Physics Branch (STS and CHA).

APPENDIX

NUMERICAL METHOD

To solve equations (1)–(5) numerically, we specify velocity and all equilibrium quantities at the center of each grid cell and the perturbed pressure, magnetic field, and density at the corner of each grid cell. The finite difference schemes are as follows:

$$v_{i+1/2,j+1/2}^{n+1} - v_{i+1/2,j+1/2}^n = \frac{\Delta t}{(\rho_0)_{i+1/2,j+1/2}} [-\beta \nabla p_1 + (J \times B)_1 + \rho_1 g]_{i+1/2,j+1/2}^{n+1/2}; \quad (A1)$$

$$(A_1)_{i+1/2,j+1/2}^{n+3/2} - (A_1)_{i+1/2,j+1/2}^{n+1/2} = \Delta t [v \times B_0]_{i+1/2,j+1/2}^{n+1}; \quad (A2)$$

$$(B_1)_{i,j}^{n+3/2} = (\nabla \times A_1)_{i,j}^{n+3/2}; \quad (A3)$$

$$(p_1)_{i,j}^{n+3/2} - (p_1)_{i,j}^{n+1/2} = -\Delta t \left(\bar{v}_x \frac{\partial p_0}{\partial x} + \bar{v}_y \frac{\partial p_0}{\partial y} + ik \bar{v}_z \bar{p}_0 + \Gamma \bar{p}_0 \nabla \cdot v \right)_{i,j}^{n+1}; \quad (A4)$$

$$(\rho_1)_{i,j}^{n+3/2} - (\rho_1)_{i,j}^{n+1/2} = -\Delta t \left(\bar{v}_x \frac{\partial \rho_0}{\partial x} + \bar{v}_y \frac{\partial \rho_0}{\partial y} + ik \bar{v}_z \bar{\rho}_0 + \bar{\rho}_0 \nabla \cdot v \right)_{i,j}^{n+1}. \quad (A5)$$

We use the perturbed vector potential A_1 to ensure $\nabla \cdot B = 0$ in our numerical calculation. The explicit expressions of the x-component of momentum and induction equations are as follows.

The x-component of equation (A1) is

$$\begin{aligned} (v_x)_{i+1/2,j+1/2}^{n+1} - (v_x)_{i+1/2,j+1/2}^n &= \frac{\Delta t}{(\rho_0)_{i+1/2,j+1/2}} \{ -\beta [(p_1)_{i+1,j+1} + (p_1)_{i+1,j} - (p_1)_{i,j+1} - (p_1)_{i,j}] \\ &\quad \times 0.5/\Delta x + (J_{0y})_{i+1/2,j+1/2} \times (\bar{B}_{1z})_{i+1/2,j+1/2} - (J_{0z})_{i+1/2,j+1/2} \times (\bar{B}_{1y})_{i+1/2,j+1/2} + (J_{1y})_{i+1/2,j+1/2} \\ &\quad \times (B_{0z})_{i+1/2,j+1/2} - (J_{1z})_{i+1/2,j+1/2} \times (B_{0y})_{i+1/2,j+1/2} \}^{n+1/2}, \end{aligned} \quad (A6)$$

where

$$(J_{1y})_{i+1/2,j+1/2} = ik(\bar{B}_{1x})_{i+1/2,j+1/2} - [(B_{1z})_{i+1,j+1} + (B_{1z})_{i+1,j} - (B_{1z})_{i,j+1} - (B_{1z})_{i,j}]/(2\Delta x) \quad (A7)$$

$$\begin{aligned} (J_{1z})_{i+1/2,j+1/2} &= [(B_{1y})_{i+1,j+1} + (B_{1y})_{i+1,j} - (B_{1y})_{i,j+1} - (B_{1y})_{i,j}]/(2\Delta x) \\ &\quad - [(B_{1x})_{i+1,j+1} + (B_{1x})_{i,j+1} - (B_{1x})_{i+1,j} - (B_{1x})_{i,j}]/(2\Delta y). \end{aligned} \quad (A8)$$

The x-component of the induction equations (A2) and (A3) are

$$(A_x)_{i+1/2,j+1/2}^{n+3/2} - (A_x)_{i+1/2,j+1/2}^{n+1/2} = \Delta t [(v_y)_{i+1/2,j+1/2} (B_{0z})_{i+1/2,j+1/2} - (v_z)_{i+1/2,j+1/2} (B_{0y})_{i+1/2,j+1/2}]^{n+1}. \quad (A9)$$

$$(B_{1x})_{i,j} = [(A_z)_{i+1/2,j+1/2} + (A_z)_{i-1/2,j+1/2} - (A_z)_{i+1/2,j-1/2} - (A_z)_{i-1/2,j-1/2}]/(2\Delta y) - ik(\bar{A}_y)_{i,j}. \quad (A10)$$

The averaged values $(\bar{B}_{1x}, \bar{B}_{1y}, \bar{B}_{1z})_{i+1/2,j+1/2}$ are defined as

$$(\bar{B}_{1x})_{i+1/2,j+1/2} = [(B_{1x})_{i+1,j+1} + (B_{1x})_{i+1,j} + (B_{1x})_{i,j+1} + (B_{1x})_{i,j}]/4,$$

and the averaged values $(\bar{A}_x, \bar{v}_x, \bar{v}_y, \bar{v}_z, \bar{p}_0, \bar{\rho}_0)_{i,j}$ are defined as

$$(\bar{v}_x)_{i,j} = [(v_x)_{i+1/2,j+1/2} + (v_x)_{i+1/2,j-1/2} + (v_x)_{i-1/2,j+1/2} + (v_x)_{i-1/2,j-1/2}]/4.$$

The partial derivative of ρ, p_0, v with respect to x and y are as follows.

$$\left(\frac{\partial p_0}{\partial x} \right)_{i,j} = [(p_0)_{i+1/2,j+1/2} + (p_0)_{i+1/2,j-1/2} - (p_0)_{i-1/2,j+1/2} - (p_0)_{i-1/2,j-1/2}]/(2\Delta x),$$

$$\left(\frac{\partial p_0}{\partial y} \right)_{i,j} = [(p_0)_{i+1/2,j+1/2} + (p_0)_{i-1/2,j+1/2} - (p_0)_{i+1/2,j-1/2} - (p_0)_{i-1/2,j-1/2}]/(2\Delta y).$$

Since the perturbed quantities have the following form.

$$f_1(r, t) = f_1(x, y, t)e^{ikz}$$

and

$$\frac{\partial f_1}{\partial z} = ikf_1(r, t),$$

the two-dimensional perturbation quantities $f_1(x, y, t)$ are complex. In order to solve the equations numerically, we have to divide each equation into real and imaginary parts which are coupled to each other for $k \neq 0$.

For specifying boundary conditions, we assumed that field lines are tied to the lower boundary, and that there is no charge accumulation on and no energy and mass flow across the side boundary (Bateman *et al.* 1974).

Side boundary: $E = 0$, $\nabla \cdot E_1 = 0$, $p_1 = \rho_1 = 0$;

Lower boundary: $v = 0$

For a lower boundary condition, $v = 0$ is sufficient to solve the equations when v is defined at the corner of each grid cell. When v is defined at the center of each grid cell, we need to assume that equilibrium quantities are the same at the upper and lower cells of the lower boundary.

We use two different upper boundary conditions depending on what coordinate system we use. If we assume that the upper boundary is at a finite height in the y -coordinate the upper boundary condition is the same as the side boundary condition, but the boundary condition is not realistic for solar magnetic fields which have an open boundary. In order to take into account the open boundary we use an exponential coordinate which is transformed by

$$w = e^{-(y/2)}$$

in which the computing domain $0 \leq w \leq 1$ is equivalent to the physical domain $0 \leq y \leq \infty$. In this w -coordinate $w = 1$ (i.e., $y = 0$) is the lower boundary and $w = 0$ (i.e., $y = \infty$) is the upper boundary. At $w = 1$, the boundary condition is $v = 0$ but at $w = 0$ we specify $B_1 = 0$, $p_1 = \rho_1 = 0$. To transform the coordinate from y to w all the y derivatives are changed as

$$\frac{\partial f}{\partial y} \rightarrow \frac{\partial f}{\partial w} \left(-\frac{1}{2} w \right).$$

In this paper we assume that coronal arcades have a finite upper boundary. The stability of a coronal arcade with open boundary will be studied later.

The time-dependent computation is initiated by a random velocity perturbation to an initial steady equilibrium state. After the perturbation, we calculate B_1 , ρ_1 , and p_1 at $t = \Delta t/2$ and then calculate v at $t = \Delta t$. After the initial step, B_1 , ρ_1 , and p_1 , are advanced in time with the time step Δt alternately with v until we reach the linear growth rate.

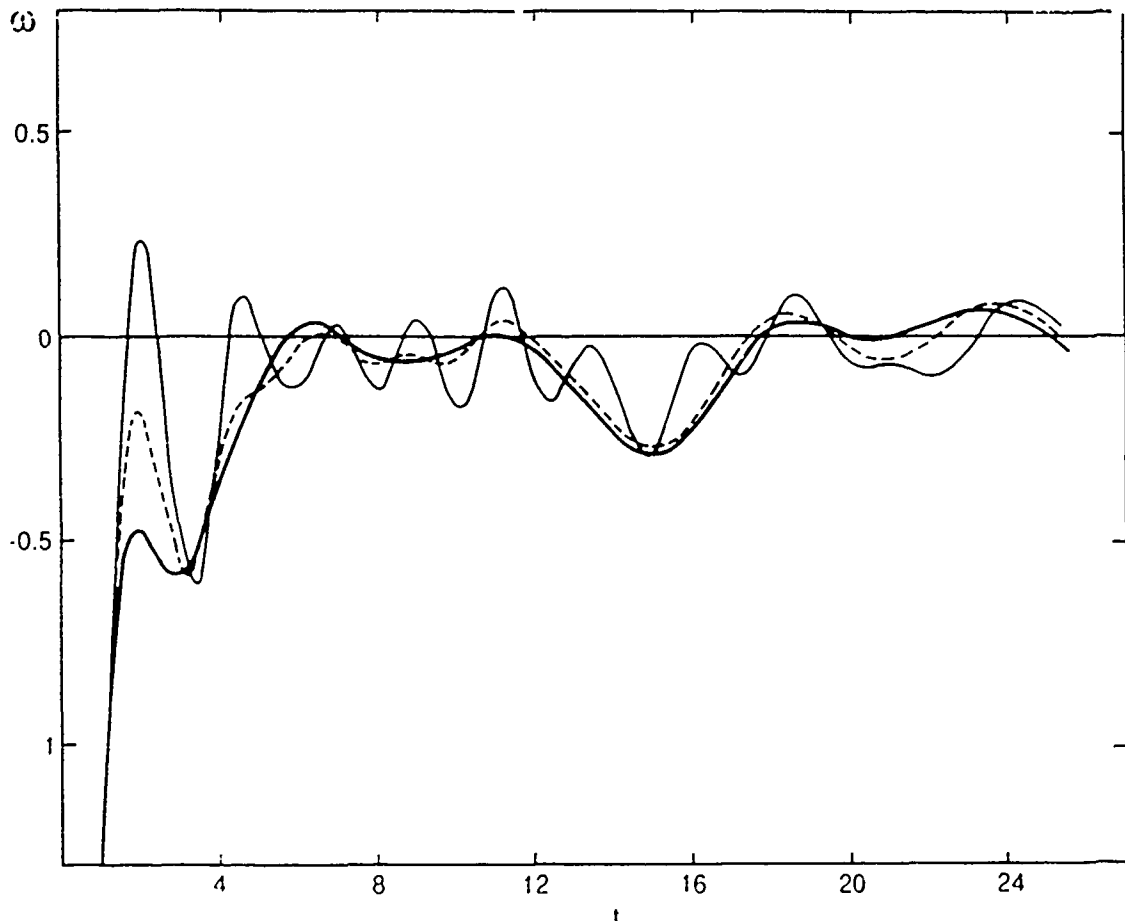


FIG. 11.—Growth rate of a stable equilibrium, ω , vs. time for different values of the artificial viscosity coefficient. The light solid line is for $v = 0.0001$, the dotted line is for $v = 0.0003$, and the heavy solid line is for $v = 0.0005$.

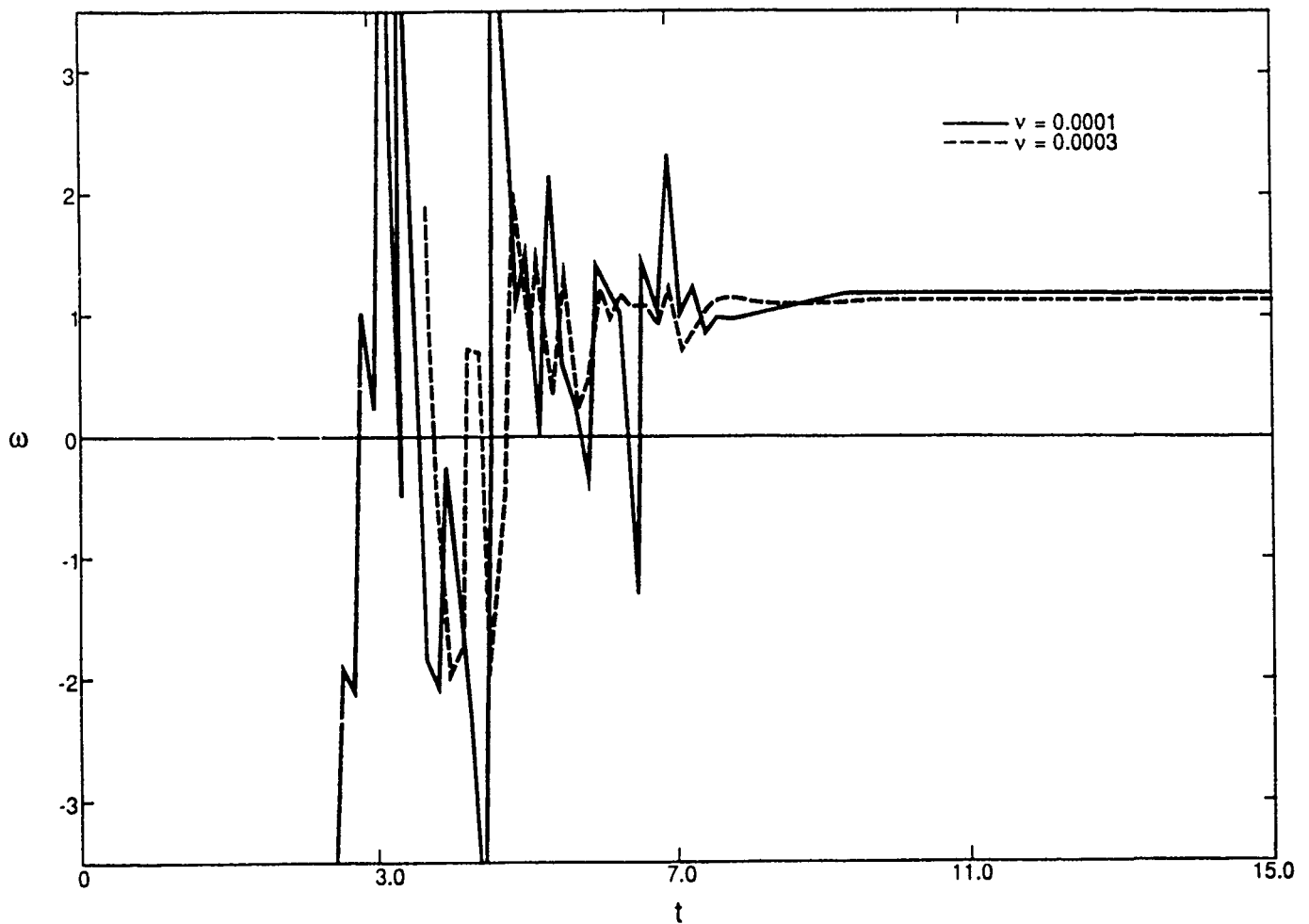


FIG. 12.—Growth rate of an unstable equilibrium, ω , vs time for different values of the artificial viscosity coefficient. The solid line is for $\nu = 0.0001$, and the dotted line is for $\nu = 0.0003$.

We add an artificial viscosity term, $\rho_0 \nu \nabla^2 v$, to the momentum equation (1) to stabilize a numerical instability which develops in a gravitationally stratified atmosphere. When numerical instability develops, the velocity is distributed randomly and oscillates in time with very short periods. We find that the artificial viscosity term is not needed in the absence of gravity. Figure 11 shows how the growth rate of a stable equilibrium changes with time for different ν values. The figure shows that the growth rate keeps oscillating around zero as time progresses, which is a typical phenomenon for a stable equilibrium. For $\nu = 1 \times 10^{-4}$ the growth rate oscillates randomly with short periods but for $\nu = 3 \times 10^{-4}$ and 5×10^{-4} the oscillations are more orderly and have longer periods. Figure 12 shows how the growth rate of an unstable equilibrium saturates to a linear growth rate and how the linear growth rate depends on the magnitude of ν . For $\nu = 1 \times 10^{-4}$, the growth rate oscillates randomly with high amplitudes before it saturates to a linear growth rate while for $\nu = 3 \times 10^{-4}$ the oscillation is less random and the saturation occurs earlier. We find that the linear growth rate decreases as we increase the magnitude of ν , for $\nu = 1 \times 10^{-4}$, 3×10^{-4} , and 5×10^{-4} , the linear growth rates are $\omega = 1.07$, 1.01 , and 0.97 , respectively. The result indicates that we should use as small value of ν as possible in order to not alter the stability result. Too small value causes not only numerical instability but also a longer saturation time. It is found that $\nu = 3 \times 10^{-4}$ is the optimum value for an equilibrium with open boundary, but we can reduce the value down to $\nu = 1 \times 10^{-4}$ for an equilibrium with a finite upper boundary. In this study, we choose $\nu = 3 \times 10^{-4}$.

With a finite upper boundary, a low (or zero) value of ν does not cause severe numerical instability. A severe numerical instability occurs only when the time step Δt violates the Courant-Friedrichs-Lewy (CFL) condition. We have to check the CFL condition when we increase magnetic shear because higher magnetic shear causes a lower transit time of an Alfvén wave across each grid cell.

REFERENCES

- | | |
|---------------------------------------------------------------------------------------------------------------------------------------|------------------------------------------------------------------------------------------------------------------------------------------------------|
| Bateman, G. and Peng, Y. K. M. 1977 <i>Phys. Rev. Letters</i> , 38 , 829. | Canfield, R. C., Priest, E. R., and Rust, D. M. 1974, <i>Flare-related Magnetic Field Dynamics</i> , ed. Y. Nakagawa and D. M. Rust (Boulder: NCAR). |
| Bateman, G., Schneider, W., and Grossmann, W. 1974, <i>Nucl. Fusion</i> , 14 , 669. | Galindo, T. J. 1987, <i>Solar Phys.</i> , 108 , 265. |
| Bateman, G. 1978, <i>MHD Instabilities</i> (Cambridge: MIT Press). | Galindo, T. J., and Schindler, K. 1984, <i>Ap. J.</i> , 277 , 422. |
| Bernstein, I. B., Frieman, E. A., Kruskal, M. D., and Kulsrud, R. M. 1958, <i>Proc. Roy. Soc. London, A</i> , 244 , 17. | Hain, K., Lust, R., and Schluter, A. 1957, <i>Zs. Ap.</i> , 43 , 36. |
| Birn, J., and Schindler, K. 1981, in <i>Solar Flare Magnetohydrodynamics</i> , ed. E. R. Priest (London: Gordon and Breach), Chap. 6. | Heyvaerts, J., Priest, E. R., and Rust, D. M. 1977, <i>Ap. J.</i> , 216 , 123. |
| | Hood, A. W., and Anzer, U. 1987, <i>Solar Phys.</i> , 111 , 333. |

AN, SUESS, AND WU

Hood, A. W., and Priest, E. R. 1980, *Solar Phys.*, **66**, 113
 Jockers, K. 1976, *Solar Phys.*, **50**, 405.
 ——— 1978, *Solar Phys.*, **56**, 37.
 Liggett, M., and Zirinn, H. 1984, *Solar Phys.*, **91**, 259.
 Low, B. C. 1975, *Ap. J.*, **197**, 251.
 ——— 1977, *Ap. J.*, **212**, 234.
 ——— 1984, *Ap. J.*, **286**, 772.

Melville, J. P., Hood, A. W., and Priest, E. R. 1986, *Solar Phys.*, **105**, 291
 Mighuolo, S., and Cargill, P. J. 1983, *Ap. J.*, **271**, 820
 Moore, R. L. 1988, *Ap. J.*, **324**, 1132
 Priest, E. R. 1984, *Solar Magnetohydrodynamics*, (Dordrecht Reidel)
 Ray, A., and Van Hoven, G. 1982, *Solar Phys.*, **79**, 353
 Sakurai, T. 1976, *Pub Astro. Soc. Japan*, **28**, 177
 Zwingman, W. 1989 *Solar Phys.*, **11**, 309

CHANG-HYUK AN and S. T. WU: Center for Space Plasma and Aeronomic Research, University of Alabama in Huntsville, Huntsville AL 35899

S. T. SUESS: NASA/MSFC, Space Science Lab., ES-52, Huntsville, AL 35812

PROPAGATING AND NONPROPAGATING COMPRESSION WAVES IN AN ISOTHERMAL ATMOSPHERE WITH UNIFORM HORIZONTAL MAGNETIC FIELD

Z. E. MUSIELAK¹

NASA/Marshall Space Flight Center

C.-H. AN

University of Alabama in Huntsville

AND

R. L. MOORE AND S. T. SUESS

NASA/Marshall Space Flight Center

Received 1988 November 3; accepted 1989 February 13

ABSTRACT

We present, for the first time, full analytical solutions to the wave equations for *steady* vertical compression waves in an isothermal hydrostatic atmosphere with uniform horizontal magnetic field. There are two classes of waves: (1) upward waves, those which are excited from below by a horizontal perturbing surface; and (2) downward waves, those which are excited from above by a horizontal perturbing surface. We show that in the steady state approach the behavior of these two classes of waves is different. The upward waves are non-propagating (standing) waves for any wave frequency. For each frequency, there is a critical height in the atmosphere below which the upward wave is a regular standing wave and above which the wave is an evanescent standing wave. The critical height is the height at which a local characteristic frequency, defined by the local fast mode speed divided by twice the scale height of the isothermal atmosphere, equals the wave frequency. This characteristic frequency, which we call the local critical frequency, increases with height because the Alfvén velocity increases with height. Above the critical height reflection on the density gradient dominates the behavior of the upward waves. The downward waves are propagating waves for all frequencies that are higher than the acoustic cutoff frequency obtained for the same isothermal atmosphere without magnetic field. If the frequency of the downward wave is at or below this cutoff, the wave is an evanescent wave. These results show that the finding by Thomas, that the cutoff frequency for vertically propagating magnetoacoustic waves in an isothermal atmosphere with horizontal magnetic field is the same as for isothermal atmosphere with no magnetic field, is true only for the downward waves.

Subject headings: hydromagnetics — Sun: oscillations — Sun: atmosphere — wave motions

1. INTRODUCTION

A number of authors have considered propagation of magnetohydrodynamic (MHD) waves in an isothermal hydrostatic atmosphere suffused by a uniform, oblique (or, in a special case, horizontal) magnetic field. Many have used a local dispersion relation in which the stratification of the atmosphere gives rise to cutoff frequencies (McLellan and Winterberg 1968; Stein and Leibacher 1974; Thomas 1982; Musielak and Rosner 1987; see also reviews by Priest 1982; Thomas 1983; Campos 1987 and references therein). This approach is justified only when the vertical wavelength is much smaller than the atmospheric characteristic scale height (the WKB approximation). It has been shown recently (Thomas 1982, 1983; Campos 1987; Musielak 1988) that many results previously obtained were outside the range of validity of the local dispersion relation approach and that the cutoff frequencies were incorrectly calculated.

In order to obtain the correct cutoff frequencies, either a global dispersion relation for MHD waves is needed or exact analytical solutions of the wave equations derived for stratified atmospheres are required. The first case was considered by Yu (1965), Deutsch (1967) and Nye and Thomas (1974), who calculated a special case when the background atmosphere is isothermal with a horizontal magnetic field that decreases exponentially with height. In this approach, the wave equation leads to a global dispersion relation which is the same in the whole atmosphere and is not restricted to short vertical wavelengths; this allows properly defining the true cutoff frequencies. However, this approach is very limited and cannot be applied to more realistic situations. Similarly, in the second case the exact analytical solutions of the MHD wave equations have been found only in the limited situation of an isothermal atmosphere with a uniform magnetic field.

A special case of uniform and purely horizontal magnetic field was considered Summers (1976) who obtained approximate solutions in the limit of low- and high- β plasma case (where β is ratio of sound speed to the Alfvén velocity) and showed that in the limit of low- β plasma the resulting solution represents a standing wave. He also found the formal solutions given in terms of hypergeometric functions. More recently, Thomas (1982) and Campos (1985) calculated the cutoff frequency by solving the wave equation for velocity perturbations and found exact analytical solutions which, they thought, were valid for the whole physical space of the considered model and for any direction of wave propagation. Also, they concluded that the cutoff frequency is *not* affected by the strength of the uniform horizontal magnetic field and therefore does not depend on the Alfvén velocity; instead they

COMPRESSION WAVES IN ISOTHERMAL ATMOSPHERE

suggested that the filtering of magnetoacoustic waves through the atmosphere is a pure compressive phenomenon, being thereby identical to the filtering of acousto-gravity waves. There are, however, two important problems with their approach as well as with Summers approach—namely, they *did not obtain* full solutions to the wave equation (see § III and Appendix A for physical and mathematical arguments, respectively) and *did not specify* the direction in the atmosphere from which the waves are excited. It must be emphasized that the latter point is essential for any inhomogeneous media as the physical conditions and their variation with distance from the wave source are different in different directions, therefore waves excited upward (against gravity) and downward (in the direction of gravity) with respect to the wave source behave differently.

It is our main goal to obtain first full analytical steady solutions to the wave equation derived for compression vertical waves in an isothermal atmosphere with uniform horizontal magnetic field, and to show that the solution for the waves excited from below is different from that for the waves excited from above. We shall derive and solve the wave equations for the velocity perturbations and for the magnetic field perturbations, finding that the latter show different spatial variations than the velocity perturbations.

We begin our presentation with some physical considerations concerning two simple cases: the "cold" plasma case and high- β plasma case. It is shown that in the case of cold plasma, compression waves behave similarly to purely transverse Alfvén waves and that there are two distinct solutions to the wave equations: standing and propagating waves for the upward and downward directions, respectively. We also introduce a characteristic frequency (called here a local critical frequency) that determines, for a given wave frequency, the height in the atmosphere at which wave reflection becomes important. By comparing these results to those given by Thomas (1982), we find that no standing wave solutions and no local critical frequencies are obtained in his approach. Therefore, his solutions *cannot* describe the behavior of the upward waves in the limit of cold plasma. However, when the limit of high- β plasma is considered, Thomas's solutions with the acoustic cutoff frequency determining the type of solutions are recovered. This implies that Thomas's results describe only the behavior of the downward waves.

After considering these two simple cases, we present the full solutions to the general wave equations describing the behavior of vertical compression waves in our model (§ IV) and then show how to select physical solutions (§ V). We find that the upward waves correspond to the upward waves in the cold plasma case; the local critical frequency has the same role and the same physical meaning in both cases. The downward waves correspond to the downward waves in the high- β plasma case, the acoustic cutoff frequency determines whether the waves can or cannot propagate. This is the same result as that found by Thomas (1982), although he apparently did not realize that the result does not apply to the upward waves but only to the downward waves. In § VI, we discuss possible applications of the obtained results to solar and stellar physics.

II. BASIC FORMULATION AND WAVE EQUATIONS

Throughout this paper, we assume that the background atmosphere is in hydrostatic equilibrium with uniform acceleration of gravity ($\mathbf{g} = -g\hat{z}$), and that the atmosphere is a perfect gas with uniform temperature T_0 . Hence, the density variation is given by $\rho_0(z) = \rho_{00} \exp(-z/H)$, where H is the density (and pressure) scale height and ρ_{00} is the gas density at $z = 0$. We also take the atmosphere to be permeated by a horizontal uniform magnetic field given by $\mathbf{B}_0 = B_0 \hat{x}$; in this case the magnetic field has no effect on the equilibrium of the atmosphere. The density scale height is determined by $H = V_s^2/\gamma g$, where $V_s[(\gamma R T_0/\mu)^{1/2}]$ is the adiabatic sound speed. Hence, the model atmosphere is specified by the free parameters: B_0 , T_0 , ρ_{00} , g , γ and μ , which are constant in the whole atmosphere.

We assume that both velocity and magnetic field perturbations depend solely on height, z , and time, t , and given by $\mathbf{U}(z, t) = u(z, t)\hat{z}$ and $\mathbf{B}(z, t) = B_0 + b(z, t)\hat{x}$ (see Fig. 1). As shown in this figure, we introduce the coordinate system with the plane $z = 0$ dividing the atmosphere into two half-spaces characterized by decreasing (positive z) or increasing (negative z) density with distance from $z = 0$. This leads to plasma β [denoted here as V_s/V_a , where $V_a = B_0/(4\pi\rho_0)^{1/2}$ is the Alfvén velocity] being arbitrary at the plane $z = 0$ and only in a special case does $\beta(z = 0) = 1$. Because ρ_{00} is an arbitrary parameter, the plane $z = 0$ can be placed anywhere in the atmosphere. We also find it useful to assume that the wave source is located on this plane, i.e., that the plane itself generates the waves (see Fig. 2). We assume that the plane (to be called the forcing plane or horizontal perturbing surface) produces upward and downward propagating magnetoacoustic waves, and we study the steady state wave behavior. It is obvious from a physical point of view that the conditions for waves in the upward and downward directions are significantly different because, far from the forcing plane, upward and downward waves are in a medium with very low and very high- β plasma, respectively. We discuss this in detail in the following sections.

The MHD equations are considered in the approximation that the gas pressure is a scalar and that displacement currents and electrostatic forces are neglected. We apply the MHD equations to our model of the atmosphere and then linearize them by assuming that the perturbations about the basic state are small and adiabatic. This leads to the following equations for conservation of mass, energy, momentum and magnetic flux:

$$\frac{\partial \rho}{\partial t} + \rho_0 \left(\frac{\partial}{\partial z} - \frac{1}{H} \right) u = 0, \quad (1)$$

$$\frac{\partial p}{\partial t} - \rho_0 g u + \rho_0 V_s^2 \frac{\partial u}{\partial z} = 0, \quad (2)$$

$$\rho_0 \frac{\partial u}{\partial t} + \frac{\partial p}{\partial z} + \rho g + \frac{B_0}{4\pi} \frac{\partial b}{\partial z} = 0, \quad (3)$$

and

$$\frac{\partial b}{\partial t} + B_0 \frac{\partial u}{\partial z} = 0. \quad (4)$$

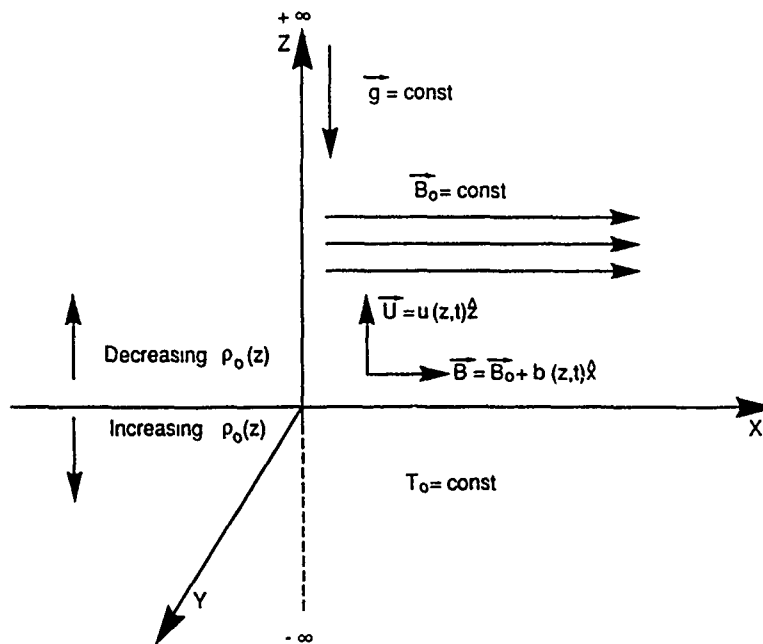


FIG. 1.—Definition of the pertinent symbols relating the directions between the gravity, g , the uniform background magnetic field, B_0 , the perturbed velocity, U , and the perturbed magnetic field, B . Note also that the density $\rho_0(z)$ decreases with height according to hydrostatic equilibrium in an isothermal atmosphere; hence, both β and V_s decrease exponentially with height.

In equations (1)–(4), the perturbations of density, pressure, velocity and magnetic field are represented by ρ , p , u , and b , respectively. Equations (1)–(4) show that we are considering only MHD waves with an x -component of the perturbed magnetic field; these are purely compressional (magnetoacoustic) waves that oscillate vertically, perpendicular to the magnetic field lines.

The wave equation for the velocity perturbation u may be obtained by eliminating ρ , p , and b from equations (1)–(4). This gives (see also Nye and Thomas 1974)

$$\frac{\partial^2 u}{\partial t^2} - (V_s^2 + V_a^2) \frac{\partial^2 u}{\partial z^2} + \frac{V_s^2}{H} \frac{\partial u}{\partial z} = 0. \quad (5)$$

In the previous studies of this problem, only the wave equation for the velocity perturbation has been considered. However, as known from studies of Alfvén waves (see Ferraro and Plumpton 1958) the velocity and magnetic field perturbations behave

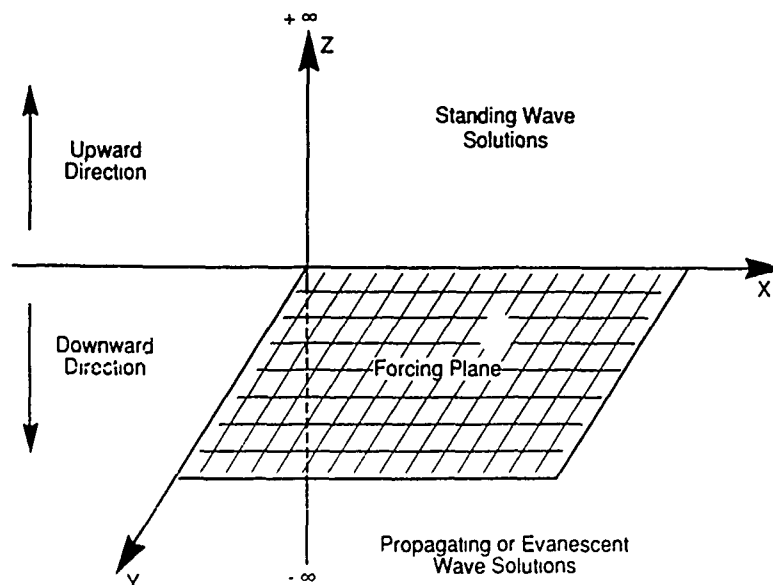


FIG. 2.—Sketch of the forcing plane imagined in the physical considerations by which we select the wave solutions for upward and downward waves. These steady state solutions show (1) that all upward waves are standing waves for any frequency and any values of the parameters of the model atmosphere (for $B_0 > 0$ and H finite), and (2) that the downward waves are either propagating or evanescent waves depending only on whether the frequency is higher or lower than the cutoff frequency $\omega_c = V_s/2H$ set by the temperature of the atmosphere (and by g , γ , and μ).

differently in a stratified medium. Therefore, we also derive the wave equation for the magnetic field perturbation b and for the perturbations in density and pressure. We begin with the magnetic field perturbation and eliminate all the variables from equations (1)–(4) in terms of b . This gives the wave equation in the form:

$$\frac{\partial^2 b}{\partial t^2} - (V_s^2 + V_a^2) \frac{\partial^2 b}{\partial z^2} + \frac{V_s^2 - V_a^2}{H} \frac{\partial b}{\partial z} = 0. \quad (6)$$

By comparing this equation to equation (5), one sees that the wave equations are different, which means that the MHD variables u and b show different spatial dependence in an isothermal atmosphere. We find that the wave equations for redefined variables p/p_0 and ρ/ρ_0 satisfy the same wave equation as for the magnetic field b ; this formally allows us to deal with only two wave equations of different forms (for u and b) and when the latter is solved the solutions for both p and ρ are immediately known. The wave equations (5) and (6) fully describe the downward and upward waves below and above our wave source. If there are no gradients ($H \rightarrow \infty$) the solutions to the wave equation represent magnetoacoustic waves propagating with the phase velocity $V_f^2 = V_s^2 + V_a^2$ resulting from compressional stresses in both the gas pressure and the magnetic field pressure.

III. PHYSICAL CONSIDERATIONS

Before the full solutions to the wave equations (5) and (6) are obtained for the model described in the previous section, we begin with two simple cases, the limits of cold plasma ($\beta = 0$) and high- β plasma ($\beta \gg 1$). We discuss physical implications for the wave behavior that result from considering these simplifications and find that upward and downward waves behave differently. By comparing our results with those obtained by Thomas (1982), we conclude, on the basis of physical arguments, that the behavior of the upward waves in the case of cold plasma cannot be described by Thomas's approach (see also Appendix A for mathematical arguments) and therefore his approach is of limited applicability. Thus, we conclude that a new treatment of this problem (in the case of finite temperature) is necessary. Our interpretation of the full solutions, presented in § V, is guided by our understanding of the simple limiting cases considered here.

a) Limit of Cold Plasma

To consider the compression waves in the limit of cold plasma, we assume that $V_s \rightarrow 0$ and $g \rightarrow 0$ to give the density scale height $H = \text{const}$. Then, equations (5) and (6) are reduced to the form which is identical to that describing purely transverse Alfvén waves; this means that the fast mode waves propagating across the field lines behave similarly to Alfvén waves propagating along the magnetic field lines. Note that this similarity is only mathematical as the main physical differences between the two types of waves still remain. In the case considered here, the fast waves are purely compressional waves and exist because of the field compression, while Alfvén waves are purely transverse and tension stress of the magnetic field is responsible for their existence. Despite this physical difference, the basic propagation equations are the same and therefore insight into the wave propagation properties may be gained by using the results previously obtained for Alfvén waves propagating in a stratified medium with a vertical and uniform magnetic field (Ferraro and Plumpton 1958; Hollweg 1978; Leroy 1980; Rosner, Low, and Holzer 1986, and references therein; see also An *et al.* 1989, for a numerical time-dependent approach).

To describe the behavior of compression waves propagating across the field lines in the cold plasma, we begin with transformation of equations (5) and (6) using a new variable $\eta = \omega/\omega_a(z)$, where $\omega_a(z) = V_a(z)/2H$, and change wave variables as follows: $u(z, t) = u_1(\eta, t) = u_2(\eta)e^{-i\omega t}$ and $b(z, t)/(\rho_0)^{1/2} = b_1(z, t) = b_2(\eta, t) = b_3(\eta)e^{-i\omega t}$. This gives

$$\eta^2 \frac{d^2 u_2}{d\eta^2} + \eta \frac{du_2}{d\eta} + \eta^2 u_2 = 0, \quad (7)$$

and

$$\eta^2 \frac{d^2 b_3}{d\eta^2} + \eta \frac{db_3}{d\eta} + (\eta^2 - 1)b_3 = 0, \quad (8)$$

which are the Bessel type of equations with the solutions given by $u_2 = C_1 J_0(\eta) + C_2 Y_0(\eta)$ and $b_3 = C_3 J_1(\eta) + C_4 Y_1(\eta)$; J and Y are Bessel and Weber functions, respectively, and subscripts 0 and 1 determine the order of the functions.

Now, we must introduce the forcing plane and obtain solutions in the upward and downward directions. It can be easily shown that in the model considered here, by analogy with Alfvén waves in an isothermal atmosphere (An *et al.* 1989), the upward waves have finite transit time (exponential increase of the phase velocity) to reach infinity and therefore they are always *standing waves*; this means that the standing wave solutions are unavoidable for the upward direction. However, for downward waves the transit time to reach infinity is infinite (exponential decrease of the phase velocity) which means that these waves are *propagating waves*.

The obtained solutions to equations (7) and (8) describe standing waves if the constants of integration $C_{1,2,3,4}$ are real numbers. For the upward waves, then, we can apply the boundary condition of finite amplitude at $z = +\infty$ (see Fig. 2) to determine two of these constants. We find that both Weber functions (Y_0 and Y_1) are infinite at $\eta = 0$ and by physical reasoning (finite wave energy density) these solutions have to be excluded by assuming $C_2 = C_4 = 0$. Hence, the solutions for the upward waves are given in the form: $u_1 = C_1 J_0(\eta)e^{-i\omega t}$ and $b_2 = C_3 J_1(\eta)e^{-i\omega t}$. The functions J_0 and J_1 are plotted in Figures 3a and 3c which show that both functions can be divided into two separate parts, namely, the part with and the part without nodes. The latter part is the wave in the region of atmosphere where reflection dominates (see An *et al.* 1989) as the wavelength becomes longer than the local density scale height; in this region the wave is called here *evanescent standing wave*. The other part with nodes is in the region of the atmosphere where the wavelength is shorter than the local density scale height and therefore there is little reflection, in this region, the standing

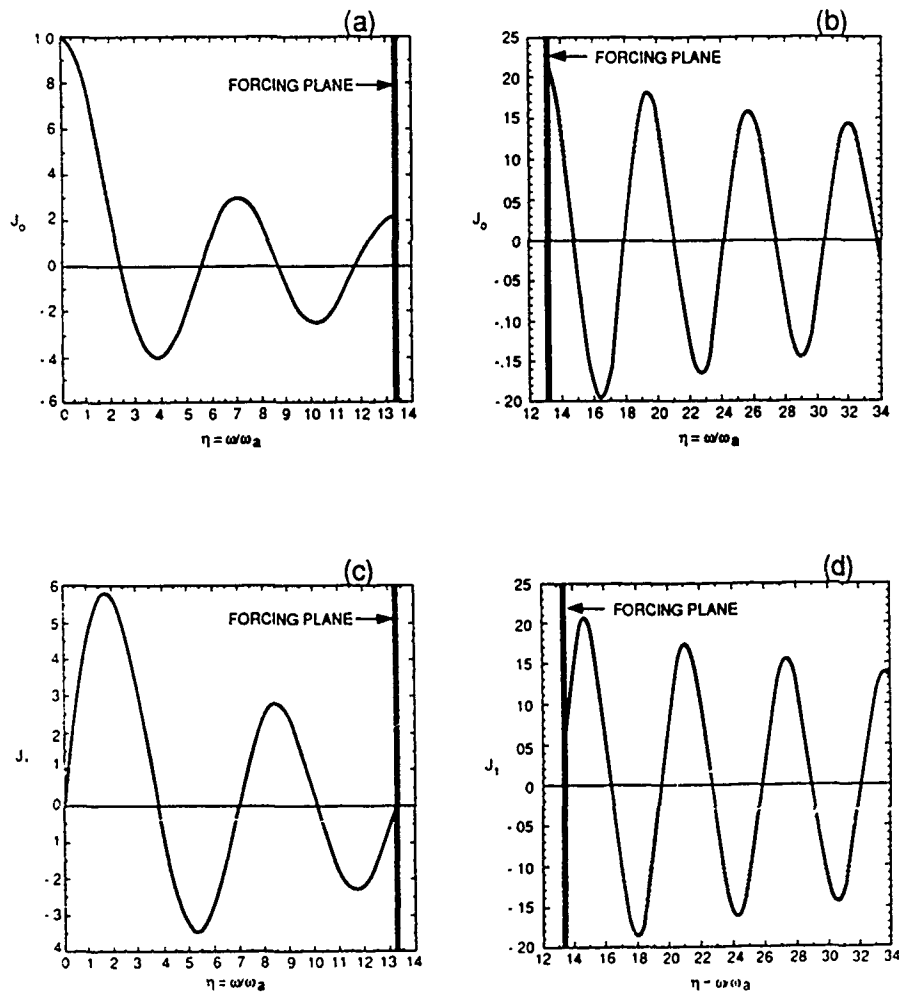


FIG. 3.—Upward and downward waves in the cold plasma case. The upward standing wave solutions, given by the zeroth and first-order Bessel function, are plotted for the velocity and magnetic field perturbations in Figs. 3a and 3c, respectively. The downward propagating wave solutions are presented in Figs. 3b and 3d for the velocity and magnetic field perturbations, respectively. The forcing plane is located at $\eta = 13.4$.

wave is formed from two opposite propagating waves and is called here *regular standing wave*. The fact that the steady state solutions describing behavior of compression waves in low- β plasma represent standing waves was first shown by Summers (1976). However, he did not discuss this problem in terms of the upward and downward waves and did not pay attention to wave reflection. Our paper deals with both these problems in detail.

The transition between the region of evanescent and regular standing waves does not take place at one particular point but gradually through the vicinity of the height at which the condition $\omega = \omega_a$ is satisfied. It was recently shown by An *et al.* (1989) that at this height wave reflection dominates in the wave behavior. Hence, it is arbitrary but reasonable to adopt the point where $\omega = \omega_a$ (or $\lambda = 4\pi H$) to the boundary between the two regions. That is, for $\omega > \omega_a$ the upward wave solutions are reasonably called regular standing waves. Above this height, $\omega \leq \omega_a$ and the upward waves reasonably called evanescent standing waves. Note that for finite ω , the condition $\omega \leq \omega_a$ is satisfied above some height for any wave frequency, which means that the evanescent standing waves are unavoidable steady state solutions for the upward waves. Hence, at any given height, as the wave frequency ω is decreased, reflection becomes dominant and propagation becomes suppressed as ω drops below ω_a . We therefore call ω_a the *local critical frequency*. Sometimes, this frequency is also called the cutoff frequency (e.g., Campos 1987) by analogy to the acoustic cutoff frequency, the latter, however, is the same (global) frequency for the whole atmosphere (see the next subsection) which makes it different from the local critical frequency.

Now, we consider the waves that propagate downward from the forcing plane. Because the propagation time to $z = -\infty$ is infinite for any wave frequency, the downward waves are propagating waves for all wave frequencies, there is no cutoff frequency for downward propagation in the cold plasma limit. For propagating waves, both constants C_2 and C_4 must be purely imaginary and equal to C_1 and C_3 in magnitude. Hence, the solutions can be written in the form: $u_2 = C_1[J_0(\eta) - iY_0(\eta)]$ and $b_3 = C_3[J_1(\eta) - iY_1(\eta)]$. These solutions represent downward propagating waves for any real constants C_1 and C_3 . We plot the real part of these solutions in Figures 3b and 3d.

To summarize, the results presented in this subsection demonstrate similarities in the behavior between compressional and transverse (Alfvén) waves considered in a cold plasma medium. We see that there are two distinct classes of steady state solutions.

standing and propagating waves existing for the upward and downward directions with respect to the wave source, respectively (see Fig. 2). We find that the upward waves become evanescent standing waves above some height for any wave frequency, and below that height the upward wave is a regular standing wave composed of two oppositely directed propagating waves. The height in the atmosphere at which the upward waves become the evanescent standing waves is roughly the height at which the condition $\omega = \omega_a$ is satisfied, this means that ω_a is the local critical frequency. The downward waves are propagating waves for any wave frequency.

Finally, we need to compare the results obtained here to those given by Thomas (1982) and find out whether the same conclusions, concerning the wave behavior, can be drawn from his results. As shown in Appendix A, Thomas's solutions are represented by descending power solutions, which means that they apply to the singular point at $z = -\infty$ (large β) and *cannot* be valid in the vicinity of the singular point $z = \infty$ ($\beta = 0$) for any real wave frequency. However, as demonstrated by the solution to the cold plasma case, the steady state solution for the upward waves must include the point $z = \infty$. Therefore, Thomas's results are mathematically flawed for the upward waves. The full solutions to the problem of the wave behavior in an isothermal and stratified atmosphere with uniform horizontal magnetic field are presented in section 4.

b) Limit of High- β Plasma

In the model considered here (see § II), the limit of high- β , ($V_0/V_a \gg 1$) plasma is naturally expected for the downward waves because V_a decreases with depth (see Fig. 1). Thus, we assume that the wave source (or the plane $z = 0$) is located in the region of sufficiently high density to have the condition $\beta \gg 1$ fulfilled everywhere below the plane. This means that the whole medium for downward propagating waves is a high- β plasma and that in this limit the wave equations (5) and (6) are reduced to the well-known wave equation for acoustic waves propagating vertically in an isothermal atmosphere (Lamb 1945; Moore and Spiegel 1964). In this case, the phase velocity approaches V_s and the waves mimic the behavior of acoustic waves. Hence, they are either *propagating waves* for $\omega > \omega_s$ or *evanescent waves* for $\omega \leq \omega_s$, with $\omega_s (= V_s/2H)$ being constant in the whole atmosphere and called the acoustic cutoff frequency. This shows that the acoustic cutoff frequency has a distinctly different role than the local critical frequency ω_a , the cutoff ω_s determines the behavior of the downward wave solutions and ω_a determines the height at which the upward waves transition from regular standing waves to evanescent waves.

The conclusion that the condition $\omega > \omega_s$ is necessary to have propagating wave solutions was obtained by Summers (1976) from his approximate solutions and also by Thomas (1982) and Campos (1985) who solved the wave equation (5) without any approximation by reducing it to the hypergeometric form (see Appendix A). In this paper, we confirm their results but would like to emphasize that those results concern only downward propagating waves because, in the steady state approach, *there are no propagating wave solutions for the upward direction*. The latter was demonstrated in the previous subsection for the cold plasma case and will also be extended on the general case of finite temperature (see §§ IV and V). Each upward steady solution is a standing wave, even though below a critical height this standing wave is composed of upward and downward propagating waves. Summers (1976), Thomas (1982), and Campos (1985) missed the point that the propagation cutoff at ω_s is only a property of the downward waves.

IV. FULL ANALYTICAL SOLUTIONS TO THE WAVE EQUATIONS

In this section, we present the transformed form of the wave equations (5) and (6), discuss their mathematical properties, and give full solutions to these equations. The physical interpretation of the obtained solutions can be found in the next section.

a) Transformed Wave Equations and Their Properties

After having presented the wave equations and discussed the wave behavior in the limits of cold and high- β plasma, we now proceed to obtain full solutions to equations (5) and (6). To do this, we transform these equations using the plasma β and change variables as follows: $u(z, t) = u_1(\beta, t) = u_2(\beta)e^{-i\omega t}$ and $b(z, t) = b_1(z, t)(\rho_0)^{1/2} = b_2(\beta, t) = b_3(\beta)e^{-i\omega t}$. This gives

$$\frac{d^2 N_i}{d\beta^2} + \frac{P_i(\beta)}{\beta} \frac{dN_i}{d\beta} + \frac{Q_i(\beta, \alpha_i)}{\beta^2} N_i = 0, \quad (9)$$

where

$$P_i(\beta) = \frac{1 + a_i \beta^2}{1 + \beta^2}, \quad (10)$$

$$Q_i(\beta, \alpha_i) = \frac{c_i \beta^2 - d_i}{1 + \beta^2}, \quad (11)$$

with $i = 1, 2$, $N_i = [u_i, b_i]$, $a_i = [3, 5]$, $c_i = [\alpha_i^{-2}, (3 + \alpha_i^2)]$, $d_i = [0, 1]$ and

$$\alpha_i = \frac{\omega_s}{\omega},$$

being an arbitrary constant parameter.

From a mathematical point of view equation (9) shows one singular point on the real finite axis ($\beta = 0$) and, according to the results of § IVc, one singular point at $\beta = \infty$, both these points are *regular singular points*. To find the full solutions to equation (9), we begin by obtaining the solutions in the vicinity of the regular singular point at $\beta = 0$ and then discuss the range of validity of these solutions. As shown in the next subsection, the solutions obtained at $\beta = 0$ do not cover the whole space and therefore we must also explore solutions at the singular point $\beta = \infty$ and at the ordinary point $\beta = 1$. After obtaining full solutions to equation (9), we shall select the physical solutions for the upward waves and for the downward waves (see § V).

b) Singular Point Solutions at $\beta = 0$

The solutions in the vicinity of the real singular point can be obtained by assuming that all the functions in equation (9) are analytical and by making the series expansion of P_i , Q_i , and N_i about $\beta = 0$. For P_i and Q_i , this gives

$$P_i(\beta) = \sum_{n=0}^{\infty} p_{in} \beta^n = 1 - (a_i - 1) \sum_{n=1}^{\infty} (-1)^n \beta^{2n}, \quad (12)$$

and

$$Q_i(\beta, \alpha_i) = \sum_{n=0}^{\infty} q_{in} \beta^n = -d_i - (c_i + d_i) \sum_{n=1}^{\infty} (-1)^n \beta^{2n}, \quad (13)$$

with all odd coefficients being zero. It is easily seen that these series expansions converge only for $\beta < 1$, which restricts the solutions to where $V_a > V_s$. In addition, the series expansions (12) and (13) show a discouraging slowness in converging when $\beta \rightarrow 1$. Thus, to present the full solutions to equation (9), we must also obtain the solutions in the vicinity of the point $\beta = 1$ as well as the solutions for $\beta > 1$. We deal with these problems separately in the next two subsections.

Now, we are looking for the solutions given by the series expansion following the standard procedure in solving differential equations in the vicinity of singular points (e.g., Murphy 1960), and obtain

$$N_i(\beta) = \sum_{n=0}^{\infty} \Phi_{in} \beta^{n+\lambda}, \quad (14)$$

where λ is a free parameter to be determined from the indicial equation and $\Phi_{in} = [\phi_n, \psi_n]$ are the expansion coefficients for the velocity and magnetic perturbations, respectively; ϕ_0 and ψ_0 are arbitrary constants. Note also that the coefficients ϕ_n and ψ_n depend on the constant parameter α_i , but to present the results in a more compact form this is not explicitly shown in the above equation. The same convention is to be assumed in later parts of this paper where only dependence on β and t is emphasized. It is easy to demonstrate that the indicial equation shows two solutions: $\lambda_1 = \lambda_2 = 0$ for the velocity perturbations, and $\lambda_{1,2} = \pm 1$, for the magnetic field perturbations. Because in the first case both roots are zero, the solutions always contain a logarithmic term. In the latter case, the roots are nonzero integers and therefore we need to test whether the logarithmic term occurs in the solution. Following Murphy (1960), we calculate $\delta = \lambda_1 - \lambda_2 = 2$ and look for the constant $\psi_{(\delta=2)}$. It appears that ψ_2 is not an arbitrary constant. Thus the logarithmic term will also exist in the solution for the magnetic field.

Solutions for the velocity perturbations are given in the following form:

$$u_1(\beta, t) = [C_1 \mathcal{J}_0(\beta) + C_2 \mathcal{Y}_0(\beta)] e^{-i\omega t}, \quad (15)$$

where

$$\mathcal{J}_0(\beta) = \sum_{n=0}^{\infty} \phi_{2n} \beta^{2n}, \quad (16)$$

with $\phi_0 = 1$ and

$$\phi_{2n} = \frac{1}{(2n)^2} \sum_{m=0}^{n-1} (-1)^{n-m} (4m + \alpha_s^{-2}) \phi_{2m}, \quad (17)$$

valid for all $n \geq 1$. C_1 and C_2 are arbitrary constants of integration to be determined from boundary conditions. In the following parts of this paper, the letter C will be always used to denote the constant of integration.

In addition, we have

$$\mathcal{Y}_0(\beta) = \mathcal{J}_0(\beta) \ln(\beta) + \sum_{n=1}^{\infty} \phi'_{2n} \beta^{2n}, \quad (18)$$

where $\phi'_0 = 0$ and

$$\phi'_{2n} = \frac{1}{(2n)^2} \sum_{m=0}^{n-1} (-1)^{n-m} \left[(4m + \alpha_s^{-2}) \left(\phi'_{2m} - \frac{1}{n} \phi_{2m} \right) + 4m \phi_{2m} \right], \quad (19)$$

valid for all $n \geq 1$.

The solutions for the perturbed magnetic fields are given by

$$b_2(\beta, t) = [C_3 \mathcal{J}_1(\beta) + C_4 \mathcal{Y}_1(\beta)] e^{-i\omega t}, \quad (20)$$

where

$$\mathcal{J}_1(\beta) = \sum_{n=0}^{\infty} \psi_{2n} \beta^{2n-1}, \quad (21)$$

with $\psi_0 = 0$, $\psi_2 = -\alpha_i^{-2}/2$, and

$$\psi_{2n} = \frac{1}{4n(n-1)} \sum_{m=0}^{n-1} (-1)^{n-m} (8m + \alpha_i^{-2}) \psi_{2m}, \quad (22)$$

valid for all $n > 1$.

In addition, we have

$$\mathcal{Y}_1(\beta) = \mathcal{J}_1(\beta) \ln(\beta) + \sum_{n=1}^{\infty} \psi'_{2n} \beta^{2n-1}, \quad (23)$$

where $\psi'_0 = 1$, $\psi'_2 = (\alpha_s^{-2} - 8)/4$, and

$$\psi'_{2n} = \frac{1}{4n(n-1)} \sum_{m=0}^{n-1} (-1)^{n-m} \left\{ (8m + \alpha_s^{-2}) \left[\psi'_{2m} - \frac{2n-1}{2n(n-1)} \psi'_{2m} \right] + 8m \psi'_{2m} \right\}, \quad (24)$$

valid for all $n > 1$.

It is easily seen from the above equations that in the limit of $\beta \ll 1$, the functions \mathcal{J}_0 and \mathcal{J}_1 reduce to Bessel J_0 and J_1 functions of the zeroth and first order, respectively. The same is true for the functions \mathcal{Y}_0 and \mathcal{Y}_1 which, in this limit, become Weber functions of the zeroth and first order, respectively. Therefore, we may call the functions obtained here generalized Bessel and Weber functions.

Note that regular Bessel and Weber functions which result from equations (7) and (8) depend on the argument η instead of β ; both arguments are, however, related by $\beta = \alpha_s \eta$. To make the comparison between regular and generalized Bessel and Weber functions, we transform $\mathcal{J}_{0,1}(\beta) \rightarrow \mathcal{J}_{0,1}(\eta)$ and $\mathcal{Y}_{0,1}(\beta) \rightarrow \mathcal{Y}_{0,1}(\eta)$ with $\eta < \alpha_s^{-1}$ resulting from the condition that $\beta < 1$. The results plotted in Figure 4 present the zeroth order generalized Bessel and Weber functions obtained for two different values of α_s (0.025, 0.075) and compared to the regular Bessel and Weber functions. In addition, the figure shows that the region of validity of the results is very sensitive to the parameter α_s and that convergence of $\mathcal{J}_0(\eta)$ and $\mathcal{Y}_0(\eta)$ does not occur for all $\eta < \alpha_s^{-1}$, but instead only for $\eta \lesssim 0.5 \alpha_s^{-1}$; the latter is indicated in Figure 4 by the last zero of these functions before they diverge. It should be also mentioned that for small η both generalized functions become identical to their regular counterparts and that this does not depend on α_s .

c) Singular Point Solutions at $\beta = \infty$

As shown in previous subsection, the solutions obtained at the point $\beta = 0$ are not valid for all β . Thus, as the next step, we find the solutions for $\beta > 1$, which is equivalent to obtaining the solutions in the vicinity of $\beta = \infty$. To do so, we define a new variable $\chi = 1/\beta$ which allows finding the solutions for large β . Using $M_i(\chi) = N_i(\beta)$, we write the wave equation (9) in the form:

$$\frac{d^2 M_i}{d\chi^2} + \frac{P_i(\chi)}{\chi} \frac{dM_i}{d\chi} + \frac{Q_i(\chi, \alpha_s)}{\chi^2} M_i = 0, \quad (25)$$

where

$$P_i(\chi) = \frac{\chi^2 - e_i}{1 + \chi^2}, \quad (26)$$

$$Q_i(\chi, \alpha_s) = \frac{c_i - \chi^2}{1 + \chi^2}, \quad (27)$$

and $e_i = [1, 3]$.

Now, the wave equation (25) shows only one regular singular point on the finite real axis ($\chi = 0$ or $\beta = \infty$), and we may again write the series expansion of functions P_i and Q_i in the following form:

$$P_i(\chi) = \sum_{n=0}^{\infty} p_{in} \chi^n = -e_i - (1 + e_i) \sum_{n=1}^{\infty} (-1)^n \chi^{2n}, \quad (28)$$

$$Q_i(\chi, \alpha_s) = \sum_{n=0}^{\infty} q_{in} \chi^n = c_i + (1 + c_i) \sum_{n=1}^{\infty} (-1)^n \chi^{2n}. \quad (29)$$

These series are convergent when the condition $\chi < 1$ ($\beta > 1$) is satisfied, which restricts the solutions to where $V_a < V_s$.

Again, we are looking for the solutions given by a series expansion and obtain

$$M_i(\chi) = \sum_{n=0}^{\infty} \Psi_{in} \chi^{n+\lambda}, \quad (30)$$

where λ is a free parameter to be determined from the indicial equation, and $\Psi_{in} = [\phi_n, \psi_n]$ are the expansion coefficients with ϕ_0 and ψ_0 being arbitrary but nonzero constants for the velocity and magnetic field perturbations, respectively. Note also that the coefficients Ψ_{in} depend on the parameter α_s . In this case, the indicial equation shows, in the case considered here, two complex roots defined by $\lambda_{1,2} = 1 \pm i[(\omega^2 - \omega_s^2)/\omega_s^2]^{1/2}$ for the velocity perturbations, and by $\lambda_{1,2} = 2 \pm i[(\omega^2 - \omega_s^2)/\omega_s^2]^{1/2}$ for the magnetic field perturbations. Calculating $\delta = \lambda_1 - \lambda_2$, we find that this quantity is not an integer; thus, the solutions do not contain the logarithmic term. Because the roots are complex, the coefficients ψ_{in} are also complex. The solutions (30) represent either periodically oscillating functions when the condition $\omega > \omega_s$ is satisfied or nonoscillating functions in the opposite limit. Physical consequences of this are discussed in the next section.

Solutions for the velocity perturbations are given in the form:

$$u_1(\chi, t) = [C_1 Z_0^+(\chi) + C_2 Z_0^-(\chi)] e^{-i\omega t}. \quad (31)$$

where

$$Z_0^\pm(\chi) = \exp [\pm i(\alpha_s^{-2} - 1)^{1/2} \ln \chi] \sum_{n=0}^{\infty} \phi_{2n}^\pm \chi^{2n+1}, \quad (32)$$

with $\phi_0 = 1$. The real and imaginary parts of ϕ_{2n}^\pm are given by

$$\operatorname{Re}(\phi_{2n}^\pm) = \frac{1}{2n(n^2 + \alpha_s^{-2} - 1)} \sum_{m=0}^{n-1} (-1)^{n-m} \left[n \left(2m + 1 + \frac{\alpha_s^{-2}}{2} \right) + \alpha_s^{-2} - 1 \right] \operatorname{Re}(\phi_{2m}^\pm), \quad (33)$$

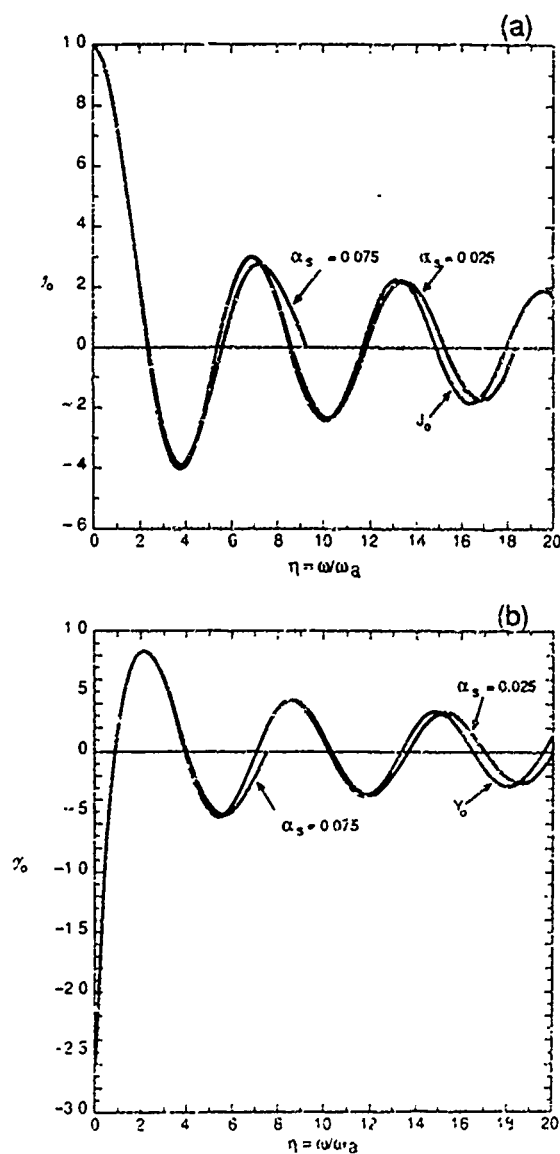


FIG. 4

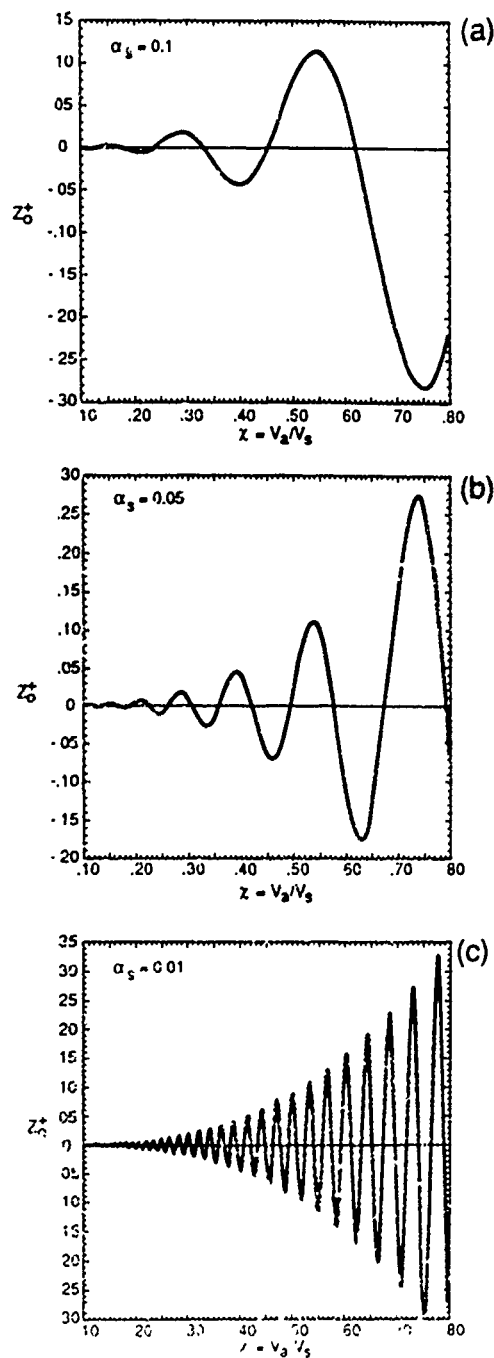


FIG. 5

FIG. 4—Example basis functions for the velocity solution in the $\beta < 1$ region of the model atmosphere with arbitrary B_0 and T_0 . The zeroth order generalized Bessel, J_0 , and Weber, Y_0 , functions are plotted for different $\alpha_s = \omega_0/\omega$, (a) and (b), respectively. The plots are made for two different values of α_s and compared to regular Bessel and Weber functions obtained for the $\alpha_s = 0$ case. Because the generalized Bessel and Weber functions do not converge for all the arguments η , the calculations are stopped at the last node before the functions diverge.

FIG. 5—Velocity solutions obtained in the vicinity of the singular point $\beta = x$ for the case of arbitrary B_0 and T_0 . The examples plotted are for three different parameters α_s in (a), (b), and (c) respectively. It is seen that the wave amplitude decreases in the downward (increasing z) direction.

and

$$\operatorname{Im}(\phi_{2n}^{\pm}) = \pm \frac{(\alpha_s^{-2} - 1)^{1/2}}{2n(n^2 + \alpha_s^{-2} - 1)} \sum_{m=0}^{n-1} (-1)^{n-m} \left(n - 2m - 1 - \frac{1}{2} \alpha_s^{-2} \right) \operatorname{Im}(\phi_{2m}^{\pm}), \quad (34)$$

valid for all $n \geq 1$.

For the magnetic field perturbations, we obtain

$$b_2(\chi, t) = [C_3 Z_1^+(\chi) + C_4 Z_1^-(\chi)] e^{-i\omega t}, \quad (35)$$

where

$$Z_1^{\pm}(\chi) = \exp[\pm i(\alpha_s^{-2} - 1)^{1/2} \ln \chi] \sum_{n=0}^{\infty} \psi_{2n}^{\pm} \chi^{2(n+1)}, \quad (36)$$

with $\psi_0 = 1$, and

$$\operatorname{Re}(\psi_{2n}^{\pm}) = \frac{1}{n(n^2 + \alpha_s^{-2} - 1)} \sum_{m=0}^{n-1} (-1)^{n-m} \left[2n(m+1) + n \left(1 + \frac{\alpha_s^{-2}}{4} \right) + \alpha_s^{-2} - 1 \right] \operatorname{Re}(\psi_{2m}^{\pm}), \quad (37)$$

and

$$\operatorname{Im}(\psi_{2n}^{\pm}) = \pm \frac{(\alpha_s^{-2} - 1)^{1/2}}{n(n^2 + \alpha_s^{-2} - 1)} \sum_{m=0}^{n-1} (-1)^{n-m} \left(n - 2m - 3 - \frac{\alpha_s^{-2}}{4} \right) \operatorname{Im}(\psi_{2m}^{\pm}), \quad (38)$$

valid for all $n \geq 1$.

As an example, we plot in Figure 5 the real part of the function Z_0^+ (eq. [31]) with real coefficients ϕ_{2n} (eq. [33]) for three different parameters α_s . The figure shows that the solutions are very sensitive to the parameter α_s , and they have an oscillatory shape with the amplitude increasing for increasing argument χ .

d) Ordinary Point Solutions at $\beta = 1$

The results presented in two previous subsections show that the solutions obtained at singular points $\beta = 0$ and $\beta = \infty$ cannot be extended to the vicinity of $\beta = 1$. Thus, we must find the solutions at this point as well.

We transform the wave equation (9) using the new variable $\xi = \beta - 1$ and define $L(\xi) = N(\beta)$. This gives

$$\frac{d^2 L_i}{d\xi^2} + P(\xi) \frac{dL_i}{d\xi} + Q(\xi, \alpha_s) L_i = 0, \quad (39)$$

where

$$P(\xi) = \frac{1 + a_i(1 + \xi)^2}{[1 + (1 + \xi)^2](1 + \xi)}, \quad (40)$$

$$Q(\xi, \alpha_s) = \frac{c_i(1 + \xi)^2 - d_i}{[1 + (1 + \xi)^2](1 + \xi)^2}. \quad (41)$$

Now, one sees that for both cases $i = 1$ and 2 , $\xi = 0$ is the ordinary point and the method of finding the solutions (e.g., Murphy 1960) differs from that considered for the regular singular point. Note also that the solutions found in the vicinity of the ordinary point cannot be extended to the vicinity of the singular points $\beta = 0$ and $\beta = \infty$. The important result is, however, that the solutions obtained at the singular points and at the ordinary point show overlapping regions of common validity and thus they may cover the whole physical space when the appropriate matching conditions are applied (Appendix B).

Making the expansion of functions P_i and Q_i similar to those given by equations (12) and (13), we find that the coefficients p_{in} and q_{in} are given by

$$p_{in} = -\frac{1}{2}[4p_{i(n-1)} + 3p_{i(n-2)} + p_{i(n-3)}], \quad (42)$$

valid for all $n \geq 3$ and with $p_{i0} = (1 + a_i)/2$, $p_{i1} = -1$ and $p_{i2} = (5 - a_i)/4$; and

$$q_{in} = -\frac{1}{2}[6q_{i(n-1)} + 7q_{i(n-2)} + 4q_{i(n-3)} + q_{i(n-4)}], \quad (43)$$

valid for all $n \geq 4$ and with $q_{i0} = (c_i - d_i)/2$, $q_{i1} = -c_i - 3d_i/2$, $q_{i2} = (c_i - 11d_i)/4$ and $q_{i3} = 4d_i$.

Then, the solution can be obtained as

$$L(\xi) = [C_1 L_{1i}(\xi) + C_2 L_{2i}(\xi)] e^{-i\omega t}, \quad (44)$$

where

$$L_{1i}(\xi) = 1 + \sum_{n=2}^{\infty} \phi_{in} \xi^n, \quad (45)$$

and

$$L_2(\xi) = \xi + \sum_{n=2}^{\infty} \psi_n \xi^n. \quad (46)$$

The expansion coefficients ϕ_n and ψ_n can be evaluated from the following recursion relation:

$$[\phi_n; \psi_n] = -\frac{1}{n(n-1)} \left\{ \sum_{m=1}^{n-1} m[\phi_m; \psi_m] p_{i(n-m-1)} + \sum_{m=0}^{n-2} [\phi_m; \psi_m] q_{i(n-m-2)} \right\}, \quad (47)$$

valid for all $n \geq 2$ and with coefficients $[\phi_{i0}; \phi_{i1}]$ and $[\psi_{i0}; \psi_{i1}]$ being arbitrary constants. The coefficients ϕ_{in} and ψ_{in} are evaluated with the assumptions: $(\phi_{i0} = 1, \phi_{i1} = 0)$ and $(\psi_{i0} = 0, \psi_{i1} = 1)$, respectively. In Figure 6, we plot the solutions (45) and (46) for the velocity perturbations for different α_s . It is shown that the results are very sensitive to the parameter α_s and, even more important, their range of validity significantly decreases for decreasing α_s . In the limit of $\alpha_s \rightarrow 0$, the range approaches zero and one does not need to be concerned with the ordinary point solutions. In addition, the solutions are not symmetric about $\beta = 1$ (see Fig. 6a and 6e and Figs. 6b and 6f). By comparing Figures 6c and 6d, one may also find that the functions L_1 and L_2 for the velocity perturbations show a 90° shift and have greatly different amplitudes ($L_1/L_2 \approx 70$).

V. SELECTION OF PHYSICAL SOLUTIONS

In the previous section, we presented the solutions to the wave equation (9) obtained in the vicinity of two singular points and one ordinary point and discussed the importance of the parameter $\alpha_s = \omega/\omega$ in determining the range of validity of the solutions. These results are summarized in Figure 7, which shows that there is no one expansion that converges to the solution for the whole space and that the expansions are different in the vicinity of the ordinary and regular singular points. That is, there is one general solution that spans the whole atmosphere, but each of our three expansions converges to this solution over only a part of the atmosphere. Even so, together these expansions constitute a full general solution because there is overlap between the adjacent regions of convergence.

From our general solution, we seek two classes of physical solutions, the upward and downward waves excited above and below a forcing plane. In this section, we find the upward and downward solutions in each of the three regions of convergence and show how to match the adjacent solutions to obtain solutions that cover the whole atmosphere. We assume that the forcing plane is located at the height in the atmosphere where $\beta = 1$ and consider the solutions in the upward and downward directions. One should note, however, that the point $\beta = 1$ is not a special point in the atmosphere; in general, the matching procedure described in Appendix B can be applied to any location of the forcing plane and the solutions that cover the whole atmosphere are always obtained.

a) The Upward Direction

As discussed in § III, the upward waves are standing waves as a result of reflection on the density gradient. Far above the forcing plane, the solutions are given by equations (15) and (20), which represent real functions describing standing wave solutions for any arbitrary (but real) constants of integrations. However, as shown by equations (18) and (23), the functions \mathcal{Y}_0 and \mathcal{Y}_1 contain the logarithmic term which makes these solutions infinite when $\beta \rightarrow 0$. Therefore, we exclude these unphysical solutions by taking $C_2 = C_4 = 0$. This gives the physically acceptable solutions, describing finite-amplitude wave behavior far away from the forcing plane, in the following form: $u_1(\beta, t) = C_1 \mathcal{J}_0(\beta) e^{-i\omega t}$ and $b_1(\beta, t) = C_3 \mathcal{J}_1(\beta) e^{-i\omega t}$, which represent the standing wave solutions for real constants C_1 and C_2 . However, as shown in the previous section, these solutions cannot be extended down to the ordinary point but instead roughly to the point $\beta \approx 0.5$. The solutions in the region of $1 \geq \beta \geq 0.5$ are described by the ordinary point solutions (eq. [44]) and are plotted in Figure 6c. The full solutions for the velocity perturbations are presented in Figure 8 for the whole space above the forcing plane. This plot requires matching the function \mathcal{J}_0 to the solutions given by equation (44). The matching point is chosen at $\beta = 0.6$ and the matching procedure is described in Appendix B.

The results shown in Figure 8 represent standing wave solutions and, similar to the results of § IIIa, we may again separate the solution into two parts that correspond to the evanescent and regular standing waves. In the case considered here, this height depends also on V_s which means that the local critical frequency, introduced in § IIIa for the upward compression waves in a cold plasma, must be generalized to the case of $T_0 > 0$. In order to do so, we return to our original equation (9) and find that only Q_s shows a dependence on the wave frequency ω and it can be written as $\omega^2/(\omega_a^2 + \omega_s^2)$. To check how our results depend on this ratio of frequencies, we assume that $\omega = \omega_{as}$ [with $\omega_{as} = (\omega_a^2 + \omega_s^2)^{1/2}$] at the forcing plane ($\alpha_s = 0.707$) and find that the solutions represent evanescent standing waves (Fig. 9) for the whole space above the forcing plane. This illustrates that frequency ω_{as} has the same physical meaning as ω_a for purely transverse Alfvén waves, i.e., it separates the evanescent and regular standing wave solutions and determines the height at which wave reflection becomes dominant (see § IIIa). Note also that for the forcing plane located at the height where $\beta \ll 1$, the local critical frequency ω_{as} reduces to ω_a which is in agreement with the results of § IIIa. Thus, we may call the frequency ω_{as} the local critical frequency for the upward compression waves.

b) The Downward Direction

According to the results obtained in §§ IIIb and IV, the solutions for the downward waves are given by equations (31) and (35) far away from the forcing plane and by equation (44) close to the plane. The roots of the indicial equation presented in § IVc show that these solutions represent propagating waves when $\omega > \omega_s$ and evanescent waves in the opposite case. Because the result is independent of any critical frequencies (either ω_{as} or ω_a), the frequency ω_s is the cutoff frequency for the downward compression waves. This cutoff frequency is the same (global) for the whole atmosphere and in this way is different than the local critical frequency ω_{as} introduced in the previous subsection for the upward compression waves.

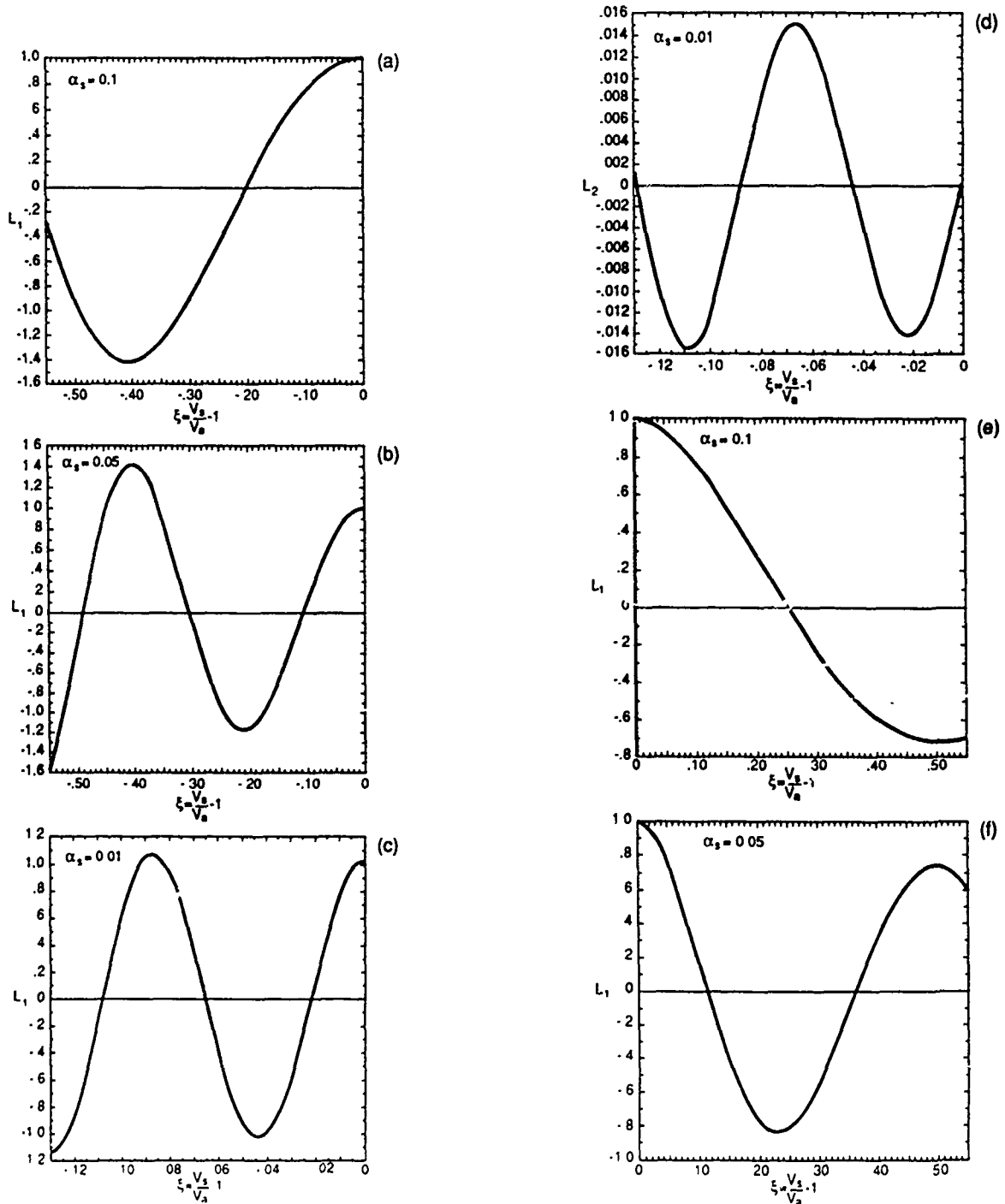
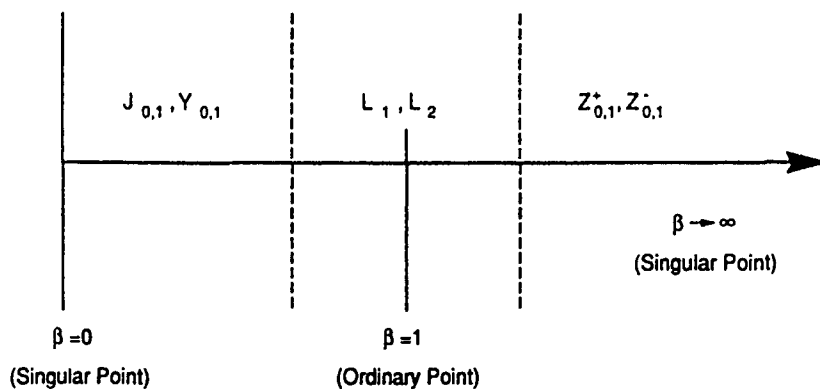


FIG. 6.—Example basis functions L_1 and L_2 for the velocity solution in the vicinity of $\beta = 1$ in the model atmosphere with arbitrary B_0 and T_0 . In (a) and (b), L_1 is plotted on the low- β side of $\beta = 1$ for two different parameters α_3 . In (c) and (d), L_1 and L_2 are plotted for the same α_3 , note that as a result of small α_3 , the solutions are restricted to lower $|\xi|$ than in the previous panels. Finally, in (e) and (f), L_1 is plotted on the high- β side for two different parameters α_3 .

The physically accepted (i.e., downward propagating) solutions for the downward compression waves are given by $u_1(\chi, t) = C_1 Z_0^+(\chi) e^{-i\omega t}$ and $b_2(\chi, t) = C_3 Z_1^+(\chi) e^{-i\omega t}$ which describe the propagating wave solutions for any real C_1 and C_3 with the coefficients ϕ and ψ defined by equations (33) and (37), respectively. Note also that real parts of nonoscillatory terms in equations (32) and (36) describe a decrease in the wave amplitudes required by the conservation of wave energy fluxes. The solutions close to the forcing plane (vicinity of the ordinary point) are given by equation (44) and are plotted in Figures 6e and 6f. The full solutions for this half of the space where $\beta \leq 1$ are presented in Figure 10, which shows the propagating waves with decreasing amplitude. The figure also demonstrates that the wavelength increases for the downward propagation (compare to Fig. 5a); however, the latter is a superficial effect caused by using variable β instead of χ . In order to plot the full solutions for the downward propagation, we matched the function Z_0^+ to the solutions (44) at the point $\beta = 1.3$. The procedure described in Appendix B.

FIG. 7.—Schematic presentation of the full solutions to the velocity wave equation in β space

VI. DISCUSSION

In this paper, we consider the behavior of vertical compression waves in an isothermal atmosphere with a uniform horizontal magnetic field and present, for the first time, the full analytical solutions to the wave equations obtained for both velocity and magnetic field perturbations. The problems discussed here have already been studied by other authors (Summers 1976; Thomas, 1982, 1983; Campos 1985, 1987); however, their results and conclusions are incomplete in light of our results. The basic conclusion from the previous studies is that the filtering of magnetoacoustic waves through the atmosphere is a purely compressive phenomenon and that these waves behave identically to acoustogravity waves. Here, we show, however, that in the considered model of the atmosphere waves behave differently for upward and downward excitation and that only the downward waves behave in the way found by Thomas and Campos.

In the steady state approach considered here, the upward waves are standing waves for *any wave frequency*. The standing wave solutions can be spatially separated into two different parts: evanescent and regular standing waves. The height at which the transition takes place can be evaluated from the condition $\omega = \omega_{as}$, with $\omega_{as} = (\omega_a^2 + \omega_g^2)^{1/2}$ being called the local critical frequency. At heights where $\omega < \omega_{as}$, reflection on the density gradient dominates in the wave behavior. The local critical frequency ω_{as} has the same physical meaning as the frequency ω_a for the upward Alfvén waves in an isothermal atmosphere with uniform vertical magnetic field. The critical frequency ω_{as} increases with height in the atmosphere because of the increase in ω_a with height. Hence,

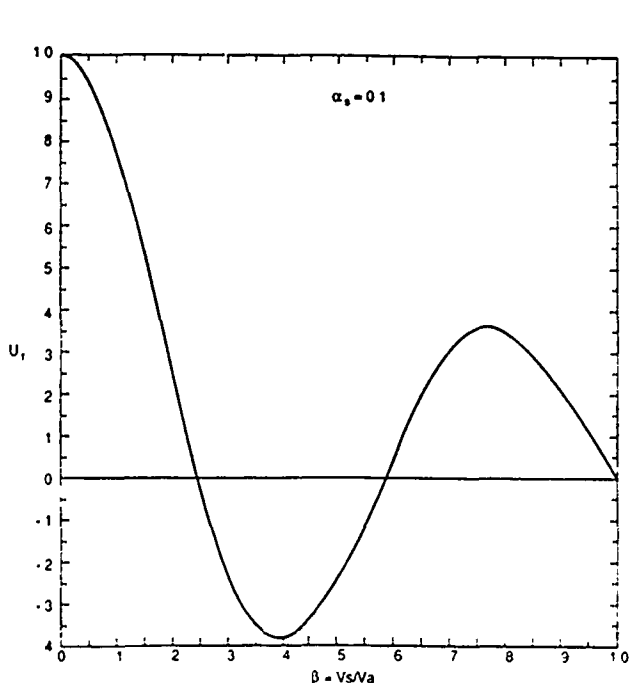


FIG. 8

FIG. 8—An example full standing wave solution for velocity perturbations plotted in β space for the upward compression waves. The forcing plane is located at $\beta = 1$, and the matching point is 0.6.

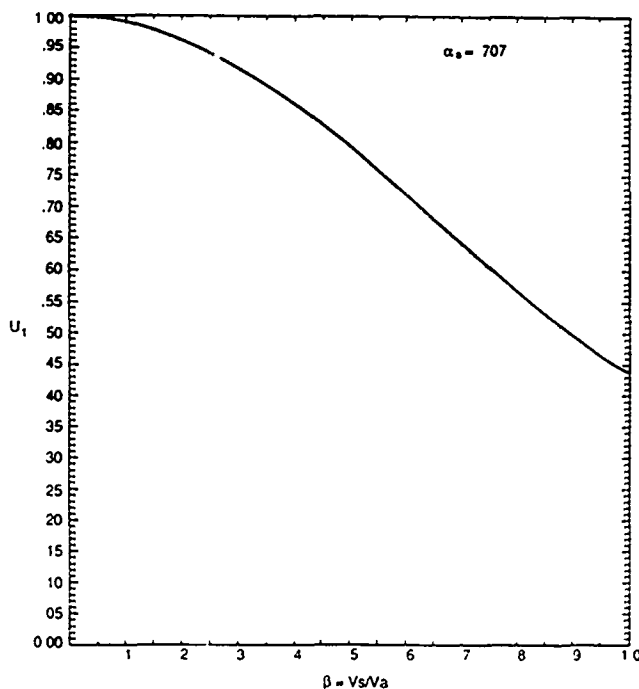


FIG. 9

FIG. 9—An example full evanescent standing wave solution for velocity perturbations plotted in the β space for the upward compression waves. The forcing plane is located at $\beta = 1$ which corresponds to wave frequency being the same as the local critical frequency ω_{as} at the forcing plane. The matching point is 0.4. Because the wave is evanescent, this illustrates that ω_{as} in the atmosphere with temperature $T_0 > 0$ corresponds to ω_a in the cold plasma case.

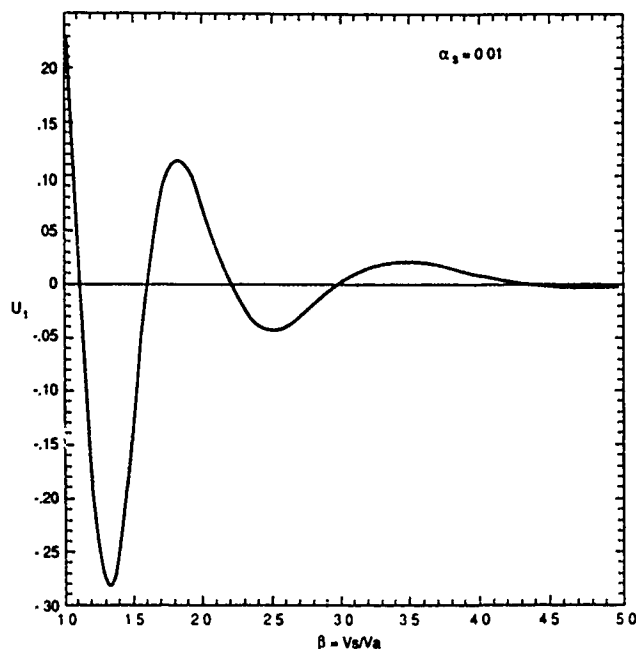


FIG. 10.—An example full propagating wave solution for velocity perturbations plotted in β space for the downward compression waves. The forcing plane is located at $\beta = 1$, the parameter $\alpha_s = 0.01$, and the matching point is 1.3.

the condition for strong reflection of a wave of frequency ω is met above some height. This effect may be significant for the behavior of the upward compression waves in a stellar atmosphere as it may lead to wave trapping in the atmosphere.

The discussion presented above concerns only the steady state case which is reached when all transient effects vanish and a standing wave pattern is formed. However, before this happens one may expect to see propagating waves in the upward direction. These waves interfere with reflected waves propagating in the downward direction and form standing waves when the reflected wave superposes on the upward propagating wave (An *et al.* 1989). For this transient phenomenon, the critical frequency ω_{as} plays the role of a local cutoff frequency defined at the height where the forcing plane is located (say z_0). Thus, in order to excite the upward propagating waves, the condition $\omega > \omega_{as}(z_0)$ must be satisfied; otherwise, the forcing plane excites nonpropagating (evanescent) waves. These few brief statements only signalize more general problems in the propagation of transient waves which are, however, beyond the scope of this paper.

For the downward direction, the waves are propagating waves for those frequencies that are higher than the acoustic cutoff frequency, ω_i . In this respect, magnetoacoustic waves indeed behave like acoustogravity waves but only in the downward direction with respect to the wave source. Thus, our results confirm, but also clarify Thomas and Campos's conclusions. We should mention that the acoustic cutoff frequency (or more precisely its ratio to the wave frequency, α_s) becomes also an important parameter for the standing wave solutions obtained in the upward direction. In general, this parameter determines the domain of validity of the ordinary point solutions and in the limit of cold plasma ($\beta \rightarrow 0$) the domain approaches zero. Then, the singular point solutions obtained at $\beta = 0$ cover the whole physical space and the form of the solution is identical to the solution describing Alfvén waves in an isothermal atmosphere with uniform vertical magnetic field. In this limit, no cutoff frequency can be defined for the downward direction and magnetoacoustic waves are always propagating waves.

To apply our results to solar (or stellar) physics problems, we must specify the wave source in the atmosphere. Assuming that the major source of magnetoacoustic waves is the highly turbulent part of the solar convective zone (Musielak and Rosner 1987), then the downward propagating waves become purely acoustic waves in deep solar layers where they can be refracted due to the temperature gradient and may contribute to the observed solar global oscillations. These problems are beyond the scope of this paper as the temperature gradient is not taken into account in our approach. Thus, our most important result for the solar (and stellar) physics is that the upward propagating magnetoacoustic waves may also become trapped waves if the atmosphere at a certain level is filled with enough nearly horizontal magnetic field. If this occurs in the photosphere, then magnetoacoustic waves cannot transfer the energy required for the heating of solar (stellar) chromospheres and coronae. On the other hand, this trapping effect might contribute to the observed small amplitude solar (stellar) p -mode oscillations.

We are indebted to D. H. Hathway and J. H. Thomas for their extensive comments on the manuscript of our paper. The research has been supported by the NASA Space Plasma Physics and Solar and Heliospheric Physics Branches in the Office of Space Science and Applications. C. H. A. has also been supported by NASA HQ Grant (NAGW-9) and Air Force Grant (AFOSR-88-0013). This work was completed while Z. E. M. held an NRC-NASA/MSFC Research Associateship.

APPENDIX A

LIMITS OF VALIDITY OF THOMAS'S SOLUTIONS

To show the limits of validity of the solutions obtained by Thomas (1982), we follow Nye and Thomas (1976) and, using their notation, transform the wave equation (5) to the hypergeometric form:

$$x(1-x) \frac{d^2 w}{dx^2} + (1-2x) \frac{dw}{dx} - \Omega^2 w = 0, \quad (\text{A1})$$

where w is the vertical wave amplitude, $x = -V_s^2/V_a^2$, $\Omega = \omega H/V_s$, and H is the density scale height. As shown by Thomas (1982), this equation can be transformed to a form of Legendre's differential equation by making the transformation $\xi = 1 - 2x$. This gives

$$(1-\xi^2) \frac{d^2 w}{d\xi^2} - 2\xi \frac{dw}{d\xi} - \Omega^2 w = 0, \quad (\text{A2})$$

and the solutions can be found as Legendre functions of zeroth order and of degree ν defined by

$$\nu = -\frac{1}{2} \pm (1 - 4\Omega^2)^{1/2}. \quad (\text{A3})$$

According to Thomas, these are full solutions to equation (A2) which means that they cover the whole physical space including the point $\xi = 1$ that corresponds to a very low- β ("cold") plasma. In addition, he showed that in order to have propagating wave solutions ν must have a nonzero imaginary part, which requires $4\Omega^2 > 1$ or $\omega > \omega_c$, and concluded that the cutoff frequency for magnetoacoustic waves is not affected by the magnetic field and thereby is identical to the cutoff obtained for acoustic waves propagating in a stratified medium.

It is shown in this paper that from a physical point of view, his conclusions are valid only for the downward (in the direction of gravity) propagating magnetoacoustic waves and *cannot* apply to the upward waves. Here, we show that also from mathematical point of view Thomas's solutions are *not valid* in the vicinity of the point $\xi = 1$. This results from the theory of differential equations (Murphy 1960) showing that all solutions to equation (A2) diverge around $\xi = 1$ for *all* real constants Ω^2 that *cannot* be given in the form $\Omega^2 = \nu(\nu + 1)$, with ν being a nonnegative integer. As shown by equation (A3), this is the case considered here.

Let us discuss these problems in detail. From mathematical point of view, equation (A2) shows singular points at $\xi = \pm 1$ and ∞ with roots of the indicial equation given by $(0, 0)$, $(0, 0)$ and $(\xi \pm 1, -\xi)$, respectively (Murphy 1960). The zeroth roots always lead to a logarithmic term in one of the two solutions. The form of the second solution depends on whether ν is a positive integer or not. In the former case, a nonlogarithmic solution (given by a Legendre function) becomes a Legendre polynomial that converges for all ξ including the point $\xi = 1$ (e.g., Hochstadt 1986). However, in the latter case, Legendre functions *do not* converge in the vicinity of the point $\xi = 1$ and the solutions are given either by ascending powers of ξ valid for all $|\xi| < 1$ (expansion about the singular point $\xi = \pm 1$) or by descending powers of ξ valid for all $|\xi| > 1$ and corresponding to the singular point at $\xi = \infty$ (Murphy 1960). In the case considered here, we are interested in the descending power solutions with ν being a complex quantity and find that the point $\xi = 1$ and its vicinity *cannot* be included in the solutions.

Thus, our major conclusion from this appendix is that Thomas's solutions must be given by the descending power solutions (Legendre functions of noninteger degree) and that they *do not* cover the point $\xi = 1$ and its vicinity. Because of this restriction, the obtained solutions describe only downward waves as to describe the upward waves the full solutions for the upward direction have to be given; the latter are missing in Thomas's approach and therefore any procedure to construct the upward solutions using Thomas's results is mathematically flawed.

APPENDIX B

MATCHING THE SOLUTIONS

As shown in § V, we must match the solutions given in the form of series expansions. In general, the forms of the solutions to be matched can be written as $F(x) = C_0 f(x)$ and $G(x) = C_1 g_1(x) + C_2 g_2(x)$, where $C_{0,1,2}$ are arbitrary constants. We assume that $C_0 = 1$ and obtain the matching conditions in the form:

$$f(x)|_{x=x_0} = C_1 g_1(x)|_{x=x_0} + C_2 g_2(x)|_{x=x_0}, \quad (\text{B1})$$

$$f'(x)|_{x=x_0} = C_1 g'_1(x)|_{x=x_0} + C_2 g'_2(x)|_{x=x_0}, \quad (\text{B2})$$

where x_0 is the matching point and the prime (') denotes the derivative with respect to x .

Now, we may evaluate constants C_1 and C_2 from equation (B1) and (B2). This gives

$$C_1 = \frac{f'(x)g_2(x) - f(x)g'_2(x)}{g'_1(x)g_2(x) - g_1(x)g'_2(x)} \Big|_{x=x_0}, \quad (\text{B3})$$

and

$$C_2 = \frac{f(x) - C_1 g_1(x)}{g_2(x)} \Big|_{x=x_0}. \quad (\text{B3})$$

Applying these results to the solutions obtained for the upward direction (see § V), we calculate

$$\mathcal{J}'_0(\beta) = 2 \sum_{n=0}^{\infty} n \phi_{2n} \beta^{2n-1} \Big|_{\beta=\beta_0}, \quad (\text{B4})$$

$$L'_1(\beta - 1) = \sum_{n=2}^{\infty} n \phi_n (\beta - 1)^{n-1} \Big|_{\beta=\beta_0}, \quad (\text{B5})$$

and

$$L'_2(\beta - 1) = 1 + \sum_{n=2}^{\infty} n \psi_n (\beta - 1)^n \Big|_{\beta=\beta_0}. \quad (\text{B6})$$

Then, assuming $\beta_0 = 0.6$ and using equations (B1) and (B2), we obtain $C_1 = -0.0197$ and $C_2 = -2.05$.

For the downward propagation, we calculate

$$\begin{aligned} Z'_0\left(\frac{1}{\beta}\right) &= \cos \left[(\alpha_s^{-2} - 1)^{1/2} \ln \left(\frac{1}{\beta} \right) \right] \sum_{n=0}^{\infty} (2n+1) \phi_{2n} \left(\frac{1}{\beta} \right)^{2n} \Big|_{\beta=\beta_0} \\ &\quad - \beta (\alpha_s^{-2} - 1)^{1/2} \sin \left[(\alpha_s^{-2} - 1)^{1/2} \ln \left(\frac{1}{\beta} \right) \right] \sum_{n=0}^{\infty} \phi_{2n} \left(\frac{1}{\beta} \right)^{2n+1} \Big|_{\beta=\beta_0}. \end{aligned} \quad (\text{B7})$$

Assuming that $\beta_0 = 1.3$, we substitute equations (B5), (B6), and (B7) into equations (B1) and (B2), and obtain $C_1 = 0.242$ and $C_2 = -2.04$.

REFERENCES

- An, C. H., Musielak, Z. E., Moore, R. L., and Suess, S. T. 1989, *Ap. J.*, in press.
 Campos, L. M. B. C. 1985, *Geophys. Ap. Fluid Dyn.*, **32**, 217.
 ———, 1987, *Rev. Mod. Phys.*, **59**, 363.
 Deutsch, R. J. 1976, *Stud. Cercet. Fiz.*, **19**, 807.
 Ferraro, V. C. A., and Plumpton, C. 1958, *Ap. J.*, **127**, 459.
 Hochstadt, H. 1986, *The Functions of Mathematical Physics* (New York: Dover).
 Hollweg, J. V. 1978, *Solar Phys.*, **56**, 305.
 Lamb, H. 1945, *Hydrodynamics* (New York: Dover).
 Leroy, B. 1980, *Astr. Ap.*, **91**, 136.
 McLellan, A., and Winterberg, F. 1968, *Solar Phys.*, **4**, 401.
 Moore, D. W., and Spiegel, E. A. 1964, *Ap. J.*, **139**, 48.
 Murphy, G. M. 1960, *Ordinary Differential Equations and Their Solutions* (New York: Van Nostrand).
 Musielak, Z. E. 1988, *Ap. J.*, submitted.
 Musielak, Z. E., and Rosner, R. 1987, *Ap. J.*, **315**, 371.
 Nye, A. H., and Thomas, J. H. 1974, *Solar Phys.*, **38**, 399.
 ———, 1976, *Ap. J.*, **204**, 573.
 Priest, E. R. 1982, *Solar Magnetohydrodynamics* (Dordrecht: Reidel).
 Rosner, R., Low, B. C., and Holzer, T. E. 1986, *Physics of the Sun*, Vol. 2 (Dordrecht: Reidel).
 Stein, R. F., and Leibacher, J. 1974, *Ann. Rev. Astr. Ap.*, **12**, 407.
 Summers, D. 1976, *Quart. J. Mech. Appl. Math.*, **29**, 117.
 Thomas, J. H. 1982, *Ap. J.*, **262**, 760.
 ———, 1983, *Ann. Rev. Fluid Mech.*, **15**, 321.
 Yu, C. P. 1965, *Phys. Fluids*, **8**, 650.

C.-H. AN: Department of Mechanical Engineering and Center for Space Plasma and Aeronomic Research, University of Alabama in Huntsville, Huntsville, AL 35899

R. L. MOORE, Z. E. MUSIELAK, and S. T. SUESS: Space Science Laboratory, ES52, NASA/Marshall Space Flight Center, Huntsville, AL 35812

REFLECTION AND TRAPPING OF TRANSIENT ALFVÉN WAVES PROPAGATING IN AN ISOTHERMAL ATMOSPHERE WITH CONSTANT GRAVITY AND UNIFORM MAGNETIC FIELD

C.-H. AN

Department of Mechanical Engineering and Center for Space Plasma and Aeronomic Research, University of Alabama in Huntsville

AND

Z. E. MUSIELAK, R. L. MOORE, AND S. T. SUESS

Space Science Laboratory, NASA Marshall Space Flight Center

Received 1989 January 30; accepted 1989 March 13

ABSTRACT

We have studied transient propagation of Alfvén waves in an isothermal atmosphere with constant gravity and uniform vertical magnetic field as an initial-value problem using a time-dependent linear magnetohydrodynamic numerical model. The initial value approach allows us to undertake investigations not accessible to analytic models, e.g., direct demonstration of partial reflection from the wave front propagating in an inhomogeneous medium, transient waves approaching the analytic solution, and direct demonstration of resonance at certain driving frequencies.

Our results show that the Alfvén wave transit time from the wave source to infinity is finite and the wave exhibits continuous partial reflection which becomes total reflection as the front approaches infinity. As the reflected waves propagate down and interfere with the upward-propagating waves, a standing wave pattern forms in the region of the interference, and the numerical solution approaches the analytic standing wave solution as the reflected wave superposes completely on the upward propagating wave. As soon as complete superposition is broken, the standing wave becomes a transient propagating wave. The total reflection causes the waves to be trapped in the cavity that extends from the wave source to infinity and in which the wave energy is stored. We find a resonant frequency at which the amplitude of the stored wave energy increases parabolically with time.

Our results suggest that the reflection of Alfvén waves (of sufficiently long period) from the outer corona is an intrinsic phenomenon for any stellar atmosphere stratified by gravity and with an open magnetic field, and that therefore such waves may be trapped in the stellar atmosphere.

Subject headings: hydromagnetics — stars: atmospheres — stars: coronae — Sun: atmosphere — wave motions

1. INTRODUCTION

The propagation of Alfvén waves in the solar atmosphere has been studied in connection with heating of the atmosphere and solar wind acceleration. Since the solar atmosphere is gravitationally stratified with gradients in both the temperature and the magnetic field, the study requires abandoning the WKB approximation, especially for long-period Alfvén waves. The equation governing the wave propagation in a realistic solar atmosphere is extremely complicated to solve analytically. Thus, for analytical studies, the problem has generally been simplified by assuming a uniform magnetic field, uniform gravity, and a one-dimensional atmosphere which varies only along the direction parallel to gravity. Linear theory leads to a second-order differential equation solved for the first time by Ferraro (1954) and Ferraro and Plumpton (1958). With the assumption of a steady sinusoidal time dependence, they obtained a standing wave solution, which implies no wave (and also no energy) propagation through the medium.

In order to avoid this difficulty, Hollweg (1972) divided the atmosphere into two parts that are characterized by different scale heights. He imposed a boundary interface (transition region) which divides the atmosphere into the chromosphere and the corona. He specified ascending and descending wave solutions below the interface boundary, but only an ascending wave solution above the boundary. He obtained the wave solu-

tion for the whole atmosphere by matching the two different wave solutions at the boundary and found a resonant phenomenon which shows a peak in the wave energy flux above the boundary at certain frequencies. The resonant phenomenon was believed to be due to wave reflection at the boundary and was used to explain coronal heating and solar wind acceleration. Following Hollweg (1972), numerous authors (Hollweg 1978, 1984; Leroy 1980; Leroy and Schwartz 1982; Schwartz and Leroy 1982; Leer, Holzer, and Flå 1982; Schwartz, Cally, and Bel 1984; Zugzda and Locans 1982; Rosner, Low, and Holzer 1986) studied Alfvén wave propagation in the solar atmosphere by dividing it into several layers. However, the interpretation of the resonant phenomenon varied. Zugzda and Locans (1982) claimed that the resonant phenomenon is due to an error in the procedure, and Leer, Holzer, and Flå (1982) emphasize that the resonant phenomenon cannot be considered as a mechanism of coronal heating and solar wind acceleration. In addition, the approach itself deserves comment. First, imposing an artificial upper boundary for the transition region exaggerates the reflectivity from the transition region. If we solve the wave equation with a smoothly varying layer, we may find a lower reflectivity. Finally, the assumption of a uniform atmosphere above the upper boundary neglects the propagation of Alfvén waves in the gravitationally stratified upper corona. We therefore believe that

Alfvén wave propagation in the upper corona has not yet been properly treated.

Because of the importance of Alfvén wave propagation through the transition region into the corona for coronal heating and solar wind acceleration we need to study such wave propagation in a more realistic solar atmosphere with a realistic corona, transition region, and chromosphere. However, before we consider this problem, we must first understand how Alfvén waves propagate in the corona. Since an analytic study with a steady sinusoidal time dependence produces only a standing wave solution, we use a time-dependent magnetohydrodynamic (MHD) numerical simulation method to get more physical insight into the wave behavior. The numerical calculation enables us to study transient MHD wave propagation through an initially unperturbed medium and to see how the wave character (i.e., wavelength, amplitude, propagation speed, etc.) vary in response to the nonuniform medium. We also study how the propagating wave is continuously reflected and how the wave undergoes total reflection as it propagates to infinity. Finally, for better understanding of observations, it is important to study transient wave propagation, since the wave drivers in the Sun may not have a long enough lifetime to reach a steady state.

In this paper we restrict our attention to Alfvén waves propagating in an isothermal and stratified atmosphere with constant gravity and uniform vertical magnetic field. We will first review published analytic solutions and then present the numerical results.

II. REVIEW OF ANALYTIC SOLUTIONS

As shown first by Ferraro and Plumpton (1958), full analytic solutions to the linearized Alfvén wave equation can be given in terms of Bessel functions. However, in order to obtain these solutions, a simple model has to be assumed; namely, one must consider an isothermal and stratified medium with constant gravity and with uniform vertical background magnetic field. Under these conditions, the plasma pressure and density can be given in the following form:

$$\rho = \rho_0 e^{-\lambda z}, \quad p = p_0 e^{-\lambda z}, \quad (1)$$

where ρ_0 and p_0 are the values of density and pressure at $z = 0$, respectively; note that we are using the Cartesian system with x the horizontal and z the vertical coordinate. The Alfvén velocity is given by

$$V_A = V_{0A} e^{(\lambda/2)z}, \quad (2)$$

where V_{0A} is the Alfvén speed at $z = 0$ and λ is defined as the inverse of the gravitational scale height, $H_g = RT/g$. Here R is the gas constant, T is the temperature, and g is gravitational acceleration. Then, after Ferraro and Plumpton (1958), assuming steady sinusoidal time dependence, the general solution for the velocity and magnetic perturbations V_x and B_x is given by

$$\begin{aligned} V_x(z, t) &= [A_1 J_0(\omega/\omega_A) + A_2 Y_0(\omega/\omega_A)] e^{i\omega t}, \\ B_x(z, t) &= \rho_0^{1/2} [A_3 J_1(\omega/\omega_A) + A_4 Y_1(\omega/\omega_A)] e^{i\omega t}. \end{aligned} \quad (3)$$

Here, J_0 (J_1) and Y_0 (Y_1) are the Bessel functions of the first and second kind of order zero (first), respectively. A_1 , A_2 , A_3 , and A_4 are constants to be determined by the boundary conditions, and ω_A is defined by

$$\omega_A = V_A/2H_g. \quad (4)$$

The explicit form of the argument of the Bessel function, ω/ω_A , is

$$\frac{\omega}{\omega_A} = \frac{\omega}{\omega_{0A}} e^{-(\lambda/2)z},$$

where $\omega_{0A} = V_{0A}/2H_g$.

Note that for any real constants A_1 and A_2 (or A_3 and A_4) the solution (3) represents a standing wave solution (see § IIa). This solution has been extensively studied in the literature (Hollweg 1978; Leroy 1980; Leer, Holzer, and Flå 1982; Rosner, Low, and Holzer 1986) in the context of propagating and reflecting Alfvén waves. It has been shown that there exists a characteristic height for a given ω , which separates the solution into two parts: sinusoidal ($\omega \gtrsim \omega_A$) and nonoscillating ($\omega \lesssim \omega_A$) wave solutions (Campos 1987).

a) Ascending Propagation

In this section we will consider why the analytic solution shows a standing rather than a traveling wave and will comment on previous work attempting to avoid the standing wave solution. First of all, however, we must specify the region of wave generation and the direction of the wave propagation in order to check whether the solution (3) diverges as $z \rightarrow \infty$. If we assume that the wave is generated at $z = 0$ and propagates to $z = \infty$, this leads to $V_0(\omega/\omega_A) \rightarrow \infty$ as the argument approaches zero, and the condition $A_2 = 0$ is necessary to prevent infinite wave energy infinitely far from the source, which is physically unreasonable. With $A_2 = 0$ and A_1 nonzero, equation (3) describes a standing wave solution.

For an isothermal atmosphere with constant gravity, plasma pressure and density decrease exponentially, as shown by equation (1). Hence the Alfvén wave velocity increases exponentially with height, and the wave reaches infinity in a finite time. Also, it eventually becomes totally reflected because the wavelength becomes infinitely longer than the density scale height. The Alfvén wave transit time to infinity can easily be calculated from equation (2), giving

$$t_\infty = \int_0^\infty \frac{dz}{V_A} = 2t_A, \quad (5)$$

where $t_A = H_g/V_{0A}$.

Hence, physically, there is interference between the ascending and the reflected descending wave, and this constitutes the standing wave expressed by equation (3) with $A_2 = 0$. In other words, the standing wave solution of Ferraro and Plumpton (1958) is unavoidable under the assumption of uniform gravity, uniform magnetic field, and steady sinusoidal time dependence.

Previous authors attempted to avoid the standing wave solution by dividing the atmosphere into two parts—corona and chromosphere—and by specifying the outward propagating solution above the interface boundary (transition region); Hollweg (1972) and Zugzda and Locans (1982) specify a Hankel function representing a wave propagating from a wave source (see eq. [9] for the Hankel function) and Schwartz, Cally, and Bel (1984) and Leer, Holzer, and Flå (1986) impose an ascending plane wave solution above the interface boundary. The imposition of an ascending plane wave solution implies that the density scale height is infinite above the interface boundary, i.e., the reflection due to the finite density scale height is neglected. In addition, the specification of the Hankel

function might not properly describe wave propagation in the upper corona because the function diverges as $z \rightarrow \infty$.

In order to study the propagation of Alfvén waves in the corona, we will employ two approaches: (1) Use a time-dependent MHD simulation method to study wave propagation to infinity, wave reflection due to the density gradient, and interference between the outgoing and incoming waves. (2) Abandon constant gravity and study the wave propagation in spherical geometry with gravity $g \sim 1/r^2$. In this paper, we give results from the first approach. We plan to deal with the second problem in a separate paper.

b) Descending Propagation

The wave solution, equation (3), is also valid for descending wave propagation, but we have to determine the coefficients A_1 and A_2 from the boundary conditions. If we assume that the wave is generated at $z = 0$ and propagates to $z = -\infty$, the asymptotic solution of the Bessel functions, $J_0(\xi)$ and $Y_0(\xi)$, for $\xi \equiv \omega/\omega_A \rightarrow \infty$ (when $z \rightarrow -\infty$) becomes finite. How can we then determine A_1 and A_2 ? We believe that the answer lies in a physical, rather than mathematical, argument. If the descending Alfvén wave transit time to $z = -\infty$ is infinite, the wave is a traveling wave with one of A_1 and A_2 being real and the other imaginary. We can calculate the transit time of a descending wave from equation (5) by integrating from $z = 0$ to $z = -\infty$ and can easily show that the transit time is infinity, implying a traveling wave. The wavelength of a descending wave decreases exponentially, and the wave can be approximated to a WKB wave. Thus, the propagation of descending waves will not be considered further in this paper.

III. TRANSIENT WAVE PROPAGATION

To study transient wave propagation, we solve the time-dependent one-dimensional linearized ideal MHD equations numerically for an oscillatory transverse perturbation at the lower boundary (An, Suess, and Wu, 1989). The equations are

written in dimensionless form by normalizing velocity with V_{0A} of equation (2), and by normalizing magnetic field and pressure with their values at $z = 0$. The height is normalized by density scale height H_g and time t by t_A of equation (5). We assume that gravity is constant and the magnetic field is uniform and is parallel to gravity, and that the wave propagates only along the field lines. Since the Alfvén velocity increases exponentially as the wave propagates upward, we will violate the Courant-Friedrichs-Lewy (CFL) numerical stability condition unless we increase the grid size exponentially. For this reason, we transform the coordinates from z to η , where η is defined by

$$\eta = e^{-z/2}. \quad (7)$$

Here, λ becomes unity for the equations in dimensionless form. At the lower boundary, we impose an oscillatory transverse velocity perturbation with

$$v_x = 0.01 \cos \omega t, \quad (8)$$

which excites an Alfvén wave, and specify that the perturbed magnetic field is zero at the upper boundary—which is physically reasonable because the magnetic field behaves as a rigid bar because of finite magnetic field strength and zero density at $\eta = 0$. The transformation presented by equation (7) has several advantages. First, the uniform grid size $\Delta\eta$, since Δz increases exponentially and the transit time of the Alfvén wave across Δz is constant for the exponentially increasing Alfvén speed with height, we can avoid the numerical instability. Second, for upward propagation we can cover $0 \leq z \leq \infty$ in the computing domain and study in detail wave reflection from infinity. Third, we can impose nonartificial boundary conditions at $z = \infty$. The following results are all based on the η coordinates.

a) Ascending Wave Propagation

Figures 1a and 1b show the computed upward-propagating Alfvén wave with frequency $\omega = 4\pi$. The perturbation ampli-

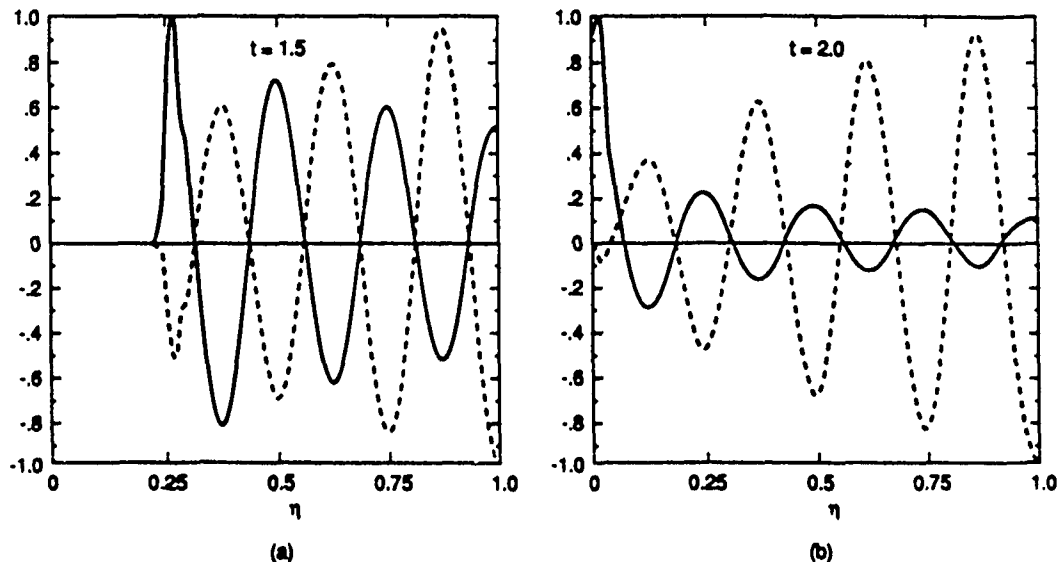


FIG. 1.—Upward transient Alfvén wave propagation with frequency $\omega = 4\pi$ in an atmosphere stratified by uniform gravity and having a uniform vertical magnetic field. The solid line is for the velocity, and the dashed line is for the perturbation magnetic field amplitude at (a) $t = 1.5$ and (b) $t = 2.0$. The horizontal axis stands for the height with $\eta = 0$ and $\eta = 1$ corresponding to $z = \infty$ and $z = 0$, respectively. The vertical axis represents the amplitudes of velocity and magnetic field normalized by the maximum value at each time. The wiggles in the first half-wavelength are due to the abrupt initiation of the wave in our simulation.

tude is finite at $t = 0$ and oscillates with time. Because of the finite amplitude at $t = 0$, there is a noticeable transient wave front followed by a smooth oscillatory wave train. Since we give the perturbation at $z = 0$, the wave propagates from $\eta = 1$ to $\eta = 0$. The solid and dashed lines represent the velocity and magnetic field perturbations, respectively. Before the waves reach $\eta = 0$ (i.e., $z = \infty$) the velocity and magnetic field perturbations propagate with a 180° phase difference. At $t = 2$ the magnetic wave reaches $\eta = 0$ as predicted by equation (5). (Note that t is normalized by t_A in our dimensionless equations.)

Figures 2a, 2b, and 2c show the velocity wave propagation at $t = 2.890$, 4.00, and 4.99, respectively, after the initial transient front reflects from $\eta = 0$. In each figure, the solid line is the analytic standing wave solution, and the dotted line is the numerical traveling wave solution. The amplitude is normalized by the maximum value at each time. At $t = 2.890$, the initial transient has reflected back to $\eta \approx 0.4$, and the train is a superposition of reflecting and ascending waves forming the analytic standing wave solution between $\eta = 0$ and $\eta \approx 0.4$. At $0.4 \leq \eta \leq 1.0$ the ascending waves propagate upward (toward $\eta = 0$) without being interfered with by the reflecting waves, which have not yet reached this region. At $t = 4.0$ the initial transient front returns to $\eta = 1$, forming a complete superposition with the ascending wave, and the whole region is well represented by the analytic standing wave solution. As the reflected wave reaches $\eta = 1$, it is reflected and interacts with the oscillating wave source. A fraction of the energy of the incident wave is absorbed by the wave source if there is a phase difference between the two. At $t = 4.99$, the initial transient front has reflected from $\eta = 1$ and propagated upward to reach $\eta = 0.5$. Because of the initial transient wave train, complete superposition is broken and the numerical solution becomes a transient propagating wave, departing from the analytic standing wave solution at $0.5 \leq \eta \leq 1$. Our numerical result shows that complete superposition occurs at $t = 4, 8, 12$, and so forth, at which times the numerical solution reproduces the analytic standing wave solution. When complete superposition is broken at other intermediate times, the numerical solution is simply a transient propagating solution. Figure 3 shows that the magnetic perturbation also approaches the analytic standing wave solution as the reflected initial transient front returns to $\eta = 1$ and forms a complete superposition on the ascending wave. The solid line is the analytic standing wave solution for the perturbed magnetic field (with $A_4 = 0$ in eq. [3]), and the dotted line is the numerical wave solution. The wave is also a transient propagating wave when complete superposition is broken at $t \geq 4$.

b) Wave Reflection

i) Partial Reflection

Much effort has been devoted to the calculation of the reflection coefficient of an Alfvén wave propagating through a non-uniform medium. A commonly used method is to divide the atmosphere into several layers and apply the matching boundary conditions at each layer (e.g., Hollweg 1978). From analytic studies, many authors (Leroy 1980; Leer, Holzer, and Flå 1982; Rosner, Low, and Holzer 1986) have suggested that there is continuous partial reflection for waves with wavelength longer than the density scale height. Since the analytic solution with steady state sinusoidal time dependence, $e^{i\omega t}$, holds only for $t \gg 1$ and does not describe the wave propagation through

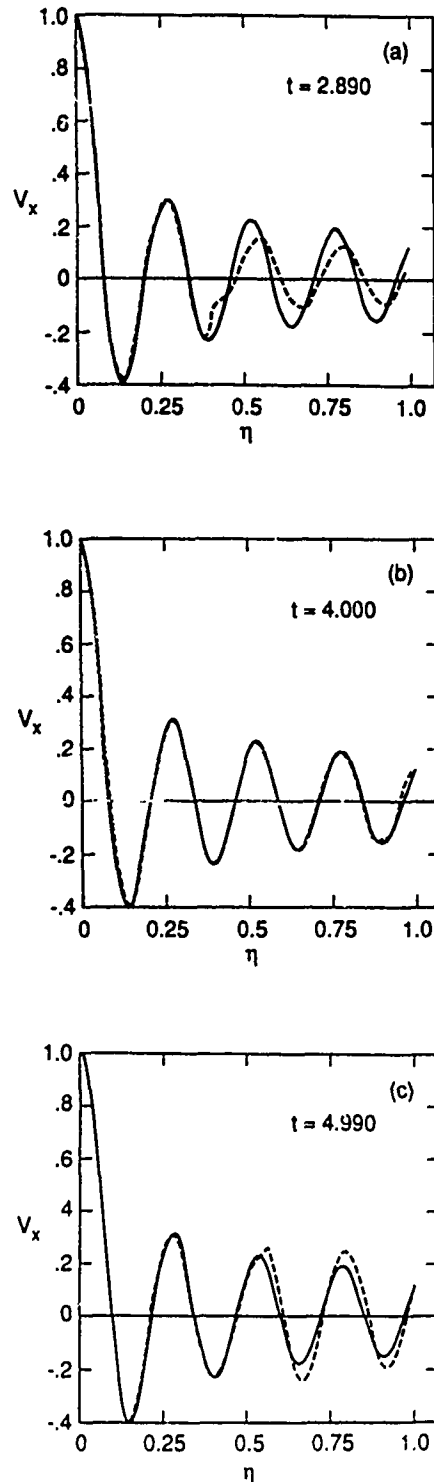


FIG. 2.—The transient propagating wave approaches and departs from the analytic standing wave solution as the transient wave train interferes completely with the ascending wave and breaks the complete superposition. The solid curve is the analytic standing wave solution, and the dashed curves are the computed waves at (a) $t = 2.890$, (b) $t = 4.0$, and (c) $t = 4.99$. The amplitudes are normalized by the maximum value at each time here and in Fig. 3. At $t = 4.0$ the initial transient front returns to $\eta = 1$, forming a complete superposition with the ascending wave, and the whole region becomes the analytic standing wave solution. At $t = 4.99$ the initial transient front reflects from $\eta = 1$ to $\eta = 0.5$ and breaks the complete superposition, showing a transient propagating wave in the region.

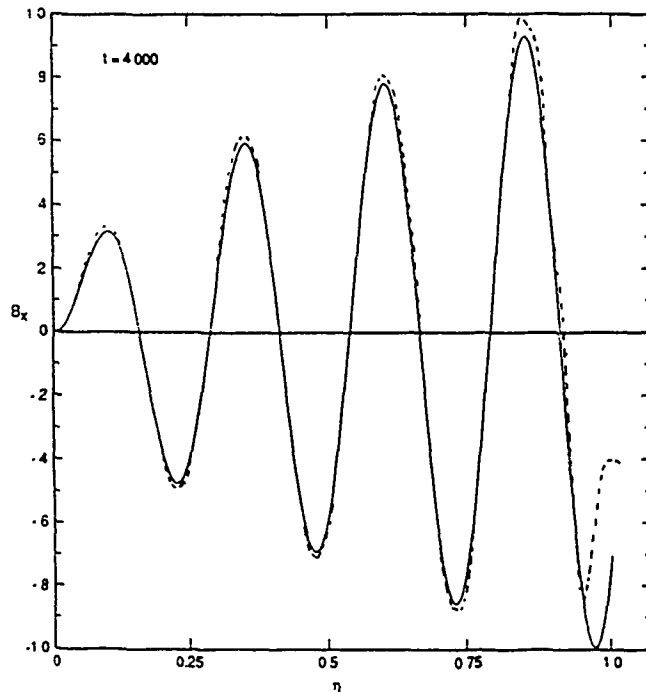


FIG. 3.—The magnetic wave also approaches the analytic standing wave solution as the initial wave front reflects back to $\eta = 1$ and interferes with the ascending wave at $t = 4$. The solid curve is the analytic solution, and the dashed curve is the numerical solution. At $t = 4.99$ the magnetic wave also shows a transient propagating wave in $0.5 \leq \eta \leq 1$.

an undisturbed medium, the continuous partial reflection from a propagating wave cannot be properly studied by the analytic approach. Here we study how energy is reflected as the wave propagates to $z = \infty$ by calculating the magnetic and kinetic energy in every half-wavelength at specific intervals in time. If there is no reflection, the energy in each half-wavelength should be the same. Figures 4a and 4b show the kinetic and magnetic energy in each half-wavelength for $t = 1.40$, $t = 1.65$, and $t = 1.90$, which are a half-period apart for the frequency $\omega = 4\pi$. The vertical axis is the magnitude of the energy, and the horizontal axis represents the position of each wavelength at a specific time interval. For example, for $t = 1.65$, 1 stands for the position of the first half-wavelength and 6 means the position of the next to last half-wavelength counted from $\eta = 1$ (or $z = 0$). The energy of the last half-wavelength is not considered here because it is strongly disturbed by the transient effect of the wave front. Since the times are a half-period apart, the position of a half-wavelength designated by a number on the horizontal axis is the same for the three different times. Figures 4a and 4b show the oscillatory change of the kinetic and magnetic energy between adjacent half-wavelengths which is superposed on the gradual decrease of the energy from the first to the last half-wavelength. The oscillatory change of the energy between adjacent half-wavelengths is amplified as the wave front moves closer to $\eta = 0$, as we see by comparing the energy change at $t = 1.4$ and $t = 1.65$. At $t = 1.9$, the oscillatory change of the energy is noticeable even between the first and second half-wavelengths, and the energy difference between the seventh and the sixth is significant: a 3.6% decrease for kinetic energy and a 7.2% increase for magnetic energy. At $t = 1.98$, the kinetic and magnetic energy changes between the seventh and the sixth are about twice as large as

the changes at $t = 1.90$, while at $t = 1.40$ the magnetic energy of the sixth increases over the fifth by 0.6% and the kinetic energy decreases by 0.5%.

To interpret these results, we ask the following questions: Are the oscillatory changes in magnetic and kinetic energy due to partial reflection? If so, then why does the oscillatory behavior of the magnetic energy have 180° phase difference from the kinetic energy?

As the wave front passes through heights where the wavelength is shorter than the density scale height, the wave sees the atmosphere as a nearly uniform medium and undergoes negligible reflection. As the wave front moves to the height where the wavelength is longer than the scale height, the wave sees the medium as nonuniform, and partial reflection occurs. At $t = 1.45$, the wavelength of the wave front with $\omega = 4\pi$ is about

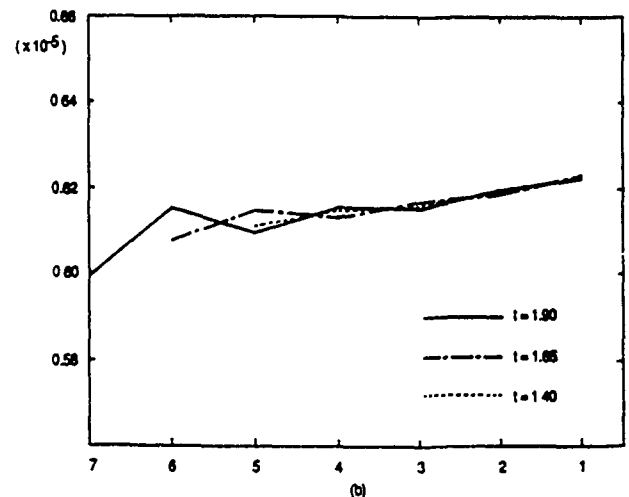
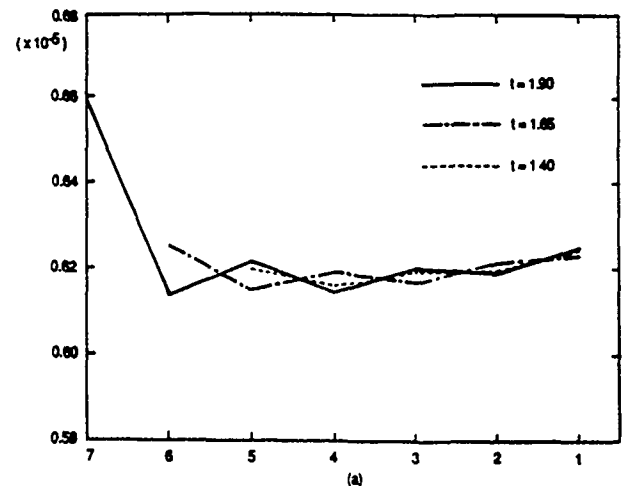


FIG. 4.—Variation of (a) magnetic and (b) kinetic wave energy in each half-wavelength, for different times, due to continuous reflection. The numbers on the horizontal axis stand for the position of each half-wavelength at each time, with a higher number designating a half-wavelength closer to the wave front, which is propagating from right to left. The vertical axis stands for the magnitude of the energy in dimensionless form. These plots show that because of continuous reflection the energy difference between the sixth and seventh half-wavelengths increases significantly after $t = 1.90$. The magnetic energy increase and the kinetic energy decrease in the seventh compared with the sixth half-wavelength are due to the fact that the medium at the wave front behaves approximately as a rigid boundary for the magnetic wave but as a free boundary for the velocity wave.

1.8 times the density scale height and noticeable partial reflection may occur. We therefore believe that the kinetic and magnetic energy differences between the fourth and fifth half-wavelengths at $t = 1.45$ are due to the partial reflection. We note that the increment of the magnetic energy and the decrement of the kinetic energy of the fifth over the fourth are due to different behaviors in the perturbed magnetic field, B_x , and velocity, v_x , near the wave front. Since the magnetic field strength is uniform, while the plasma density decreases exponentially with height, the magnetic tension force becomes larger than the inertia force as the wave front propagates upward. Thus, the medium at the wave front eventually behaves as a rigid boundary for the magnetic field but as a free boundary for the velocity. This causes the reflected magnetic wave to have a 180° phase difference from the upgoing magnetic wave, and the reflected velocity wave to have the same phase as the upgoing velocity wave. Since the fifth half-wavelength for $t = 1.4$, the sixth for $t = 1.65$, and the seventh for $t = 1.90$ are just behind the wave front and have the wave amplitude of opposite sign to the amplitude of the front, the reflection from the front causes the magnetic amplitude (and so the magnetic energy) to increase and the velocity amplitude (and so the kinetic energy) to decrease at the half-wavelength next to the front. As the reflected wave propagates downward, it increases and decreases the amplitudes of lower half-wavelengths alternately, causing the oscillatory change of kinetic and magnetic energy. At $t = 1.9$, the wave front passes $\eta_c = 0.04$, at which point $\omega/\omega_A = 1$ and the energy differences between the seventh and the sixth half-wavelengths become significant. For $\omega/\omega_A < 1$, the Bessel function $J_0(\omega/\omega_A)$ has no zero points, so there are no nodes between $\eta = 0$ and η_c . Note that η_c corresponds to a finite height z_c , above which the plasmas oscillate in the same phase. Thus, the physical meaning of η_c for transient wave propagation is as follows: As the wave front passes over η_c , the wavelength becomes more than 10 times longer than the density scale height, resulting in strong continuous partial reflection. This leads to total reflection of the upward wave train and sets up a nonoscillating standing wave above the critical height. By comparing the energy differences between the sixth and the seventh half-wavelengths for $t = 1.90$ and $t = 1.98$, we find that reflection increases rapidly once the wave front passes over η_c . As the wave front reaches infinity, the wavelength becomes infinite and partial reflection becomes total reflection.

Since we include artificial viscosity in our numerical model, the energy difference between each adjacent half-wavelength may be due to viscosity rather than to partial reflection. In order to understand the effect of viscosity on the energy differences, we vary the wave frequency and viscosity coefficient. Figure 5 shows the kinetic energy change at each half-wavelength at $t = 1.9$. The dotted line is for $\omega = 4\pi$, and the solid lines are for $\omega = 8\pi$. The dimensionless artificial viscosity coefficient, ν , is specified in the figure. The left axis shows the wave energy for $\omega = 8\pi$ and the right axis shows the energy for $\omega = 4\pi$. Since the wavelength for $\omega = 8\pi$ is half the wavelength for $\omega = 4\pi$, the first and second half-wavelengths of $\omega = 8\pi$ have the same position as the first half-wavelengths of $\omega = 8\pi$ have the same position as the first half-wavelength of $\omega = 4\pi$. In order to take this into account, the lower horizontal axis shows the position of each half-wavelength for $\omega = 8\pi$, while the upper horizontal axis is for $\omega = 4\pi$. By comparing the results for $\omega = 4\pi$ and 8π and $\nu = 0.0002$, we can see the following. First, the energy difference between the 14th and the

13th half-wavelengths for $\omega = 8\pi$ is 2%, which is about half the difference for $\omega = 4\pi$. Second, the oscillatory change of the energy for $\omega = 4\pi$ is larger than for $\omega = 8\pi$; for $\omega = 4\pi$ there is a noticeable oscillatory change above the third half-wavelength, while for $\omega = 8\pi$ the noticeable change occurs above the ninth which corresponds to the fifth for $\omega = 4\pi$. The lower oscillatory change for $\omega = 8\pi$ is due to less reflection. However, the continuous decrease of the energy from the first to the last half-wavelength is more significant for $\omega = 8\pi$ than for $\omega = 4\pi$. If the decrease were due to partial reflection, then the result would contradict our physical argument that a longer wavelength undergoes more reflection. For shorter wavelengths, the wave energy damping due to the artificial viscosity is higher, causing more rapid decrease of the energy with height. In order to further confirm the effect of artificial viscosity, we double the magnitude of the viscosity coefficient for $\omega = 8\pi$. Figure 5 shows that the oscillatory changes for $\nu = 0.0002$ and $\nu = 0.0004$ are nearly identical, but the continuous decrease of the energy from the first to the last half-wavelength for $\nu = 0.0004$ is more significant than for $\nu = 0.0002$. This result confirms that the continuous decrease of the energy from the first to the last half-wavelength is due to viscous dissipation, and the continuous reflection shows up as the oscillatory change of the energy superposed on the continuous decrease due to the artificial viscosity.

ii) Total Reflection and Interference

In the previous section, we found that the ascending waves undergo total reflection, causing them to be trapped in a cavity extending from infinity to the wave source. In this section we will study the transient nature of wave trapping and interference for various wave frequencies. This study is motivated by the results of Hollweg (1972, 1978) showing a resonant phenomenon for certain wave frequencies, those for which $J_0(\omega/\omega_A) = 0$. Since the atmosphere is essentially a cavity with upper boundary at $\eta = 0$, similar resonant phenomena may occur in our numerical solutions for the resonant frequencies found by Hollweg.

First, we generate waves with frequency $\omega = 6.65$ for which $J_1(\omega/\omega_A) = 0$ at $z = 0$. With this frequency $J_0(\omega/\omega_A)$ at $z = 0$ has a local maximum value. Figure 6a shows the time variation of velocity amplitude at $\eta = 0.5$. The figure shows greatly reduced amplitude between $t = 7$ and $t = 9$. The magnetic field amplitude shows a time variation similar to that of the velocity. We interpret the strong transient variation of the amplitudes to be due to destructive interference between the upward and reflected downward waves. Figure 6b presents the time variation of the kinetic energy integrated over the whole propagation region, demonstrating severe destructive interference between $t = 4$ and $t = 8$.

Next, we generate the wave with frequency $\omega = 7.45$ for which the zeroth-order Bessel function, the solution of perturbed velocity (eq. [3] with $A_2 = 0$), becomes zero at $\eta = 1$ (or $z = 0$). Figure 7a shows that whenever the ascending wave interacts with the reflected descending wave, the velocity amplitude at $\eta = 0.5$ increases approximately linearly with time, implying that there is always constructive interference. The magnetic perturbation shows a similar tendency. The continuous constructive interference at this frequency is dramatically seen in Figure 7b, which shows the time variation of kinetic energy integrated over the whole propagation region. The figure shows that the amplitude of the kinetic energy increases with the square of time; all the input energy is stored

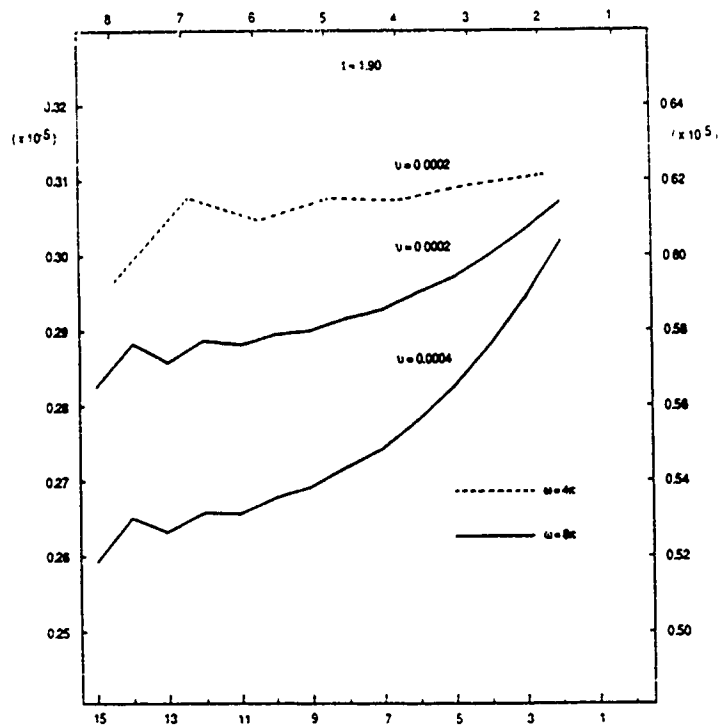


FIG. 5.—Change of kinetic energy in each half-wavelength at $t = 1.9$ for different frequencies and different magnitudes of artificial viscosity. The dashed line is for $\omega = 4\pi$, and the solid lines are for $\omega = 8\pi$. The two solid lines are distinguished by different magnitudes of the artificial viscosity coefficient v . The upper solid curve has $v = 0.0002$ (the same as for the dotted curve), and the lower one has $v = 0.0004$. The vertical axis represents the magnitude of kinetic energy, and the horizontal axis represents the position of each half-wavelength. In order to make a close comparison between $\omega = 4\pi$ and $\omega = 8\pi$, we specify different scales on the right (for $\omega = 4\pi$) and the left (for $\omega = 8\pi$) vertical axes, and upper (for $\omega = 4\pi$) and lower (for $\omega = 8\pi$) horizontal axes. The effect of partial reflection is represented by the oscillatory change in the energy which is superposed on the continuous decrease of the energy due to artificial viscosity.

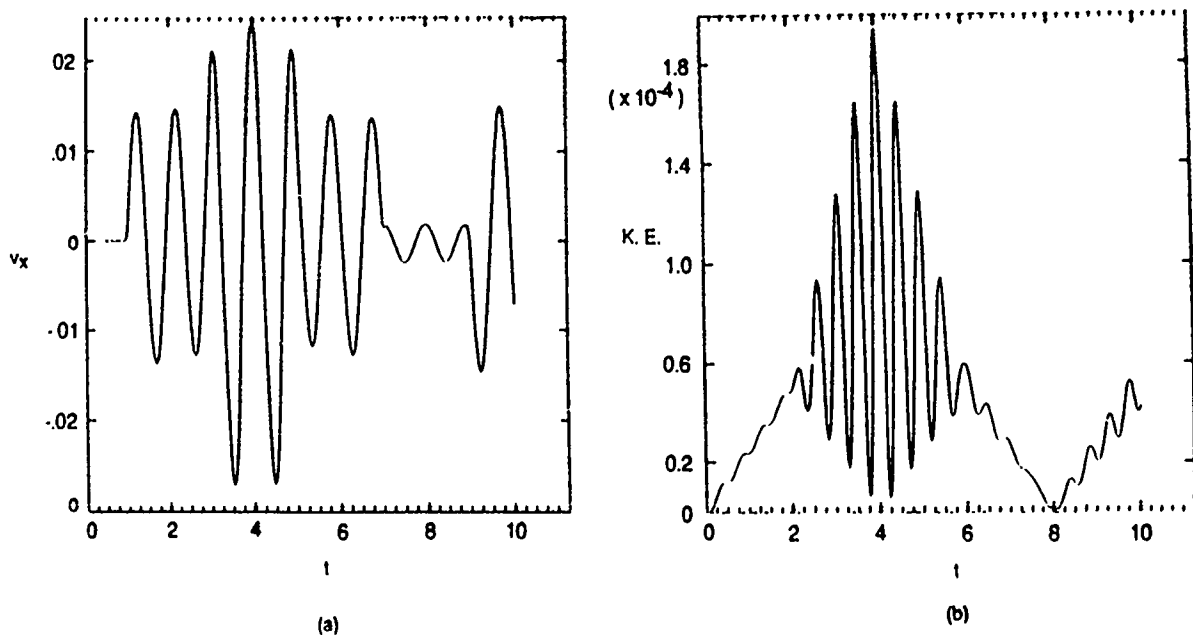


FIG. 6.—(a) Time variation of the velocity (v_x) at $\eta = 0.5$ with wave frequency $\omega = 6.65$, at which $J_1(\omega/\omega_A) \approx 0$. Apparently because of destructive interference between the ascending and descending waves, the amplitude shows strong modulation. The vertical axis is the amplitude of the velocity, and the horizontal axis is time. (b) Time variation of kinetic energy integrated over $0 \leq \eta \leq 1$. Because of destructive interference, the energy waves and waves with time.

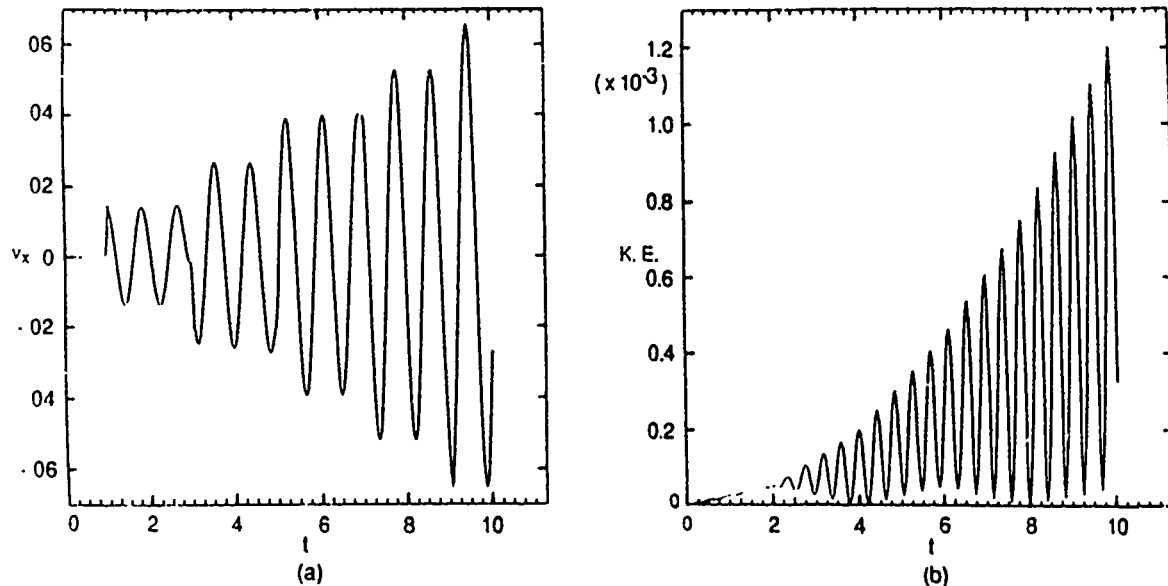


FIG. 7.—(a) Time variation of velocity amplitude at $\eta = 0.5$ for frequency $\omega = 7.45$ at which $J_0(\omega/\omega_A) \approx 0$. Apparently because of constructive interference, the amplitude increases nearly linearly with time. (b) Time variation of kinetic energy integrated from the wave source to infinity with frequency $\omega = 7.45$. Because of constructive interference (or resonance), the amplitude increases as the square of time.

in the cavity. This continuous constructive interference resembles the resonant phenomenon found by Hollweg (1972, 1978), who showed that the peak of transmitted energy density is at the frequencies for which $J_0(\omega/\omega_A) = 0$ at $\eta = 1$. The amplitude of magnetic energy increases as the kinetic energy, but with a 180° phase difference.

We believe that the resonant phenomenon found in this study is essentially the same as that found by Hollweg (1972, 1978) studying Alfvén wave propagation from the chromosphere into the corona. For $\omega = 7.45$ the amplitude of the analytic solution of velocity at $z = 0$ is nearly zero, but we force the velocity at the wave source to oscillate with a finite amplitude. As the initial wave front reflects back and interferes with the ascending wave, the solution becomes the analytic standing wave shown in Figure 2. A characteristic of the analytic standing wave solution is that if we increase the amplitude at $z = 0$, the amplitude above $z = 0$ increases proportionately. However, the amplitude of the propagating wave does not immediately go to the analytic value (about 10^3 times the initial amplitude) because it takes time for the perturbation to reach all heights. During that time, the ascending and descending waves interfere constructively to increase the amplitude continuously. It will take about 2×10^4 wave periods for our numerical peak to reach the analytic value. On the other hand, for $\omega = 6.65$ the amplitude of the analytic solution for velocity is a local maximum at $z = 0$. As the wave source is forced to oscillate, the amplitude at $z = 0$ decreases below the analytic value, which decreases the amplitude of the analytic solution above $z = 0$ proportionately. Again, the amplitude of the transient wave does not decrease to the analytic value immediately. The ascending and reflected descending waves continuously interfere with each other to decrease the amplitude.

IV. DISCUSSION AND CONCLUSION

We have studied Alfvén wave propagation in an isothermal and stratified atmosphere with constant gravity and uniform vertical magnetic field. The problem dates back to Ferraro and Plumpton (1958), but there has been confusion because

Ferraro and Plumpton's solution is a standing wave solution, which seems unrealistic for the solar atmosphere. Many attempts have been made to avoid the standing wave solution and obtain a realistic traveling wave by dividing the atmosphere into two parts, corona and chromosphere, and by specifying an ascending traveling wave solution in the corona. Here, we have concentrated on understanding the wave propagation by reviewing the analytic solutions and physically interpreting them by studying the wave propagation using a time-dependent MHD numerical model.

We find that the analytic standing wave solution of Ferraro and Plumpton with steady sinusoidal oscillations is unavoidable for an isothermal atmosphere with constant gravity and uniform vertical magnetic field. This atmosphere has an exponentially decreasing plasma density and an exponentially increasing Alfvén speed. This results in finite transit time of the Alfvén wave to infinity and total reflection. The steady sinusoidal time dependence for the perturbed quantities in the analytic study is valid only after sufficient time has elapsed for the outgoing and reflecting waves to interact to form a steady standing wave. All attempts to avoid the standing wave solution have resorted to specifying upward-propagating waves at the upper boundary or a discontinuous atmosphere which sets the character of the solutions. We, as an alternative, studied the wave propagation in a continuous atmosphere by using a time-dependent linear MHD numerical model.

Our numerical results reveal that as the wave front approaches infinity, partial reflection due to the density gradient continuously increases. As the wave front reaches infinity, the reflection becomes total. The transient wave front reflects back, leaving a steady standing wave train behind. We have compared the standing wave train with the analytic solution and found excellent agreement. We found a noticeable partial reflection as the wave front approaches the height at which $\omega \leq \omega_A$ and above which the plasma oscillates in the same phase. In other words, there is noticeable continuous reflection when the wavelength is longer than density scale height because the wave then sees the atmosphere as a rapidly chang-

ing medium. When the wave front approaches infinity, the wavelength becomes infinite and the wave sees the medium as a discontinuity, causing total reflection. The total reflection causes the waves to be trapped in a cavity, extending from the wave source to infinity, in which the wave energy is stored. We find that there is a resonant frequency at which the stored energy increases with the square of time. We suggest that the resonant phenomenon in this study is the same as found by Hollweg (1972, 1978), who calculated the peak of energy flux at the resonant frequency to be several orders of magnitude higher than the value at a nonresonant frequency. It will take about 2×10^4 wave periods for our numerical peak to reach the analytic value, by which time our linear approximation breaks down. Our recent study for nonlinear Alfvén wave propagations shows that the resonant amplitude grows to about 20 times the initial value and becomes saturated and transient propagation continues. The study implies that the resonance should be treated nonlinearly and is physically important only when the lifetime of the wave source is long enough.

Zugzda and Locans (1982) suggested that there would be no resonance peak in transmitted energy if we specified unit wave energy flux rather than unit velocity; at a large reflection coefficient in the lower atmospheric layers, there arise nearly standing waves with a node at the lower boundary ($z = 0$) for resonance frequencies. Zugzda and Locans claimed that if we give a forced oscillation with a unit velocity, the velocity above the lower boundary will be proportionately high, but with a unit energy flux the velocity will not be high. However, we note that the amplitude at the lower boundary is finite, if not unity, for the unit energy flux. As long as the velocity amplitude at the lower boundary is finite, no matter how small it is, the velocity amplitude above the boundary will approach the analytic value of a resonance peak for the resonance frequencies. In other words, we will find resonance peaks of Hollweg even if we specify unit energy flux rather than unit velocity. It is not clear why Zugzda and Locans (1982) did not find the reson-

ance, even though their approach is similar to Hollweg's for the calculation of the reflectivity.

We have demonstrated the accuracy of our numerical simulation method by its close reproduction of the analytic solutions for vertical Alfvén waves in an isothermal atmosphere with constant gravity. This means that the same simulation method will be valid for study of MHD wave propagation in more realistic stellar atmospheres.

Recently, we have studied fast-mode wave propagation in an atmosphere stratified by a uniform gravity and magnetized by a uniform horizontal magnetic field (Musielak *et al.* 1989) analytically. The results demonstrated that the ascending fast mode also undergoes reflection in the corona, implying that the reflection is a common phenomenon for both fast and Alfvén waves propagating upward in a stratified stellar atmosphere. Even though the density of a real atmosphere might not decrease to zero at infinity, as for the uniform-gravity case, the density stratification can cause the wavelength of the waves to be much longer than the density scale height at some location in the corona. Then, the waves begin undergoing continuous partial reflection as they propagate above that height. This partial reflection is totally neglected by authors imposing only outgoing wave solutions at the upper boundary. We believe that the possibility of partial reflection of the MHD waves in the corona may be important for coronal heating and solar wind acceleration.

We are grateful to D. H. Hathaway and J. V. Hollweg for valuable comments on this paper. The research has been supported by NASA HQ grant NAGW-9 and Air Force grant AFOSR-88-0013 (C. H. A.) and by the NASA Space Plasma Physics and Solar and Heliospheric Physics Branches in the Office of Space Science and Applications. This work was completed while Z. E. M. held a NRC-NASA/MSFC Research Associateship.

REFERENCES

- An, C.-H., Suess, S. T., and Wu, S. T. 1989, *Ap. J.*, **337**, 989.
 Campos, L. M. B. C. 1987, *Rev. Mod. Phys.*, **59**, 363.
 Ferraro, V. C. A. 1954, *Ap. J.*, **119**, 393.
 Ferraro, V. C. A., and Plumpton, C. 1958, *Ap. J.*, **127**, 459.
 Hollweg, J. V. 1972, *Cosmic Electrodyn.*, **2**, 423.
 ———, 1978, *Solar Phys.*, **56**, 305.
 ———, 1984, *Ap. J.*, **277**, 392.
 Leer, E., Holzer, T., and Flå, T. 1982, *Space Sci. Rev.*, **33**, 161.
 Leroy, B. 1980, *Astr. Ap.*, **91**, 136.
 Leroy, B., and Schwartz, S. J. 1982, *Astr. Ap.*, **112**, 84.
 Musielak, Z. E., An, C.-H., Moore, R. L., and Suess, S. T. 1989, *Ap. J.*, in press.
 Rosner, R., Low, B. C., and Holzer, T. E. 1986, *Physics of the Sun*, ed. P. A. Sturrock, T. E. Holzer, D. M. Mihalas, and R. K. Ulrich (Dordrecht: Reidel), **2**, 135.
 Schwartz, S. J., Cally, P. S., and Bel, N. 1984, *Solar Phys.*, **92**, 81.
 Schwartz, S. J., and Leroy, B. 1982, *Astr. Ap.*, **112**, 93.
 Zugzda, Y. D., and Locans, V. 1982, *Solar Phys.*, **76**, 77.

C.-H. AN, Center for Space Plasma and Aeronomic Research, University of Alabama in Huntsville, Huntsville, AL 35899

R. L. MOORE, Z. E. MUSIELAK, and S. T. SUESS, Space Science Laboratory, ES52, NASA Marshall Space Flight Center, Huntsville, AL 35812

IV. SOLAR INTERPLANETARY COUPLING STUDIES

There were three papers published; two papers in Solar Physics dealing with the initiation of solar disturbances propagating into interplanetary environment and one paper in J. of Geophysical Research describing the interactions of the propagating plasmoid and solar wind in three-dimensions.

Shear-Induced Instability and Arch Filament Eruption:
An MHD Numerical Simulation in Solar Phys., (to appear)
1991.

Model Calculations of Rising Motions of Prominence Loops
in Solar Phys. (to appear) 1991.

A Time-dependent, Three-dimensional, MHD Numerical Study
of Interplanetary Magnetic Draping Around Plasmoid in
the Solar Wind in J. of Geophysical Res. (to appear)
1991.

SHEAR INDUCED INSTABILITY AND ARCH FILAMENT ERUPTION:
A MAGNETOHYDRODYNAMIC (MHD) NUMERICAL SIMULATION

by

S. T. Wu and M. T. Song*
Department of Mechanical Engineering and
Center for Space Plasma and Aeronomic Research
The University of Alabama in Huntsville
Huntsville, Alabama 35899 U.S.A.

and

P. C. H. Martens
Harvard-Smithsonian Center for Astrophysics
Cambridge, Massachusetts 02138 U.S.A.

and

Lockheed Palo Alto Research Laboratories
Palo Alto, California 94304 U.S.A.

and

M. Dryer
Space Environment Laboratory
National Oceanic and Atmospheric Administration
Boulder, Colorado 80303 U.S.A.

SOLAR PHYSICS

Accepted 1991

Running Heading: Corona, Filament Eruption, Shear Instability,
Magnetohydrodynamics (MHD)

*Permanent Address: Purple Mountain Observatory, Nanjing, China

ABSTRACT

We investigate, via a two-dimensional (nonplanar) MHD simulation, a situation wherein a bipolar magnetic field embedded in a stratified solar atmosphere (i.e. arch-filament-like structure) undergoes symmetrical shear motion at the footpoints. It was found that the vertical plasma flow velocities grow exponentially leading to a new type of global MHD-instability that could be characterized as a "Dynamic Shearing Instability", with a growth rate of about $\sqrt{8} \bar{V}_A a$, where \bar{V}_A is the average Alfven speed and a^{-1} is the characteristic length scale. The growth rate grows almost linearly until it reaches the same order of magnitude as the Alfven speed. Then a nonlinear MHD instability occurs beyond this point. This simulation indicates the following physical consequences: the central loops are pinched by opposing Lorentz forces, and the outer closed loops stretch upward with the vertically-rising mass flow. This instability may apply to arch filament eruptions (AFE) and coronal mass ejections (CMEs).

To illustrate the nonlinear dynamical shearing instability, a numerical example is given for three different values of the plasma beta that span several orders of magnitude. The numerical results were analyzed using a linearized asymptotic approach in which an analytical approximate solution for velocity growth is presented. Finally, this theoretical model is applied to describe the arch filament eruption as well as CMEs.

1. INTRODUCTION

More than a quarter century ago, Gold and Hoyle (1960) suggested that horizontal photospheric motion can move the footpoints of magnetic field lines and twist the flux tubes because of the highly electric conducting plasma at the photospheric levels. A number of investigators (Tanaka and Nakagawa, 1973; Low and Nakagawa, 1975; Low, 1977; Klimchuk, Sturrock and Yang, 1988; Klimchuk and Sturrock, 1989) studied the evolution of force-free fields and its role in energy storage (build-up) for solar flares.

All of these studies were limited to the case of magnetostatics; self-consistent dynamical effects were ignored. Recently, Wu et al. (1983, 1984, 1986) presented a self-consistent MHD model for the purpose of examining flare energy build-up and wave-mass interactions due to shear and converging-diverging motions at the photospheric level. Most recently, Mikic et al. (1988) and Biskamp and Welter (1989) have presented numerical results on the dynamical evolution of a magnetic arcade type due to shear motion. However, their models are restricted to symmetric boundary conditions, while in this study self-consistent boundary conditions were used (see, for example, Wu and Wang, 1987; Nakagawa et al. 1987).

In this paper, we use the time-dependent MHD simulation model devised by Wu et al. (1983) to reveal a nonlinear solution for the evolution of the magnetic field configuration driven by shear motion. In this solution, we find that the plasma velocity

in the vertical plane perpendicular to the shear, grows exponentially in a process which can be analytically described by a linear MHD instability. This upward velocity steadily increases until it reaches the average Alfvén speed. At later times, a nonlinear instability sets in. A field line pinch occurs in the lower shear region in the numerical results. At the same time, mass and field line expulsion appears in higher parts of the region and the closed field tends to open locally. We suggest that these new effects (i.e., mushroom cloud-like flow, pinch and expulsion) can explain the formation of current sheets, the opening of a closed bipolar field, and the ability of particle streams to escape from the solar surface. Specifically, we suggest that this model applies to the eruption of arch filament systems (AFEs) and their relation to non-flare-associated coronal mass ejections (CMEs). The mathematical description of the model and numerical results are given in Section 2. A general physical interpretation of these results is presented in Section 3. An application of this model to specific coronal phenomena is given in Section 4, and the concluding remarks are presented in Section 5.

2. NUMERICAL SIMULATION

In order to illustrate how shear induced non-equilibrium occurs, we use a theoretical model in which a two-dimensional bipolar field undergoes a steady shear velocity at the footpoints of its magnetic loops. The shearing motion is sketched in Figure 1(a), and the initial bipolar field is shown explicitly in Figure

1(b).

First, we perform a simulation of the dynamic response of the bipolar field to the shear. Then we use an analytical method to interpret the simulation results. The simulation model is based on a two-dimensional, time-dependent, MHD model (Wu, et al. 1983, Hu and Wu, 1984) with an improved FICE (Full-Implicit-Continuous-Eulerian) numerical scheme (Wu and Wang, 1987). Symmetrical side boundary conditions have been replaced with non-reflecting boundary conditions. This implies that the physical phenomena are determined by the solution at a specific time and are not determined by the specified boundary conditions as in the case studied by Mikic et al. (1988). The physical conditions on these two side boundaries are determined mathematically through compatibility relations that are given in detail by Wu and Wang, (1987). Thus, the computation domain (i.e., $|x| \leq 8.4 \times 10^3$ km, $0 \leq y \leq 8 \times 10^3$ km) consists of three free non-reflecting boundaries (i.e. top, and sides), while the bottom boundary ($y = 0$) is created with the method of projected characteristics (Nakagawa, et al. 1987; Hu and Wu, 1984). The basic equations for this model are the time-dependent MHD equations with infinite conductivity, no viscosity and symmetry in one direction (Wu et al. 1983). Solar gravity, plasma pressure gradients, and compressibility are explicitly considered. None of these characteristics were considered in the work of Mikic et al. (1983), and Biskamp and Welter (1989) have only considered compressibility in a special way.

The initial conditions are (see Fig. 1b),

$$\left. \begin{aligned} \rho_0 &= \rho_c \exp \left[-\frac{gy}{RT_c} \right], \quad T_0 = T_c, \quad v_x, v_y, v_z = 0, \\ B_{x0} &= B_0 [\cos(ax)] e^{-ay}, \quad B_{y0} = -B_0 [\sin(ax)] e^{-ay}, \quad B_{z0} = 0, \\ a &= \pi/2x_0, \quad x_0 = 8.4 \times 10^3 \text{ km}. \end{aligned} \right\} \quad (1)$$

The plasma parameters are taken to be $\rho_c = 1.67 \times 10^{-12} \text{ g cm}^{-3}$ and $T_c = 10^5 \text{ K}$. These parameters are representative for solar conditions at the higher chromosphere and lower corona. The computation grid points are:

$$x_i = -8.4 \times 10^3 + (i-1)\Delta x, \quad i = 1, 2, \dots, 22$$

$$y_j = (j-1)\Delta y, \quad j = 1, 2, \dots, 11$$

$$\Delta x = \Delta y = 8 \times 10^2 \text{ km} \sim 1 \text{ arc sec.}$$

The non-reflecting boundary conditions, as noted above, are used for the top ($y = y_{11}$), left hand side ($x = x_1$), and right hand side ($x = x_{22}$). The conditions at the bottom boundary ($y = y_1$) are taken as follows:

$$\rho = \rho_c, \quad T = T_c, \quad B_y = B_{y0}, \quad v_x = 0, \quad \text{but } v_y, v_z = 0,$$

$$v_z = \begin{cases} w_c \sin(ax), & \text{if } |x| \leq 5.2 \times 10^3 \text{ km} \\ \frac{(6.8 \times 10^3 - |x|)}{1.6 \times 10^3} w_c (\text{sgn } x) \sin(5.2 \times 10^3 a), & \text{if } 5.2 \times 10^3 < |x| \leq 6.8 \times 10^3 \text{ km} \\ 0, & \text{if } 6.8 \times 10^3 < |x| < 8 \times 10^3 \text{ km}, \end{cases} \quad (2)$$

The other physical quantities (p, T, v_y, B_x, B_z) are computed by

means of the compatibility equations for the non-reflecting boundary condition which assures the consistency of the numerical computation.

In order to understand the general physical behaviour of the nonlinear solution from the mathematical model, we have performed three numerical experiments. These three cases use combinations of magnetic field intensity and magnitudes of the shear velocity. The results for these three cases are described as follows:

(i) Large Plasma Beta ($\beta_0 \approx 15.4$)

In this numerical experiment, we chose the initial plasma beta (β_0) to be 15.4. This is not a physically realistic case for a solar active region; but it does provide a basis for comparison with the other cases. This case corresponds to a local, exceedingly low, magnetic field strength of 2.12 gauss at the origin, $x = y = 0$, as shown in Fig. 1b. The shear velocity, w_c , was taken to be 5 km s^{-1} . Figure 2 shows the evolution of the magnetic field lines due to the shear motion at $200 \text{ s} \leq t \leq 3200 \text{ s}$. It is useful to examine the evolutionary behaviour at various Alfvén times (defined as $\tau_A = [\Delta y \text{ (or } \Delta x)]/v_A \approx 1700 \text{ s}$). During the early stages of evolution (that is, within the first Alfvén time), the magnetic field lines rise together in an orderly fashion in response to the shearing motion. This behavior is also presented in the analytical solution of Low (1981) and the force-free numerical solutions of Klimchuk and Sturrock (1989) although they do not consider dynamics and gravitational effects. After the first Alfvén time period, the

evolutionary behaviour of the field lines becomes more complicated. Nonlinear interactions take place between the shear-induced mass motion, magnetic field and gravity with the result that in some regions the field lines are bunched together to form a current sheet (see Fig. 2g and 2h). Further understanding of these phenomena is provided by the representation of the shear induced mass motion as shown by the vectorial velocity field in Figure 3. Notice that the inclusion of magnetohydrodynamic effects, in contrast to the kinematic study of Low (1981), causes upward mass motion in addition to the up-lifting of the magnetic field lines because the plasma has to move with the field lines under the conditions of infinite conductivity as manifested by the upward component of Lorentz force. Note, however, that some of the uplifted plasma (in the region displaced from the origin) slows down under the action of gravity, reverses direction, and falls back to the surface. Most of the motion, however, is upward. These upward mass motions are also found by Mikic et al (1988) and Biskamp and Welter (1989). However, these workers did not include compressibility, pressure gradient, and gravitation as noted above. The present study, which does so explicitly, demonstrates a different evolution in the later stages.

This induced upward motion can be explained via our governing equations. When we introduce the shear motion (v_z), an axial field component, B_z , will be induced through the induction equation. The additional magnetic field will cause an additional

magnetic pressure gradient in the momentum equation. This additional pressure gradient induces both the horizontal (v_x) and upward (v_y) motions as shown in Figure 3. Subsequently, the mass motion interacts with both the magnetic field and gravity. Closer to the surface, the combined effect is dominated by gravity, and the result is the cluster of magnetic field lines in which a current sheet is formed as shown in Figures 2(g) and 2(h) at nearly twice the Alfvén time.

Figure 4 shows the plasma properties (i.e. density, temperature and pressure enhancement in terms of percentage change from the initial values at each level) at the end of this simulation ($t = 3600$ s; more than $2 \tau_A$). These properties are shown at various heights (Y_1, Y_2, Y_4, Y_6 , and Y_{10} , as shown in Figure 1b) as a function of horizontal distance. These results also help to explain the magnetic field line distribution. That is, the high density magnetic field region shown in Figures 2(g) and 2(h) within the mid-horizontal range (at the altitudes: Y_2, Y_4) corresponds to the increase of plasma density by 20% (i.e. $\Delta\rho/\rho_0 \sim 0.2$), temperature decrease of 20% (i.e. $\Delta T/T_0 \sim -0.2$), and magnetic field strength ($\Delta B/B_0$) increase by a factor of 3. These properties are similar to those for a current sheet. With these properties in mind, let us now turn our attention to the plasma flow patterns as shown in Figure 3. The plasma flow rises initially above the zone of maximum shear velocity. At later times (say, from 1000 to 2000 s), the plasma flow moves toward the central region in a pattern reminiscent of a mushroom cloud.

In the later stages as shown in Figures 3g and 3h, the significant plasma motion is again concentrated in the neighborhood of the sheared region. This is also the region where the magnetic field lines have been clustered as seen in Figures 2g and 2h.

(ii) Intermediate plasma beta (i.e. $\beta_0 = 1.54$)

In this case, our simulation is performed with an initially modest magnetic field strength ($B_0 = 21.3$ G) and with a shear velocity (w_c) of 15 km s^{-1} . The qualitative behaviour of the evolution of the vectorial fields (i.e., magnetic and velocity fields) and plasma parameters (i.e., density, temperature, and pressure) are similar to the Case (i). Therefore, we shall not repeat a full presentation. Nevertheless, there are some interesting features that appear in the evolutionary results of the magnetic and velocity fields as shown in Figure 5.

The most pronounced result is the induced velocity distribution shown on the right side panels of Figure 5. The high velocity of the ascending movement in the central region is especially notable. As a result, the closed bipolar field tends to be opened up. We attribute this to the force created by the ascending movement of mass motion initiated by the shear prescribed at the lower boundary. The highest velocity attained by the mushroom cloud-like ascending mass motion is about 25 km s^{-1} at $t = 700 \text{ s}$ (i.e., ~ 4 Alfvén times) after introduction of the shear motion. The corresponding plasma parameters can be summarized as follows: the density decreases by about 50% at the

legs of the intermediate loops marked by the footpoints x_4 , x_5 , and x_6 as labeled in Figure 1b. Again, the pinch effects discussed for Case (i) occur and a current sheet is formed where the density increases by 25%; the temperature decreases by 30%; and the field strength increases by a factor of 2.

(iii) Low plasma beta (i.e. $\beta_0 = 0.06$)

In this case the initial magnetic field strength is increased to a more realistic value of 106.3 G without changing the other plasma parameters. The initial plasma beta is equal to 0.06 which is twenty-five times smaller than Case (ii) and two hundred fifty times smaller than Case (i). Again, the evolution of the magnetic field and velocity field exhibits patterns similar to those of Cases (i) and (ii). Figure 6 shows the evolution of the magnetic field and the velocity vector field for this case. The maximum upward velocity is a factor of 4 higher than for Case (ii) and a factor of 40 higher than for Case (i). We note that the time required to reach the maximum velocity is much shorter than in the other two cases.

In order to examine this phenomenon further, we plotted in Figure 7 the planar maximum absolute velocity (i.e.

$(v_x^2 + v_y^2)^{1/2}_{\max}$) in the neighborhood of the apex of the arcade as a function of time for the three different cases. We chose to plot this parameter instead of the upward velocity, v_y , because the representative parameter $(v_x^2 + v_y^2)^{1/2}$ is related to our analytical analysis that is discussed later (and in the Appendix). Actually, the numerical results show that the

horizontal velocity, v_x , is only 25% of the vertical velocity, v_y . First, we point out the change of scales that was required for the three Cases (i), (ii), and (iii). Second, we direct attention to the common features: an approximately linear initial phase followed by a smooth transition to an explosive upward mass motion. The latter phenomenon is representative of the upward regions as discussed earlier.

It is interesting to relate these results to the magnetic field evolution. For example, we direct attention to Figures 2, 5 and 6 where, in the early stages of the evolution, the change of field lines is regular with a slowly ascending movement. This upward motion is also present in the force-free analyses of Low (1981) and Klimchuk and Strurrock (1989), and the numerical incompressible simulations of Mikic et al. (1988), and Biskamp and Welter (1989). However, the change of field lines in the present case becomes quite irregular in the later stages of the evolution. From Figures 2, 5, and 6, we notice that the lower field lines are pinched together and the upper field lines tend to open up when the maximum planar velocity exceeds the Alfven speed. The Alfven speed for these three cases is 4.67 km s^{-1} , 46.7 km s^{-1} and 232 km s^{-1} respectively. The maximum footpoint shear motion, v_z , is slow compared to the Alfven velocity in the latter two cases but fast compared with resistive diffusion in all three cases. Thus a sequence of essentially quasi-static, force-free states with frozen-in magnetic fields is found in the early stages, which ends when the magnitude of planar maximum

velocity exceeds the Alfvén speed, and the system becomes unstable. We claim that this is a shear-induced instability that could not be found in the earlier numerical simulations that omitted compressibility, pressure gradient, gravity, and the different treatment of boundary conditions. We shall return to this point later for further discussion utilizing analytical results.

3. FURTHER INTERPRETATION OF THE SIMULATION RESULTS

From these simulation results, we have found that the buoyancy force leads to a mushroom cloud-like ascending movement that pushes the closed magnetic field upward. In order to understand this result further, we supplement our numerical simulation with an approximate analytical solution:

Creation of Mushroom Cloud-like Ascending Motion

From the numerical simulation of all three cases, we observe that the shear-induced mushroom cloud-like ascending movement can be ascribed to the out-of-plane component of the magnetic field, B_z . This component gives an upward magnetic pressure gradient (i.e. $\nabla(B_z^2/8\pi)$) which causes the ascending movement of magnetic field and corresponding plasma flows. On the other hand, we notice that no B_z component is generated near the origin ($x = 0, y = 0$) due to shear. This leads to a downward force, such that we observe the field lines being squeezed together to form a current sheet as shown in Figures 2, 5, and 6. This point can be illustrated further by using a linear approximation. The justification for the use of linear theory is seen from the

numerical results that show that the initial stage of the shear-induced motion behaves regularly as shown in Figures 2,3,5 and 6.

A closed form linearized solution for the induced field component B_z is the following (for the derivation, see the Appendix):

$$\frac{B_z}{\sqrt{4\pi\rho_0}} = c_1 e^{-ay} \cos(ax) \cos[Lax(e^{-ay}) \cos(ax)] \sin[(t+t_0)L\omega_0] \quad (3)$$

This result expresses that the induced magnetic field B_z rises from the lower boundary (i.e., $y = 0$) and spreads upward with a characteristic time scale $L\omega_0$, where L is defined by Eq. (A.8). It could be noticed from Eq. (3) that B_z decreases exponentially with respect to the increase of y (height), because the term, $\cos[Lax(e^{-ay})(\cos(ax))^{-1}]$ in the central region, varies slowly with height.

Finally, the coefficient c_1 corresponds to the shear velocity (w_c). The part of the total upward Lorentz force

$(-J_x B_z = -\frac{\partial}{\partial y} \frac{B^2}{2})$ that causes upward acceleration is independent of the sign of the coefficient c_1 (or w_c).

Shear-induced Instability

From the simulation results shown in Figure 7, we found earlier that instability sets in when the absolute maximum planar velocity exceeds the Alfvén speed. In order to substantiate this claim, we performed a linearized analysis in which an approximate linearized solution for the planar velocities (u, v) was constructed as shown in the Appendix (Eq. (A.13)). These

velocities are as follows:

$$\begin{aligned} u_1 &= \delta' e^{-2ay} \sin(2ax) \\ v_1 &= \delta' e^{-2ay} [1 + \cos 2(ax)]. \end{aligned} \quad (4)$$

The electric current along the z-axis can be estimated to the first order, as:

$$\frac{4\pi}{c} J_z = \frac{\partial B_y}{\partial x} - \frac{\partial B_x}{\partial y} = 16 a^2 B_0 e^{-3ay} \cos ax \int_0^t \delta' dt, \quad (5)$$

which means that the Lorentz force $1/c (J_z B_x - J_x B_z)$ leads to ascending flow, because it has been shown in the Appendix that δ' is always positive and has an exponential growth rate as shown in Eq. (A.16). We have identified this phenomenon as the shear-induced instability since the numerical simulation results shown in Figure 7 are consistent with the analytical analysis. It is further noted from numerical results that the term $-1/c J_x B_z$ is always upward.

The results for the evolution of the magnetic field configuration shown in Figures 2, 5 and 6 show clearly the two-stage evolution that we discussed earlier. The first stage of the evolution can be described by the linearized solution given in Eq. (4). The second stage of the evolution involves the pinching together of field lines in the region where the shear motion was applied. If the three factors noted earlier (compressibility, pressure gradients, and gravity) had been absent, we believe that our results would have been similar to those of Mikic et al. (1988). Our current sheet, however,

developed horizontally, whereas, their current sheet was vertical. We explain this phenomenon by examining the distribution of upward component of the Lorentz force (i.e. $1/c (J_z B_x - J_x B_z)$). To illustrate this viewpoint, we use the results for $\beta_0 = 0.06$ because this case best resembles the real physical conditions in active regions. The results are plotted in Figure 8. The left-most panels show the horizontal distribution of the vertical component of the Lorentz force at different heights from Y_1 to Y_{10} [as shown in Figure 1b] at 25 s after the introduction of the shear motion at the lower boundary. As noted earlier, the Alfvén time for this case is ~ 35 s. This result clearly indicates the first stage of the evolution due to the introduction of shear. All the forces are in the upward direction which means that all field lines are lifted up in an orderly fashion. The magnitude of these forces is of the order of 3×10^{-9} dyne/cm². The middle panels show the resultant upward component of the Lorentz force at $t = 100$ s which is about three Alfvén periods. These results are reflected in the nonlinear nature of the evolution in which the Lorentz forces have both upward and downward direction at the intermediate altitudes.

This bi-directional nature of the Lorentz forces causes the field lines to be pinched together in the lower regions as shown, for example, in Figure 6 for $\beta_0 = 0.06$. This particular feature is most pronounced in the results shown in the right-most panels which show the vertical component of Lorentz force at $t = 213$ s;

this is about seven Alfven periods after the introduction of the shear. We note that the vertical component of this Lorentz force decreases at high levels, but, in lower levels (i.e. Y_1 and Y_2), two very strong oppositely-directed vertical components of Lorentz force ($\sim 3 \times 10^{-7}$ dyn/cm²) appear. The force at Y_1 is upward and the force at Y_2 is downward. These two forces cause the field lines to be pinched together as shown in Figure 6c. Further discussion of this point will be included in the next section as part of a general scenario for shearing motions of magnetic arches or bipolar regions.

4. SCENARIO

From these simulation results, supported by the linearized analytical solution, a physical scenario is proposed for the formation of an "Arch Filament System (AFS)" and its eruption as part of a more general scenario for "Coronal Mass Ejections (CMEs)". A schematic representation of this scenario is presented in Figure 9. After introduction of shear motion at a bi-polar region, all of the field lines will first be lifted up in an orderly fashion due to the shear-induced upward Lorentz force before the absolute maximum upward velocity reaches the local Alfven speed; this is the linear stage of the evolution. When this upward velocity is in the neighborhood of the local Alfven speed, the lower parts of the magnetic field lines are pinched together, and an arch filament system is formed. At the same time, the upper part of the magnetic field lines is pushed upward, and a certain amount of mass is carried upward. This

upward mass motion is shown in Figure 10 in terms of contours of $\Delta\rho$ and Δp that move upward at all but the lowest gravitationally-bound heights.

Finally, when this absolute upward velocity exceeds the Alfvén speed, the shear-induced instability sets in as shown by the numerical results of Figure 7 and the analytical solution in the Appendix (Eq. (A.16)). In the following we compare this scenario with the available observations.

Arch filament systems and coronal mass ejections have been investigated by many authors (Bruzek, 1967, 1968, 1969; Bumba and Howard, 1965; Martres et al. 1966; Harrison 1986). These authors have noted that arch filament systems (AFS) always connect areas of opposite polarities and cross the neutral line in the longitudinal magnetic field. Bruzek (1969) has pointed out that the occurrence of AFS is associated with evolution of young bipolar spot groups. As for the motion of AFS, its characteristic feature is its expansion in height with an ascending velocity of $16 - 25 \text{ km s}^{-1}$ with footpoints rooted in the two opposite spot regions. This behaviour is quite similar to the early stage of the simulated magnetic field line evolution and mass motion shown in Figures 2, 3, 5 and 6 where the apex of the magnetic loops is rising but their legs have little lateral movement. It was further noted that the AFS has both descending and ascending motions in loops. Bruzek (1968) attributed this phenomenon to the mass injection at one leg and its return to the chromosphere via another leg that has opposite polarity. On the

other hand, shearing motion, if it has a line-of-sight component, would always lead to a blue shift in one leg and red shift in the other. Therefore observations of flows in filaments are not evidence of shearing. However, such evidence is not needed since the relative motion of bipolar spots is both necessary and sufficient evidence of shearing. Nevertheless, this concept of descending and ascending motion is based on Doppler shift measurements which can easily, at least partially, be recognized as complementary evidence of horizontal shear motion that occurs on both sides of the neutral line. This statement considers the fact that the spot group area is often not strictly perpendicular to the line-of-sight of the observer; thus the Doppler shift velocity must have an appreciable horizontal component (Harvey and Harvey, 1976).

On the basis of our numerical simulations, the analytical solution and observed characteristics, a physical model for the formation of AFS and subsequent CME can be constructed as follows. First, a young bipolar sunspot group emerges from the sub-photosphere. As it rises, its area increases and the neutral line dividing the opposite polarities gets longer and longer. Then a portion of the field can be reasonably regarded as a two-dimensional bipolar field (as is used in our mathematical model). In the meantime, the opposite polarity areas rotate with respect to each other. Associated with this rotation are horizontal shear motions that appear on both sides of the neutral line (thereby justifying our construction of the shearing

velocity used herein). The Lorentz force generated by this process (see, for example Figure 8) pushes the magnetic loops upward during an initial stage. At the later times, the magnetic field becomes distorted, nonlinear MHD effects force field lines to pile-up and, then, the pinch phenomenon ensues. Such pinched magnetic flux tubes could be identified as arch filaments which are visible as a set of dark loops. The simulation has shown that in this region the plasma has high density and low temperature. From the analytical solution, we notice that the growth time $(V_A a)^{-1}$ of the shearing instability is about 30 min which is a typical average life time of AFS. Thus, this simulation model may be appropriate to describe the formation of AFS and the eruption which leads to some CMEs.

5. CONCLUDING REMARKS

We have used a time-dependent, nonplanar MHD model for a bipolar magnetic region that was subjected to shearing motion at its foot points. The characteristic plasma beta was varied over a wide range - from 15.4 to a more realistic value of 0.06. Common features were identified for all cases with the differences primarily occurring in the timing of the events vis-a-vis the characteristic Alfvén times. An essentially linear, early phase of upward mass motion was followed until the Alfvén speed was reached, and a shear-induced instability is initiated. This nonlinear instability may be the basic mechanism for arch filament formation and subsequent coronal mass ejections.

In our opinion, the early evolution in our simulation is in

accord with quasi-static evolution of magnetic arcades demonstrated by Klimchuk and Sturrock (1989). In their work, a very low beta plasma was assumed, and therefore the magnetic field is unaffected by pressure and gravitational forces. Our simulations are also in accord with the dynamic evolution of magnetic arcades demonstrated by the numerical simulations of Mikic et al. (1988) and Biskamp and Welter (1989) in both the early and intermediate stages of this evolution despite their neglect of compressibility, pressure gradient, and gravity. We did not find the reconnection and formation of an ejected plasmoid, as Mikic et al (1988) did, since we assumed electrical resistivity and viscosity to be zero. During the late stages of the evolutionary development, when the plasma velocities surpassed the Alfvén speed, our numerical simulations demonstrate nonlinear instability and catastrophic upward motion at high altitudes.

As a final remark, it can be shown that these numerical results are valid over a wide range of parameters according to the scaling rule for dynamic similitude. For example, the present numerical results, computed on the basis of $T_0 = 10^5$ K and $\rho_0 = 1.67 \times 10^{-12}$ g cm⁻³, can be scaled to initial conditions of $T_1 = 10^6$ K and $\rho_1 = 1.67 \times 10^{-13}$ g cm⁻³ by introducing a set of scaling parameters; $t_1 = \sqrt{\lambda} t_0$, $L_1 = \lambda L_0$, $v_1 = \sqrt{\lambda} v_0$, $T_1 = \lambda T_0$, $\rho_1 = \lambda^{-1} \rho_0$, $p_1 = p_0$ and $B_1 = B_0$ which leave the governing equations invariant for a given plasma beta. In a recent study of similitude theory, Wu et al. (1988) have shown that the

present results also apply to the physical condition represented by these different initial conditions.

As another example of the use of dynamic similitude, we may pose the following question: if the footpoints are moved slowly enough that the evolution is quasi-static, would the magnetic field closely approximate the static equilibrium states? Although, we suggested above (as did Mikic et al., 1988, and Biskamp and Welter, 1989) that the answer is 'yes', the reader is reminded of the values of the shearing velocity v_z used in the present studies (e.g., 15 km sec^{-1} , maximum, for $\beta_0 = 0.06$) and in the above mentioned work (30 km sec^{-1} , assumed by Mikic et al. 1988 for $\beta \sim 0.03$). Although these maximum footpoint shearing velocities are much less than the Alfvén speed, they are a factor of about 10 larger than observed photospheric velocities.

In summary, we consider the results given here to be representative of a realistic dynamical evolution of the posed physical problem of sheared magnetic arches and their evolution into arch filament eruption and coronal mass ejections.

Finally, we remark on the relevance of our results to the observations of some CMEs as reported by Harrison (1986). The major point of his work is that a small x-ray burst is often found at the very onset of a CME, often followed by a large x-ray flare later on during the CME. In the present work, the formation of the current sheet coincides with the rapid increase in the velocity of the upper portion of the field lines. One could interpret the latter, as already discussed, as the onset of

CME, while the current sheet formation could lead to a burst of energy dissipation (not shown here) which would be visible as a small x-ray burst. The simultaneity of these two events is consistent with the observations of Harrison (1986). This could be another indication that these numerical results indeed represent a basic mechanism for the initiation of CMEs.

ACKNOWLEDGEMENT

The work performed by STW was supported by Air Force Office of Scientific Research grant AFSOR-88-0013, National Aeronautics and Space Administration/Headquarters grant NAGW-9, and National Oceanic and Atmospheric Administration contract (50RANR-7000104). The work of PM was supported at CFA by NASA Grant NAGW-112. The work of MD was supported in part by NASA Interagency Order 17,015.

REFERENCES

- Biskamp, D. and Welter, H., 1989, Solar Physics 120, 49.
- Bruzek, A., 1967, Solar Physics 2, 451.
- Bruzek, A., 1968, in K. O. Kiepenheuer (ed.), 'Structure and Development of Solar Active Region', IAU Symposium 35, 293.
- Bruzek, A., 1969, Solar Physics, 3, 29.
- Bumba, V. and Howard, R., 1965, Astrophysical Journal, 141, 1492.
- Courant, R. and Hilbert, D., 1962, Methods of Mathematical Physics, Interscience Publ. New York, London.
- Gold, T. and Hoyle, F., 1960, Monthly Notices of the Royal Astronomical Society, 120, 89.
- Hagyard, M. J., 1990, Memorie dell Societa Astronomica Italiana (in press)

- Harrison, R., 1986, *Astron. Astrophys.*, 162, 283.
- Harvey, J. W. and Harvey, K. L., 1976, *Solar Physics* 47, 233.
- Hu, Y. Q. and Wu, S. T., 1984, *Journal of Computational Physics*, 55, 33.
- Klimchuk, J. A., Sturrock, P. A. and Yang, W.-H., 1988, *Astrophys. J.*, 335, 456.
- Klimchuk, J. A. and Sturrock, P. A., 1989, *Astrophys. J.*, 345, 1034.
- Krall, K. R., et al., 1982, *Solar Physics*, 79, 59.
- Low, B. C., 1977, *Astrophysical Journal*, 212, 234.
- Low, B. C., 1981, *Astrophysical Journal*, 251, 352.
- Low, B. C., and Nakagawa, Y., 1975, *Astrophysical Journal*, 199, 237.
- Martres, M. J., et al., 1966, *Annual Review of Astronomy and Astrophysics*, 29, 245.
- Mikic, D. Z., Barnes, D. C., and Schnack, D. D., 1988, *Astrophysical Journal*, 328, 830.
- Nakagawa, Y., Hu, Y. Q. and Wu, S. T., 1987, *Astronomy and Astrophysics*, 179, 354.
- Svestka, Z., 1976, *Solar Flares*, D. Reidel, Dordrecht-Holland.
- Tanaka, K. and Nakagawa, Y., 1973, *Solar Physics*, 33, 187.
- Wu, S. T., Hu, Y. Q., and Nakagawa, Y., 1983, *Astrophysical J.*, 266, 366.
- Wu, S. T., Hu, Y. Q., and Krall, K. R., 1984, *Solar Physics*, 90, 117.
- Wu, S. T., Hu, Y. Q., Nakagawa, Y. and Tandberg-Hanssen, E., 1986, *Astrophysical J.*, 306, 751.
- Wu, S. T., and Wang, J. F. 1987, *Computer Methods in Applied Mechanics and Engineering*, 64, 267.
- Wu, S. T., Wang, S., Wang, A. H., and Dryer, M., 1988, *Adv. Space Sci.*, 3 (11), 221.

APPENDIX

To obtain an asymptotic solution for the relationship between the footpoint shearing velocity, w , and B_z in the first stage (linear stage) of evolution during which ρ , p , T , B_x , B_y vary slightly, we write:

$$\begin{aligned} \rho &= \rho_0 + \rho_1, \quad p = p_0 + p_1, \quad T = T_0 + T_1, \quad B_x = B_{x0} + B_{x1}, \\ B_y &= B_{y0} + B_{y1}, \quad B_z = B_{z1}, \quad v_x = v_{x1}, \quad v_y = v_{y1}, \quad v_z = v_{z1}. \end{aligned} \quad (\text{A.1})$$

where subscript 0 and 1 indicate the zero-order and first-order quantities. And, $|v_{x1}|, |v_{y1}|, |v_{z1}| \ll \frac{B_0}{\sqrt{4\pi\rho_0}} = \text{Alfvén speed}$, $B_{z1} \ll B_0$. Inserting (A.1) into Eqs. (2.4) and (2.7) formerly given by Wu et al. (1983) and leaving out the higher-order quantities, we obtain the linearized equations

$$\begin{aligned} \frac{\partial v_{z1}}{\partial t} &= \frac{B_{x0}}{\sqrt{4\pi\rho_0}} \cdot \frac{\partial (B_{z1}/\sqrt{4\pi\rho_0})}{\partial x} + \frac{B_{y0}}{\sqrt{4\pi\rho_0}} \frac{\partial (B_{z1}/\sqrt{4\pi\rho_0})}{\partial y} \\ &\quad - \frac{b}{2} \frac{B_{y0}}{\sqrt{4\pi\rho_0}} \cdot \frac{B_{z1}}{\sqrt{4\pi\rho_0}}, \end{aligned} \quad (\text{A.2})$$

$$\frac{\partial (B_{z1}/\sqrt{4\pi\rho_0})}{\partial t} = \frac{B_{x0}}{\sqrt{4\pi\rho_0}} \frac{\partial v_{z1}}{\partial x} + \frac{B_{y0}}{\sqrt{4\pi\rho_0}} \frac{\partial v_{z1}}{\partial y},$$

where $\rho_0 = \rho_c \cdot e^{-by}$, $b = g/RT_c$. To solve Eq. (A.2), we construct the auxiliary equations:

$$\begin{aligned} \frac{\partial v_z^*}{\partial t} &= B_{x0}(4\pi\rho_0)^{-1/2} \cdot \frac{\partial (B_z^*/\sqrt{4\pi\rho_0})}{\partial x} + B_{y0}(4\pi\rho_0)^{-1/2} \frac{\partial (B_z^*/\sqrt{4\pi\rho_0})}{\partial y} \\ \frac{\partial (B_z^*/\sqrt{4\pi\rho_0})}{\partial t} &= B_{x0}(4\pi\rho_0)^{-1/2} \frac{\partial v_z^*}{\partial x} + B_{y0}(4\pi\rho_0)^{-1/2} \frac{\partial v_z^*}{\partial y}. \end{aligned} \quad (\text{A.3})$$

$$\text{Substituting: } F^+ = \frac{v_z^* + \frac{B_z^*}{\sqrt{4\pi\rho_0}}}{2}, \quad F^- = \frac{v_z^* - \frac{B_z^*}{\sqrt{4\pi\rho_0}}}{2},$$

Eq. (A.3) reduces to

$$\begin{aligned} \frac{\partial F^+}{\partial t} &= B_0 (4\pi\rho_c)^{-1/2} \cdot e^{-(a-b/2)y} \left(\cos ax \cdot \frac{\partial F^+}{\partial x} - \sin ax \cdot \frac{\partial F^+}{\partial y} \right), \\ \frac{\partial F^-}{\partial t} &= B_0 (4\pi\rho_c)^{-1/2} \cdot e^{-(a-b/2)y} \left(-\cos ax \cdot \frac{\partial F^-}{\partial x} + \sin ax \cdot \frac{\partial F^-}{\partial y} \right). \end{aligned} \quad (\text{A.4})$$

Since solving Eq. (A.4) is equivalent to solving its corresponding ordinary differential equation (Courant and Hilbert, 1962) it is easy to write down the solutions as follows:

$$\begin{aligned} F^+ &= \phi (e^{-ay} \cos ax, t\omega_0 + f(ax) \cdot (e^{-ay} \cos ax)^{-1+b(2a)^{-1}}), \\ F^- &= \psi (e^{-ay} \cos ax, t\omega_0 - f(ax) \cdot (e^{-ay} \cos ax)^{-1+b(2a)^{-1}}), \end{aligned} \quad (\text{A.5})$$

where

$$\omega_0 = aB_0(4\pi\rho_c)^{-1/2}, \quad f(x) \equiv \int_0^x (\cos x')^{-b/2a} \cdot dx'.$$

Considering the boundary value of v_z (the nature of shearing) and using Eq. (A.5) we can find the following solutions

$$\begin{aligned} v_z^* &= c_1 e^{-ay} \cdot \cos ax \cdot \cos(L\xi) \cdot \sin(L\eta), \\ \frac{B_z^*}{\sqrt{4\pi\rho_0}} &= c_1 e^{-ay} \cdot \cos ax \cdot \sin(L\xi) \cdot \cos(L\eta), \end{aligned} \quad (\text{A.6})$$

where

$$\xi \equiv (t + t_0)\omega_0, \quad \eta \equiv f(ax) \cdot (e^{-ay} \cos ax)^{-1+b(2a)^{-1}}.$$

t_0 , L and c_1 are integration constants. Back to solving Eq. (A.2)

suppose v_{z1} , $\frac{B_z}{\sqrt{4\pi\rho_0}}$ satisfies the equality (A.6) except that L , c_1 are now not constants but functions of x, y . Thus

$$v_{z1} = c_1(x, y) \cdot e^{-ay} \cdot \cos(ax) \cdot \cos(L(x, y) \cdot \xi) \cdot \sin(L(x, y) \cdot \eta),$$

$$\frac{B_{z1}}{\sqrt{4\pi\rho_0}} = c_1(x, y) \cdot e^{-ay} \cos(ax) \cdot \sin(L(x, y) \cdot \xi) \cdot \cos(L(x, y) \cdot \eta) \quad (A.7)$$

Inserting (A.7) into (A.2), c_1 and L can be determined uniquely by solving two ordinary differential equations. First, L satisfies the equation:

$$\cos ax \cdot \frac{\partial L}{\partial \xi} - \sin ax \cdot \frac{\partial L}{\partial y} = Q(x, y, L)$$

$$Q(x, y, L) \equiv - (b/4) \sin(ax) \cdot \sin(2L\xi) \sin(2L\eta) \quad (A.8)$$

$$[\bar{\xi} \sin(2L\eta) - \eta \sin(2L\bar{\xi})]^{-1},$$

with boundary condition $L|_{y=0} = L(x)$. After L has been found, $(\ln c_1)$ can be obtained in the same manner using the following equation

$$\cos(ax) \frac{\partial(\ln c_1)}{\partial x} - \sin(ax) \cdot \frac{\partial(\ln c_1)}{\partial y} = [\bar{\xi} \cdot \operatorname{tg}(L\bar{\xi}) - \eta \cdot \operatorname{ctg}(L\eta)] \cdot Q(x, y, L) \quad (A.9)$$

In fact, we only apply (A.7) to explain the physical nature in the lower shearing region where $\bar{\rho}_0 \approx 0.8 \rho_c$, therefore L and c_1 can roughly be regarded as constants.

It is difficult to find an asymptotic solution for v_x and v_y . Let us consider Case (iii) of strong magnetic field, in which the inertial force and $-7p$ and ρg can safely be ignored. Inserting (A.1) into (2.2) and (2.3) of Wu et al (1983), the

linearized equations are given as follows:

$$\begin{aligned} -\frac{\partial v_{x1}}{\partial t} &= \frac{1}{4\pi} B_{y0} \left(\frac{\partial B_{x1}}{\partial y} - \frac{\partial B_{y1}}{\partial x} \right) - \frac{1}{4\pi} B_{z1} \frac{\partial B_{z1}}{\partial x}, \\ -\frac{\partial v_{y1}}{\partial t} &= -\frac{1}{4\pi} B_{x0} \left(\frac{\partial B_{x1}}{\partial y} - \frac{\partial B_{y1}}{\partial x} \right) - \frac{1}{4\pi} B_{z1} \frac{\partial B_{z1}}{\partial y}, \end{aligned} \quad (A.10)$$

where the terms $-\frac{1}{4\pi} B_{z1} \frac{\partial B_{z1}}{\partial x}$, $-\frac{1}{4\pi} B_{z1} \frac{\partial B_{z1}}{\partial y}$ that are second-order quantities must be kept in view of actual mathematical manipulation. From (A.7) the partial Lorentz Force can be written as

$$\begin{aligned} - (4\pi \bar{\rho}_0)^{-1} \cdot B_{z1} \cdot \frac{\partial B_{z1}}{\partial x} &= (c_1^2 a/2) \cdot (\eta' + \eta_1) \cdot e^{-2ay} \\ &\quad \cdot \sin(2ax) \cdot \sin^2(L\zeta), \\ - (4\pi \bar{\rho}_0)^{-1} \cdot B_{z1} \cdot \frac{\partial B_{z1}}{\partial y} &= (c_1^2 a/2) \cdot \eta' \cdot e^{-2ay} [1 + \cos(2ax)] \\ &\quad \cdot \sin^2(L\zeta), \end{aligned} \quad (A.11)$$

where η' and η_1 are slow-varying functions of x, y . The representations for η' , η_1 are very complicated in the case with gravity but as we only deal with the lower central part of the domain where $\rho = \text{const.}$ $\eta = ax \cdot e^{-ay} \cdot (\cos ax)^{-1}$, $B_{z1} = B_z^*$. Therefore η' and η_1 asymptotically approach the case with no gravity. In such case η' and η_1 take simple forms as:

$$\begin{aligned} \eta' &= (\cos \bar{\eta})^2 + \bar{\eta} \cdot \cos \bar{\eta} \cdot \sin \bar{\eta}, \\ \eta_1 &= Le^{ay} \cdot \cos \bar{\eta} \cdot \sin \bar{\eta} \cdot (\sin ax)^{-1}, \\ \bar{\eta} &= Le^{ay} \cdot ax \cdot (\cos ax)^{-1}. \end{aligned} \quad (A.12)$$

Figure 11 shows the behaviour of η' and η_1 . Note that if Le^{ay} is less than 0.5, then $0 < \eta_1 < \eta' = 1$. Therefore we will pay no

attention to the difference between η' and $\eta' + \eta_1$ within the range $|ax| < \pi/4$. (A.11) reminds us of analogy between shearing velocity and force, so we suppose velocity having a mushroom-like form as:

$$\begin{aligned} v_{x1} &= \delta' e^{-2ay} \sin ax, \\ v_{y1} &= \delta' e^{-2ay} [1 + \cos (2 ax)], \end{aligned} \quad (\text{A.13})$$

where δ' is a function of t, x, y (but weakly depends on x, y) being determined later. Inserting (A.13) into the linearized equations of (2.5) and (2.6), of Wu et al. (1983) the time variation of current J_{z1}/c can be found as

$$\frac{\partial}{\partial t} \left(\frac{\partial B_{y1}}{\partial x} - \frac{\partial B_{x1}}{\partial y} \right) = 16 a^2 B_0 \delta' e^{-3ay} \cdot \cos (ax). \quad (\text{A.14})$$

In deriving Eq. (A.14) the weak dependence of δ' on x, y has been used. Differentiating (A.10) with respect to t and inserting (A.14) and (A.11) into it and then letting it go to limitation when y goes to zero, we obtain one equation

$$\begin{aligned} \frac{\partial^2}{\partial t^2} \delta' |_{y=0} &= 8 v_A^2 a^2 \cdot \delta' |_{y=0} + (c_i^2 a/2) \cdot \eta' |_{y=0} \cdot \\ &\quad \cdot L\omega_0 \sin [2L\omega_0 (t + t_0)] \end{aligned} \quad (\text{A.15})$$

to determine δ' uniquely (here $v_A^2 = B_0^2/4\pi\rho_0$). Noticing δ', η' only weakly depend on x, y , Eq. (A.15) can be regarded as an ordinary differential equation and, therefore, can be easily integrated with respect to t . Giving the initial condition: $\delta' |_{y=0} = 0, \frac{d\delta'}{dt} |_{y=0} = 0$ when $t = 0$, we obtain an asymptotic solution as:

$$\delta''|_{y=0} = [(\alpha+\beta)/2] \cdot \exp(-\sqrt{8} v_A a t) + [(\alpha-\beta)/2] \exp(-\sqrt{8} v_A a t) - \alpha \cdot \frac{\sin [2L\omega_0(t + t_0)]}{\sin [2L\omega_0 t_0]} \quad (\text{A.16})$$

with

$$\alpha = \frac{L\omega_0 a c_1^2 \eta''|_{y=0}}{8(L^2\omega_0^2 + 2v_A^2 a^2)} \sin(2L\omega_0 t_0) - \frac{L\eta' c_1^2 / v_A}{8\sqrt{2} (L^2+2)} > 0$$

$$\beta = \frac{L^2\omega_0^2 c_1^2 \eta''|_{y=0}}{8\sqrt{2} v_A \cdot (L^2\omega_0^2 - 2v_A^2 a^2)} \cos(2L\omega_0 t_0) - \frac{L^2 \eta' c_1^2 / v_A}{16(L^2+2)} > 0$$

Generally, we can find an approximate solution for the average $\bar{\delta}'$, the representation of which is the same as (A.16) except for the substitutions $\delta''|_{y=0}$, $\eta''|_{y=0}$, v_A^2 by $\bar{\delta}'$, $\bar{\eta}'$, \bar{v}_A^2 , where

$$\bar{\delta}' = \int_0^{Y_2} \delta' dy / Y_2, \quad \bar{\eta}' = \int_0^{Y_2} \eta' dy / Y_2, \quad \bar{v}_A^2 = v_A^2 \cdot \int_0^{Y_2} e^{-2ay} dy / Y_2.$$

From (A.16) it can be seen that δ' will grow exponentially, and that the shearing velocity c_1 acts like a "seed". If there is no "seed", the mushroom flow velocities (v_x , v_y) will never arise. The growth rate is independent of c_1 but depends on the Alfvén speed $v_A = B_0 / \sqrt{4\pi\rho}$. Therefore shear motion can induce linear MHD-instability. However this instability soon attains saturation, and the flow becomes quasi-steady and increases gradually until the velocities (v_x , v_y) exceed v_A .

Figure 1. (a) Sketch of a two-dimensional bipolar magnetic field that is subjected to a footpoint shearing motion as indicated by the arrows.

(b) Explicit bipolar magnetic topology prior to the shearing motion (see Equation (1)). The photospheric boundary extends to $|x| = 8.4 \times 10^3$ km in both directions from the origin. The vertical extent into the corona is to $y = 8 \times 10^3$ km. The positions $y = y_1, y_2, \dots, y_{10}$ indicate the vertical levels at which horizontal surveys will be shown of various physical quantities during the shearing motion at the footpoints.

Figure 2. Magnetic field line evolution as a function of time during induced footpoint shearing motion for Case (i): $\beta_0 = 15.4$ and the Alfvén time, $\tau_A = 1700$ s. The horizontal axis represents the distance from $x_1 \dots x_{22}$ as shown in Figure 1(b).

Figure 3. Vectorial velocity field, $(v_x^2 + v_y^2)^{1/2}$, as a function of time during induced footpoint shearing motion for Case (i): $\beta_0 = 15.4$; $\tau_A = 1700$ s.

Figure 4. Changes (relative to the initial local values) of density, temperature, and pressure at the end of the simulation (Case (i): $\beta_0 = 15.4$), $t = 3600$ s which is more than two Alfven time periods. The distributions are plotted along the entire horizontal scale of the domain and at various levels; Y_1 , Y_2 , Y_4 , Y_6 , and Y_{10} as shown in Figure 1b. All the values are normalized by a reference quantity as indicated.

Figure 5. Evolution of magnetic field lines and vectorial velocity fields at various times for Case (ii): $\beta_0 = 1.54$. The characteristic Alfven time for this case is $\tau_A = 174$ s.

Figure 6. Evolution of magnetic field lines and vectorial velocity fields at various times for Case (iii): $\beta_0 = 0.06$. The characteristic Alfven time for this case is $\tau_A = 35$ s.

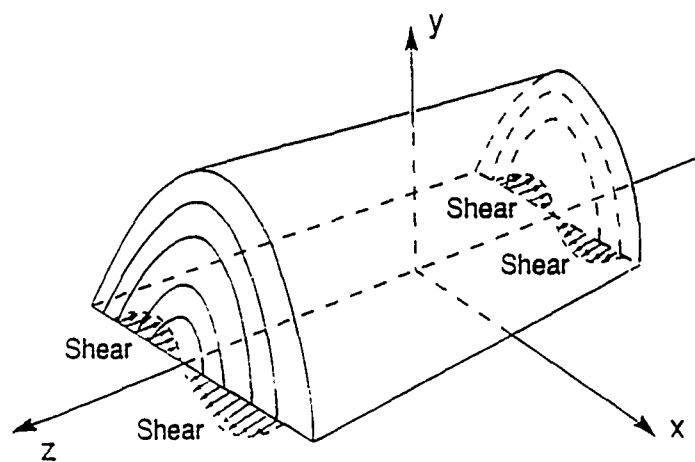
Figure 7. Maximum vectorial velocity that is representative of the upward vertical mass motion for Cases (i), (ii), and (iii). Note the change of scales. The representative Alfven times for the three cases ($\beta_0 = 15.4$, 1.54 , and 0.06 , respectively) are $\tau_A = 1700$ s, 174 s, and 35 s.

Figure 8. The total y -component of the Lorentz force per unit area at $t = 25$ s, 100 s, and 213 s and at various levels in the solar atmosphere ($y = y_1, y_2, \dots$ etc.). The representative Alfven time for case (iii) is 35 s. At $t = 100$ s (about $3\tau_A$) during the nonlinear stage of evolution, the Lorentz forces at the intermediate heights have a combination of upward and downward directions that causes magnetic field line pinching (see text). This pinch effect is more pronounced at $t = 213$ s (about $7\tau_A$) at lower altitudes. The horizontal axis represents the distance $x_1 \dots x_2$ as shown in Figure 1(b) also shown for Figures 2 - 6.

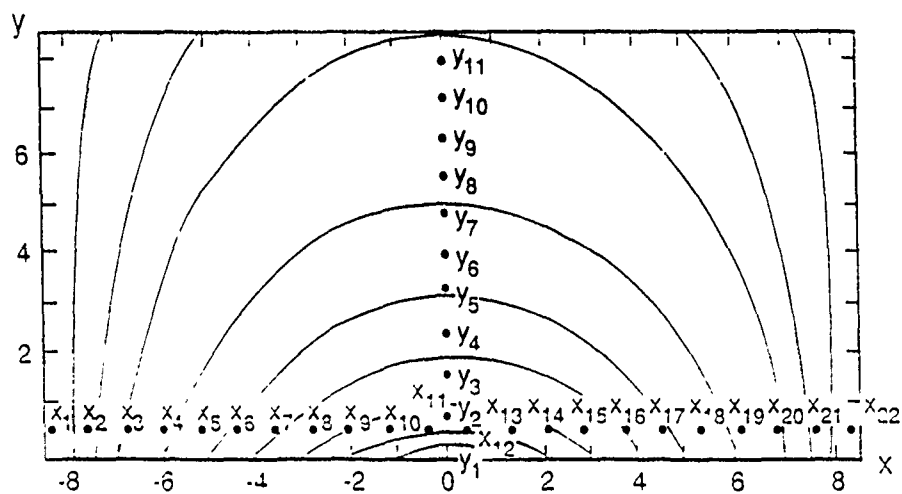
Figure 9. Scenario for the formation of an arch filament system (AFS) and upper level movement outward in the initial stage of a coronal mass ejection (CME) as a result of shear-induced instability.

Figure 10. Contours of pressure and density changes, $\Delta p/p_0$ and $\Delta \rho/\rho_0$, for case (ii) [$\beta_0 = 1.54$] at several times.

Figure 11. Behaviour of n' and n_1 . See Appendix (Equation A.12).



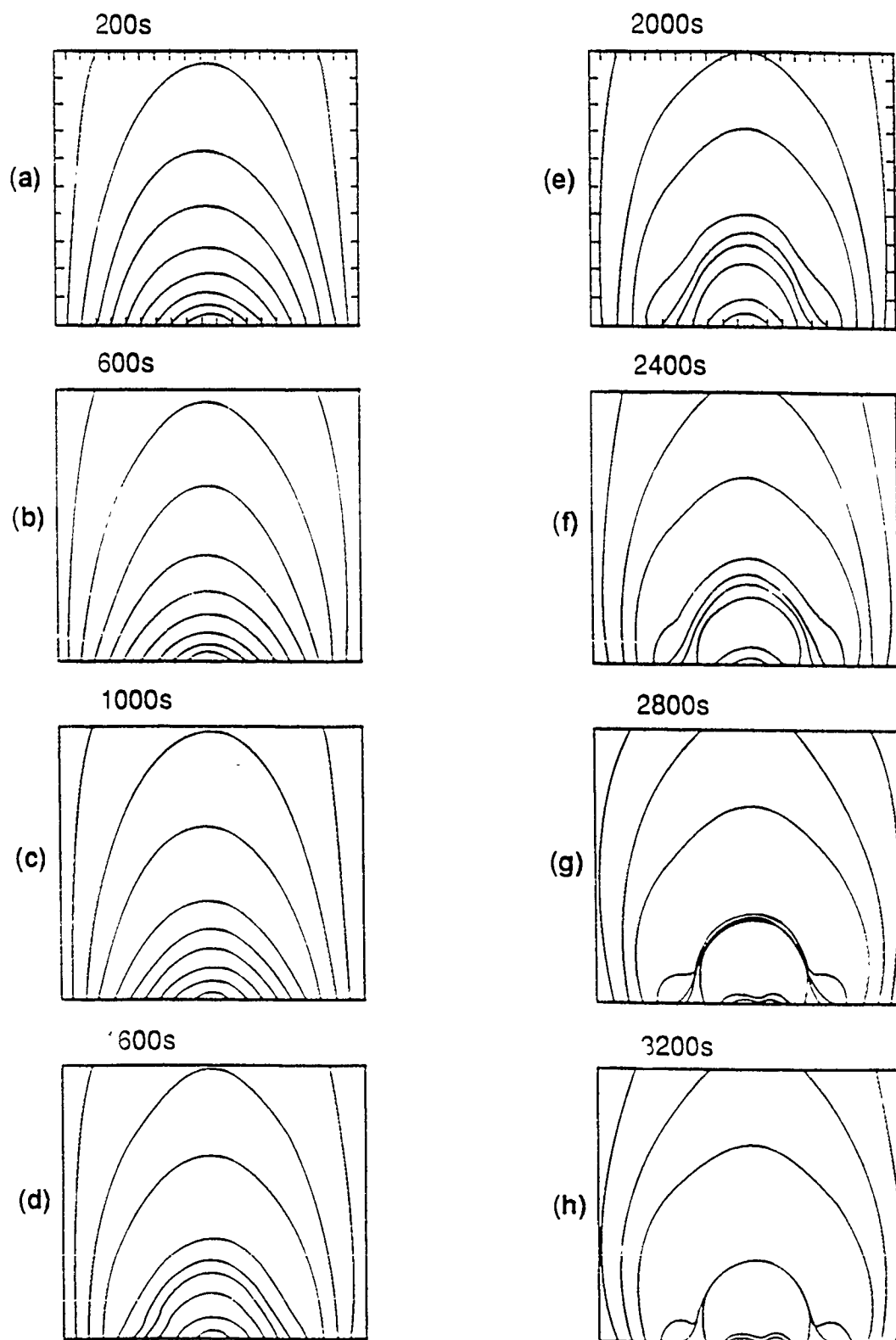
(a)



(b)

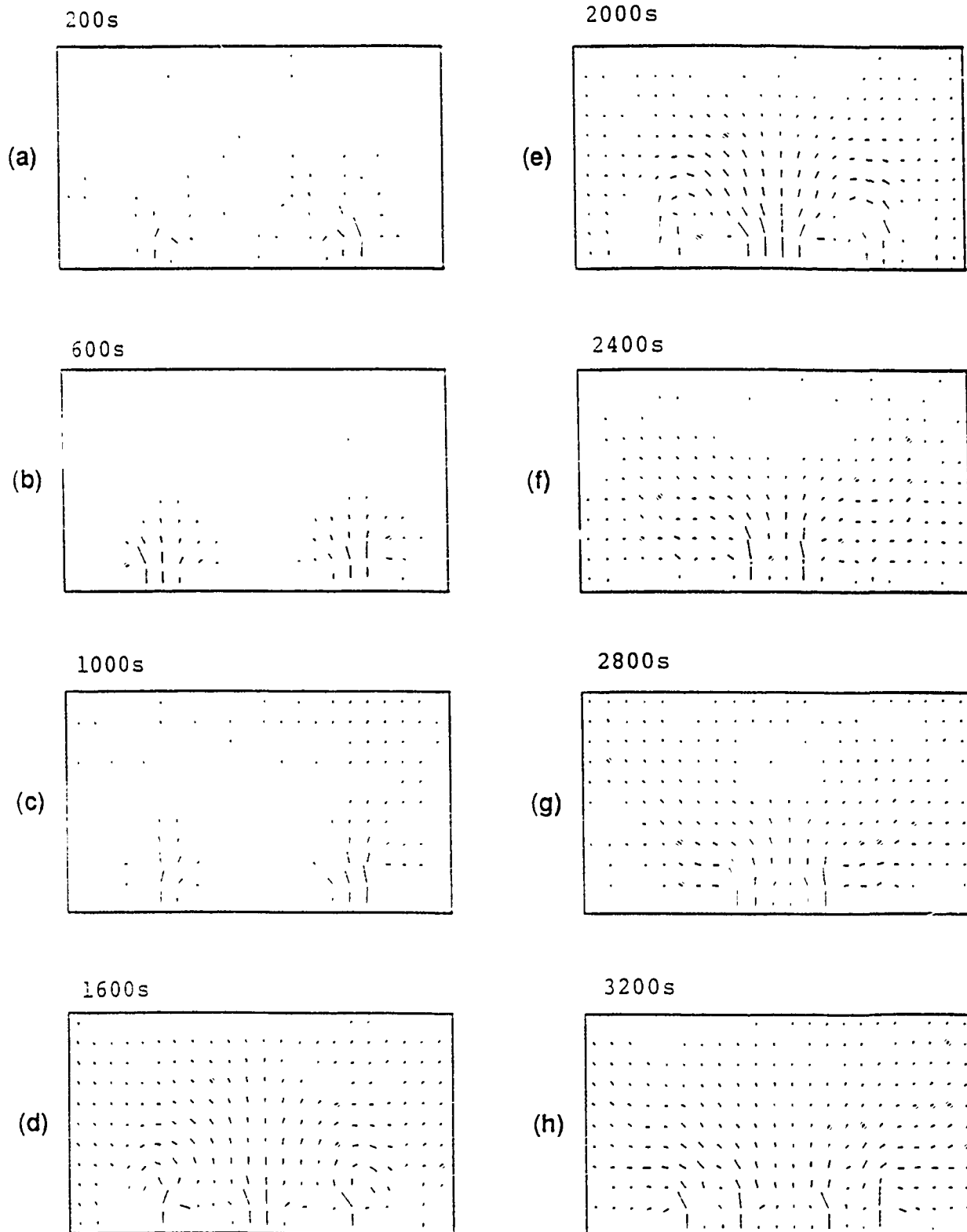
Figure 1

Figure 2



$\beta. \sim 15.4, \tau_a \sim 1700s$

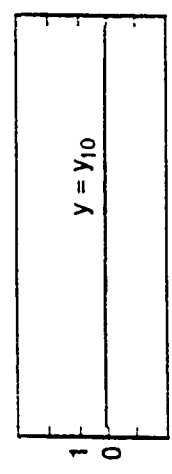
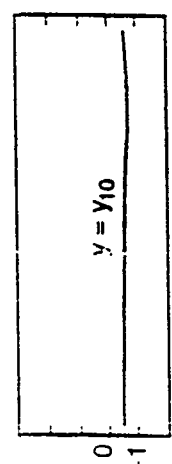
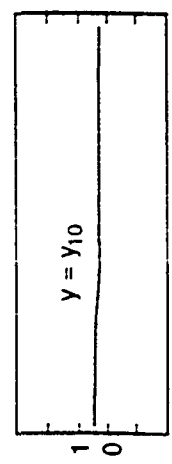
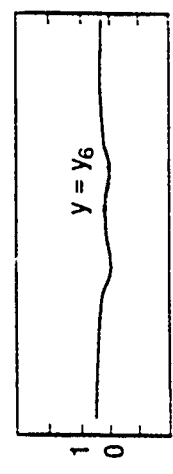
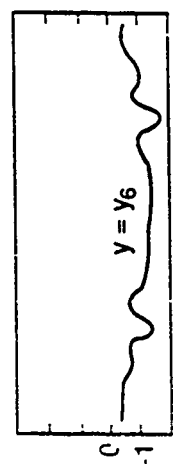
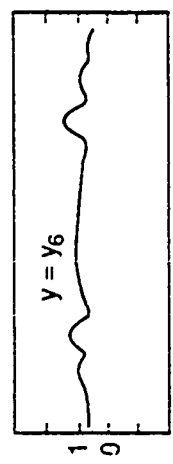
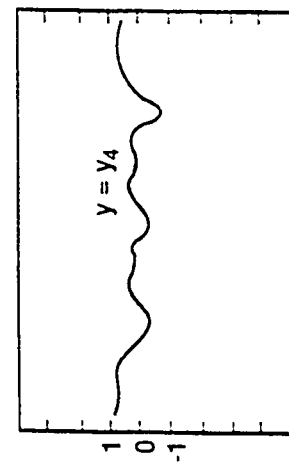
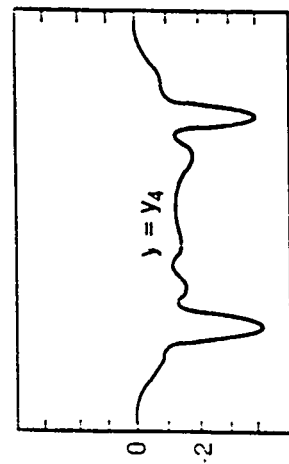
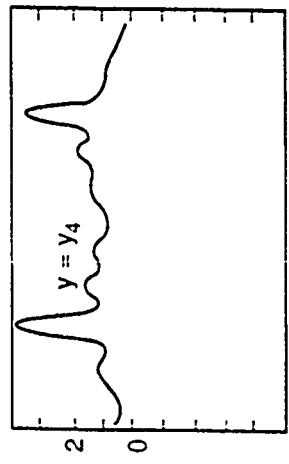
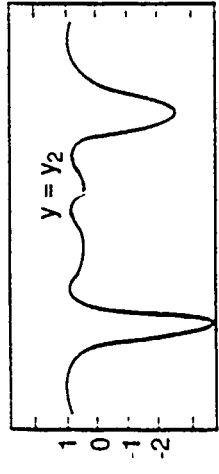
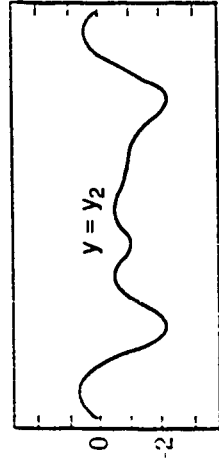
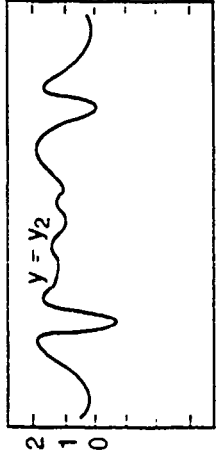
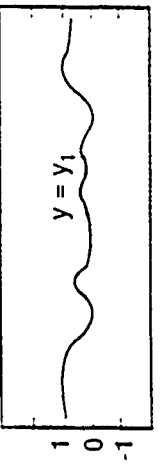
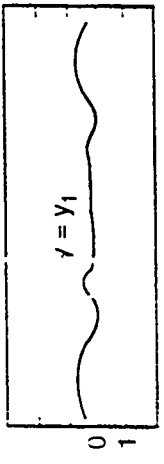
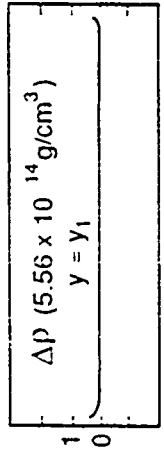
Figure 3



$\Delta\rho/\rho_0$ ($\rho_0 = 5.56 \times 10^{-14} \text{ g/cm}^3$)

$\Delta T/T_0$ ($T_0 = 4500 \text{ K}$)

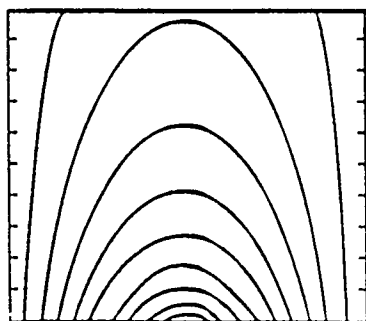
$\Delta p/p_0$ ($p_0 = 7.43 \times 10^1 \text{ dyne/cm}^2$)



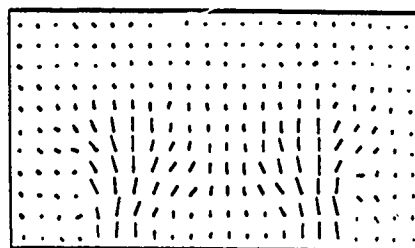
$$\beta_o = 1.54$$

Magnetic Field Line

Velocity

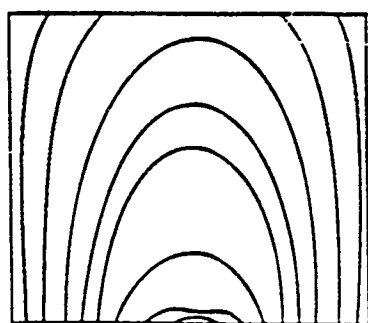


(a)

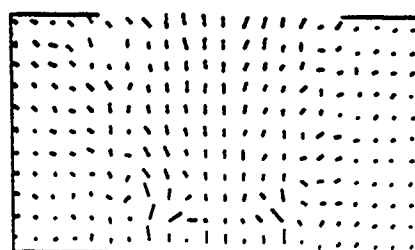


(d)

Time = 100 s

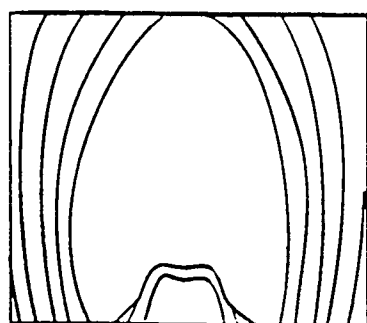


(b)

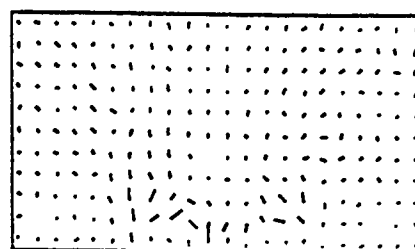


(e)

Time = 450 s



(c)



(f)

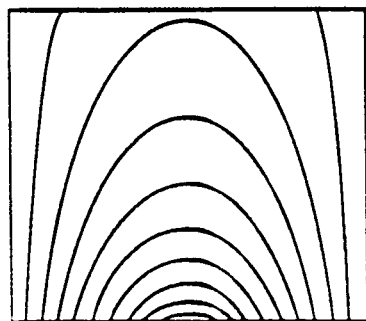
Time = 700 s

$$\beta_o = 0.06$$

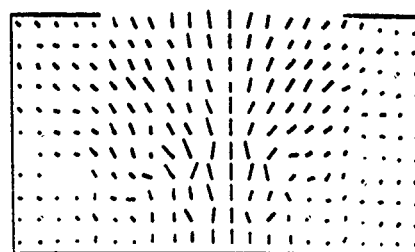
Magnetic Field Line

Velocity

Time = 75 s

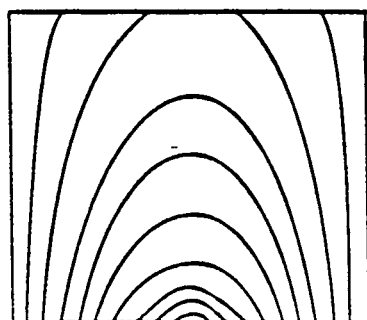


(a)

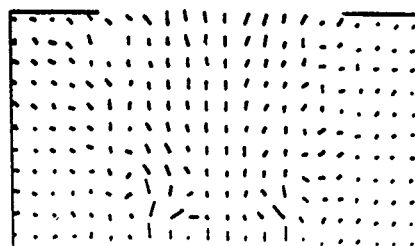


(d)

Time = 175 s

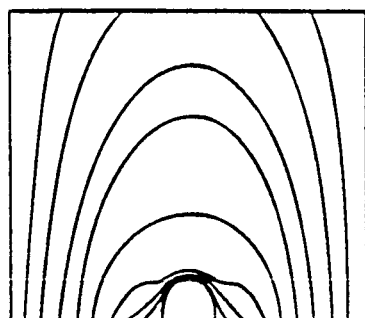


(b)

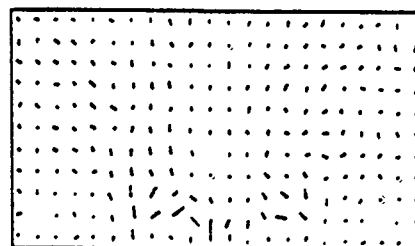


(e)

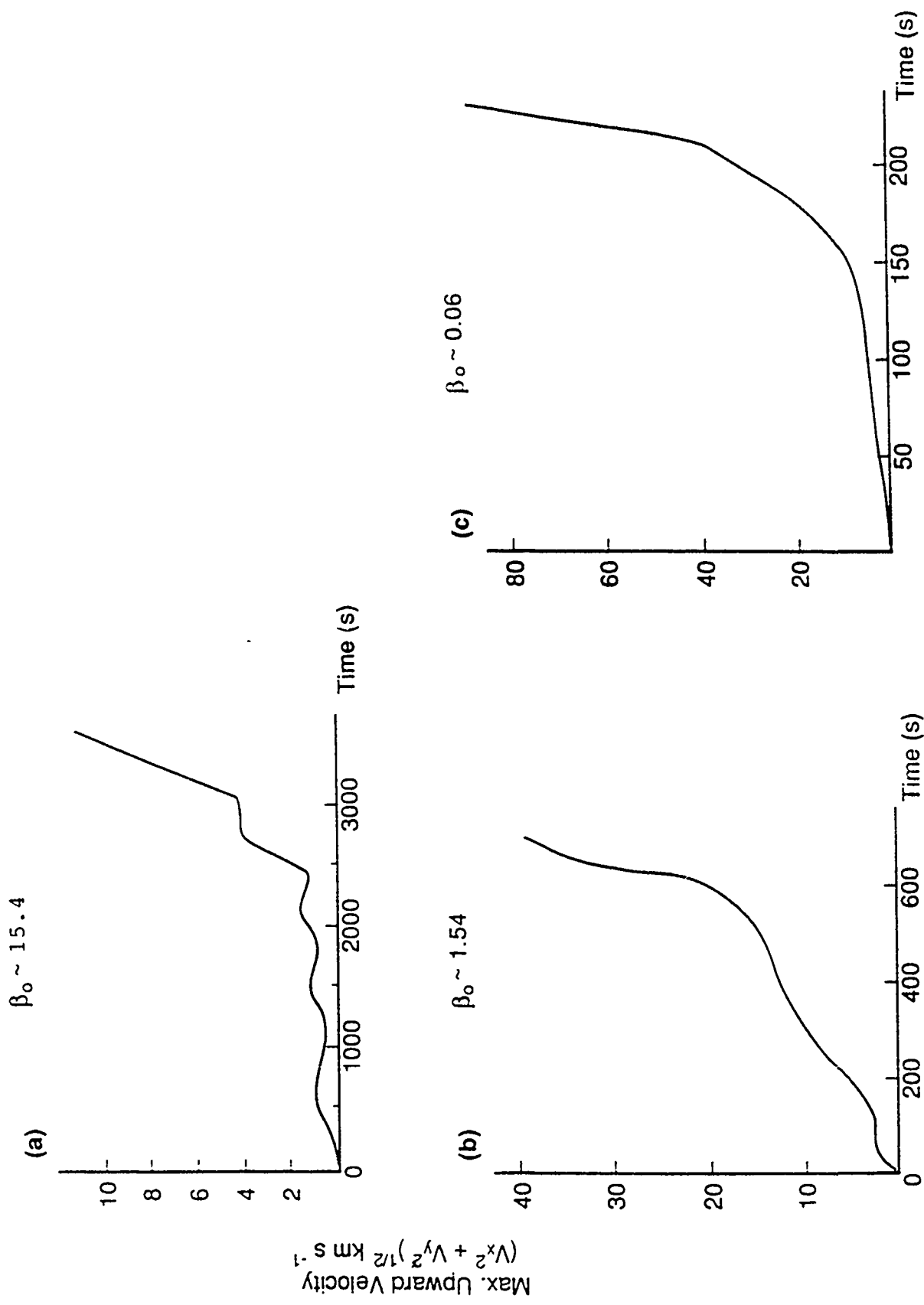
Time = 225 s



(c)

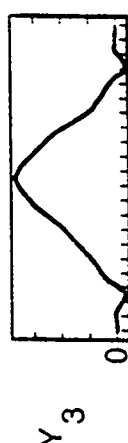
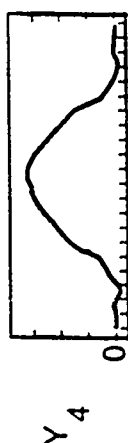
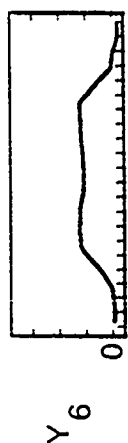
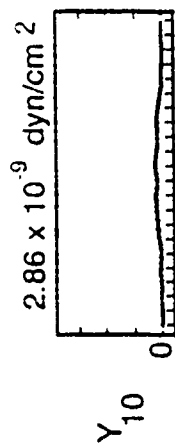


(f)

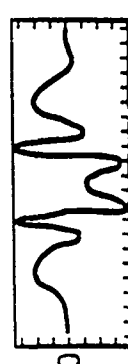
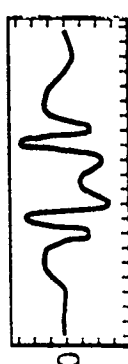
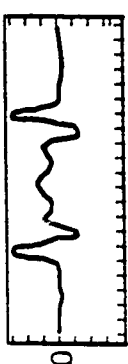
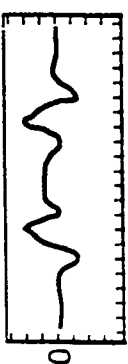
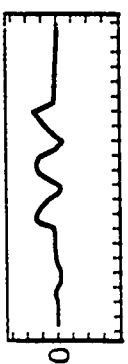
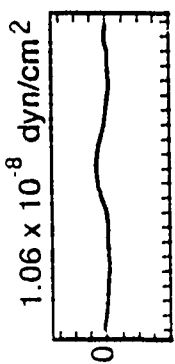


Total y - Component Lorentz Force $\frac{1}{C} [(J_Z B_X - J_X B_Z)]$ at Different Times

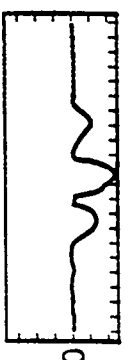
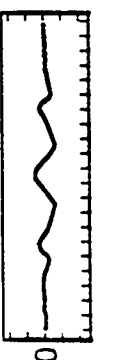
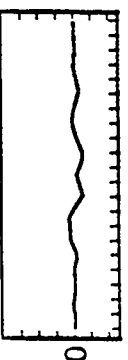
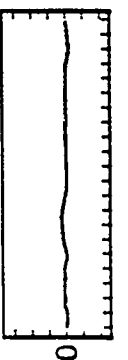
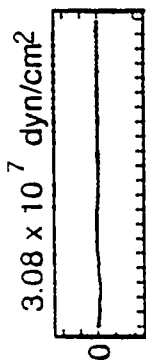
t = 25 s

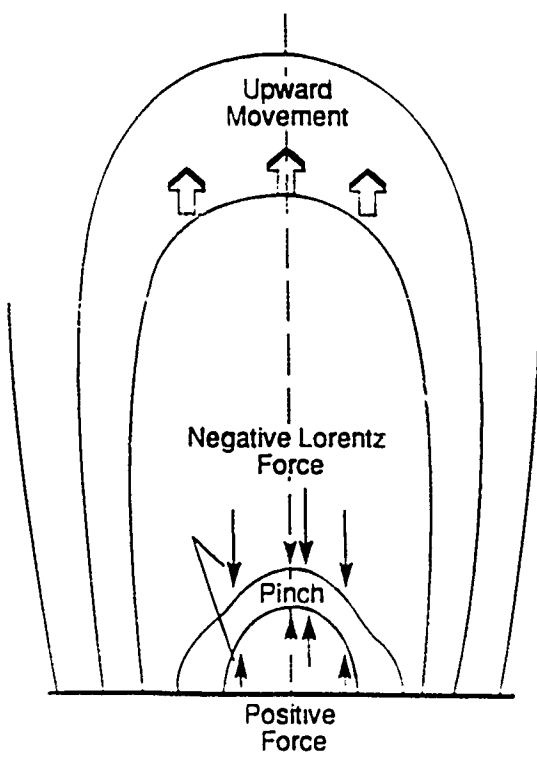


t = 100 s



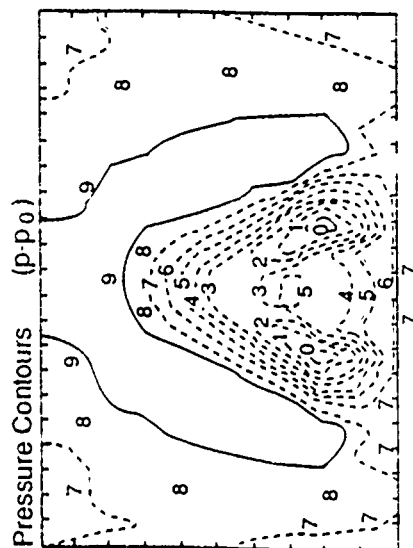
t = 213 s





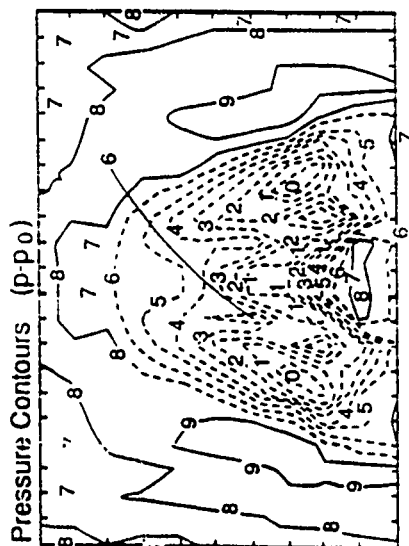
$$\beta_0 = 1.54$$

Time = 300 s



Broken Lines	Δp
0	-28.3×10^{-11} (dyne/cm ²)
1	-24.3×10^{-11} (dyne/cm ²)
2	-20.3×10^{-11} (dyne/cm ²)
3	-16.3×10^{-11} (dyne/cm ²)
4	-12.3×10^{-11} (dyne/cm ²)
5	-8.4×10^{-11} (dyne/cm ²)
6	-4.4×10^{-11} (dyne/cm ²)
7	-0.39×10^{-11} (dyne/cm ²)
8	3.6×10^{-11} (dyne/cm ²)
9	7.6×10^{-11} (dyne/cm ²)
10	11.6×10^{-11} (dyne/cm ²)

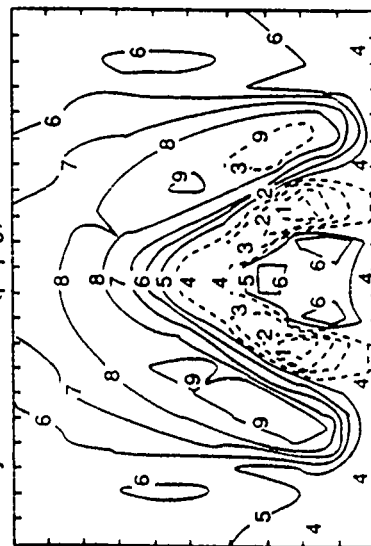
Time = 400 s



Broken Lines	Δp
0	-31.5×10^{-11} (dyne/cm ²)
1	-26.9×10^{-11} (dyne/cm ²)
2	-22.2×10^{-11} (dyne/cm ²)
3	-17.6×10^{-11} (dyne/cm ²)
4	-12.9×10^{-11} (dyne/cm ²)
5	-8.3×10^{-11} (dyne/cm ²)
6	-3.6×10^{-11} (dyne/cm ²)
7	$+1.0 \times 10^{-11}$ (dyne/cm ²)
8	5.7×10^{-11} (dyne/cm ²)
9	10.3×10^{-11} (dyne/cm ²)
10	15.0×10^{-11} (dyne/cm ²)

157

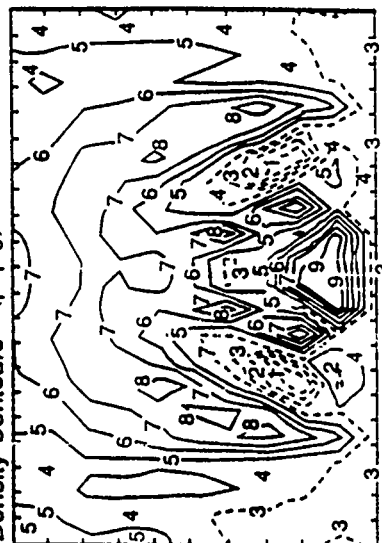
Density Contours (p-p₀)



Broken Lines	Δp
0	57.8×10^{-15} (g/cm ³)
1	-44.0×10^{-15} (g/cm ³)
2	-30.1×10^{-15} (g/cm ³)
3	-16.3×10^{-15} (g/cm ³)
4	-2.5×10^{-15} (g/cm ³)
5	11.3×10^{-15} (g/cm ³)
6	25.1×10^{-15} (g/cm ³)
7	38.9×10^{-15} (g/cm ³)
8	52.7×10^{-15} (g/cm ³)
9	66.5×10^{-15} (g/cm ³)
10	80.4×10^{-15} (g/cm ³)

(10a)

Density Contours (p-p₀)



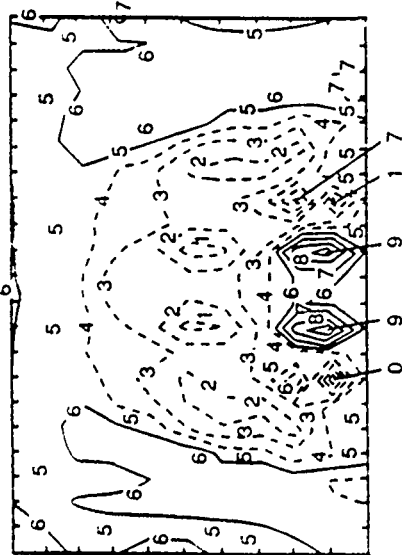
Broken Lines	Δp
0	-57.7×10^{-15} (g/cm ³)
1	-40.7×10^{-15} (g/cm ³)
2	-23.7×10^{-15} (g/cm ³)
3	-6.7×10^{-15} (g/cm ³)
4	10.3×10^{-15} (g/cm ³)
5	27.3×10^{-15} (g/cm ³)
6	44.3×10^{-15} (g/cm ³)
7	61.3×10^{-15} (g/cm ³)
8	78.2×10^{-15} (g/cm ³)
9	95.2×10^{-15} (g/cm ³)
10	112.2×10^{-15} (g/cm ³)

(10b)

$$\beta_0 = 1.54$$

Time = 500 s

Pressure Contours ($p-p_0$)

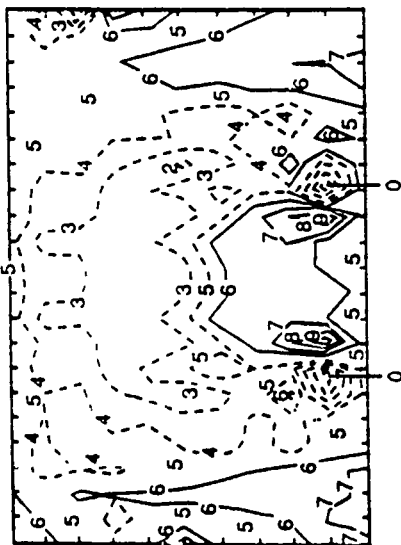


Δp

Broken Lines

Time = 600 s

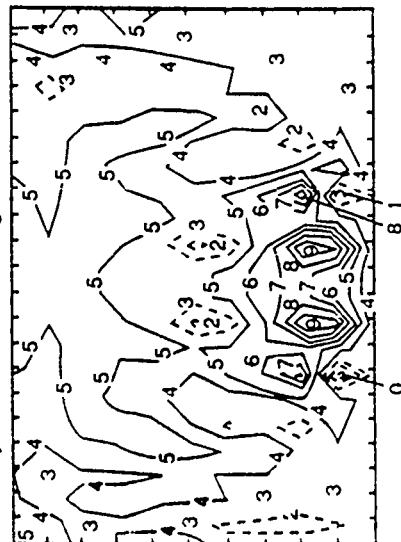
Pressure Contours ($p-p_0$)



Δp

Broken Lines

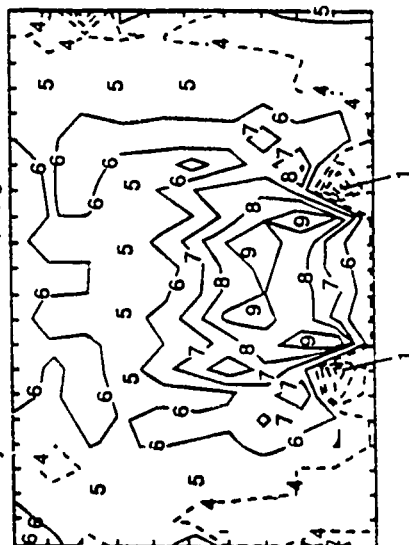
Density Contours ($\rho-\rho_0$)



$\Delta \rho$

Broken Lines

Density Contours ($\rho-\rho_0$)

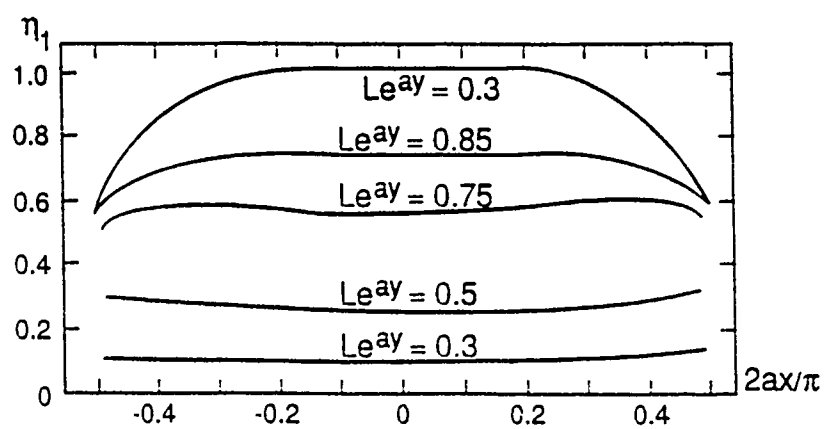
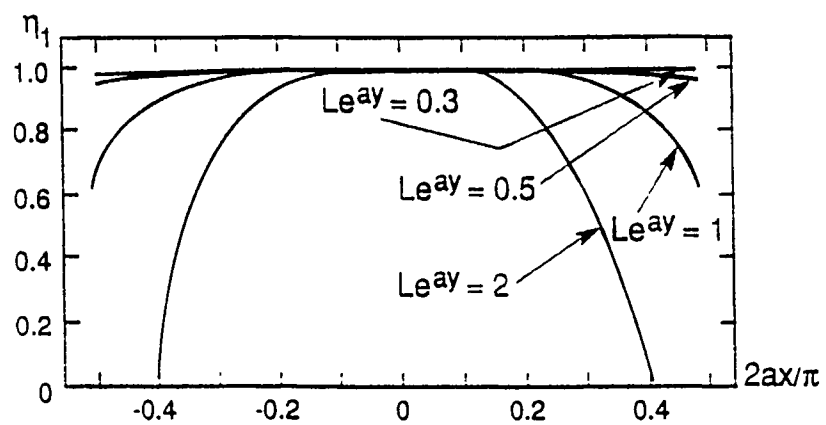


Δp

Broken Lines

(10c)

(10d)



MODEL CALCULATIONS OF RISING MOTIONS OF PROMINENCE LOOPS

Tyan Yeh

Space Environment Laboratory, NOAA Environmental Research Laboratories

Boulder, CO 80303, U.S.A.

and

S. T. Wu

Center for Space Plasma and Aeronomic Research, The University of Alabama in Huntsville

Huntsville, AL 35899, U.S.A.

Abstract. Model calculations are presented for the rising motion of the top section of a prominence loop, which is represented by a straight flux rope immersed in a coronal medium permeated with a bipolar magnetic field. Initially the prominence is at rest, in equilibrium with the surrounding coronal medium. When the magnetic monopoles that account for the source current for the bipolar field strengthen, the upward hydromagnetic buoyancy force overcomes the downward gravitational force so that the prominence is initiated into upward motion. The illustrative examples show that prominences can move away from the solar surface by the action of hydromagnetic buoyancy force if the disturbances are large.

SOLAR PHYSICS

Submitted June 1990

1. Introduction

A new dynamical model of prominence loops was recently constructed on the basis of the theory of hydromagnetic buoyancy force for flux ropes (Yeh, 1989). A prominence loop immersed in the solar atmosphere is regarded as an extraneous body, in the sense that it is magnetically separated from its surrounding medium. Thus, its magnetic field, mass density, temperature, and motion are quite different from those of the surrounding medium. The important feature is the polarization current induced on the periphery of the prominence that makes the ambient magnetic field tangential. The exertion of the ambient hydromagnetic pressure gives rise to the hydromagnetic buoyancy force. Its predominant constituent is the diamagnetic force which amounts to the force exerted on the currents in the prominence by the external currents that sustain the coronal magnetic field. For a prominence to be stationary in equilibrium with its surrounding medium, the hydromagnetic buoyancy force counterbalances the gravitational force exerted by the massive Sun. When the coronal magnetic field evolves, the changed diamagnetic force no longer matches the gravitational force. Once the forces become unbalanced, the prominence is initiated into motion. The evolving motion may be either upward or downward, depending on whether the hydromagnetic buoyancy force is greater or less than the gravitational force. That the evolving motion of prominence filaments is driven by the instability evolution of the global magnetic field has recently inferred from observations (Kahler et al., 1988).

In this paper we apply the dynamical theory to study the motion of the top section of a prominence loop arched above the solar surface. The calculation presented is mathematically one-dimensional in space (viz., the heliocentric distance) although it involves two dimensional geometry (see Figure 1). The governing equations for the dynamical evolution are MHD equations of motion supplemented with equations of mass conservation, flux conservation, and energy conservation. Since we are mainly interested in the dynamics of prominences, energetics is dealt with only to the extent necessary to provide a closed system of equations for the dynamics. Accordingly, in our present calculations we neglect all entropy-generating processes that are pertinent to the thermodynamics of prominences.

Several illustrative examples of dynamical evolution of a prominence loop are shown. First, we construct an equilibrium configuration for a prominence loop immersed in a coronal

medium that has a bipolar magnetic field permeated into a magnetohydrostatic atmosphere. For a prominence loop to be stationary, it must have neither translational motion as a whole nor expansional motion relative to its axis. The former requires that the downward pull of the gravitational force exerted by the Sun is counterbalanced by the upward lift of the hydromagnetic buoyancy force exerted by the surrounding coronal medium. The latter requires that the outward push of the pressure gradient due to the difference in internal and external gas pressures is counterbalanced by the inward pinch of the Lorentz force density due to the internal currents. Next, we calculate the motion of the prominence loop when the equilibrium is disturbed by the temporal change of the bipolar field. The change can be caused by strengthening and/or displacement of the magnetic monopoles for the bipolar field. These examples demonstrate that the prominence can move away from the solar surface when the disturbances are sufficiently large.

The model calculations illustrate the mechanism involving hydromagnetic buoyancy force that is likely important in the eruption of prominences. Such calculations in conjunction with analytical study also serve to narrow down the ranges of the parameters as an aid to MHD numerical simulations of the eruptive motion of prominences. Very often the difficulties with numerical simulations lie in the large number and extensive range of the pertinent parameters that characterize the phenomenon under study (Wu, 1988).

2. Assumptions

The geometry of the prominence loop may be described by its axis and its cross-section. We assume that the varying cross-section is well accounted for by a circular cross-section whose radius changes in time. In this treatment of the top section of a prominence loop, a prominence is represented by a flux rope with a straight axis, whose heliocentric distance may change. The corona is represented by a magnetized medium that has a transverse magnetic field, perpendicular to the axis of the prominence, which is bipolar and a longitudinal magnetic field, parallel to the axis, which varies with the heliocentric distance only. The current that produces the bipolar field is on the solar surface, to be accounted for by a couple of magnetic monopoles on the photosphere. These monopoles are chosen to be line monopoles to make the problem two-dimensional. The current that produces the longitudinal magnetic

field is in the corona. The coronal current is in magnetohydrostatic equilibrium with a stratified gas pressure of the gravitated coronal gas.

The prominence loop carries helical field lines. The helical magnetic field in the straight prominence is represented by

$$\mathbf{B}_E = \mathbf{i}_z B_0 \left(1 - \frac{q^2}{Q^2}\right)^{1/2} + \mathbf{i}_\phi \frac{1}{2} \mu J_0 q \quad (1)$$

in cylindrical coordinates (z, q, ϕ) , with the azimuthal angle ϕ measured from the radial line pointing downward (μ being the magnetic permeability in mks units). The axial component decreases from the axial value B_0 at the axis $q=0$ to zero at the boundary $q=Q$. The azimuthal component increases from zero at the axis to the boundary value $B_B \equiv \frac{1}{2} \mu J_0 Q$ at the boundary. The total axial flux is $\Psi_E \equiv \frac{2}{3} \pi Q^2 B_0$ and the total azimuthal flux is $\frac{1}{4} Q^2 \mu J_0$ per unit axial length. This helical field is produced by the current density

$$\mathbf{J}_E = \mathbf{i}_z J_0 + \mathbf{i}_\phi \mu^{-1} \frac{B_0}{Q} \frac{q/Q}{(1 - q^2/Q^2)^{1/2}} \quad (2)$$

which has an axial component that is uniform and an azimuthal component that increases from zero at the axis to infinity at the boundary. The total axial current is $I_E \equiv \pi Q^2 J_0$ and the total azimuthal current is $\mu^{-1} B_0$ per unit axial length. The Lorentz force density

$$\mathbf{J}_E \times \mathbf{B}_E = \mathbf{i}_q \left(\mu^{-1} \frac{B_0^2}{Q} - \frac{1}{2} \mu J_0^2 Q \right) \frac{q}{Q} \quad (3)$$

acting at various mass elements of the prominence is in the radial direction, perpendicular to the axis of the prominence loop. It increases from zero at the axis to $\mu^{-1} B_0^2/Q - \frac{1}{2} \mu J_0^2 Q$ at the boundary, in proportion to the radial distance. The axial current produces a pinching force toward the axis whereas the azimuthal current produces an anti-pinching force away from the axis.

The immersion of the prominence loop in the coronal medium incurs a polarization current that keeps the helical field lines separated from the external field lines of the corona. The induced current, which is concentrated in a thin peripheral layer by virtue of the high electrical conductivity of the solar plasma, produces a magnetic field that makes the ambient field tangential by cancelling the radial component of the coronal field on the interface and essentially doubling the azimuthal component there (Yeh, 1983). With the coronal mass density

p_∞ , the coronal gas pressure p_∞ , and the coronal magnetic field $\mathbf{B}_\infty \equiv \mathbf{1}_z B_{\infty z} + \mathbf{B}_{\infty \perp}$ pre-existing at the site of the prominence, the ambient magnetic field on the outer surface of the current layer is

$$\mathbf{B}_\Lambda(\phi) = \mathbf{1}_z B_{\infty z} \Big|_{q=Q} + \mathbf{1}_\phi 2(\mathbf{1}_\phi \cdot \mathbf{B}_{\infty \perp}) \Big|_{q=Q} + \mathbf{1}_\phi \frac{\mu I_E}{2\pi Q} \quad (4)$$

The boundary magnetic field on the inner surface is

$$\mathbf{B}_B(\phi) = \mathbf{1}_\phi \frac{\mu I_E}{2\pi Q} \quad (5)$$

The polarization current, given by $\mathbf{i}_p \equiv \mathbf{1}_q \times \mu^{-1}(\mathbf{B}_\Lambda - \mathbf{B}_B)$ per unit circumferential length, shields off the coronal field from permeating into the prominence. Across the massless layer of peripheral current the sum of gas pressure and magnetic pressure is invariant. The ambient gas pressure

$$p_\Lambda(\phi) = p_\infty \Big|_{q=Q} \quad (6)$$

on the outer surface is essentially equal to the pre-existing coronal gas pressure at the periphery since the gas pressure in the external region is hardly perturbed by the intrusion of the prominence. The boundary gas pressure

$$p_B(\phi) = p_\infty \Big|_{q=Q} + \frac{1}{2} \mu^{-1} B_{\infty z}^2 \Big|_{q=Q} + 2 \mu^{-1} B_{\infty \perp}^2 \Big|_{q=Q} \cos^2 \phi + \frac{I_E}{\pi Q} B_{\infty \perp} \Big|_{q=Q} \cos \phi \quad (7)$$

on the inner surface has a circumferential inhomogeneity which is spatially transformed from that of the ambient hydromagnetic pressure. The gas pressure inside the prominence is well represented by

$$p_E(q, \phi) = \left[p_0 - \left(p_\infty + \frac{1}{2} \mu^{-1} B_{\infty z}^2 \right) \Big|_{q=Q} \right] \left(1 - \frac{q^2}{Q^2} \right) + p_\infty(q, \phi) + \frac{1}{2} \mu^{-1} B_{\infty z}^2(q, \phi) + \mu^{-1} B_{\infty \perp}^2(q, \phi) + \mu^{-1} B_{\infty \perp}^2 \Big|_{q=0} \left(2 \frac{q^2}{Q^2} \cos^2 \phi - 1 \right) + \mu^{-1} \left(B_{\infty z}^2 \Big|_{q=Q} - B_{\infty z}^2 \Big|_{q=0} \right) \frac{q^2}{Q^2} \cos 2\phi + \frac{I_E}{\pi Q^2} B_{\infty \perp} \Big|_{q=Q} q \cos \phi \quad (8)$$

It varies from the axial value p_0 at the axis to the boundary value p_B . The gradient of this gas pressure yields the force density

$$-\nabla p_E = -\nabla \left(p_\infty + \frac{1}{2} \mu^{-1} B_{\infty z}^2 + \frac{1}{2} \mu^{-1} B_{\infty \perp}^2 \right) + \mathbf{1}_r \frac{I_E B_{\infty \perp}}{\pi Q^2} \Big|_{r=r_1} + \mathbf{1}_q \frac{2p_0 - \left(2p_\infty + \mu^{-1} B_{\infty z}^2 \right) \Big|_{r=r_1}}{Q} \frac{q}{Q}, \quad (9)$$

ignoring insignificant terms. The force term proportional to q/Q represents a radial force

density that results from the difference between the internal gas pressure and the circumferential average of the external hydromagnetic pressure. The other terms, resulting from the circumferential inhomogeneity of the ambient hydromagnetic pressure, represent the spatial spreading or the hydromagnetic buoyancy force, the latter amounts to $I_r \rho_\infty GM_\odot / r_0^2 + I_r \Gamma \mu^{-1} B_{\infty L}^2 / R_\odot + I_E \times B_\infty / \pi Q^2$ by virtue of the magnetohydrostatic state of the coronal medium (see Equations (27) and (21)). The coefficient Γ has the value of 2 in the above elucidation.

The prominence moves with the velocity

$$u_E = I_r u_0 + I_q V \frac{q}{Q} \quad (10)$$

which consists of a translational velocity common to all mass elements of the prominence loop and an expansional velocity proportional to the distance from the axis. The translational motion is driven by the part of the force density that is uniform and the expansional motion is driven by the part of the force density that is in various radial directions. The former part includes the gravitational force exerted by the Sun and the hydromagnetic buoyancy force exerted by the surrounding medium. The latter part includes the Lorentz force that results from the interaction among the internal currents inside the prominence and the gradient force that results from the difference in the internal and external gas pressures.

The dynamical evolution of the prominence depends on its inertia. We assume that the mass density is uniform over the cross-section, ignoring the higher-order effect of the spatial variation of the mass distribution. The value of mass density ρ_E may change in time.

3. Governing Equations

A prominence which is located initially equidistant from the two magnetic monopoles will remain so when its heliocentric distance changes temporally. The prominence loop is characterized by eight parameters: r_0 , Q , u_0 , V , ρ_E , B_0 , J_0 , and p_0 .

The characterizing parameters evolve in accordance with the differential equations:

$$\frac{d}{dt} r_0 = u_0 \quad (11)$$

$$\frac{d}{dt} Q = V \quad (12)$$

$$\rho_E \frac{d}{dt} u_0 = -\rho_E \frac{GM_\odot}{r_0^2} + \rho_\infty \frac{GM_\odot}{r_0^2} + J_0 B_{\infty L} + \Gamma \frac{\mu^{-1} B_{\infty L}^2}{R_c} , \quad (13)$$

$$\rho_E \frac{d}{dt} V = \frac{2p_0 + \mu^{-1} B_0^2}{Q} - \frac{2p_\infty + \mu^{-1} B_{\infty L}^2 + \frac{1}{2} \mu J_0^2 Q^2}{Q} , \quad (14)$$

supplemented by the temporal invariances of the total mass, the axial magnetic flux, the azimuthal magnetic flux, and the total thermal energy:

$$\pi Q^2 \rho_E = M_E , \quad (15)$$

$$\frac{2}{3} \pi Q^2 B_0 = \Psi_E , \quad (16)$$

$$\frac{1}{2} Q^2 J_0 = \frac{1}{2\pi} I_E , \quad (17)$$

$$\frac{3}{2} \pi Q^2 \left[\frac{1}{2} p_0 + \frac{1}{2} \left(p_\infty + \frac{1}{2} \mu^{-1} B_{\infty L}^2 \right) \right] = E_E . \quad (18)$$

For a prominence to be initially in stationary equilibrium with the surrounding coronal medium the requisite current density is

$$J_0 = \frac{\rho_E - \rho_\infty}{B_{\infty L}} \frac{GM_\odot}{r_0^2} - \Gamma \frac{\mu^{-1} B_{\infty L}}{R_c} \quad (19)$$

in terms of the mass density (or the requisite ρ_E in terms of the current density) and other quantities. The requisite magnetic field is

$$B_0 = \pm \left(2\mu p_\infty + B_{\infty L}^2 + \frac{1}{2} \mu^2 J_0^2 Q^2 - 2\mu p_0 \right)^{1/2} \quad (20)$$

(in either direction) in terms of the gas pressure (or the requisite p_0 in terms of the magnetic field) and other quantities. The first constraint makes the upward hydromagnetic buoyancy force counterbalance the downward gravitational force. The second constraint makes the outward forces due to the gas pressure and the axial magnetic field of the prominence counterbalance the inward forces due to the hydromagnetic pressure of the ambient medium and the axial current of the prominence.

4. Coronal Medium

We choose the line monopoles for the bipolar magnetic field to have the strengths $\pm \Psi_M$ and an angular separation of $2\theta_M$, subtended at the center of the Sun. The two line mono-

poles produce the bipolar magnetic field

$$B_{\infty L} = 1_n B_{\infty L} \quad (21)$$

in the midplane between them. Its direction, from the positive monopole to the negative monopole, is perpendicular to the midplane. Its magnitude is

$$B_{\infty L} = \frac{\Psi_M}{\pi} \frac{R_\odot \sin \theta_M}{r^2 - 2r R_\odot \cos \theta_M + R_\odot^2} \quad (22)$$

at a heliocentric distance of r . There, the associated magnetic pressure has the gradient

$$-\nabla_{\frac{1}{2}} \mu^{-1} B_{\infty L}^2 = 1_r \frac{\mu^{-1} B_{\infty L}^2}{R_c} \quad (23)$$

in the vertical direction, with the radius-of-curvature

$$R_c = \frac{1}{2} \frac{r^2 - 2r R_\odot \cos \theta_M + R_\odot^2}{r - R_\odot \cos \theta_M} \quad (24)$$

for the circular field line. (By virtue of the current-freeness of the bipolar field, the gradient force of its magnetic pressure is exactly opposite to its tensile force density.) This magnetic pressure gradient is enhanced by a factor

$$\Gamma = \frac{2}{(1 - Q^2/q_M^2) [(1 - Q^2/q_M^2)^2 + 4(Q^2/q_M^2) \sin^2 \phi_M]} \quad (25)$$

by the polarization current

$$i_p = 1_z \mu^{-1} B_{\infty L} \frac{2q_M^2(Q^2 + q_M^2) \cos \phi - 4Qq_M^3 \cos \phi_M}{[Q^2 - 2Qq_M \cos(\phi - \phi_M) + q_M^2][Q^2 - 2Qq_M \cos(\phi + \phi_M) + q_M^2]} \quad (26)$$

Here $q_M \equiv (r_0^2 - 2r_0 R_\odot \cos \theta_M + R_\odot^2)^{1/2}$ is the distance from the prominence to either monopole and $\phi_M \equiv \sin(R_\odot \sin \theta_M / q_M)$ is the azimuthal angle for the monopole. The field strength $B_{\infty L}$ increases with Ψ_M and maximizes when $\cos \theta_M$ is equal to $2rR_\odot / (r^2 + R_\odot^2)$. In terms of the field strength on the solar surface midway between the two monopoles, the monopole strength has the value

$$\Psi_M = 2\pi \frac{1 - \cos \theta_M}{\sin \theta_M} R_\odot B_{\infty L} \Big|_{r=R_\odot} \quad (27)$$

The monopole strength Ψ_M and the separation angle θ_M may undergo temporal changes.

We choose the longitudinal magnetic field

$$B_{\infty 1} = 1_7 B_{\infty 1} \quad (28)$$

produced by the coronal current to be horizontal. The associated current density is $1_7 \mu^{-1} dB_{\infty 1} / dr$. It provides a magnetic force in the force balance

$$-\frac{d}{dr} \left(p_{\infty} + \frac{1}{2} \mu^{-1} B_{\infty 1}^2 \right) = \rho_{\infty} \frac{GM_{\odot}}{r^2} \quad (29)$$

between the gravitational force and the gradient of hydromagnetic pressure. In addition to the equation of force balance, two more constraints are needed in order to determine the vertical variation of the coronal mass density, gas pressure, and longitudinal magnetic field. We shall assume that the gas pressure varies in proportion to the mass density and the magnetic pressure varies in proportion to the gas pressure, viz.,

$$p_{\infty} = KT_{\infty} \rho_{\infty} \quad (30)$$

$$B_{\infty 1}^2 = \frac{B_{\infty 1}^2|_{r=R_{\odot}}}{p_{\infty}|_{r=R_{\odot}}} p_{\infty} \quad (31)$$

These assumptions ensure that the pressure and mass density decrease with the heliocentric distance. The constant T_{∞} signifies the coronal temperature (K being the gas constant for the solar plasma). These assumptions allow us to calculate the mass density by numerical integration of the differential equation

$$\frac{d}{dr} \rho_{\infty} = - \frac{1}{1 + \frac{1}{2} \mu^{-1} B_{\infty 1}^2|_{r=R_{\odot}} / p_{\infty}|_{r=R_{\odot}}} \frac{GM_{\odot}}{KT_{\infty}} \frac{\rho_{\infty}}{r^2} \quad (32)$$

from the solar surface.

5. Conditions for Upward and Outward Accelerations

For the translational motion to have an upward acceleration away from the Sun, the hydromagnetic buoyancy force must overcome the gravitational force. The former will exceed the latter if the bipolar field is sufficiently large so that

$$B_{\infty L} > \frac{1}{\frac{1}{2} + \left[\frac{1}{4} + \Gamma \mu^{-1} G M_{\odot} (\rho_E - \rho_{\infty}) / r_0^2 J_0^2 R_c \right]^{1/2}} \frac{G M_{\odot}}{r_0^2} \frac{\rho_E - \rho_{\infty}}{J_0} \quad (33)$$

On the other hand, for the expansional motion to have an outward acceleration away from the axis, the outward force must overcome the inward force. The former will exceed the latter if the surrounding medium has a hydromagnetic pressure sufficiently small so that

$$p_{\infty} + \frac{1}{2} \mu^{-1} B_{\infty L}^2 < p_0 + \frac{1}{2} \mu^{-1} B_0^2 - \frac{1}{4} \mu J_0^2 Q^2 \quad (34)$$

Upon the use of the equilibrium values at $t=0$ and the conservation invariants, the condition for an upward acceleration can be written

$$B_{\infty L} > B_{\infty L} \Big|_{t=0} \left(\frac{r_0|_{t=0}}{r_0} \right)^2 \frac{1 - (\rho_{\infty}/\rho_E|_{t=0})(Q/Q|_{t=0})^2}{1 - \rho_{\infty}|_{t=0}/\rho_E|_{t=0}} \quad (35)$$

if we ignore the higher-order part of the diamagnetic force associated with the pre-existing gradient of the coronal magnetic pressure. The condition for an outward acceleration can be written

$$p_{\infty} + \frac{1}{2} \mu^{-1} B_{\infty L}^2 < \left\{ p_{\infty}^* \Big|_{t=0} + \frac{1}{2} \mu^{-1} B_{\infty L}^2 \Big|_{t=0} + \frac{1}{4} \mu^{-1} B_0^2 \Big|_{t=0} \left[\left(\frac{Q|_{t=0}}{Q} \right)^{2/3} - 1 \right] + \frac{1}{8} \mu J_0^2 \Big|_{t=0} Q^2 \Big|_{t=0} \left[1 - \left(\frac{Q}{Q|_{t=0}} \right)^{4/3} \right] \right\} \left(\frac{Q|_{t=0}}{Q} \right)^{2+4/3} \quad (36)$$

It follows from the inequality (35) that in the region where ρ_{∞} is small, the translational motion will have an upward acceleration when the encountered bipolar magnetic field $B_{\infty L}(t)$ is not less than its initial value by a factor of $(r_0|_{t=0}/r_0)^2$. On the other hand, it follows from the inequality (36) that the expansional motion will have an outward acceleration in the region where $p_{\infty} + \frac{1}{2} \mu^{-1} B_{\infty L}^2$ is less than its initial value when $Q(t)$ is less than $Q|_{t=0}$ and in the region where $p_{\infty} + \frac{1}{2} \mu^{-1} B_{\infty L}^2$ is sufficiently less than its initial value when $Q(t)$ is greater than $Q|_{t=0}$.

6. Numerics

In mks units, the magnetic permeability has the value $\mu = 4\pi \times 10^{-7} \text{ T}^2 \text{ m}^3/\text{J}$, the gravitational constant times solar mass has the value $G M_{\odot} = (6.67 \times 10^{-11} \text{ N} \cdot \text{m}^2/\text{kg}^2) \times (1.99 \times 10^{30})$

kg), and the gas constant for the proton-electron plasma has the value $K = (1.38 \times 10^{-23} \text{ J/deg}) \div \frac{1}{2}(1.67 \times 10^{-27} \text{ kg} + 9.11 \times 10^{-31} \text{ kg})$. To facilitate the numerics, we choose to measure time, length, and magnetic field in the units of one hour, one helioradius, and one gauss, respectively, viz., $t_{\text{ref}} = 3.6 \times 10^3 \text{ s}$, $r_{\text{ref}} = 6.96 \times 10^8 \text{ m}$, and $B_{\text{ref}} = 10^{-4} \text{ T}$. We further choose to measure speed, mass density, pressure, current density, and temperature in the units of $r_{\text{ref}}/t_{\text{ref}}$, $(\mu^{-1} B_{\text{ref}}^2)(r_{\text{ref}}/t_{\text{ref}})^2$, $\mu^{-1} B_{\text{ref}}^2$, $\mu^{-1} B_{\text{ref}}/r_{\text{ref}}$, and $(r_{\text{ref}}/t_{\text{ref}})^2/K$. Namely, $u_{\text{ref}} = 193.3 \text{ km/s}$, $\rho_{\text{ref}} = 2.129 \times 10^{-13} \text{ kg/m}^3$ (corresponding to $1.274 \times 10^8 \text{ electrons/cm}^3$), $p_{\text{ref}} = 7.958 \times 10^{-3} \text{ J/m}^3$, $J_{\text{ref}} = 1.143 \times 10^{-7} \text{ A/m}^2$, and $T_{\text{ref}} = 2.263 \times 10^6 \text{ deg}$.

In these normalized units, both the magnetic permeability, given by $(4\pi \times 10^{-7} \text{ T}^2 \text{ m}^3/\text{J})/(B_{\text{ref}}/J_{\text{ref}} r_{\text{ref}})$, and the gas constant, given by $(1.65 \times 10^4 \text{ J/kg/deg})/(u_{\text{ref}}^2/r_{\text{ref}})$, have the numerical value of unity whereas the gravitational constant times solar mass has the numerical value of $5.102 \text{ helioradius}^3/\text{hour}^2$, given by $(1.333 \times 10^{20} \text{ m}^3/\text{s}^2)/(r_{\text{ref}} u_{\text{ref}}^2)$.

7. Illustrative Examples

For the magnetohydrostatic coronal atmosphere, we choose a mass density of $3 \times 10^7 \text{ electrons/cm}^3$, a temperature of $2 \times 10^6 \text{ }^\circ\text{K}$ (hence $T_\infty = 0.8838$) and a longitudinal magnetic field of 2 gauss at the solar surface. For the magnetic monopoles, to have a transverse magnetic field of 10 gauss at the solar surface midway between the two monopoles, we choose

$$\Psi_M = 5.497 \text{ gauss} \cdot \text{helioradius}, \quad \theta_M = 10^\circ.$$

The calculated profiles are shown in Figure 2.

For a stationary prominence loop, we choose a height of $5 \times 10^4 \text{ km}$, a radius of $2 \times 10^4 \text{ km}$, a mass density of $5 \times 10^{11} \text{ electrons/cm}^3$, and a temperature of $5 \times 10^4 \text{ }^\circ\text{K}$ so that:

$$r_0 = 1.0718, \quad Q = 0.02874, \quad \rho_0 = 3924.2, \quad p_0 = 86.704.$$

At the site where the prominence resides we have

$$\rho_\infty = 16.535, \quad p_\infty = 14.614, \quad B_{\infty||} = 1.676, \quad B_{\infty\perp} = 8.054.$$

The conditions of force balance require:

$$J_0 = 2080.9, \quad B_0 = 40.574.$$

In other words, for the prominence loop to be in stationary equilibrium with the surrounding medium, it must carry a total axial current I_E of 3.0×10^{11} amperes and carry an azimuthal current that sustains a total axial magnetic flux Ψ_E of 3.4×10^{12} webers. These values are within the ranges of typical values for quiescent prominences (Tandberg-Hanssen, 1974). It is seen from

$$\rho_E \frac{GM_0}{r_0^2} = 17428.7, \quad \rho_\infty \frac{GM_0}{r_0^2} = 73.61, \quad \frac{I_E B_\infty}{\pi Q^2} = 16759.7, \quad \Gamma \frac{\mu^{-1} B_\infty^2}{R_c} = 595.4$$

that the gravitational force is largely counterbalanced by the zeroth-order diamagnetic force (due to the prominence current). The hydrostatic buoyancy force is very small, accounting for only 0.42%. Even the higher-order part of the diamagnetic force (due to the inhomogeneity of the coronal magnetic field) is small, only 3.55% of the zeroth-order part. On the other hand, it is seen from

$$P_0 = 86.704, \quad \frac{1}{2} \mu^{-1} B_0^2 = 823.14, \quad \frac{1}{4} \mu J_0^2 Q^2 = 893.82, \quad p_\infty = 14.615, \quad \frac{1}{2} \mu^{-1} B_\infty^2 = 1.405$$

that the pinching force of the axial current is largely counterbalanced by the anti-pinching force of the azimuthal current and to a less extent by the internal gas pressure. The ambient hydromagnetic pressure provides only a very small pinching. To facilitate comparison, these values may be translated to $(2\mu p_\infty)^{1/2} = 5.4063$ gauss, $\frac{1}{2} \mu J_0 Q = 29.903$ gauss, and $(2\mu p_0)^{1/2} = 13.168$ gauss. The plasma beta at the axis is 0.1053. The transverse projection of the field lines in the equilibrium configuration is as shown in Figure 1. With the ratio $\mu I_E / \Psi_M = 0.9684$, the bipolar field has two neutral points located at $q = 0.187$, $\phi = \pm 118.7^\circ$. Figure 3 shows the peripheral distribution of the polarization current with $q_M = 0.194$ and $\phi_M = 63.4^\circ$. It flows in the direction of the prominence current in the lower periphery $|\phi| < 82.6^\circ$ and flows in the opposite direction in the upper periphery. It is zero at the two points where the two neutral points would be located in the case I_E happens to be zero. Of course, the total polarization current sums up to zero.

Now, we consider the motion of the prominence loop when the equilibrium is disturbed. We consider motions caused by temporal changes of the bipolar magnetic field due to the strengthening of the monopoles. Figure 4 shows the evolution caused by

$$\frac{d}{dt} \Psi_M = 20.0 \text{ gauss} \cdot \text{helioradius}/\text{hour} \quad \text{for } 0 < t < 10 \text{ hours} .$$

The initial increase in the bipolar field makes the hydromagnetic buoyancy force exceed the gravitational force, so that the prominence rises from its equilibrium position. The prominence keeps moving upward, even during $0.6 < t < 3.5$ when the hydromagnetic buoyancy force is not large enough to cause a small deceleration. Likewise, the radius of the prominence keeps increasing. Its rate of increase is small in this case because the encountered coronal hydromagnetic pressure decreases very slowly. To see the dependence on the strength of disturbance, we show in Figure 5 the evolutions caused by smaller values of $d\Psi_M/dt$. It is seen that the prominence may move up and down if the disturbance is small. With a sufficiently large disturbance, the prominence will move away from the Sun.

8. Discussion

For a prominence to be in equilibrium with the coronal medium, the six parameters r_0 , Q , ρ_L , B_0 , J_0 , and p_0 that characterize the property of the prominence loop are related by two constraints. They determine two of the parameters in terms of the remaining four parameters. We depict these constraints by showing the requisite values of $\frac{1}{2}\mu QJ_0$ and B_0 for various values of r_0 , Q , ρ_L , p_0 , ρ_∞ , T_∞ , $B_{\infty\parallel}$, and $B_{\infty\perp}$, in the neighborhood of the equilibrium used in the example (see Figures 6 and 7).

Figure 6 shows the variations of the requisite values for equilibria when the height, the size, the mass density, or the gas pressure of the prominence has other values. Both the requisite current and the requisite magnetic field are larger for a prominence at a greater height if the prominence is not located very close to the solar surface. This is so because the bipolar magnetic field decreases in height faster than the solar gravity when the height is above a certain value. The increased pinching force due to a larger requisite current requires an increase in the requisite magnetic field in order to have a matching outward force. Next, a larger value

of the prominence radius increases the boundary magnetic field although the requisite prominence current density remains the same. The increased pinching force is to be counterbalanced by an increased anti-pinching force to be provided by a larger axial magnetic field. On the other hand, a larger value of the mass density of the prominence requires both a larger prominence current and a larger magnetic field. The increased gravitational force is to be matched by an increased diamagnetic force for counterbalancing. The consequential increase in the pinching force is matched by an increase in the anti-pinching force to be provided by a larger axial magnetic field. Finally, a greater value of the gas pressure in the prominence requires a matching decrease in the magnetic pressure so that the total hydromagnetic pressure is kept unchanged.

Figure 7 shows the variations when the coronal mass density, temperature, longitudinal magnetic field, or transverse magnetic field at the site of the prominence has other values. A larger value of the coronal mass density requires a smaller prominence current and a larger gas pressure in the prominence. The increased hydrostatic buoyancy force due to a larger coronal mass density necessitates a smaller diamagnetic force (to be provided by a smaller prominence current) so that together they provide the same upward force to counterbalance the unchanged downward gravitational force. The increase in the pinching force due to a larger ambient pressure (the decrease in the pinching force by a smaller prominence current being rather small) necessitates a larger anti-pinching force to be provided by an increased axial magnetic field. Next, a change in either the coronal temperature or in the longitudinal magnetic field of the corona does not affect the required prominence current because the balancing between the gravitational force and the hydromagnetic buoyancy force is not affected at all. However, the change does affect the requisite axial magnetic field. A larger value of the coronal temperature or the longitudinal magnetic field makes the ambient hydromagnetic pressure larger. The increased pinching force is to be matched by an increased anti-pinching force to be provided by a larger axial magnetic field. Finally, a larger value of the transverse magnetic field of the corona requires a smaller prominence current in order to produce the same diamagnetic force to counterbalance the unchanged gravitational force. The consequential decrease in the pinching force necessitates a decrease in the axial magnetic field in order to produce a smaller anti-pinching force in the equilibrium.

In the illustrative examples, not only in the equilibrium but also during the motion, the hydromagnetic buoyancy force is largely dominated by the zeroth-order diamagnetic force $I_E \times B_\infty$. The higher-order part of the diamagnetic force due to the inhomogeneity of the coronal magnetic field only amounts to a few percent and the hydrostatic buoyancy force is even much smaller. Their percentages diminish in heliocentric distance. Thus, without the action of the zeroth-order diamagnetic force due to the prominence current, prominences are not able to move away from the solar surface.

Actually, when the prominence is close to the photospheric surface, the diamagnetic force is enhanced by the mirror-current effect (Kuperus and Raadu, 1974). The polarization current induced on the photosphere will exert an additional upward force on the prominence current in the amount of $\mu I_E^2 R_\odot^2 / 2\pi r_0 (r_0^2 - R_\odot^2)$ (cf. Van Tend and Kuperus, 1978). Inclusion of this force will modify Equation (13) to

$$\rho_E \frac{d}{dt} u_0 = -\rho_E \frac{GM_\odot}{r_0^2} + \rho_\infty \frac{GM_\odot}{r_0^2} + j_0 B_{\infty L} + r \frac{\mu^{-1} B_{\infty L}^2}{R_c} + \mu j_0^2 \frac{Q^2 R_\odot^2}{2 r_0 (r_0^2 - R_\odot^2)} \quad (37)$$

Accordingly, for the prominence in the illustrative example the requisite current density reduces to $J_0 = 1426.5$ and the requisite magnetic field reduces to $B_0 = 26.44$. With the monopoles strengthening at the rate of $d\Psi_M/dt = 20$, the disturbed prominence rises slightly slower. See Figure 8. This is due to a smaller prominence current. The reduced $I_E B_{\infty L}$ is not sufficiently compensated by the added $\mu I_E^2 R_\odot^2 / 2\pi r_0 (r_0^2 - R_\odot^2)$.

In conclusion, the calculations show the importance of the hydromagnetic buoyancy force in the dynamics of prominence loops.

Acknowledgements

This work was supported by U. S. Air Force Office of Scientific Research under the contract AFOSR-88-0013.

References

- Kahler, S. W., Moore, R. L., Kane, S. R., and Zirin, H.: 1988, *Astrophys. J.* **328**, 824.
- Kuperus, M. and Raadu, M. A.: 1974, *Astron. Astrophys.* **31**, 189.
- Van Tend, W. and Kuperus, M.: 1978, *Solar Phys.* **59**, 115.
- Tandberg-Hanssen, E.: 1974, *Solar Prominences*, D. Reidel Publ. Co., Dordrecht, Holland.
- Wu, S. T.: 1988, *Solar Phys.* **115**, 81.
- Yeh, T.: 1983, *Astrophys. J.* **264**, 630.
- Yeh, T.: 1989, *Solar Phys.* **124**, 251.

CAPTIONS

Figure 1. Magnetic configuration resulting from the interaction between a couple of magnetic monopoles on the solar surface and a large current carried by the prominence, with a polarization current induced on the interface.

Figure 2. Profile of a stratified magnetohydrostatic corona at 2×10^6 °K, with a mass density of 3×10^9 electrons/cm³, a longitudinal magnetic field of 2 gauss and a transverse magnetic field of 10 gauss at the solar surface.

Figure 3. Peripheral distribution of the polarization current in the equilibrium configuration.

Figure 4. Temporal evolution of the prominence as the monopole strength changes in time, with $d\Psi_M/dt = 20$ gauss·helioradius/hour.

Figure 5. Temporal evolutions of the prominence for disturbances with various values of $d\Psi_M/dt$.

Figure 6. Requisite values of $\frac{1}{2}\mu QJ_0$ and B_0 for an equilibrium prominence with various values of r_0 , Q , ρ_E , or p_0 .

Figure 7. Requisite values of $\frac{1}{2}\mu QJ_0$ and B_0 for an equilibrium prominence in a coronal medium with various values of ρ_∞ , T_∞ , $B_{\infty||}$, or $B_{\infty\perp}$.

Figure 8. Temporal evolutions of the prominence when the mirror-current effect is included in the hydromagnetic diamagnetic force, with $d\Psi_M/dt = 20$ gauss·helioradius/hour (thick lines). Dashed lines indicate the corresponding evolution without the mirror-currents.

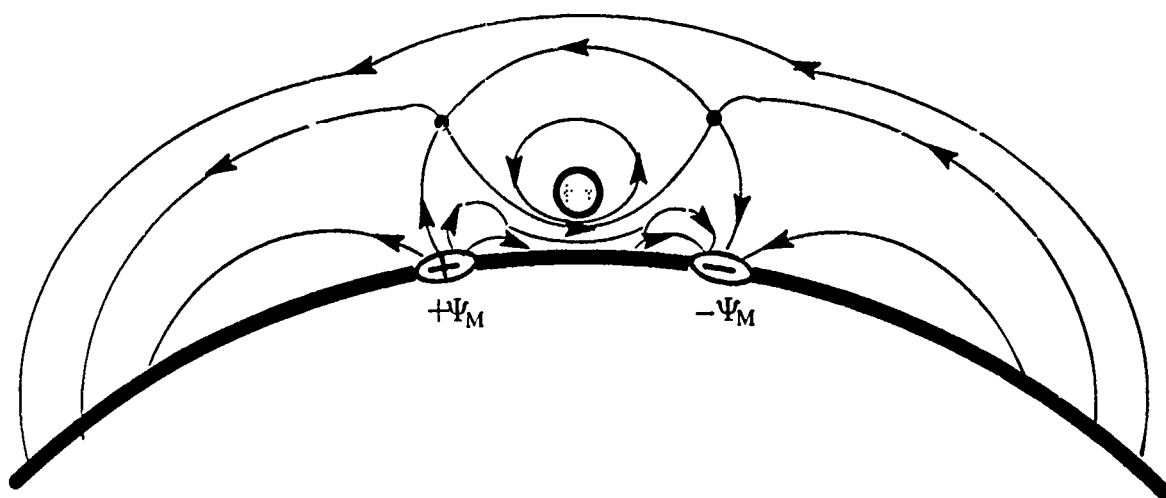


Figure 1

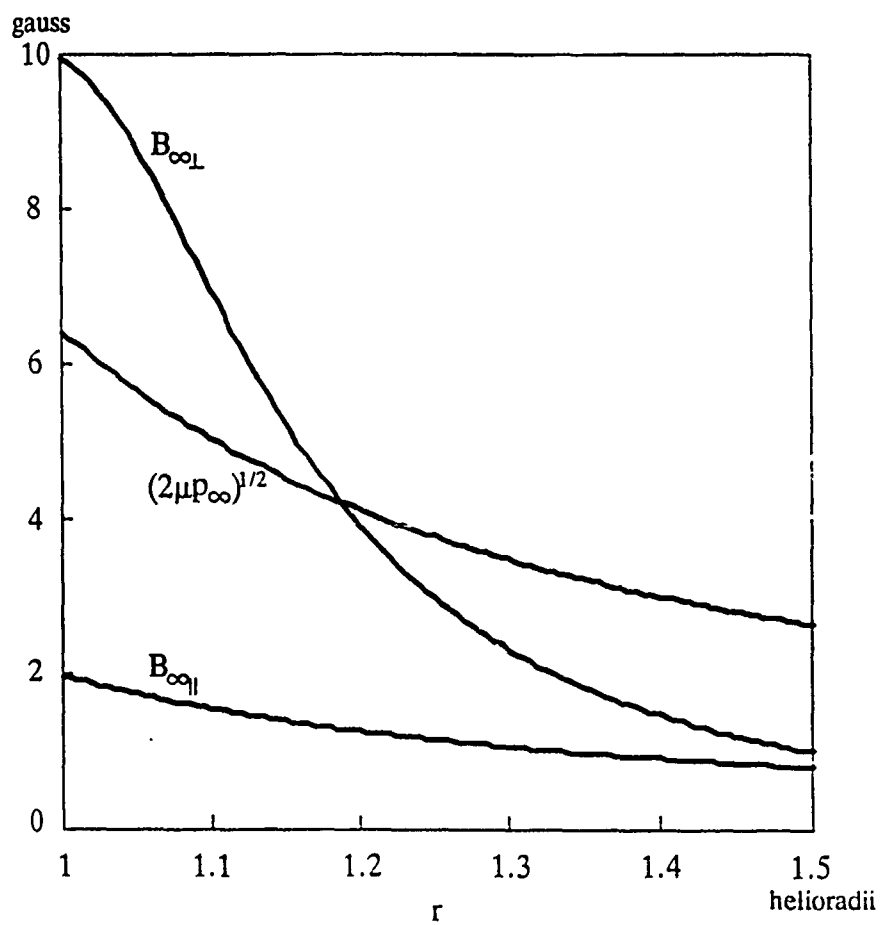


Figure 2

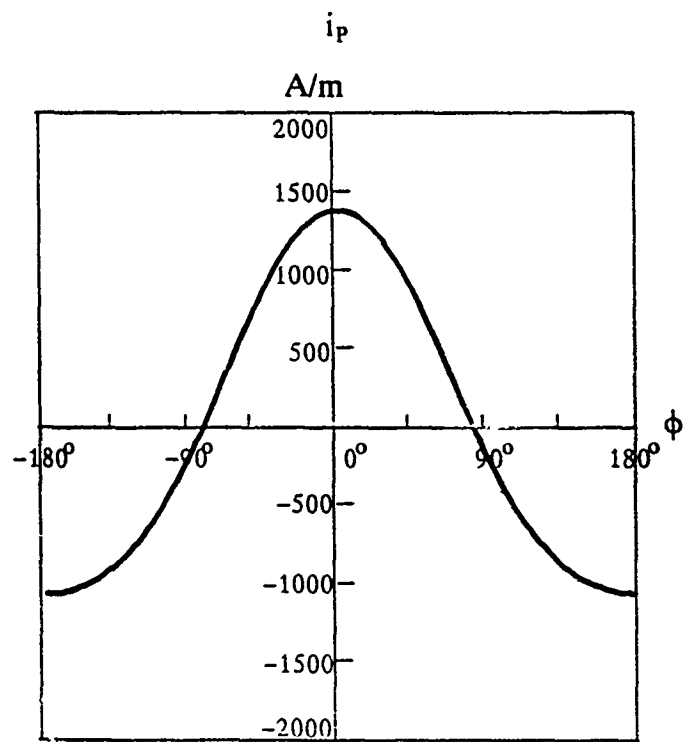


Figure 3

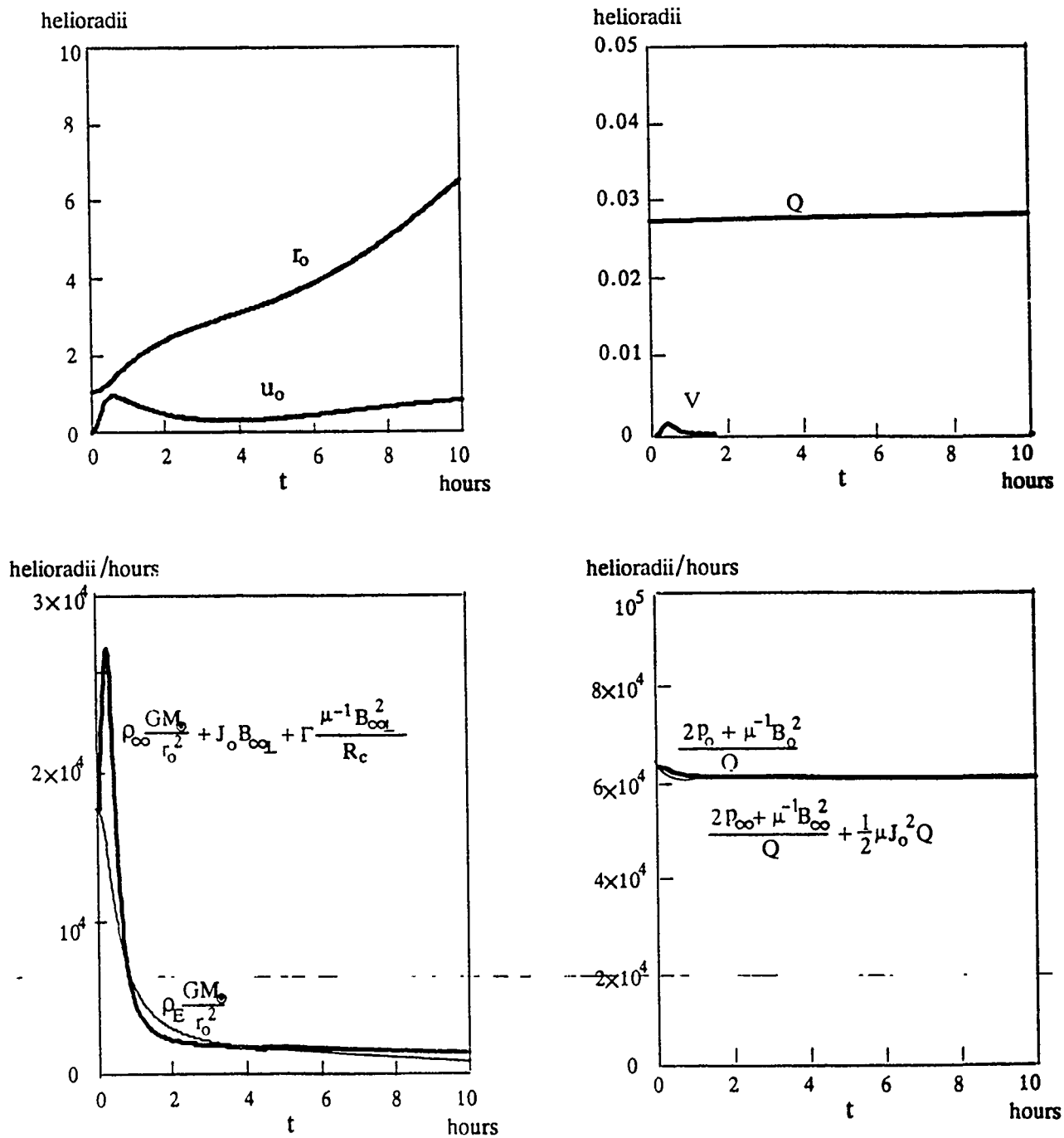


Figure 4

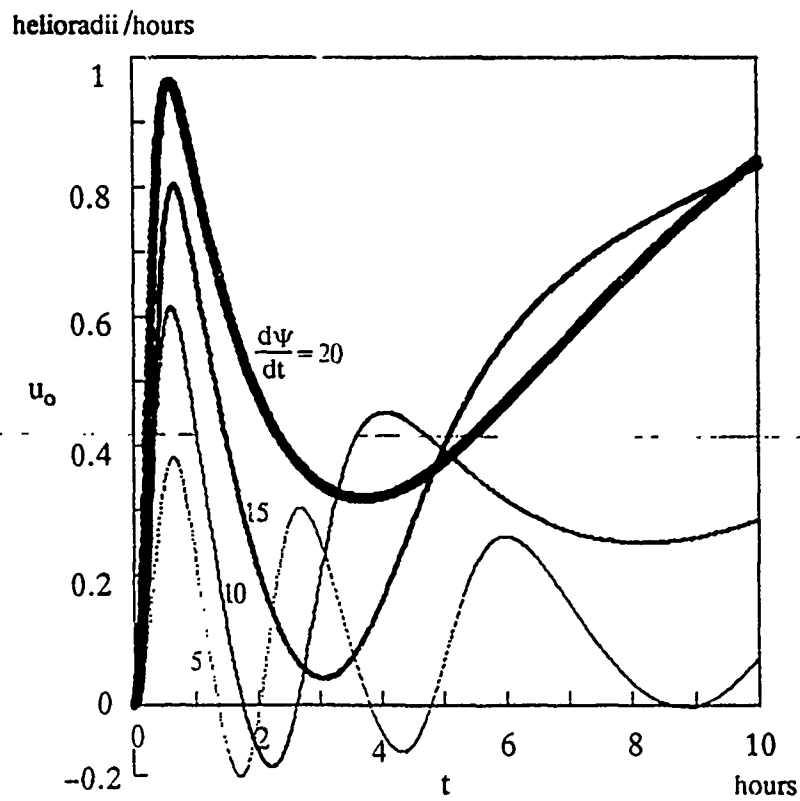
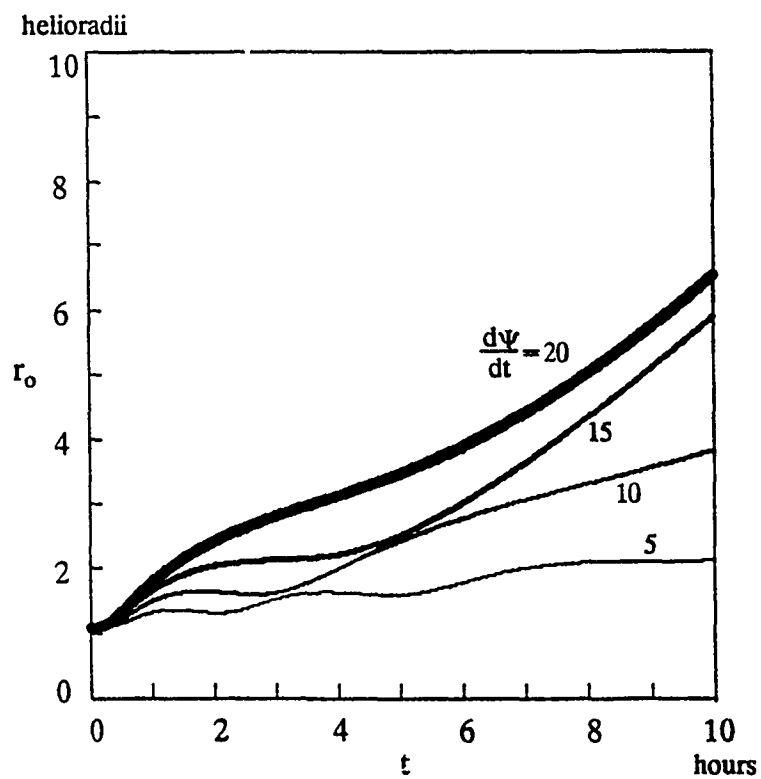


Figure 5

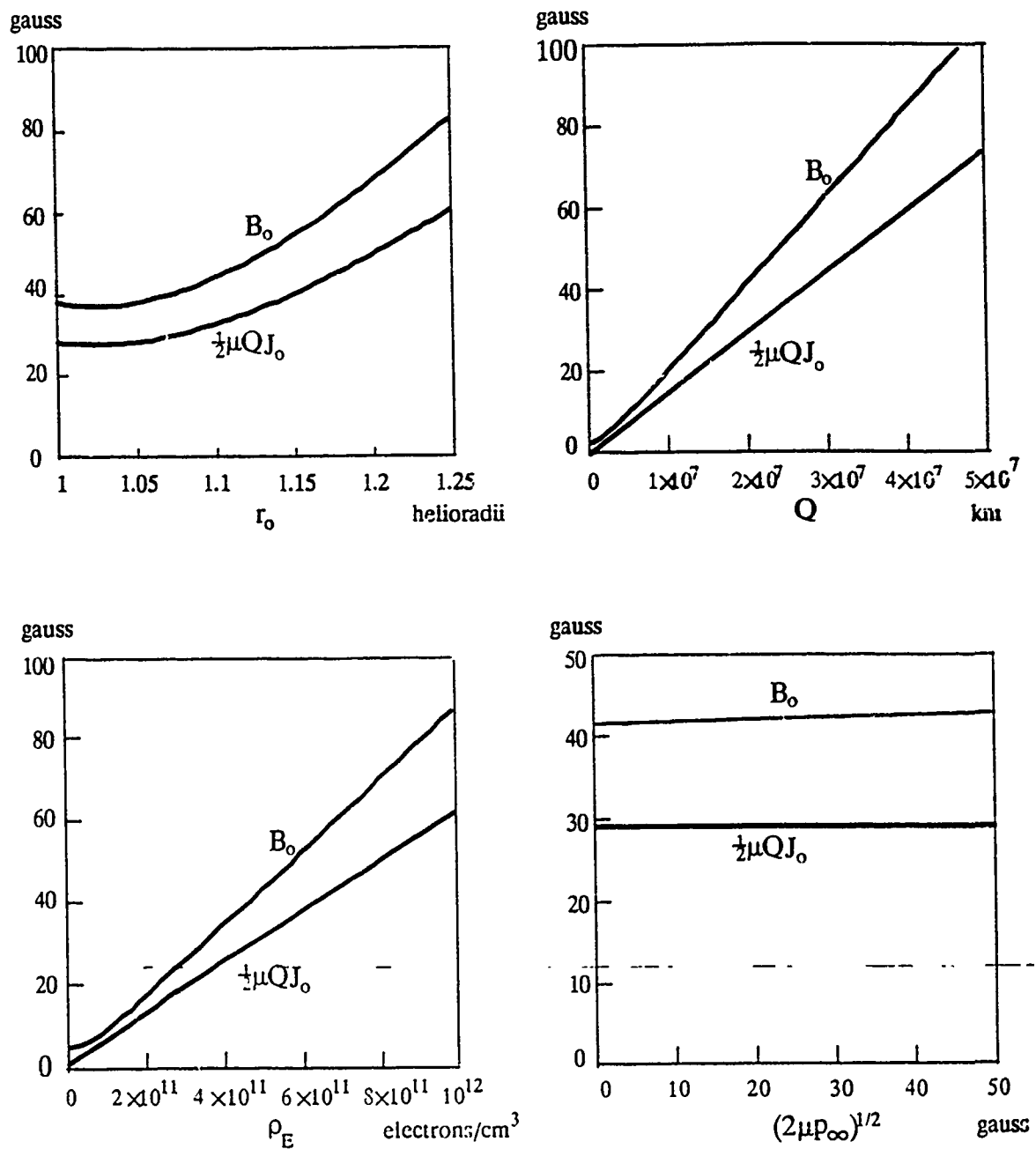


Figure 6

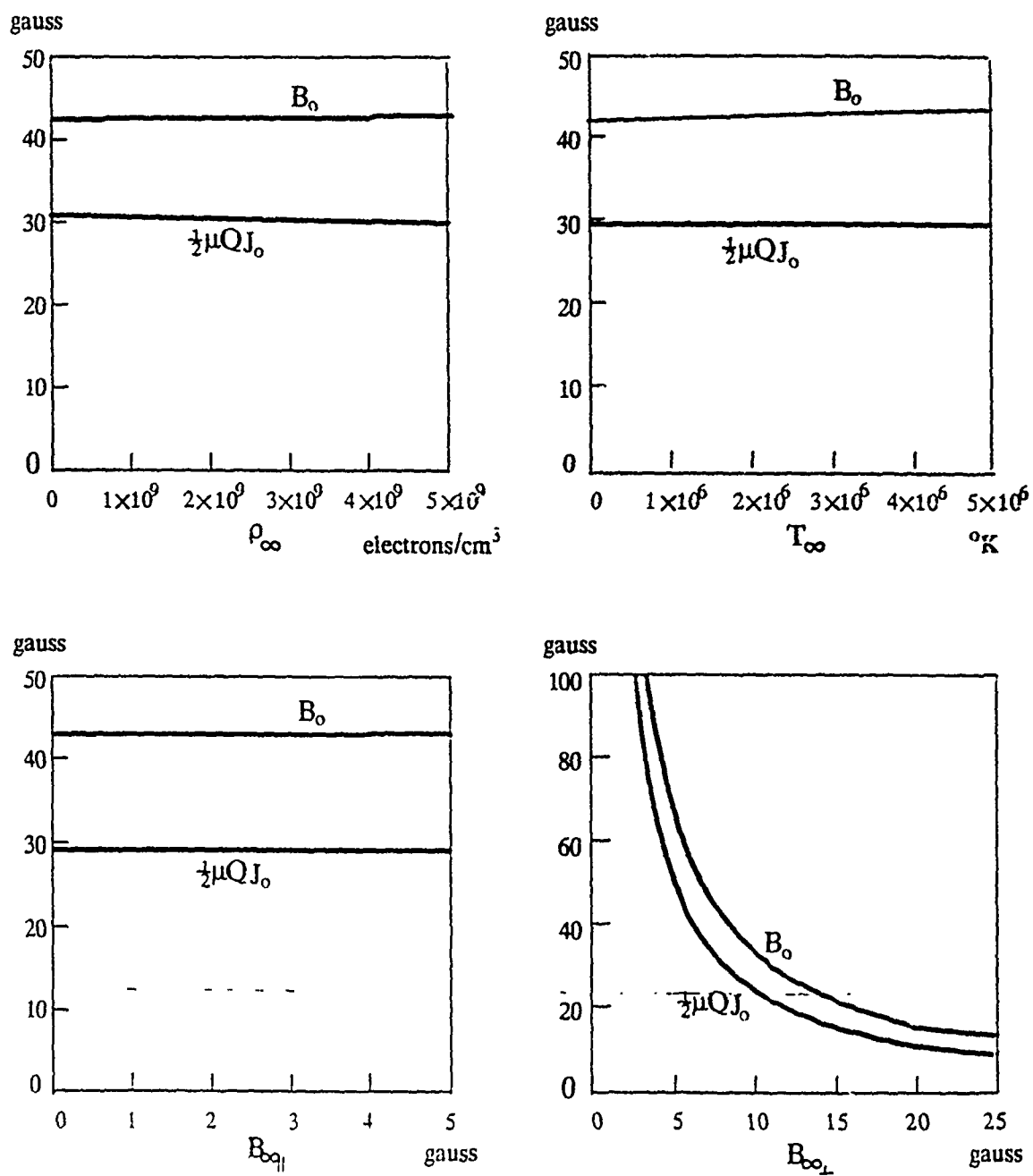


Figure 7

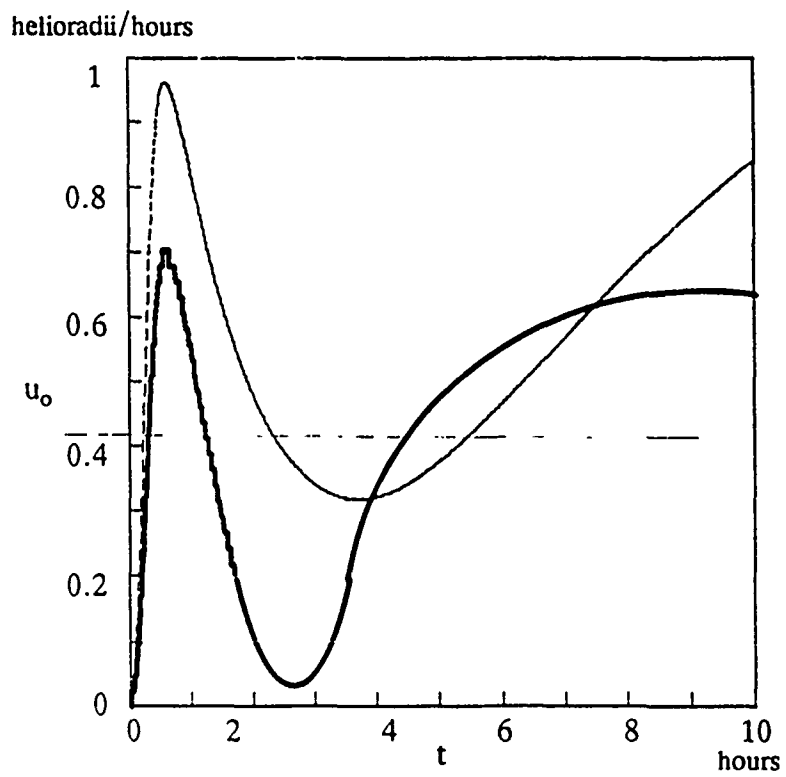
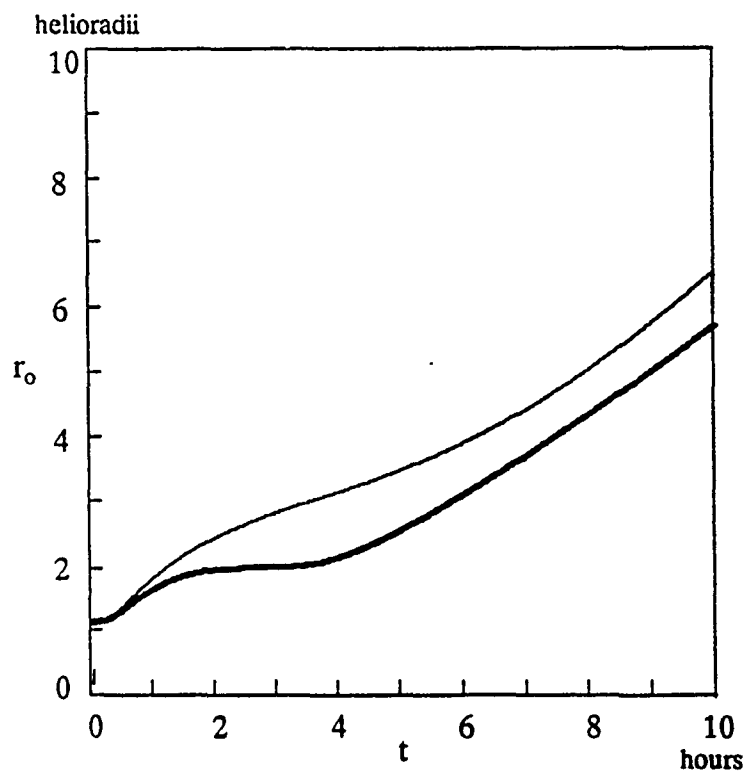


Figure 8

**A TIME-DEPENDENT, 3-D MHD NUMERICAL STUDY OF
INTERPLANETARY MAGNETIC DRAPING AROUND
PLASMOIDS IN THE SOLAR WIND**

by

**T. R. Detman,¹ M. Dryer,¹ T. Yeh,² S. M. Han,³
S. T. Wu,⁴ and D. J. McComas⁵**

September 1990 (revised)

Submitted to

Journal of Geophysical Research

To appear 1991

¹ Space Environment Laboratory, NOAA Environmental Research Laboratories, R/E/SE, 325 Broadway, Boulder, Colorado 80303-3328, USA

² Cooperative Institute for Research in the Environmental Sciences, University of Colorado, Boulder, Colorado 80309, USA

³ Department of Mechanical Engineering, Tennessee Technological University, Cookeville, Tennessee, 38505, USA

⁴ Center for Space Plasma and Aeronomic Research and Department of Mechanical Engineering, University of Alabama in Huntsville, Huntsville, Alabama 35899, USA

⁵ Los Alamos National Laboratory, Los Alamos, New Mexico 87545, USA

ABSTRACT

A spheroidal plasmoid is injected into a representative steady state solar wind at the lower computational boundary of a 3-D MHD model at 18 solar radii. The field line topology of the injected plasmoid resembles the streamline topology of a spherical vortex. Evolution of the plasmoid and its surrounding interplanetary medium is described out to approximately 1 AU for three cases with different values for the velocity imparted to the plasmoid.

In the first case a plasmoid is injected with a velocity equal to that of the steady-state background solar wind at the lower boundary (250 km s^{-1}). In the second and third cases, the plasmoid is injected with peak velocities of twice and three times the background velocity.

A number of interesting features are found. For instance, the evolving plasmoid retains its basic magnetic topology, although the shape becomes distorted. As might be expected, the shape distortion increases with the injection velocity. Development of a bow shock occurs when it is injected with a velocity greater than the sum of the local fast magnetosonic speed and the ambient solar wind velocity. The MHD simulation demonstrates magnetic draping around the plasmoid.

INTRODUCTION

Solar radio heliographic evidence (Riddle, 1970; Smerd and Dulk, 1971; Stewart et al., 1982) suggests that plasmoids are injected into the interplanetary medium during flare and/or eruptive prominence episodes. Riddle (1970) and Smerd and Dulk (1971) reported oppositely-polarized radioheliograph sources during a westward-ejected plasmoid on 1–2 March 1969. Riddle (1970) estimated densities in the source region as $N_e \gtrsim 6 \times 10^6 \text{ cm}^{-3}$ at both $2 R_\odot$ and $5 R_\odot$ where R_\odot is the solar radius, $6.95 \times 10^5 \text{ km}$. He also estimated magnetic fields of $H \gtrsim 0.8 \text{ G}$ at $2 R_\odot$ and $H \gtrsim 0.08 \text{ G}$ at $5 R_\odot$. Riddle suggests a configuration analogous to a smoke ring puffed out from the site of the flare. Smerd and Dulk hypothesized that the internal field structure was carried with the plasmoid into interplanetary space. Stewart et al. (1982) detected a plasmoid on 27 April 1980 with the Culgoora radioheliograph; the measurements strongly suggested the presence of closed magnetic fields within the plasmoid. Based on the plasma emission mechanism (from a hot, dense, magnetically confined configuration), they estimated the field magnitude to be $> 0.6 \text{ G}$ at $2.5 R_\odot$. They also estimated the densities to be $3.5\text{--}5.7 \times 10^7 \text{ cm}^{-3} \pm 30\%$. More recently, Gopalswamy and Kundu (1989), with the Clark Lake radioheliograph, inferred the presence of a slow-moving plasmoid following a flare on 2 February 1986. Assuming the presence of gyrosynchrotron emission at 50, 73.8, and 138.5 MHz, the plasmoid's electron density was estimated to be on the order of $10^5\text{--}10^6 \text{ cm}^{-3}$; the magnetic field magnitude was estimated to be 1–2 G.

Draping of IMF lines has been postulated (Gosling and McComas, 1987; McComas and Gosling, 1988) to occur when a CME or a plasmoid plows through the interplanetary medium, stacking up IMF lines on its front side. The nature of such draping was considered in these papers. Additional studies that support these ideas are also presented by McComas et al. (1988), who examined draping beyond 1 AU, and McComas et al. (1989), who proposed a test of IMF draping based on *in situ* measurements. The present exploratory numerical study was done to examine the stability, evolution and draping associated with one possible mag-

netic configuration for such plasmoids. In this paper we are not considering “rope-like” magnetic configurations which have been invoked to explain the interplanetary “magnetic cloud” observations of Klein and Burlaga (1982). It also is important to make a distinction between the numerical simulations discussed in this paper and those made in the 1970’s (Wu et al. 1978; Dryer et al, 1979) for coronal transient behavior. The latter works (and a number of related studies, e.g. Steinolfson and Hundhausen, 1988) demonstrated that magnetic field lines will be distorted and forced (by virtue of high conductivity) around ejecta similar to that in CMEs. In these simulations of the initial boundary value problem, the time dependent coronal behavior was initiated by a change of thermodynamic properties (i.e. an energy increase) in or around a localized region at the boundary of the computational domain— the base of the corona, for example. The present study is physically different. The perturbing agent is a “projectile” that is injected with a prescribed momentum into the pre-existing solar wind flow. As noted in recent reviews (Burlaga, 1989; and Gosling, 1990), no dynamical numerical simulations have yet been made of the coupled plasmoid-solar wind, “projectile” problem. Preliminary results of the work presented here were described in Dryer et al. (1989). There are three primary advantages of MHD simulations: (1) they present global, rather than local views of the interaction; (2) they are dynamic; and (3) they are intrinsically quantitative, rather than qualitative, in their results.

In this paper we first discuss the method of computation, followed by a discussion of the results for several cases of plasmoid injection. We conclude with some remarks on the plasmoid deformation, on the topological changes caused by numerically induced reconnection, and on the draping of the IMF.

METHOD

Our 3-D model (Dryer et al., 1986; Han et al., 1988, 1989) has a computational domain with the lower boundary at $18 R_{\odot}$, the upper boundary at $225 R_{\odot}$, and the side boundaries covering 90° of latitude centered on the equator and 90° of heliographic longitude. The grid resolutions are respectively $3 R_{\odot}$ in radius, 3° in longitude and 3° in latitude; thus the numerical grid is $70 \times 31 \times 31$. The model uses the two-step, Lax-Wendroff finite difference approximation to the equations of ideal MHD with the addition of artificial viscosity (Han et al., 1988). Our model uses the pseudo-conservation form of the equations to be solved:

$$\frac{\partial \mathbf{U}}{\partial t} + \frac{\partial \mathbf{F}}{\partial R} + \frac{1}{R \sin \theta} \frac{\partial \mathbf{G}}{\partial \theta} + \frac{1}{R \sin \theta} \frac{\partial \mathbf{H}}{\partial \phi} = \mathbf{S}, \quad (1)$$

where \mathbf{U} is the variable vector, \mathbf{F} , \mathbf{G} , and \mathbf{H} are flux vectors and \mathbf{S} is the source vector (Han et al., 1988). Equation (1) expresses the induction equations, and conservation of mass, momentum and energy, without thermal conduction. Thus, except at shocks, the plasma behaves adiabatically. Due to the use of the pseudo-conservation law form, the Rankine-Hugoniot conditions are satisfied at any shocks which develop. This scheme is, however, inherently diffusive and requires added explicit numerical diffusion (artificial viscosity) to stabilize it if any shocks are present. The combination of inherent and explicit numerical diffusion causes shocks to spread over 5 to 10 grid points and facilitates magnetic reconnection when oppositely directed fields are compressed together. All input to the computational domain takes place at the lower boundary. The lower boundary is chosen at $18 R_{\odot}$ because it was just beyond the critical points of the representatively chosen steady-state solar wind. There is nothing special about this location other than that the flow there is both supersonic and superalfvenic.

We begin with a representative, steady-state solar wind. Steady-state conditions at $18 R_{\odot}$ were selected by trial and error to obtain a match with observed conditions at 1 AU. See, for

example, Han et al. (1989). The IMF is assumed to be unipolar (outward) everywhere. Thus this model contains no magnetic sectors and no heliospheric current sheet. The plasmoid is introduced by a time-dependent perturbation of the lower boundary surface at $18 R_{\odot}$. Consider a plasmoid moving away from the Sun. Conditions on the surface at $18 R_{\odot}$ will be perturbed in a particular way as the plasmoid moves across that surface. We perturb conditions on our model's lower boundary at $18 R_{\odot}$ in just such a way.

The configuration of the plasmoid is analogous to the Hill vortex (Hill, 1894; Lamb, 1932) in fluid dynamics; i.e., the magnetic field lines have the same topology as the streamlines in a smoke ring. Thus we are exploring numerically the suggestion made by Riddle (1970). Specifically, Hill's spherical vortex (Milne-Thomson, 1955) is described in terms of a Stokes stream function,

$$\psi = \frac{3}{4} V \left(1 - \frac{r^2}{a^2}\right) r^2 \sin^2 \theta' \quad (r < a), \quad (2)$$

which represents inviscid fluid motion within a sphere of radius a , in spherical coordinates (r, θ', ϕ') centered on the sphere. V is the (constant) flow velocity far from the spherical vortex.

The stream function yields the velocity within the spherical vortex:

$$W(r, \theta') = \frac{3}{2} V \left[\hat{e}_r \left(1 - \frac{r^2}{a^2}\right) \cos \theta' - \hat{e}_{\theta'} \left(1 - 2\frac{r^2}{a^2}\right) \sin \theta' \right]. \quad (3)$$

Therefore the radial velocity is zero at the interface, $r=a$.

The vorticity, ζ is given by

$$\zeta = \hat{e}_{\phi'} \frac{15V}{2a^2} r \sin \theta' \quad (r < a). \quad (4)$$

Thus the vortex lines are circles perpendicular to the axis of symmetry, and the vorticity has a constant value on any such circle. This Hill's vortex is surrounded by a fluid that streams past it

with a velocity, V . The tangential velocity is continuous at the interface $r = a$. Stagnation points exist at the leading and trailing polar points ($\theta' = 0, \pi$) of the sphere, and a ring vortex exists at $r = a/2^{1/2}$ and $\theta' = \pi/2$. The motion of the fluid outside the spherical vortex is the same as if the sphere were a *solid* sphere of the same radius. The stream function for the external flow is

$$\psi = -\frac{1}{2} V \left(1 - \frac{a^3}{r^3}\right) r^2 \sin^2 \theta' \quad (r > a). \quad (5)$$

In a contour plot of ψ , such as Figure 1, contour lines correspond to streamlines.

We have used this classical fluid vortex as the analog for our magnetic plasmoid. Specifically, we take ψ to be a flux function instead of a stream function which then yields magnetic field instead of flow velocity. Also the perturbation which injects the plasmoid into the model must be specified in time and the heliocentric spherical coordinates of the MHD model θ and ϕ on the $R = 18 R_{\odot}$ surface such that axial symmetry is maintained. Current density is the analog of vorticity and we have two neutral points analogous to the stagnation points of the Hill vortex. Current in the plasmoid flows in a loop around the axis of symmetry which points in the radial direction away from the Sun. Thus, the stream function for Hill's vortex is used to describe a magnetic plasmoid. The magnetic field at the center of the sphere reaches a peak value of $-3/2$ times the steady state value (150 nT), i.e. the field in the center of the plasmoid is toward the sun, while outside the plasmoid the field is directed away from the Sun. In adapting the Hill stream function to generate a magnetic plasmoid we made two significant alterations: (1) we constrain the perturbation to be limited in both space and time; and (2) the configuration of our plasmoid has both poloidal and toroidal field components. The magnitude of the poloidal component relative to the toroidal is arbitrarily set at a factor of 1/10. Figure 1 shows only the toroidal component. We have not considered other ratios. A plasmoidal field

line is like a "slinky" toy with the two ends held together. The final flux function for the field outside the plasmoid is:

$$\psi = -\frac{1}{2} V \left(1 - \frac{a^3 (b-r)}{r^3 (b-a)} \right) r^2 \sin^2 \theta' \quad (a < r < b). \quad (6)$$

The toroidal field component has the form:

$$B_\phi = -\frac{1}{20} B_0 \left(1 - \frac{r^2}{a^2} \right) \frac{r}{a} \sin \theta' \quad (r < a), \quad (7)$$

where B_0 is the steady state value of the radial component of the IMF. For this study we have chosen $a = 18 R_\odot \times 18^\circ = 3.9 \times 10^6$ km, see Figure 1 (b), and $b = 2a$. The density and temperature inside the plasmoid are taken to be $1.4 \times 10^3 \text{ cm}^{-3}$ and 1.1×10^6 K respectively, the same as the background values at the input location, $18 R_\odot$. There the sound speed is 174 km s^{-1} and Alfvén speed is 87 km s^{-1} . Thus the 250 km s^{-1} steady state flow speed at the lower boundary is super-sonic and super-Alfvénic.

We present three cases. In Case One, the plasmoid enters the grid with no change in velocity from the steady state. In Case Two, the velocity at the center of the plasmoid reaches a factor of 2.0 above the steady-state velocity; and in Case Three, 3.0 times the steady-state velocity. A cosine profile is used to smoothly taper from the peak velocity at the center of the plasmoid down to match the steady state velocity at a radius b from the center of the plasmoid.

Since we have made modifications to the original stream function as described by Hill, e.g. the spatial confinement described by (6), the toroidal component described by (7), and the velocity perturbations described in the preceding paragraph, it is possible that our final input boundary perturbation may no longer be strictly solenoidal. We investigated two methods of enforcing solenoidality on the input boundary perturbation, so as to avoid introducing magnetic monopoles into the grid. The first, described in Yeh and Dryer (1985) is based on Fara-

day's law of magnetic induction applied to the model boundary at $18 R_{\odot}$. We implemented this method in an iterative scheme which adjusted B_R on the lower boundary until Faraday's law was satisfied. The second method, the one we settled on for all computations described herein, is more direct, but involves field quantities inside the grid. We start with the second order centered difference formula for $\nabla \cdot \underline{B}$ at $I=2$, the first interior radial grid position. We then solve this for B_R at $I=1$, substituting 0 for the value of $\nabla \cdot \underline{B}$. This gives,

$$B_R(1, J, K) = \frac{R_3^2}{R_1^2} B_R(3, J, K) + \frac{R_2^2}{R_1^2} \Delta R (\Delta B_{\theta} + \Delta B_{\phi}) \quad (8)$$

where

$$\Delta B_{\theta} = \frac{(\sin \theta_{J+1} B_{\theta_{J+1}} - \sin \theta_{J-1} B_{\theta_{J-1}})}{2R_2 \Delta \theta \sin \theta_J}$$

$$\Delta B_{\phi} = \frac{(B_{\phi_{K+1}} - B_{\phi_{K-1}})}{2R_2 \Delta \phi \sin \theta_J}$$

Here $B_R(I, J, K)$ is the value of B_R at grid point (I, J, K) where I, J, K are the grid indices in the R, θ , and ϕ directions respectively. We use (8) to find B_R for all points on the lower boundary at each time step, i.e. for all J and K . This guarantees that $\nabla \cdot \underline{B} = 0$ at $I=2$ at each time step. Any departures from $\nabla \cdot \underline{B} = 0$ further inside the grid are thus due only to numerical error, which is discussed below.

The validity and accuracy of the numerical method used for this study are discussed by Han et al. (1988). In addition, we made several diagnostic checks to assess the validity of the numerical calculation. In the first check, we computed the total energy within the entire computational domain for the exceptionally stringent Case Three. The total energy in the model grid (the sum of kinetic, thermal, magnetic, and potential) increased smoothly from the background value of 5.73×10^{31} ergs at $t = 0$ h to 6.18×10^{31} ergs at $t = 15$ h as the plasmoid was

injected. Total energy then decreased slowly to 6.15×10^{31} ergs at $t = 48$ h. Plasmoid injection thus added 0.45×10^{31} ergs to the model grid, and 0.03×10^{31} ergs were subsequently lost (some through the sides of the grid). This indicates conservation of energy to 0.5% of total energy or 7% of the added energy. We consider this satisfactory. In the second diagnostic check, we estimated the effect of numerical round-off, etc., on the requirement of solenoidality ($\nabla \cdot \underline{B} = 0$). For this purpose we calculated the total (fictitious) monopole force, $\underline{B} \nabla \cdot \underline{B}$, and compared it with the Lorentz force, $(\nabla \times \underline{B}) \times \underline{B}$ as a function of time. The result was that the former was typically 1% of the latter, indicating a very acceptable level of non-solenoidality in the computation. The Lorentz force, for this particular case, was generally one to three orders of magnitude lower than the pressure and gravitational forces, thereby indicating the fictitious monopole force to be insignificant.

RESULTS

For the three cases noted above, we will describe a number of features pertaining to the unit IMF vectors. The IMF unit vectors indicate direction, but not magnitude, which changes by orders of magnitude between the inner and outer boundary of the model. We also present several contour plots of the physical parameters at a representative radius for the first case, 3-D plots of IMF lines for all three cases, and finally time series plots of magnetic field components as they would be observed by a spacecraft located in the path of the plasmoid.

Unit IMF Vectors

Figure 2 shows the unit IMF vectors in the equatorial plane at four times ($t = 24$ h, 48 h, 72 h and 96 h) during the interplanetary evolution of the Case One plasmoid that was inserted at the lower boundary ($18 R_{\odot}$) at the background solar wind velocity (250 km s^{-1}). As the plasmoid is convected outward, increasing B_{ϕ} due to the Archimedian spiral causes asymmetry in the external and internal currents which combine to force the nose of the evolving, ellipsoid-like volume eastward. (To an observer facing the Sun east is on the left.) While the nose

moves eastward, the tail moves westward. Thus, distortion occurs but with no net deflection of the plasmoid from the radial direction. The approximate boundary of the plasmoid is sketched-in at $t=96\text{h}$ in Figure 2. This result is in agreement with the observationally based suggestion that shockless (i.e., co-moving) plasmoids have no net average deflection (Gosling et al., 1987b).

Case Two and Case Three are shown in Figure 3 and Figure 4, respectively, for approximately the same times as for the first case. Here, the plasmoid enters the lower boundary with peak velocities of twice and three times, respectively, the background solar wind velocity. As the plasmoid approaches the outer grid boundary at $225 R_{\odot}$ its final velocity is about 420 km s^{-1} in Case Two, and about 490 km s^{-1} in Case Three. Hence, for these two cases, the plasmoid is always moving at super-characteristic speeds. For comparison, the plasmoid's final velocity in Case One was about the same as the ambient solar wind speed at $225 R_{\odot}$, 360 km s^{-1} . We have sketched (in Figures 3 and 4) the approximate location of the plasmoid surface. These figures also show the locations of the bow shocks. Shock locations were obtained from contour plots of entropy rise, and overlaid using a light table. The thicknesses of these shocks are a numerical artifact, as discussed earlier. Note the deflection across the shock of the vectorial directions from the original Archimedian spiral. These shock are quasi-parallel on the east flank, and quasi-perpendicular on the west, thus little or no change in direction is evident in those locations. Similar deflections occurred in Case One, however in that case, the deflection was caused by non-linear fast mode waves. The increased magnetic pressure and curvature forces and the increased shock-induced thermal pressure on the leading (anti-sunward) surface of the plasmoid, together flatten it from its original shape. Its relatively flatter shape, compared with Case One, is evident.

It should be noted that, because of the coarse grid size in our numerical simulation, we do not track the precise boundary of the plasmoid. This limitation of the simulation might be improved with an extensive study of finer grid sizes, but that is beyond the scope of this study.

Thus, our sketch of the plasmoid's boundary is only a reasonable approximation. In spacecraft measurements, such boundaries are believed to be indicated by onset of bi-directional electron heat flux signatures, as well as the bi-directional energetic particle flux signatures mentioned earlier (Paimier et al., 1978; Gosling et al., 1987a; Marsden et al., 1987)

Contours of Physical Parameters at $R = 129 R_{\odot}$

Another way of examining the properties of the evolving plasmoid and its interplanetary environs is to plot contours of the dependent variables on a spherical segment at various heliocentric radii. Figure 5(a,b) shows, for Case One, contours of constant plasma number density and temperature at $t = 72$ h on a spherical surface at $R = 129 R_{\odot}$. (The mass density labels are shown in units of $10^{-13} \text{ kg km}^{-3}$). Note that the "cross section" is nearly circular, with number densities at 16 cm^{-3} in the center and 20 cm^{-3} at the plasmoid's surface (where the pressure is continuous). Although the plasmoid's motion for Case One is passive, accelerating at the same rate as the solar wind, the inhomogeneity of the upstream, spiral IMF produces a larger, fast-mode compression on the westward (right) side of the plasmoid: up to 21 cm^{-3} as compared with only 19 cm^{-3} on the eastward (left) side.

It is interesting to note that the major distortion of the plasmoid is always seen (Figure 2) in the equatorial plane, where the effect of the spiral IMF is maximized. At the moderate heliolatitudes (about $\pm 20^\circ$) the change in the spiral angle is small (Han et al., 1988), with a negligible effect on the spheroid's distortion in the meridional plane.

Perspective views of IMF Lines

A 3-D view of a few IMF lines is shown in Figure 6(a-c) for Case One at $t = 48$ h, 72 h, and 96 h. These figures show a box which is 1 AU on each edge. Only 15, originally Archimedean, field lines in the equatorial plane, separated in heliolongitude by $\Delta\phi = 6^\circ$, are used in this presentation. Their projections onto the lower plane of the box, parallel to the equatorial plane, are shown as dotted lines. The plasmoid's field lines are not shown in this figure. The

observer is located at 8 AU, $\theta = 60^\circ$ (the solar co-latitude), and $\phi = 20^\circ$ (where the X-axis along the lower left side of the box points in the $\phi = 0^\circ$ direction).

Note that, in Figure 6(a), the fourth IMF line from the left is seen to go around the plasmoid then loop back through the center of the plasmoid. This is the first indication that reconnection (caused by numerical diffusion) has occurred for those IMF lines that come into close proximity to the neutral points at the nose and tail of the plasmoid. In this model reconnection results from the coarse grid and the highly diffusive Lax-Wendroff numerical scheme. Although reconnection is exaggerated in these simulations, it does satisfy the rigorous definition adopted by Spicer (1990). It does show the type of global changes in magnetic topology real reconnection would produce. The idea that the external IMF and the internal plasmoid field lines may reconnect was first proposed, to our knowledge, by McComas et al. (1988). Although the magnetic configuration of the plasmoid is changed relatively little by this reconnection, the global view of external and internal field lines shows that the plasmoid's topology is now that of a torus rather than that of a sphere. A number of IMF plots show lines looping back through the "hole in the donut" one or more times. We estimate our grid magnetic Reynolds number to be of the order of 300 near the neutral point at the nose of the plasmoid.

The viewing perspective for Case Two, illustrated in Figure 7, is the same as used in Figure 6. Figure 7(a-c) shows the IMF at $t = 24$ h, 48 h, and 72 h. The computed topology of one field line belonging to the plasmoid itself is shown in Figure 7(c). This configuration supports the speculation of Smerd and Dulk (1971) concerning the left- and right-hand polarization of plasma spiraling around self-contained magnetic field lines based on their radioheliograph observations of a plasmoid near the Sun.

In Case Three, increased pressure forces cause greater distortion of the shape of the plasmoid. In Case One the shape is roughly spherical while in Case Three the shape is roughly hemispherical with the flat side toward the sun. As expected for Case Three, the IMF draping seen in Figure 8 is more pronounced than the other cases, and a stronger bow shock is pro-

duced. We have shown, in this figure, a single set of co-rotating field lines at three different times. One particular field line is emphasized at the three times shown in this figure in order to demonstrate its ever-increasing amount of draping.

Time series of magnetic field components

Figure 9(a-c) shows the magnetic field signatures which a spacecraft sitting in the equatorial plane and in the path of the plasmoid near the axis of symmetry would experience. In Case One where no draping is expected, the magnitude of B_ϕ first decreases as the plasmoid arrives. In Cases Two and Three, the signature of draping is evident as an increase in the magnitude of B_ϕ (eastward deflection) as the plasmoid approaches. B_ϕ deflects eastward due to the compression of field lines stacked up on the front of the advancing plasmoid. In Case Two the magnitude of B_ϕ is increased moderately, about 60%; in Case Three it is increased by 120%. These results suggest a linear relation between the injection velocity and the amount of draping. Note, also, that a moderate rotation of the field occurs within the plasmoid, lasting for many hours. In this respect our plasmoid resembles the magnetic cloud observations of Klein and Burlaga (1982), however, the behavior of $|\mathbf{B}|$ in Figure 9, together with that of β , lower panel, indicate that the spheroidal plasmoid, as we have modeled it, is not a good candidate to explain the magnetic cloud observations of Klein and Burlaga (1982). A prominent feature of the spheroidal plasmoid is the region of reversed sign of the radial field component in the central region. An adjunct of this is a surrounding shell of high β associated with the zero crossing of the radial field component. However, the dynamics are non-trivial as indicated by the region of very low β in the central region of the plasmoid in Case Three (lower right panel). We have not searched spacecraft data for signatures resembling those of our plasmoid.

CONCLUDING REMARKS

We have combined our 3-D Interplanetary Global Model (3-D IGM) with a diamagnetic plasmoid (in analogy to a spherical vortex) to demonstrate the dynamical evolution of a plasmoid in an ideal conducting medium. The entrance of a plasmoid into the 3-D computational

domain is effected by time-dependent conditions on the lower boundary ($18 R_{\odot}$). We simulated plasmoids to study their evolution and as a means to study IMF draping. Although the microscale position of the IMF/plasmoid boundary was not demonstrated due to use of MHD (fluid) approximations and coarse grid resolution, the large-scale topology of both sets of field lines is reasonably well-approximated.

Several numerical experiments were performed. In Case One, the plasmoid was convected with the ambient solar wind speed across the lower boundary with no deviation from the background solar wind velocity (250 km s^{-1}) at that boundary. In Case Two (and Case Three), the plasmoid entered with additional momentum such that the peak velocity was twice (three times) that of the lower boundary's steady-state value.

In Case Two, the plasmoid also survives injection into the computational domain and, in fact, generates a bow shock as would be expected in this "projectile" experiment. The plasmoid becomes flattened; its radial extent is less than that in Case One, and its transverse extent is greater. As in Case One, reconnection changes the topology from a spheroid to a torus. In addition, substantial draping of the IMF is apparent on the front, westward side of the plasmoid, thereby supporting the suggestions of Gosling and McComas (1987) and McComas and Gosling (1988). All of these characteristics are, as expected, enhanced for Case Three.

It is impossible to present here all of the evidence available to the investigators. For example, one of our most used graphical aids has been animated 1D traces of various quantities along a radial line near the plasmoid axis of symmetry. Another, which we have chosen not to present, is color contour plots in equatorial and meridional planes. Yet another is "real" 3D stereoscopic views of magnetic field lines such as those presented in Figures 6, 7, and 8. These were achieved by making 35mm "left" and "right" slide pairs where the "eye" positions differed by $\Delta\phi = 3^\circ$. These are viewed with a hand held viewer which holds two slides, one for each eye.

Although not shown here, we noted that the force free condition, $(\nabla \times \underline{B}) \times \underline{B} = 0$, was never exactly satisfied but the maximum angular separation of \underline{J} , i.e. $(\nabla \times \underline{B})$, and \underline{B} was usually less than 10° . This lends support to the use of force free models such as by Suess (1988) and Burlaga (1988) which have been relatively successful in predicting observed field orientations in magnetic clouds (as reviewed by Gosling, 1990, and Burlaga, 1989). It also encourages us to try to accommodate the more complex boundary conditions presented by the "rope-like" low beta configurations.

The present study demonstrates a valuable, dynamically self-consistent, new MHD simulation tool for studying the development of plasmoids as they propagate outward into the interplanetary space. This 3-D tool clearly allows the study of IMF draping around such plasmoids out of the ecliptic where it is difficult to sketch the spiraling of the IMF on conically-shaped surfaces – even on an intuitive basis. This capability is particularly important in light of the upcoming (October 1990) launch of the out-of-ecliptic ULYSSES mission.

ACKNOWLEDGMENT

This work was supported in part by NASA Order No. 17,015 to NOAA Space Environment Laboratory (MD,TRD); by AFOSR Grant 88-0013 (TY); by NOAA Contract 40RANR7-08459 (SMH); and by NOAA Contract 50RANR-700099 and AFOSR Grant 88-0013 (STW). Work at Los Alamos National Laboratory was performed (DJM) under the auspices of the U.S. Department of Energy with support from NASA under S04039-D. We wish to thank Zdenka Smith and Michel Poquerusse for a number of stimulating discussions on the numerical algorithms of the 3-D IGM (Interplanetary Global Model) and the physics of plasmoids. Also, we thank Howard Garcia and the anonymous referees for many useful suggestions during the preparation of this manuscript.

REFERENCES

- Burlaga, L.F., Magnetic Clouds, in *Physics of the Inner Heliosphere* (E. Marsch and R. Schwenn, Eds.), D. Reidel Publ. Co., Dordrecht, in press. 1989.
- Burlaga, L.F., Magnetic Clouds and Force-Free Fields with Constant Alpha, *J. Geophys. Res.*, **93**, 7217, 1988.
- Dryer, M., S.T. Wu, R.S. Steinolfson, and R.M. Wilson, Magnetohydrodynamic models of coronal transients in the meridional plane, II, Simulation of the coronal transient of 1973 August 21, *Astrophys. J.*, **227**, 1059, 1979.
- Dryer, M., T.R. Detman, S.T. Wu, and S.M. Han, Three-Dimensional MHD Simulations of Interplanetary Plasmoids, *Adv. Space Res.*, **9**(4), 75, 1989.
- Dryer, M., S.T. Wu, and S.M. Han, Three-Dimensional, Time-Dependent, MHD Model of a Solar Flare-Generated Interplanetary Shock Wave, in *The Sun and the Heliosphere in Three Dimensions* (R.G. Marsden, Ed.), D. Reidel Publ. Co., Dordrecht, pp. 135-140, 1986.
- Gopalswamy, N., and M.R. Kundu, A Slowly Moving Plasmoid Associated with a Filament Eruption, *Solar Phys.*, **122**, 91, 1989.
- Gosling, J.T., Coronal Mass Ejections and Magnetic Flux Ropes in Interplanetary Space, in *Physics of Magnetic Flux Ropes* (C.T. Russell, E.R. Priest, and L.C. Lee Eds.), Geophysical Monograph #58, American Geophysical Union, pp.343-364, 1990.
- Gosling, J.T., and D.J. McComas, Field Line Draping About Fast Coronal Mass Ejecta: A Source of Strong Out-of-the-Ecliptic Interplanetary Magnetic Fields, *Geophys. Res. Lett.*, **14**, 355, 1987.
- Gosling, J.T., D.N. Baker, S.J. Bame, W.C. Feldman, R.D. Zwickl, and E.J. Smith, Bidirectional Solar Wind Electron Heat Flux Events, *J. Geophys. Res.*, **92**, 8519, 1987a.

- Gosling, J.T., M.F. Thomsen, S.J. Bame, and R.D. Zwickl, The Eastward Deflection of Fast Coronal Mass Ejecta in Interplanetary Space, *J. Geophys. Res.*, **92**, 12,399, 1987b.
- Han, S.M., S.T. Wu, and M. Dryer, A Three-Dimensional, Time-Dependent Numerical Modeling of Supersonic, Superalfvenic MHD Flow, *Computers and Fluids*, **16**, 81, 1988.
- Han, S.M., S.T. Wu, and M. Dryer, A Transient, Three-Dimensional MHD Model for Numerical Simulation of Interplanetary Disturbances, in *Proceedings of STIP Symposium on Retrospective Analyses* (M.A. Shea and D.F. Smart, Eds.), Book Crafters Publ. Co., Chelsea, MI, in press, 1989.
- Hill, M.J.M., On a Spherical Vortex, *Roy. Soc. London-Phil. Trans. Series A.*, **35**, 219, 1894.
- Klein, L.W., and L.F. Burlaga, Interplanetary Magnetic Clouds at 1 AU, *J. Geophys. Res.*, **87**, 613, 1982.
- Lamb, H., *Hydrodynamics* (Sixth Edition), Dover Publications, New York, NY, pp. 245-246, 1932.
- Marsden, R.G., T.R. Sanderson, C. Tranquille, K.-P. Wenzel, and E.J. Smith, ISEE 3 Observations of Low-Energy Proton Bidirectional Events and Their Relation to Isolated Magnetic Structures, *J. Geophys. Res.*, **92**, 11,009, 1987.
- McComas, D.J., and J.T. Gosling, Magnetic Field Draping about Coronal Mass Ejecta, in *Proceedings of the Sixth International Solar Wind Conference* (V.I. Pizzo, T.E. Holzer, and D.G. Sime, Eds.), NCAR/TN-306-Proc., Vol. I, pp. 291-297, 1988.
- McComas, D.J., J.T. Gosling, D. Winterhalter, and E.J. Smith, Interplanetary Magnetic Field Draping About Fast Coronal Mass Ejecta in the Outer Heliosphere, *J. Geophys. Res.*, **93**, 2519, 1988.

- McComas, D.J., J.T. Gosling, J.L. Phillips, S.J. Bame, J.G. Luhmann, and E.J. Smith, Electron Heat Dropouts in the Solar Wind: Evidence for Interplanetary Magnetic Field Reconnection? *J. Geophys. Res.*, **94**, 1465, 1989.
- Milne-Thomson, L.M., *Theoretical Hydrodynamics* (Third Edition), The MacMillan Company, New York, NY, pp. 527-528, 1955.
- Palmer, I.D., F.R. Allum, and S. Singer, Bidirectional Anisotropies in Solar Cosmic Ray Events: Evidence for Magnetic Bottles, *J. Geophys. Res.*, **83**, 75, 1978.
- Riddle, A.C., 80 MHz Observations of a Moving Type IV Solar Burst, March 1, 1969, *Solar Physics* **13**, 448, 1970.
- Smerd, S.F., and G.A. Dulk, 80 MHz Radioheliograph Evidence on Moving Type IV Bursts and Coronal Magnetic Fields, in *Solar Magnetic Fields*, (R. Howard, Ed.), IAU Symposium No. 43, D. Reidel Publ. Co., Dordrecht, pp. 616-641, 1971.
- Spicer, D.S., Three Dimensional Reconnection in Astrophysical Plasmas, *Adv. Space Res.* **10**, (9)43, 1990.
- Stewart, R.T., G.A. Dulk, K.V. Sheridan, L.L. House, W.J. Wagner, C.J. Sawyer, and R. Illing, Visible Light Observations of a Dense Plasmoid Associated with a Moving Type IV Solar Radio Burst, *Astron. Astrophys.*, **116**, 217, 1982.
- Suess, S.T., Magnetic Clouds and the Pinch Effect, *J. Geophys. Res.*, **93**, 5437, 1988.
- Wu, S.T., M. Dryer, Y. Nakagawa, S.M. Han, Magnetohydrodynamics of atmospheric transients, II, Two-dimensional numerical results for a model solar corona, *Astrophys. J.*, **219**, 324, 1978.
- Yeh, T., and M. Dryer, A Constraint on Boundary Data for Magnetic Solenoidality in MHD Calculations, *Astrophys. and Space Sci.* **117**, 165, 1985.

FIGURE TITLES

Figure 1. (a) Modified spherical vortex of radius a . Each contour, together with its mirror image, shows the surface of a cylindrical stream tube. The stream function was modified to make the flow uniform beyond the radius $b = 2a$. Note the region of reversed flow in the central region of the vortex. In (b) the geometry and relative size of the plasmoid is shown as it is introduced into the model grid by perturbation of the lower computational boundary. The diameter of the plasmoid at $R = 18 R_{\odot}$ is $r = 18 R_{\odot} \times 18^{\circ} = 3.9 \times 10^6$ km.

Figure 2. Distortion (Case One) of the initially spherical plasmoid is indicated by unit IMF vectors in the solar equatorial plane at four different times. In Case One, the plasmoid is *convected* into the solar wind with the initial background solar wind velocity of 250 km s^{-1} at $18 R_{\odot}$.

Figure 3. Distortion (Case Two) of the initially spherical plasmoid as indicated by unit IMF vectors in the solar equatorial plane. The plasmoid is *injected* into the solar wind with peak velocities of twice the initial background solar wind velocity of 250 km s^{-1} at $18 R_{\odot}$. The approximate trace of the plasmoid surface in the equatorial plane is sketched-in. Shock position was transferred from a matching contour plot of entropy increase.

Figure 4. Distortion (Case Three) of the initially spherical plasmoid as indicated by unit IMF vectors in the solar equatorial plane. The plasmoid is *injected* into the solar wind with three times the initial background solar wind velocity.

Figure 5. Density (a) and temperature (b) contours on a segment of a spherical shell through the Case One plasmoid at $R = 129 R_{\odot}$ and $t = 72 \text{ h}$. The viewing perspective is toward the Sun; thus "west" is to the right, "east" to the left. The density labels are given units of $10^{-13} \text{ kg km}^{-3}$; $320 \times 10^{-13} \text{ kg km}^{-3}$ is equivalent to a number den-

sity of 19 cm^{-3} . Note the asymmetry in the compression and adiabatic heating on the west compared with that on the eastward side of the plasmoid.

Figure 6. Initially-equatorial IMF lines at $t = 48 \text{ h}$, 72 h , and 96 h for Case One. The plasmoid's field lines are not shown in this figure. The viewing perspective is from 8 AU , $\theta = 60^\circ$, $\phi = 20^\circ$.

Figure 7. Initially-equatorial IMF lines at $t = 24 \text{ h}$, 48 h , and 72 h for Case Two. The viewing perspective is from 8 AU , $\theta = 60^\circ$, $\phi = 20^\circ$. In (c) we have traced out one field line of the plasmoid and indicated the location of the bow shock on the floor of the 1 AU cube.

Figure 8. Initially-equatorial IMF lines at $t = 24 \text{ h}$, 48 h , and 68 h for Case Three. The plasmoid's field lines are not shown in this figure. The viewing perspective is from 8 AU , $\theta = 60^\circ$, $\phi = 20^\circ$.

Figure 9. Time series plots of magnetic field components (upper panels) as seen by a spacecraft located at 0.72 AU and sitting 1.5° below and 1.5° to the west of the radial extension of the plasmoid's initial axis of symmetry. The corresponding time series of plasma beta ($\beta = 2nkT/(B^2/8\pi)$) are shown in the lower panels for Cases One, Two and Three. The shaded regions indicate the approximate plasmoid boundaries.

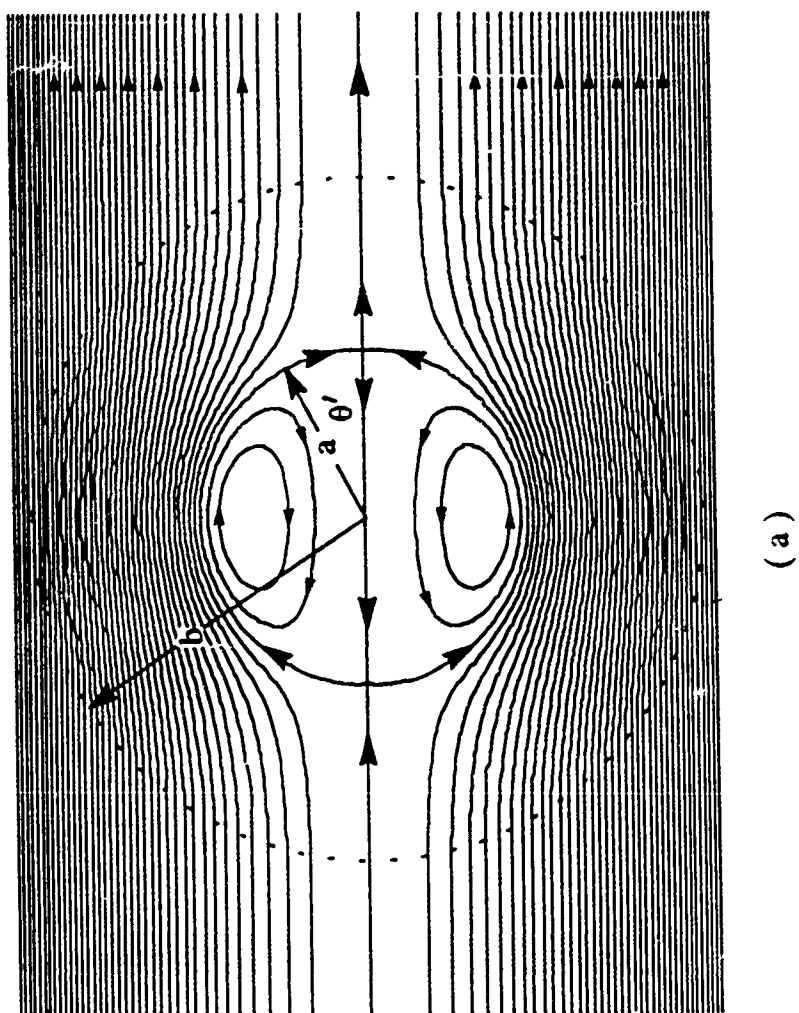
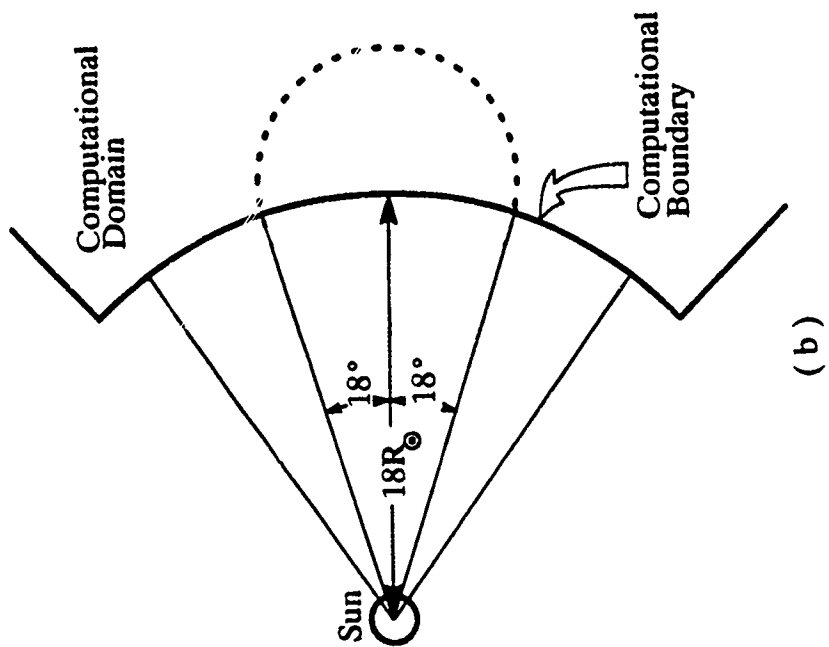


Figure 1

Hill Magnetic Bubble, Case One IMF unit vectors in equatorial plane

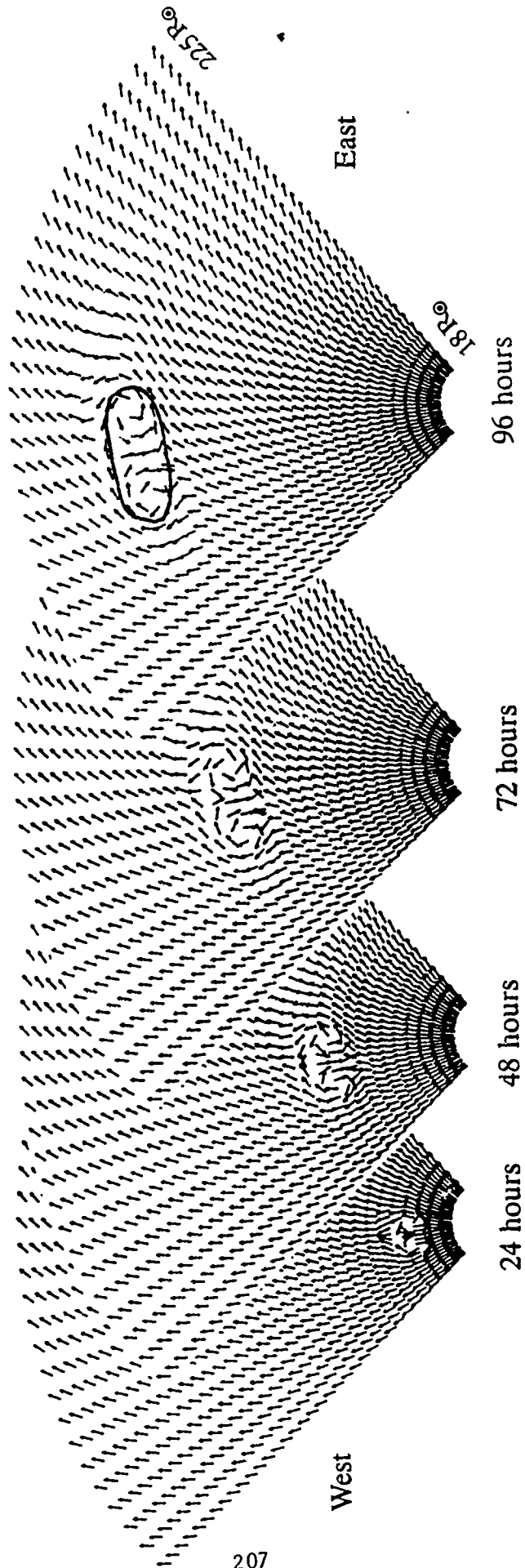


Figure 2

Hill Magnetic Bubble, Case Two IMF unit vectors in equatorial plane

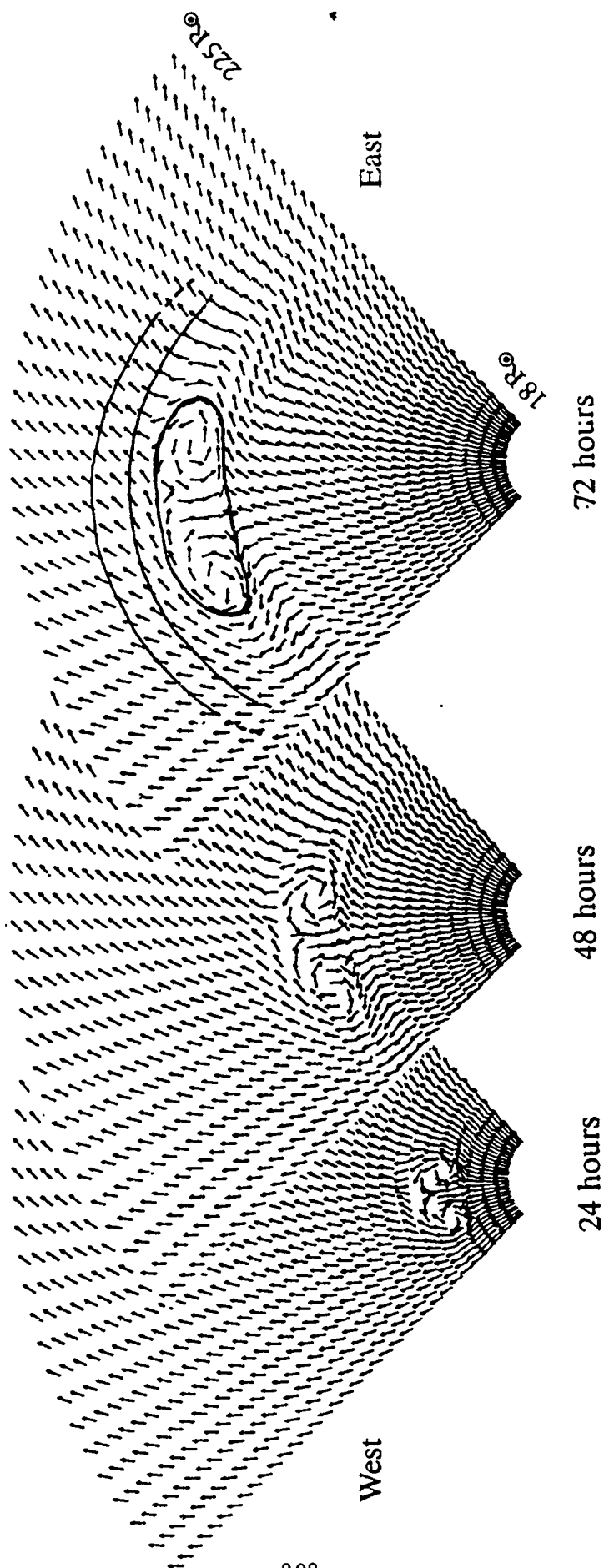


Figure 3

Hill Magnetic Bubble, Case Three

IMF unit vectors in equatorial plane

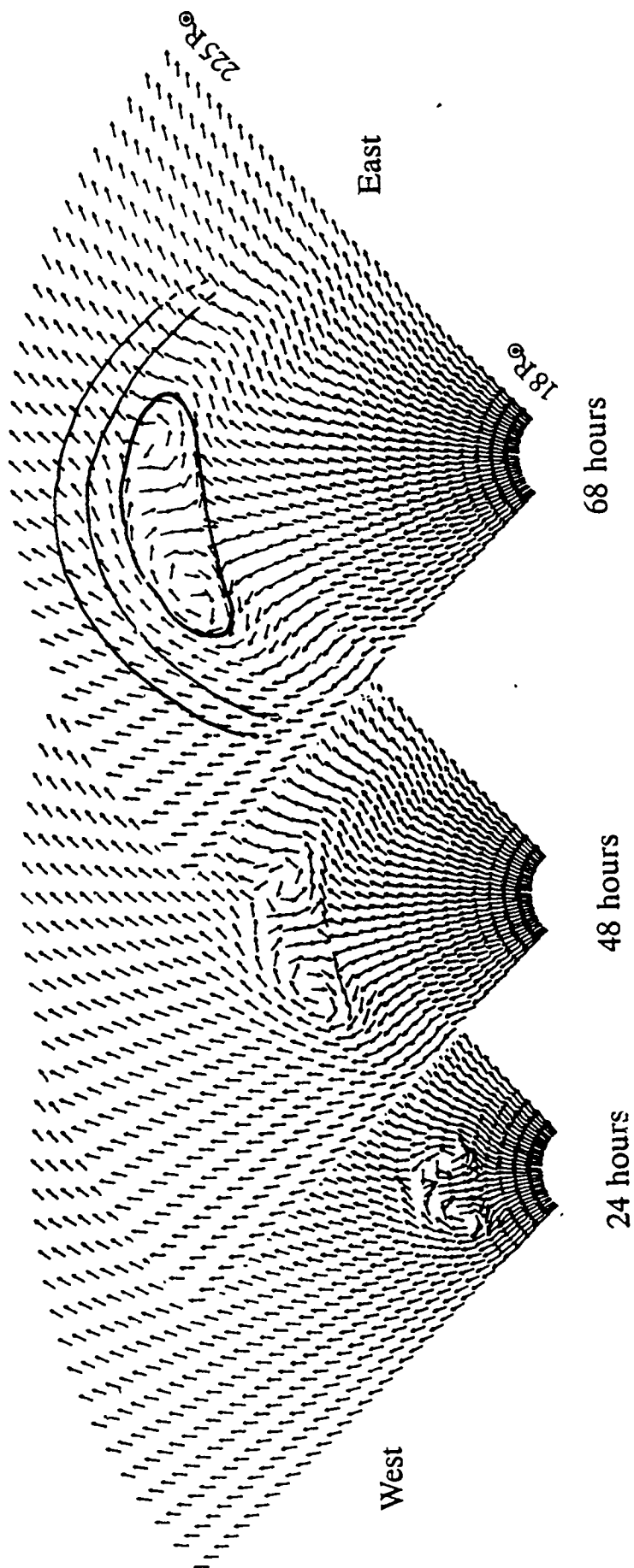
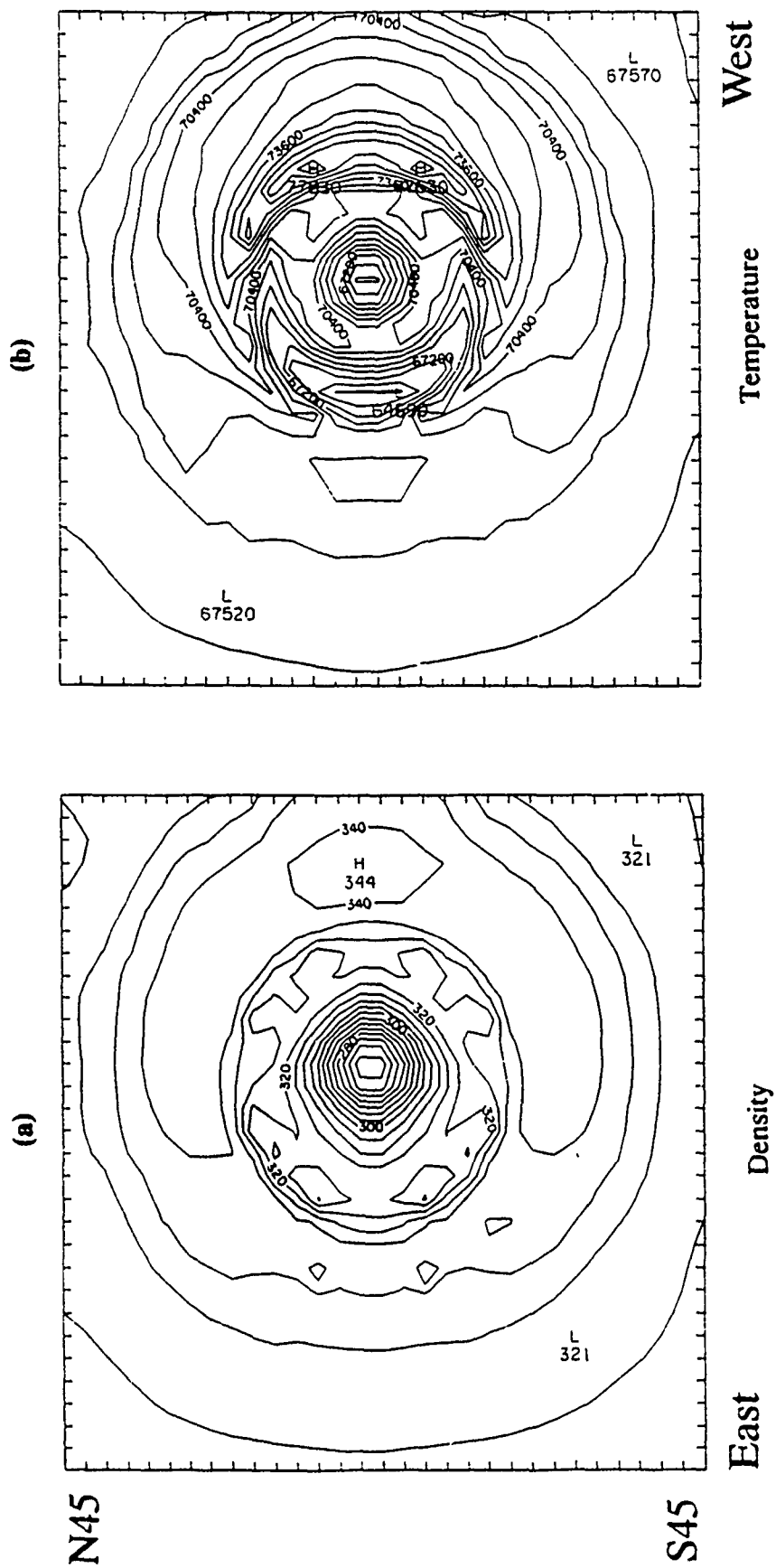
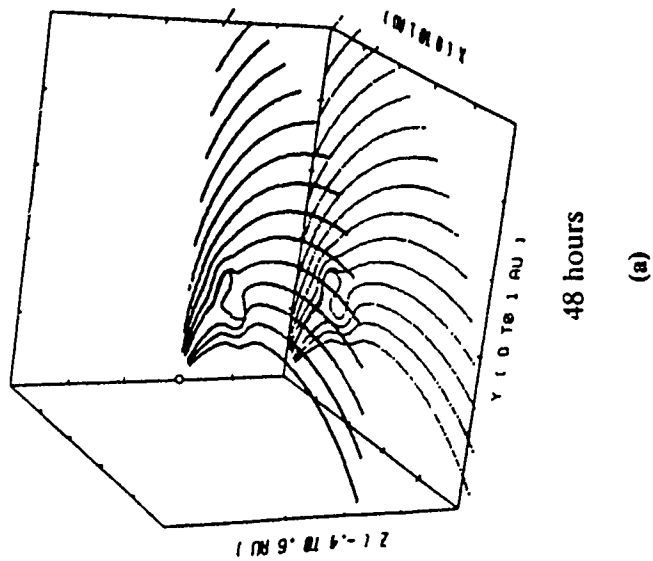


Figure 4

Figure 5

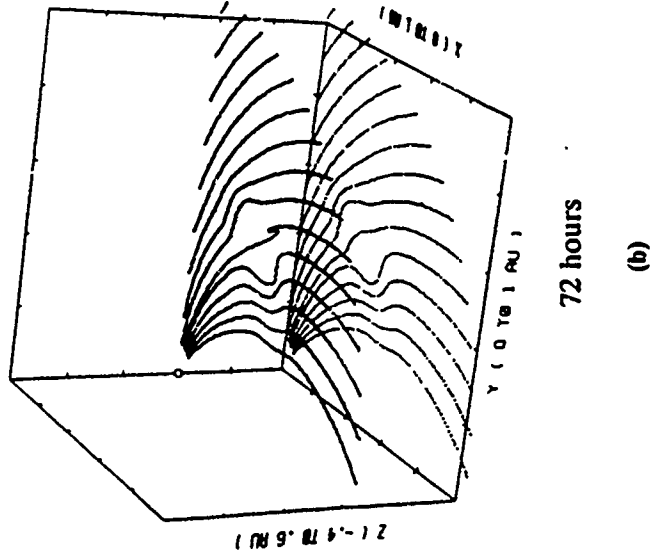


Magnetic Field Lines Case One



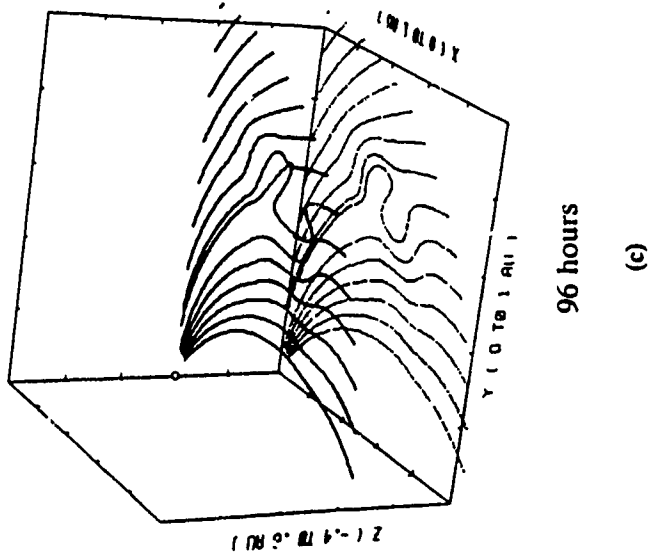
48 hours

(a)



72 hours

(b)

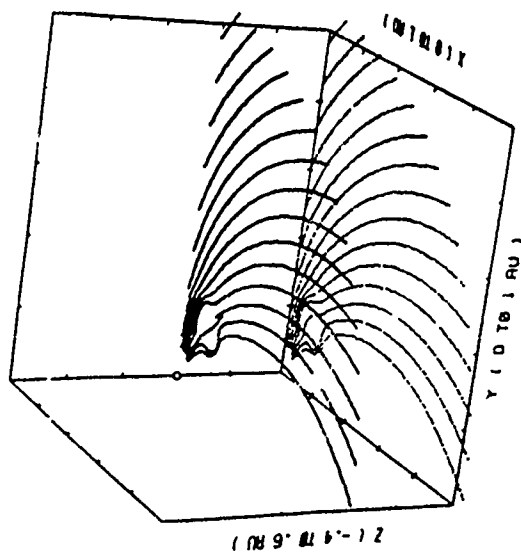


96 hours

(c)

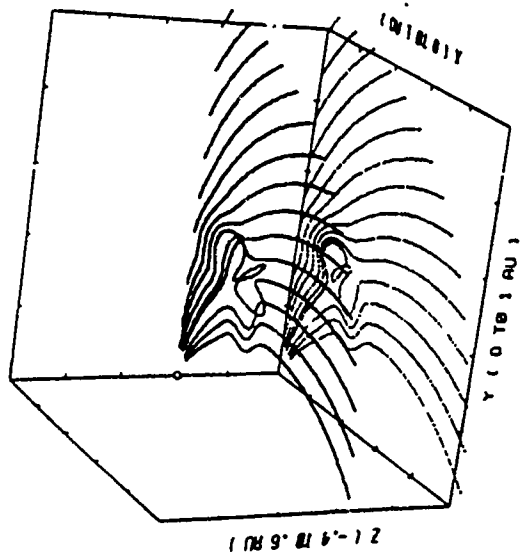
Figure 6

Magnetic Field Lines Case Two



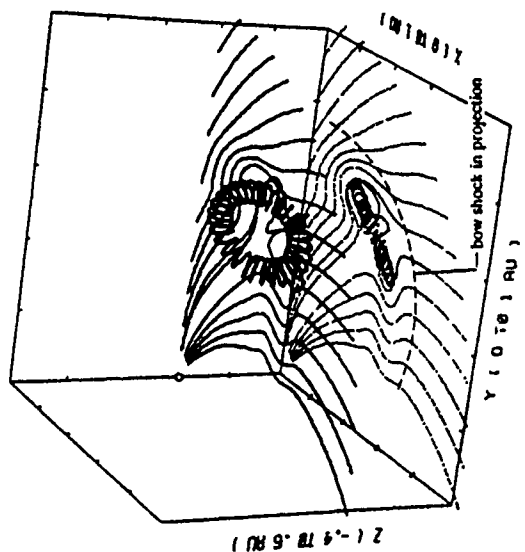
24 hours

(a)



48 hours

(b)



72 hours

(c)

Magnetic Field Lines Case Three

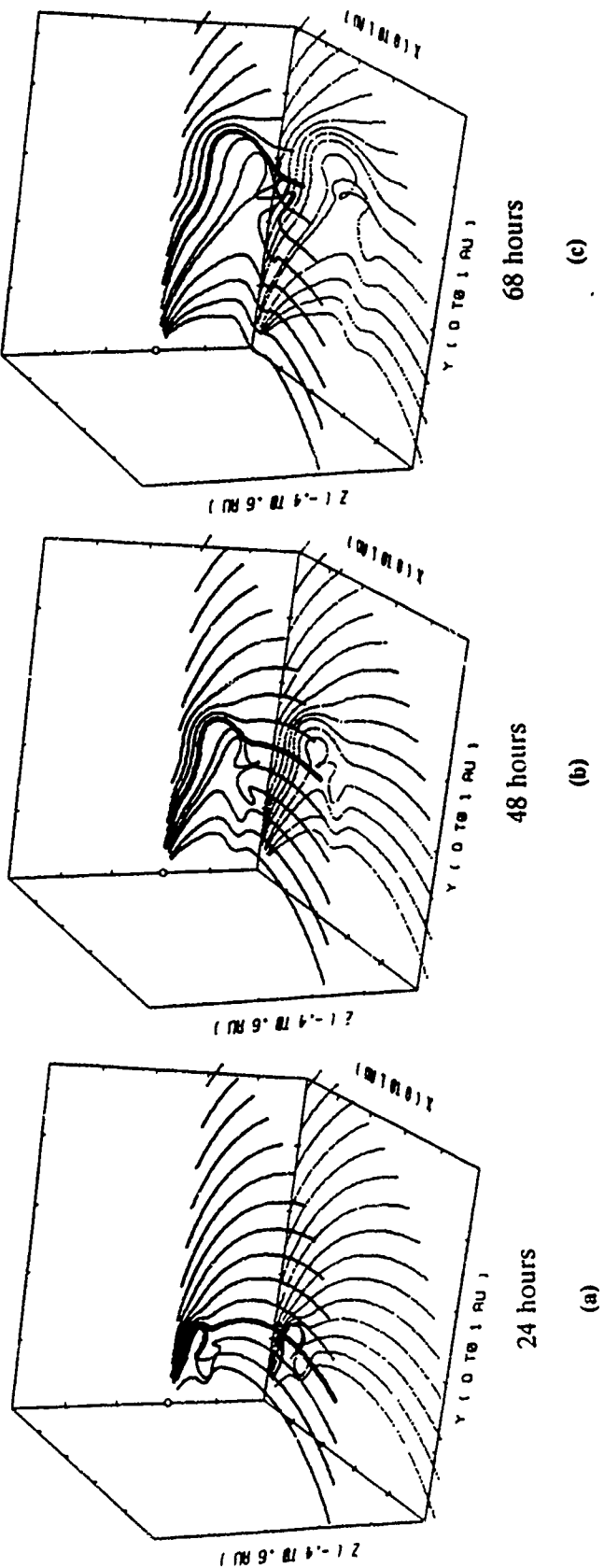


Figure 3

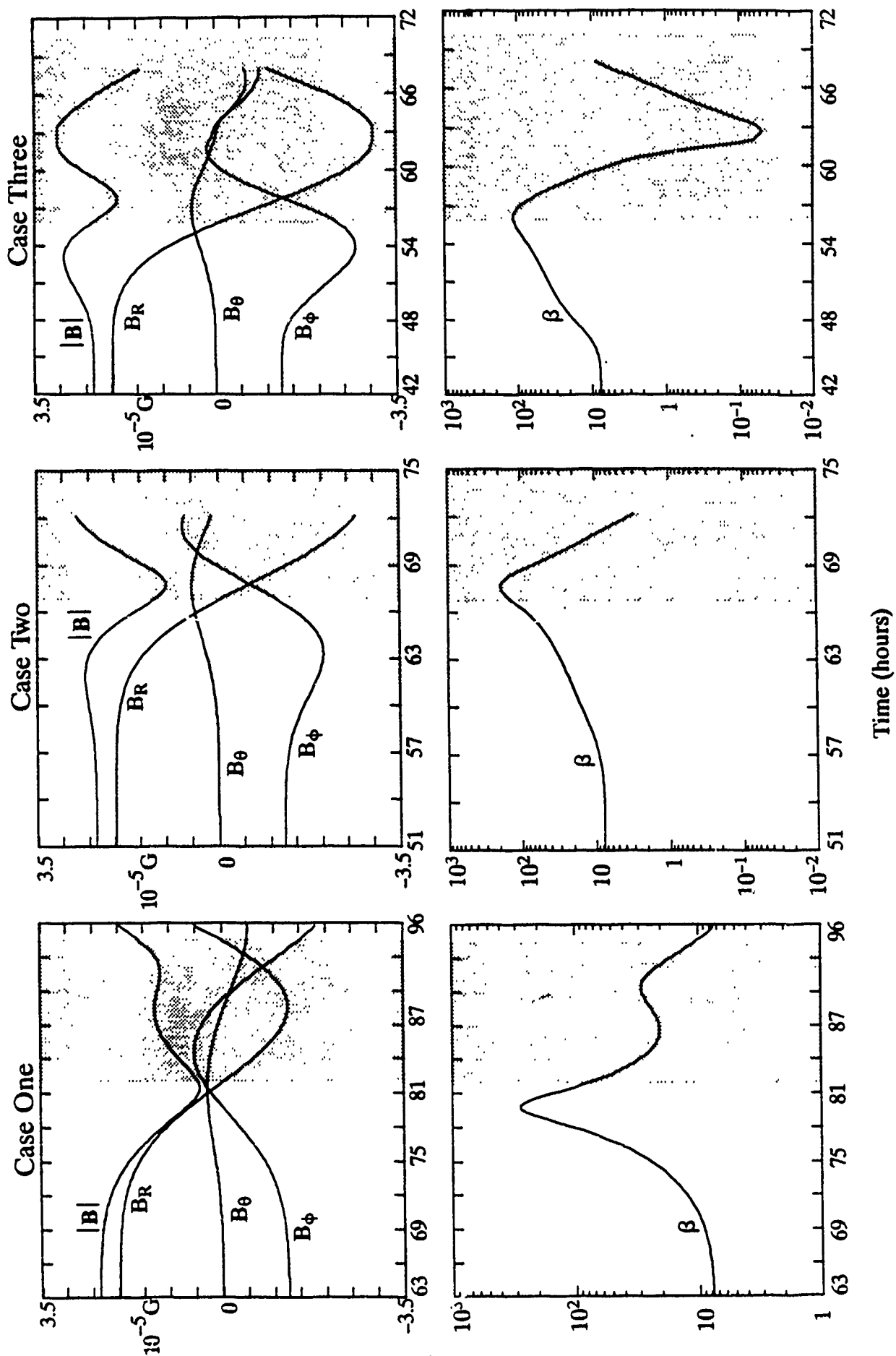


Figure 9

V. NUMERICAL MODELING OF GLOBAL INTERPLANETARY ENVIRONMENT

In this section, we reported the newest three-dimensional, time-dependent magnetohydrodynamic model of extended corona. This model provided steady and time-dependent solar wind solutions in three dimensions. Thus, it can be used as a diagnostic tool for the calibration of instruments for observation using the steady solution. The evolutionary solution can be utilized for the examination of the disturbed solar wind due to solar disturbances. The preliminary results deduced from this model will be published as an invited paper in the J. Adv. Space Research. Another paper is also included in this section which describes the interplanetary consequences due to solar disturbances.

Numerical Simulation of Solar Disturbances and Their
Interplanetary Consequences in 1990 IAU Symposium on
"Basic Plasma Processes on the Sun" E. R. Priest and V.
Krishan (eds), 331-340.

Numerical Simulation of Extended Corona in J. Adv. Space
Res. (to appear) 1991.

NUMERICAL SIMULATIONS OF SOLAR DISTURBANCES AND THEIR INTERPLANETARY CONSEQUENCES

M. DRYER¹, S. T. WU², and T. R. DETMAN¹

¹Space Environment Laboratory
National Oceanic and Atmospheric Administration
R/E/SE, 325 Broadway
Boulder, Colorado 80303-3328
USA

²Center for Space Plasma and Aeronomic Research, and
Department of Mechanical Engineering
University of Alabama in Huntsville
Huntsville, Alabama 35899
USA

ABSTRACT. Responses of the solar atmosphere and interplanetary medium to simulated solar disturbances were studied by time-dependent, MHD numerical simulations. This deterministic initial-boundary value problem was attacked in the classical way: a representative steady state is first established, then input parameters at the lower near-Sun boundary are perturbed. We discuss a number of 2- and 3-dimensional examples of coronal mass ejection (CME) simulations and some current controversies concerning the basic process of CME initiation. Footpoint shearing motion is tested to see whether it can provide a reasonable mechanism for CME development from arch filament configurations.

We also demonstrate possible interplanetary consequences to CME-like disturbances by using 3-D simulations to determine the dynamic response of the solar wind to a plasmoid injection from an eruptive filament or prominence. We also discuss the separate possibility whereby a plasmoid may be generated in the interplanetary medium by a solar-generated shock that propagates through a heliospheric current sheet. Application of the 3-D model for the interpretation of interplanetary scintillation observations is also discussed.

1. INTRODUCTION

1.1 Near-Sun Activity

The origin of coronal mass ejections (CMEs) is one of the major topics currently under active debate. Observations by white-light coronagraphs led to the first ideas and models for CMEs. Coronagraph images are produced by Thomson scattering of photospheric photons by coronal electrons. In addition to the problem of CME origin, the problems of CME propagation and evolution in interplanetary space are also important topics which provide the backdrop for this paper.

A variety of phenomenological descriptions have been applied to the transient white-light images detected by coronagraphs. First OSO-7 and then Skylab, P78-1, and SMM have contributed to the observations. As observed in the solar-occulted plane of sky (Howard et al., 1985), these traveling images have been called curved fronts, spikes, bubbles, loops, blobs, etc. Some workers considered them to be more-or-less planar struc-

tures or helical, magnetically bound loops that escaped the Sun's gravitational attraction; other workers considered them to be compressions (followed by rarefactions) in the corona, produced by near-surface energy conversion that expanded quasi-spherically. Their rate of occurrence and solar-cycle dependence are in statistical dispute, with differences (one per day vis-a-vis two per day) most likely caused by variations in coronagraph design, resolution, and duty cycle. About half of the CMEs are associated with filament eruptions (easily detected at the solar limbs); some are associated with solar flares (not easily detected near the limbs because of the awkward remote-sensing line of sight from Earth); some are associated with both of the above; and sometimes there are no optical, radio, or x-ray observations temporally and spatially associated with CMEs (Munro and Sime, 1985; Webb and Hundhausen, 1987).

Three theoretical descriptions (reviewed by Dryer, 1982) have been offered: (a) White-light "loops" are magnetically driven by stresses in the curved, moving plasma column; (b) White-light "loops," followed by depleted brightness, are quasi-spherical shells of compressed coronal plasma followed by rarefactions; these "loops" are produced by a localized, near-surface change of properties in or near active regions; (c) Very-large-scale coronal magnetic topologies become unstable and trigger CMEs in some way.

Klimchuk (1989) has discussed theoretical ideas for physical mechanisms of CME initiation. He first identifies three basic questions:

- "1) What causes the disruption of the large-scale magnetic field/plasma configuration?
- 2) How does the system evolve once the disruption begins?
- 3) How does the disruption trigger solar flares?"

Klimchuk addresses the first question within the framework of quasi-static evolutionary models. The second, he suggests, "will require a fully time-dependent MHD treatment." As noted by Dryer and Wu (1985), this point has been studied extensively. The third question is "likely [he noted further] to involve non-MHD plasma processes." Neither Klimchuk nor we discuss this third question. In SECTION 2 below, we discuss a numerically demonstrated MHD treatment that, in our opinion, is relevant to both the first and second questions.

1.2 Interplanetary Activity

Several radio astronomers (Hewish and Duffett-Smith, 1987; and Hewish and Bravo, 1986) have interpreted their observations of interplanetary scintillation (IPS) to be associated with geomagnetic activity. Scintillations of distant radio galaxies' radiation are caused by density fluctuations in the intervening solar wind. These fluctuations can be used to generate maps of enhanced and depleted solar wind density. These workers (see, also, Tappin et al., 1988) introduced an ability to generate "interplanetary images" of compressed and rarified solar wind plasmas once each day.

A controversy stems from the radio interpretation of these maps when the density-enhanced regions are back-projected to the Sun. The point of ejection is (according to Hewish, 1988) within (or within a 45° circle surrounding) a coronal hole. Hewish (1986) therefore inferred that an erupting stream within a coronal hole emits very-high-momentum flux that expands into a large (~ 90°) heliolongitudinal expanse and persists for several days. This high efflux of energy, he claims, is the source of geomagnetic storms. He asserts that solar flares are peripheral events.

The alternative view, as expressed by most of the solar physics community, is that the energy influx to the interplanetary medium is due to magnetic eruptions which produce a complicated interaction of shocks, com-

pressions, and rarefactions. The net result [suggested by the 2-D and 3-D numerical MHD simulations by Dryer, Smith, and Wu (1988)] is the high dynamic pressure and IMF amplitude, negative B_z that are required for geomagnetic activity.

A number of transient interplanetary events (often preceded by shocks) have been described by spacecraft investigators as "magnetic clouds," or "plasmoids" (see the review by Burlaga, 1989). These magnetic clouds are characterized by: (1) a rotation of the IMF polarity through a large angle during a temporal interval of about a day, (2) an IMF magnitude which is higher than average, and (3) a solar wind temperature which is lower than average. It is not known if the global topology is disconnected from the Sun (i.e., a plasmoid); if the IMF is still connected to the Sun at both ends (i.e., extension of a solar loop arcade as suggested by Gold, 1959); or if the propagating shocks introduce large-amplitude MHD waves in their wake that cause the IMF to twist, then unwind, with one end rooted in the Sun and the other in interstellar space (Dryer, Wu, and Gislason, 1983). The plasmoid and extended loop are currently attracting much attention together with the notion of twisted, nearly-force-free, IMF "flux ropes."

Another interesting observational inference (based on *in situ* observations) is concerned with the IMF external to the magnetic cloud. Gosling (1989) has reviewed work that suggests that IMF draping around the object occurs in the sheath region between a bow shock and the presumed boundary of the "CME." Although there is no objective criterion for identifying the boundary of a "magnetic cloud" (Burlaga, 1989), this inference is reasonable, particularly if the object (CME, magnetic cloud, etc.) moves relative to the background solar wind with a velocity greater than the local magnetosonic speed.

2. RESULTS

2.1 Shear-Induced Instability

Figure 1 shows the schematic representation of a dipole magnetic field in an initial state of equilibrium in a stratified atmosphere. A 2 $\frac{1}{2}$ -D (i.e., non-planar) MHD model is used to simulate the response of the exponentially stratified atmosphere to a photospheric shearing motion as indicated by the sinusoidal velocity profile in Figure 1. It was found that upward plasma flow velocities are generated in the vertical direction. The velocities grow exponentially at first, with a growth rate equal to $\sqrt{8} (\bar{V}_A a)$, where \bar{V}_A is the average Alfvén speed and a^{-1} is the characteristic length scale. The growth rate is saturated by the Lorentz force, but growth continues until it reaches the same order of magnitude as the Alfvén speed. MHD instability, which we suggest may be called "shearing-induced instability" (SII), occurs shortly thereafter. Physically, the simulation suggests that the central magnetic field lines are pinched, and the outer loops stretch upward with a tendency to open. This process may be considered as one of the fundamental mechanisms for CME initiation (Wu, Song, Martens, and Dryer, 1990).

The SII was studied for three values of plasma beta, $\beta = 15.4$, 1.54, and 0.08. The characteristic Alfvén velocities for these three cases are, respectively: 4.67, 46.7, and 232 km s⁻¹. Figure 2 shows the maximum upward velocity within the computational domain as a function of time. The peak shearing velocity (Figure 1) was 5 km s⁻¹ for the two high values of β and 15 km s⁻¹ for the (more realistic) lowest value. The growth rate for

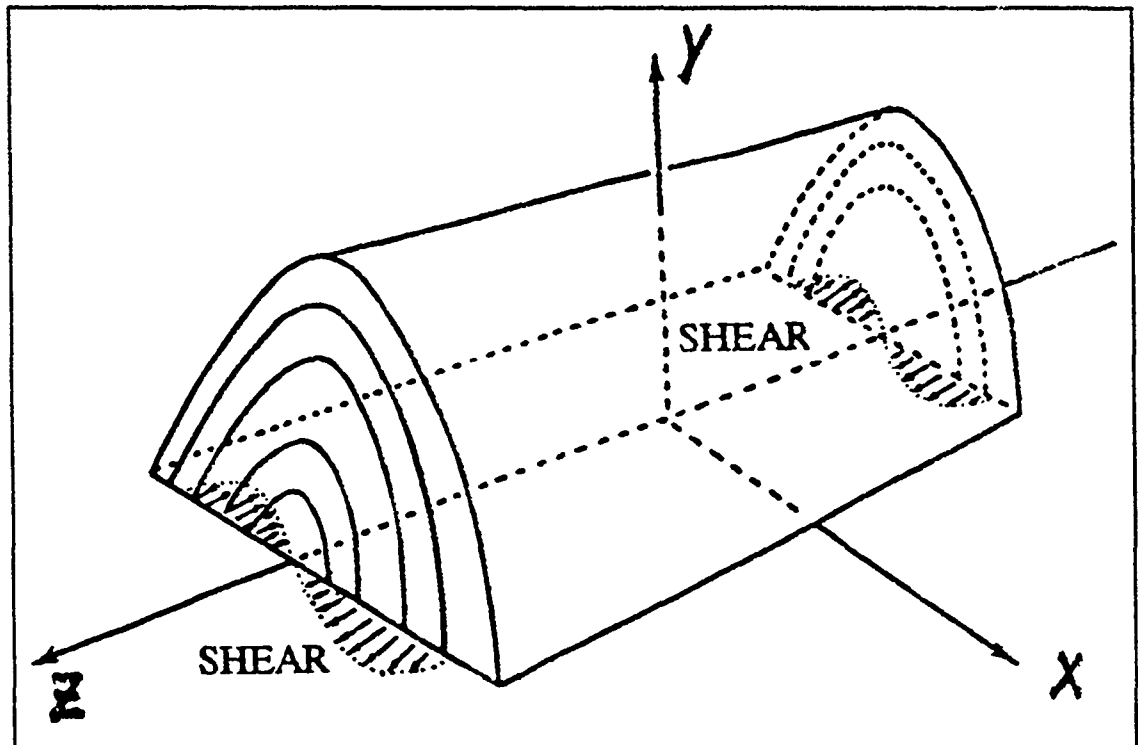


Figure 1. Schematic representation of an initial magnetic field (dipole) arcade which is subsequently sheared at the photosphere by the indicated velocity profile. The computational domain is: $x = \pm 8.4 \times 10^3$ km, and $y = 8 \times 10^3$ km. (Wu, Song, Martens, and Dryer, 1990.)

these upward velocities became unstable when the maximum deviation of the field at the coronal base reached shear angles of 63° , 48° , and 21° for $\beta = 15.4$, 1.54 , and 0.06 , respectively. Thus, instability is indicated for moderate shearing angles when the plasma betas are low, as expected in the lower corona.

It is important to note that the forcing function is a finite-amplitude perturbation upon a stable configuration that eventually becomes unstable. Reduction of the peak shearing velocity of 15 km s^{-1} to a more gentle value, say 0.15 km s^{-1} , could be accomplished via the principle of dynamic similitude (c.f., Wu et al., 1988). The computational run time must then be longer. In the present case of $\beta = 0.06$ (the "prototype"), the same realistic beta could be maintained for the "model," together with the same Struhal, Euler, and Froude numbers as well as the same ratio of magnetic to kinetic energy for a dissipationless fluid.

As suggested above, however, there is a problem in this particular case. The prototype ran for 7 Alfvén periods, where the Alfvén time was 35 seconds. Because of the desired hundred-fold decrease of shearing velocity, the model's rather excessive temporal requirement, τ_M , would be:

$$\tau_M = 7 \times 35 \times 10^2 = 24,500 \text{ s.}$$

2.2 Solar-Injected Plasmoid into the Solar Wind

Using the 3-D code of Han, Wu, and Dryer (1988), Detman et al. (1990) have simulated the injection of an initially spherical plasmoid into the solar

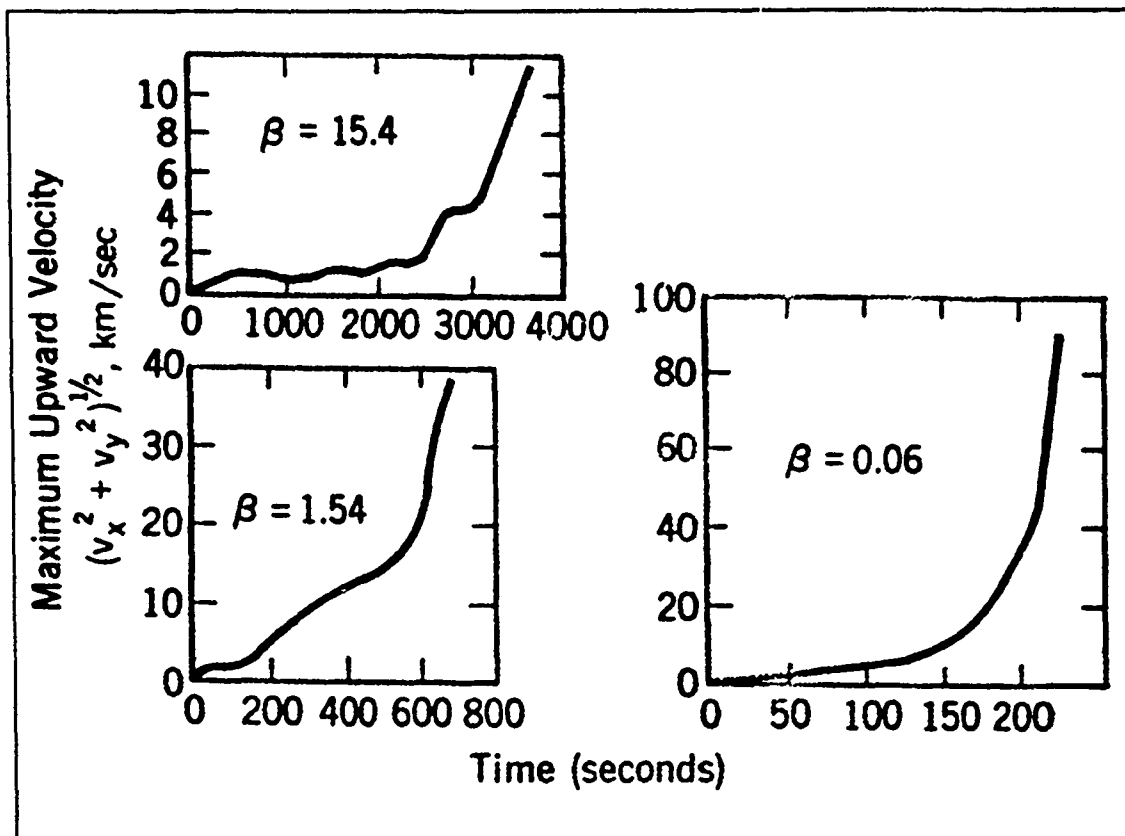


Figure 2. Maximum upward velocity in the computational domain (Figure 1) when photospheric shearing of a dipole magnetic field takes place. Note that "shearing-induced instability" takes place at $t \approx 200$ s, for $\beta = 0.06$, after approximately seven Alfvén times. (From Wu, Song, Martens, and Dryer, 1990.)

wind. The plasmoid possessed both toroidal and poloidal magnetic field components, like a set of concentric "slinky toys" placed end to end. The plasmoid survived the injection and continued to propagate through the solar wind, even producing a substantial shock wave when injected at a speed greater (relative to the background solar wind velocity) than the magnetosonic speed. The approximate positions of the plasmoid and its shock wave, and the draping of the IMF around the plasmoid, were determined. Figure 3 shows a 3-D view of some representative IMF lines and their draping around the plasmoid. A representative magnetic field line within the plasmoid is also shown.

It is interesting to note that some reconnection (due to numerical diffusion) takes place between some of the plasmoid field lines and IMF lines that come into close proximity to the neutral points on the front and rear positions of the plasmoid.

2.3 Plasmoid Created at Heliospheric Current Sheet

In a separate numerical experiment, Dryer et al. (1989) showed how a cigar-shaped plasmoid might be generated by a shock wave that propagates through a flat heliospheric current sheet. The high total pressure, formed by the 3-D shock wave just within its outermost envelope, decreases to low values within the central portion, i.e., near the IMF reversal zone. The high pressure gradient, generated by the outward-moving, large-scale

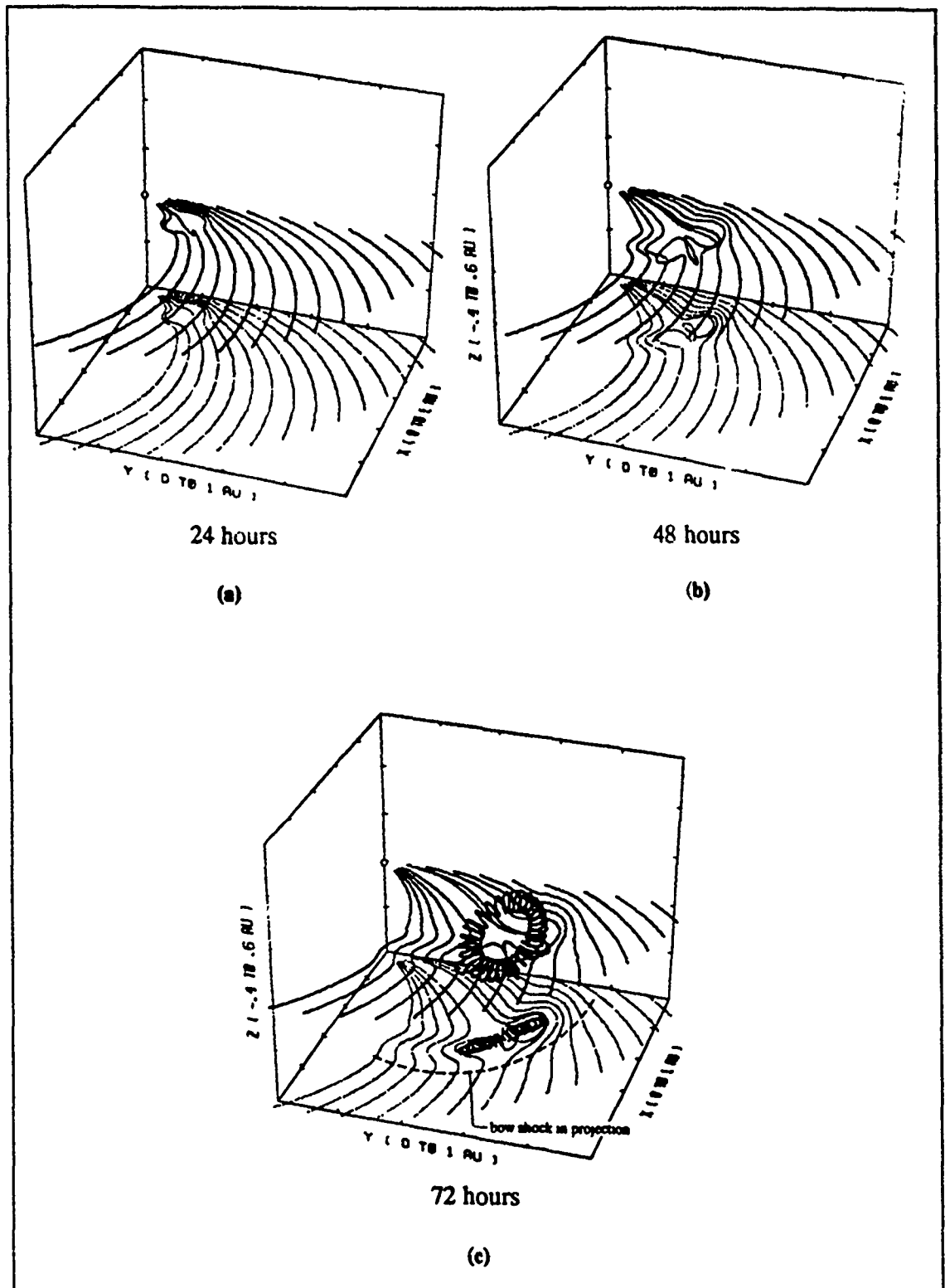


Figure 3. A 3-D view of the IMF as it is deflected by the bow shock, its draping around the solar-generated plasmoid, and a single helical magnetic field line within the plasmoid. Initially equatorial IMF lines are shown at $t = 24, 48$, and 72 hours in panels (a), (b), and (c), respectively. The viewing perspective is from 8 AU , $\theta = 60^\circ$, $\phi = 20^\circ$, where θ is the heliocolatitude and ϕ is the heliolongitudinal angle measured from the lower left of the 1 AU -sized box. (Detman et al., 1990.)

heliospheric shock wave, forces the opposite-directed IMF field lines together and causes them to reconnect.

Figure 4 shows the initial stage of reconnection at what will be the leading edge of the cigar-shaped plasmoid. Reconnection also takes place at the rear, pinching off the opposite-directed IMF as the entire structure propagates through the solar wind. The "cigar" would be oriented in a direction transverse to the outward motion of the large-scale global disturbance.

4. CONCLUDING REMARKS

We have briefly summarized some of our ongoing work in the field of non-planar and 3-D numerical simulations of solar disturbances and their possible interplanetary consequences. The classical initial boundary-value approach is scrupulously followed to ensure a deterministic response whenever a stable initial state is perturbed by a set of observationally in-

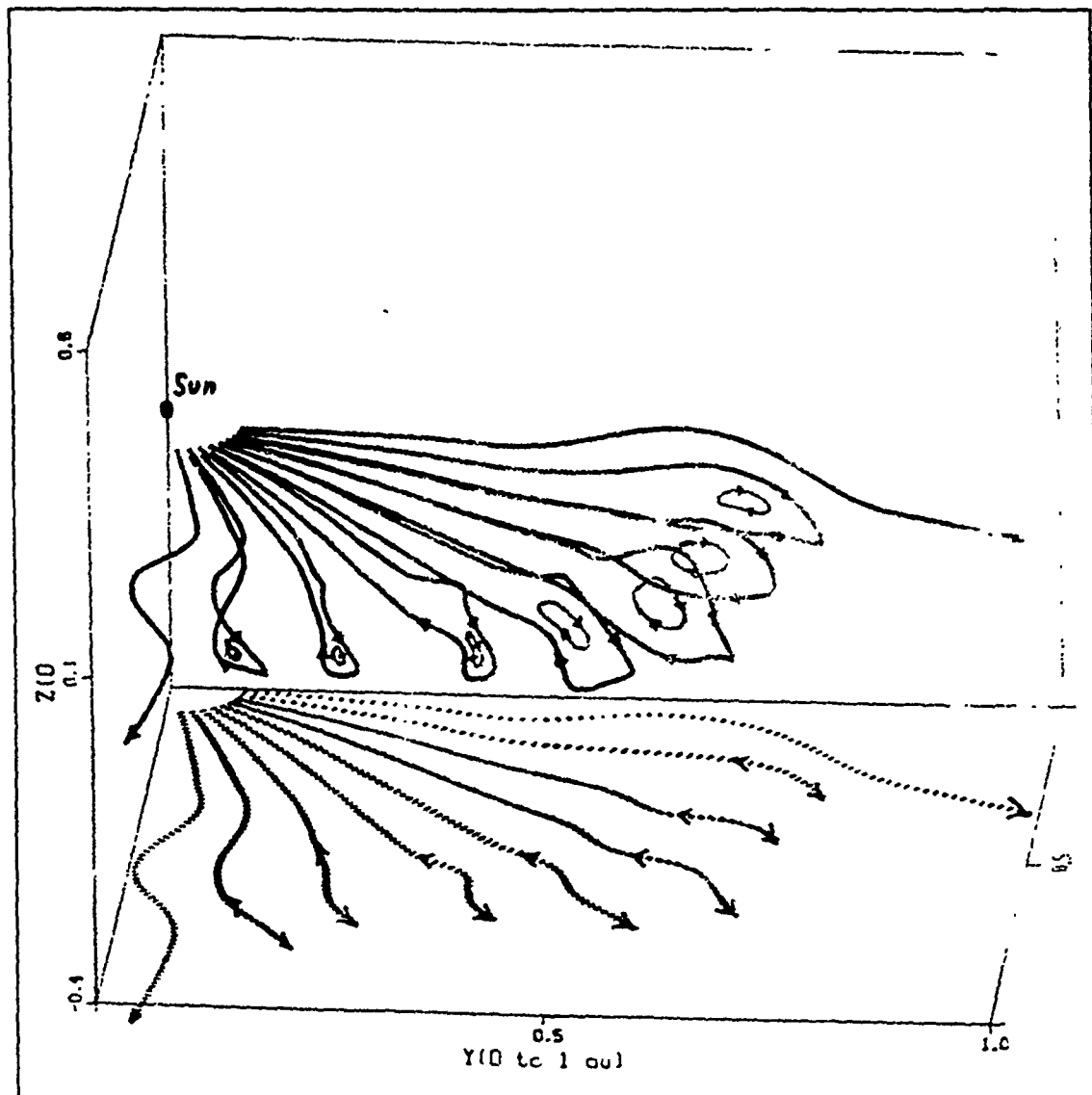


Figure 4. Initial stage of a cigar-shaped plasmoid that is formed in the interplanetary medium by the propagation of a shock wave through a flat heliospheric current sheet. (Dryer et al., 1989; S.M. Han, private comm., 1989.)

ferred parameter changes. Numerical experiments of this kind are a necessary step beyond the "cartoon" stage, and must be undertaken with the solution of the mathematical expressions for well-known physical laws together with reasonably chosen assumptions. The insight derived from simulations such as the three described here are essential for understanding large-scale global processes. Only investigation by multiple, in situ, spacecraft missions can confirm or refute the global predictions of such 3-D numerical experiments. Such missions have yet to be undertaken.

5. ACKNOWLEDGMENT

This work was supported in part by NASA Order No. 17,015 to NOAA Space Environment Laboratory (MD, TRD), and by NOAA Contract 50RANR-700099, NAGW-9, and AFOSR Grant 88-0013 (STW). We wish to thank Z. Smith, R. Zwickl, S. M. Han, S. W. Kahler, T. G. Forbes, J. A. Klimchuk, and D.J. McComas, for their help and advice.

6. REFERENCES

- Burlaga, L. F. (1989), in E. Marsch and R. Schwenn (eds.), Physics of the Inner Heliosphere, D. Reidel Publ. Co., Dordrecht, in press.
- Detman, T. R., Dryer, M., Yeh, T., Han, S. M., Wu, S. T., and McComas, D. J. (1990), in preparation.
- Dryer, M. (1982), Space Sci. Rev., 33, 233.
- Dryer, M., Detman, T. R., Wu, S. T., and Han, S. M. (1989), Adv. Space Res., 9(4), 75.
- Dryer, M., Smith, Z. K., and Wu, S. T. (1988), Astrophys. Space Sci., 144, 407-425.
- Dryer, M., and Wu, S. T. (1985), J. Geophys. Res., 90, 559.
- Dryer, M., Wu, S. T., and Gislason, G. (1983), in M. Neugebauer (ed.), Proceedings of the Fifth International Solar Wind Conference, NASA Conference Publ. No. 2280, p. 735.
- Gold, T. (1959), J. Geophys. Res., 64, 1665.
- Gosling, J. T. (1989), in C. T. Russell (ed.), Physics of Magnetic Flux Ropes, Amer. Geophys. Union Monograph, in press.
- Han, S. M., Wu, S. T., and Dryer, M. (1988), Computers & Fluids, 16, 82.
- Hewish, A. (1988), Solar Phys., 116, 195.
- Hewish, A., and Bravo, S. (1986), Solar Phys., 106, 185.
- Hewish, A., and Duffett-Smith, P. J. (1987), Planet. Space Sci., 35, 487.
- Howard, R. A., Sheeley, N. R., Jr., Michels, D. J., and Koomen, M. J. (1985), J. Geophys. Res., 90, 8173.
- Klimchuk, J.A. (1989), in K. Phillips (ed.), Proceedings of the Thermal-Nonthermal Flares Workshop II, Rutherford-Appleton Laboratory Report, RAL-89-102, Didcot, U.K., pp. 1-6 to 1-8.
- Munro, R. H., and Sime, D. G. (1985), Solar Phys., 97, 191.
- Tappin, S. M., Dryer, M., Han, S. M., and Wu, S. T. (1988), Planet. Space Sci., 36, 1155.
- Webb, D. F., and Hundhausen, A. J. (1987), Solar Phys., 108, 383-401.
- Wu, S. T., Song, M. T., Martens, P., and Dryer, M. (1990), in preparation.
- Wu, S. T., Wang, S., Wang, A. H., and Dryer, M. (1988), Adv. Space Res., 8(11), 221-226.

DISCUSSION

FORBES: Was the initial state in your sheared arcade example potential or force-free? If so, it seems to me that your result completely contradicts the work of J. J. Aly which shows that such a disruption, which opens the field, by shearing should be impossible.

DRYER: The initial state is, indeed, a potential force-free magnetic arcade. When the footpoints are moved, they are moved rather rapidly. For example, the lowest beta case ($\beta = 0.06$) had a peak shearing velocity of 15 km/sec. Consequently, the system quickly evolves into a non-force-free system with pressure gradients. Thus, the force-free results of Aly do not apply. Also, the instability only results in a rapid expansion of loops and locally fast mass flows after the mean Alfvén speed is exceeded. This instability, moreover, does not necessarily open the magnetic field. You will recall that there is no resistivity in this model, nor are there any anti-directed fields where numerical reconnection could, in principle, take place. Thus, this model does not address the question of field-line-opening.

KUNDU: I am a little confused by your referring to flares as the cause of IPS-producing shocks rather than high-speed streams from coronal holes, which Tony Hewish believes. Since you showed Hewish's data, when you talked about IP shocks, I would like to know what the present status is with regard to flares versus coronal holes as the cause of IP shocks.

DRYER: Our use of Hewish's IPS data is decoupled from his interpretation that high speed streams from coronal holes are responsible for geomagnetic storms. If a transiently-developing coronal hole suddenly (say, on a few-hour time scale) develops, a shock could certainly develop. I have a constructive and friendly disagreement with Tony who believes that flares are peripheral events *vis-à-vis* geomagnetic storms. I believe otherwise. You will recall that IPS data contains no information about the IMF (which, if southerly-directed, is important for storm triggering); hence my comment above about decoupling. Of course, even a steady-state hole could develop a shock that develops in the corotating frame. My point is that *any* temporal and/or spatial solar inhomogeneity (*c.f.*, flare, eruptive prominence, or hole) could produce a shock. Hewish's point, however, about a transient event, followed by a *long-lasting* energy output (be it a flare or whatever) is an important point that is worth investigation. To this purpose, Zdenka Smith and I have recently completed a 2D MHD parametric study that is relevant to this point. A final point is worth making: there are no observables of erupting streams from coronal holes. Transient coronal hole area changes are not sufficient, in my opinion, to claim that a shock will propagate from such an event. The case for flares is well-established.

SWARUP: How does the intensity of shocks vary with solar distance in your models?

DRYER: When the temporal duration of an input pulse is short, say less than a few hours, the strongest part of the shock will decay similarly to a classical blast wave with shock speed $\sim R^{-1/2}$ where R is the heliocentric radius. If the energy input is long-lasting, say some 5-15 hours (as suggested by long duration X-ray flares) the shock could move out at a constant velocity (*i.e.*, as a piston-driven shock) for some tenths of an AU before decelerating as noted above in the frame of the background, moving solar wind.

PRIEST: (i) Is the plasma beta much smaller than unity in magnetic clouds and in your magnetic bubble?

(ii) If so, why should the plasma density changes be directly proportional to the initial density?

DRYER: (i) Your first question relates to our "magnetic bubble" numerical experiment. We were interested in examining the dynamics of a particular configuration and the response (*c.f.*, field draping) of the ambient solar wind and its interplanetary magnetic field to its projectile-like motion. Although we were not interested at this exploratory stage to make any comparisons with spacecraft-observed "magnetic clouds" the particular choice of the parameters (n, T, B ,) within our input bubble produced plasma betas greater than unity. We would expect that other, judiciously-chosen, parameter combinations could produce betas less than one - as found in the observations. It is not clear, incidentally that the latter are bubbles - or whether they are gigantic loops with both ends rooted in the Sun.

(ii) The density fluctuations that give rise to IPS are experimentally correlated with *in situ* density measurements by Tappin (1986) and more rigorously, recently, by Zwickl *et al* (AGU abstract, 1988).

UBEROI: In your analogy of magnetic bubble to Hill's vortex did you take care of the fact that some conservation theorems valid for vortices do not hold good for MHD theory?

DRYER: Thank you for bringing this possibility to my attention. No, we did not take this point into consideration.

Invited Paper, COSPAR Symposium S.9
"Space Observations of the Solar Corona
and the Origin of the Solar Wind"

The Hague, The Netherlands,
June 27-29, 1990

NUMERICAL SIMULATION OF EXTENDED CORONA

S. T. Wu and Ai-Hwa Wang

Center for Space Plasma and Aeronomic Research
and Department of Mechanical Engineering
The University of Alabama in Huntsville
Huntsville, AL 35899 U.S.A.

ABSTRACT

A three-dimensional, time-dependent magnetohydrodynamic (MHD) model is presented for the study of coronal dynamics. The model, written in spherical coordinates, extends from the solar surface ($1R_{\odot}$, where $1R_{\odot} = 6.95 \times 10^5$ km) to $15 R_{\odot}$. This model was developed with two major issues in mind, namely for interpretation of various steady state and evolutionary dynamical structures in the corona. In order to achieve these objectives we have employed two different numerical techniques to seek solutions for these two different, but related, problems: steady state structures and evolutionary structures. These two numerical techniques are: (i) relaxation technique for steady state structures; and (ii) FICE (Full-Implicit-Continuous-Eulerian) technique for evolutionary structures.

To illustrate this model, we present numerical results for examples of both the steady state and evolutionary structure of the corona. These results show the additional physical features which cannot be shown by a two-dimensional model. Finally, on the basis of the exploratory calculation, we outline some interesting physical features which can be considered for the observing programs of future space missions such as SOHO, OSO, CORONAS, etc.

I. INTRODUCTION

Since the Skylab-ATM experiments in the seventies, we have recognized that the corona is in a transient state in contrast to the previous understanding whereby the corona is always in a quiet orderly state (Billings, 1966). It is also further realized that the relationship between the flare and the coronal mass ejection is not as consistently intimate as originally thought (Hildner et al. 1976). In order to understand the physics of this fascinating phenomena of so-called "coronal transients", a number of theoretical models has been presented in the literature (Hundhausen et al. 1984). All of these theoretical models are based on magnetohydrodynamic theory. The methodology used to treat these theoretical models could be classified into two categories: (i) analytical methods and (ii) numerical methods. Those models treated by analytical methods have to conform to certain strict conditions in which a full description of nonlinear dynamical behavior is difficult to achieve; nevertheless, the solutions are exact. On the other hand, the models treated by numerical methods could obtain global descriptions of nonlinear dynamics, but these descriptions are not unambiguous and may mislead the physical interpretations. A further limitation to these two categories is the fact that all of these models are confined to a two-dimensional geometry. Thus, it is inevitable that some arguments in the interpretation of observations have taken place.

In this paper, we present a newly developed *three-dimensional*, time-dependent, magnetohydrodynamic model for an extended corona. We will suggest that this model could be used to understand the physical processes from the comparison of this model's results with observational data. The theoretical description of the model presents the basis for the addition of dissipative mathematical terms that could be used to understand additional physical processes from specific observational data. The theoretical description of the model are included in Section II. The numerical results are presented in Section III. Finally, the concluding remarks are included in Section IV.

II. ANALYSES

Mathematical Model

In this study, we have assumed that the solar atmosphere behaves as a single fluid with negligible dissipative effects. With these assumptions, the time-dependent magnetohydrodynamic (MHD) equations that describe

atmospheric flows in three-dimensions for a spherical coordinate system can be written as follows:

$$\frac{\partial \rho}{\partial t} = -\frac{1}{r^2} \frac{\partial(r^2 \rho v_r)}{\partial r} - \frac{1}{r \sin \theta} \frac{\partial(\rho v_\theta \sin \theta)}{\partial \theta} - \frac{1}{r \sin \theta} \frac{\partial(\rho v_\phi)}{\partial \phi} \quad (1)$$

$$\begin{aligned} \frac{\partial v_r}{\partial t} = & -v_r \frac{\partial v_r}{\partial r} - \frac{v_\theta}{r} \frac{\partial v_r}{\partial \theta} - \frac{v_\phi}{r \sin \theta} \frac{\partial v_r}{\partial \phi} - \frac{1}{\rho} \left\{ \frac{\partial(\rho RT)}{\partial r} + B_\theta \left(\frac{\partial B_\theta}{\partial r} - \frac{1}{r} \frac{\partial B_r}{\partial \theta} \right) \right. \\ & \left. - B_\phi \left(\frac{1}{r \sin \theta} \frac{\partial B_r}{\partial \phi} - \frac{\partial B_\phi}{\partial r} \right) \right\} + \frac{v_\phi^2 + v_\theta^2}{r} - \frac{B_\phi^2 + B_\theta^2}{\rho r} - \frac{GM}{r^2} \end{aligned} \quad (2)$$

$$\begin{aligned} \frac{\partial v_\theta}{\partial t} = & -v_r \frac{\partial v_\theta}{\partial r} - \frac{v_\theta}{r} \frac{\partial v_\theta}{\partial \theta} - \frac{v_\phi}{r \sin \theta} \frac{\partial v_\theta}{\partial \phi} - \frac{1}{\rho} \left\{ \frac{\partial(\rho RT)}{r \partial \theta} - B_r \left(\frac{\partial B_\theta}{\partial r} - \frac{1}{r} \frac{\partial B_r}{\partial \theta} \right) \right. \\ & \left. - B_\phi \left(\frac{1}{r \sin \theta} \frac{\partial B_\theta}{\partial \phi} - \frac{\partial B_\phi}{r \partial \theta} \right) \right\} - \frac{v_r v_\theta - v_\phi^2 \cot \theta}{r} - \frac{B_r B_\theta - B_\phi^2 \cot \theta}{\rho r} \end{aligned} \quad (3)$$

$$\begin{aligned} \frac{\partial v_\phi}{\partial t} = & -v_r \frac{\partial v_\phi}{\partial r} - \frac{v_\theta}{r} \frac{\partial v_\phi}{\partial \theta} - \frac{v_\phi}{r \sin \theta} \frac{\partial v_\phi}{\partial \phi} - \frac{B_r}{\rho} \frac{\partial B_\phi}{\partial r} - \frac{B_\theta}{r} \frac{\partial B_\phi}{\partial \theta} - \frac{1}{r \rho \sin \theta} \\ & \left(\frac{\partial(\rho RT)}{\partial \phi} - B_r \frac{\partial B_r}{\partial \phi} - B_\theta \frac{\partial B_\theta}{\partial \phi} \right) - \frac{B_\phi}{\rho r} (B_r + B_\theta \cot \theta) - \frac{v_\phi}{r} (v_r + v_\theta \cot \theta) \end{aligned} \quad (4)$$

$$\frac{\partial B_r}{\partial t} = \frac{1}{r \sin \theta} \left\{ \frac{\partial}{\partial \theta} (\sin \theta (v_r B_\theta - v_\theta B_r)) - \frac{\partial}{\partial \phi} (v_\phi B_r - v_r B_\phi) \right\} \quad (5)$$

$$\frac{\partial B_\theta}{\partial t} = \frac{1}{r \sin \theta} \frac{\partial}{\partial \phi} (v_\theta B_\phi - v_\phi B_\theta) - \frac{1}{r} \frac{\partial}{\partial r} [r (v_r B_\theta - v_\theta B_r)] \quad (6)$$

$$\frac{\partial B_\phi}{\partial t} = \frac{1}{r} \frac{\partial}{\partial r} [r (v_\phi B_r - v_r B_\phi)] - \frac{1}{r} \frac{\partial}{\partial \theta} (v_\theta B_\phi - v_\phi B_\theta) \quad (7)$$

$$\begin{aligned} \frac{\partial T}{\partial t} = & -(\gamma - 1) T \left\{ \frac{1}{r^2} \frac{\partial(r^2 v_r)}{\partial r} + \frac{1}{r \sin \theta} \frac{\partial(v_\theta \sin \theta)}{\partial \theta} + \frac{1}{r \sin \theta} \frac{\partial v_\phi}{\partial \phi} \right\} \\ & - v_r \frac{\partial T}{\partial r} - \frac{v_\theta}{r} \frac{\partial T}{\partial \theta} - \frac{v_\phi}{r \sin \theta} \frac{\partial T}{\partial \phi} \end{aligned} \quad (8)$$

where the dependent variables are the density ρ , temperature T , velocity (v_r, v_θ, v_ϕ), and magnetic field (B_r, B_θ, B_ϕ). The independent variables are the radius r , the meridional angle θ and azimuthal angle ϕ as well as time t . The constants are the polytropic index γ , solar total mass M and gravitational constant G . In addition, the standard equation of state ($p = \rho RT$) was used to obtain the above set of governing equations.

The region, within which we will present the numerical solution to the above set of governing equations, is shown in Figure 1. This region is bounded by the solar surface and 15 solar radii (R_s) in radial distance, by the equator and the pole in meridional distance (θ -coordinate), and by azimuthal extent (ϕ -coordinate) of 45° .

Method of Solution

The equations are solved numerically using a modified FICE (Full-Implicit-Continuous-Eulerian) scheme which is based on the original FICE scheme developed by Hu and Wu (1984) and Wu and Wang (1987). The grid spacings used are $\delta r = R_s(1 - \delta\theta)^{1/4}$, and $\delta\theta = \delta\phi = 4.5^\circ$. It should be noted that the radial spacing is not uniform and is chosen so as to: (1) assure the initial state as being in isothermal and hydrostatic equilibrium (Wang et al. 1982); (2) initialization of the computation procedure; and (3) to ensure numerical accuracy. The time step can be arbitrarily chosen because of the flexibility of the FICE scheme.

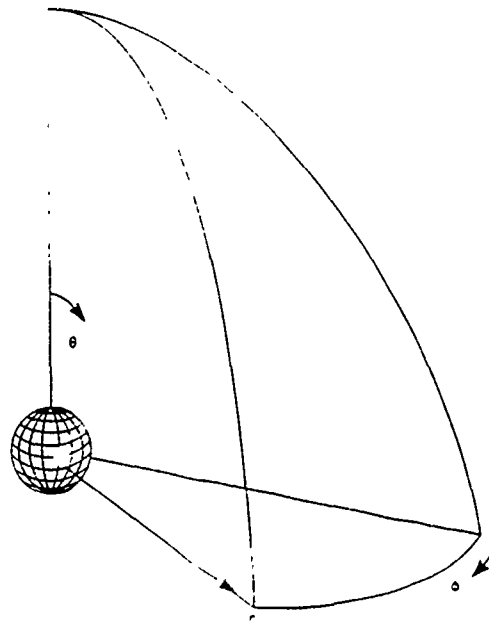


Fig. 1. A schematic description of the portion of a three-dimensional configuration in which the solution is calculated. Note that the computational domain extends from the pole to the equator within a 45° extent of heliolongitude. In the present paper, symmetry is assumed below the solar equatorial plane.

Initial State and Boundary Conditions

In order to seek a solution of this problem, we need to specify the initial conditions. These initial conditions include the magnetic field configuration, velocity field and corresponding thermodynamic properties of the plasma.

The boundary conditions are rather complicated, hence a detailed account of the derivation of the boundary conditions will be presented later (Wang and Wu, 1990). We shall only briefly describe these boundary conditions here. There are a total of six sides in which the boundary conditions need to be specified; they are:

- (1) $r = R_s$, eight compatibility conditions are obtained from the set of governing equations (Wu and Wang, 1987);
- (2) $r = 15R_s$, non-reflecting boundary conditions are used (Hu and Wu, 1984);
- (3) $\theta = 0$ (pole) and $\theta = 90^\circ$ (equator), symmetric conditions are chosen because of the chosen field configuration;
- (4) $\phi = 0$ and $\phi = 45^\circ$, the boundary conditions are obtained by extrapolation techniques.

III. NUMERICAL RESULTS

In order to carry out this simulation, we first introduced an initial state at isothermal and hydrostatic equilibrium with $\gamma = 1.67$ together with a potential field in one case and, in a separate case, a linear force-free magnetic field topology. These two separate cases were introduced into the set of governing equations in order to ensure that the isothermal and hydrostatic equilibrium does exist. We then introduced a steady-state, Parker-type, velocity field. The numerical solution of this mathematical system led to a magnetohydrodynamic equilibrium state via the relaxation technique. This MHD equilibrium state is then taken as the simulated undisturbed coronal (i.e., quiet corona) with an outflowing solar wind around multiple helmet magnetic topologies.

The initial plasma and fields (magnetic and velocity) parameters incorporated in this simulation are the following representative conditions of a non-rotating sun with an initial plasma $\beta_0 (= 16\pi n_0 k_0 T_0 / B_0^2)$ being unity, at $r = R_s$, $\theta = 90^\circ$ and $\phi = 22.5^\circ$.

- Isothermal and hydrostatic equilibrium atmosphere.

$$T_0 = 10^6 \text{ K}$$

$$\rho_0 = \rho_0^0 \exp\left(\left(\frac{1}{R_{i,1}} - 1\right) \frac{R_i g_0}{RT_0}\right)$$

where ρ_0^0 is the density (the value of $1.67 \times 10^{-16} \text{ gm cm}^{-3}$ is used in this study and g_0 is the gravity on the solar surface.

- Magnetic field configuration

- (i) A hexapole potential field (Jackson, 1962); and, in a separate calculation.
- (ii) A hexapole linear force-free field (Nakagawa et al., 1978)

- Velocity Field

$$v_r(1, \theta, \phi) = 15 \text{ km s}^{-1},$$

$$v_r(15, \theta, \phi) = 200 \text{ km s}^{-1},$$

$$v_\theta(r, \theta, \phi) = v_\phi(r, \theta, \phi) = 0.$$

Figure 2 shows the simulated morphology of the quiet corona which consists of a three-dimensional representation of the brightness (integrated density along the path of the line-of-sight), steady state solar wind velocity vectors and magnetic field for two cases: (a) initially potential field topology; and (b) initially linear force-free field topology, respectively. It is easy to recognize that the shape of the quiet corona depends on the initial magnetic field topology. The bright corona is related to the closed magnetic field configuration, and the dark region corresponds to the open field configuration which corresponds to the out-flowing solar wind from the coronal hole. Also it shows that the solar wind velocity is almost radial.

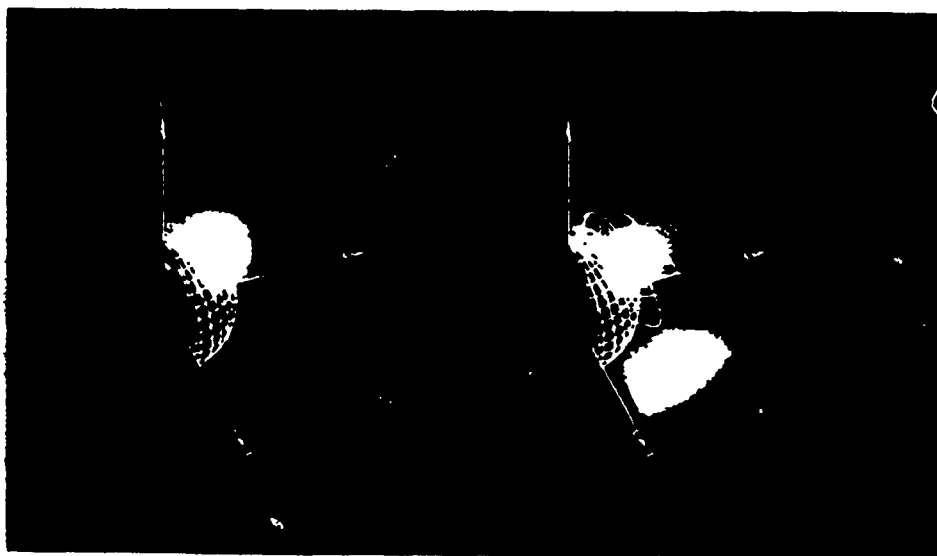


Fig. 2. The three-dimensional simulated brightness, steady state solar wind velocity vectors and magnetic field of the confined plasma corona for: (a) initially potential field configuration (upper left panel) and (b) initially linear force-free field configuration (upper right panel).

In order to examine the physical structure of the quiet, steady-state, corona, we plot the radial distribution of the density and temperature at the pole and equator for the initially potential and linear force-free magnetic field topologies, respectively, as shown in Figure 3. The radial distribution of the three velocity components (i.e., v_r , v_θ , v_ϕ) at the pole and equator is shown in Figure 4 for both types of magnetic field topology. Finally, we plot the radial distribution of Alfvén and sonic speed at the pole and equator in Figure 5.

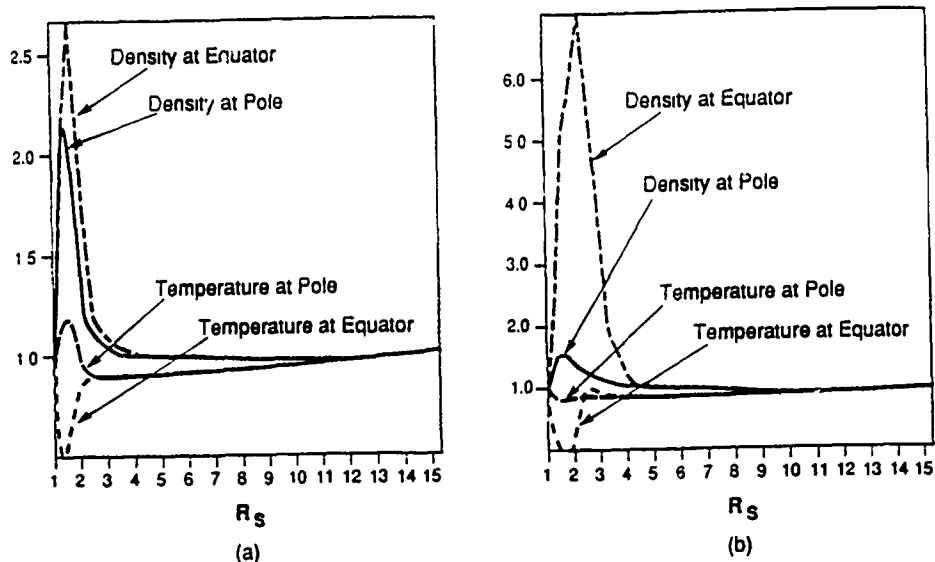


Fig. 3. Radial distribution of the density (ρ/ρ_0) and temperature (T/T_0) at the pole and the equator, respectively for; (a) initially potential field configuration and (b) initially linear force-free field configuration with ρ_0 and T_0 given in page 6 of the text.

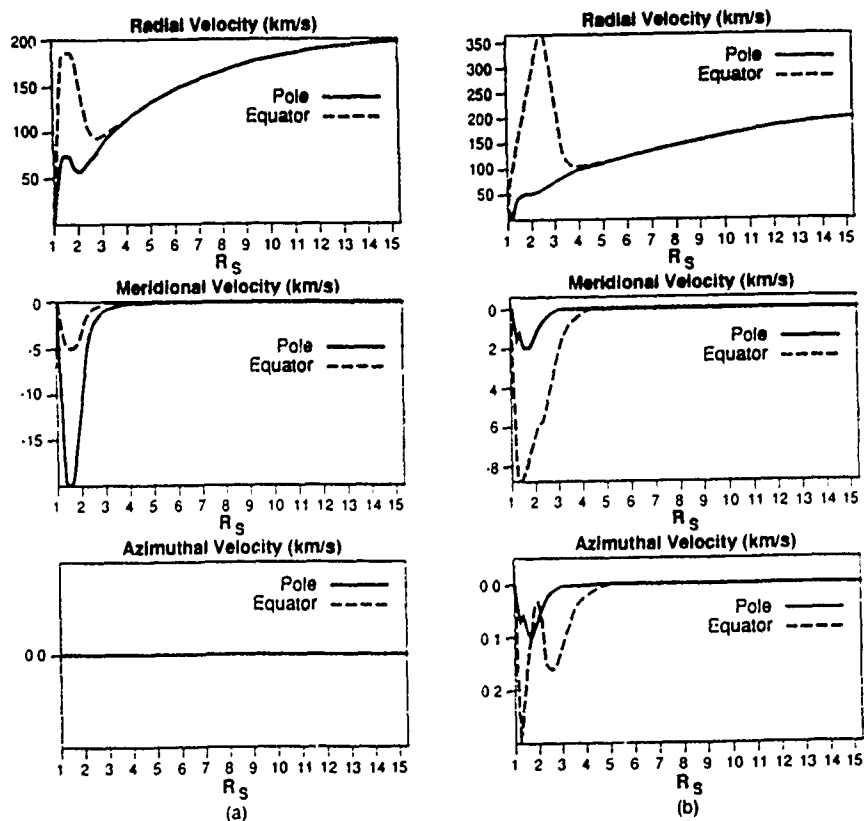


Fig. 4. Radial distribution of the three velocity components (v_r , v_θ , v_ϕ) at the pole and equator for: (a) initially potential field configuration and (b) initially linear force-free field configuration.

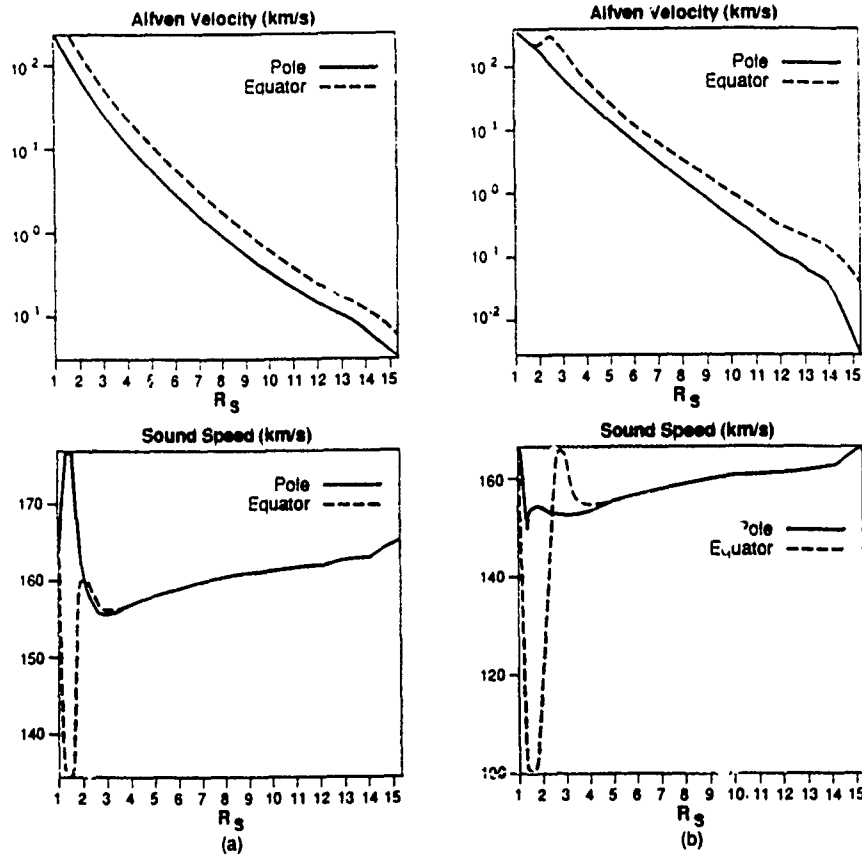


Fig. 5. Alfvénic speed and sonic speed as function of radial distance at pole and equator for (a) initially potential field configuration and (b) initially linear force-free field configuration.

Comparison of each of these parameters demonstrates the well-known inference and important fact that the magnetic field is the dominant factor that determines both the morphology and physical structure of the corona. The spatial diversity of these important, fundamental steady-state parameters is obvious.

For the completeness of this presentation, we shall show some results for a disturbed corona in Figure 6. This numerical result is obtained by introducing a pressure pulse ($p/p_0 = 10$) distributed over three grid points centered at $\theta = 35^\circ$, $\phi = 22.5^\circ$ and $r = R_s$, for the case of the initially linear force-free magnetic field topology of the quiet corona as shown in Figure 2b. In Figure 6, at $t = 600$ s, we show simulated brightness (i.e. line-of-sight integrated density enhancement), disturbed magnetic field and solar wind velocity vectors in the $\phi = 22^\circ$ plane. According to the results shown, we may interpret that the brightness was caused by the flow interaction with the magnetic field. This density enhancement consists of both the mass carried by plasma flow motion and local wave compression.

IV. CONCLUDING REMARKS

In this study, we have presented a newly-developed, three-dimensional, time-dependent magnetohydrodynamic model for the study of corona structures in both quiet and disturbed states. This model extends from the solar surface to $15 R_s$, and, thereby, includes the region of outflowing solar wind from the subsonic, sub-Alfvénic to super-sonic and super-Alfvénic regions. Therefore, we assert that it is, indeed, a model which could be used to study coronal/interplanetary coupling problems.

In these preliminary results, we clearly recognize that the magnetic field topology and strength controls both the structures and physical parameters' morphology of the corona. Also, this model has the capability to convert the fundamental physical parameters (i.e. ρ , T , v) to observables such as brightness (see Fig. 2) and doppler shifts (not shown). Therefore, we may claim that this model has the potential whereby it could be used as a diagnostic tool that can be applied to the interpretation and guidance of the observations. For example, we may use the physical properties obtained from this model to compute line profiles. As a final

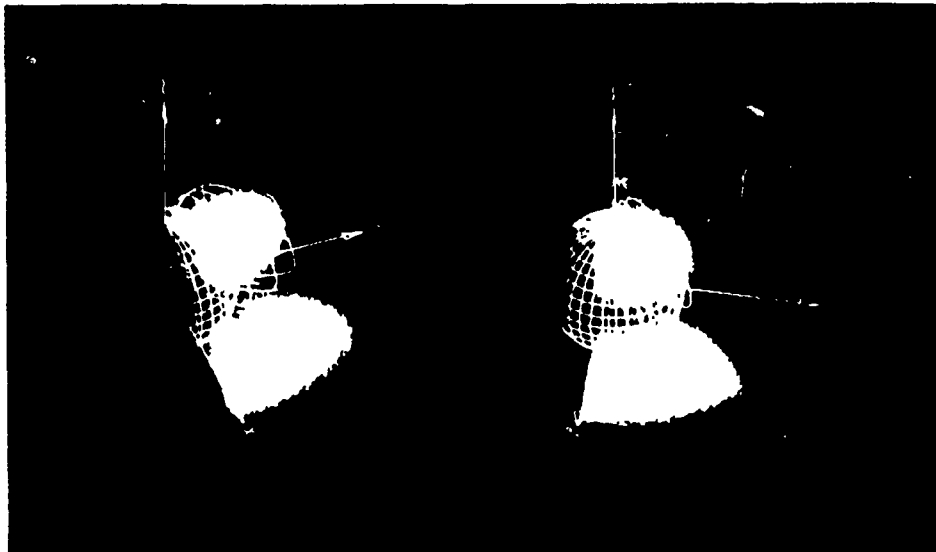


Fig. 6. The three-dimensional simulated brightness, magnetic field and solar wind velocity of a disturbed corona at 600 s after introduction of a pressure pulse (simulated flare) at solar surface of the quiet corona given in Figure 2b, (a) Viewed from $\theta = 50^\circ, \phi = -20^\circ$, and (b). viewed from $\theta = 50^\circ, \phi = 10^\circ$.

remark, we recognize that the development of this model is far from complete. The improvements can be tackled in two major categories as follows:

- Mathematical Improvement

We should establish the accuracy of the numerical results. In order to achieve this purpose, we should conduct a grid size test for this model.

- Physical Improvement

Presently, the model includes dissipative mechanisms that were not invoked for the present demonstration of its three-dimensional, temporal capability. Namely, the present model results are based on "ideal" MHD theory. We realize that dissipative MHD is important to many solar physics problems in which finite electrical conductivity, thermal conductivity, radiation and turbulence are undoubtedly present. We plan to incorporate these effects in our model via a conservative and rational step-by-step approach. However, the current ideal MHD model, because of its inherent and natural three-dimensional resemblance to the real world, is essential for the construction of solutions which resemble observed realistic topologies. We have obtained in the present demonstration, for example, induced meridional and azimuthal flows which existing two-dimensional models cannot provide.

ACKNOWLEDGEMENT

We are indebted to Dr. Murray Dryer for reading this manuscript and making invaluable suggestions and M. T. Sun for preparing the three-dimensional color graphics. This work is supported by AFOSR-88-0013, NAGW-9 and NOAA (50RANR000104).

REFERENCES

Billings, D. E., 1966. *A Guide to the Solar Corona*. Academic Press, New York

- Jackson. John David, 1962, *Classical Electrodynamics*. John Wiley and Sons, Inc.. New York,-London-Sydney
- Hildner. E.. Gosling, J. T.. MacQueen. R. M.. Munro. R. H., Poland. A. I. and Ross. C. L.. 1976, *Solar Physics*. 48. 127.
- Hu. Y. Q. and Wu. S. T., 1984, *J. Comp. Phys.* 55. 33.
- Hundhausen. A. J., Burlaga, L. F., Feldman. W. C., Gosling, J. T., Hildner, E., House, L. L., Howard. R. A., Krieger. A. S., Kundu, M. R., Low. B. C., Sheeley, N. R., Jr., Steinolfson, R. S., Stewart, R. T., Stone. R. G. and Wu, S. T., 1984, *Solar Terrestrial Physics: Present and Future*, (Butler. D. M. and Papadopoulos. K.. eds) **NASA Reference Publication 1120**, Chapter 6.
- Nakagawa. Y., Wu, S. T., and Tandberg-Hanssen. E., 1978, *Astron. Astrophys.* 69, 43.
- Wang, A. H.. and Wu, S. T., 1990, *J. Comp. Phys.* (to be submitted).
- Wang, S., Hu. Y. Q. and Wu, S. T., 1982, *Scientia Sinica (Series A)* , **XXV**, 1305.
- Wu. S. T.. and Wang, J. F., 1987, *Comp. Meth. in Applied Mechanics and Engineering*, 64. 267.

VI. FUNDAMENTAL METHODS FOR THE MODELING OF SOLAR INTERPLANETARY ENVIRONMENT

In order to obtain numerical solutions for these highly complex non-linear mathematical models, for the physical system encountered, innovative numerical techniques are called for. We have successfully developed a new numerical method to deal with mathematically ill-posed problems of extrapolation of magnetic field configurations using observations. This method is called Progress Extension Method (PEM; Wu, et al. 1990, *Astrophys. J.*) and is included in this section. A total of four papers concerning numerical methods were published and are included in this section.

Magnetohydrodynamic (MHD) Modeling of Solar Active Phenomena via Numerical Methods, in Developments in Theoretical and Applied Mechanics, S. Y. Wang, R. M. Hackett, S. L. Deleuw and S. Am. Smith (eds), 62-70, 1988.

Application of Similitude Principle to the Numerical Simulation of Solar Atmospheric Dynamics in J. Adv. Space Res., Vol. 8, Number 11, 221-226, 1988.

On the Numerical Computation of Non-linear Force-free Magnetic Fields, in Astrophys. J., Vol. 362, 698-708, 1990.

A Comparison Between Progressive Extension Method (PEM) and Iterative Method (IM) for Magnetic Field Extrapolations in the Solar Atmosphere in J. of the Italian Astronomical Soc., Vol. 61, No. 2, 477-484, 1990.

DEVELOPMENTS IN
THEORETICAL AND APPLIED MECHANICS

Volume XIV

Proceedings of the
Fourteenth Southeastern Conference on
Theoretical and Applied Mechanics

Edited by

Sam S. Y. Wang, Professor of Mechanical Engineering
Robert M. Hackett, Professor of Civil Engineering
Samuel L. DeLeeuw, Professor of Civil Engineering
Allie M. Smith, Dean, School of Engineering,
and Professor of Mechanical Engineering

SCHOOL OF ENGINEERING
THE UNIVERSITY OF MISSISSIPPI
University, Mississippi, U.S.A.

Magnetohydrodynamic (MHD) Modelling of Solar Active Phenomena Via Numerical Methods

S. T. Wu¹

Abstract

Current work of magnetohydrodynamic (MHD) modelling of solar active phenomena via the use of numerical methods is summarized. This research can be subdivided into two major categories: (i) time-dependent and (ii) time-independent models. The former can be used to describe the evolutionary physical processes of solar active phenomena: formation of loops, prominences, flares and coronal transients are examples within this category. The latter category is utilized to establish understanding of the physical dynamical structures of those long-lasting, or more accurately, quasi-stationary phenomena. Various numerical methods were used in order to adapt to the various mathematical formulations corresponding to specific physical problems. The accuracy corresponding to these numerical methods and boundary conditions have great importance on the physical results and are individually addressed. We present physical examples to illustrate the capability of the numerical methods to model the physics of the solar active phenomena. We also discuss the importance of boundary conditions and accuracy on the physical results of these simulation models.

Introduction

From the macroscopic point of view recent knowledge (e.g., Skylab monograph; 1977; 1980; 1981) clearly have established the fact that the physical processes involved in solar atmospheric dynamical phenomena can be understood only in terms of interaction between the magnetic field and plasma motion. Consideration of the observed results further indicated that there are two distinguishing features: magnetically confined and non-confined structures. The former has been recognized as the flaring loop (Webb 1981), and bright point have been recognized as examples of the former case, and the violent flaring event (Sturrock, 1980) is regarded as an example of the latter case. The physics underlining these different phenomena can be interpreted via studies of the representative magnetic field configurations and their interactions with plasma flows. For example, magnetically confined structures must exist within the closed magnetic field topology; conversely, we must consider the possibility that non-confined magnetic structures may evolve or be initiated within a closed magnetic topology. This latter possibility may take place through reconnection or even a more violent dynamical action via expulsion of magnetic field with the consequence of transformation of the originally-closed magnetic field topology into a locally open one.

¹Professor of Mechanical Engineering and Director of Center for Space Plasma and Aeronomical Research, The University of Alabama in Huntsville, Huntsville, AL 35899 U.S.A.

One way to describe these macroscopic physical mechanisms is to use magnetohydrodynamics (MHD) theory. Mathematically, this approach leads to a boundary value problem for the steady state case in order to illustrate long lived solar feature. This approach also leads to an initial boundary value problem for the time-dependent case in order to illustrate the evolution of solar active regions. Because of the mathematical complexities of these problems, the analytical approach has only limited use for simplified physical problems which becomes inadequate for comparison with observation. Nevertheless, the strength of the analytical approach is that it can provide exact solutions in some cases to a certain or specified order of approximation. On the other hand, the numerical techniques, together with high speed and large memory computers, enable theorists to perform complex analyses for highly non-linear problems. However, all numerical solutions are approximate solutions and their uniqueness and degree of accuracy are unable to be proved. Therefore, analytical solutions are still needed to help us to make a judgment on the physical reality of each of the numerical "experiments". Thus, both analytical and numerical methods complement each other for the analysis of solar active phenomena.

In this paper, we shall limit our discussion to the numerical solutions and their accuracy and resolution. Two physical examples are described in order to illustrate the capability of numerical approach. They are: (i) local heating of a coronal loop in an isothermal and stratified atmosphere; and (ii) coronal dynamical responses due to the movement of magnetic field.

Mathematical Model and Numerical Methods

The mathematical model for the physical phenomena to be studied can be described by a set of time-dependent, non-planar, adiabatic, two-dimensional, one fluid MHD equations. These coupled non-linear equations represent conservation of mass (with no sources or sinks except as prescribed as in an initial boundary problem), momentum (with no viscosity), and energy (with no dissipation except at shocks), together with the induction equations (assuming infinite electrical conductivity). This is the key equation to describe the field and plasma flow interaction. These fundamental equations are straightforward; we shall not repeat here (c.f. Wu, et al., 1983). However, the numerical methods and their accuracy are directly related to the particular physical problems under investigation and, therefore, deserve some attention.

In general, there are two fundamental numerical methods for the solution of time-dependent non-linear systems. The first one, the explicit method, is very efficient for the solution of super-sonic and super-Alfvenic flows. The second one, the implicit method, is better for the solution of sub-sonic and sub-Alfvenic flows or mixed type problems, (i.e. elliptical and hyperbolic mathematical system). Detailed descriptions of these two methods are given by Roach (1972). Applications to astrophysical MHD flows are demonstrated by Wu et al. (1979) and Wu et al. (1983, 1984, 1985) and Wu (1984a). Details concerning the numerical schemes for astrophysical MHD flows are described by Han et al. (1979) for the explicit scheme and by Wu and Wu (1984) for the implicit scheme. Conventionally, the boundary conditions used for these calculations are fixed (i.e. they do not change with time) and are chosen on the basis of the physical assumptions.

The development of the method of projected characteristics by Nakagawa (1981a,b) made it possible to formulate time-dependent boundary conditions according to self-consistent physical rules. This method was applied by Wu and Wu (1984) who modified the physical projected characteristics at the boundary by the so-called "normal" projected characteristics. This study enabled Wu

(1984b); Wu and Wang (1987) to study the correctness and accuracy of the multi-dimensional, time-dependent MHD problem that incorporated either the conventional (i.e., fixed) or temporally-evolving boundary conditions.

Figure 1 illustrates how the simulated physical situation may be affected by the choice of the boundary conditions and time step. The excess magnetic energy generated within the domain (i.e., an active region) due to horizontal photospheric shear motion was computed by conventional boundary conditions (curve A) and by the method of projected normal characteristics (curve B) as shown in Figure 1a. One notices immediately that the conventional boundary conditions over-predicts the growth rate of excess magnetic energy. Use of the conventional boundary conditions, then, would very likely lead to incorrect physical interpretations. For example, by using the results shown on curve A, we may conclude that the time scale is ~ 150 s for development of an active region to a stage when enough energy due to photospheric shear motion will be produced for an incipient flare because the energy growth rate becomes unstable. We know, however, from observation that an active region takes days to develop enough energy for a potential flare. Figure 1b shows the influence of time-step choices on the physical solution. The time-step (Δt) is equal to the ratio of the grid size (Δx) and the characteristic speed (i.e., Alfvén speed). Since the characteristic speed depends on local physical properties. Thus, when one chooses a time-step, the grid size is subsequently determined (or vice-versa).

Numerical testing is necessary to determine a satisfactory time step (or grid size); that is, the solution must become independent of the time-step (or grid size) as shown in Figure 1b. Some details of this study are discussed by Wu and Wang (1987).

Physical Results

Up to now, we have briefly summarized the presently used numerical methods and their accuracy as a consequence of boundary condition and time-step (or grid size) choices. With carefully chosen numerical methods for the appropriate physical situation, we shall present two physical examples to illustrate the ability of the numerical solution to provide a tool for the physical interpretation of observations.

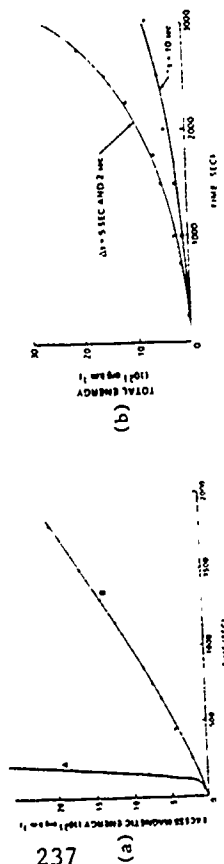


Figure 1(a) Computed excess magnetic energy (erg km^{-1}) due to photospheric shear (0.1 km s^{-1}) for initial plasma beta ($= \frac{B_0^2}{16\pi n_0 k T_0}$) being 0.54 using conventional boundary conditions (curve A) and temporally-evolving boundary conditions (curve B).
(b) Testing of the numerical solutions by time step (explicitly) and grid size (implicitly).

(1) Local Heating of a Coronal Loop in an Isothermal and Stratified Atmosphere.

In this example, we used our MHD model as described in spherical coordinates for large phenomena such as coronal loops. Further, we consider a six-lobed potential magnetic field that is embedded within an isothermal ($\sim 10^6 \text{ K}$) and hydrostatic atmosphere. The number density at the base (i.e., $R_0 = 1 R_\odot$, where R_\odot is the solar radius) is 10^8 cm^{-3} , with magnetic field strength approximately 1 Gauss, this giving plasma beta of unity at that point. Plasma beta is defined as the ratio of plasma pressure to magnetic pressure ($\frac{16\pi n_0 k T_0}{B_0^2}$).

A Temperature perturbation of a factor of 10 (i.e., $T = 10 T_0$) is introduced at the apex of a loop for 60 s. The density and temperature from the numerical solution at 200 s are presented (with disturbed magnetic field lines in the background) in Figures 2a and 2b, respectively. The corresponding three dimensional representations are shown in Figure 2c and 2d. Figure 2e shows the local vectorial representation of Eulerian (i.e., mass flow) velocity. From these results, we observe the following physical interpretations:

- the maximum density enhancement is not at the location where local heating occurs. In fact, the heating creates a rarefied regions with higher temperature (see Figures 2a and 2b). Physically, this rarefied region appears because the local heating induces a downward mass flow. There is no additional local mass source; hence, a rarefield region appears because of the conservation of mass.
- The appearance of a maximum density enhancement region above the heat source location is a result due to the propagation of a MHD fast wave which gives a local compression. This phenomena can be seen from Figure 2e. The mass flow is confined to the magnetic loop and whereas the outward wave motion is quasi-isotropic.

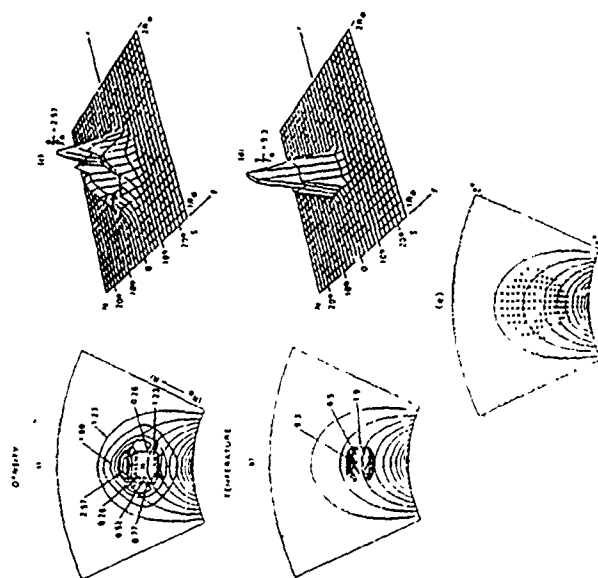


Figure 2 Numerical MHD simulation of local heating of a magnetic loop (as marked by x) at 200 s; (a) density contours (ρ/ρ_0); (b) temperature contours (T/T_0); (c) three-dimensional representation of density; (d) three-dimensional representation of temperature; and (e) vectorial representation of velocity with magnetic field lines as the background.

(11) Coronal Dynamical Responses

The same numerical model used in the previous example can also be applied to another phenomena in the corona. The initial magnetic field topology is now changed to a helmet-streamer-type configuration as shown in Figure 3b. One can then postulate a lateral motion by applying a non-uniform movement (with a maximum unrealistic velocity magnitude of 40 km s^{-1}) of magnetic field lines at the coronal base according to the pattern as shown in Figure 3a. The reason we have chosen the unrealistic high velocity is because we chose unrealistic physical domain (i.e., a hemisphere of the sun) for this simulation. The initial plasma beta (β_0) at the base is 0.1, thereby implying strong magnetic control. Evolution of the magnetic field is shown in Figures 3b through 3f and the corresponding density distribution is presented in Figure 4 at times of 500 s, 1,000 s, 1,500 s and 2,000 s respectively. Several interesting results can be noted and summarized in the following:

- (a) The diverging motion from the central axis (i.e., the neutral line) leads to rising field lines in the closed field topology. This phenomena has also been shown analytically by Low (1981) and Wu *et al.* (1985).

(b) As shown in Figure 3a, we also simultaneously introduced converging motion toward the axis of the open field configuration. As a result of this additional perturbation, high pressure regions develop on both sides of the neutral line. This high pressure acts as an "external" force to push the field lines together at a height greater than the neutral line. It appears, therefore, that there is a tendency for some of the field lines to be pinched off. Actually, reconnection in this model is impossible because the currently considered model is an ideal MHD model. However, these results indicate that there is still another mechanism that could alter the field topology, even in the absence of a dissipative reconnection mechanism. It is therefore, indicated that this additional consideration should seriously be taken into account when we interpret observed phenomena.

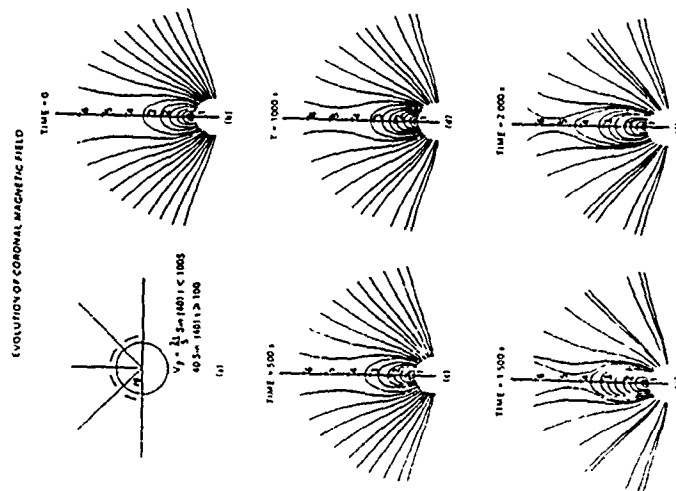


Figure 3 Computed evolution of magnetic field lines of a helmet-streamer due to the diverging and converging motion at the base.

(c) Figure 4 shows density contours that correspond to the times shown in Figure 3. The vertical axis refers to the distance (in solar radii) along the central axis. It is clearly indicated that there is a dark region (density depleted region) propagating outward along the center line with a speed of about 340 km s⁻¹ as shown, for example, by the contour labeled "j". This phenomenon is similar to that observed with the K-coronograph by Fisher and Poland (1981) and modelled by Low et al. (1981) with a kinematic approach. There exists, simultaneously, a density enhancement at the open portion of the magnetic field topology and which is closely attached to the density depleted region.

Concluding Remarks

In this paper, we have briefly summarized several numerical ideal magnetohydrodynamic (MHD) models for the study of solar active phenomena. We emphasized numerical accuracy and correction of the boundary conditions. The numerical "experiments" were concerned with three physical phenomena: (i) local heating of a coronal loop in an isothermal and stratified atmosphere and (ii) coronal dynamic responses due to the movement of magnetic field. The following important physical interpretations may be inferred from the results:

- (i) Local heating of a magnetic loop will lead to the enhancement of density of the neighboring loops through MHD wave compression.
- (ii) Converging and diverging motion of magnetic field lines at the coronal base may create the dark transient observed by Fisher and Poland (1981). Furthermore, field lines can be pinched off and may form a self-contained magnetized plasma blob that may move outward into interplanetary space.

It should be noted that all of these physical interpretations are based on ideal (non-dissipative) MHD theory. Dissipative models have been investigated by many authors Forbe and Priest (1987), Steinolfson and Van Hoven (1984) and Wu et al. (1986). We may conclude from these results that the numerical simulation approach may, perhaps, be the best way that can be used to disclose the physics from the observational data. In addition, simulations may be viewed as an invaluable aid as guidance for the design of instruments for a specific observation. In order to achieve these goals, it is important that the numerical resolution of the simulations be known. For example, the numerical resolution for the coronal dynamic simulation presented in this paper is rather poor, because the grid size is 20,000 km which converts to a picasal size of 28 arc sec. If we wish to increase the number of grid points in order to increase the computational accuracy in corresponding current observation, then even presently-available supercomputers become too small to accommodate the required memory. However, even with this coarse approximation, some general dynamical behaviors of the solar active features still could be learned. But, the grid size for our lower atmospheric simulation is 400 km which results in a sub-arc second picasal. Hence, this latter simulation is adequate to resolve the observations.

As a final remark, we should like to comment that the development of high speed, large memory computers and the advancement of numerical methods have provided a powerful tool to the theoretician. These developments enable the theoretician to attack increasingly complex, non-linear problems. But, it is essential to note that we should use these tools responsibly (just like experimentalists who must carefully design and develop their instruments) and to be careful with the accuracy and resolution of the simulations.

Acknowledgement

The author is indebted to Dr. M. Dryer for his comments and suggestions during the preparation of this manuscript. The work done was supported by a NASA Grant (NAGW-9), NASA/HSFC Grant NAG8-053 and United States Air Force Grant AFOSR-88-0013.

References

- Fisher, R. R. and A. I. Poland, 1981, *Astrophys. J.* **246**, 1004.
 Forbes, T. and E. Priest, 1987, *Rev. of Geophys.* **25**, 1583.
 Hu, Y. Q. and S. T. Wu, 1984, *J. Computational Phys.* **55**, 33.
 Han, S. H., S. T. Wu, and Y. Nakagawa, 1979, *Comput. Fluids*, **7**, 97.
 Low, B. C., 1981, *Astrophys. J.* **261**, 352.
 Low, B. C., R. H. Monro, and R. R. Fisher, 1982, *Astrophys. J.* **254**, 335.
 Nakagawa, Y., 1981a, *Astrophys. J.* **247**, 707.
 Nakagawa, Y., 1981b, *Astrophys. J.* **247**, 719.
 Orall, Frank Q. (ed.), 1981, *Solar Active Regions: A Monograph from Skylab Solar Workshop III*, Colorado Associated University Press, Boulder, Colorado 80309, USA.

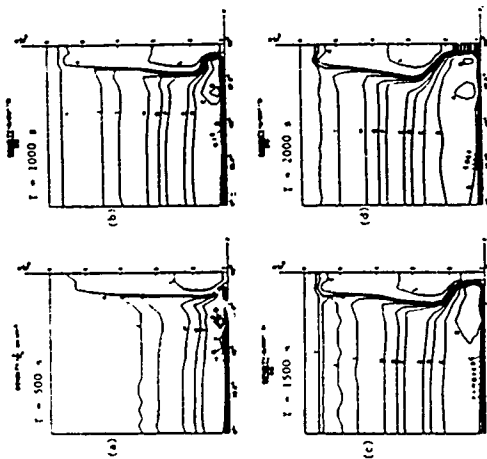


Figure 4 Computed corresponding density (ρ/ρ_0) evolution for a helmet-streamer due to diverging and converging motion at the base shown in Figure 3a.

A:	1.028	F:	1.003
B:	1.021	G:	1.001
C:	1.010	H:	0.999
D:	1.007	I:	0.992
E:	1.005	J:	0.980

- Roache, P. J., 1972, Computational Fluid Dynamics, Hermosa Publishers, Alburquerque, New Mexico, USA.
- Steinolfson, R. S. and G. Van Hoven, 1986, Phys. Fluids, **27**, 1207.
- Sturrock, P. A. (ed.), 1980, Solar Flares, A Monograph from Solar Workshop II, Colorado Associated University Press, Boulder, Colorado 80309, USA.
- Webb, D. et al., 1980 in Solar Flares (P. A. Sturrock ed.), A Monograph from Solar Workshop II, Colorado Associated University Press, Boulder, Colorado, 80309, USA.
- Wu, S. T., 1984a, Computer Simulation of Space Plasmas (H. Matsumoto and T. Sato eds.), Terra Scientific/D. Riedel Publishing Company, Tokyo, Dordrecht, Boston, Lancaster, 179.
- Wu, S. T., 1984b, Proceedings of US-Japan Seminar on Recent Advances in the Understanding of Structure and Dynamics of the Heliosphere during the Current Maximum and Declining Phase of Solar Activity. (T. Kakinuma ed.), The Research Institute of Atmospheric, Nagoya University, Japan.
- Wu, S. T., S. M. Han, and M. Dyer, 1979, Planet. Space Sci. **27**, 255.
- Wu, S. T., Y. Q. Hu, Y. Nakagawa and E. Tandberg-Hanssen, 1983, Astrophys. J. **266**, 866.
- Wu, S. T., Y. Q. Hu, K. R. Kroll, M. J. Hagyard and J. B. Smith, Jr., 1984, Solar Phys. **90**, 117.
- Wu, S. T., Y. Q. Hu, Y. Nakagawa and E. Tandberg-Hanssen, 1986, Astrophys. J. **306**, 751.
- Wu, S. T., J. J. Bao, Y. C. Xiao and J. B. Smith, Jr., 1986, Proceedings of the Solar Terrestrial Prediction Workshop, June 18-22, 1984, Observatoire de Meudon, Paris, France.
- Wu, S. T., J. J. Bao and J. F. Wang, 1986, J. Adv. in Space Res. **6**, No. 6, 53.
- Wu, S. T. and J. F. Wang, 1987, Comp. Meth. in Appl. Mech. and Eng., **64**, 267-282.
- Zirker, Jack G. (ed.) 1977, Coronal Holes and High Speed Wind Streams, A Monograph from Skylab Workshop I, Colorado Associated University Press, Boulder, Colorado 80309, USA.

APPLICATION OF SIMILITUDE PRINCIPLE TO THE NUMERICAL SIMULATION OF SOLAR ATMOSPHERIC DYNAMICS

S. T. Wu,* S. Wang,* A. H. Wang* and M. Dryer**

**Department of Mechanical Engineering and Center for Space Plasma and Aeronomic Research, The University of Alabama in Huntsville, Huntsville, AL 35899, U.S.A.*

***Space Environment Laboratory, ERL/National Oceanic and Atmospheric Administration, Boulder, CO 80303, U.S.A.*

ABSTRACT

Numerical simulation has become a tool for the investigation of detailed physical structures of solar atmospheric dynamics. This tool has become an essential part of solar physics because the complexity of nonlinear characteristics of much solar phenomena renders the achievement of analytical solutions to be difficult to obtain. Although computer technology and numerical methods have made significant progress in recent years, realistic simulation for some prototype physical systems (for example: the birth and decay of an active region) still is not possible because of the wide range of spatial and time scales that must be considered. Therefore, proper scaling rules must be recognized for the development of appropriate models. In this paper, we shall apply the similitude principle to develop these scaling rules for problems of solar atmospheric dynamics. It is found that these rules are highly dependent on the physical nature of the specific problem under consideration. A set of "similitude critiques" is presented for some specific physical conditions. Numerical examples of coronal dynamic response and active region dynamics are used to demonstrate these new ideas.

INTRODUCTION

Dimensional analysis and similitude principles (Kalikhman, /2/) have been widely used in experimental physics and hydrodynamics, because these fundamental theories enable us to study and gain the insight of physical relationships between laboratory models and their full scale prototypes. Recently, highly sophisticated computing capability has enabled theoreticians to study very complex nonlinear physical systems which are beyond the reach of analytical methods. This approach has grown quickly and has become a sub-discipline called "numerical simulation". In fact, numerical simulation is, in reality, the theoretician's experiments. Experimentalists build physical models in the laboratory with hardware. On the other hand, theoreticians build models with computer codes. Despite the availability of state-of-the-art supercomputers and advanced numerical methods, the construction of numerical simulation models for realistic prototype experiments still has encountered the following difficulties:

- (i) limitations on memory capacity and computation speed for desired resolution and accuracy of the physical system under investigation.
- (ii) even without limitations on memory capacity and computation speeds, the large number of significant computation operations will introduce inherited truncation errors that will effect the accuracy of the computation and, consequently, will prevent the realistic simulation of the prototype.

It can be noted that these two conditions contradict each other. Therefore, it is almost impossible to obtain ideally perfect simulation models. One may remedy this

issue, firstly, by constructing a simulation model on the basis of the best resolution and accuracy with optimum spatial grids and time steps (which may not be exactly identical to the prototype) and then, secondly, using classical similitude principles to scale the prototype with the simulation model and its physical characteristics.

It has been established for a long time that the characteristics of the full-scale prototype could be predicted by a small-scale model provided certain similitude rules are followed. For example, the airplane designer tests scaled models in the wind tunnel to determine the aerodynamic behaviour of the airplane that is expected in actual atmospheric flight. Similarly, the naval architect tests new hull designs in a towing basin by using a model with the same philosophy vis-à-vis ocean-traversing ships.

According to the similitude principle, in order to enable a model to simulate the physical conditions of the prototype, the model system has to be geometrically, kinematically, and dynamically similar to the prototype system. The derivations of these physical characteristics will be presented in Section II. Numerical results for solar coronal dynamics to substantiate these claims are included in Section III. The final conclusions on the application of similitude principle to solar atmospheric dynamics will be discussed in Section IV.

SIMILITUDE PARAMETERS

Let us consider an inviscid, compressible magnetohydrodynamic (MHD) flow of finite electrical conductivity and thermal conductivity in a gravitational field. The mathematical representation of this physical system results in a set of standard MHD equations. The first step is to make this set of governing equations dimensionless in order to obtain the similitude parameters. Through these dimensionless procedures, we found the following similitude parameters:

$$\left. \begin{aligned} St &\equiv \frac{L}{\tau U}, & Eu &\equiv \frac{p}{\rho U^2}, & S_m &\equiv \frac{B^2}{\rho U^2}, \\ Fr &\equiv \frac{U^2}{GL}, & Rm &\equiv \frac{UL}{\Lambda}, & S_v &\equiv \frac{c_v \theta}{U^2}, \\ S_p &\equiv \frac{c_p \theta}{U^2}, & S_k &\equiv \frac{K \theta}{L \rho U^3}, & S_d &\equiv \frac{p}{D R \theta} \end{aligned} \right\} \quad (1)$$

where the symbols τ , L , U , D , p , θ , B , G , Λ and K are the characteristic quantities for the time, length, velocity, density, pressure, temperature, magnetic field, gravitational field, electrical and thermal conductivity, respectively. Their values are given by the boundary values or other constant values reflected in the physical and mathematical nature of the problem to be investigated. The physical significance of each of these dimensionless parameters given by Eq. (1) is very clear. The reader will recognize that St , Eu , Fr and Rm are the Strouhal number, Euler number, Froude number and magnetic Reynolds numbers, respectively, that are described in many standard hydrodynamic and magnetohydrodynamics textbooks. The other dimensionless parameters S_m , S_v , S_p and S_k represent the relative importance of characteristic magnetic energy, characteristic internal energy, characteristic enthalpy, and characteristic thermal flux relative to the kinetic energy, respectively.

Based on the similitude principle (Kalikhman, /2/), the condition of similitude characteristics must satisfy the geometric and physical similitudes. In other words, the characteristic dimensionless parameters for the model and the prototype must have the same values, respectively. According to the equality of these similitude parameters, as described in Eq. (1), the scaling laws can be derived between the model and prototype.

NUMERICAL TESTS OF SIMILITUDE PRINCIPLES FOR SOLAR ATMOSPHERIC DYNAMICS

In order to illustrate the potential applicability of this method to solar atmospheric dynamic research, two examples are chosen for illustration. These are

the coronal mass ejection and mass ejection in an active region as discussed below.

Coronal Mass Ejection

In this demonstration, we employed a two-dimensional, time-dependent ideal magnetohydrodynamic model /1,3/. In this ideal MHD model (i.e., infinite electric conductivity and no thermal conduction and radiation effects) there are four independent similitude "characteristic critiques", namely, St, Eu, S_m , and Fr according to Eq. (1).

Based on similitude principle, it is necessary to keep these four independent similitude characteristic critiques identical for both model and prototype in order to have the appropriate physical similarity. Hence these are:

$$\left. \begin{aligned} St &= \frac{L_p}{\tau_p U_p} = \frac{L_m}{\tau_m U_m}, \\ Eu &= \frac{p_p}{D_p U_p^2} = \frac{p_m}{D_m U_m^2}, \\ S_m &= \frac{B_p^2}{D_p U_p^2} = \frac{B_m^2}{D_m U_m^2}, \\ Fr &= \frac{U_p^2}{G_p L_p} = \frac{U_m^2}{G_m L_m}, \end{aligned} \right\} \quad (2)$$

where the subscripts "p" and "m" represent the quantities associated with the prototype and model, respectively. As usual, it has been learned that the parameter "plasma beta (β)" is the important parameter in the MHD numerical simulation, which can be deduced by taking the ratio of Eu and S_m , such that

$$\frac{8\pi E_u}{S_m} = \frac{8\pi p_m}{B_m^2} = \frac{8\pi p_p}{B_p^2} = \beta_p = \beta_m, \quad (3)$$

This implies that the characteristic β value for the prototype and model are identical as expected.

Recently, Wang et al. /3/ and Wu et al. /5/ have numerically simulated the characteristics of mass motion and wave propagation in the solar corona caused by a radial mass ejection in neighborhood of the equator at the solar surface by using the Full-Implicit Continuous Eulerian (FICE) scheme in spherical coordinates. For the prototype, we use the following values to calculate the initial state: the coronal temperature is taken to be 10^6 K, the plasma density at the equator on the solar surface $1.67 \times 10^{-16} \text{ g} \cdot \text{cm}^{-3}$, and β is equal to 10 at this position. The computation domain is taken to be $1r_\odot \leq r \leq 4r_\odot$ and $0 \leq \theta \leq 90^\circ$, r_\odot is the radius of the sun ($6.95 \times 10^5 \text{ km}$). After obtaining the initial state, we introduce a radial mass ejection upward in the latitudinal range, $83.25^\circ \leq \theta \leq 90^\circ$, on the solar surface. The ejection velocity is distributed linearly with θ , and the maximum velocity is taken at $\theta = 90^\circ$. Temporally, the velocity increases with time until $t = 1000 \text{ s}$ when it reaches a prescribed maximum 100 km s^{-1} at 90° and remains constant at that value until the end of the computation. The total time-scale of computation is about 6000 s . So, we may take the characteristic quantities of various physical parameters for the prototype as the following:

$$\left. \begin{aligned} \tau_p &= 6000 \text{ sec}, & L_p &= 3r_\odot, \\ U_p &= 100 \text{ km} \cdot \text{s}^{-1}, & D_p &= 1.67 \times 10^{-16} \text{ g/cm}^3, \\ \theta_p &= 10^6 \text{ k}, & p_p &= 2.76 \times 10^{-2} \text{ dyne cm}^{-2}, \\ G_p &= 0.271 \text{ km s}^{-2}, & B_p &= 0.26 \text{ Gauss}. \end{aligned} \right\} \quad (4)$$

We have used the full implicit continuous eulerian scheme in spherical coordinates, as noted above, and the usual symmetrical boundary conditions at the pole and the equator, as well as the physical boundary conditions at the bottom and the computation boundary conditions at the top in the computation domain /1,3,4/. According to Eq. (2), we are allowed to choose the characteristic quantities of various physical parameters for the model. For example we take

$$L_m = L_p, D_m = D_p, U_m = 2U_p. \quad (5)$$

Then, by using Eq. (4), we obtain the other characteristic quantities for the model

$$\tau_m = \frac{1}{2} \tau_p, P_m = 4P_p, \theta_m = 4 \theta_p, \quad (6)$$

$$G_m = 4G_p, B_m = 2B_p, \beta_m = \beta_p. \quad (7)$$

It should be noted that this kind of physical phenomena contains the appropriate mass motion and wave propagation. The characteristic velocity in Eq. (5) is the velocity of mass motion in order to simulate simultaneously the characteristics of mass motion and wave propagation in the model. Then, a characteristic quantity that describes the wave propagation, namely the Alfven velocity, V_A , must be considered. From Eq. (4) - (7), we obtain

$$(V_A)_m = 2(V_A)_p \quad (8)$$

For comparison, we present the computed results of relative density at $t = 6000$ s for the prototype and at $t = 3000$ s for the model in Table 1.

TABLE 1 The Values of Relative Density* at $\theta = 87.5^\circ$ ($1.066 \leq R \leq 3.847$); ($t = 6000$ s for prototype, $t = 3000$ s for model, $\beta_p = \beta_m = 10$)

$R(=r/r_0)$	1.066	1.137	1.212	1.293	1.378	1.470	1.567
Prototype	1.123	1.198	0.848	0.415	0.257	0.179	0.107
Model	1.109	1.249	0.869	0.436	0.272	0.191	0.117
R	1.671	1.782	1.900	2.025	2.160	2.300	2.455
Prototype	0.019	-0.073	-0.087	-0.023	0.050	0.125	0.200
Model	0.035	-0.043	-0.042	0.014	0.078	0.143	0.210
R	2.618	2.791	2.976	3.174	3.384	3.608	3.847
Prototype	0.277	0.352	0.422	0.352	0.169	0.025	0.000
Model	0.278	0.343	0.396	0.318	0.151	0.023	0.000

*Relative density = $(D - D_0)/D_0$

From Table 1, it can be shown that the radial profiles of relative density for the model are in good agreement with the radial profiles of relative density for the prototype at $t = 6000$ s. Note that a leading compression, followed by a rarefaction, occurs in both cases. At other time steps the numerical results show the same agreement. This result proves that the model reflects the actual physical characteristics of the prototype in this example.

Mass Ejection in an Active Region

We consider another example of mass ejection in a small-scale region. Wu et al. /4/ have investigated the problem of mass ejection from the photosphere (a "surge" perturbation as contrasted to the above-discussed thermal pressure-pulse "flare"

perturbations) and calculated the response of the surrounding solar atmosphere. For the initial state of the prototype, the distributions of the magnetic field and plasma density are:

$$\left. \begin{aligned} B_x &= B_0 \cos \left(\frac{\pi x}{L} \right) e^{-\alpha y}, \\ B_y &= B_0 \sin \left(\frac{\pi x}{L} \right) e^{-\alpha y}, \\ \rho &= \rho_0 e^{-\int_0^y \frac{g}{RT} dy}, \end{aligned} \right\} \quad (9)$$

where $\alpha = \pi/L$, and B_x and B_y are the horizontal and vertical components of magnetic field, respectively. L , ρ_0 , B_0 are the characteristic quantities of the length (spatial scale), reference plasma density and magnetic field, respectively. We introduce a vertical mass ejection upward at $t = 0$ in the range, $5200 \text{ km} \leq x \leq 8000 \text{ km}$ on the $y = 0$ plane, with the ejection velocity distributed linearly with x and the maximum taken at $x = 8000 \text{ km}$. At the same time, the velocity increases with time until $t = 15 \text{ s}$ when it reaches its maximum, 15 km s^{-1} , at $x = 8000 \text{ km}$. The total time-scale of computation is about 700 s . We used the FICE scheme in the Cartesian coordinate system together with projected normal characteristics /1/. Then, the characteristic quantities of various physical parameters for the prototype can be taken as follows:

$$\left. \begin{aligned} \tau_p &= 700 \text{ sec}, & L_p &= 1.6 \times 10^4 \text{ km}, \\ u_p &= 15 \text{ km s}^{-1}, & D_p &= 43.175 \times 10^{-13} \text{ g cm}^{-3} \\ \theta_p &= 5 \times 10^4 \text{ K}, & p_p &= 3.45 \text{ dyne cm}^{-2} \\ G_p &= 0.271 \text{ km s}^{-2}, & B_p &= 5.59 \text{ Gauss} \end{aligned} \right\} \quad (10)$$

It may be shown that $\beta_p = \frac{8\pi p_p}{B_p^2} = 1$. In this example, we use a new choice for the characteristic quantities of the model. If we take

$$L_m = \frac{L_p}{2}, \quad D_m = D_p, \quad U_m = U_p \quad (11)$$

then, according to Eq. (2), we can obtain other characteristic quantities for the model as follows:

$$\left. \begin{aligned} \tau_m &= \frac{\tau_p}{2}, \quad p_m = p_p, \quad \theta_m = \theta_p, \\ G_m &= 2G_p, \quad B_m = B_p, \quad \beta_m = \beta_p, \end{aligned} \right\} \quad (12)$$

From Eqs. (10) and (11), it can be shown

$$(V_A)_m = (V_A)_p \quad (13)$$

in this case. For comparison, corresponding data at $t = 700 \text{ s}$ and $x = 7200 \text{ km}$ for the prototype, and at $t = 350 \text{ s}$ and $x = 3600 \text{ km}$ for the model, are given in Table 2.

TABLE 2 The Values of Relative Density* ($800 \leq y \leq 8000$ km)
($\beta_m = \beta_p = 1$)

Prototype	y(km) $\Delta\rho/\rho_0$	800 0.103	1600 0.267	2400 0.059	3200 0.045	4000 0.100	4800 0.129	5600 0.124
	t = 700 s x = 7200km	y(km) $\Delta\rho/\rho_0$	6400 0.114	7200 0.104	8000 0.044	8800 0.083	9600 0.029	10400 0.060
		y(km) $\Delta\rho/\rho_0$	12000 0.036	12800 0.026	13600 0.018	14400 0.014	15200 0.024	16000 0.049
Model	y(km) $\Delta\rho/\rho_0$	800 0.104	1600 0.282	2400 0.054	3200 0.052	4000 0.097	4800 0.124	5600 0.116
	t = 350 s x = 3600km	y(km) $\Delta\rho/\rho_0$	6400 0.116	7200 0.096	8000 0.049			

*Here, $\Delta\rho/\rho_0 = (D-D_0)/D_0$.

From these results, we again noticed that the agreement between the prototype and model is good but is not as satisfactory as the coronal mass ejection case. This is probably because we have scaled both time and space which may cause additional numerical errors. However, the qualitative behavior of physics is still acceptable.

CONCLUDING REMARKS

In this study, we may conclude the following:

- (i) Using proper similitude characteristic critiques, one set of model calculations can be used to simulate a number of prototype calculations. This implies that, when the physical size of the prototype becomes too large to handle, a small size of the model could be used to replace it. In such a way, the computing time can be improved because of the fewer required numerical operations which will also decrease the truncation error.
- (ii) The similitude principle may be considered to be a universal solution for certain types of physical problems such as those in solar atmospheric dynamics.

ACKNOWLEDGEMENT

The work done by STW, SW, and AHW is supported by NASA grant NAGW-9 and STW is also supported by Air Force grant AFOSR-88-0013.

REFERENCES

1. Y. Q. Hu and S. T. Wu, *J. Comp. Phys.*, 55, 33, 19xx
2. L. E. Kalikhman, *Elements of Magnetogas-dynamics*, Ch. 3, W. B. Saunders, Company, New York, New York, 1967.
3. S. Wang, Y. Q. Hu, and S. T. Wu, *Scientia Sinica*, Ser. A., 1305, 1982.
4. S. T. Wu, Y. Q. Hu, S. Wang, M. Dryer, and E. Tandberg-Hanssen, *Astrophys. Space Sci.*, 83, 189, 1982.
5. S. T. Wu, S. Wang, M. Dryer, A. I. Poland, D. G. Sime, C. J. Wolfson, L. E. Orwig, and A. Maxwell, *Solar Phys.*, 85, 351, 1983.

ON THE NUMERICAL COMPUTATION OF NONLINEAR FORCE-FREE MAGNETIC FIELDS

S. T. WU, M. T. SUN, AND H. M. CHANG

Department of Mechanical Engineering and Center for Space Plasma and Aeronomic Research, University of Alabama in Huntsville

AND

M. J. HAGYARD AND G. A. GARY

Space Science Laboratory, NASA/Marshall Space Flight Center

Received 1988 November 7; accepted 1990 April 18,

ABSTRACT

An algorithm has been developed to extrapolate nonlinear force-free magnetic fields from the photosphere, given the proper boundary conditions. In this paper we present the results of this work, describing the mathematical formalism that was developed, the numerical techniques employed, and comments on the stability criteria and accuracy developed for these numerical schemes. An analytical solution is used for a benchmark test; the results show that the computational accuracy for the case of a nonlinear force-free magnetic field was on the order of a few percent ($<5\%$). Then we applied this newly developed scheme to analyze a solar vector magnetogram, and the results were compared with the results deduced from the classical potential field method. The comparison shows that additional physical features of the vector magnetogram were revealed in the nonlinear force-free case.

Subject headings: hydromagnetics — Sun: chromosphere — Sun: corona — Sun: magnetic fields

1. INTRODUCTION

Observations have shown that physical conditions in the solar atmosphere are strongly controlled by solar magnetic fields. The appearance of photospheric, chromospheric, and coronal structures, including active regions and flares, seen in $H\alpha$ and in different lines in the ultraviolet and extreme ultraviolet as well as in white-light observations, provides indications of the prevalent nature and importance of solar magnetic fields. Consequently, to understand the physics of active regions, the storage and release of flare energy, and the formation of hot plasma loops and mass ejections, it is imperative that we understand and study the evolution of the Sun's magnetic field. To achieve such a goal, the logical first step is to seek a realistic representation of the configuration of the solar magnetic field from observations.

A number of efforts in modeling physical structures of the magnetic fields and the storage and release of energy in flares are based on linear, so-called constant- α force-free models of magnetic fields (e.g., Nakabawa *et al.* 1971; Nakagawa and Raadu 1972; Welleck and Nakagawa 1973). For example, Tanaka and Nakagawa (1973) used this linear force-free model to analyze the energy buildup for the 1972 August flare. More recently, Schmahl *et al.* (1982) used a linear force-free model together with solar magnetograph data, VLA microwave maps, and X-ray spectroheliograms to study the evolution of an active region's magnetic structure, a study that led to a better understanding of the observed microwave structures. The authors concluded that localized currents must have been present in the low corona to account for the bright 6 cm sources observed far from areas of strong sunspot fields, thus suggesting the presence of nonlinear (non-constant- α) force-free fields. Further evidence for the existence of nonlinear force-free fields comes from the study of Krall *et al.* (1982), they used a linear model to investigate the vector magnetic field evolution within a flare-productive active region and concluded that the constant- α force-free model could not adequately represent the structures observed in the magnetic field

of the active region. Previously, Levine (1976) has shown that changes in the value and sign of α can occur within a single active region. Recently, Gary *et al.* (1987) have used observations of an active region (NOAA AR 2684 on 1980 September 23) to show nonlinear aspects of the magnetic field. The specific investigation of the spatial distributions in the photosphere of the vertical component of the electric currents has proved the nonlinear nature of the force-free fields (Hagyard, West, and Smith 1985; Moreton and Severny 1968).

The inadequacy of linear force-free models to represent observed solar magnetic fields is demonstrated amply by these studies. A compromise approach—constructing a “patchwork quilt” representation of the field of an active region by combining fields derived from solutions of the linear equations of different values of α —has no mathematical basis, as shown by Gary (1989). Such an approach is certainly inappropriate in describing the evolution of magnetic fields when important nonlinear physical processes such as energy storage and release and magnetohydrodynamic (MHD) instabilities are involved.

In this paper a numerical scheme is presented for extrapolating nonlinear force-free magnetic fields from a source surface, i.e., from observed vector magnetic fields at the photospheric level. This kind of approach was discussed in previous works (Harvey 1967; Molodenski 1969; Nakagawa 1974), but none of them is specifically for nonlinear force-free fields. It is understood here that we deal with a Cauchy problem for a system of elliptical partial differential equations, in which both field values and their derivatives are specified at the plane $z = 0$. Mathematically, this is an ill-posed problem with an unstable solution (see, e.g., Morse and Feshbach 1953, p. 703). However, ill-posed problems are encountered in many important practical physical and technical situations (Courant and Hilbert 1962) and are being solved by the so-called regularization method (Tikhonov and Arsenin 1977). In the present study, we have developed an averaging procedure which represents a relatively simple smoothing of the derivatives; it enables us to obtain an approximate solution with reasonable accuracy. The

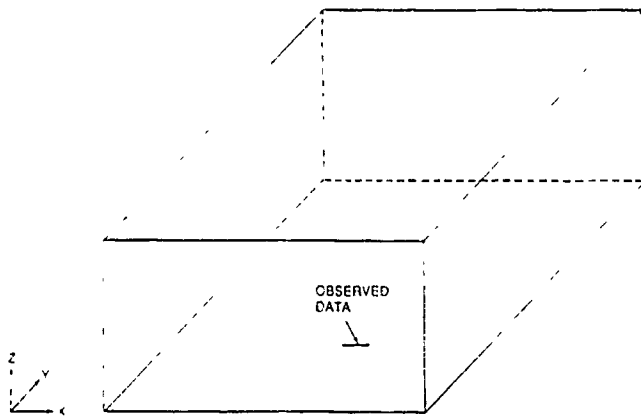


FIG. 1—Coordinate system and computational domain

The numerical algorithm presented in this paper is a straightforward extrapolation procedure with specified boundary conditions (where data can be used). The computational procedures, differencing schemes, and criteria for numerical stability are discussed in the following subsections.

a) Computational Procedures

We take as boundaries the six planes of the computational domain as shown in Figure 1. The values of the field on the lower surface are assumed known at discrete points, e.g., from measurements of the vector magnetic field at the photospheric level. The computational procedure to be used is summarized as follows.

1. At the lower surface ($z = 0$), the vector field (B_x , B_y , B_z) is prescribed at each grid point.
2. At this surface (i.e., $z = 0$), the horizontal derivatives $\partial B_x / \partial x$, $\partial B_x / \partial y$, $\partial B_y / \partial x$, $\partial B_y / \partial y$, $\partial B_z / \partial x$, $\partial B_z / \partial y$ are computed.
3. Using equation (2.9), the value of α over the plane is computed.
4. Using the results from steps 2 and 3, the vertical derivatives are computed from equations (2.6), (2.7), and (2.8).
5. With the vertical derivative of $B(x, y, 0)$ thus determined, the field $B(x, y, dz)$ is computed using an explicit extrapolation scheme.
6. Repeating steps 2–5, the complete field configuration can be determined subject to the boundary conditions, specified on the other five surfaces.

b) The Numerical Differential Scheme

In order to compute these horizontal derivatives numerically, we used second-order central differences for the interior points (Burden 1981), the specific expressions are given in the Appendix. For the computation of derivatives for points on the boundaries, the central differences cannot be used; in these cases, three-point forward (backward) formulae were used and are given in the Appendix (Greenspan 1974). It is important to note that no side boundary conditions are imposed. Equations (A3)–(A8) in the Appendix are used to extrapolate the interior field to the side walls. This forms a Cauchy problem to be solved.

Finally, to extrapolate the field components numerically in the z -direction using the derived vertical gradients, both Euler's formula and the Adams-Bashforth two-step formula were used. These formulae are also given in the Appendix. Thus, the final numerical forms for the extrapolation of the magnetic field for points interior to the domain are given by

combining equations (2.6)–(2.9) with the finite-difference formulae shown in the Appendix:

$$(B_x)_{l,m,n+1} = (\bar{B}_x)_{l,m,n} + \frac{h_z}{2h_x} [(B_z)_{l+1,m,n} - (B_z)_{l-1,m,n}] + (\alpha B_y)_{l,m,n} h_z, \quad (3.1)$$

$$(B_y)_{l,m,n+1} = (\bar{B}_y)_{l,m,n} + \frac{h_z}{2h_y} [(B_z)_{l,m+1,n} - (B_z)_{l,m-1,n}] - (\alpha B_x)_{l,m,n} h_z, \quad (3.2)$$

$$(B_z)_{l,m,n+1} = (\bar{B}_z)_{l,m,n} - \frac{h_z}{2h_x} [(B_x)_{l+1,m,n} - (B_x)_{l-1,m,n}] - \frac{h_z}{2h_y} [(B_y)_{l,m+1,n} - (B_y)_{l,m-1,n}], \quad (3.3)$$

$$(\alpha)_{l,m,n} = \frac{1}{(B_z)_{l,m,n+1}} \left[\frac{(B_y)_{l+1,m,n+1} - (B_y)_{l-1,m,n+1}}{2h_x} - \frac{(B_x)_{l+1,m,n+1} - (B_x)_{l-1,m,n+1}}{2h_y} \right], \quad (3.4)$$

where

$$(\bar{B})_{l,m,n} = \frac{1}{4} [(B)_{l+1,m,n} + (B)_{l-1,m,n} + (B)_{l,m+1,n} + (B)_{l,m-1,n}]. \quad (3.5)$$

In cases where B_z becomes so small that the computed value of α becomes inaccurate, we simply replace α by $\bar{\alpha}$, defined as

$$(\bar{\alpha})_{l,m,n} = \frac{1}{4} [(\alpha)_{l+1,m,n} + (\alpha)_{l-1,m,n} + (\alpha)_{l,m+1,n} + (\alpha)_{l,m-1,n}]. \quad (3.6)$$

These averaging formulae $(\bar{\alpha})_{l,m,n}$ and $(\bar{B})_{l,m,n}$ are used instead of the values of $(\alpha)_{l,m,n}$ and $(B)_{l,m,n}$ at the grid points as a method for smoothing the data. The selection of the grid spaces is guided according to the numerical stability criteria which are discussed in the next section.

c) Computational Domain and Numerical Stability

In general, six planes form the surface (or limits) of the computational domain. The values on the lower surface are determined from observational data; thus this surface is referred to as the "source surface," i.e., the photosphere. Values on the other surfaces are prescribed according to both physical and mathematical continuity conditions.

In the paper we employ the following conditions for the numerical stability analysis: assuming that (1) as $z \rightarrow \infty$, $(B_x, B_y, B_z) \rightarrow 0$, and (2) outside the rectangle given by $-a < x < a$, $-b < y < b$, periodic conditions are used together with von Neumann's method (Mitchell and Griffiths 1980), leads to the following conditions on h_z :

$$\frac{B_x}{B_z} \rho_x \leq \frac{1}{2} \quad \text{and} \quad \frac{B_y}{B_z} \rho_y \leq \frac{1}{2} \quad (3.7)$$

$$\frac{B_x^2 + B_y^2}{B_x B_z} \rho_x \leq \frac{1}{2} \quad \text{and} \quad \frac{B_x^2 + B_y^2}{B_y B_z} \rho_y \leq \frac{1}{2}, \quad (3.8)$$

where

$$\rho_x = \frac{h_z}{h_x}, \quad \rho_y = \frac{h_z}{h_y} \quad (3.9)$$

FORCE-FREE MAGNETIC FIELDS

mathematical formalism of this method is presented in § II, and the numerical method and procedures are included in § III. In § IV, results from a benchmark test case are given together with an analysis of the computational accuracy for this test case. To show the capability of this scheme, the data obtained from observation were analyzed by this new technique and compared with a classical potential field technique (Schmidt 1964). This comparison clearly shows that the nonuniform current features that are present can be identified with this new technique. Finally, concluding remarks are presented in § V.

II. MATHEMATICAL MODEL

The basic equation describing a force-free magnetic field is given by

$$\mathbf{J} \times \mathbf{B} = 0 \quad (2.1)$$

This may be rewritten with the aid of Ampere's law (cgs electromagnetic units),

$$4\pi\mathbf{J} = \nabla \times \mathbf{B}, \quad (2.2)$$

as

$$\nabla \times \mathbf{B} = \alpha \mathbf{B}, \quad (2.3)$$

where \mathbf{J} is the electric current density and α in general is different for each field line, although it must be constant along a given field line. This can be seen by taking the divergence of equation (2.3) to obtain

$$\mathbf{B} \cdot \nabla \alpha = 0 \quad (2.4)$$

by virtue of the solenoidal condition

$$\nabla \cdot \mathbf{B} = 0. \quad (2.5)$$

If $\alpha = 0$, the field is potential, that is, the lowest order approximation for a description of realistic solar magnetic fields. Since a potential configuration represents the lowest state of energy of a given magnetic boundary condition, it is definitely not an appropriate description for magnetic fields in active regions that produce flares. If α has the same value throughout the field domain, the resulting subclass of force-free fields is called a "constant- α " or linear field, since the field components satisfy a linear differential equation (Nakagawa and Raadu 1972). We will consider the general class of fields where α is a variable.

In component form, equations (2.3) and (2.5) form the basis of a scheme to extrapolate the force-free field when the vector magnetic field on the boundary surface is known. Some of the preliminary results were presented by Wu, Chang, and Hagyard (1985). We write the following equations using equations (2.3), (2.4), and (2.5)

$$\frac{\partial B_z}{\partial z} = \alpha B_z - \frac{\partial B_z}{\partial \alpha} \quad (2.6)$$

$$\frac{\partial B}{\partial z} = \alpha B - \frac{\partial B}{\partial \alpha} \quad (2.7)$$

$$\frac{\partial B_z}{\partial z} = \frac{\partial B_z}{\partial \alpha} - \frac{\partial B}{\partial \alpha} \quad (2.8)$$

$$\alpha = \frac{1}{B_z} \left(\frac{\partial B_z}{\partial \alpha} - \frac{\partial B}{\partial \alpha} \right) \quad (2.9)$$

$$\frac{\partial B_z}{\partial z} = \frac{\partial B}{\partial \alpha} \left(\frac{\partial B_z}{\partial z} \right) - \frac{\partial B}{\partial \alpha} \left(\frac{\partial B}{\partial z} \right) \quad (2.10)$$

We take as the lower boundary surface the plane $z = 0$. Then equation (2.9) indicates that knowing the vector field $\mathbf{B}(x, y, 0)$ over this surface is sufficient to determine locally the parameter $\alpha(x, y, 0)$. In this way, we have ensured that the source surface is a self-consistent nonlinear force-free field. Then with $\alpha(x, y, 0)$ and $\mathbf{B}(x, y, 0)$ specified, equations (2.6)–(2.8) determine $\partial \mathbf{B}(x, y, 0)/\partial z$ and thus allow the start of an integration upward with height z . The process can then be repeated, beginning with the determination of $\alpha(x, y, dz)$ from $\mathbf{B}(x, y, dz)$, again through equation (2.9). It should be noted that equation (2.10), derived from equations (2.6)–(2.9), provides an alternative method to derive $\alpha(x, y, z > 0)$. In places where B_z goes to zero, for example, along the "neutral line" in the photosphere (loci of nulls in the line of sight (B_z) component of the photospheric field), or near the tops of magnetic loops higher in the atmosphere, equation (2.9) cannot be used. In these instances, an interpolation along the field line such as that given in equation (3.6) is used to determine the value of α . This is based on the assumption that all the field lines are continuous in the neighborhood of a point, an assumption that has a physical and mathematical basis, since the present formulation does not include dissipative processes.

III. NUMERICAL METHODS

As shown by Grad (Grad and Rubin 1958; Grad 1985), the differential equation for the force-free field problem is a mixed type, having one nontrivial distinct real characteristic as in a hyperbolic equation, and two imaginary ones as in the case of an elliptical equation. For the general nonlinear case this leads to mathematical difficulties both in the specification of boundary conditions and in the nature of the solutions. A number of astrophysical examples (magnetostatic as well as force-free) have been discussed by Low (1982a) and by Lerche and Low (1982), and they summarize the present status of several classes of analytical solutions. Recently several attempts have been made to devise algorithms for calculating nonlinear force-free fields using observational boundary conditions (e.g., Sakurai 1981; Pridmore-Brown 1981; Sakurai and Makita 1986; Yang, Antiochos, and Sturrock 1986; Zwingmann 1987). The technique developed by Pridmore-Brown (1981) requires the Lorentz force to be minimized. The method of Zwingmann (1987) and Yang, Antiochos, and Sturrock (1986) have only been applied to two-dimensional problems. On the other hand, the method developed by Sakurai (1981) is a combination of the superposition of a current field on a potential field and a convergent iterative procedure. Pridmore-Brown's method has not been used with observational data, nor has it been tested against general nonlinear analytical models. However, neither Sakurai's nor Pridmore-Brown's method is convenient to apply to observational data. The present method is specifically developed for data utilization. Most recently, Aly (1988) has investigated some theoretical aspects of the construction of the nonlinear force-free magnetic field from boundary data. He has concluded that it is possible to construct such a solution with proper constraints. As a final remark, it has been known that some very useful approximations do not become exact in any known limit. For example, the von Karman–Tsien method for airfoils in subsonic flow (Liepman and Puckett 1947), shock expansion theory and its extension to axisymmetric and three-dimensional flows (Hayes and Probstein 1959), Spreiter's local linearization in transonic flow (Spreiter 1959), etc. This kind of approximation has been classified as the irrational approximation by Van Dyke (1975). The present approximation falls into this category.

These stability criteria guide us in choosing the proper grid spacings and extrapolation step (h_z). In practice, the periodic boundary conditions are not used to determine the values on the side boundaries, but the linear extrapolation based on interior points was used.

IV. COMPUTATIONAL RESULTS

In order to demonstrate this algorithm, we have carried out a numerical calculation, using as a benchmark testing case a form for the nonlinear force-free field that admits of an analytical solution. The form chosen was the analytical solution of Low (1982b) that incorporates a distorted magnetic neutral line and a highly sheared magnetic field in the vicinity of the neutral line, both important elements in flare-productive active regions (Hagyard, West, and Smith 1985; Hagyard, Moore, and Emslie 1984). Low's solution is given by the following equations:

$$B_z = -B_0 z_0 \frac{\cos \phi_i}{r}, \quad (4.1)$$

$$B_x = \frac{B_0 z_0 (x + x_0)(y - y_0)}{r R_i^2} \cos \phi_i - \frac{B_0 z_0 (z + z_0)}{R_i^2} \sin \phi_i, \quad (4.2)$$

$$B_y = \frac{B_0 z_0 (x + x_0)(z + z_0)}{r R_i^2} \cos \phi_i + \frac{B_0 z_0 (y + y_0)}{R_i^2} \sin \phi_i, \quad (4.3)$$

where

$$R_i^2 = [(y + y_0)^2 + (z + z_0)^2], \quad (4.4)$$

$$r^2 = [(x + x_0)^2 + (y + y_0)^2 + (z + z_0)^2], \quad (4.5)$$

$$\phi_i = 0.3 \ln R, \quad (4.6)$$

$$x = \frac{d[\phi_i(r)]}{dr} = -\frac{0.3}{r} \quad (4.7)$$

B_0 is the magnitude of the magnetic field strength at the origin (x_0, y_0, z_0) , where this origin is chosen to be located under the source surface. The configuration of the field lines inside the domain are determined by the position of this origin relative to the source surface. In the present study, the origin (x_0, y_0, z_0) is chosen to be $(x_0 = -\frac{1}{2}L_x, y_0 = -\frac{1}{2}L_y, z_0 = \frac{2}{3}L_z)$, and R is the normalized form of r ($R = r/R_0$).

Using these formulae, we generated the values of the magnetic field on a finite source surface forming the boundary of the domain of the calculation. The source surface numerical values were used in our numerical algorithm to extrapolate the field above the source surface. Since the analytic solutions gave the exact solutions for the field above the source surface, comparisons of our results with the analytic computations provided a stringent test of the algorithm. Figures 2-4 show the resulting comparisons between the numerical and analytic solutions.

In Figure 2, contours of the vertical field (the line-of-sight field for areas near the center of the solar disk) are shown in the x - y plane at two heights ($z = \text{constant}$) above the photosphere. Normalized to the computational size of the square base region at $z = 0$, the two levels are at $z = 0.50$ and $z = 1.0$; with a base length of $\sim 10^7$ km, these levels correspond to heights of 50,000 and 100,000 km, respectively. Since these are considerable heights up in the solar corona, comparisons between the numerical and analytical fields at these heights represent critical tests of the numerical method. As judged by the results

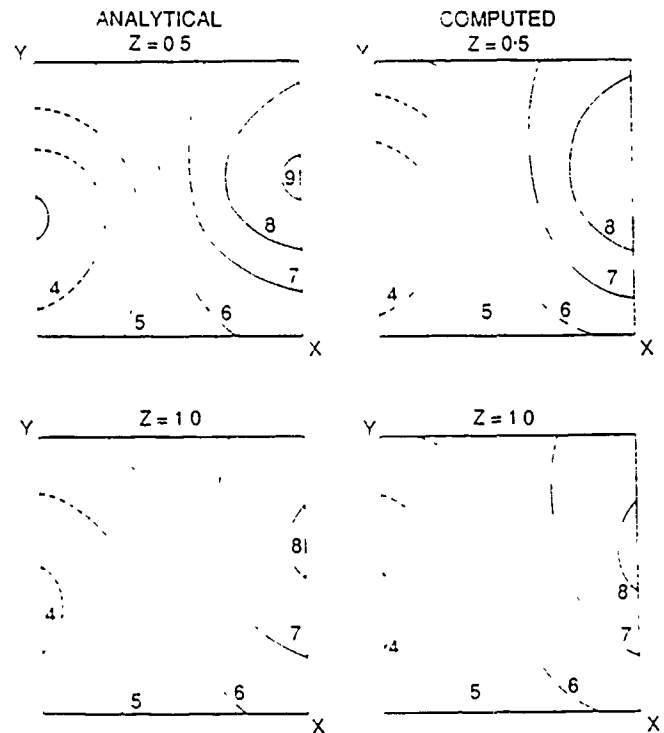


FIG. 2.—Comparison of analytical and numerical values for the B_z (line of sight) component of the magnetic field at two different heights ($z = \text{const.}$). The solid and dashed curves represent positive and negative contours of the B_z component of the nonlinear force-free magnetic field in the x - y plane at $z = 0.5$ (in the middle of the z -scale) and at $z = 1.0$ (at the top of the z -scale), where the numbers indicate the strength of the magnetic field. The numbers represent the level of magnetic strength as follows: 3 = 1000 G, 4 = 500 G, 5 = 200 G, 6 = 0 G, 7 = 200 G, 8 = 500 G, 9 = 1000 G.

shown in Figure 2, they are in good agreement at both levels as far as the strength of the vertical component of the magnetic field is concerned.

In Table 1 we present detailed quantitative comparisons for $z = 0.5$ (50,000 km). For selected grid points in the x - y plane of

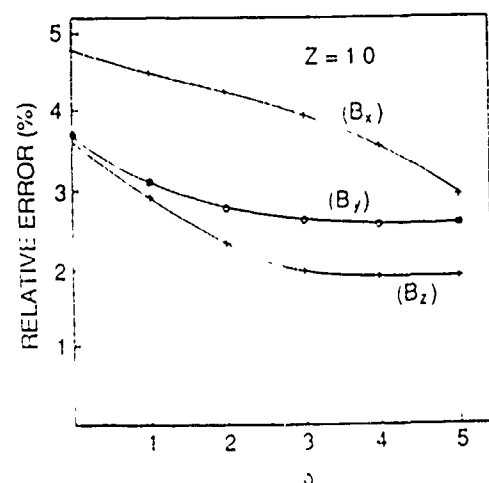


FIG. 3.—Average percentage error between the analytical and numerical solutions as a function of the parameter δ . This parameter represents how much of the domain in the x - y plane is included in the analysis of average error. $\delta = 0$ represents the initial domain. $\delta = 1$ indicates that the first row and column on all sides at the boundary of the domain are omitted in the error analysis, etc.

TABLE I
 TABLE AND VALUES OF B_1, B_2, B_3 AND C_1, C_2, C_3 FOR ANALYTICAL AND COMPUTED RESULTS FOR A 33 × 33 GRID PIV AND P

N1	N2	0.1		0.33		0.15		0.58		0.70		0.82		0.94	
		ANAL. Ytical	COM. PUTED	ANAL. Ytical	COM. PUTED	ANAL. Ytical	COM. PUTED	ANAL. Ytical	COM. PUTED	ANAL. Ytical	COM. PUTED	ANAL. Ytical	COM. PUTED	ANAL. Ytical	COM. PUTED
0.21	BX	238	250	250	253	258	256	262	257	260	254	254	250	244	250
	BY	256	083	072	092	091	098	111	098	128	100	140	107	115	108
	BZ	141	151	143	152	151	140	129	143	110	123	085	106	058	103
	AL	078	088	081	076	083	063	085	018	084	032	082	020	079	010
0.33	BX	250	238	263	246	273	250	277	251	276	251	268	247	277	239
	BY	065	078	078	086	093	094	108	097	120	101	128	111	130	113
	BZ	114	130	113	121	107	112	096	099	078	080	056	066	032	072
	AL	081	092	085	081	088	074	089	061	089	045	086	031	083	020
0.15	BX	258	226	273	212	283	253	288	257	286	256	279	248	26	231
	BY	077	079	087	087	097	094	106	098	113	102	116	110	111	109
	BZ	084	094	079	080	070	086	057	051	040	035	021	026	002	031
	AL	083	095	088	090	091	082	092	070	092	054	089	043	086	028
0.58	BX	262	219	277	211	288	257	293	261	291	262	283	250	270	277
	BY	091	087	097	096	103	099	106	100	107	101	105	103	101	100
	BZ	053	048	042	038	030	027	015	013	001	003	017	011	031	018
	AL	085	084	089	097	092	083	091	089	093	077	091	078	087	079
0.70	BX	260	219	276	211	286	256	291	261	290	259	282	249	268	231
	BY	106	095	110	106	111	105	108	100	103	097	096	091	088	088
	BZ	022	003	006	006	011	010	028	023	043	039	056	053	065	066
	AL	081	048	089	059	094	067	093	074	093	076	090	081	086	095
0.82	BX	251	228	268	213	279	251	283	253	282	252	274	247	262	238
	BY	122	100	123	111	120	106	112	099	101	096	088	090	076	082
	BZ	007	048	028	047	050	050	069	066	084	082	093	095	098	108
	AL	082	022	086	035	089	010	091	059	090	073	088	083	085	091
0.94	BX	241	209	257	216	266	250	270	253	268	253	262	251	251	217
	BY	137	102	137	110	130	103	117	098	101	097	083	093	067	085
	BZ	034	079	059	032	084	032	105	113	120	129	127	136	129	140
	AL	079	011	083	021	086	032	087	018	086	062	085	075	081	085

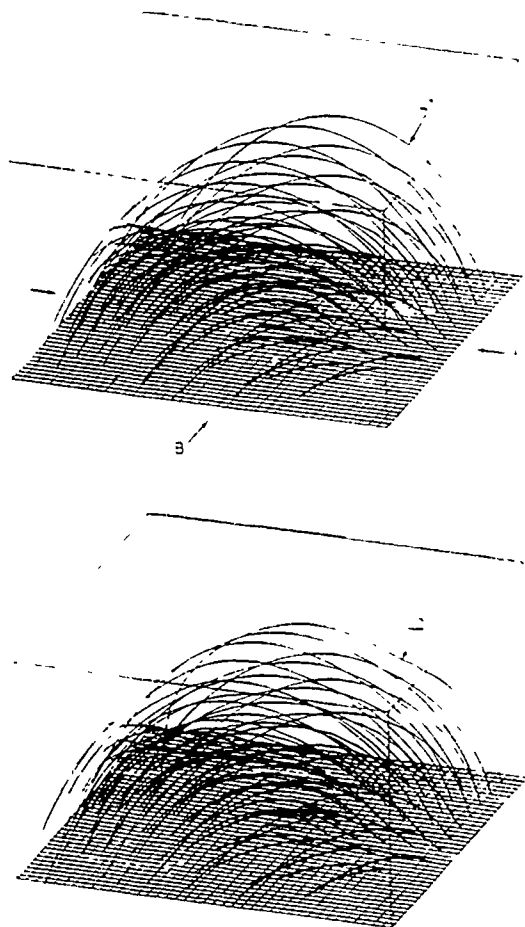


FIG. 4—Three-dimensional representation of the nonlinear force-free magnetic field. (a) analytical solution and (b) numerical solution, where L_1 and L_2 respectively represent the field line. The same footpoint is obtained by the analytical solution and the numerical solution.

33 \times 33 grid points, the table gives the analytic and computed values for all three field components and for the force-free parameter α . From data such as those in Table 1, we have calculated the mean square percentage errors in the field components at different heights as a function of the parameter δ , which is the number of rows and columns next to the boundary surfaces in the x - y plane that are omitted from the error analysis. In Figure 3 these percentage errors are plotted against the parameter δ for the level $z = 1.0$. For the case of $\delta = 0$, that is, if all grid points in the domain are included in the error analysis, the basic quantitative result is very obvious: at all height levels, including the highest, the computed solution agrees with the analytic solution to better than 5% in all field components, and the typical error is only 3%. However, the error of the α -value will be greater because α is computed from the gradients of the magnetic field and divided by B_z . Figure 3 also demonstrates that the worst errors tend to occur near the boundaries, since all errors at $z = 1.0$ tend to decrease as the grid points near the boundary are omitted in the error calculation. This result indicates the obvious result that in computations using observational data some care must be exercised in analyzing the data near the boundaries. Because the exact nature of the field outside the region is not available for use in the computation, the effects on the solution due to this outside region could not be accounted for.

Figure 4 shows the three-dimensional representation of the magnetic field lines obtained from analytical solution and numerical code, respectively. Again, by comparison of these two cases, we note that for the lower field lines (i.e., below 20,000 km) these two cases are almost identical, but the higher field lines do show some small differences, for example, the differences between field line L_1 and L_2 . These lines originate near the boundary; hence they are expected to show numerical differences. However, we are reminded, in general, that there are two steps that introduce numerical errors: (1) the extrapolation procedures and (2) the graphics procedure. With these two sources, the differences between analytical and numerical solutions are as small as shown, which indicates that we are able to establish a numerical procedure for extrapolation of the field.

Since we have shown that the numerical scheme is an acceptable one in comparison with an analytical solution, we shall now apply this scheme for real data analysis. Since observational errors may introduce spurious numerical results, this data set will test the numerical stability to nonideal data. For this purpose, we have chosen the near disk center (1980 September 15) active region AR 2665 observed by the Marshall Space Flight Center vector magnetograph for analysis. Figure 5 shows the observed B_z contours and transverse vector fields (i.e., B_x and B_y) at the photospheric level which will be used as the surface information for the numerical extrapolation of nonlinear (i.e., non-constant- α) force-free field lines. Physically this means that the intensity of the current density at each footpoint is different according to the observed value.

Figure 6a shows the three-dimensional configuration of the field lines of this active region based on this newly developed nonlinear force-free model, and Figure 6c shows the three-dimensional configuration of the field lines of the same active region found with a potential field model (Schmidt 1964). In addition, we have shown the top view of these two cases in Figures 6b and 6d, respectively. In comparing these two cases,

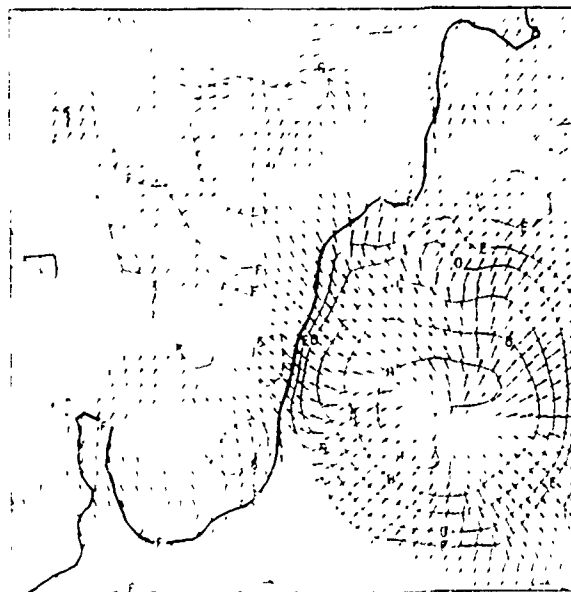


FIG. 5—Observed B_z contours and transverse vector fields (i.e., B_x and B_y) on 1980 September 15 (AR 2665) at photospheric level (i.e., $z = 0$), where A = 2000 G, B = 1500 G, C = 1000 G, D = 500 G, E = 250 G, F = 0 G, G = -250 G, H = -500 G, I = -1000 G.

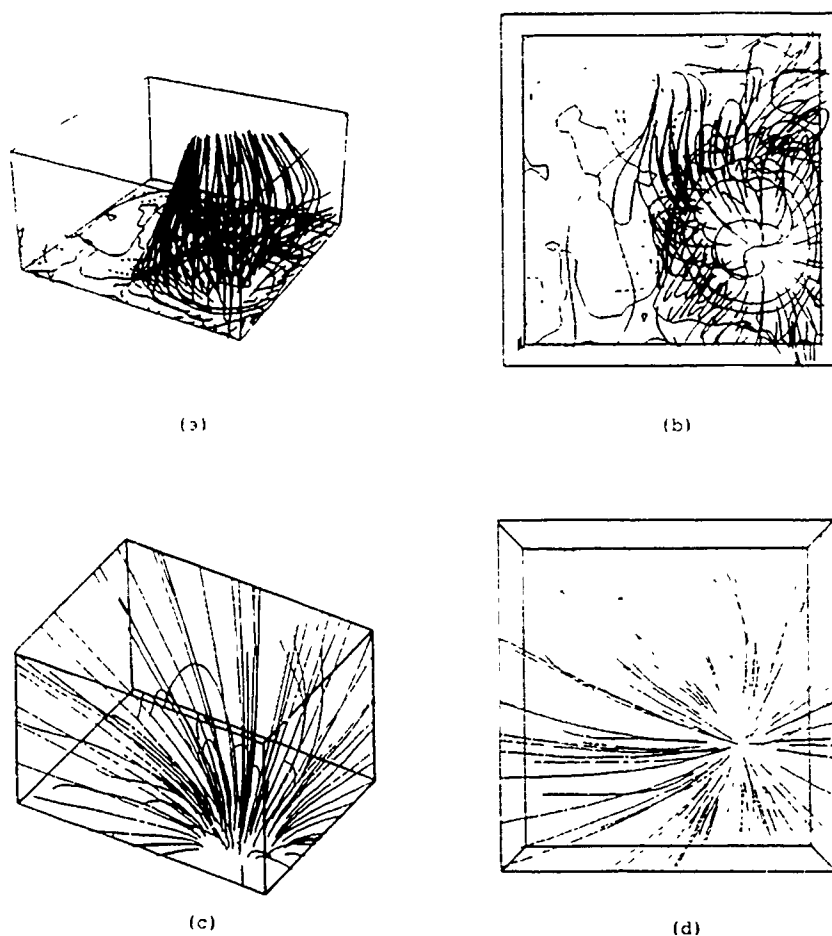


FIG. 6—(a) Numerical extrapolated three-dimensional magnetic field line using present nonlinear force-free magnetic field code based on the data given in Fig. 5. (b) Same structure as in (a) as viewed from the top. (c) Numerical extrapolated three-dimensional magnetic field lines using potential magnetic field model (Schmidt 1964) based on the data given in Fig. 5. (d) Same structure as in (c) as viewed from top.

we note that the topology of two magnetic field lines exhibits considerable differences. No shear feature appeared in the potential field representation, which is what is expected because the potential field model is a current-free model. Thus, there is much less structure exhibited in the potential field representation as compared with the nonlinear force-free rep-

resentation. For example, let us examine the field line configuration for these two cases. In the case of the nonlinear force-free field representation as shown in Figure 6a, the field lines are highly twisted topologically in the penumbral region as well as in the umbra, where field lines are open. Also, we observe from the calculation based on the analytical solution

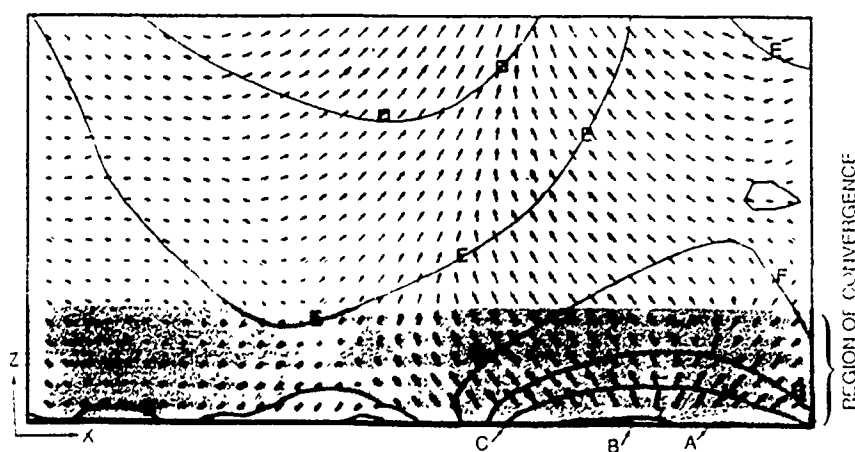


FIG. 7—Numerical computed nonlinear force-free field configuration projected on the x - z plane, based on AR 2665, 1980 September 8 where A, B, and C indicate the locations of core, umbrae, and penumbrae respectively. The other symbols indicate the field strength: D = 500 G, E = 250 G, F = 0 G, G = -250 G, H = -500 G.

that every loop has a different shear, which represents a different current intensity. Now some attention must be given to the extrapolated field configuration as shown in Figure 6a. It is obviously difficult to comment on the accuracy of this representation because there is no analytical solution or other reference which we can use for comparison. However, some theoretical assessments can be made:

1. In Figure 7 we have plotted the extrapolated field configuration shown in Figure 6a projected on the x - z plane. It is clearly indicated in this figure that the general characteristics of this extrapolate solution exhibit characteristics of a sunspot such as the core, umbrae, and penumbrae (marked by A, B, and C in Fig. 7).

2. The shaded region represents the region of realistic solu-

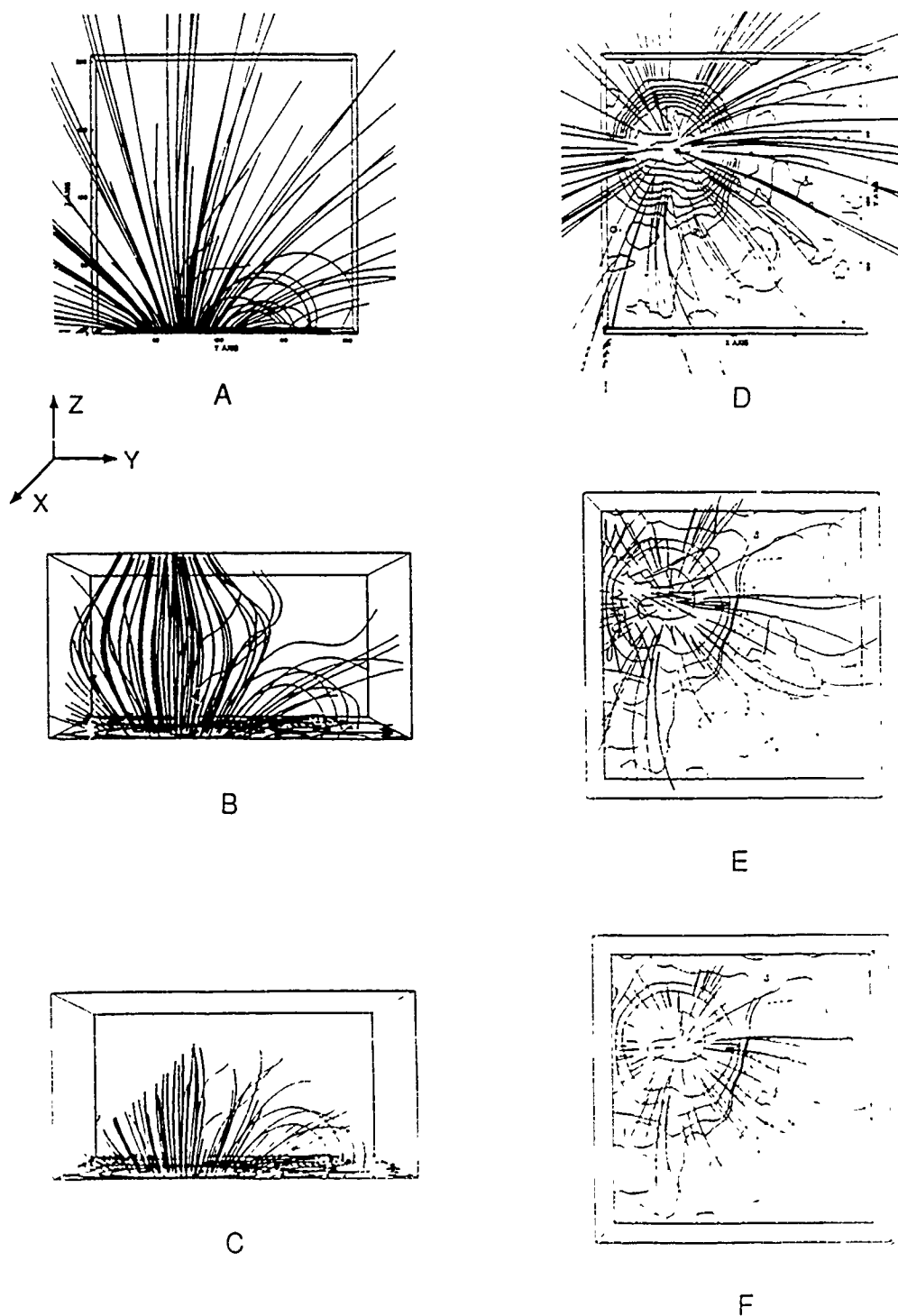


FIG. 8 — Comparison of Schmidt's method ($[a]$ and $[d]$) and the present methods for $\alpha = 0$. The left hand panel represents the side view of the extrapolation of the observed magnetic field (AR 2665, 1980 September 15), and the right-hand panel represents the top view of the extrapolation of the observed magnetic field. (a) and (d) are obtained by Schmidt's method, (b) and (e) are obtained by the present method with full height of the computation domain, and (c) and (f) are obtained by the present method with half the height of the computation domain.

tion. Beyond this region, the numerical procedure diverges from a realistic solution, as can be seen by the convergence of the field lines. This effect could be credited to the averaging procedure in our numerical calculation (see eq. [3.6]) and the range extended beyond our regularization process in addition to the finite magnetogram. However, this effect does not appear when we run the analytical tests because the analytical solution which we have chosen has regular analytical continuous behavior.

3. To assess the region of convergence further, we have employed the present numerical method to compute the potential field (i.e., $\alpha = 0$) configuration using the very same data presented in Figure 5 in comparison with Schmidt's method (1964). The procedure for carrying out this comparison is to input the potential field at the $z = 0$ level from the observed data of 1980 September 15 (AR 2665) into the present numeri-

cal algorithm by setting $\alpha = 0$. The results are compared in Figure 8. In Figure 8 we have shown the front view of the field lines (y - z plane) computed by Schmidt's method (Fig. 8a) and by the present method (Figs. 8b and 8c) on the left-hand side, and the corresponding results of the top view (x - y plane), i.e., Figures 8d-8f, on the right. From these results, we observed that those lines limited to half the height of the computations domain, which corresponds to a 45° cut [i.e., $\sim \tan^{-1}(h_x/h_z)$], are almost identical to those given by Schmidt's method. This is indeed consistent with the results we have shown in Figure 7 in describing the region of convergence.

To examine the effects of the boundaries, we use the same observed field but "move" the sunspot toward the boundary and extrapolate the nonlinear force-free field to different heights as shown in Figure 9. From these results, we note that

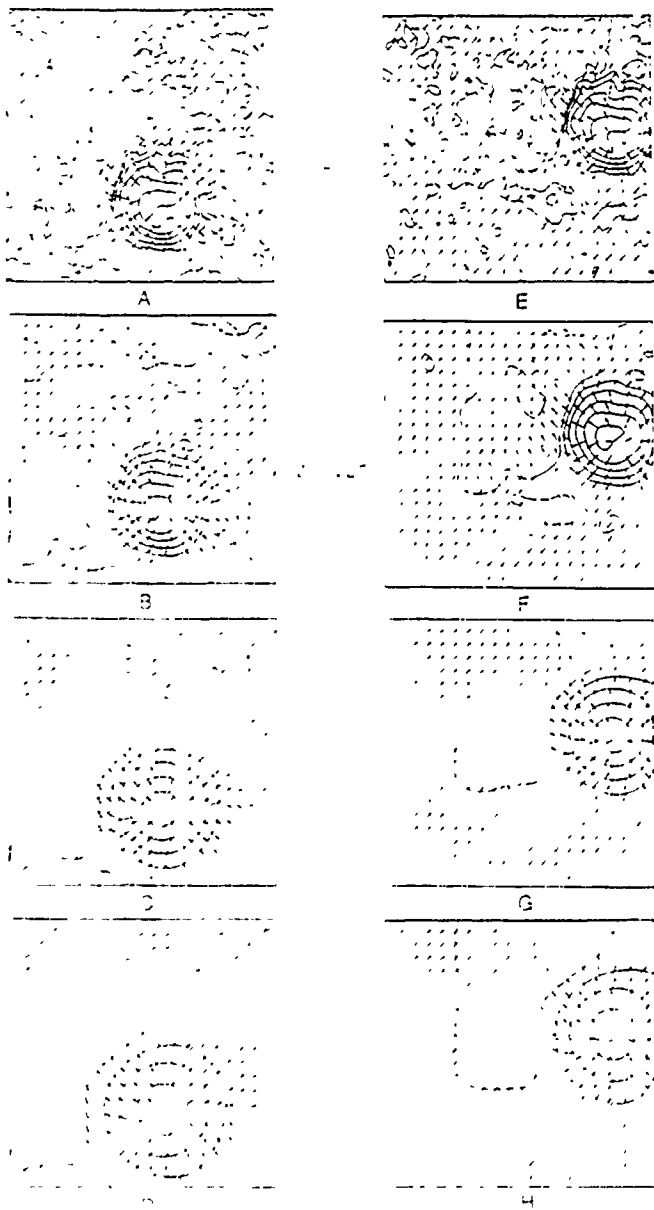


FIG. 9. Effects of the boundary on the numerical results at various heights (i.e., $z = 0, 0.25, 0.75, 1.0$).

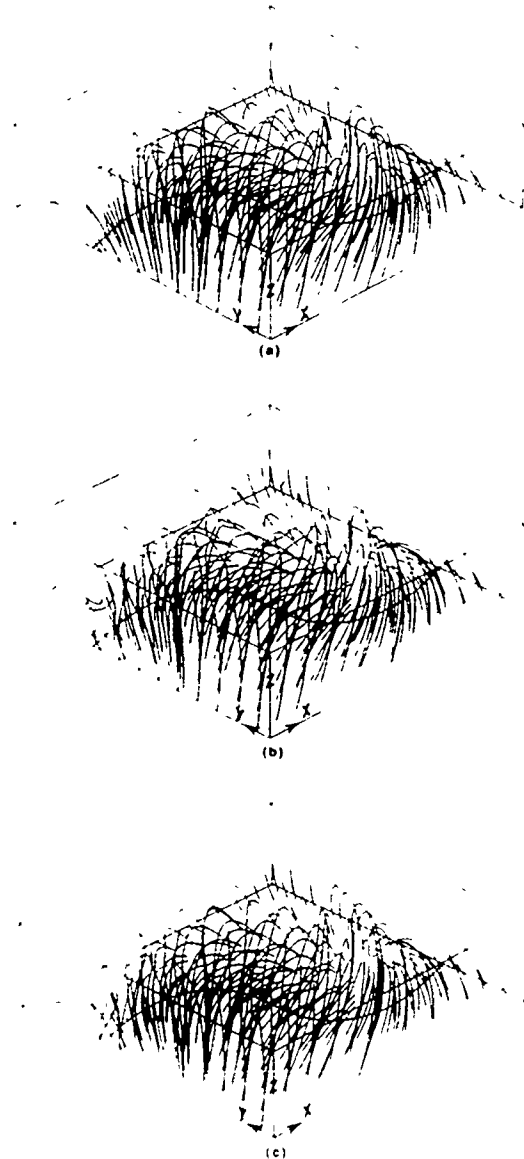


FIG. 10. Comparison of the three-dimensional magnetic field configurations extrapolated from (a) the analytical data (eqs. [4.1]–[4.5]), (b) the analytical data with random perturbation using a one-step smoothing process, and (c) the analytical data with random perturbation using a two-step smoothing process. The one-step and two-step smoothing processes represent using a four-point average as shown in eq. [3.5] once and twice, respectively.

the basic features of the sunspot are identical for both cases. However, at higher heights, significant differences on the neutral lines are seen. This is consistent with our previous comments, the accuracy of this procedure deteriorates when the solution is close to a boundary. It is important to note that since $\vec{B} \cdot \nabla \chi = 0$, a twisted field leads to localized currents which will remain localized as seen in Figure 6a.

As a final assessment of this newly developed method, we would like to show that this method is indeed stable with respect to the random noise. In order to achieve this point, we have introduced a random perturbation in the data generated by Low's analytical solution at the surface (eqs. [4.1]–[4.3]). The random perturbations were introduced at an amplitude of 10% for the transverse field (i.e., B_x and B_y) and 1% for the line-of-sight field (i.e., B_z). These results are shown in Figure 10. Figure 10a shows the results without introducing the random perturbation, Figure 10b shows the results with random perturbation with a one-step smoothing process, and the results with random perturbation together with a two-step smoothing process are presented in Figure 10c. By comparison of these results, we clearly noted that the results with two-step smoothing are converging to the true solution. Thus we may claim that the present method is a stable one with random noise perturbation.

V CONCLUDING REMARKS

In this paper we have presented numerical solutions for nonlinear force-free magnetic fields above a source surface. These numerical solutions are based on a numerical scheme which enables us to obtain nonlinear force-free solutions by extrapolation from a given surface. This newly developed algorithm was tested by using an analytical solution to the nonlinear force-free field equations, the test showed that, with the present numerical scheme, nonlinear force-free magnetic fields can be extrapolated to an accuracy of better than 5% in comparison with the analytical case in a defined region, i.e. region of con-

vergence. In addition, a numerical example based on the observational data was also presented to test the capability of this numerical nonlinear force-free model. As has been pointed out by a number of authors (Grad 1973, Kress 1977, 1978), the complete mathematical characterization of the nonlinear force-free problem has not yet been achieved. Accordingly, we do not claim to have solved the nonlinear force-free problem, we have merely presented a numerical algorithm that can be used for extrapolation of the force-free solution to within a certain accuracy. Nevertheless, because of the practical importance of force-free fields in understanding the physics of the Sun, there is strong motivation for devising a numerical approach that will serve in the interim until a satisfactory mathematical understanding is achieved. Therefore, it would be wise to note some unresolved mathematical questions when applying this numerical procedure for data analysis. (1) The accuracy deteriorates when the solution is close to the boundary. (2) The uniqueness of the solution has yet to be established (however, the preservation of the solution via various boundary values has been demonstrated; see Fig. 9).

As of now, we have achieved this initial goal, the next step is to apply this algorithm to a wide variety of actual observations of vector magnetic fields to test the numerical code under various conditions, e.g., for the magnetic field in more complex regions, and to explore the region of convergence of the numerical extrapolation. Also, the effect of noise in the observational data should be investigated.

The work done by S. T. W. and M. T. S. was partially supported by AFSOR-88-0013. S. T. W., M. T. S., and H. M. C. were partially supported by NASA grant NAGW-9. The work done by M. J. H. and G. A. G. was in part supported by NASA through the Solar Physics Branch of the Space Physics Division. We also thank S. T. Suess for reading the manuscript and giving valuable comments.

APPENDIX

FINITE-DIFFERENCE REPRESENTATION OF THE REQUIRED TERMS IN THE GOVERNING EQUATIONS

$$\left(\frac{\partial B_x}{\partial x} \right)_{l,m,n} = \frac{(B_x)_{l+1,m,n} - (B_x)_{l-1,m,n}}{2h_x} + O(h_x^2), \quad (A1)$$

and

$$\left(\frac{\partial B}{\partial x} \right)_{l,m,n} = \frac{(B)_{l+1,m,n} - (B)_{l-1,m,n}}{2h_x} + O(h_x^2), \quad (A2)$$

where the subscript l represents the components of the physical quantities (i.e., x, y, z), l, m , and n indicate the coordinates of the grid points in a three-dimensional space, and h_x and h_z are the grid spacings along the x and z -axes, respectively.

For points $l = 1$:

$$\left(\frac{\partial B}{\partial x} \right)_{1,m,n} = \frac{(B)_{2,m,n} - 4(B)_{1,m,n} + 3(B)_{0,m,n}}{2h_x} + O(h_x^2) \quad (A3)$$

For points $m = 1$:

$$\left(\frac{\partial B}{\partial x} \right)_{l,m,n} = \frac{(B)_{l,m+1,n} - 4(B)_{l,m,n} + 3(B)_{l,m-1,n}}{2h_z} + O(h_z^2) \quad (A4)$$

For points $l = l_{\max}$,

$$\left(\frac{\partial B_i}{\partial x}\right)_{l,m,n} = \frac{3(B_i)_{l,m,n} - 4(B_i)_{l-1,m,n} + (B_i)_{l-2,m,n}}{2h_x} + O(h_x^2). \quad (A5)$$

For points $m = m_{\max}$,

$$\left(\frac{\partial B_i}{\partial y}\right)_{l,m,n} = \frac{3(B_i)_{l,m,n} - 4(B_i)_{l,m-1,n} + (B_i)_{l,m-2,n}}{2h_y} + O(h_y^2). \quad (A6)$$

Euler's formula is written

$$(B_i)_{l,m,n+1} - (B_i)_{l,m,n} = h_z \left(\frac{\partial B_i}{\partial z}\right)_{l,m,n} + O(h_z^2); \quad (A7)$$

the Adams-Bashforth two-step formula is

$$(B_i)_{l,m,n+1} - (B_i)_{l,m,n} = \frac{3h_z}{2} \left(\frac{\partial B_i}{\partial z}\right)_{l,m,n} - \frac{h_z}{2} \left(\frac{\partial B_i}{\partial z}\right)_{l,m,n-1} + O(h_z^2). \quad (A8)$$

REFERENCES

- Aly, J. J. 1988, *Solar Phys.*, **120**, 19.
- Burden, R. L. 1981, *Numerical Analysis* (Boston: Prindle, Weber and Schmidt).
- Courant, R., and Hilbert, D. 1962, *Methods of Mathematical Physics*, Vol. 2. (New York: Interscience), p. 231.
- Gary, G. A. 1989, *Ap J Suppl.*, **69**, 323.
- Gary, G. A., Moore, R. L., Hagyard, M. J., and Haisch, B. M. 1987, *Ap J.*, **314**, 782.
- Grad, H. 1973, *Adv. Plasma Phys.*, **5**, 103.
- 1985, *Internat. J. Fusion Energy*, **3**, 33.
- Grad, H., and Rubin, H. 1958, in *Proc. Second Internat. Conf. on the Peaceful Uses of Atomic Energy* (Geneva), **31**, 1950.
- Greenspan, P. 1974, *Discrete Numerical Methods in Physics and Engineering* (New York: Academic), p. 28.
- Hagyard, M. J., Moore, R. L., and Emslie, A. G. 1984, *Adv. Space Res.*, **4**, 71.
- Hagyard, M. J., West, E. A., and Smith, J. B., Jr. 1985, in *Proc. Kunming Workshop on Solar Physics and Interplanetary Travelling Phenomena*, ed. C. DeJager and Chen Biao (Beijing: Science Press), p. 179.
- Harvey, J. W. 1967, Ph.D. thesis, University of Colorado, Boulder.
- Hayes, W. D., and Probst, R. F. 1959, *Hypersonic Flow Theory* (New York: Academic), p. 265.
- Krall, K. R., Smith, J. B., Jr., Hagyard, M. J., West, E. A., and Cumings, N. O. 1982, *Solar Phys.*, **79**, 59.
- Kress, R. 1977, *Angew. Zs. Math. Phys.*, **28**, 715.
- 1978, *Proc. Roy. Soc. Edinburgh, A*, **82**, 71.
- Lerche, I., and Low, B. C. 1982, *Physica*, **4D**, 293.
- Levine, R. 1976, *Solar Phys.*, **46**, 159.
- Liepmann, H. W., and Puckett, A. E. 1947, *Introduction to Aerodynamics of a Compressible Fluid* (New York: Wiley), p. 176.
- Low, B. C. 1982a, *Rev. Geophys. Space Phys.*, **20**, 145.
- 1982b, *Solar Phys.*, **77**, 43.
- Mitchell, A. R., and Griffiths, D. F. 1980, *The Finite Differences Method in Partial Differential Equations* (New York: Wiley).
- Molodenski, M. M. 1969, *Soviet Astr.—A J.*, **10**, 585.
- Moreton, G. G., and Severny, A. B. 1968, *Solar Phys.*, **3**, 282.
- Morse, P. M., and Feshbach, H. 1953, *Methods of Theoretical Physics* (New York: McGraw-Hill), p. 703.
- Nakagawa, Y. 1974, *Ap J.*, **190**, 437.
- Nakagawa, Y., and Raadu, M. A. 1972, *Solar Phys.*, **25**, 127.
- Nakagawa, Y., Raadu, M. A., Billings, D. F., and McNamara, D. 1971, *Solar Phys.*, **19**, 72.
- Prudmore-Brown, D. C. 1981, Aerospace Corporation Rept. No. ATR-81(7813)-1.
- Sakurai, T. 1981, *Solar Phys.*, **69**, 343.
- Sakurai, T., and Makita, M. 1986, in *Hydrodynamic and Magnetohydrodynamic Problems in the Sun and Stars*, ed. Y. Osaki (Tokyo: University of Tokyo), p. 53.
- Schmahl, E. J., Kundu, M. R., Strong, K. T., Bentley, R. D., Smith, J. B., Jr., and Krall, K. R. 1982, *Solar Phys.*, **80**, 233.
- Schmidt, H. U. 1964, *Physics of Solar Flares* (NASA SP-50), p. 107.
- Spreiter, J. R. 1959, *J. Aerospace Sci.*, **26**, 465.
- Tanaka, K., and Nakagawa, Y. 1973, *Solar Phys.*, **33**, 187.
- Tikhonov, A. N., and Arsenin, V. Y. 1977, *Solutions of Ill-posed Problems* (New York: Wiley).
- Van Dyke, M. 1975, *Perturbation Methods in Fluid Mechanics* (Stanford: Parabolic), p. 3.
- Welleck, R. E., and Nakagawa, Y. 1973, *Force-free Magnetic Field Computation* (NCAR-TN/STR-87).
- Wu, S. T., Chang, H. M., and Hagyard, M. J. 1985, *Proc. MSFC Workshop, Measurements of Solar Vector Magnetic Fields* (NASA CP-2374), p. 17.
- Yang, W. H., Antiochos, S. K., and Sturrock, P. A. 1986, *Ap J.*, **309**, 383.
- Zwingmann, W. 1987, *Solar Phys.*, **111**, 309.

G. A. GARY and M. J. HAGYARD: Mail Code ES 52, NASA/Marshall Space Flight Center, MSFC, AL 35812

H. M. CHANG, M. T. SUN, and S. T. WU: Department of Mechanical Engineering and Center for Space Plasma and Aeronomic Research, University of Alabama in Huntsville, Huntsville, AL 35899

A COMPARISON BETWEEN PROGRESSIVE EXTENSION METHOD (PEM) AND
ITERATIVE METHOD (IM) FOR MAGNETIC FIELD EXTRAPOLATIONS
IN THE SOLAR ATMOSPHERE

S. T. Wu and M. T. Sun
Center for Space Plasma and Aeronomic Research
and Department of Mechanical Engineering
The University of Alabama in Huntsville
Huntsville, AL 35899 USA
and
Takashi Sakurai
National Astronomical Observatory
Matsuda, Tokyo, 181 Japan

ABSTRACT

In this paper we present a comparison between two numerical methods for the extrapolation of nonlinear force-free magnetic fields, viz. (i) the Iterative Method (IM) and (ii) the Progressive Extension Method (PEM). The advantages and disadvantages of these two methods are summarized and the accuracy and numerical instability are discussed. On the basis of this investigation, we claim that the two methods do resemble each other qualitatively.

I. INTRODUCTION

It is wellknown that the magnetic fields play a dominant role in all physical features which appear in the solar atmosphere; for example, the observed filamentary structures in the chromosphere seen in H_{α} (Martin, 1980), and coronal loops seen in UV (Cneng, et al. 1982) and X-rays (Antonucci et al. 1982; de Jager et al. 1983). All these structures in the solar atmosphere are generally considered to be aligned along the magnetic field (Zirin, 1971; Poletto, et al., 1975). Physically, these structures can be interpreted as plasma confined by the magnetic field. Hence, a detailed and quantitative analysis of these structures require a quantitative knowledge of the magnetic field in the solar atmosphere. Presently, measurements of magnetic fields are

confined to the photospheric level; therefore, in higher levels (i.e. chromosphere and corona) the magnetic field can only be obtained through numerical extrapolation using the measured photospheric magnetic field as the source surface, as demonstrated in the early work of Schmidt (1964), Altschuler and Newkirk (1969), Nakagawa and Raadu (1972). All these early extrapolation methods are restricted to the linear approximation, which physically represents current-free field (potential field) or constant current-to-magnetic field ratio (linear force free field). It has been shown that these representations are far from realistic in describing the observed features in the solar atmosphere (Schmahl et al., 1982).

In order to improve our understanding of the physical structures of the solar atmosphere it is necessary to have quantitative knowledge of the magnetic field. Therefore, a number of extrapolation methods is developed to meet the demands. The mathematical model using a force free configuration on the basis for the extrapolation of photospheric vector magnetograms to obtain the coronal field has been given by Aly (1989) and Gary (1990). In particular, Gary (1990) presented an excellent summary and assessment on the present available extrapolation methods from a theoretical point of view. In this paper, a comparison between the progressive extension method (PEM) and iterative method (IM) is presented. The rationale for choosing these two extrapolation techniques for comparison is that they are based on observed photospheric level fields and have practical applications. A brief description of the theoretical background of these two techniques is presented in Section 2. Numerical results of direct comparison are included in Section 3. The discussion of advantages and disadvantages of these two techniques and their possible physical consequences are presented in section 4.

II. THEORY AND TECHNIQUES

On the assumption of magnetohydrostatic equilibrium in the solar atmosphere, the mathematical model describing such an equilibrium state may be written as

$$-\nabla p + \vec{J} \times \vec{B} - \rho \vec{g} = 0, \quad (1)$$

where p is the hydrostatic pressure and will be represented by the equation of state,

$$p = \rho RT, \quad (2)$$

with ρ and T being the mass density and temperature respectively. The other symbols have their usual meanings; B is the magnetic field and J , the current density, is related to B by

$$\vec{J} = \nabla \times \vec{B} . \quad (3)$$

Finally, \vec{g} is the gravitational acceleration. Physically, there are three different orders of approximation to determine the magnetic field configuration. The first and second order approximations are the current free (potential) and force-free magnetic field, respectively. Within these orders of approximation the magnetic force vanishes, and the pressure force is balanced by the gravitational force which leads to the hydrostatic equilibrium in the solar atmosphere. Under these circumstances, the mathematical model for the magnetic field configuration can be represented by

$$\nabla \times \vec{B} = \alpha \vec{B} , \quad (4)$$

This expression possesses three different physical meanings, which are: (i) $\alpha = 0$, corresponds to the current free case in which the magnetic field is potential, (ii) $\alpha = \text{constant}$, corresponds to the linear force-free magnetic field which implies a constant current-to-magnetic field ratio in a region and (iii) $\alpha = \alpha(r)$, corresponds to the nonlinear force-free field which implies a non-constant current-to-magnetic field ratio in a region.

Finally, the third order of approximation is the magnetohydrostatic equilibrium in the solar atmosphere which is given by Eq. (1). If there is information on B and p on the source surface, it is possible to extrapolate B and p upward. Since there only are measurements of the magnetic field on the source surface (photosphere), it is not possible to extrapolate magnetohydrostatic equilibrium field-configurations at the present time.

In the meantime, we shall focus our attention on the nonlinear force-free field configuration. For the purpose of this paper, we have selected two techniques for this investigation. These two techniques are progressive extension method (PEM) (Wu et al., 1985, 1990) and iterative method (IM) (Sakurai, 1981). A brief description of these two methods is presented below:

Progressive Extension Method (PEM)

The progressive extension method is formulated as an initial-value problem (i.e., Cauchy problem) using a finite difference scheme which is similar to a Taylor expansion. A detailed description of this method is given by Wu et al. (1990). They have demonstrated the usefulness of this method, and the numerical algorithm has been verified by extrapolation of an analytical solution (Low, 1982).

Iterative Method (IM)

A number of authors (see references in Gary, 1990) have utilized an iterative method originated by Grad and Rubin (1958) to extrapolate the nonlinear force-free magnetic field from boundary data. For convenience, we simply choose the iterative method developed by Sakurai (1981) in this study. His method is based the integral equation representation of Eq. (1), and the discretization is made by the technique of finite element method. A detailed description of this technique was given by Sakurai (1981), and we shall not repeat it here.

III. NUMERICAL RESULTS

In order to make comparison between the PEM (Progressive Extension Method) of Wu et al. (1985, 1990) and the IM (Iterative Method) of Sakurai (1981), we have chosen the vectoral magnetic field observed at Okayama Astrophysical Observatory on May 26, 1985 (Sakurai and Makita, 1986) as the boundary for extrapolation using these two methods. The observed magnetic field vector is shown in Figure 1.

MC526C DATE 83/5/26 TIME(JST) 10 2 13 -11 13 5
OBSERVED FIELD VECTOR

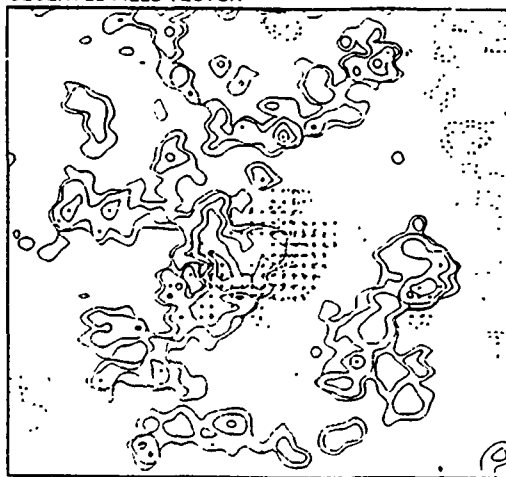


Figure 1. Magnetic field vector observed at Okayama Astrophysical Observatory on May 26, 1983. Solid and dotted contours show positive and negative longitudinal fields, respectively, with levels $\pm 10, 20, 50, 100, 200, 500$ G. Arrows indicate the transverse vector.

Mem. S.A.It., 1990

Using these observational data as a source surface, we obtained the nonlinear force-free field configuration by using the above mentioned two methods as shown in Figure 2, where Figure 2a is obtained by using the IM and Figure 2b by using PEM. In addition we have extrapolated the potential field configuration using PEM in comparison with the potential field given by Sakurai and Makita (1986), see Figure 3. From these results, observe that the deduced magnetic field configurations albeit not identical, in fact, qualitatively resemble each other to a large extent.

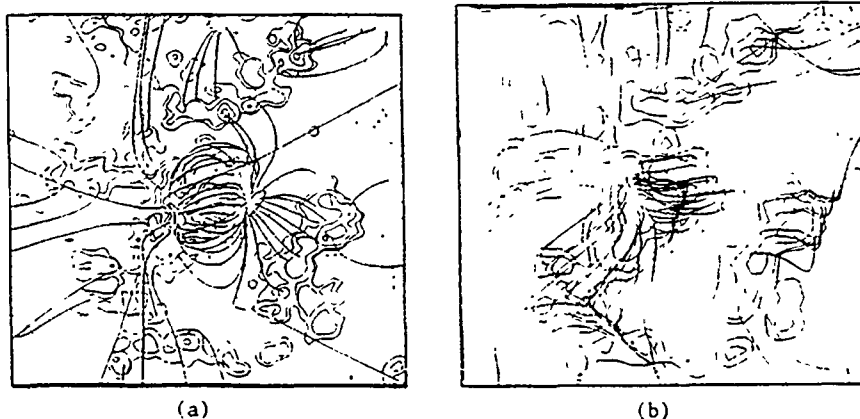


Figure 2. Nonlinear force-free field lines computed by (a) Iterative Method (IM) and (b) by Progressive Extension Method (PEM) using the data shown in Figure 1.

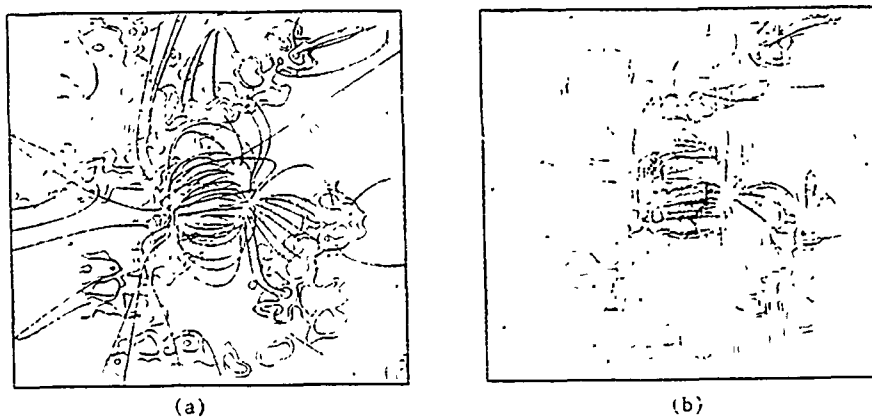


Figure 3. (a) Potential field lines computed by IM and (b) potential field lines computed by PEM using the observation given in Figure 1.

IV. DISCUSSION

Before we analyze the causes of these differences seen in the two extrapolations we review the fundamental differences between the two methods. These differences can be summarized as follows:

1. The Iterative Method (IM) specifies the value of α on a portion of the boundary plane (e.g. on a positive field region) and cannot assign the value of α on the whole boundary plane, since that would introduce an inconsistency in the extrapolation process. The values of α in the whole boundary plane are determined by the observed data for PEM. In this fashion, there is an electric current only along the particular field line in the IM extrapolation, while the electric current is distributed in the whole domain of calculation for the PEM extrapolation.
2. The IM type of extrapolation is convergent only for small values of α . Physically, this implies that the electric current in the region of interest must be small. On the other hand, the PEM type of extrapolation does not have this limitation. However, the accuracy of the computed α -value deteriorates at the points near the neutral line (i.e. $B_z \rightarrow 0$). This may cause a misrepresentation of the magnetic field configuration. The grid size of the extrapolation is controlled by the numerical stability criteria as given by Wu et al. (1990).
3. The fact that the value of α is assigned at one of the two foot points of a particular field line in the IM while the values of α are determined on the entire boundary surface in the PEM makes it difficult to match and compare the field lines for these two different methods.

On the basis of these differences of extrapolation procedures, we may understand why the magnetic field configurations obtained from the same data with these two methods are not identical. For example, Figure 2, shows some differences in magnetic field-line configurations, but the lines connecting different regions of polarities are quite similar. Note that for two regions of opposite polarities near the right center, the PEM extrapolation doesn't show any connection by field lines, while the IM type extrapolation does. However this is due simply to the fact that the field lines in this region are very low and short, and cannot be discerned in this drawing. Plots of the front view of Figure 2b, clearly indicate that the regions are connected by field lines (marked by A) as shown in Figure 4.

Mem. S.A.It., 1990

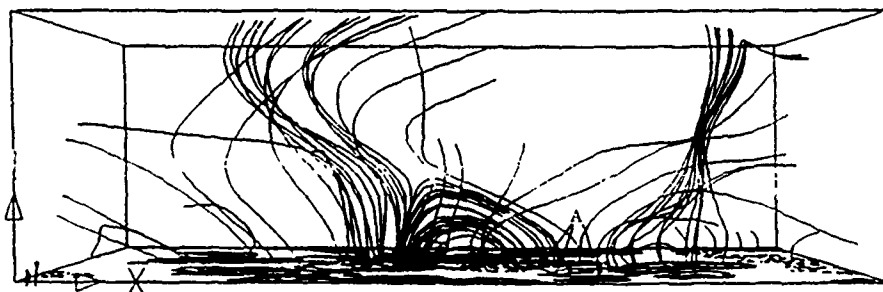


Figure 4. The front view of the nonlinear force-free field computed by PEM using the observation given in Figure 1. It should be noted that the field lines near the top are not accurate due to numerical procedure as discussed by Wu et al. (1990).

We further notice that the configuration of the field lines obtained by IM extrapolation is very similar to a potential field line configuration. This is because the IM requires that the value of α be small (i.e. slightly deviating from potential). On the other hand, the PEM extrapolation does not have this limitation. It is understood that the degree of deviation from a potential field depends on the value of α , that is the strength of the local electric current. Therefore, the configuration of magnetic field lines is affected.

In summary, we conclude:

- (i) Both methods do produce qualitatively similar results.
- (ii) The accuracy of PEM has been verified by an analytical solution (Wu et al. 1990); verification of IM is still needed.
- (iii) There are limitations on the value of α for IM, but not for PEM.
- (iv) The accuracy for PEM deteriorates when the height of extrapolation exceeds one third the horizontal length, because of the propagation of the accumulated numerical errors at each level (Wu et al. 1990).

ACKNOWLEDGEMENT

The authors wish to acknowledge Drs. E. Tandberg-Hanssen and A. Gary for reading the manuscript and giving valuable comments. The work done by S. T. Wu and M. T. Sun was supported by NASA grant NAGW-9 and AFSOR grant ASFOR-88-0013.

Mem. S.A.I., 1990

REFERENCES

- Altschuler, M. D. and Newkirk, G., Jr.: 1969, Solar Physics, 9, 131.
- Aly, J. J.: 1989, Solar Physics, 120, 19.
- Antonucci, E, Gabriel, A. H., Acton, L. W., Culhand, J. L. Doyle, J. G., Liebacher, J. W., Machado, M. E., Orwig, L. E. and Rapley, C. G.: 1982, Solar Physics, 78, 107.
- Cheng, C. C, Bruner, E. C., Tandberg-Hanssen, E., Woodgate, B. E., Shine, R. A., Kenny, P. JU., Henze, W., and Poletto, G.: 1982, Ap. J., 253, 353.
- deJager, C., Machado, M. E., Schadee, A., Strong, K. T., Svestka, Z., Woodgate, B. E. and van Tend, W.: 1983, Solar Physics, 84, 205.
- Gary, G. A.: Mem. della Soc. Astr. Italiana, this issue.
- Grad, H. and Rubin, H.: 1958, in Proc. 2nd International Conference Peaceful Uses of Atomic Energy, Vol. 13, Geneva, United Nations, p. 190.
- Low, B., C.: 1982, Solar Physics, 77, 43.
- Martin, S. F.: 1980, Solar Physics, 68, 217.
- Nakagawa, Y. and Raadu, M. A.: 1972, Solar Physics, 25, 127
- Poletto, G., Vaiana, G. S., Zombeck, M. V., Krieger, A. S. and Timothy, A. F.: 1975, Solar Physics, 44, 83.
- Sakurai, T.: 1981, Solar Physics, 69, 343.
- Sakurai, T. and Makita, M.: 1986, in Y. Osaki (ed.) Hydrodynamics and Magnetohydrodynamic Problems in the Sun and Stars, University of Tokyo, 53.
- Schmal, E., Kundu, M. R., Strong, K. T., Bentley, R. D., Smith, J. B., Jr., and Krall, K. R.: 1982, Solar Physics, 80, 233.
- Schmidt, H. U.: 1964 in W. N. Hess (ed.), Physics of Solar Flares, NASA SP-50, 107.
- Wu, S. T., Chang, H. M. and Hagyard, M. J.: 1985, NASA CP-2347, 17.
- Wu, S. T., Sun, M. T., Chang, H. M., Hagyard, M. J., and Gary, G. A.: 1990, Astrophys. J. (in press).

CONCLUDING REMARKS

Under this grant, significant contributions are made for understanding the photosphere-corona-interplanetary couplings. The highlights of these findings can be summarized into three areas as follows:

- (i) Shear induced instability as a mechanism for the occurrence of Coronal Mass Ejections (CMEs).
- (ii) A three-dimensional, time-dependent magnetohydrodynamic (MHD) model of extended corona.
- (iii) Progressive-Extension-Method for the extrapolation of non-linear force-free magnetic field.

The basis of these results have laid the groundwork for further development of the prediction science and technologies for forecasting solar flares and geomagnetic storms. For example, the shear induced instability leads to CMEs which could be tested by observations in which a critical value of "shear" could be obtained. Then, this could be used as one of the parameters for the prediction of CMEs. The current understanding is, the CME has great significant correlation with the occurrence of geomagnetic storms.

In this scenario, we would recommend the following specific subjects for further investigation:

1. Numerical Simulation of the Formation and Evolution of the Active Region.

To perform such a study, we need to employ the PEm to extrapolate the magnetic field configuration from the observations. Using this realistic magnetic field configuration as the initial condition for our three-dimensional MHD model, compute the evolution of the physical plasma parameters and fields to determine the critical values of these physical parameters for

occurrence of solar activities.

2. Numerical Accuracy Tests for MHD Models

In order to learn the reliability of these numerical simulations, these MHD models need to be tested carefully in which limitations on these models should be established.

3. Real-Time Tests

If the results in (2) are positive, we should document these models to transfer them to the proper Air Force Laboratory for real-time tests. Thus, a prediction technology could be developed for the protection of satellite systems and others.